

# The Outer Halos of Elliptical Galaxies – Implications for their Formation Histories



Rhea-Silvia Remus





# **The Outer Halos of Elliptical Galaxies – Implications for their Formation Histories**

**Dissertation**

der Fakultät für Physik der  
Ludwig–Maximilians–Universität (LMU) München

**Ph.D. Thesis**

at the  
**Ludwig–Maximilians–Universität (LMU) München**

submitted by

**Rhea-Silvia Remus**

born on April 22<sup>nd</sup> 1983 in Hamburg

Munich, May 11<sup>th</sup> 2015

1<sup>st</sup> Evaluator: Prof. Dr. Andreas Burkert

2<sup>nd</sup> Evaluator: Prof. Dr. Harald Lesch

Date of the oral exam: 13<sup>th</sup> July 2015

*Für meine Eltern, Sabina, Christoph  
und meinen Sonnenschein,*

*die hellsten Sterne am Himmel*



# Contents

<b>Zusammenfassung</b>	<b>xi</b>
<b>Abstract</b>	<b>xiii</b>
<b>1 Introduction</b>	<b>1</b>
1.1 Structure Formation in the Universe . . . . .	1
1.2 Galaxies and their Properties . . . . .	9
1.2.1 Morphology: Basic Classifications . . . . .	11
1.2.2 Environmental Dependence . . . . .	14
1.2.3 Classification II: Kinematic Properties . . . . .	17
1.3 Dynamical Processes . . . . .	20
1.3.1 Equilibrium . . . . .	20
1.3.2 Disturbing the Equilibrium: Accretion and Merging . . . . .	22
1.3.3 Relaxing the System: Phase Mixing, Violent Relaxation and Dynamical Friction . . . . .	24
1.3.4 Involving the Gas: The Impact of Dissipation . . . . .	25
1.3.5 The Galaxy Cluster Environment . . . . .	26
1.4 The Radial (Surface) Density Profiles of Galaxies . . . . .	27
1.4.1 Surface Brightness Profiles: What is Observed . . . . .	28
1.4.2 Radial Density Profiles: Deprojecting Observations . . . . .	29
1.5 Elliptical Galaxies: Scaling Relations . . . . .	35
1.5.1 Properties at Present Day . . . . .	35
1.5.2 Properties at Higher Redshifts . . . . .	37
<b>2 Numerical Simulations: From Isolated Mergers to Magneticum</b>	<b>41</b>
2.1 The Tree-SPH Code Gadget . . . . .	43
2.2 Binary Merger Simulations . . . . .	44
2.2.1 Binary Merger Simulations Used in this Work . . . . .	47
2.3 Cosmological Zoom-In Simulations . . . . .	49
2.3.1 Cosmological Zoom-In Simulations Used in this Work . . . . .	53
2.4 The Magneticum Pathfinder Simulation Set . . . . .	55
2.4.1 Galaxy Classification . . . . .	59
2.4.2 Brightest Cluster Galaxies from Box3 hr Used in this Work . . . . .	63
2.4.3 Galaxies from Box4 uhr Used in this Work . . . . .	63

<b>3</b>	<b>The Dark Halo – Spheroid Conspiracy and the Origin of Elliptical Galaxies</b>	<b>69</b>
3.1	Introduction . . . . .	69
3.2	The Dark Halo – Spheroid Conspiracy . . . . .	71
3.2.1	Density and Velocity Dispersion Slopes . . . . .	74
3.2.2	The Influence of Gas and Star Formation on the Density Slope . . . . .	78
3.2.3	Evolution of the Slopes . . . . .	82
3.3	Summary and Discussion . . . . .	85
<b>4</b>	<b>The Dark Halo – Spheroid Conspiracy: Evolution with Redshift</b>	<b>89</b>
4.1	Introduction . . . . .	89
4.2	The Mass-Size Relation . . . . .	91
4.3	Dark Matter Fractions . . . . .	94
4.4	Conspiracy Evolution with Redshift . . . . .	97
4.4.1	Slope Evolution with Redshift . . . . .	98
4.4.2	Correlating Galaxy Properties with the Total Density Slope . . . . .	100
4.5	Mocking the Slopes: “Observing” our Simulations . . . . .	102
4.6	Summary and Discussion . . . . .	107
<b>5</b>	<b>A “Universal” Density Profile for the Stellar Halos of Galaxies</b>	<b>111</b>
5.1	Introduction . . . . .	111
5.2	Fitting a Power-Law to the Outer Stellar Halo . . . . .	113
5.2.1	Milky Way Mass Galaxies . . . . .	114
5.2.2	Including other Mass Ranges . . . . .	120
5.3	A “Universal” Density Profile for the Stellar Halo of Galaxies: the Einasto Profile . . . . .	122
5.4	Summary and Discussion . . . . .	130
<b>6</b>	<b>Tracing the Outer Halo</b>	<b>133</b>
6.1	Introduction . . . . .	133
6.2	Number Statistics . . . . .	134
6.3	What do the Different Kinds of Tracers Trace? . . . . .	141
6.4	Surveying the Outer Halo: Shells, Streams and other Features . . . . .	147
6.4.1	Shells . . . . .	149
6.4.2	The $\sigma$ -Bump . . . . .	151
6.5	Summary and Discussion . . . . .	153
<b>7</b>	<b>Summary, Discussion and Conclusions</b>	<b>157</b>
<b>A</b>	<b>Additional work</b>	<b>163</b>
A.1	The Mystery of the $\sigma$ -Bump . . . . .	164
A.2	The Origin of the Cold Gas in Isolated Elliptical Galaxies . . . . .	166
A.3	The Dynamics of Spheroidal Galaxies from Cosmological Simulations . . . . .	170
A.4	Connecting Angular Momentum and Galactic Dynamics . . . . .	172
A.5	Testing Fundamental Galaxy Properties in the Magneticum Simulations . . . . .	174
A.6	A Refined Sub-Grid Model for Black Hole Accretion and AGN Feedback . . . . .	176
A.7	On the Magnetic Fields in Voids . . . . .	178
A.8	Disk Properties in the New Modified SPH . . . . .	180

---

<b>B Magneticum Box4 uhr Galaxies</b>	<b>183</b>
<b>Bibliography</b>	<b>234</b>
<b>List of Figures</b>	<b>237</b>
<b>List of Tables</b>	<b>239</b>



# Zusammenfassung

Es ist bekannt, dass die äußeren Halos der Galaxien wichtige Informationen über die Entstehungsgeschichte und die durch Verschmelzungen von Strukturen verursachten Entwicklungen der zentralen Galaxien speichern, da die Relaxationszeiten in den Außenbereichen wesentlich länger sind als im Zentralbereich. Daher bleibt die Erinnerung an diese Ereignisse dort wesentlich länger erhalten. Die Verschmelzungsgeschichte gibt Einsicht in die fundamentalen Prozesse, die zum Wachstum der Galaxien und zur Veränderung ihrer Morphologien beitragen. Die Entschlüsselung dieser Information wird massiv dazu beitragen, unser Verständnis der verschiedenen Mechanismen der Strukturentwicklung zu erweitern. Des Weiteren gewinnt in diesem Bereich der Galaxien die Dunkle Materie im Vergleich zu den Sternen an Dominanz, wodurch diese Region perfekt geeignet ist, um das Zusammenspiel der Sterne mit der Dunklen Materie zu untersuchen. Diese dynamische Interaktion der kollisionsfreien Komponenten der Galaxien kann das Erscheinungsbild einer Galaxie signifikant prägen, wenn auch über deutlich längere Zeiträume hinweg als gasbedingte Prozesse. Ein besseres Verständnis dieser dynamischen Prozesse kann maßgeblich dazu beitragen, Licht in die dunklen Bereiche der Galaxien und ihrer Entstehung zu bringen.

In dieser Dissertation nutzen wir die kombinierte Stärke idealisierter, hochaufgelöster Simulationen individueller Galaxien und großer kosmologischer Simulationen, um einige der Informationen zu entschlüsseln, die in den äußeren Halos der Galaxien verborgen sind. Mittels der hochaufgelösten Simulationen kann der Einfluss einzelner physikalischer Prozesse auf die dynamischen Strukturen der Galaxien im Detail untersucht werden, während die großen kosmologischen Simulationen ein statisch relevantes Sample an Galaxien verschiedenster Massen in unterschiedlichen Umgebungen bereitstellen.

Der Fokus des ersten Teils der Dissertation liegt auf der Untersuchung des Zusammenspiels von Dunkler Materie und stellarer Komponente im Falle sphärischer Galaxien wie beispielsweise Ellipsen. Wir zeigen, dass diese Interaktion mittels des gemeinsamen Potentials stattfindet und die Komponenten sich so anordnen, dass ihr Gesamtprofil isotherm ist und die Gesamtdichteverteilung einem Potenzprofil der Form  $\rho \propto r^{-2}$  entspricht. Dieser Zustand, wenn er erreicht ist, erweist sich als ausgesprochen stabil. Das Gas, das auf deutlich kürzeren Zeitskalen interagiert und seine Energien mittels Dissipation umverteilen kann, stört diesen Prozess und verursacht eine deutliche Komprimierung der Gesamtdichteverteilung, die dadurch eher einem Potenzprofil der Form  $\rho \propto r^{-3}$  entspricht. Solange das Gas innerhalb der Galaxie Sterne bilden kann, wird der dynamische Gleichgewichtszustand zwischen den stoßfreien Komponenten nicht erreicht, jedoch sorgt jedes gasarme Akkretionsereignis für einen Schub in diese Richtung. Dies wird auch durch die Tatsache verdeutlicht, dass dynamisch weiter entwickelte Systeme einen größeren Anteil an Dunkler Materie im Zentrum besitzen und der Anteil der Sterne, die innerhalb der Galaxie selbst geboren wurden, kleiner ist. Generell sehen wir, dass die Gesamtdichteverteilung der sphärischen Galaxien bei höheren Rotverschiebungen komprimierter ist.

Zusammenfassend schlußfolgern wir, dass der Gleichgewichtszustand, den kollisionsfreie Systeme anstreben, einen hervorragenden Testfall bietet, um einen Eckpfeiler der modernen Kosmologie – die Existenz Dunkler Materie – zu überprüfen, da nur in einem solchen Falle die Dunkle Materie und die Sterne auf eine Art miteinander interagieren, dass sich ein Dichteprofil obengenannter Form ausbildet.

Im zweiten Teil dieser Dissertation analysieren wir Informationen, die in den stellaren Halos der Galaxien verschlüsselt sind. Wir zeigen, dass das Dichteprofil aller stellarer Halos von ähnlicher Form ist und sich durch ein gekrümmtes Exponentialgesetz beschreiben lässt. Diese universelle Form ist dabei unabhängig von der Morphologie der Galaxie im Zentrum. Der Krümmungsgrad kann als Indiz dafür gewertet werden, wie viele (kleinere) Strukturen die Galaxie bereits verschlungen hat, da der stellare Halo im Wesentlichen durch Akkretion kleinerer Strukturen wächst. Dies liegt darin begründet, dass die Gasdichte in den äußeren Bereichen der Galaxien dauerhaft zu niedrig ist, um einen signifikanten Anteil an Sternen zu erzeugen. Mittels eines derartigen universalen Dichteprofiles ist es nunmehr möglich, die Abweichungen von diesem Profil zu bestimmen und daraus Details der Akkretionsgeschichte individueller Galaxien zu rekonstruieren, da die unterschiedlichen Akkretionsprozesse (wie zum Beispiel der Einfall kleiner oder großer (Zwerg-)Galaxien oder das Akkretieren einzelner Sterne von vorbeifliegenden Strukturen) unterschiedliche Signaturen im Halo hinterlassen. Daher schlagen wir vor, dem detaillierten Verständnis der Signaturen der einzelnen Akkretionsprozesse in der Zukunft eine größere Bedeutung zukommen zu lassen, um die ergiebigen Informationen, die in den stellaren Halos enthalten sind, auswerten zu können, wodurch ein deutlicher Fortschritt im Verständnis sowohl der akkretionsgetriebenen als auch der sekularen Entwicklung von Galaxien erreicht würde.

# Abstract

The outer halos of galaxies are known to store vital information about the formation history and merger-induced evolution of their central galaxies, since the relaxation timescales are much larger than in the innermost parts and thus the memory of the events is conserved over a long period. This information provides fundamental insights into the processes of mass growth and morphological changes, broadening our understanding of the different mechanisms of structure formation. Additionally, the radius regime where the stellar component starts to dominate over the dark matter component is the perfect place to study the interplay between dark matter and stars. This interaction between the collisionless components of a galaxy, although much slower than the gas-induced processes, significantly alters the appearance of a galaxy in the long term. A better understanding of those processes can help to shed light on the dark sides of the galaxies.

In this work, we use the combined strength of idealized high-resolution simulations of individual galaxies and large cosmological simulations to unveil some of the information encoded in the outer halos of galaxies. The high resolution simulations allow us to disentangle the impact of selected physics on the formation and evolution of galaxies in particular, while the large cosmological simulations provide a statistically meaningful sample of galaxies covering a large range in masses and environments. The first part of this thesis focuses on the interplay between dark matter and stars, revealing that both parts actually do interact through their common potential by re-ordering into a stable state where the total halo is isothermal and its density distribution follows a  $\rho \propto r^{-2}$  profile. The gas, which dissipates energy and sinks towards the center on much shorter timescales, disturbs this process, forcing the total halo into a more compact state with approximately  $\rho \propto r^{-3}$ . Therefore, as long as gas is present, the collisionless attractor state can not be reached, but every dry merger evolves the system towards it. This is also apparent by the fact that more evolved halos have higher central dark matter fractions and smaller amounts of stars formed in situ, and that the slopes are generally steeper at high redshifts. We conclude that the equilibrium attractor state of dry merging systems provides a new test case for  $\Lambda$ CDM and prove that, if  $\Lambda$ CDM is correct, the dark matter and the stars do communicate through their common gravitational potential.

The second part of this thesis deals with the information provided by the stellar halo. We show that the radial density profiles of all stellar halos have a universal shape which can be described by a curved exponential, independent of the morphology of their central galaxy. The strength of the curvature appears to be an indication for the amount of merging a galaxy suffered, since the stellar halo mostly grows through merging as the cold gas density in the halo region is much too low to cause a significant amount of star formation at all redshifts. With such a universal shape at hand, it is possible to study the deviations from this shape to learn about the details of the stellar accretion history of a galaxy, since different types of events leave distinct signatures. We suggest that more emphasis on the understanding of those different signatures is needed in the future to fully exploit the rich information contained in the outer halos, to learn more about the accretion driven but also the secular evolution of galaxies.



# Chapter 1

## Introduction

In 1924, Edwin Hubble showed that many of the faint “nebulae” observed all over the sky were actually not part of the Milky Way stellar system, but stellar systems of their own, similar to our own galaxy, albeit much farther away (Hubble, 1925)<sup>1</sup>. Only five years later, in 1929, he found that the relative velocities of those galaxies are higher the larger their distance to the Milky Way (Hubble, 1929). With this breakthrough he had discovered that the universe in which we are living is not static, but expanding. This realization significantly altered mankind’s view of the universe we are living in, and brought new exciting questions into the focus of the everlasting search for knowledge, which has always been a major mainspring in the advancement of humanity. The most fundamental questions regarding the newly explorable Universe were the issue of the origin of those objects discovered all over the (nearby) Universe, the search for the mechanisms that cause the structure formation and the nature of those stellar islands, which strongly vary in shape and mass. In this chapter we will provide an overview of our current knowledge regarding these topics, and thus set the groundwork for the questions addressed in this thesis.

### 1.1 Structure Formation in the Universe

In 1964, Penzias and Wilson detected a temperature excess of 3.5 K at a wavelength of  $\lambda = 7.35$  cm, merely by accident, using a horn-reflector antenna to measure radio waves (Penzias & Wilson, 1965). They found this signal to be spread isotropic over the whole sky, independent of daytime or seasons. Thus it could not originate from any known source inside the solar system or our galaxy. An explanation was introduced by Dicke et al. (1965), who suggested that this signal might actually be a remnant of an early stage of the Universe, when it was much denser and hotter than at present day, and dominated by radiation, as already proposed by Gamow (1946, 1948).

To date, research has unveiled the following picture about the earliest epochs of the Universe: At the very beginning, all matter in the Universe was compressed in a tiny space, and the temperature was extremely high. In this early phase, the Universe was dominated by radiation, and all matter in the Universe was in a plasma state, with the particles much too energetic for the strong and electroweak

---

<sup>1</sup> It had been speculated before by Thomas Wright (1750, reprint from 2014) that the faint nebulae could be made from many distant stars, as well as by Immanuel Kant in 1755, who did not know how right he was when he suggested that some of the observed nebulae are actually distant “island universes” similar to our own galaxy, the Milky Way. Kant even explained the different elliptical shapes to simply be a projection effect, from face-on to edge-on, which is pretty close to the true nature of observations of spiral galaxies (Kant, 1755, reprint, pp. 39).

forces to bind them together and build up nuclei or even atoms. The photons were bouncing between the particles in this plasma, and as such the Universe was an opaque uniform mass. However, our Universe is expanding, and thus it effectively cools down while its average density decreases. At a certain point the Universe became cold enough for quarks and gluons to form neutrons and protons, but not yet cold enough for the electrons to be captured by the nuclei to form atoms. This required the temperature to decrease even more. At a temperature of about 3000 K, the motion of particles had slowed down enough for the electromagnetic force to be strong enough to bind the electrons to the nuclei, and the nuclei and electrons combined to form atoms. This happened about 380000 years after the Universe was born, and we nowadays call this epoch the time of recombination. At that point, the baryonic matter in the Universe decoupled from the radiation, and the Universe became transparent. As a result, the photons were not absorbed or scattered anymore but could travel freely, still retaining in their energy distribution the memory of the temperature of the Universe in the moment of recombination.

In a continuously expanding universe, electromagnetic waves are stretched according to the scale factor  $a(t)$  of the universe, which describes the relative distances between distant points in space as a function of time (where today corresponds to  $a(t_0) = 1$  and  $a(0) = 0$  to the beginning of the Universe). The wavelength  $\lambda_{\text{em}}$  of a photon emitted at a time  $t_{\text{em}}$  is therefore observed at present day with a wavelength  $\lambda_{\text{obs}} = \lambda_{\text{em}}/a(t_{\text{em}})$ . Since  $a(t < t_0) < 1$ , the observed wavelength  $\lambda_{\text{obs}}$  is larger than the one at emission,  $\lambda_{\text{em}}$ , which in visual light corresponds to a relative shift of the photons wavelength from blue to red. This gives rise to the term “redshift”, defined as

$$z = \frac{\lambda_{\text{obs}} - \lambda_{\text{em}}}{\lambda_{\text{em}}} = \frac{1}{a(t_{\text{em}})} - 1. \quad (1.1)$$

In an expanding universe with a monotonic expansion law  $a(t)$ , every redshift value  $z$  thus corresponds to a unique time  $t$  in the past.

The photons that were released at the time of recombination (i.e., shortly after the Universe was born) became red-shifted until today as a result of the expansion of the Universe, while their energy distribution kept its characteristic shape, and now corresponds to a temperature of about 3 K. This is the signal found by Penzias and Wilson, a remnant of the radiation emitted in a very early phase of the Universe, now called the cosmic microwave background (CMB). With their discovery, Penzias and Wilson found the earliest image of the Universe that can be detected, and this recognition opened the door for a new approach to understand the cosmology of our Universe.

The fact that the energy distribution of the CMB is the nearest to a perfect blackbody distribution that has yet been observed indicates that before the time of recombination matter and radiation were in thermal equilibrium in those early phases of the Universe. Since the CMB photons encode the physical conditions in the Universe at the time of recombination, they might also remember possible anisotropies. The fact that Penzias and Wilson found the radiation from the CMB to be isotropic on large scales already suggested that any existing fluctuations at the time of recombination were not large; however, their detection methods were not accurate enough to detect small-scale deviations. Therefore, a series of new instruments was built to enable all-sky surveys of the CMB to detect small fluctuations in the temperatures and polarisations, if those existed. There were several attempts to measure the CMB using ground-based and airborne observatories, but the real breakthrough came with space-based probes. The first of those satellites was COBE, launched in 1989, followed by WMAP (launched in 2001) and recently Planck, which was launched in 2009. These missions, ground based, airborne, and space-based, confirmed the CMB to be isotropic on large scales and from its black body

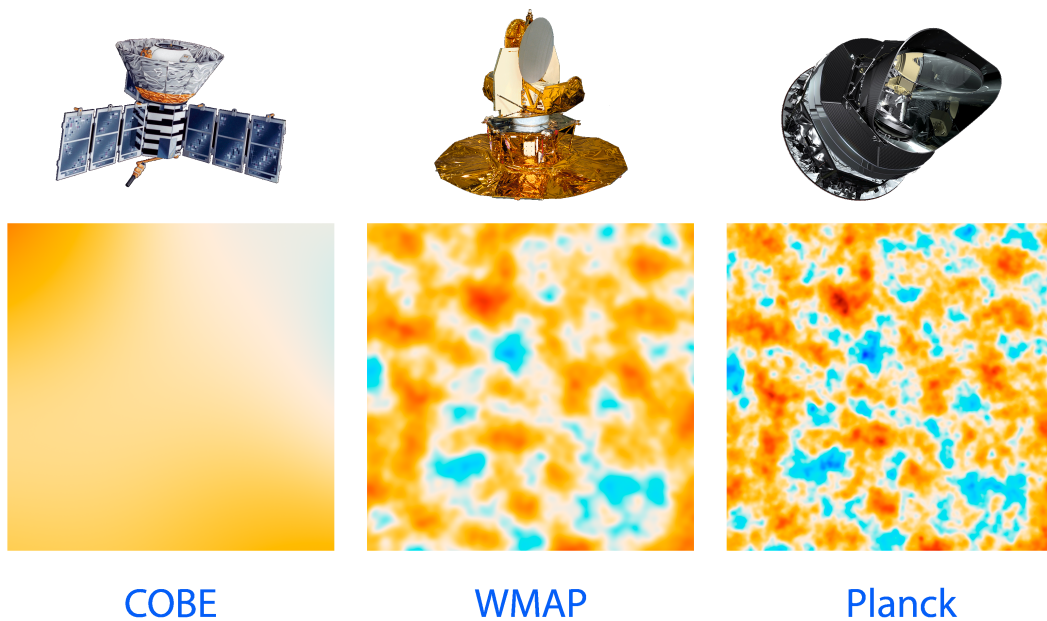


**Figure 1.1:** Schematic overview of the resolutions of the CMB maps provided by the COBE, WMAP, and Planck missions. The images of the CMB are taken from the actual observations. Image credit: NASA/JPL-Caltech/ESA.

radiation spectrum to have a present-day temperature of 2.7 K. The satellite missions proved that the CMB has small scale distortions in the temperature distribution, on the order of  $13.4 \mu\text{K}$  (from COBE, Smoot et al., 1992), effectively limiting the scales of the initial density fluctuations in our Universe. A comparison between the resolutions of those three probes is shown in Fig. 1.1.

From those fluctuations, it is possible to put constraints on the underlying cosmology of the Universe. To understand this, we first have to take a look at the theoretical approach to cosmology: Many theories about the basic properties of space and time have been discussed in the literature since Albert Einstein in 1915 published his work presenting General Relativity (Einstein, 1915). Most of the early models tried to solve the field equations for a static universe, where the visible matter was the only matter component and all parts of the universe have essentially existed forever in their present-day form. Einstein himself favored a model where the universe was spherical, but to keep it static he had to introduce a new form of “anti-gravity”, the cosmological constant  $\Lambda$  (Einstein, 1917). Another well-known model was the de Sitter-model, where the universe basically has no mass but a positive cosmological constant. This universe could have positive, negative or flat curvature (de Sitter, 1916a,b, 1917).

However, many of the discussed models, including those two mentioned above, were essentially special cases of the model introduced by Alexander Friedmann (1922). His comparatively simple solution of the equations of general relativity follows from the assumptions of an isotropic and homogeneous universe, and describes a non-static universe, which is expanding (and subsequently contracting in case of a closed universe). In his work from 1922, Friedmann discussed only the model for a closed universe, but in its generalized form it can also be flat or open (for more details see Remus 2009; Mo

et al. 2010, pp. 112ff; and Longair 2008). From the Friedmann equations we can derive the evolution of the scale factor of the universe as

$$\frac{\dot{a}(t)^2}{a(t)^2} = H_0^2 \left( \frac{\Omega_m}{a(t)^3} + \Omega_\Lambda + \frac{\Omega_r}{a(t)^4} + \frac{\Omega_k}{a(t)^2} \right), \quad (1.2)$$

where

$$H_0 = \frac{\dot{a}(t_0)}{a(t_0)} \quad (1.3)$$

is the present-day ( $a(t_0) \equiv 1$ ) expansion rate, also known as the ‘‘Hubble constant’’ as a reference to Edwin Hubble’s discovery that the Universe is expanding, often represented as

$$H_0 = h \, 100 \frac{\text{km}}{\text{s Mpc}}. \quad (1.4)$$

The  $\Omega$  parameters are normalized to the critical density of the universe

$$\rho_{\text{crit}} \equiv \frac{3H_0^2}{8\pi G}, \quad (1.5)$$

and represent the densities of the different constituents:

**Matter:**  $\Omega_m$  describes the matter content (ordinary baryonic as well as dark matter), which is non-relativistic and pressure-less on cosmological scales:  $\Omega_m = \Omega_b + \Omega_{\text{DM}}$ .

**Radiation:**  $\Omega_r$  describes relativistic particles such as photons. This component was dominant in the very early phases of the universe, but plays no significant role at later times, after recombination.

**Dark Energy:**  $\Omega_\Lambda$  describes an energy density that does not dilute with the scale factor, and can be interpreted as vacuum energy or the cosmological constant. Depending on the values of the other parameters, it may lead to accelerated expansion of the universe starting at a certain point in time, and will then eventually become the dominant component.

**Curvature:**  $\Omega_k = 1 - \Omega_0$ , where  $\Omega_0 = \Omega_m + \Omega_r + \Omega_\Lambda$ , describes the geometry of the universe. If  $\Omega_k = 0$ , the universe is flat. If  $\Omega_k > 0$ , the curvature is positive, which in an isotropic and homogeneous universe corresponds to a spherical geometry. If  $\Omega_k < 0$ , the curvature is negative, and in the isotropic case this implies a hyperbolic geometry.

A universe where dark energy and cold dark matter are present is commonly called a  $\Lambda$ CDM universe. Here, ‘‘cold’’ means that the particles of the (as yet hypothetical) dark matter decoupled after they had become non-relativistic, move at velocities significantly slower than the speed of light, and are of comparatively high mass<sup>2</sup>.

Since the observed CMB is a picture of the state of the Universe at the time of recombination, it can provide information to validate the basic assumptions of the Friedman model and constrain

---

<sup>2</sup> In comparison to ‘‘hot’’ dark matter, where the particles have velocities close to the speed of light and are very light. As a possible candidate for such hot dark matter, neutrinos were discussed. A third form of dark matter which has been in the focus of several recent studies is ‘‘warm’’ dark matter, which basically means that the dark matter particles carry a small initial thermal velocity.

the underlying cosmological parameters to set limits on the amount of the different components: As already seen from the earliest observations, the Universe is isotropic on large scales, and only on small scales distortions can be detected. This has been confirmed by all three space-borne probes measuring the CMB, independent of their spatial resolution. This supports the first of the two basic assumptions of the Friedmann model, and under the assumption that the Milky Way is not a special point in the Universe<sup>3</sup>, Friedmann's second assumption is also valid.

The information about the cosmological parameters is encoded in the temperature variations in the CMB. These anisotropies originate from small density fluctuations present at the time of recombination. Since the baryonic matter was in a plasma state before recombination, it behaved like a fluid: Whenever a local under-density appears, the matter streams into the free space, in this process causing a new relative under-density in its previous position. This under-density in turn causes matter to stream back. With time, this process should effectively have smeared out all density variations. In a universe that contains (cold) dark matter, however, this will not happen: The dark matter has decoupled earlier than the baryons, and due to small initial quantum density fluctuations which get stretched during the initial exponential expansion phase of the universe, they build up tiny over-densities, effectively causing shallow potential wells. In the presence of those wells, the baryons cannot smear out the over-densities anymore since their influence on the dark matter is small. They stream into the wells and compress, until the radiation pressure gets strong enough to counteract the gravitational forces, pushing the baryons back from the well. Those baryons that are at the bottom of a well oscillate less strongly than the baryons that are at the under-dense regions, where the gravitational forces are small. At the time of recombination, those oscillations which are currently in the bottom of the wells or the top of the hills show up as slightly hotter or colder parts in the CMB.

Thus, from those small fluctuations a temperature power spectrum of the CMB can be calculated, as shown in Fig. 1.2 from the Planck mission data (Planck Collaboration et al., 2015). Oscillations which only had enough time before recombination for half an oscillation build up the first big peak, those which had time for a full oscillation show up as the second peak, and so on. From the heights and positions of those peaks, the cosmological parameters can be constrained. Tab. 1.1 provides an overview of the results from the three different space-borne probes (the results from WMAP-3 and WMAP-7 are used for the cosmological parameters in the different simulations studied throughout this thesis).

The parameter that is most difficult to constrain from the CMB is the dark energy parameter  $\Omega_\Lambda$ . However, Perlmutter et al. (1998) and Riess et al. (1998) found strong indications that the expansion of the Universe is actually accelerating and not slowing down, corresponding to a parameter  $\Omega_\Lambda > 0$  and thus confirming the existence of such a dark energy component that counteracts the gravitational forces. They used type Ia supernovae (SN Ia) as standard candles and compared their measured brightnesses at different redshifts. In type Ia supernovae, a well-defined relationship exists between the luminosity at maximum and the width of the lightcurve. Thus, by measuring how fast the brightness falls off with time it is possible to determine the absolute luminosity, and comparing this with the measured brightness then yields the distance to the supernova. The surprising result was that the observed supernovae were fainter for a given redshift than would be expected for a universe expanding with a constant rate (or a universe with a decelerating expansion). With the independent measurements of both the CMB and the SN surveys,  $\Omega_\Lambda$  can be constrained much better, which has already been

<sup>3</sup> This is also called the Cosmological Principle, which basically means that the Universe is homogeneous, i.e., it looks on average the same for any given observer anywhere in the Universe. As a Principle, it was introduced by E. Milne (Milne, 1933a,b), but it is similar to Copernicus' idea of a non-centered Earth.

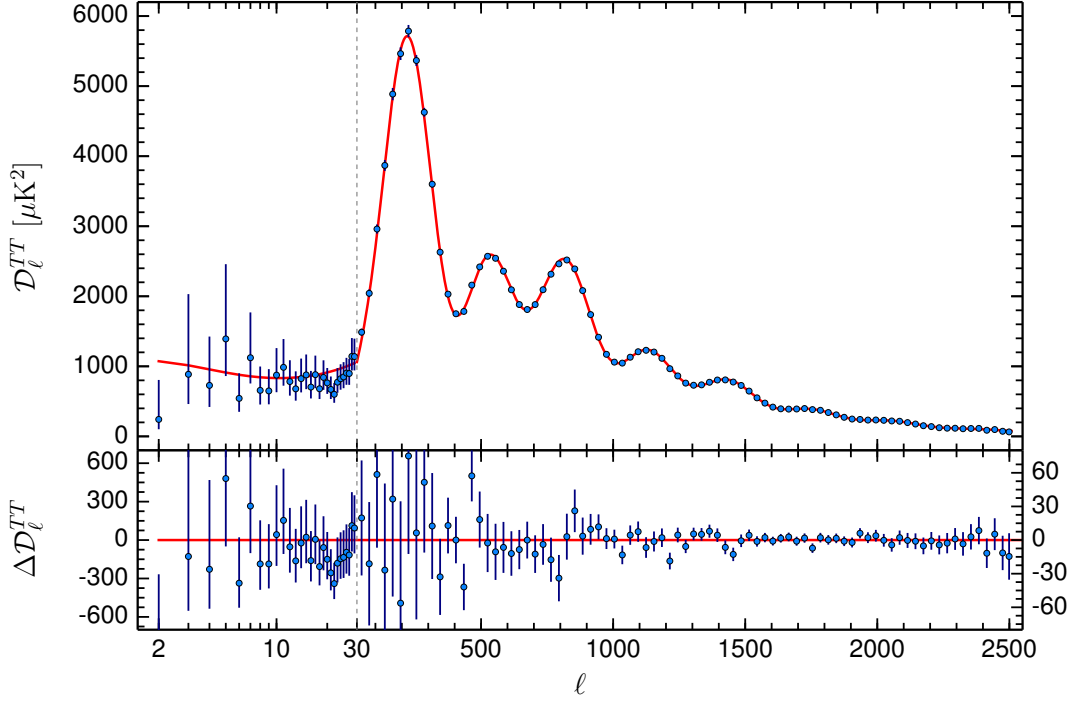


**Figure 1.2:** Fig. 1 taken from Planck Collaboration et al. (2015): **Upper panel:** Temperature power spectrum from the Planck data (blue filled circles) with the best fitting  $\Lambda$ CDM model shown as red line. **Lower panel:** Residuals from the best fitting  $\Lambda$ CDM model, with error bars showing the  $1\sigma$  uncertainties.

**Table 1.1:** Cosmological parameters from COBE, WMAP3, WMAP7, and Planck

	COBE <sup>(a)</sup>	WMAP <sup>(b)</sup>	WMAP-3 <sup>(c)</sup>	WMAP-7 <sup>(d)</sup>	Planck <sup>(e)</sup>
$\Omega_\Lambda$	0.80	$0.73 \pm 0.04$	$0.716 \pm 0.055$	$0.727 \pm 0.03$	$0.685 \pm 0.013$
$\Omega_m$	0.20	$0.27 \pm 0.04$	$0.237 \pm 0.034$	$0.2713 \pm 0.029$	$0.315 \pm 0.013$
$\Omega_b$	0.02	$0.044 \pm 0.004$	$0.041 \pm 0.001$	$0.0455 \pm 0.0028$	$0.0490 \pm 0.0005$
$h$	1	$0.71 \pm 0.23$	$0.735 \pm 0.032$	$0.704 \pm 0.025$	$0.6731 \pm 0.0096$
$f_{\text{bar}}$	0.1	$0.17 \pm 0.03$	0.173	0.167	0.156
$t_{\text{universe}}$	—	$13.7 \pm 0.2$ Gyr	—	$13.77 \pm 0.13$ Gyr	$13.813 \pm 0.038$ Gyr

<sup>a</sup> for vacuum dominated CDM from Wright et al. (1992). However, they also show that COBE data is likewise consistent with other CDM models without vacuum energy as well as hot dark matter models.;

<sup>b</sup> Bennett et al. (2003);

<sup>c</sup> Spergel et al. (2007);

<sup>d</sup> Komatsu et al. (2011);

<sup>e</sup> Planck Collaboration et al. (2015);

included in the data shown for Planck and some of the WMAP releases shown in Table 1.1. As can be seen from the results of all surveys, a  $\Lambda$ CDM universe is in good agreement with the measured values for the cosmological parameters, which thus justifies using this cosmology as background for studies of the Universe, even if the parameters measured from the probes differ slightly.

In a  $\Lambda$ CDM universe, structures grow hierarchically through merging of small structures, building up the larger structures. At the very early phases, the tiny density perturbations collapse into larger dark matter structures, gaining angular momentum through tidal torques during those merging events (Peebles, 1969; Danovich et al., 2015). The gas accumulates in those dark matter halos, it cools, redistributes angular momentum, and condenses at the centers of those halos. Up to this moment, the Universe is dark, since no stars have formed yet. Thus, this period in the lifetime of the Universe is still poorly understood due to its lack of information in the form of observable photons. The primordial gas in the centers of those halos at some point formed the first stars (so-called Population III stars), however, the exact formation processes are still unknown. Since there are no metals yet to help cooling the gas, leading to fragmentation, it has been speculated that those first stars must have been very massive. Their lifetimes therefore must have been relatively short, and at the end of their lives a significant part of their mass collapsed into a small space, forming the first black holes (BHs). Those BHs are thought to be the seeds of the supermassive black holes which can be found in the centers of many, if not all, massive galaxies at present day (e.g., Kormendy & Richstone, 1995; Scott et al., 2013). The first stars also lead to the first enrichment of the surrounding gas with metals heavier than Lithium, which enable a more efficient cooling including fragmentations of the molecular clouds, which permits the formation of less massive stars. This second generation of stars, Population II, can still be observed today in the very low-mass stellar populations.

Through continuous infall of small structures and smooth accretion from streams, larger structures form, continuously supplied with new gas, supporting star formation. The more gas is accreted onto a galaxy, the more efficiently stars are formed. Those stars that have been formed within the centers of the dark matter halos by the galaxy itself are called in-situ stars. At about a redshift of  $z = 2$  the star formation efficiency reaches a maximum, and huge amounts of gas are transformed into stars, as shown in Fig. 1.3. Many galaxies at  $z = 2$  are still very gas rich, but the first gas-poor, stellar dominated systems are found as well (van Dokkum et al., 2009; van de Sande et al., 2013; Barro et al., 2013; Marsan et al., 2015). Now, a complex interplay of gas accretion along cold streams (Dekel & Birnboim, 2006; Dekel et al., 2009) versus gas depletion due to star formation dominates the galaxies (e.g. Bouché et al., 2010). However, as the galaxies become even more massive, the feedback from the stellar winds, growing black holes, and dying stars feeds a hot gaseous halo around those central galaxies, which, at some point, (nearly) cuts the gas inflow from the cold streams towards the galactic centers. This happens between  $z = 2$  and  $z = 1$  for most of the massive systems, and with the decreasing amount of available gas, the major driver of structure growth becomes the merging of structures, and most new stars in a galaxy are accreted instead of formed in situ. These stars are called ex-situ stars, as they were born in another galaxy and only later added to the content of their present-day host galaxy. This picture of galaxy growth, which, in its early phase is dominated by accretion of gas along filaments or through mergers with other gas-rich objects and in its later phase by the (nearly gas-less) merging of systems, is called the two-phase scenario of galaxy growth (Zhao et al., 2003; Oser et al., 2010, 2012).

Surveys of large areas of the sky have enabled a detailed mapping of the visible structures within a significant part of the Universe: up to redshifts of  $z \approx 0.25$  for the SDSS survey (York et al., 2000; Eisenstein et al., 2011), which so far is the largest of such surveys containing about 300000 galaxies,

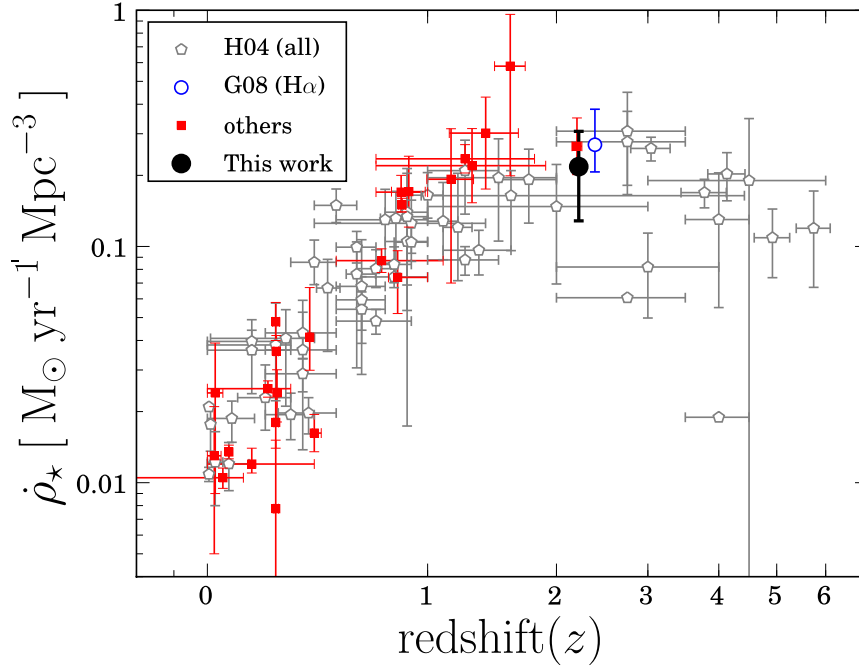


**Figure 1.3:** *Fig. 3 from Hayes et al. (2010). Cosmic star formation rate density at different redshifts, determined by several different surveys and different wavebands (see references within Hayes et al. (2010)). At a redshift of about  $z = 2$ , the cosmic star formation rate density has a maximum.*

including a red-galaxy sample up to  $z = 0.7$  and a quasar survey up to  $z = 5$ ; up to  $z \approx 0.3$  for the 2dF survey (Colless et al., 2001) including  $\approx 250000$  galaxies; up to  $z \approx 0.6$  for the CNOC2 survey including 5000 galaxies (Yee et al., 2000; Carlberg et al., 2000). Fig. 1.4 shows the distribution of galaxies as seen in the SDSS survey. The filamentary structure of our Universe is clearly visible, supporting the idea of hierarchical growth of structures in the Universe from small isolated galaxies to conglomerations of several galaxies called “galaxy groups”, up to thousands of galaxies within one massive dark matter halo, called “galaxy clusters”. Even those galaxy clusters and groups can cluster by themselves, building up super clusters. Merging of structures as well as smooth accretion are currently thought to occur along those filaments, and this view is supported by simulations of large cosmological volumes, which also show such filamentary structures. Simulations of this kind started with dark-matter-only volumes like the Millenium simulation (Springel et al., 2005c), and were extended to fully baryonic simulations of large volumes, with the largest of those fully baryonic simulations currently available being one of the boxes from the Magneticum Pathfinder simulation set (Hirschmann et al., 2014; Remus et al., 2015a; Teklu, Remus, et al., 2015a), which is part of the study presented in this thesis. For more details on those cosmological simulations, especially on the Magneticum simulation set, see Sec. 2.4.

To date,  $\Lambda$ CDM has successfully passed observational verification. Currently, assuming the Universe to be a dark-energy containing, acceleratedly expanding, cold dark matter universe is a solid working hypothesis, since deviations from this model (e.g. slightly warm dark matter, slight curvature) that would be compatible with observations would only slightly change the basic mechanisms of structure formation and evolution.

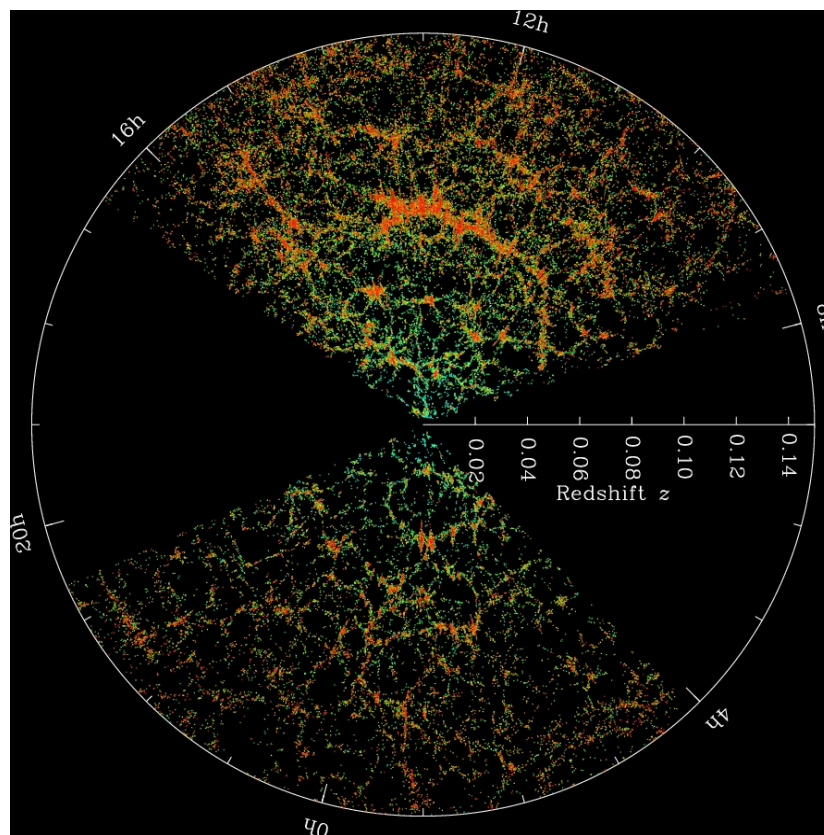


**Figure 1.4:** The cosmic web as seen from the galaxy distribution determined from the SDSS, out to a redshift of  $z = 0.14$ , in both directions perpendicular to the galactic disk of the Milky Way. Each point shows a galaxy, with the color according to the density of the galaxies environment. The most clustered regions are shown in red, with the most clearly visible clustering in the upper part of the wedge being the so-called Sloan Great Wall clustering of galaxies. Image credit: Sloan Digital Sky Survey ([www.sdss.org](http://www.sdss.org)).

## 1.2 Galaxies and their Properties

Classically, the term “galaxy”<sup>4</sup> was used only for the visible, baryonic islands which, as Hubble had shown in 1924, were not part of our own galaxy, the Milky Way. These galaxies clearly show different morphologies, of which two different kinds of structures are immediately distinguishable: elliptically

<sup>4</sup> From Greek *γαλαξίας* (*κύκλος*), milky circle (*γάλα*: milk). In Greek mythology, the origin of the stellar band at the sky which we know today to be the projection of the disk of our own stellar system, was explained as follows: Zeus, the father of all gods, had betrayed his wife, the goddess Hera, with a mortal. He still wanted the son he gained from this affair, Hercules, to have immortal strength, which could be only achieved by suckling milk from Heras breasts. Zeus sneaked Hercules to Heras breast while she was asleep, however, the little fellow, hero as he was, sucked a bit too strong and Hera awakened, pushing the stranger boy aside, thereby spreading her milk all over the sky (see Pseudo-Eratosthenes, *Katasterismoi*, 44 and Hygin, *Poetic Astronomicon*, 2.43). While the aition (myth of origin) today is known to be untrue, the name still remains, even if we now do not call it a milky circle but merely a milky way (which was already changed by the Romans, as shown in *Metamorphoseon, liber primus, verse 168 & 169* by Ovid (von Albrecht, 1994)). In most European languages, we still use the translated name for our own galaxy, the Milky Way, while the Greek name “galaxy” is applied generally to all stellar islands in the Universe.

shaped stellar systems without clearly visible dust or gas structures, and the more diverse family of flattened, disk like galaxies which clearly exhibit bright (young) stars and dust and gas lanes, alongside with spiral structures similar to the appearance of our own galaxy.

However, with detailed measurements of the radial line-of-sight velocity profiles of nearby disk galaxies (e.g., Oort, 1940; Rubin et al., 1965; Rubin & Ford, 1970; Rubin et al., 1978), it became successively evident that there had to be a non-visible component surrounding the bright parts of the galaxies (Rubin et al., 1980): Since the velocity profiles did not decrease with radius as expected for systems which strongly decrease in mass density with increasing radius, there had to be additional matter around those galaxies which could not be detected with the available telescopes. This non-visible component, which had to be much more massive than the visible part of the galaxy, was called “dark matter” due to its lack of light emission (see for example Zwicky 1937 or Spitzer 1942 referring to the results presented by Oort 1940). That component is even more dominant in clusters of galaxies, and it was already shown by Zwicky (1937) using the motions of galaxies in the Coma cluster, that there had to be a huge amount of this non-visible dark matter. This became even more evident in weak lensing observations of merging galaxy clusters like the Bullet cluster (Clowe et al., 2006), where most of the baryonic matter in form of the hot gas is in the center between both merging clusters, while the majority of the matter measured through weak lensing is clearly outside this central region closely correlated with the visible galaxies. This is due to the fact that, while the baryonic gas component is not collisionless and thus collides and accumulates at the center between both merging galaxy clusters after the first passage, the collisionless matter like dark matter and stars pass through each other and will only eventually merge after additional passages.

The puzzling discovery of this matter which could only be detected due to its gravitational impact on galaxies and clusters led to many heated debates on its nature, ranging from normal but low-luminous matter in form of MACHOs (Massive Astrophysical Compact Halo Objects, which are objects made of “normal” baryonic matter which do not emit radiation, like starless planets, lonely black holes, neutron stars, brown dwarfs, and others), to special particles called WIMPs (Weakly Interacting Massive Particles, massive particles that only interact with normal matter through the weak force). Tentative explanations also include the MOND theories (MODified Newtonian Dynamics), which postulate that gravity acts differently on large scales than on small scales, see (Milgrom, 1983a,b,c) and do not require actual dark matter.

There is still an ongoing debate whether a dark matter component does exist or not, however, while the MOND theories can predict some of the observed properties on galactic scales, they still fail to explain Bullet-cluster-like structures, and lack a working cosmological background theory. Assuming an additional form of non-visible matter, on the contrary, is in good agreement with our current understanding of the underlying cosmology, as explained in the previous section. The most likely candidate for dark matter particles are WIMPs, since objects like MACHOs cannot be the source of all the missing matter; if MACHOs were the reason for the flattened velocity profiles of disk galaxies, there would have to be a tremendous amount of those objects in the halos of galaxies. In that case, each MACHO, when passing in front of the visible part of a galaxy like Andromeda, should lead to a micro-lensing event, i.e., the background light should be gravitationally focused due to the presence of a massive object in front of the galaxy. Alcock et al. (2000) and Alcock (2009) searched for MACHOs in front of the Magellanic Clouds and found that they can only account for a maximum of 20% of the missing matter and a 100% MACHO dark matter is ruled out (Alcock et al., 2000). A similar study using the Andromeda galaxy to search for MACHOs is presented by Riffeser et al. (2008), who suggest that there might be biases in the detection methods and as such it could still

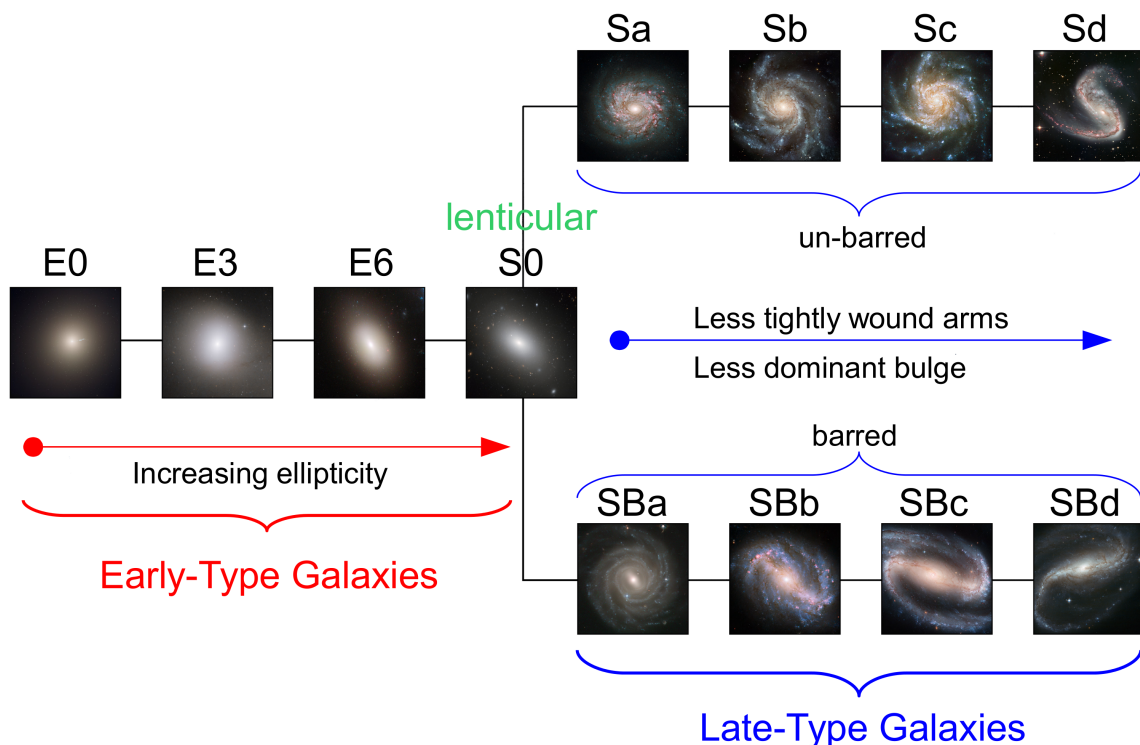


**Figure 1.5:** Illustration of the classification of galaxies due to their morphology, using example galaxies from observations with the Hubble space telescope. This scheme is based on the classification introduced by Edwin Hubble in 1936. Image credit: NASA, ESA, M. Kornmesser, labeling by the author.

be that MACHOs can contribute significantly to the dark matter content (also private communication with A. Riffeser).

In our picture of a  $\Lambda$ CDM universe, we can summarize that galaxies consist of an extended, spherical (or triaxial) halo of dark matter, with a baryonic component in its center which is composed of stars, cold gas and dust, and in case of the most massive halos a hot gas component which basically follows the distribution of the dark matter. Merging substructures can provide small satellite galaxies like the Magellanic Clouds, surrounding the main galaxy until they finally are disrupted by tidal forces and leave stream-like structures in the faint stellar outskirts of the galaxies, building up a so-called stellar halo around the central galaxy.

Thus, the visible galaxy only is a very small fraction of the actual galaxy, although it is by far its most studied part. In the following, some basic properties of galaxies are presented, to prepare the ground for the study presented in this thesis.

### 1.2.1 Morphology: Basic Classifications

Already in 1926, Edwin Hubble suggested to classify the extragalactic nebulae into different categories according to their morphology (Hubble, 1926, 1927): **Elliptical galaxies (E)**, which basically have a spheroidal shape without any substructures. They are classified according to their degree of

flatness, from round (E0) to flat (E7). Hereby, the number specifies the ellipticity  $e$

$$e = \frac{a - b}{a}, \quad (1.6)$$

where  $a$  is the long and  $b$  is the short axis. Most galaxies which cannot be classified as ellipticals are classified as **spiral galaxies** due to their wound stellar arms. Those come in two different flavours: **Barred (SB)** spirals exhibit a strong bar in the center, with the spiral arms usually starting at the ends of the bar, while **normal (S)** spirals do not show a bar-like structure. In the centers of most spirals, a bright spheroidal component can be found, called the bulge. For both barred and normal galaxies, Hubble distinguished between three different classes (a,b,c) according to the amount of unwinding of the arms (from a to c the arms are less tightly wound) and the dominance of the bulge component (from a to c the bulge becomes less dominant). In Fig. 1.5, an illustration of Hubble's classification scheme is shown, similar to the schematic view of his classification which he showed in his paper from 1936 (Hubble 1936, see also Buta et al. 2007). This diagram is often referred to as the Hubble "tuning fork". Hubble himself believed this classification to be a temporal sequence, that is the ellipticals evolve into spirals with time, with an S0-state as transient form between the most flattened form of elliptical and the spirals of class Sa or SBa. Therefore, he called all elliptical galaxies including the hypothetical class of S0 galaxies "early-type" galaxies, and the spiral galaxies "late-type" galaxies. Even though this presumed sequential evolution of galaxies is now known to be incorrect, those terms are still used today.

In general, early-type galaxies have no (or very little) gas which forms stars, and therefore their stellar content is on average old, causing the galaxies to appear "red". For this reason, early-type galaxies were often called "red and dead", as they do not refresh their stellar content by forming stars themselves. In contrast, late-type galaxies usually show signs of (strong) star formation activity, especially in the spiral arm structures, and therefore seem to be "blue". However, their bulge components have colors similar to those of early-type galaxies, and the (cold) gas fraction in the bulges is low. Thus, the Hubble sequence for late-type galaxies is also a description of the amount of relative star formation, as the bulge fraction decreases from a to c, the star formation becomes more dominant.

With increasing observational resolution, the detailed structures of galaxies became visible. This applied mostly to the spiral galaxies and led to several revisions of the Hubble tuning fork, from which only those that are still in use nowadays will be briefly presented in the following.

Most prominently, Alan Sandage, based on the work by Edwin Hubble, firmly established the **S0** class of armless disks, introducing the name **lenticular**, and added a new classification criterion to all spiral galaxies: He found that many spiral galaxies, especially barred spirals, have ring-like structures (Sandage, 1961). Whenever the spiral arms spring directly from the bar (or the core of the bulge-region), he classified the galaxy as "s", in contrast to those galaxies where the spiral arms start tangential from a ring-structure, which he classified as "r". An example for such a ring galaxy is shown in the left panel of Fig. 1.6. This revised version of the Hubble sequence is called the Hubble-Sandage classification.

Another major revision of the Hubble-Sandage classification was introduced by Gerard de Vaucouleurs (de Vaucouleurs 1957, 1963 as well as Buta et al. 2007 and references therein). He realized that many galaxies had only small bulges, looking more like a mixture between the barred and non-barred galaxies introduced by Hubble. Motivated by these observations he introduced a 3-dimensional classification scheme, where normal bar-less galaxies are now denoted by an "A", and transitional classes can be identified as "SAB" or "SBA", depending on which structure is more dominant. These



**Figure 1.6:** Three examples for galaxies which cannot be fit into the original picture of galaxy morphology as suggested by Hubble. **Left panel:** NGC 2217, an example for a galaxy exhibiting an outer and an inner ring, as well as a bar. Those rings were added as morphological classification criterion by Sandage in 1961. Thus, NGC 2217 is a beautiful example for a double-ringed, barred galaxy of type RSBrsa. Image credit: ESO **Middle panel:** NGC 1275, the BCG of the Perseus galaxy cluster, is an example for a cD-type galaxy according to the Morgan classification scheme. In addition to “normal” BCGs, this one has strong flows of cold gas reaching towards its center, causing the peculiar spider-like structures. Image credit: NASA, ESA and Andy Fabian (University of Cambridge, UK) **Right panel:** Arp 273 is a system of two merging galaxies with a mass ratio of  $\approx 1 : 5$ . The upper galaxy shows multiple newly formed blue stellar clusters, and in its upper arm a dwarf galaxy is embedded. Image credit: NASA, ESA and the Hubble Heritage Team (STScI/AURA)

classes were augmented to include transitional classes for the lenticulars, and also stages intermediate between lenticular and spiral galaxies (0/a). This transitional scheme also included the inner ring notation introduced by Sandage, and it is at present day the most used classification scheme. The classification was also broadened to include the transition to **irregular galaxies (I)**, denoted by a “d” for spirals with very open arms, and an “Im” for irregular galaxies similar to the Magellanic clouds. Furthermore, he added the outer ring structures to the classification, denoted by “R”. An example for such an outer ring galaxy is shown in the left panel of Fig. 1.6, where the galaxy exhibits both an inner and an outer ring. This galaxy, according to de Vaucouleurs classification scheme, is a classical (R)SB(rs)0/a. Additionally, all systems which show signs of heavy distortions were called **peculiar (P)**, and many of them situated in the local Universe can be found in Arps Atlas of Peculiar Galaxies (Arp, 1966; Kanipe & Webb, 2006). One example of such a peculiar system is shown in the right panel of Fig. 1.6 for the case of two merging spiral galaxies, where both systems already exhibit signs of strong distortions of their spiral arms and heavy star formation activity, indicating that there has already occurred a first passage between those two galaxies (for more details on massive binary merger events, see Sec. 2.2).

Parallel to those classifications based purely on morphology, Morgan invented a classification which incorporated information about the stellar content in form of the averaged spectral type of the stars (Morgan, 1958). Subsequently, he could show that spiral galaxies with small or no bulges are dominated by bright, massive (A-type-like) stars, while the stellar content of ellipticals and bulge-dominated galaxies is generally old (K-type star dominated). From this classification scheme, only

the **cD** classification has survived, where the “D” describes a galaxy which is rotationally symmetric, while the “c” stands for a very massive galaxy with an extended envelope (Matthews et al., 1964). This special form of elliptical galaxy can mostly be found in the centers of massive galaxy clusters, and is the common classification for those brightest cluster galaxies (**BCGs**, see middle panel of Fig. 1.6).

For a more detailed discussion on the different classification schemes including those not discussed above, see Buta et al. (2007) and the chapters by John Kormendy and Ron Buta in the collection of reviews by Falcón-Barroso & Knapen (2013). While there have been many revisions for the spiral type galaxies, the classification for elliptical galaxies due to their ellipticity had not been changed since they do not exhibit any significant morphological differences apart from their ellipticity. However, while the morphological type of spiral galaxies is correlated with several properties like bulge dominance, gas content and color, the ellipticity correlates virtually with almost no property of the ellipticals (Tremaine, 1987). Therefore, Kormendy & Bender (1996) suggested to revise the Hubble-Sandage tuning fork with regard to ellipticals according to the deviations of the shapes their isophotes from exact ellipses, since these deviations are closely correlated with the kinematic properties of ellipticals. They introduced two classes of ellipticals, “boxy (b)” and “disky (d)”, with ellipticals with exactly elliptical isophotes as an intermediate state in between those two classes. We will come back to this revision in Sec. 1.2.3 when we discuss the kinematic properties of galaxies. However, we will now first take an excursion into the environmental dependencies of galactic properties.

## 1.2.2 Environmental Dependence

In our present-day Universe, galaxies are not distributed randomly but along the cosmic web which was introduced before. The most massive dark matter halos, the galaxy clusters, usually sitting at the intersections of at least three filaments, can host thousands of (massive) galaxies, with the most massive galaxies at their centers, the BCGs. These massive galaxies usually are elliptical galaxies, classified as cD, and composed of a bright, spheroidal component and a shallow halo around them which smoothly merges with the intra-cluster light which is generated by stars stripped from the accreted galaxies or accreted smoothly from the environments (Gallagher & Ostriker, 1972; White, 1976; Merritt, 1983; Malumuth & Richstone, 1984; Murante et al., 2004). These clusters have total masses of more than  $M_{\text{tot}} > 1 \times 10^{14} M_{\odot}$ , and can even reach total masses of an order of magnitude more than this (see Sec. 2.4.2 for more details on galaxy clusters). Most of the baryonic mass is contained in a hot gaseous component<sup>5</sup>, which is distributed similarly to the dark matter and shines brightly in X-ray observations, while galaxies only contribute little to the baryonic content of clusters.

Nevertheless, the galaxy content of galaxy clusters is of utmost interest, since these are the densest environments which can be found in the Universe and therefore excellent laboratories to understand the impact of environment on galactic properties such as morphology and gas content. Most of the galaxies in clusters are gas-poor, and recent detailed observations of the galaxies in the Virgo Cluster revealed, that many of those galaxies which still have H I gas disks show strong indications of ram-pressure stripping which rips the gas off the galaxies (Abramson et al., 2011; Vollmer et al., 2012; Boissier et al., 2012), effectively starving them by removing the gas and thus also the ability to form

<sup>5</sup> In the most massive galaxy clusters, those hot gaseous halos can become dense enough that the timescales on which the gas is cooling radiatively (due to bremsstrahlung) become small enough to cause condensation of cold gas in the central BCG. This is most likely the reason for the cold flows which can be seen for example in the Phoenix-Cluster BCG, as shown in Fig. 1.6. These galaxy clusters are called “cool core clusters”, see also Semler et al. (2012) for more details on cool core clusters from the SPT survey (see also Mo et al., 2010, pp. 413ff and pp. 760ff).

new stars (see also Jaffé et al., 2015, who showed that galaxies can already be starved at the first infall). This is in agreement with results found by Bamford et al. (2009) and Tojeiro et al. (2013) who showed that red spiral galaxies, i.e. galaxies which morphologically are spiral galaxies but do not form new stars due to the lack of larger gas reservoirs and are therefore dominated by an older population of stars, are mostly found in the outskirts of galaxy clusters.

In contrast, voids, which are the underdense regions in the cosmic web, contain only low numbers of galaxies. Pan et al. (2012) identified 1054 voids in the northern hemisphere segments of the SDSS survey, which in total contain 8046 galaxies with magnitudes above  $-20.09\text{mag}$ , accounting for about 7% of all galaxies in those segments. These voids have radii between 10 and 30  $\text{Mpc}/h$ ,<sup>6</sup> and their borders are made up by the filaments in the cosmic web. Galaxies which can be found in voids tend to be not very massive and either spirals or of (merging) irregular shapes (e.g., Szomoru et al., 1996; Kreckel et al., 2012). Results from the AMIGA survey of galaxies in low-density environments have shown that 82% of those galaxies are spirals, with the majority having small bulges (Sulentic et al., 2006). Void galaxies are usually gas-rich, albeit their star formation rates are not too high since the galaxies are small (Beygu et al., 2015), however, if compared to galaxies of similar mass in denser environments, their star formation rates are similar (Ricciardelli et al., 2014). Kreckel et al. (2014) also found indications for ongoing assembly of those galaxies, i.e., ongoing small mergers as well as gas accretion onto the galaxies from the surroundings. Recently, Beygu et al. (2013) and Alpaslan et al. (2014) showed that many of those galaxies which live in void environments are actually ordered in a chain along fine filaments (Alpaslan et al. 2014 introduced the name “tendrils” for those ultra-thin structures), from which they actually accrete their gas. Indications for such behaviour had already been seen for the galaxies in the Bootes-Void (Szomoru et al., 1996). Early-type galaxies are very rare in void environments, and those which can be found there sit at the intersections of small void-filaments (i.e., three out of 55 galaxies studied in the Void Galaxy Survey by Kreckel et al., 2012). Nevertheless, even if the number of galaxies in voids are low, there are still enough galaxies to cause winds to magnetize the voids (Beck et al., 2013, and references therein, and App. A.7).

Most galaxies live in group environments (Eke et al., 2004; Wilman et al., 2005), that is conglomerations of three (loose groups) up to hundreds of galaxies, with total halo masses between  $1 \times 10^{13} M_{\odot} < M_{\text{tot}} < 1 \times 10^{14} M_{\odot}$ . Most interesting are the so-called compact groups, which are groups of at least four galaxies that show strong signs of ongoing interactions (Hickson, 1982). In those environments, from loose groups where the galaxies show only weak signs of interactions (like warped disks) to compact groups with ongoing merger processes, the violent merging processes that lead to changes in the morphologies of galaxies can be studied best, especially since the likelihood for merging events is much higher in groups than in any other environment (Mamon, 1992). For more details on galaxy groups see Remus (2009) and references therein. A special form of galaxy groups are fossil groups. Those groups, although as massive as the other types of groups, consist of solely one massive early-type galaxy at their centers, with the next massive group member at least two magnitudes less bright than the main galaxy (Jones et al., 2003, but also La Barbera et al. 2009), and have X-ray-bright gas halos. These massive galaxies sometimes resemble the properties of the galaxies at the centers of galaxy clusters, indicating that galaxy clusters are pre-processed in groups. For example, Remus (2009) found from cosmological simulations that all 10 galaxy clusters in their simulation have accreted at least one galaxy group during their lifetime, with the most massive cluster

<sup>6</sup> Szapudi et al. (2014b,a) recently reported that they discovered a supervoid with a radius of  $220 \pm 50 \text{Mpc}/h$  at its redshift centered around  $z \approx 0.22$ , which they assume to be the cause of the “Cold Spot” seen in the CMB. This would be the largest void in the known Universe.

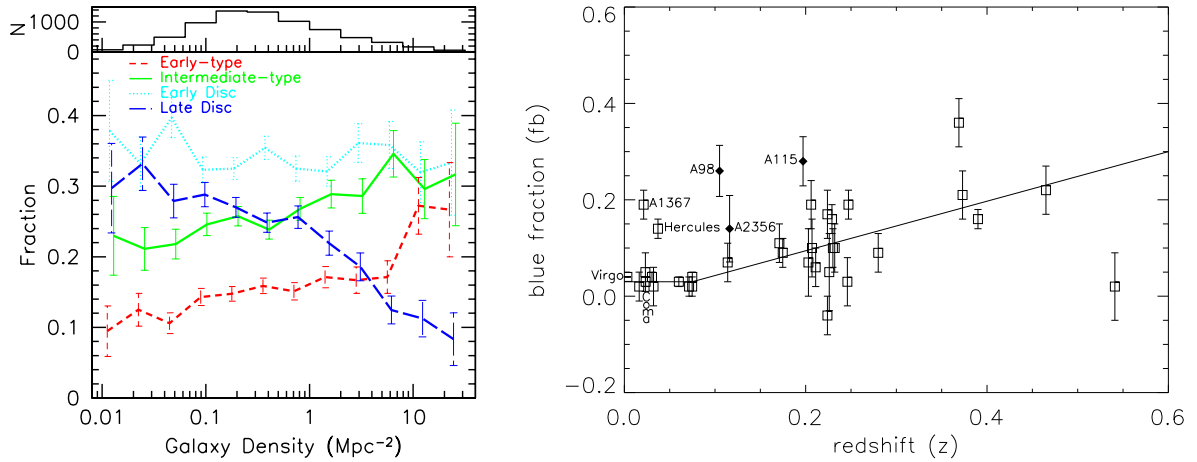


**Figure 1.7:** *Left panel:* Fig. 12 taken from Goto et al. (2003b). The number density of galaxies of different morphologies is shown depending on their environmental density for galaxies from the SDSS survey. The morphology-density relation is shown for early-type galaxies as red dashed line, for disk galaxies as blue long dashed (*c/d* types) or cyan dotted (*a/b* types) lines, and for intermediate galaxies like *S0* galaxies as green solid line. The upper panel shows the number of total galaxies found in each environmental density bin. *Right panel:* Fig. 7 taken from Metevier et al. (2000). The fraction of blue galaxies with respect to the total number of galaxies within clusters at different redshifts is shown. The increase of the number of blue galaxies with redshift is called Butcher-Oemler effect, and this figure includes the original data points from the work by Butcher & Oemler (1984) and new data from the work by Metevier et al. (2000).

having accreted three groups. However, their most massive cluster had only  $4 \times 10^{14} M_{\odot}$ .

Generally, as shown for example by Dressler (1980) and Goto et al. (2003b) (for galaxies from SDSS, see also left panel of Fig. 1.7), there exists a morphology-density relation for galaxies<sup>7</sup>: In the field environment, the number of early-type galaxies is comparatively low, and most galaxies are either late-type galaxies or irregulars. With increasing density of the environment, i.e., in galaxy group environments, the number of early-type galaxies, especially *S0* galaxies, increases compared to the number of late-type galaxies. In the most dense environments, the galaxy clusters, early-type galaxies are the dominant morphological type, and especially elliptical galaxies can be found most often in such overdense environments. The morphology-density relation already clearly states that there is a morphological transition from late-type to early-type galaxies, which can be induced by merger events in dense environments, but might also be caused by gas stripping processes in the hot halo environments of those dense regions. Thus, understanding the details of those stripping and merging processes is one of the cornerstones in understanding the formation histories and morphological changes of galaxies at low redshifts.

At higher redshifts, the fraction of blue (gas-rich and star forming) galaxies tends to be higher. This was found in a survey of 33 galaxy clusters by Butcher & Oemler (1984) at different redshifts up to  $z \approx 0.6$ , and therefore named the Butcher-Oemler-Effect. The right panel of Fig. 1.7 shows the

<sup>7</sup> Indications for a dominance of compact spheroidal systems in a “nebula-cluster” environment have already been presented by Wolf (1901), who thereby discovered the nowadays well known Coma cluster of galaxies in the observational catalogue of nebulae presented by D’Arrest (1865). He also noticed that there are galaxies with a compact core and a shallow surrounding halo in this environment, which we nowadays know to be the BCGs, of which Coma actually has more than one.

relation found by Butcher & Oemler (1984), including three more galaxy clusters (Metevier et al., 2000). Since the discovery of this increase in the blue fraction with redshift, this effect has been studied in several surveys, for example by Goto et al. (2003a) for the galaxy cluster sample selected from SDSS, and by Zenteno et al. (2011) for galaxy clusters detected with the South Pole Telescope (SPT) due to their signal in the CMB (Sunyaev-Zel'dovich effect<sup>8</sup>).

### 1.2.3 Classification II: Kinematic Properties

Next to the morphology, kinematic properties observationally accessible through the radial (line-of-sight) velocity and velocity dispersion profiles of galaxies are one of the most important sources of information on galaxy properties. As already discussed before, observations of the rotation curves of disk galaxies have led to the realization that a huge amount of the actual mass of a galaxy is invisible, and can only be measured via its gravitational impact on the visible baryonic components. Measuring the kinematic properties of galaxies out to large radii is one way to learn about this component, as the radial velocity profiles and rotation profiles directly reflect the gravitational potential of the galaxies, and therefore can even provide information about the dark parts of the galaxies. However, the outskirts are regions of very low baryonic densities, thus have nearly no star formation and consist mostly of old stars, and therefore are very difficult to measure observationally. This is one of the ongoing challenges for observers, and parts of this thesis deal with gaining a better understanding of the information encoded in these outskirts.

Nevertheless, the kinematics also provide interesting information about the visible parts of galaxies, and those are much better understood so far. One of the basic kinematic properties of galaxies is closely correlated with their morphology: Stars and gas in late-type galaxies usually rotate fast around the galaxies' centers, and their motion is strongly ordered. The stellar orbits in late-type galaxies are dominated by circular orbits around the galactic center, building up the extended disks, and only the bulge components show non-ordered motions, in agreement with their spheroidal appearance. Therefore, late-type galaxies usually have low mean velocity dispersions in their central parts (up to a few kpc), and relatively high velocities. Early-type galaxies, on the other hand, have less ordered motion, and thus their average velocity dispersion is high and can reach up to  $\sigma \approx 300$  km/s or even more (Forbes & Ponman, 1999).

Until recently, early-type galaxies have been seen as smooth, amorphous, old stellar systems, with the most massive ones (BCGs and fossil group central galaxies) having boxy isophotes and the lion's share having disk isophotes, following the classification introduced by Kormendy & Bender (1996). As these authors have shown, boxiness and diskiness are closely correlated with kinematic properties of the ellipticals: Boxy ellipticals usually show no or only very little signs of rotation, and occasionally even exhibit minor-axis rotation, while disk ellipticals rotate comparatively fast and mostly along the major axis. Additionally, the boxy isophotes indicate strong anisotropy and triaxiality, while disk isophotes correlate with nearly isotropic, oblate-shaped ellipticals.

However, compared to the large variety in morphology and diversity in kinematic components as bulges, rings, bars, that can be found in spiral galaxies, early-type galaxies seemed rather poor. This picture has been changed by the results of a new survey called Atlas<sup>3D</sup>, where the kinematic properties of the central areas (within approximately one effective radius  $R_{\text{eff}}$ , the radius which includes half

<sup>8</sup> The Sunyaev-Zel'dovich effect, also called SZ-effect, is a "shadow" of the intra-cluster medium (ICM) on the CMB, caused by inverse Compton scattering of the CMB photons in the hot ICM gas (Zeldovich & Sunyaev, 1969; Sunyaev & Zeldovich, 1980)

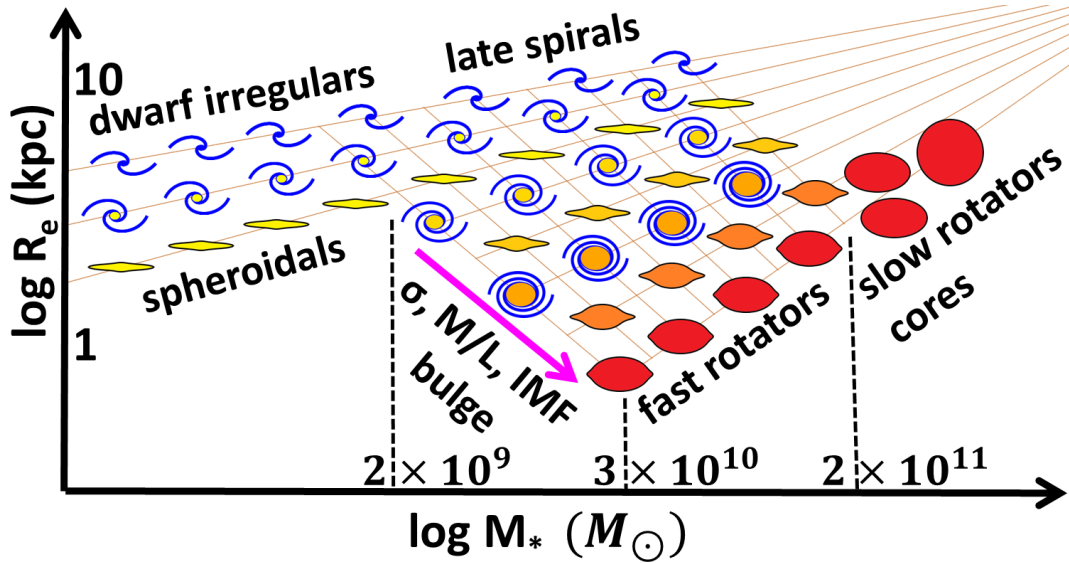


**Figure 1.8:** Fig. 1 taken from Cappellari et al. (2011b): Illustration of the classification scheme introduced by Cappellari et al. (2011b), suggesting that there exists a smooth transition between spiral and elliptical galaxies, from spirals with large bulges to fast rotating S0 galaxies. For a given mass, the spirals are generally larger than the fast rotating early-type galaxies, suggesting that such a transformation mechanism has to shrink the galaxy while basically conserving (or only slightly enhancing) the mass. The most massive galaxies, however, the slow rotators, must clearly have formed from a different channel through accretion of structures, growing in both mass and size.

the light of the galaxy) of a volume-limited ( $1.16 \times 10^5 \text{ Mpc}^3$ ) sample of local galaxies have been studied, with special emphasis on the early-type galaxies in this survey (Cappellari et al., 2011a). They selected all galaxies in their sample fields which were within a distance of 42 Mpc and brighter than  $-21.5 \text{ mag}$ , which roughly corresponds to stellar masses of  $M_* \leq 6 \times 10^9 M_\odot$ . From those 871 galaxies, 8% are elliptical and 22% are S0 galaxies, so that the studied sample of early-type galaxies consists of 260 objects. Those galaxies were observed in several different wavelengths, enabling a detailed investigation of the gas components (hot, molecular, and H I gas) (Young et al., 2011; Davis et al., 2011; Young et al., 2013) as well as a high resolution two-dimensional mapping of the stellar (and gaseous) kinematics. Emsellem et al. (2007) had already shown from a small selected sample of early-type galaxies (SAURON survey) that the apparent specific angular momentum  $\lambda_R$  of those galaxies,

$$\lambda_R = \frac{\langle R|V| \rangle}{\langle R \sqrt{V^2 + \sigma^2} \rangle} \quad (1.7)$$

with  $\langle R|V| \rangle$  as an approximation for the angular momentum  $\vec{L} = \vec{R} \times \vec{V}$  can be used to distinguish between fast and slow rotating early-type galaxies (see also Jesseit et al. 2009). Here,  $V$  and  $\sigma$  are the line-of-sight velocity and velocity dispersion, respectively, and  $R$  is the projected distance to the center of the galaxy. Galaxies dominated by a rotating component have a smaller velocity dispersion component, thus  $\lambda_R$  tends towards 1, while for non-rotating or slowly rotating galaxies, where the dispersion is much larger than the mean velocity, the  $\lambda_R$  parameter is close to 0.

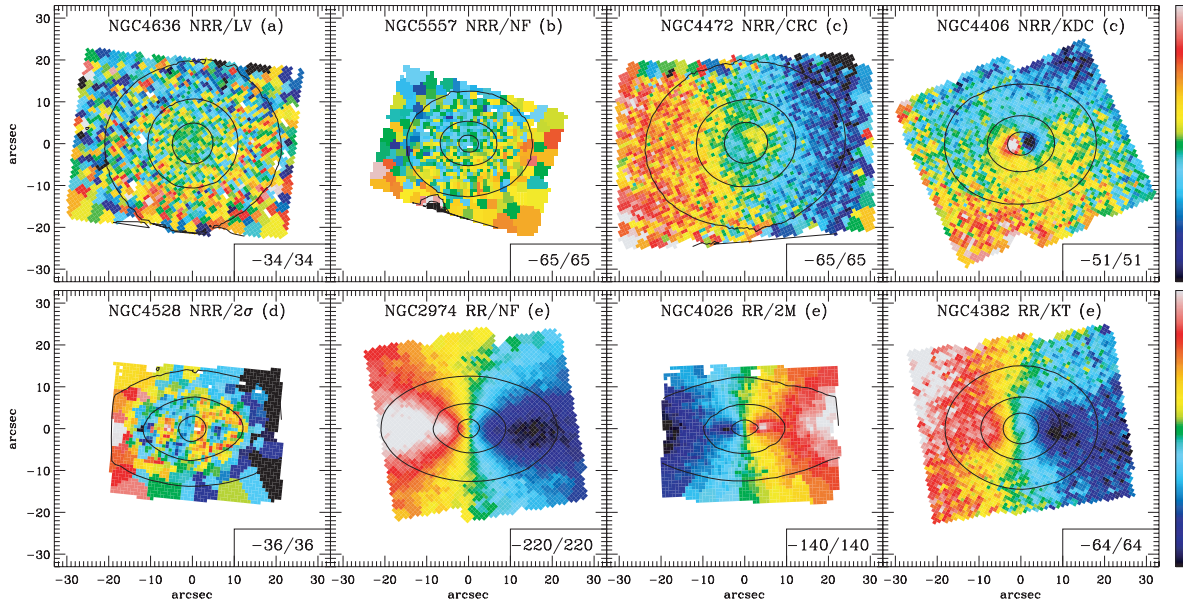


**Figure 1.9:** Fig. 1 taken from Krajnović et al. (2011), showing examples of the mean velocity maps for each of the eight classes of features identified in the Atlas<sup>3D</sup> survey, with the photometric major-axis for each galaxy oriented horizontally. The numbers in the lower right corners of each map mark the range of the plotted velocities in km/s, and the colors correspond to those values. From left to right, top to bottom, the following features are shown: no rotation at all (LV), normal feature (NR) slow rotator, counter-rotating core (DRD) slow rotator, kinematically distinct core (KDC) slow rotator, double peak in  $\sigma$ -map ( $2\sigma$ ) slow rotator, normal feature (NR) fast rotator, double maxima (2M) fast rotator, and kinematically twisted (KT) fast rotator. More details in the text and in Krajnović et al. (2011).

Emsellem et al. (2007) already suggested to classify the galaxies with  $\lambda_R < 0.1$  as slow rotators, and galaxies with  $\lambda_R > 0.1$  as fast rotators. With the extended Atlas<sup>3D</sup> survey, this has been proven to be a solid classification for early-type galaxies (Emsellem et al., 2011). In addition, Emsellem et al. (2011) showed that almost all of the most massive galaxies are slow rotators, albeit their number is small (14%) compared to the number of fast rotating early-type galaxies. However, they did not find a clear correlation between the boxy and disk isophotes and the slow and fast rotator classification, even if many of the slow rotators are boxy. Based on these results, Cappellari et al. (2013) suggested a new classification scheme as shown in Fig. 1.8, indicating that there exists a smooth transition between spirals with large bulge components and fast-rotating early-type galaxies, hinting at a possible transformation scenario. In this picture, slow rotators clearly stand out as the massive end of all transformations, similar to what had already been suggested by Kormendy & Bender (1996) for the boxy ellipticals. Cappellari et al. (2011b) also showed that the slow rotators usually live in the most dense regions, while the environmental dependence of the fast rotators is similar to the morphology-density relation of early-type galaxies as discussed above.

However, while this classification into slow and fast rotators is useful in the sense that it correlates with observable parameters such as mass, size, and even environment, a detailed analysis of the velocity maps of the early-type galaxies in the Atlas<sup>3D</sup> survey reveals the existence of several kinematic features (Krajnović et al., 2011). Examples of those features are shown in Fig. 1.9: Double maxima

(2M, 2nd row, 3rd column) and kinematic twists (KT, lower right panel) are found in the family of fast rotators, while kinematically distinct cores (KDC, upper right panel) are a common feature in slow rotating galaxies. Some of those slow rotating galaxies even show no sign of ordered motion at all, and thus are called low-level velocity galaxies (LV, upper left panel of Fig. 1.9). Galaxies with counter rotating cores (CRC, 1st row, 3rd panel) occur in both families, as well as the  $2\sigma$  galaxies (lower left panel). This last feature cannot be seen in the velocity maps but only in the velocity dispersion maps, where there are two off-center, but symmetric peaks. The majority of all early-type galaxies, nevertheless, is still featureless (NF, second column in Fig. 1.9), and slow rotating early-type galaxies more often tend to possess features. Understanding the origin of those features will possibly provide insight into the different channels that are important for the formation of early-type galaxies.

While these results have proven that early-type galaxies are not at all featureless, dead systems, the current survey was limited to the innermost parts of the galaxies (the area within the projected effective radius). More kinematic features are likely to appear if larger radii are included in the study, as has been already shown for a small subset of the Atlas<sup>3D</sup> by Foster et al. (2013) and Brodie et al. (2014), who studied the kinematics in the outskirts of early-type galaxies using globular clusters (GCs) as tracer population (see Chap. 6 for more details). More extended studies are planned for the future, using instruments like MUSE to measure the kinematics. In addition, extremely deep optical imaging (Duc et al., 2015) with the aim to find remnants of (recent) merger events will also help to understand the complex mechanisms that lead to the formation of the most massive stellar structures in the Universe.

## 1.3 Dynamical Processes

Kinematic and morphological features like those discussed in the previous subsections can provide many insights into the processes which are currently ongoing or have led to the formation of galaxies as we know them today. However, a solid theoretical framework is needed to interpret the origins of the observed features. In this subsection, we will briefly describe the most important mechanisms that influence the dynamical collisionless multi-body systems of galaxies. While there are many more important processes involved whenever gas plays an important role, the main focus of this thesis will be on the dynamical properties of spheroidal galaxies where the gas fraction only plays a minor role, and therefore we will only shortly discuss the relevant aspects of the influence of the gas.

### 1.3.1 Equilibrium

In an undisturbed, relaxed, collisionless, spherical, gravitational system, the average kinetic energy content  $E_{\text{kin}}$  of the system is in equilibrium with its average potential energy  $E_{\text{pot}}$ . This state is well described by the (scalar) virial theorem:

$$E_{\text{kin}} = \frac{k}{2} E_{\text{pot}} \quad (1.8)$$

with  $k = -1$  for gravitating systems. For the total energy content  $E_{\text{tot}} = E_{\text{kin}} + E_{\text{pot}}$  of such a system this implies that  $E_{\text{tot}} = 0.5E_{\text{pot}} = -E_{\text{kin}}$ . In case of a spherically symmetric gravitating system, the average kinetic energy can be calculated from the average squared velocities  $\langle v^2 \rangle$  of the particles and

their total mass  $M$  as

$$E_{\text{kin}} = \frac{1}{2} M \langle v^2 \rangle, \quad (1.9)$$

and the mean potential energy of the system can be calculated as

$$E_{\text{pot}} = -\frac{G M^2}{R}, \quad (1.10)$$

where  $R$  is a suitably defined “gravitational radius” and  $G$  is the gravitational constant. Using the virial theorem, this leads to a simple correlation between the system’s mean velocity, mass and radius (denoted as  $v_{\text{vir}}$ ,  $M_{\text{vir}}$  and  $R_{\text{vir}}$ , respectively):

$$\frac{1}{2} M_{\text{vir}} v_{\text{vir}}^2 = \frac{1}{2} \frac{G M_{\text{vir}}^2}{R_{\text{vir}}}; \quad (1.11)$$

$$\Rightarrow v_{\text{vir}}^2 = \frac{G M_{\text{vir}}}{R_{\text{vir}}}, \quad (1.12)$$

see also Mo et al. (2010), Binney & Tremaine (2008) and Goldstein et al. (2002) for more details. The virial mass and the virial radius are correlated as

$$M_{\text{vir}} = \frac{4\pi}{3} R_{\text{vir}}^3 \rho_{\text{crit}} \Delta \quad (1.13)$$

with  $\Delta$  a variable that describes the amount of overdensity of the virialised halo as a fraction of the critical density of the Universe (see Eq. 1.5)  $\rho_{\text{crit}}$ , and it depends on the applied cosmology. This is, of course, a rather crude approximation to the real states of galaxies, and the underlying equilibrium state to which galaxies evolve through their lifetimes is a multi-component problem and thus much more complex. Nevertheless, especially for galaxy clusters and globular clusters, the virial theorem is a good approximation to measure masses and radial extends. This is especially useful in the case of galaxy clusters, since the dark matter is the most dominant constituent in those structures. On the downside, most clusters in the Universe are not relaxed, especially in their outskirts, and thus those measurements are only approximations.

In practice, especially in observations,  $\Delta = 200$ , that is an overdensity of 200 times the critical density of the Universe, is often used to approximate the virial mass and radius, and thus are denoted as  $M_{200}$  and  $R_{200}$ . As reported for example by Kravtsov (2013), there is also a close relation between the stellar half-mass radius  $r_{1/2}$  of a central galaxy (i.e., the radius which contains half the stellar mass of the galaxy) and the  $R_{200}$  of the total halo, namely  $r_{1/2} \approx 0.015 R_{200}$ .

In such a spherical system which is in a relaxed equilibrium state, the time that a test mass (for example a stellar particle or a satellite galaxy) needs to orbit once through this system, the so called **dynamical time**, can be calculated as

$$t_{\text{dyn}} = \sqrt{\frac{3\pi}{16G\bar{\rho}}} \quad \text{with} \quad \bar{\rho} = \frac{3M}{4\pi R^3} \quad (1.14)$$

the average density in the halo, as long as the test mass is small enough compared to the host system. This is similar to the so-called **free-fall time**  $t_{\text{ff}} = t_{\text{dyn}} / \sqrt{2}$ , the time that a uniform, pressure free sphere needs to collapse into a point mass (Mo et al., 2010, p. 14). The free-fall time is often used to calculate the time which a particle that can redistribute its energy (for example a gas particle) needs to fall into the center of the halo (see also App. A.2 where this timescale is actually related to our results for the origin of the cold gas in spheroidal galaxies).

### 1.3.2 Disturbing the Equilibrium: Accretion and Merging

While the idea of a relaxed state of a collisionless system is useful to analytically solve equations of motions and calculate potentials, in reality most systems are not relaxed and far from an equilibrium state. In a standard  $\Lambda$ CDM universe, structures grow hierarchical through merging processes, and especially at low redshifts this is the most important mechanism of significant mass growth. Even most disk galaxies show signs of structure accretion, for example in form of streams like the Sagittarius stream in our own galaxy, the Milky Way. All those processes significantly disturb the equilibrium. The most important processes in those interaction scenarios are tidal stripping and galaxy merging.

**Tidal stripping** is a process which can happen to any two particle systems that pass each other in close proximity. In such a case, particles especially at the outskirts of those systems, which are less strongly bound, gain energy through the tidal forces between those systems, that is part of the orbital energy of the encounter is transformed into internal energy, increasing the binding energy between those two bodies and potentially causes the systems to merge eventually. However, this only happens in case that the speed of the encounter is high enough so that the deformations due to the tidal forces are lacking behind the encounter event, since otherwise the effects would cancel each other. Even in case that the systems do not finally merge, they exchange particles during the close passage due to the tidal forces, and those non-merging events are called fly-by events.

Depending on the mass ratio of the two merging particle systems, different kinds of structure can be caused by the tidal forces: If an intruder system is small compared to the main system, e.g., if a dwarf galaxy is accreted by a large galaxy, it is orbiting inside the dark matter halo of the host galaxy, while it feels the tidal forces from the host. As it is not a point mass, the particles of the satellite feel slightly different forces, depending on their internal binding energy. Those stars which are farther at the outskirts of the satellite feel the strongest forces, and the transfer of energy rips them away from the dwarf galaxy's center, causing them to form leading or trailing tails in front or behind the orbit of the satellite inside the host halo potential. In time, the satellite gets more and more disrupted, building up a long, thin stream along the orbit of the satellite. The most well known example of such a tidal stream caused by the dispersion of a satellite galaxy in its host galaxies halo is the Sagittarius stream around the Milky Way (Newberg et al., 2002). In general, smaller systems need longer to be fully dispersed, and as such the remnants of the accretion of small satellites can be seen the longest in the stellar halo of the host galaxy.

If the two merging systems have nearly the same mass, both feel similarly strong tidal forces. In those cases, the outer, least bound particles of those systems feel a similar strong transfer of energy and are accelerated, i.e., ripped from the galaxies and form long tails. This mechanism is most efficient for encounters of dynamically cold systems, i.e., late-type galaxies, while there are hardly any tails in encounters of dynamically hot systems, i.e., early-type galaxies. The orbit of the encounter also plays an important role: if the orbital angular momentum and the disk angular momentum are aligned, the tidal tails are the most prominent, while they are the least prominent in case of a retrograde encounter (see also Toomre & Toomre 1972). One of the most famous examples of a galaxy pair with extended tidal tails are the well studied Antennae galaxies with tidal tails extending for more than 100 kpc, but there are many more galaxy pairs in the nearby Universe which exhibit more or less extended tidal tails, indicating that merging events between two (late-type) galaxies of similar mass are not an uncommon event.

If the orbital energy and angular momentum of two interacting systems is low enough, the systems will eventually merge. This event is called **galaxy merging**, and it is considered to be one of the most

important building blocks of galaxy formation. The higher the orbital energy and angular momentum of the encounter, the longer it takes for the stellar systems to merge, that is to transfer the orbital energy into the internal energy of the newly formed system. If the orbital energy of an encounter between two galaxies is negative, the orbit is called “elliptical” (or bound), if the orbital energy of the encounter is positive, the orbit is called “hyperbolic” (or unbound). Systems which collide on a bound orbit will always merge eventually. Interacting systems on an originally hyperbolic orbit will most likely not be able to merge, however, since the tidal interactions during the encounter (the first passage) already transfer orbital energy into internal energy of the systems, this might deplete enough orbital energy and enable a successive merging event, as long as the angular momentum of the orbit is not too large.

As the outermost areas of the galaxies merge first, and the stellar parts of the galaxies usually live at the centers of extended dark matter halos, the dark matter parts are the first ones to merge. As the baryonic parts of the galaxies live at the deepest parts of the potential, they survive as individual objects much longer than their surrounding dark matter halos, and therefore it is possible for two galaxies to be still in the process of merging while they are already moving around in a common, large dark halo. This is, for example, the case in clusters of galaxies, but also already in compact groups (Remus, 2009, and references therein). While the likelihood for a merging event in a group environment is high due to the enhanced galaxy density, in a cluster environment, on the contrary, it is very unlikely for all galaxies but the BCG to undergo a merging event: since the velocity dispersion of the cluster is much higher ( $\sigma \approx 1000$  km/s) than the internal velocities of the satellite galaxies on their orbits in the cluster, a merger event is nearly impossible as their encounter speed is too high to bind them (Mo et al., 2010).

In a merger event between two galaxies of similar mass, the properties of the resulting galaxy depend on the properties of the progenitor galaxies and the orbit of the encounter. Merger events between two galaxies where one is much more massive than the other one, however, usually only slightly change the morphology of the main progenitor galaxy, as their contribution to the mass is low and many of their stars are ripped away while they are still in the outer parts of the main progenitor (however, since in-situ star formation does basically not occur in the outer halos of galaxies, those accreted stars from small satellite mergers are most likely the main building blocks of the stellar outer halos of galaxies). Mergers with a (stellar) mass ratio between 1:1 and 3:1 are usually called “major merger”, while mergers with (stellar) mass ratios larger than 3:1 are called “minor merger”. While one single minor merger event can hardly change the morphology of a galaxy significantly, several minor merger events in a row can, similar to a major merger event, alter the appearance of a galaxy significantly (see for example Oser et al., 2010; Mo et al., 2010, and references therein).

In general, smaller systems need longer to be fully dispersed, and as such the remnants of the accretion of small satellites can be seen the longest in the stellar halo of the host galaxy. The remnants of such encounters, like tidal streams of shells, are a powerful tool to analyse the potential of the host galaxy and gather information about the mass accretion events of the host galaxy. Throughout this thesis, the impact of merger events on the host galaxies’ dark matter and stellar halos will be discussed in more detail, especially in the light of information which is encoded in the outskirts of the halos about the formation history of a galaxy. For more details on simulations of merger events see Chap. 2, for more details on the theory of dynamical interactions during galaxy encounters see Binney & Tremaine (2008), Mo et al. (2010) and references therein.

### 1.3.3 Relaxing the System: Phase Mixing, Violent Relaxation and Dynamical Friction

There are several processes that lead to a relaxation of a collisionless system once it is distorted (some of those processes also continue even when the system is relaxed). The most important ones of those relaxation processes are phase mixing, violent relaxation, and dynamical friction. **Phase mixing** is a process that occurs in every galaxy whether it is relaxed or not. It basically describes the fact that two particles that at a given time have nearly the same orbit with similar velocities inside a common potential, will separate with time due to the slight differences in their phase-space characteristics without changing their energy contents (Binney & Tremaine, 2008, pp. 379). Thus, stars that are formed inside the same molecular cloud will redistribute over the whole galaxy in time. Similarly, the tidal streams formed from a satellite galaxy orbiting in a galaxy potential will lose their coherence with time, until they finally are broadly distributed inside the stellar halo of the host galaxy. However, even if the phase mixing has seemingly dissolved information about the origin of the stars inside a satellite, in phase space the information is still present (as long as a system did not undergo violent relaxation). Therefore, this could be used to estimate the origin of stars inside a galaxy, but since phase space information is extremely difficult to gain observationally, it is only rarely used. Mixing usually occurs on timescales similar to the dynamical time (see Eq. 1.14), but can also be much longer.

**Violent relaxation**, on the other hand, only occurs in systems where the gravitational potential changes. If a potential is changed, for example due to a merger event, the energies of the orbits of the (collisionless) particles change accordingly until a new equilibrium state is reached, and the system “reorders” itself. This is discussed in detail by Lynden-Bell (1967), who also showed that violent relaxation usually takes place on timescales similar to the free-fall time, and is thus a relatively fast process (explaining the choice of the name). However, the end state of a relaxed system in a cosmological context is not fully understood yet, and the statistically approach used so far has several difficulties (Mo et al., 2010, pp. 254). Nevertheless, this is an extremely interesting problem, especially in the light of new observations of galaxies which are strong lenses, where a direct measurement of the total density profiles is possible, as will be discussed later on. The nature of this relaxed state is one of the key questions this thesis tries to address, and as such it will be in the main focus of chapters 3 and 4.

One additional process which is important in re-ordering a collisionless system is **dynamical friction**. This process occurs in all systems with collisionless particles of different masses. If a particle with a higher mass is moving through a cloud of particles with lower masses, part of its energy and momentum are transferred to the particles with lower mass, thus slowing down the more massive particle while slightly speeding up the lower mass particles. Basically, the gravitational force of the field of less massive particles is dragging at the more massive particle while it is moving with a higher velocity than its surrounding particles, slowing it down. As a consequence, the orbit of the massive particle decays as its orbital energy is decreasing. This leads to a segregation of masses, with more massive particles orbiting farther inside the potential than less massive particles. The time that a particle (or a bound system of particles like a satellite galaxy) of mass  $M_{\text{Sat}}$  needs to orbit from its initial orbit at the outskirts into the center of the potential of the host halo of mass  $M_{\text{Host}}$  due to dynamical friction is (for the approximation of a circular orbit) given as

$$t_{\text{df}} \approx \frac{1.17}{\ln(M_{\text{Host}}/M_{\text{Sat}})} \left( \frac{M_{\text{Host}}}{M_{\text{Sat}}} \right) \frac{1}{10 H(z)}, \quad (1.15)$$

where  $\frac{1}{10 H(z)} \approx r_{\text{Host}}/v_{\text{circ}}$  is used as an approximation (see Mo et al., 2010, pp. 557 and references therein). Thus, dynamical friction is faster the more massive the infalling particle/system is. This

estimate of the dynamical friction timescales can change depending on the properties (e.g., mass loss, presence of a gaseous component) and the orbit of the system. However, the fact that it is generally faster for more massive systems is always valid.

### 1.3.4 Involving the Gas: The Impact of Dissipation

So far we have only considered collisionless systems, that is systems which only interact through gravity. However, most galaxies also contain a gas component, which usually splits up in a cold gas disk (mostly in late-type galaxies, but they can also appear in early-type galaxies as discussed before) and a hot, spheroidal halo surrounding the whole galaxy. In contrast to the collisionless parts of a galaxy, the gas can redistribute energy much more efficient, and thus especially redistribute the angular momentum, transporting it from the outskirts of the galaxies to their inner parts (see for example Teklu et al., 2015b, and references therein). This ability to redistribute energy enables the gas to cool and settle in a disk perpendicular to the major axis of the angular momentum vector on circular orbits, therefore causing the existence of disk galaxies. While this is an important process already during the undisturbed, secular evolution of a galaxy, where the star formation is driven by the clumping of the gas in the central parts of the galaxies in those disks, it also significantly alters the outcome of merging events.

If cold gas is present during a merger event, it already collides during the first encounter, leading to enhanced star formation on very short timescales, so called star burst events (e.g., Mihos & Hernquist, 1996), as well as enhanced activity of the central black hole (enhanced AGN activity). This is also observed in case of the Antennae system and other ongoing merger events. Even on large scales, that is galaxy cluster mergers, where the hot component that does not form stars is the dominant gas component, the gas behaves different from the collisionless components, as can be seen in case of the Bullet cluster: While the collisionless components of the merging clusters are far apart from each others and have not merged yet, X-ray observations show that the hot gas component leaves a clear strong signal in between those two components. This indicates that the Bullet cluster already had its first encounter, which caused the hot halos of both clusters to collide and settle in the common center of mass of those two merging clusters, while the collisionless components take longer to redistribute the orbital energy and build up a new, massive cluster structure. This again shows that the same processes that are important on galaxy scales, are also important on the largest scales where the dark matter component is even more dominant than on galaxy scales.

Commonly, in case of galaxy encounters we distinguish between two different kinds of merger events: **dry merger** are merger events in which only very little or no cold gas is involved, while merger events with a large amount of cold gas involved are called **wet merger**. In the major merger scenario, dry merger events usually lead to the formation of a spheroidal galaxy. Even in case of a cold gas fraction of 20% in the progenitor galaxies, i.e., the amount of cold gas found in typical present-day massive spiral galaxies, the final galaxy after the merger event resembles a spheroidal, albeit the remaining cold gas settles in a small gas disk at its centers. In a wet major merger, however, the resulting galaxy after the merger event might as well be a disk galaxy with a strong bulge at its center (Springel & Hernquist, 2005; Schlach Berger, 2014).

In the minor merger scenario, the effects of the gas are similar to the major merger scenario, especially if the mass ratios are close to the major merger case. One special case should, nevertheless, be mentioned at this point: Observationally it is known that late-type galaxies are also surrounded by dwarf galaxies, as it is the case for the Milky Way and Andromeda. Therefore, merging events are very

likely, and as mentioned before they do not influence the morphology of the main galaxy drastically as long as the merger events are not too many and the mass ratios between the infalling satellite and the main galaxy are large (10:1 or more). Still, the accretion of a satellite onto the disk transports energy from the encounter to the disk, and thus leads to a heating of the disk, which basically means that the stellar disk is getting thicker with each merger and effectively is destroyed (Purcell et al., 2009). Therefore, the likelihood to find spiral galaxies with thin disks like the Milky Way or Andromeda should be low. The reason why spiral galaxies with thin disks still exist despite the high fraction of minor merger events in the hierarchical Universe is the presence of the gas: Due to its ability to redistribute energy, the gas component in the disk can absorb most of the kinetic energy brought in by the merger event and dissipate it, and even might regrow a disk after the merger event if enough gas is present (Moster et al., 2010). Thus, the gas stabilizes the disk, and therefore, as long as a galaxy can replenish its gas disk, minor merger events of mass ratios 10:1 or larger can effectively not destroy the disk.

### 1.3.5 The Galaxy Cluster Environment

If a galaxy enters a very dense environment, i.e., a galaxy cluster, there are further processes that can significantly alter the appearance of a galaxy and disturb its internal secular evolution processes. As mentioned before in Sec. 1.2.2, the number of spheroidal galaxies in the dense environments is enhanced compared to the field. However, the likelihood for a merger event of two random galaxies inside a cluster potential is very low, because the velocities of galaxies in the cluster potential are so large that encounters between two galaxies do not lead to a capture and successive merging. However, if such a high speed encounter between two galaxies is happening, orbital energy is still transferred from the encounter to the internal energy of the galaxies. This effectively results in a heating of the galaxies, which means the particles within the galaxies become less bound, especially in the outskirts, and eventually even get stripped from the galaxy and feed the intra-cluster light component. Every high-speed encounter lessens the binding energy of the particles, puffing up the galaxies and enabling particle stripping. This process is called **galaxy harassment**. The less compact an object, the more sensitive are its outskirts to harassment processes, and thus harassment could transform a disk galaxy into a small compact spheroidal by ripping away the outer areas and only leaving the central bulge component behind.

Another important process in cluster environments is **ram-pressure stripping**, where first the hot halo and then even the cold gas component are stripped from a (disk) galaxy while it moves inside the cluster environment due to the pressure caused by the hot gas halo of the cluster (see Sec. 1.2.2 for more details on observations of ram pressure stripping inside the Virgo cluster). Jaffé et al. (2015) have shown that one orbital period inside a galaxy cluster halo can be sufficient to strip a galaxy off its gas, nevertheless, the presence of molecular gas might actually lower the efficiency of ram-pressure stripping since the gas of the hot halo is too thin to strip off molecular gas from a galaxy effectively. However, there is an additional process which is efficient in a cluster environment, which is called **strangulation**: Inside the cluster environment, galaxies (but the BCG) cannot accrete new gas from its environment, i.e., they cannot replenish their cold gas once star formation has drained the galaxy. Both processes together lead to a very fast and efficient shut off of the star formation, and thus to a change of the appearance, from a blue to a red spiral. Once the massive stars have died, the galaxy loses its spiral appearance and morphologically transforms into a spheroidal.

Those processes all apply to all galaxies in a cluster environment but the BCG. As the BCGs are

in the centers of the cluster potentials, and dynamical friction causes all satellite galaxies in time to sink to the bottom of the cluster potential, the BCGs are actually constantly fed with new galaxies to merge with, and this process is thus called **galactic cannibalism**. This also explains the extremely large stellar masses of the BCGs, as dynamical friction is especially efficient in driving the most massive satellite galaxies into the center, thus feeding the BCG with several massive merger events during its lifetime. The stripped material from those merger event could also explain the build-up of the shallow halos surrounding those BCGs (e.g., Gallagher & Ostriker, 1972; White, 1976; Merritt, 1983; Malumuth & Richstone, 1984; Mo et al., 2010, and references therein). In addition, since the BCG is sitting at the center of the cluster potential, cooling flows from the hot halo can additionally feed the BCG with cold gas, and thus even enable low amounts of star formation, as discussed before.

Hence, to fully understand the formation processes of galaxies, all the effects mentioned above have to be considered. Therefore, in simulations of galaxy formation in a cosmological context, those processes have to be modeled as accurately as possible, which is one of the ongoing challenges in cosmological simulations (see also Chap. 2 and App. A.8).

## 1.4 The Radial (Surface) Density Profiles of Galaxies

The density and velocity profiles of a galaxy provide the possibility to measure the depth and profile of the potential well in which the galaxy resides, the dynamical state of the galaxy, and the mass distribution. These properties change during the formation and evolution of a galaxy, as it experiences several encounters during its lifetime, growing from small to large structures, as explained before, but also forming stars continuously, building up a so-called in-situ fraction. Those profiles, therefore, provide important information about the underlying dynamics of the different classes of galaxies we observe, and might give us important constraints on the different channels of evolution that exist in nature. However, the full three-dimensional profiles cannot be measured directly from observations, but are always limited to two-dimensional information, as the galaxies can only be observed as projections on the sky. While measurements of the rotation curves can provide information about the luminous as well as the dark parts of the galaxies, density distributions can usually only be obtained for the luminous parts of the galaxies. In these cases, a radial surface brightness profile is measured for the luminous component, most often along the major axis of the projected galaxy.

In combination with the measurements of the rotational velocity, the radial distribution of the dark component can be indirectly measured through the deviation of the measured rotational velocity profile from the rotational velocity profile which would be expected if the visible matter would be the only matter in the galaxy (which was, as mentioned before, the method used by Rubin et al. (1965) and Rubin et al. (1980) to “detect” dark matter around galaxies). However, this strongly depends on the conversion from light to mass, which is depending on the initial mass function (IMF) used to calculate the probability distribution function of stars with different masses. Until recently, this had been assumed to be more or less constant for all galaxies in the Universe, however, this view is currently being challenged since there are multiple indications for the opposite to be true, i.e., the IMF to be not universal (e.g., Cappellari et al., 2012; Ferreras et al., 2013; van Dokkum & Conroy, 2011, 2012).

Another method to measure the density distribution of the dark components of galaxies is through strong lensing (e.g., Kochanek, 2006; Treu & Ellis, 2014): when a galaxy is sufficiently massive, its gravitational field can noticeably bend the path of light passing through it and its vicinity. If such

a galaxy has a much more distant, high-redshift galaxy directly behind it along the line of sight, this background galaxy will appear to the local observer as one or more distorted images around the lensing galaxy (see for example Koopmans et al. 2006; Bolton et al. 2008; Sonnenfeld et al. 2013a for samples of spheroidal galaxies which are strong lenses and Féron et al. 2009; Treu et al. 2011 for a sample of disk galaxy lenses). In such cases it is possible, using numerical modeling of the light paths, to determine the total mass distribution (i.e., dark plus visible components) of the lensing galaxy, up to the radius of the lensed image(s). While in this case the total mass distribution is measured, and thus a direct measurement of the potential well of the galaxy is possible, a model for the stellar mass to light ratio is still needed to disentangle the mass distributions of luminous and dark components (for example Sonnenfeld et al., 2012). Thus, strong lensing galaxies are a powerful tool to measure the total mass and density profiles of galaxies. Unfortunately, however, such strong lensing configurations are rare.

In the following a short overview of the observed surface brightness profiles is presented, followed by an overview of the theoretical density profiles which, in projection, were discussed to describe the observed two-dimensional brightness profiles. In addition, we will also briefly introduce profiles which are used to model the dark matter component of structures from galaxies to galaxy clusters.

#### 1.4.1 Surface Brightness Profiles: What is Observed

The surface brightness profiles of early-type and late-type galaxies are known to be very different. One of the first descriptions of the radial luminosity profiles of a sample of 15 ellipticals was presented by Hubble (1930), who found that the luminosity profiles of those ellipticals can be well described by the following formula:

$$I_{\text{Hub}}(r) = I_{\text{eff}} \left( \frac{r}{r_{\text{eff}}} + 1 \right)^{-2} \quad (1.16)$$

where  $r_{\text{eff}}$  is the effective radius of the spheroidal, i.e., the radius which contains half of the luminosity from the galaxy, and  $I_{\text{eff}}$  the luminosity at the effective radius. While this was working sufficiently well for those 15 galaxies, de Vaucouleurs (1948) demonstrated that the surface brightness profiles of early-type galaxies are actually better described as

$$\log I_{R^{1/4}}(r) = \log I_{\text{eff}} \left( \left( \frac{r}{r_{\text{eff}}} \right)^{\frac{1}{4}} - 1 \right). \quad (1.17)$$

This profile is called **de Vaucouleurs  $R^{1/4}$  profile**.

However, there are several early-type galaxies which cannot be fit well by the de Vaucouleurs  $R^{1/4}$  profile but show significantly flatter or more strongly curved profiles. Thus, Sérsic (1963) introduced an exponential profile that could account for these deviations:

$$I_{\text{Sér}}(r) = I_{\text{eff}} \exp \left\{ -b_n \left( \left( \frac{r}{r_{\text{eff}}} \right)^{\frac{1}{n}} - 1 \right) \right\}, \quad (1.18)$$

which is now called the **Sérsic profile**. Hereby,  $n$  is the so-called Sérsic index, which is indirectly proportional to the curvature of the profile and can be any positive real number, and  $b_n$  is a constant which is chosen such that the scale radius  $r_e$  equals the effective radius.  $I_e$  is again the luminosity

within the effective radius. The de Vaucouleurs  $R^{1/4}$  profile is a special case of this profile with a Sérsic index of  $n = 4$ .

As shown for example by Caon et al. (1993), the Sérsic index correlates with the effective radius of a galaxy, with more concentrated spheroidals having smaller Sérsic indices and more extended galaxies having larger Sérsic indices. The most extended and massive spheroidals in the Universe, the BCGs, thus have the largest Sérsic indices which can be as large as  $n = 16.5$  (Caon et al., 1993). Generally, for elliptical galaxies, the Sérsic indices vary between  $2 < n < 6$  (Binney & Tremaine, 2008), but for dwarf ellipticals it can be as low as  $n = 0.5$  (Mo et al., 2010). Bright ellipticals also show significant deviations in the center from the best-fitting Sérsic profile, with the surface brightness profiles in the centers showing a deficit compared to the Sérsic profile. For faint ellipticals, this deficit cannot be seen. These galaxies show the opposite behaviour, with a light excess in their centers, showing a power-law like behaviour. This led to the assumption that there might actually be a difference between the “cored” and “power-law” ellipticals. However, recent results of large surveys have shown that there is in fact a smooth transition in the core properties of elliptical galaxies and thus there is no dichotomy between bright and faint galaxies but only an evolution trend (e.g., Ferrarese et al., 2006, and references therein).

For a Sérsic index of  $n = 1$ , the Sérsic profile becomes a simple **exponential law**:

$$I_{\text{Exp}}(r) = I_{\text{eff}} \exp \left\{ -b_1 \left( \frac{r}{r_{\text{eff}}} - 1 \right) \right\} = I'_e \exp \left\{ -b_1 \frac{r}{r_{\text{eff}}} \right\}. \quad (1.19)$$

The observed surface brightness profiles of the disks of spiral galaxies tend to follow such an exponential law, as already shown by de Vaucouleurs (1959) and Freeman (1970). While the disks follow an exponential surface brightness profile, the bulges of those late-type galaxies behave similar to early-type galaxies, following a Sérsic profile with small Sérsic indices of about  $2 < n < 4$ .

Thus, the Sérsic index which describes a galaxy, is a good measure for the type of galaxy, with late-type galaxies having smaller Sérsic indices and early-type galaxies having larger Sérsic indices. This has been shown for example for SDSS galaxies (Maller et al., 2009) as well as for galaxies in the GAMA survey (Lange et al., 2015).

Since the stellar outskirts of galaxies are faint due to the low densities and the lack of young stars, it is difficult to directly measure the total luminosity  $L$  of a galaxy. Thus, one approach that is often used in observations is to fit one of the above profiles to the measured surface brightness profile and calculate the total luminosity from the integral of the fitted surface brightness profiles as

$$L = \int I(r) d^2r. \quad (1.20)$$

With this method, it is possible to effectively eliminate the background brightness from the measurement of the total luminosity of a galaxy.

### 1.4.2 Radial Density Profiles: Deprojecting Observations

To describe the intrinsic three-dimensional structure of a galaxy, it is useful to construct models of galaxies for which it is possible to analytically calculate the depth and shape of the potential well and the velocity distributions from the intrinsic mass density distribution. The two-dimensional projections of those models should furthermore fit the properties of observed galaxies. There are several different models discussed in the literature, of which we will in the following present those that will

be important in the course of this work. All of the commonly used models assume the systems to be spherically symmetric, and in an equilibrium state. While it is known from observations that most systems are more likely (slightly) elliptical or even triaxial, those models are still a good first approximation. Since their properties can be solved analytically in most cases, which is not the case for most triaxial and elliptical models, they are nevertheless a useful tool to understand the properties of the potentials and the mass (and light) distributions of galaxies.

### Single Power Law Profiles: An Isothermal Sphere

A first simple approach to model the density distribution of a spheroidal galaxy is to assume a density which constantly decreases with radius. In this case, the density can be described by a power law of the form

$$\rho(r) = \rho_0 \left( \frac{r}{r_s} \right)^\gamma, \quad (1.21)$$

with the characteristic density  $\rho_0$  and the power law slope  $\gamma < 0$ . The special case of  $\gamma = -2$  is called the singular isothermal sphere:

$$\rho_{\text{Iso}}(r) = \rho_0 \left( \frac{r}{r_s} \right)^{-2}. \quad (1.22)$$

Using the fact that the mass distribution can be calculated from the density profile as

$$M(r) = 4\pi \int_0^r r'^2 \rho(r') dr', \quad (1.23)$$

the rotational velocity profile of the isothermal sphere equals

$$v_{\text{circ}}^2 = \frac{G M(r)}{r} = 4\pi G \rho_0 r_s^2. \quad (1.24)$$

Thus, the rotational velocity of the isothermal sphere is constant at all radii. One benefit of the single power law profiles is that they can be easily transformed from two to three dimensions and vice versa as  $\rho_{2D} \propto r^{\gamma-1}$ .

While it is possible to always find a radius range in the observed surface brightness profiles of observed galaxies where a single power law profile is a good fit, the full radius regime usually cannot be fit by a single power law profile. Nevertheless, the rotational velocity profile of the isothermal sphere is flat, which resembles the observations. Since the observed rotational velocity profiles reflect the contributions of all mass components of a galaxy, i.e., the luminous and dark matter, this could indicate that the total (stellar and dark matter) radial density profile can be described by a single power law profile, even if the individual components alone follow different laws. One of the main goals of this thesis is to address this issue, and to understand the interplay between the dark and luminous components of (spheroidal) galaxies.

### Double Power Law Profiles

As the single power law is not sufficient in describing the full radius range of the observed surface brightness profiles, double (broken) power laws have been discussed to solve the issue. These double

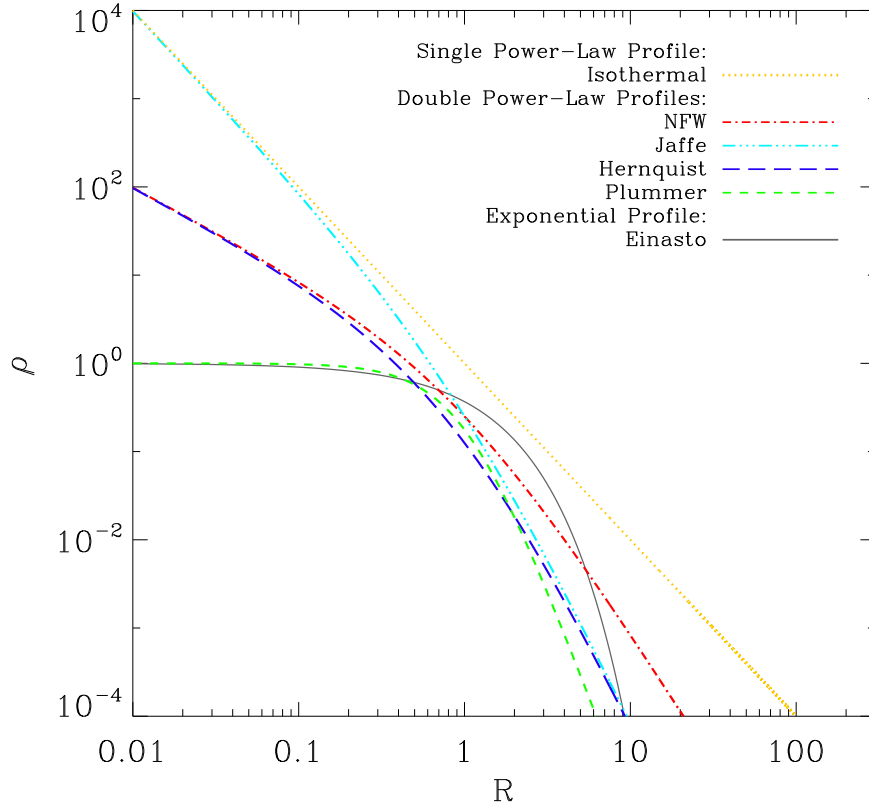


**Figure 1.10:** Examples for the different radial density profiles, normalized to  $\rho_0 = 1$  and  $r_s = 1$ , and  $\alpha = 1$  in case of the Einasto profile. Shown are the profile of the singular isothermal sphere (yellow dotted line), the Plummer profile (green dashed line), the Jaffe profile (cyan dash-dot-dot-dotted line), the Hernquist profile (blue long-dashed line), the NFW profile (red dash-dotted line) and the Einasto profile (grey solid line).

power laws are generally given by

$$\rho(r) = \frac{\rho_0}{\left(\frac{r}{r_s}\right)^{\beta_1} \left(1 + \left(\frac{r}{r_s}\right)^{\beta_3}\right)^{(\beta_2 - \beta_1)/\beta_3}}, \quad (1.25)$$

with  $\rho_0$  the characteristic density and  $r_s$  the scale radius. They follow one power law with  $\rho \propto r^{-\beta_1}$  in the inner part and a second power law with  $\rho \propto r^{-\beta_2}$  in the outskirts with a smooth transition in the mid-radius regime. The third exponent  $\beta_3$  measures the sharpness of the transition.

As for the isothermal sphere, the broken power laws also only apply to spherically symmetric systems in equilibrium. The most commonly used profiles, for which the corresponding mass and gravitational potentials have analytical expressions, are:

- **The Plummer Profile:** Already before the first measurements of the surface brightness profiles of extragalactic nebula, Plummer (1911) presented a profile to describe the radial density

distribution of stars in globular clusters:

$$\rho_{\text{Plum}}(r) = \frac{\rho_0}{\left(1 + \left(\frac{r}{r_s}\right)^2\right)^{\frac{5}{2}}}. \quad (1.26)$$

This is a broken power law profile with exponents  $\beta_1 = 0$ ,  $\beta_2 = 5$ , and  $\beta_3 = 2$ . It has a flat inner core and decreases steeply outside of the scale radius  $r_s$ , as shown as green dashed line in Fig. 1.10.

- **The Jaffe Profile:** One of the first intrinsic profiles to describe the density distributions of spheroidal galaxies and bulges was introduced by Jaffe (1983):

$$\rho_{\text{Jaffe}}(r) = \frac{\rho_0}{\left(\frac{r}{r_s}\right)^2 \left(1 + \frac{r}{r_s}\right)^2}. \quad (1.27)$$

This profile, with  $\beta_1 = 2$ ,  $\beta_2 = 4$ , and  $\beta_3 = 1$ , has an inner slope which is identical to the isothermal sphere, but steepens at the outskirts to fall off with a power law slope of  $-4$  (cyan dash triple-dotted line in Fig. 1.10). In projection, this profile is similar to the de Vaucouleurs  $R^{1/4}$  profile in the outskirts but deviates strongly in the inner parts. With its steep inner slope it resembles the power-law-excess-galaxies and is therefore sometimes still used today to model less massive spheroidals, however, it is not sufficient to describe the more massive, cored galaxies.

- **The Hernquist Profile:** In 1990, L. Hernquist introduced a density profile that resembled the de Vaucouleurs  $R^{1/4}$  profile better than the Jaffe profile (Hernquist, 1990). The equation he presented was

$$\rho(r) = \frac{M r_s}{2\pi r} \frac{1}{(r + r_s)^3}, \quad (1.28)$$

which can be rewritten as

$$\rho_{\text{Hern}}(r) = \frac{\rho_0}{\frac{r}{r_s} \left(1 + \frac{r}{r_s}\right)^3}, \quad (1.29)$$

with  $\beta_1 = 1$ ,  $\beta_2 = 4$ , and  $\beta_3 = 1$  (blue long dashed line in Fig. 1.10). For the Hernquist profile, the stellar half-mass radius (i.e., the radius which contains half of the stellar mass of a galaxy) can be calculated from the scale radius as  $r_{1/2} = (1 + \sqrt{2})r_s$ . With its excellent resemblance of the de Vaucouleurs  $R^{1/4}$  profile in projection it is the density profile which is most commonly used to especially model the mass distributions of the bulges in late-type galaxies, but also massive ellipticals. The effective radius  $r_{\text{eff}}$ , which can be calculated from the de Vaucouleurs  $R^{1/4}$  profile, can thus be calculated directly from the Hernquist profile as  $r_{\text{eff}} \approx 1.8153 r_s \approx 3/4 r_{1/2}$  (Hernquist, 1990). Both, the Jaffe and the Hernquist profiles, are part of the family of **Dehnen profiles**, which include all density profiles with  $\beta_2 = 4$  and  $\beta_3 = 1$ , and an arbitrary  $\beta_1$  (Dehnen, 1993). Generally, properties like mass distribution and intrinsic velocity dispersion can be solved analytically for many Dehnen models (especially with  $0 \leq \beta_1 \leq 3$ ), in some cases even for the projected properties (e.g.,  $\beta_1 = 0, 1, 2$ ), which makes those models particularly useful for modeling galaxies.

- **The NFW Profile:** The previously discussed profiles were all motivated by the wish to analytically model the observed surface brightness profiles of galaxies (or stellar clusters), and intended to understand the distribution and behaviour of the luminous matter in galaxies. Using cosmological  $N$ -Body dark-matter-only simulations, Navarro et al. (1996, 1997) found that the radial density distributions of dark matter halos in their simulations could always be fitted by profiles of a similar shape. The profile they presented is

$$\rho_{\text{NFW}}(r) = \frac{\rho_0}{\frac{r}{r_s} \left(1 + \frac{r}{r_s}\right)^2}, \quad (1.30)$$

which resembles a double power law profile with  $\beta_1 = 1$ ,  $\beta_2 = 3$ , and  $\beta_3 = 1$ . In contrast to the Jaffe and Hernquist profiles, the NFW profile has a total mass that diverges logarithmically for  $r \rightarrow \infty$ , while it is similar to the Hernquist profile at small radii (see red dash-dotted line in Fig. 1.10). Interestingly, as shown by Navarro et al. (1996), the two free parameters of the NFW profile,  $\rho_0$  and  $r_s$ , are correlated. Thus, calculating the radius within which the density of the dark halo is larger than 200 times the critical density of the Universe ( $\rho_{\text{crit}}$ ) and thus the mass of the halo within this radius  $r_{200}$ , enables to define a concentration parameter  $c_{\text{NFW}}$

$$c_{\text{NFW}} \equiv \frac{r_{200}}{r_s}. \quad (1.31)$$

For a given mass of a halo, this concentration parameter is nearly the same for all halos, and it decreases with increasing mass, indicating that more massive dark matter halos are less concentrated than less massive ones. This has been confirmed by observations of the hot gas content in galaxy clusters through its X-ray emissions by Pointecouteau et al. (2005), who also found a decreasing concentration parameter of their best-fitting NFW profile with cluster mass. Those observations of X-ray properties of galaxy clusters have furthermore confirmed that the NFW profile is generally a proper description of the density profiles of galaxy clusters (e.g., Pratt & Arnaud 2005; Pointecouteau et al. 2005).

In summary, the double power law profiles can, in their projected form, successfully explain some of the observed surface brightness profiles: the Hernquist profile is, in projection, a good approximation to the de Vaucouleurs  $R^{1/4}$  profile, and the Plummer profile can describe (in some cases) the density distribution of globular clusters. The NFW profile seems to be a good description of the dark matter density distributions, as indicated for example by strong lensing observations of galaxy clusters. However, none of the profiles can actually mimic the Sérsic profile which has been most successful in describing the surface brightness profiles of observed spheroidals.

### A More Realistic Approach: Exponential Profiles

None of the double power law profiles can mimic all configurations of the Sérsic profile because the Sérsic profile has three free parameters, and with the Sérsic index  $n$  it has a parameter which modifies the curvature of the profile and thus the profile is not limited to one clear shape as it is the case for the single and double power-law profiles. A similar, however three dimensional, profile was introduced by Einasto (1965) in an approach to fit stellar profiles of galaxies like Andromeda and the Milky Way

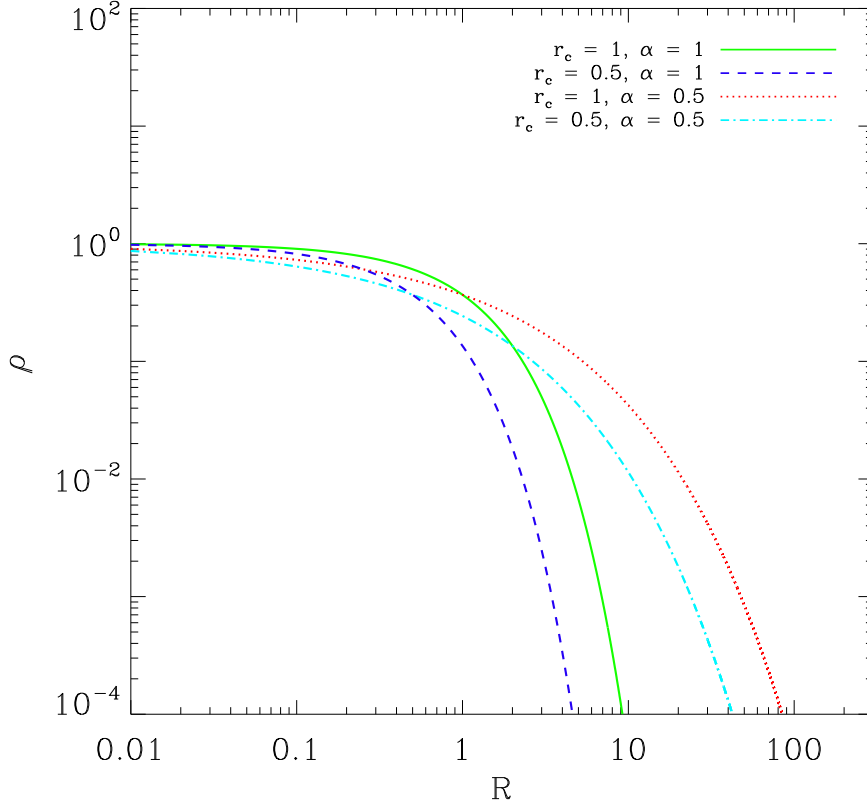


**Figure 1.11:** The Einasto profile for four different combinations of the free parameters  $r_c$  and  $\alpha$ , with the third free parameter,  $\rho_0$ , is fixed to the value of  $\rho_0 = 1$  for all test cases since it only shifts the profile in vertical direction. The green solid line shows the Einasto profile for  $r_c = 1$  and  $\alpha = 1$ , as in Fig. 1.10. The blue dashed line shows the profile for a smaller core-radius of  $r_c = 0.5$  and  $\alpha = 1$ , the profile with  $r_c = 1$  and  $\alpha = 0.5$  is shown as red dotted line, and  $r_c = 0.5$  and  $\alpha = 0.5$  is shown as cyan dash-dotted line. As can be seen, the scale radius shifts the profile in horizontal direction, while the power-law slope parameter  $\alpha = 1$  determines the profiles curvature.

(Einasto, 1974). The **Einasto profile** is characterised by its power-law logarithmic slope  $\alpha_{\text{Ein}}$ :

$$\rho_{\text{Ein}}(r) = \rho_0 \exp\left\{-\left(\frac{r}{r_c^{\text{Ein}}}\right)^{\alpha_{\text{Ein}}}\right\}, \quad (1.32)$$

where  $\rho_0$  is the central density and  $r_c^{\text{Ein}}$  is the radius at which the density has decreased to  $1/e$  of its central value (see also Retana-Montenegro et al., 2012). For  $\rho_0 = 1$ ,  $r_c^{\text{Ein}} = 1$  and  $\alpha_{\text{Ein}} = 1$ , the Einasto profile has a flat inner part similar to the Plummer profile, while it bends towards very steep slopes at large radii, steeper than all other three-dimensional profiles discussed before, as shown as grey solid line in Fig. 1.10.

Fig. 1.11 shows how the profile changes if the parameters are varied: A smaller core radius  $r_c^{\text{Ein}} = 0.5$  causes only a shift in horizontal direction towards smaller radii (blue dashed line). A smaller curvature parameter  $\alpha_{\text{Ein}} = 0.5$ , on the other hand, significantly changes the curvature of the

profile (red dotted line). The smaller  $\alpha_{\text{Ein}}$ , the less strongly curved is the radial density profile, and the shallower the outer halo. This is similar to the observations for the correlation between the compactness of a spheroidal galaxy and its Sérsic index obtained from the Sérsic fit to the surface brightness, with more compact spheroidals having smaller Sérsic indices, as  $\alpha_{\text{Ein}}$  behaves like  $1/n$ .

While originally introduced to describe stellar systems, the most common present-day application of the Einasto profile is to describe the distribution of the dark matter halos. This originates from the fact that it has been shown in several studies to be a better fit to the simulated dark matter distributions than the NFW profile (Merritt et al., 2006; Gao et al., 2008; Stadel et al., 2009; Navarro et al., 2010; Klypin et al., 2014), especially for the most massive structures. Observations of galaxy clusters using strong and weak lensing, for example, have shown that the dark matter density distribution in those clusters is shallower in the center than predicted by the standard NFW profile (Newman et al., 2013). This flatter inner cores, however, can be well described by an Einasto profile, as shown in Fig. 1.10 (see also Sereno et al. 2015). This is also supported by theoretical work of Navarro et al. 2004, 2010, who also showed that the Einasto profile is, especially in the inner parts, a better fit to the dark matter profiles of simulated halos.

On the downside, the Einasto model does not have analytic solutions for many of its properties. One approach to clarify this matter, especially in the light of strong lensing detections, is presented by Retana-Montenegro et al. (2012), but there is still no simple transformation of the three dimensional to the two dimensional projected profile, which would be necessary to compare the results from the Einasto profile fits directly with the Sérsic profile fits and apply the Einasto model to the radial density distributions of the luminous matter in galaxies. However, with new advanced simulations including baryons, a more direct approach using stellar radial density profiles of galaxies simulated in a cosmological context will enable a comparison between the observations and theoretical models, which is another major goal of this work.

## 1.5 Elliptical Galaxies: Scaling Relations

The main focus of this thesis is on early-type galaxies and the understanding of the imprints of their formation histories in their present-day properties. Thus, in the last section of this chapter, the key relations between their properties at present day and higher redshifts will be presented from an observational point of view, followed by a short introduction of our current understanding of how early-type galaxies form, evolved from a combined approach of observations and simulations. From the morphology-density relation it was already introduced that spheroidal galaxies are more common in denser environments. In addition, the most massive galaxies in the Universe are ellipticals, which implies that the mechanisms that lead to the formation of spheroidal galaxies must be present at all mass scales, from dwarf to giant galaxies. Especially in the light of the huge mass range which is covered by this type of galaxies, one of the most interesting questions is whether the observed relations between their different properties like mass, size, luminosity and velocity dispersion, are the same at all mass ranges and whether or not they change with time.

### 1.5.1 Properties at Present Day

Probably the best-known relation between two key properties of early-type galaxies is the **Faber-Jackson relation**, which describes the correlation between the luminosity  $L$  of a galaxy and its (line-of-sight) velocity dispersion  $\sigma$  to be  $L \propto \sigma^4$  (Faber & Jackson, 1976). This basically means that

more luminous galaxies have larger velocity dispersions, that is they are less strongly supported by rotation. For the most massive spheroidals, a similar result was found by Emsellem et al. (2011) for the Atlas<sup>3D</sup> survey, where they showed that the most massive galaxies are the slow rotators. However, in the Atlas<sup>3D</sup> survey no general correlation between the rotational properties and the mass of the spheroidals was found.

The Faber-Jackson relation, however, has turned out to be a projection of a much more fundamental relation valid for early-type galaxies: the **Fundamental Plane**. This was introduced by Jorgensen et al. (1996), and it describes the relation between three basic galaxy properties, effective radius  $r_{\text{eff}}$ , central velocity dispersion and the mean surface brightness within the effective radius  $\langle I \rangle_e$ . In its general form, the Fundamental Plane can be written as

$$\log r_{\text{eff}} = a \log \sigma + b \log \langle I \rangle_e + \text{const.} \quad (1.33)$$

The two free parameters,  $a$  and  $b$ , depend on the waveband in which the luminosities of the galaxies are measured. For example, Jorgensen et al. (1996) found for  $r$ -band luminosities that  $a = 1.24 \pm 0.07$  and  $b = -0.82 \pm 0.02$ . Bernardi et al. (2003) found similar values for early-type galaxies from the SDSS survey and showed that the Fundamental Plane is also similar in  $i$ ,  $g$  and  $z$ . More recently, La Barbera et al. (2010a) presented results on a Fundamental Plane study from the SPIDER survey, which contains observations in even more wavebands (grizYJHK), and found that the parameter  $a$  varies between  $a = 1.38 \pm 0.02$  in  $g$ -band to  $a = 1.55 \pm 0.02$  in  $K$ -band, while the variance in  $b$  is negligible. They also presented the Faber-Jackson relation for those wavebands, showing that the slope of the relation is similar for all wavebands. In addition, La Barbera et al. (2010c) presented strong indications of a dependence of the Fundamental Plane on the density of the environment.

A similar relation is found if the stellar mass surface density  $\Sigma_* = M_*/2\pi r_{\text{eff}}^2$  of the galaxies is used instead of the surface brightness  $\langle I \rangle_e$ . This relation is thus called the **mass-Fundamental Plane** (Hyde & Bernardi, 2009; Bezanson et al., 2013a):

$$\log r_{\text{eff}} = a_m \log \sigma + b_m \log \Sigma_* + \text{const}_m. \quad (1.34)$$

The right panel of Fig. 1.12 shows the mass-Fundamental Plane at present day, as presented by Bezanson et al. (2015), for quiescent (red) and star-forming (blue) galaxies separately. As can be clearly seen, there is basically no difference between the mass-Fundamental Planes of both types of galaxies. Hyde & Bernardi (2009) also showed from the scatter of the mass-Fundamental Plane is smaller than the scatter found for the Fundamental Plane, for all wavebands.

There is one more scaling relation which needs to be considered: the **stellar mass-size relation**. This relation exists for both early- and late-type galaxies, as shown for the SDSS sample of galaxies already by Shen et al. (2003). For the elliptical galaxies, this relation can be written as:

$$r_{\text{eff}} = r_0 \left( \frac{M_*}{10^{11} M_\odot} \right)^\zeta, \quad (1.35)$$

with  $\zeta = 0.56$  and  $r_0 = 4.16$  kpc for SDSS spheroidals (Shen et al., 2003; van de Sande et al., 2013). The grey scatter plot on the left panel of Fig. 1.12 shows the mass-size relation and its scatter as obtained from the SDSS survey. At a given mass, late-type galaxies have larger radii than early-type galaxies of the same mass (see Fig. A.5 for the mass-size relations of both late- and early-type galaxies). This is basically seen for all stellar masses but the very high mass end, however, at that mass range there are nearly no late-type galaxies. Baldry et al. (2012) studied the mass-size relation

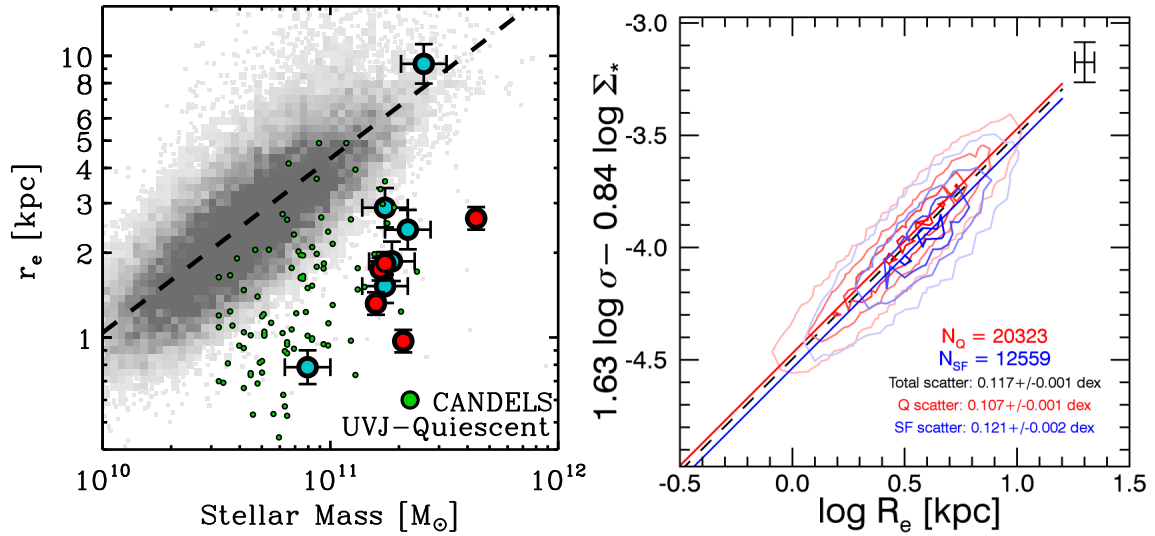


**Figure 1.12:** *Left panel:* Fig. 13a from van de Sande et al. (2013): Mass-size relation for early-type galaxies at present day from SDSS (grey scatterplot). Higher redshift observations from CANDELS at  $1.4 < z < 2.1$  are shown as green circles, while the red (cyan) filled circles show observations presented by van de Sande et al. (2013) (Bezanson et al. 2013b) at  $1.5 < z < 2$  ( $z \approx 1.5$ ). *Right panel:* Fig. 11a from Bezanson et al. (2015): Mass Fundamental Plane for quiescent (red) and star-forming (blue) galaxies at  $z = 0$  from a sample of galaxies selected from the SDSS survey.

for galaxies from the GAMA survey, which focusses on smaller mass galaxies, and find a tilt at the low mass end for early-type galaxies compared to the relation found from SDSS galaxies by Shen et al. (2003). However, in a recent re-analysis of the galaxy sample from SDSS, Mosleh et al. (2013) found a flattening of the mass-size relation for early-type galaxies for masses below  $M \leq 4 \times 10^{10} M_\odot$ , similar to the results from the GAMA survey. Nevertheless, even at low masses, blue late-type galaxies still are larger than their early-type counterparts of equal mass. The mass-size relation for spirals and ellipticals also holds in the lowest density environment, as shown by Fernández Lorenzo et al. (2013), who found that the mass-size relation for their sample of isolated spheroidals from the AMIGA survey is in excellent agreement with the relation found by Shen et al. (2003).

## 1.5.2 Properties at Higher Redshifts

Recently, with the advent of new techniques to observe objects even at high redshifts, a continuously growing number of galaxies at high redshifts have been detected. While for those galaxies at extremely high redshifts up to  $z = 10$  (Bouwens et al., 2011) in the Hubble Ultra Deep Field a detailed analysis of morphology or dynamical and kinematic properties is not possible, this can be done for galaxies up to redshifts of about  $1 < z < 3$ . Properties like dynamical mass, stellar mass, star formation rate and radial extend of individual or small samples of early-type galaxies within this redshift range have lately been studied by several authors (e.g., van Dokkum et al., 2009; van de Sande et al., 2011; Bezanson et al., 2013b; van de Sande et al., 2013), with the currently highest redshifted early-type galaxy having a spectroscopic redshift of  $z \approx 3.35$  (Marsan et al., 2015). In addition, large surveys of galaxies at redshifts of  $1 < z < 3$  have enabled the statistical analysis of global properties like

luminosity, mass or size of (early-type) galaxies for larger samples of objects (e.g., Trujillo et al., 2006; Williams et al., 2010; Fernández Lorenzo et al., 2011; Szomoru et al., 2012, 2013; van der Wel et al., 2014, and references therein). There is a growing body of literature in this field of research, especially focussing on the properties of high-redshift early-type galaxies, their possible progenitors and the question which galaxies at present day have been evolving from such spheroidal galaxies at high redshifts.

With those data sets available, the evolution of the scaling relations found at present day, can be studied. As suggested by Holden et al. (2010) and Fernández Lorenzo et al. (2011) for redshifts up to  $z \approx 1$ , and more recently by van de Sande et al. (2014) for redshifts of  $z \approx 2$ , the Fundamental Plane is already in place at those redshifts, however, it is shifted with respect to the present-day Fundamental Plane towards higher values of  $a_m \log \sigma + b_m \log \Sigma_*$  for the same value of  $\log r_{\text{eff}}$ . Nevertheless, they do not report strong indications for a tilt of the plane, although the data from Fernández Lorenzo et al. (2011) might indicate such a slight tilt. Similarly, Bezanson et al. (2015) showed that, at  $z \approx 0.7$ , the mass-Fundamental Plane was also in place but shifted towards higher values. This indicates that, at higher redshifts, the velocity dispersions of (early-type) galaxies are higher compared to those of (early-type) galaxies of the same mass at present day (Bezanson et al., 2015). In addition, the shift of the Fundamental Plane at higher redshift also implies that there are very compact and bright galaxies at high redshift, for which there are nearly no counterparts at present day (Fernández Lorenzo et al., 2011).

This tendency, that galaxies of the same mass are more compact at higher redshifts than at present day is visible also in the shift of the mass-size relation for both quiescent (early-type) and star forming (late-type) galaxies (e.g., Williams et al. 2010 for all types of galaxies and Szomoru et al. 2012 for a sample of early-type galaxies at about  $z = 2$ ), however, at all redshifts the late-type galaxies are larger than the early-type galaxies of the same mass. The colored symbols in the left panel of Fig. 1.12 show examples of the mass-size relation of early-type galaxies at higher redshifts, as presented by van de Sande et al. (2013). The mass-size relation evolves such that, at a given mass, the size of the galaxy is proportional to the redshift as

$$r_{\text{eff}} \propto (1+z)^\epsilon, \quad (1.36)$$

with  $\epsilon$  varying from study to study due to the scatter, which is large. For example, Trujillo et al. (2006) report  $\epsilon = -0.40 \pm 0.06$ , Szomoru et al. (2012) report  $\epsilon = -0.94 \pm 0.16$ , van de Sande et al. (2013) find a value of  $\epsilon = -1.02 \pm 0.05$ , while van der Wel et al. (2014) present an even larger value of  $\epsilon = -0.48 \pm 0.06$  for their early-type galaxies. The latter cover the largest redshift range with their study, up to  $z = 3$ . They also report that the number density of compact ( $r_{\text{eff}} < 2$  kpc) early-type galaxies with stellar masses  $M > 10^{11} M_\odot$  increases between  $z = 3$  and  $z = 1.5 \dots 2$ , followed by a strong decrease at lower redshifts.

Interestingly, compact galaxies with  $r_{\text{eff}} < 2$  kpc at redshifts of  $z \approx 2$ , even if they are relatively massive ( $M_* > 10^{10.8} M_\odot$ ), cover a similar range in ellipticities as present-day early-type galaxies, however, many of them are disk dominated (van der Wel et al., 2011; Chevance et al., 2012). This becomes especially evident if the Sérsic indices of those high redshift compact galaxies are compared to the distributions of present-day Sérsic indices for early and late-type galaxies. As shown by Chevance et al. (2012), most of the high redshift compact galaxies have Sérsic indices which closely resemble those found for present-day late-type galaxies and differ strongly from the distribution of Sérsic indices found for present-day early-types. Most of the galaxies studied by Chevance et al. (2012) have Sérsic indices around  $2 < n < 3$ , while typical early-type galaxies at present day usually have Sérsic

indices of about  $4 < n < 6$ . However, as shown by Szomoru et al. (2012), Sérsic profiles are good fits to the observed surface brightness profiles of high redshift compact galaxies.

These differences in the properties of low and high redshift early-type galaxies suggest that the formation mechanisms at high redshifts vary from those channels of early-type formation which are dominant at present day. One interesting approach to understand those differences is to study present-day early-type galaxies which have similar properties as those at high redshifts, as local galaxies are much easier to study in great detail. One such sample of present-day counterpart of the high redshift compact galaxies was studied by Saulder et al. (2015), however, they found that all counterpart galaxies in their sample have too low masses compared with the high redshift compact galaxies.

Recently, it has been shown that minor mergers actually play a crucial role for the formation of early-type galaxies, as minor merger events can grow a compact spheroidal into a more extended spheroidal without adding a tremendous amount of mass (e.g., Hilz et al., 2012, 2013). This can successfully explain the evolution of the mass-size relation of galaxies, however, it is also evident that minor mergers cannot be the only channel to grow spheroidal galaxies, as many present-day early-type galaxies most likely have not been spheroidals at high redshifts. Nevertheless, it can explain why we do not see many compact massive galaxies today, since those galaxies live usually in dense environments, as shown by the morphology-density relation, where minor merger events are a common event.

In addition, gas physics and accretion of gas are much more dominant at high redshifts than at low redshifts, and the channels of gas accretion should be considered as well. Dekel & Birnboim (2006) proposed that galaxies at high redshifts are fed by streams of cold gas which can penetrate the halo and feed the central galaxy unless the halo is not too massive. Once the halo is too massive, the streams are shock-heated by its hot gas atmosphere, and the cold stream breaks down, leading to a starvation of the galaxy. This idea is supported by Dekel et al. (2009), who showed simulations of such streams, suggesting that streams are especially important to explain the different morphologies of galaxies and the observed  $z = 2$  extended, massive, star-forming galaxies (e.g., Genzel et al., 2008; Förster Schreiber et al., 2009, 2011). In this scenario, those extended gas disks can collapse in their central parts and might even be able to form bulges without merger events being involved, thus only through secular evolution.

In this context, recent simulations of spheroidal galaxies aim at a more cosmologically driven evolution scenario: Oser et al. (2010, 2012) used zoom simulations of halos selected from a cosmological parent simulation to study the formation of spheroidals in a more physical scenario. They suggested a two-phase formation scenario: At high redshifts of  $z \gtrsim 2$ , galaxy formation is driven by the accretion of cold gas which leads to a high star formation rate inside the galaxy. These stars, which are formed inside the parent galaxy, are called “in-situ” stars. This gas dominated phase is subsequently followed by an accretion dominated phase of galaxy growth, where the mass growth is dominated by merging of the parent galaxy with small or large structures, while the gas plays a less dominant role. We will show in Chap. 4 that these galaxies used by Oser et al. (2010) also successfully reproduce the observed mass-size evolution.

However, isolated simulations of galaxy formation are always biased due to the applied selection criteria. Therefore, the newest set of simulations introduced to study galaxy formation in a cosmological context while simultaneously providing a statistically relevant sample of all morphological kinds of galaxies, are fully hydrodynamic cosmological simulations. One of the first of such simulations was the set of OWLS simulations (Schaye et al., 2010), with their main focus on understanding the impact of different subgrid physics, especially the feedback processes, on galaxy formation and evo-

lution. More recently, three new simulation sets are available which are dedicated to understand the formation of galaxies in the Universe, the Eagle simulations Schaye et al. (2015), the Illustris simulations (Vogelsberger et al., 2014), and the Magneticum Pathfinder simulations (Hirschmann et al., 2014; Remus et al., 2015a; Teklu et al., 2015b). Since this thesis involves analysing the properties of spheroidal galaxies formed in several different types of simulations, from isolated binary merger via cosmological zoom simulations to full cosmological boxes, the following chapter will be dedicated to introducing the different simulation methods in detail.

## Chapter 2

# Numerical Simulations: From Isolated Mergers to Magneticum

To study the formation and evolution of any structure in the universe it is necessary to follow its growth through cosmic time. However, observations can only provide a snapshot of one single moment in the object's lifetime. Since most processes in the universe evolve on timescales that are much longer than a human lifetime, it is nearly impossible to observe the evolution of any object in an astronomer's life, especially regarding massive galaxies. Thus, in order to understand the evolution and formation history of a galaxy, simulations are a valuable tool.

The need for this kind of evolutionary study arose even before computers were invented, and thus the first "simulation" aiming at understanding the origin of galaxies with peculiar structures was not a calculation on a computer but an experiment with light bulbs done by Erik Holmberg in 1941 (Holmberg, 1941). Holmberg used 74 light bulbs to simulate the gravitational interactions between two "disk" galaxies, each of them consisting of 37 bulbs. The light intensity is assumed to be proportional to the mass of each "mass element" represented by a bulb, and the gravitational forces are measured using photometry of the experiment at each timestep. The position of the bulbs is changed according to the gravitational forces measured this way, and thus the evolution of the system is simulated. With this experiment, Holmberg already found that the tidal interactions between two disk galaxies cause tidal arms, and he was able to explain some of the peculiar structures already observed in merging systems at that time. The left panel of Fig. 2.1 shows a snapshot from this "simulation", presented as Fig. 4 by Holmberg (1941).

It took a few years until the first real simulations started the era of computational astrophysical studies of galaxies. Best known are the simulations presented by Toomre & Toomre (1972) and Toomre (1974), where the authors presented simulations of two merging disk galaxies performed with a few hundred particles to understand the origin of what is known today as tidal tails and bridges, caused by the gravitational interaction of systems in the process of merging. Astonishingly, their results showed that the work Holmberg had done 30 years earlier with his graphical integrations turned out to be surprisingly accurate in its explanation of the origin of the tail structures. Fig. 2.1 demonstrates this by showing Holmberg's results on the left side and the result from a similar setup presented by Toomre (1974) (Fig. 9 therein) on the right side.

With increasing computational power, higher resolutions and larger simulations became possible, opening the doors to extended studies of merging systems with the aim to explain the peculiar shapes

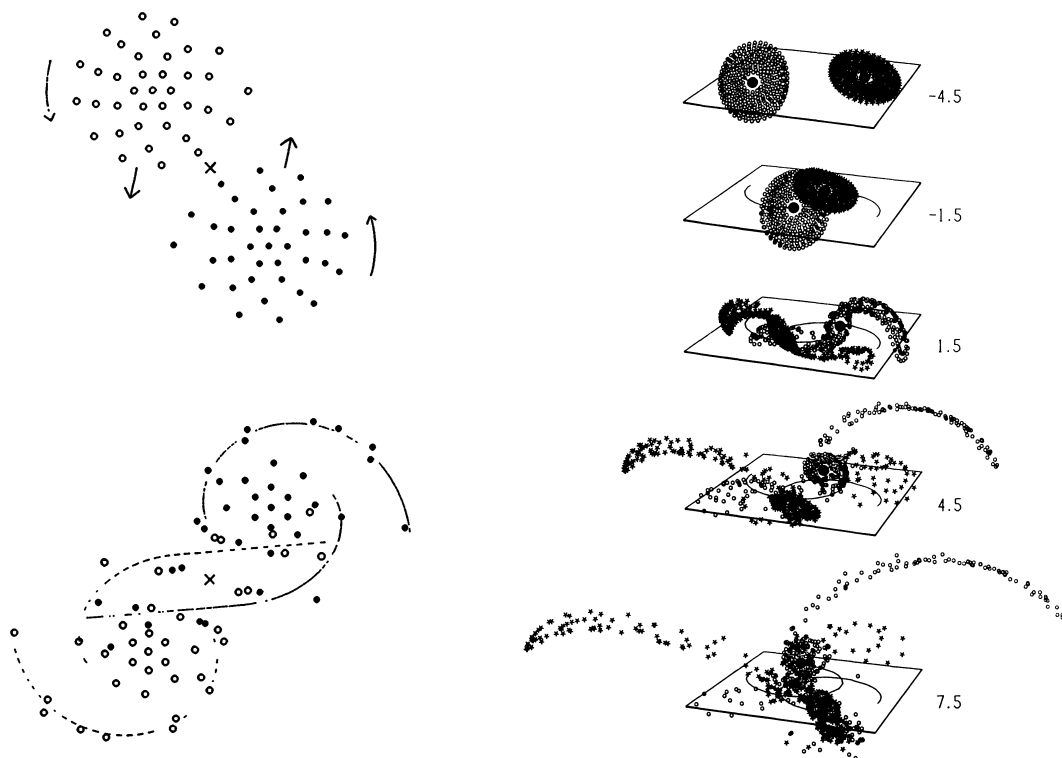


**Figure 2.1:** *Left panel: Fig. 4 taken from Holmberg (1941). “Merger” event from the flashbulb experiment. The upper part shows the initial setup of the flashbulbs with the direction in which the “disks” move and rotate, the lower panel shows the mixing that occurs in the first encounter of both disks. Right panel: Fig. 9 taken from Toomre (1974). Merger event of the simulation of two disk galaxies. The middle panel shows the stage of the first encounter, similar to the lower part of the figure in the left hand panel. In the lower panels, the tidal arms are clearly visible while the merger evolves.*

observed in several galaxies as presented for example by Arp (1966). Explanations were provided for several of those peculiarities, including ring-galaxies like Hoag’s Object (e.g., Bournaud & Combes, 2003), the Mice galaxies (e.g., Toomre & Toomre, 1972), or the Antennae system (e.g., Toomre & Toomre, 1972; Karl et al., 2010; Kotarba et al., 2010; Karl et al., 2013) and the effects of gas on the merging structures (e.g., Mihos & Hernquist, 1996). Another interesting suggestion was made by Toomre (1977) who proposed that elliptical galaxies can be produced by a merger between two spiral galaxies. This was studied subsequently in an extensive amount of simulations with more realistic models for the initial disk galaxies, for example White (1978, 1979a,b); Gerhard (1981); Negroponte & White (1983); Barnes (1988), later on also including additional physics (Hernquist, 1989; Barnes & Hernquist, 1996; Springel, 2000; Naab & Burkert, 2003; Springel et al., 2005a; Naab et al., 2006a; Cox et al., 2006; Burkert et al., 2008; Johansson et al., 2009a,b; Bois et al., 2010, 2011; Novak et al., 2012).

Those studies significantly broadened our understanding of merger processes in the universe, but with even more powerful computers and advanced simulation codes the need of understanding structure formation in a cosmological context grew. With the Millenium simulation, Springel et al. (2005c)

provided a large “universe” made inside a computer, even if it was a dark-matter-only universe still lacking baryons. This simulation has been used in hundreds of studies to understand gravitational cosmological processes on all scales, from galaxy merger histories to the evolution of the large scale structure. Already much earlier, re-simulations of selected halos from similar dark-matter-only simulations with higher resolutions and additional baryonic physics (e.g., Katz & White, 1993; Navarro & White, 1994; Bartelmann & Steinmetz, 1996; Dolag et al., 1999; Steinmetz & Navarro, 1999; Borgani et al., 2006) introduced interesting new ways to understand the evolution of galaxies, but also added new computational challenges in the form of proper inclusion of gas physics to the spectrum of problems addressable with the power of computation. This is an ongoing process, which just recently advanced to a new state with brand new, fully hydrodynamical cosmological simulations like Illustris (Vogelsberger et al., 2014), Eagle (Schaye et al., 2015) and Magneticum (Dolag et al., in prep), with the latter being in the focus of several analyses presented in this work.

## 2.1 The Tree-SPH Code Gadget

In galactic astrophysics, two different kinds of code types dominate the field: Eulerian grid codes and Lagrangian particle codes with smoothed particle hydrodynamics (SPH). In grid codes, the simulation volume is divided into cells, and all physical processes are treated as fluxes between the cells. In those codes, mixing between gas phases of different temperatures happens implicitly, but at high Mach numbers there exist problems with the Galilean invariance. In addition, adding gravity to the codes is somewhat difficult since no direct particle interactions can be calculated. This is especially problematic in simulations of dark matter and stars, since those components are collisionless. In contrast, SPH codes treat all physics as particle-particle interactions, sampling the hydrodynamical properties and using hydrodynamic equations in their Lagrangian form to calculate the dynamical interactions. In order to avoid diverging forces if the distances between two particles become very small, the gravitational interactions are (gradually) suppressed on small scales. This scale is called the softening length. SPH codes are Galilean invariant, and the self-gravity of the gas is treated naturally with the same accuracy as for the stars and dark matter which interact directly through gravity. However, the mixing of gas phases with different temperatures is completely suppressed, and artificial viscosity needs to be added at the particle level to improve the description of the gas physics and to accurately follow shocks. Recently, a new type of code has been presented (Springel, 2010), which combines both positive properties of Grid and SPH codes by treating the gas on a moving mesh grid calculated around each particle as a Voronoi tessellation.

In this thesis, all simulations were performed using extended versions of the parallel TreePM-SPH-code GADGET-2 (Springel, 2005) called P-GADGET-3. TreePM-SPH codes determine the hydrodynamic properties using SPH, and the gravitational interactions are calculated using a Tree walk algorithm (see Hernquist & Katz 1989 for more detail on Tree-SPH.) P-GADGET-3 is based on an entropy-conserving formulation of SPH (Springel & Hernquist, 2002).

To model the physics of the gas from which the stars are formed, additional processes and gas properties must be considered. In its standard version, P-GADGET-3 includes radiative cooling for a primordial mixture of hydrogen and helium (Katz et al., 1996), and star formation as well as the associated supernova feedback are included as sub-grid models according to Springel & Hernquist (2003), assuming a Salpeter initial mass function (IMF) (Salpeter, 1955). In case of cosmological simulations, additional heating due to the time dependent UV background is included (Haardt &

Madau, 1996). The interstellar medium is treated as a two-phase medium (McKee & Ostriker, 1977; Efstathiou, 2000; Johansson & Efstathiou, 2006), where dense cold clouds are in pressure equilibrium with the thin hot gas they are embedded in.

To solve the issues of the phase-mixing problem, artificial conductivity schemes (Price, 2008) can be implemented, for example those presented by Dolag et al. (2005), as well as thermal conduction (Dolag et al., 2004). A more recent approach to this matter is presented by Beck et al. (2015), see also App. A.8, where we also show the impact of this schemes on disk galaxy properties.

In the more advanced models used in this thesis, namely the *Magneticum Pathfinder* simulations (see Sec. 2.4), the metallicity of the gas and stars is also considered, modeling the continuous formation of metals from the early universe through all stellar generations (Tornatore et al., 2004, 2007). This subgrid model considers the contributions from both Type II and Type Ia supernovae, gradually releasing energy and metals with a time delay due to the lifetimes of the different stellar populations. For this subgrid model, a Chabrier IMF (Chabrier, 2003) is assumed instead of the Salpeter IMF. This treatment also includes the dependence of the gas cooling on the local metallicity in a self-consistent way. It also accounts for the kinetic feedback mimicking the effect of star formation driven winds (Springel & Hernquist, 2003).

In addition, black holes can be included in the simulations as sink particles. In that case, the black hole feedback is modelled as described by Springel et al. (2005b) or Hirschmann et al. (2014): The black hole sink particle accretes gas from its surrounding medium according to a Bondi-Hoyle accretion model, limited to the Eddington limit, and returns thermal energy to the surrounding medium. If two black holes enter each other's smoothing length and their relative velocities are below the local sound speed, they are assumed to merge instantly.

However, in case of cosmological simulations or unequal-mass mergers, the dynamical friction is not sufficient in slowing down the black holes enough, since dynamical friction is not well resolved as it has the strongest impact on small scales where artificial forces due to the low resolutions are larger than the impact of dynamical friction. To solve this issue, the black holes are pinned to the galaxies' centers of mass, assuming that when these merge, the black holes are merging, too (Johansson et al., 2009b). However, pinning has an unwanted side effect: whenever the distances, at which the black holes are "searching" for the center of mass at every timestep, becomes larger than the distance between the two centers of mass, the black hole in the less deep potential jumps immediately to the other potential minimum, effectively inhabiting now exactly the same position as the second black hole. Thus, both black holes are merged much too early in those cases, even before the potential minima have merged. Therefore, we see that this is a rather crude implementation which needs further revision. Another approximation used in the standard models that needs improvements is the neglect of radiative feedback from the black holes. A new approach to this matter has been recently suggested by Steinborn et al. (2015), see also App. A.6.

## 2.2 Binary Merger Simulations

The classical formation scenario for an elliptical galaxy is the major merger scenario, where two initial spiral galaxies with similar mass are set up artificially and collided on a specified orbit. The final remnant of such a merger event is a spheroidal galaxy, where the gas has mostly been transformed into stars during a massive starburst caused by the merger event, or has fed the black hole in the center. A small gas disk may remain, depending on the amount of gas used to model the initial disk galaxies.

Therefore, in a first step the disk galaxies are set up artificially, and they are tested to be stable, i.e., they do not collapse by themselves with time. In many modern binary merger simulations, including those studied in this thesis, the initial spiral galaxies are set up according to the model described by Springel et al. (2005b) and Johansson et al. (2009b) as follows:

**Dark Matter Halo** As discussed in Sec. 1.4.2 the radial dark matter density profiles of galaxies can be well described by an NFW-profile (Eq. 1.30). Nevertheless, the NFW density distribution does not have an analytical distribution function (Springel et al., 2005b), and its mass does not converge. Therefore, a Hernquist profile (Eq. 1.29, Hernquist 1990) is usually used to model the dark matter halos instead, which has the same behaviour as the NFW profile in the inner parts but is steeper at large radii (see also Fig. 1.10 for a comparison of the two profiles), i.e., its mass converges, and it has an analytical distribution function. The Hernquist halo is chosen such that its density distribution contains the same amount of mass as a corresponding NFW halo inside a radius of  $r_{200}$  (radius where the density is 200 times the critical density of the universe) and that the inner density profiles are equal. This implies that the scale radii of the NFW and the Hernquist profiles are correlated, and there is indeed a correlation presented by Springel et al. (2005b), where the correlation only depends on the concentration  $c = r_{200}/r_s$  of the halo. In our simulation setups, we use Hernquist halos with  $c = 9$ , and the masses and radii are calculated according to Eq. 2.2 and Eq. 2.3 (see also Johansson et al. 2009b). This concentration is a good approximation to present-day halos, but different values for the concentration can be chosen, especially in case of modelling higher redshift disk galaxies (Bullock et al., 2001).

**Stellar Components** Stars are set up in two different components, namely a disk and a bulge component. The bulge is, like the dark matter, modeled using a Hernquist profile, however, it is scaled such that the mass in the bulge  $M_b = m_b M_{\text{tot}}$  is a fraction  $m_b$  of the total mass  $M_{\text{tot}}$  and the bulge scale length is parametrized according to the scale-length of the disk. The disk component is modeled to fit an exponential surface density profile

$$\Sigma_*(r) = \frac{M_*}{2\pi h^2} \exp\left(-\frac{r}{r_d}\right), \quad (2.1)$$

with  $h$  the Hubble parameter from Eq. 1.4,  $r_d$  the scale height of the disk and  $M_* = m_d M_{\text{tot}} - M_{\text{disk}}$  ( $m_d$  is the fraction of the total mass that is inside the disk, including both stars and gas). The density in  $z$ -direction of the disk is modeled assuming an isothermal sheet with constant scale-height  $z_0$ , parametrized by the scale-length of the disk as  $z_0 \approx 0.1 \dots 0.2 r_d$ . The scale-length itself is determined by the spin-parameter of the halo (Mo et al., 1998, see also Master's thesis by Teklu (2014) and Sec. A.4), which is a free parameter, assuming that the angular momentum of the disk,  $J_{\text{disk}}$  is proportional to the angular momentum of the halo  $J_{\text{halo}}$  due to angular momentum conservation. Then,  $J_{\text{disk}} = m_d J_{\text{halo}}$  (see also Johansson et al., 2009b). In the simulations used in this work the bulge scale radius is chosen to be  $b = 0.2 h$  and the bulge mass fraction is  $m_b = 0.01367$ . For the disks, we assume a disk mass fraction of  $m_d = 0.041$ , a scale height of  $z_0 = 0.2 r_d$ , and the scale-length  $r_d$  is calculated assuming a spin of  $\Lambda = 0.033$ .

**Gas Disks** If gas is included in the simulation, it is assumed to be present only in the disk component. In that case, the mass fraction of the total disk,  $m_d$ , is split up between the stellar and the disk component, depending on the fraction of gas relative to the stars. The gas disk is modeled to fit an exponential surface density profile as well, using the same scale-length as the disk (Eq. 2.1

but with  $M_{\text{gas}}$  instead of  $M_*$ ). For the scale height, the situation is more complicated, since it changes due to star formation and feedback processes as well as cooling effects which cause the temperature to be variable. Therefore, it is computed due to the subgrid models used for the calculation, assuming that the scale-height follows directly from self-gravitation and pressure in the disk. For our simulations we adopt different gas fractions, ranging from no gas to 80% initial gas fraction.

**Black Holes** In each disk galaxy a black hole can be implemented as a sink particle in the minimum of the potential of the modeled galaxy. Those black holes can grow through accretion, depending on the subgrid model that has been chosen (see Sec. 2.1). In case of merger simulations, an additional criterion for the merging of the black holes needs to be added. In the model presented by Springel et al. (2005b) it is assumed that the black holes merge instantly once they are within each other’s softening lengths. Concerning the positioning of the black hole during the simulation, Johansson et al. (2009b) pinned the black hole to the potential minimum of the galaxy at each time step to prevent the black hole from wandering around the galaxy during the merger event. In the simulations used in this work, the seed black holes always have a mass of  $M_{\text{BH}} = 10^5 M_{\odot}$ .

It is also possible to use a spheroidal galaxy resulting from a merger simulation as initial spheroidal galaxy to simulate a binary merger between a spheroidal and a disk or between two spheroidals. Each galaxy has a spin plane orthogonal to the direction of the spin vector, i.e., along the plane of the disk in case of spiral galaxies. In addition, both galaxies are set up on an orbit for the merger, and the planes of the orbits are called orbital planes. For both galaxies, the inclination angles between their individual spin and orbital planes are called  $i_1$  and  $i_2$ . The orbit has a pericenter, and the angles between the spin plane and the connecting line between the galaxies centers at the pericenter are called pericenter arguments  $\omega_1$  and  $\omega_2$ . A schematic of this setup is shown in Fig. 2.3. All combinations of inclination angles and pericenter arguments are possible, however, some are more likely than others (Khochfar & Burkert, 2006). If two galaxies rotate in the same direction, the merger is called prograde, if their spins are orientated in opposite directions it is called retrograde. In case that the inclination angles of both galaxies are either  $i = 0^\circ$  or  $i = 180^\circ$ , we call the merger “in plane”.

In all mergers used during the course of this work, the two galaxies are set-up on (nearly) parabolic orbits which is a likely event according to Khochfar & Burkert (2006) who studied the distribution of orbits of merging galaxies from a cosmological simulation. Their initial distance is  $R_{\text{init}} = 0.5 (r_{\text{vir}}^{(1)} + r_{\text{vir}}^{(2)})$  with  $r_{\text{vir}}$  the virial radius of each galaxy, and the pericenter distance is chosen as  $r_{\text{peri}} = r_{\text{d}}^{(1)} + r_{\text{d}}^{(2)}$ . The simulation is usually performed until the final stage is reached, e.g., a spheroidal has formed. One example of such a binary merger of two equal-mass disk galaxies is shown in Fig. 2.2 for six different timesteps, including the initial state (upper left panel) and the final state of this run (lower right panel).

In the following subsection we describe the binary merger simulations used in different parts of this thesis: All of them are included in the analysis performed in Chap. 3, and the 1:1 binary merger event 11 OBH2 13 is used for parts of the studies presented in Chap. 6. Additionally, the spiral galaxy used as initial condition for these merger simulations is part of the study shown in Sec. 6.2.

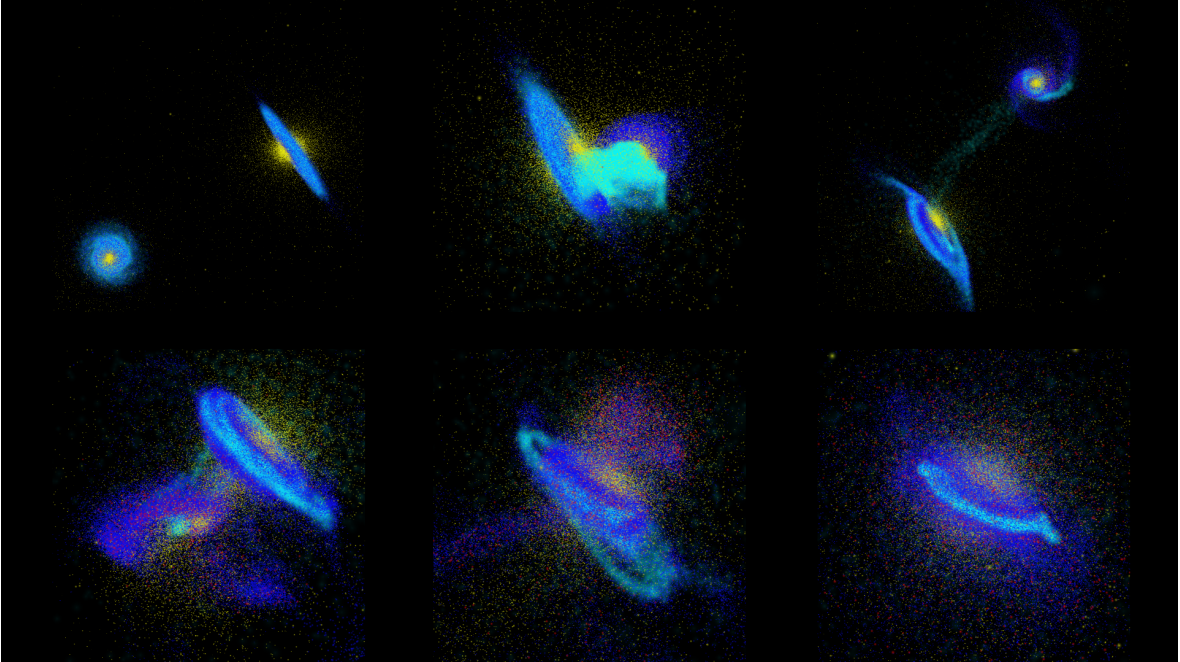


**Figure 2.2:** Visualisation of a 3:1 Binary Merger event (31 OBH8 13), showing six different timesteps. **Upper left:** initial setup. Blue stars are disk stars, yellow stars are bulge stars, the gas is shown in turquoise. **Upper middle:** First encounter of the galaxies. The interactions between the gas particles is clearly visible. New stars formed from the gas are shown in red. **Upper right:** Maximum distance between the galaxies after the first encounter. Both disks are disturbed and tidal arms have formed in both galaxies. The cold gas has built up a bridge between both galaxies. **Lower left:** Second encounter. The smaller galaxy is in the process of being disrupted, and it shows a starburst, with most of its gas being transformed into stars. **Lower middle:** 2.5 Gyr after the beginning of the simulation the small galaxy has been completely disrupted and its stars have been accreted by the larger galaxy. **Lower right:** After 3 Gyr the merger is over and the galaxy relaxes. The spirals have turned into an elliptical, but due to the large initial gas fraction the newly formed elliptical still has a clearly visible gas lane. All stars have mixed, even if the former disk stars still show a dominance along the major plane of the resulting elliptical.

### 2.2.1 Binary Merger Simulations Used in this Work<sup>9</sup>

We analyze a set of 10 high resolution ellipticals formed in such a major merger scenario, which we will refer to as Binary Ellipticals hereafter. For a detailed description of the simulations used in this work, especially the details of the setup of the progenitor spirals, see Johansson et al. (2009a) and Johansson et al. (2009b). Our sample of simulations consists of 4 spiral-spiral mergers with a mass ratio of 1:1 for the progenitor galaxies, 5 spiral-spiral mergers with a mass ratio of 3:1 and one mixed merger. For the mixed merger we collide a spiral galaxy with an elliptical which is a remnant of a 3:1 spiral-spiral merger itself.

The galaxies were set up following the method presented in Springel et al. (2005b). The dark halo virial velocity for all primary galaxies except 31 OBH2 09 320 is  $v_{\text{vir}} = 160 \text{ km s}^{-1}$ , halo 31 OBH2 09 320 is set up with  $v_{\text{vir}} = 320 \text{ km s}^{-1}$ . Here  $v_{\text{vir}}$  defines the dark matter virial mass

<sup>9</sup> This subsection is directly cited from Remus et al. (2013).

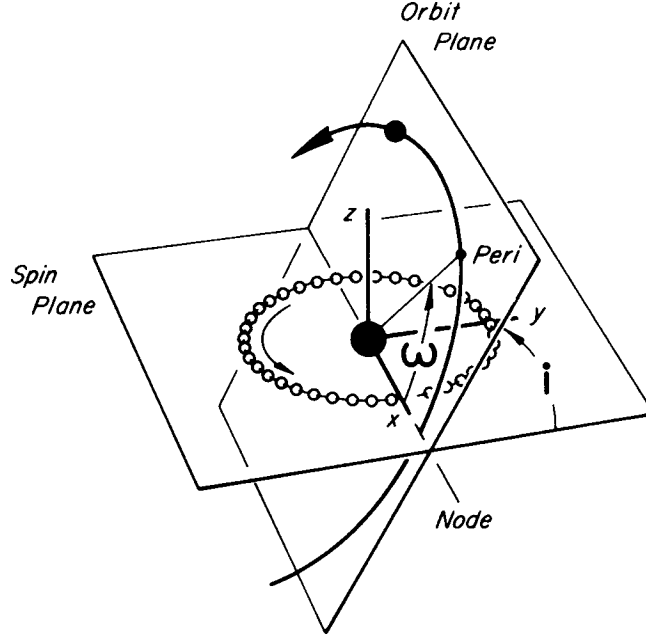


**Figure 2.3:** Fig. 6a taken from Toomre & Toomre (1972), illustrating the orbital encounter geometry as described in the text.

and virial radius of the spiral galaxy:

$$M_{\text{vir}} = \frac{v_{\text{vir}}^3}{10GH_0} \quad (2.2)$$

$$r_{\text{vir}} = \frac{v_{\text{vir}}}{10H_0} \quad (2.3)$$

The disks are set up with different initial gas fractions,  $f_{\text{gas}} = 0.0$ ,  $f_{\text{gas}} = 0.2$  and  $f_{\text{gas}} = 0.8$ , with the rest being disk stars. Simulation 11 OBHNB0 13 is a simulation without a bulge and a gas fraction of  $f_{\text{gas}} = 0.0$ . All of the simulations, except 31 ASF2 13 and 31 ASF2 13, also include Black Holes (BH) as sink particles and BH feedback.

We adopt three orbital geometries, G13, G09 and G01, according to Naab & Burkert (2003). Since we were interested in studying the effects of the initial gas fraction and the merger ratios on the merger remnant, we choose for the majority of our simulations the same orbital configurations, the G13 orbit. This orbit geometry corresponds to an inclination of  $i_1 = -109^\circ$  and a pericenter argument of  $\omega_1 = 60^\circ$  for the first progenitor galaxy (in case of an unequal-mass merger the more massive galaxy) and  $i_2 = 180^\circ$  and  $\omega_2 = 0^\circ$  for the second progenitor galaxy. Both galaxies approach each other on parabolic orbits, with the merger taking place at about 1.5 Gyr after we started the simulation. The simulations were evolved to 3 Gyr. The G09 and G01 orbits were included to understand the impact of the orbit on the remnant. For the G09 orbit, the parameters are  $i_1 = -109^\circ$  and  $\omega_1 = 0^\circ$  for the first progenitor galaxy and  $i_2 = 180^\circ$  and  $\omega_2 = 0^\circ$  for the second progenitor galaxy, the G01 orbit matches a geometry of  $i_1 = 0^\circ$ ,  $\omega_1 = 0^\circ$  and  $i_2 = 180^\circ$ ,  $\omega_2 = 0^\circ$ . All three orbits are parabolic, with

**Table 2.1:** Binary merger simulation sample at a timestep of 3 Gyr

Model	Ratio <sup>(a)</sup>	Orbit <sup>(b)</sup>	$f_{\text{gas}}$ <sup>(c)</sup>	$M_{\text{Gal}}$ <sup>(d)</sup>	$M_{\text{DM}}$ <sup>(e)</sup>	$N_{\text{Gal}}$ <sup>(f)</sup>	$f_*^{\text{new(g)}}$	$R_{1/2}$ <sup>(h)</sup>	$f_{\text{DM}}$ <sup>(i)</sup>	$f_{\text{DM}}^{0.5}$ <sup>(k)</sup>
11 OBH2 13	1:1	G13	0.2	1.28	2.84	712 870	10.71	4.67	0.24	0.14
11 OBH2 09	1:1	G09	0.2	1.29	2.82	713 997	11.21	4.45	0.23	0.13
11 OBH0 13	1:1	G13	0.0	1.33	2.71	742 490	0.00	6.14	0.29	0.18
11 OBHNB0 13	1:1	G13	0.0	0.97	2.78	548 320	0.00	7.56	0.46	0.32
mix 11 OBH2 13	1:1	G13	0.2	1.45	2.97	809 734	11.79	5.34	0.26	0.15
31 OBH2 13	3:1	G13	0.2	0.84	1.99	466 326	9.34	4.75	0.29	0.17
31 OBH8 13	3:1	G13	0.8	0.76	2.06	416 201	50.84	2.40	0.15	0.08
31 ASF2 13	3:1	G13	0.2	0.85	2.00	469 070	9.77	4.53	0.28	0.16
31 ASF2 01	3:1	G01	0.2	0.85	2.01	474 622	11.63	3.96	0.24	0.13
31 OBH2 09 320	3:1	G09	0.2	6.72	15.90	465 699	10.14	9.37	0.28	0.17

<sup>a</sup> initial mass ratio of the two galaxies;

<sup>b</sup> Orbit type according to Naab & Burkert (2003);

<sup>c</sup> Initial gas fraction of the disks of the progenitor galaxies;

<sup>d</sup> Stellar masses within 10% of the dark matter virial radius in  $10^{11} M_{\odot}$ ;

<sup>e</sup> Dark matter masses within 10% of the dark matter virial radius in  $10^{11} M_{\odot}$ ;

<sup>f</sup> Number of stellar particles within 10% of the dark matter virial radius;

<sup>g</sup> Fraction of newly formed stars since the start of the simulation in comparison to the total number of stars at the final output time  $t = 3$  Gyr;

<sup>h</sup> Effective radius of the stellar component of the galaxy, calculated as three dimensional half-mass radius, in kpc;

<sup>i</sup> Fraction of dark matter relative to the stellar component within the half-mass radius;

<sup>k</sup> Fraction of dark matter relative to the stellar component within  $0.5 R_{1/2}$ .

a pericentric distance of  $r_{\text{peri}} = r_{\text{d},1} + r_{\text{d},2}$ , with  $r_{\text{d},1}$  and  $r_{\text{d},2}$  the disk scale radii for the first respective the second progenitor galaxy. G13 and G09 are orbits where the orientations of the progenitor disks are not in the orbital plane, while G01 is a retrograde orbit with the progenitors being in the orbital plane. For more details on these orbits see Naab & Burkert (2003). Table 2.1 contains a summary of all simulation parameters used for this study.

The mass resolution for all binary merger simulations is  $M_{\text{DM}} = 2.25 \times 10^6 M_{\odot} h^{-1}$  for dark matter particles and  $M_{\text{gas}} = M_{\text{stars}} = 1.30 \times 10^5 M_{\odot} h^{-1}$  for gas and star particles. The gravitational softening length was set to  $\epsilon_{\text{DM}} = 0.083 h^{-1}$  kpc for dark matter particles and to  $\epsilon_{\text{gas}} = \epsilon_{\text{stars}} = 0.02 h^{-1}$  kpc for gas and star particles. For all simulations we used  $h = 0.71$  and a baryonic mass fraction of  $\Omega_{\text{B}} = 0.044$ .

## 2.3 Cosmological Zoom-In Simulations

While binary mergers are perfect simulations to test the influence of orbital properties and sub-grid physics in detail, they are still set up artificially. To study the formation of elliptical galaxies within the cosmological context, i.e., through multiple mergers, zoom-simulations of individual halos selected from a dark-matter-only cosmological simulation are a convenient tool. This technique allows to significantly increase the resolution in a small volume of interest, while still taking the long range gravitational forces of the surrounding cosmological structures into account.

The first study using a zoom-simulation technique to analyse the baryonic galaxy content and formation history of an X-ray cluster was presented by Katz & White (1993), for the case of one single cluster. Shortly afterwards, Bartelmann & Steinmetz (1996) used 4 zoom-resimulations of galaxy clusters to investigate strong lensing and X-ray properties, while Dolag et al. (1999) included magnetic fields in their analysis of cluster properties, using 10 clusters. On galaxy scales, Navarro & White (1994) used four zoom-simulation to understand the dynamics of baryons within galaxies. A larger set of galaxies was used in Steinmetz & Navarro (1999) to investigate the origin of the Tully-Fisher relation and its dependence on the baryonic physics included in the simulations. More recently, studies dedicated to the detailed understanding of galaxy formation, using more advanced physics and/or very high resolutions, have used the zoom-simulation technique: For example, in the Aquarius project (Springel et al., 2008), six Milky Way mass dark matter halos were selected from a dark-matter-only parent simulation and re-simulated in higher resolution to understand the formation channels of Milky-Way mass galaxies, however, without baryons. Another well-known, recent zoom-simulation is the Eris simulation (Guedes et al., 2011), which is a zoom simulation of a Milky-Way type galaxy with extremely high resolution and additional baryonic physics included. The halo was chosen to resemble the mass of the Milky Way and to have a quiet late formation history without significant merging events, according to what is assumed for the Milky Way’s formation history. For spheroidal galaxies, an extended sample of zoom-simulations including baryons was presented by Oser et al. (2010), where galaxies were selected covering the whole mass range  $7 \times 10^{11} M_{\odot} < M_{\text{tot}} < 3 \times 10^{13} M_{\odot}$  of massive galaxies. This sample of spheroidals has also been used for the Atlas<sup>3D</sup> comparison study by Naab et al. (2014), which analyses the origin of dynamical structures observed within spheroidal galaxies by means of their formation history. Similarly, however set-up with more baryonic physics and a slightly different numerical approach, Schlachtberger (2014) used zoom-simulations of four isolated spheroidals to investigate the origin of the cold gas disks that have been observed in many spheroidal galaxies lately (see App. A.2 for more information on the details of this study). Regarding galaxy cluster studies, zoom-simulations have been used extensively (e.g., Borgani et al., 2006). However, since those structures are very extended, simulations with high enough resolutions to study the individual galaxies inside the clusters in detail are extremely expensive and have only recently become available.

To perform a zoom-simulation, first of all a low resolution (dark matter only) cosmological simulation is needed. To model the initial conditions for the cosmological simulation, at first all particles are placed on a cubic grid for the entire box. All particles have the same mass, and are homogeneously distributed. In the second step, a power-spectrum is applied to all particles. The power-spectrum specifies how likely each wavelength is present in the simulation, and it determines the initial displacements of the particles. Thus, after applying the power-spectrum to the particle grid, there are density fluctuations in the particle distribution of the initial conditions which lead to the filamentary growth of structures in the box during the simulation. With this set of initial conditions that is determined by the choice of the cosmological parameters, the box is evolved until  $z = 0$ . This box is called the “parent” simulation.

From this parent simulation, the halos are selected at  $z = 0$ , and all particles which are at any given time of the simulation part of the structure that should be simulated with higher resolution are identified and traced back in time. The whole volume containing these particles is then selected as high resolution region. This volume can either be restricted to those particles directly, causing the high-resolution region to have an amorphous shape, or be a box or a sphere containing all selected particles plus additional particles within the region. The latter is used to prevent low resolution particles from

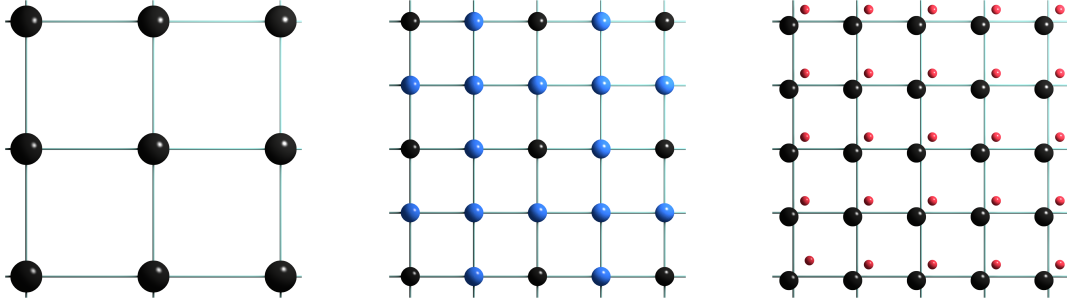


**Figure 2.4:** Two-dimensional illustration of the construction of the initial conditions of zoom-simulations from a parent cosmological simulation. **Left panel:** Example grid of the parent simulation for 9 dark matter particles (black balls). **Middle panel:** Same as left panel but with twice the spacial resolution. Each dark matter particle (black balls) has spawned three new dark matter particles (blue balls), placed of the intersections of the new, spatially enhanced grid. The mass of the particles has been reduced by a factor 4. **Right panel:** Same as middle panel, but now all dark matter particles are shown in black. Each dark matter particle has spawned a gas particles with the gas particles mass according to the assumed baryon fraction split from the original mass of the dark matter particle, effectively lowering the mass of the dark matter particle. Each gas and dark matter particle pair is placed on the grid such that their center of mass is on the intersection point of the grid, and momentum is conserved.

the surrounding areas to intrude into the high resolution volume, as those low-resolution particles have much higher masses and cause artificial dynamical friction when it drags the lower-mass particles in its wake. However, this procedure can become very computationally costly if the volumes are large due to the increasing amount of particles included in the high-resolution volume.

In the next step, the particles inside the volume where a higher resolution should be achieved, are split into multiple particles, while the individual particle mass is lowered accordingly. For example, to double the spatial resolution, each particle is split up in  $2^3$  particles with a mass of  $\frac{1}{2^3} = \frac{1}{8}$  the mass of the parent particle. A two-dimensional representation of this process is shown in Fig. 2.4: In the left panel, the original grid is shown for 9 particles. The particles, illustrated as black balls, are placed on the intersections of the gridlines. The resolution is increased by increasing the number of particles, as shown in the middle panel: The original particles are still at the same positions (black balls), but their masses are reduced (i.e., in the figure the radii of the balls are smaller). Within the grid of old particles, each particle has spawned three more particles (blue balls) placed on the new intersections of the new grid lines. Since one particle has split up into four, the mass of each particle is  $1/4$  of the original particle mass. In three dimensions, the process is the same but each particle is split up into 8 particles instead of 4. If the resolution should be  $n$ -times higher, the particles are split up into  $n^3$  particles with each  $1/n$  of the original mass.

In the high-resolution volume, baryons are often added as well. Since at the initial redshifts there are no stars formed yet, those new particles are all gas particles, and they all have the same mass, however, their mass is smaller than the mass of the dark matter particles. The gas particles are split from the dark matter particles, effectively lowering the dark matter mass of each particle. Hereby, the mass of the gas particles is usually calculated from the baryon fraction of the Universe. This baryon fraction can be calculated from observations of the cosmic microwave background (CMB,

see Sec. 1.1), and according to WMAP7 the baryon fraction is  $f_{\text{bar}} \approx 16.8\%$  (Komatsu et al., 2011). According to the newest survey of the CMB, the Planck Survey, the baryon fraction of the universe is  $\frac{\Omega_b}{\Omega_m} = f_{\text{bar}} \approx 15.6\%$  (Planck Collaboration et al., 2015). Both particles together still have the same mass as the dark matter particle had before the introduction of the baryons. Also, both particles are still close to the same points of the grid where the parent particle was placed, but now their common center of mass is at the intersection while the particles themselves are slightly displaced such that their distance is the mean inter-particle distance and their momentum is conserved. This splitting is shown in the right panel of Fig. 2.4 for the two-dimensional case. The black balls mark the dark matter particles, the red balls illustrate the gas particles. Both are placed slightly off the grid, but since the dark matter particles are much heavier than the gas particles their displacement is much smaller.

The high-resolution volume is surrounded by a lower resolution volume, where the particle mass is higher but the number of particles is lower. Often, the same resolution is used as in the original parent simulation, and sometimes more than one low-resolution volume is used. Those low resolution particles are important to calculate the gravitational long-range forces on the high-resolution volume, however, if they intrude they can cause unphysical distortions. Thus, a careful selection of the high-resolution volume is important for a successful zoom-simulation.

With the new grid and the baryons in place, the power-spectrum is again applied to all particles. The power-spectrum is the same as for the parent simulation, however, for the high-resolution volume, the smaller modes of the power spectrum that have not been used for the parent simulation since the resolution was not high enough to include those small modes, are included down to the Nyquist frequency which corresponds to the mean particle separation in the high-resolution volume (Springel et al., 2008). Once the particles have been displaced, the initial conditions are set up and the simulation can be run until the desired redshift. One example of such a zoom-simulation is shown in Fig. 2.5, where the upper left panel shows the distribution of the baryons in the high resolution volume, and the amoeba-shape of the high-resolution area is still visible. Only gas particles (red points) can be seen since there are no stars formed yet, however, the filamentary structure of the particle distribution caused by the power-spectrum is clearly visible. Five more different redshifts are shown, with more stars visible each time (yellow points) and less gas. In the final stage, at  $z = 0$ , the simulation reveals a beautiful example of a counterpart to what would be a compact group in observations (see also Diploma thesis by Remus (2009) for more details on the dark matter properties of this compact group). In case of this zoom-simulation, the three most massive satellite galaxies still have enough resolution to be studied by themselves, which is a rare case since normally each halo hosts one main galaxy in its center and several small satellites. Even on group mass scales, compact groups are a rare case to find in a simulation. Of course, in case of the zoom-simulation of a cluster, there are many massive satellites, but no re-simulations of such a massive structure has been used in the course of this thesis since they are computationally expensive. For more detailed descriptions of the zoom-in re-simulation technique, see for example Borgani et al. 2006; Springel et al. 2008; Oser et al. 2010; Schlachtberger 2014.

The zoom-simulations included in this thesis are described by Oser et al. (2010) and Oser et al. (2012), and we will shortly summarize the basic properties the following section as far as they concern the analyses discussed in this work. They are used in the studies presented in Chap. 3 and Chap. 4. In App. A.2, we also refer to a set of zoom-simulations, however, since they are not part of the main body of this thesis they are not discussed in the following subsection. For more details on these specific simulations, see Schlachtberger (2014).

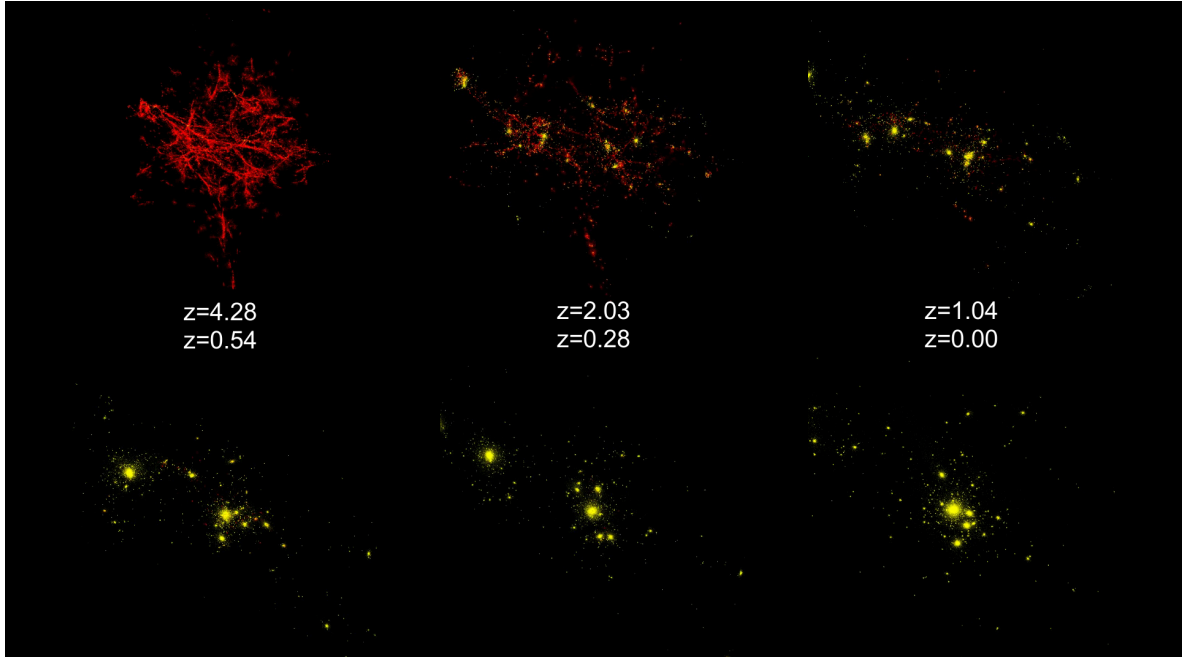


**Figure 2.5:** Visualisation of a Cosmological Zoom-In simulation (0069\_2), showing six different redshifts. Gas is shown in red, stars are shown in yellow. In contrast to the binary merger simulations, all stars in the Cosmological Zoom-in simulations are formed from the gas. **Upper left:**  $z = 4.28$ . The filaments of gas from which the final galaxies are built up are clearly visible, while there are only very few stars formed yet. **Upper middle:**  $z = 2.03$ . Structures of gas form inside the most dense gas regions. **Upper right:**  $z = 1.04$ . While there is less and less gas, more and more stellar clumps are formed, which start to merge and build up larger structures. **Lower left:**  $z = 0.548$ . **Lower middle:**  $z = 0.28$ . A small group of medium sized galaxies has formed. **Lower right:**  $z = 0$ . The final galaxy group has formed. Its central galaxy with its three massive satellites is clearly visible, surrounded by several smaller satellite structures. Pictures taken from a movie by L. Oser.

### 2.3.1 Cosmological Zoom-In Simulations Used in this Work<sup>10</sup>

Our sample consists of 17 zoom-in re-simulations of individual halos, hosting a central spheroidal galaxy at  $z = 0$ . Additionally, we included four companion ellipticals, i.e., massive spheroids that are substructures within larger halos. We will refer to the central spheroidal galaxies as CosmoZoom ellipticals hereafter, and to the substructures as CosmoZoom Companions.

The parent cosmological box of  $72^3 h^{-3} \text{ Mpc}^3$  was simulated using  $512^3$  DM particles with a particle mass of  $M_{\text{DM}} = 2 \times 10^8 M_{\odot} h^{-1}$  and a comoving gravitational softening length of  $2.52 h^{-1} \text{ kpc}$ . A WMAP3 (Spergel et al., 2007),  $\Lambda$ CDM cosmology was adopted, with  $\sigma_8 = 0.77$ ,  $\Omega_{\Lambda} = 0.74$ ,  $\Omega_{\text{m}} = 0.26$  and  $h = 0.72$  and an initial slope for the power spectrum of  $n_s = 0.95$ .

From this dark-matter-only simulation, halos of different masses, ranging from  $10^{11} M_{\odot} h^{-1}$  to  $10^{13} M_{\odot} h^{-1}$ , were selected at  $z = 0$ . All dark matter particles closer than  $2 \times r_{200}$  to the halo center at any snapshot are traced back in time. We replace all dark matter particles identified that way by dark matter and gas particles at higher resolution with  $\Omega_{\text{DM}} = 0.216$  and  $\Omega_{\text{B}} = 0.044$ . The details of the re-simulation method are described in Oser et al. (2010).

<sup>10</sup> This subsection is directly cited from Remus et al. (2013).

**Table 2.2:** *CosmoZoom ellipticals sample at  $z = 0$* 

Model	$M_*^{\text{tot(a)}}$	$M_{\text{Gal}}^{\text{(b)}}$	$M_{\text{DM}}^{\text{(c)}}$	$N_{\text{Gal}}^{\text{(d)}}$	$f_*^{\text{new(e)}}$	$R_{1/2}^{\text{(f)}}$	$f_{\text{in situ}}^{\text{(g)}}$	$f_{\text{DM}}^{\text{(h)}}$	$f_{\text{DM}}^{0.5 \text{(i)}}$
0040_2	25.98	5.00	19.02	84 786	2.02	12.91	23.07	0.43	0.29
0053_2	16.26	6.95	19.25	117 809	1.43	13.03	—	0.37	0.23
0069_2	18.08	4.94	13.28	83 804	1.49	8.84	21.78	0.31	0.20
0089_2	10.76	5.23	11.36	88 772	0.57	10.43	16.43	0.34	0.22
0094_2	9.69	4.79	12.49	81 258	0.80	7.53	25.99	0.27	0.15
0125_2	8.66	4.34	11.06	73 546	0.90	9.08	22.45	0.33	0.20
0162_2	6.28	3.64	8.42	61 808	2.11	9.78	12.92	0.40	0.27
0163_2	7.04	3.52	7.17	59 701	0.90	10.38	14.96	0.37	0.27
0175_2	6.91	3.68	9.94	62 401	1.05	7.37	26.96	0.31	0.20
0190_2	5.83	3.15	5.84	53 401	2.72	6.99	14.67	0.29	0.20
0204_2	5.87	2.69	5.95	45 554	1.63	6.50	15.63	0.25	0.15
0204_4	5.73	2.93	5.38	398 025	1.40	6.36	23.86	0.20	0.11
0215_4	6.03	3.14	6.70	425 565	1.50	4.25	36.14	0.19	0.10
0408_4	2.85	1.66	2.29	224 648	0.94	4.51	20.88	0.16	0.10
0501_4	2.72	1.68	3.18	227 403	2.70	3.27	39.31	0.19	0.10
0616_4	2.52	1.72	2.68	232 935	4.00	5.02	29.90	0.27	0.17
0664_4	2.11	1.23	2.38	166 379	2.46	2.81	38.12	0.16	0.08

<sup>a</sup> Total stellar mass within the dark matter virial radius in  $10^{11} M_{\odot}$ ;

<sup>b</sup> Stellar mass within 10% of the dark matter virial radius in  $10^{11} M_{\odot}$ ;

<sup>c</sup> Dark Matter mass within 10% of the dark matter virial radius in  $10^{11} M_{\odot}$ ;

<sup>d</sup> Number of stellar particles within 10% of the dark matter virial radius;

<sup>e</sup> Fraction of newly formed stars since a redshift of 0.27, which is approximately 3 Gyr, for comparison with the major merger sample;

<sup>f</sup> Effective radius of the stellar component of the galaxy, calculated as three dimensional half-mass radius, in kpc;

<sup>g</sup> Fraction of stars formed in situ taken from Oser et al. (2012) in %;

<sup>h</sup> Fraction of dark matter relative to the stellar component within the half-mass radius;

<sup>i</sup> Fraction of dark matter relative to the stellar component within  $0.5 R_{1/2}$ .

These simulations use cooling for a primordial gas composition and star-formation but do not include any black hole treatment. The initial conditions were created using GRAFIC and LINGERS (Bertschinger, 2001). The simulations were evolved from  $z \sim 43$  to  $z = 0$ .

To achieve a proper resolution even for the smaller halos we performed the re-simulations at two different resolutions. The most massive halos were re-simulated with twice the spatial resolution of the original dark-matter-only box. In these re-simulations the particle masses are  $M_{\text{DM}} = 2.1 \times 10^7 M_{\odot} h^{-1}$  and  $M_{\text{gas}} = M_{\text{stars}} = 4.2 \times 10^6 M_{\odot} h^{-1}$  with gravitational softening set to  $\epsilon_{\text{DM}} = 0.89 h^{-1}$  kpc and  $\epsilon_{\text{gas}} = \epsilon_{\text{stars}} = 0.4 h^{-1}$  kpc for dark matter, gas and star particles, respectively. To study the effects of the gas physics and the stellar component on the dark matter, the halos of this re-simulation level were also re-simulated with dark matter only at the same resolution.

For the less massive halos we used four times the spatial resolution of the original box, and particle masses of  $M_{\text{DM}} = 3.6 \times 10^6 M_{\odot} h^{-1}$  for the dark matter particles and  $M_{\text{gas}} = M_{\text{stars}} = 7.4 \times 10^5 M_{\odot} h^{-1}$  for the gas and star particles with gravitational softening set to  $\epsilon_{\text{DM}} = 0.45 h^{-1}$  kpc and  $\epsilon_{\text{gas}} = \epsilon_{\text{stars}} = 0.2 h^{-1}$  kpc respectively. Table 2.2 contains all ellipticals extracted from the re-simulations used for

**Table 2.3:** *CosmoZoom companion sample at  $z = 0$* 

Model	$M_{\text{Gal}}^{(a)}$	$M_{\text{DM}}^{(b)}$	$N_{\text{Gal}}^{(c)}$	$f_*^{\text{new}(d)}$	$R_{1/2}^{(e)}$	$v_{\text{max}}^{(f)}$	$f_{\text{DM}}^{(g)}$	$f_{\text{DM}}^{0.5(h)}$
0040_s1	3.28	10.13	55 581	2.05	6.62	445.0	0.28	0.18
0069_s1	1.32	3.57	22 451	1.15	4.31	317.5	0.30	0.20
0069_s2	1.67	5.34	28 393	1.52	4.54	339.5	0.30	0.20
0069_s3	1.42	3.71	24 013	3.72	3.84	340.0	0.29	0.19

- <sup>a</sup> Stellar mass within 10% of the dark matter virial radius in  $10^{11} M_{\odot}$ ;
- <sup>b</sup> Dark Matter mass within 10% of the dark matter virial radius in  $10^{11} M_{\odot}$ ;
- <sup>c</sup> Number of stellar particles within 10% of the dark matter virial radius;
- <sup>d</sup> Fraction of newly formed stars since a redshift of 0.27, which is approximately 3 Gyr, for comparison with the major merger sample;
- <sup>e</sup> Effective radius of the stellar component of the galaxy, calculated as three dimensional half-mass radius, in kpc;
- <sup>f</sup> Maximum circular velocity at infall into the parent halo;
- <sup>g</sup> Fraction of dark matter relative to the stellar component within the half-mass radius;
- <sup>h</sup> Fraction of dark matter relative to the stellar component within  $0.5 R_{1/2}$ .

this study, and Table 2.3 contains the companion halos, labeled with the name of their host central halo followed by an S and the number of the substructure.

## 2.4 The Magneticum Pathfinder Simulation Set

Several large simulations of cosmological boxes have been performed in the last 15 years, for example Millenium (Springel et al., 2005c), Millenium II (Boylan-Kolchin et al., 2009), Horizon (Teyssier et al., 2009), Bolshoi (Klypin et al., 2011) and the extended MultiDark simulation set where the Bolshoi simulation is part of (Prada et al., 2012; Klypin et al., 2014), however, they usually only contained dark matter since the inclusion of baryonic physics was computationally expensive and most subgrid models were not tested for cosmological simulations. A very recent development in the field of galaxy studies from simulations are fully hydrodynamical simulations of cosmological boxes with enough resolution to study the galaxies within them in detail. Examples for such simulations are the OWLS simulations (Schaye et al., 2010), dedicated to understand the impact of different sub-grid physics on the evolution and formation of galaxies, the Eagle simulations (Schaye et al., 2015) which are similarly constructed to the Magneticum simulations but only focussed on the analysis of galactic structures and therefore their box-sizes are limited to smaller boxes of maximum 100 Mpc boxlength, and Illustris (Vogelsberger et al., 2014). Here, we present another set of such new fully hydrodynamical cosmological simulations called Magneticum Pathfinder<sup>11</sup>.

The Magneticum Pathfinder simulations (Dolag et al., in prep.) are a set of hydrodynamical cosmological boxes with volumes ranging from  $(896 \text{ Mpc}/h)^3$  to  $(18 \text{ Mpc}/h)^3$  and resolutions of  $m_{\text{Gas}} = 2.6 \times 10^9 M_{\odot}/h$  up to  $m_{\text{Gas}} = 3.9 \times 10^5 M_{\odot}/h$ , performed with P-Gadget-3.

Throughout all simulations, a WMAP7 (Komatsu et al., 2011)  $\Lambda$ CDM cosmology is adapted with  $\sigma_8 = 0.809$ ,  $h = 0.704$ ,  $\Omega_{\Lambda} = 0.728$ ,  $\Omega_{\text{M}} = 0.272$  and  $\Omega_{\text{B}} = 0.0456$  and an initial slope for the power spectrum of  $n_s = 0.963$ . They include kinetic feedback from galactic winds following Springel

<sup>11</sup> [www.magneticum.org](http://www.magneticum.org)

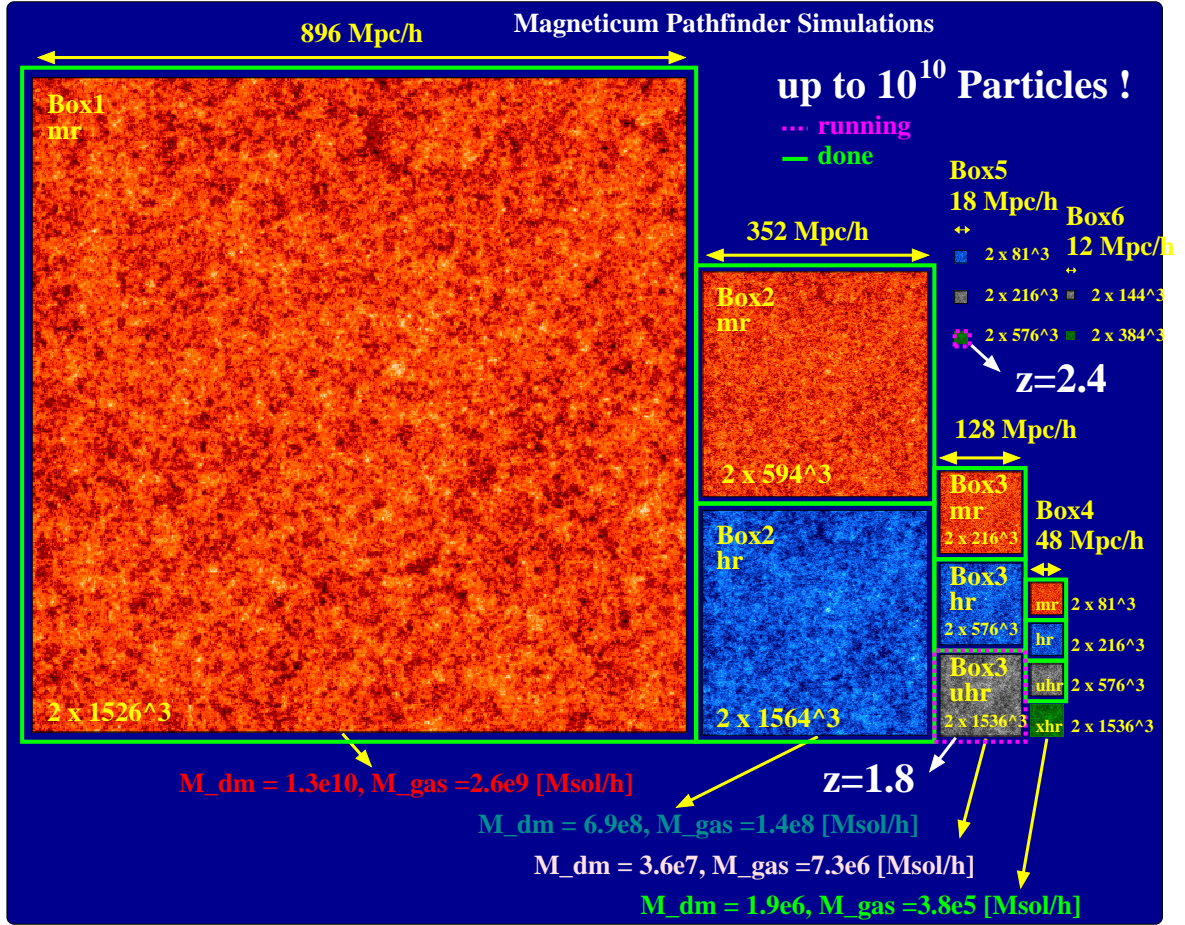


**Figure 2.6:** Schematic overview of all boxes of the Magneticum Pathfinder simulation set, ranging from Box1 with 896 Mpc/h side length to Box6 with 12 Mpc side length, and resolutions from mr to xhr covering a dark matter mass range of  $10^{10}M_{\odot}$  to  $10^6M_{\odot}$ . Boxes which are run down to  $z = 0$  are marked with green frames, boxes currently running are marked with magenta dotted frames, while boxes that still need to be started are not marked with any color. For more details see Table 2.4. Courtesy of Klaus Dolag and the Magneticum Pathfinder team.

& Hernquist (2003), and the metal enrichment and star-formation descriptions follow the pattern of metal production (Tornatore et al., 2004, 2007). Each gas particle can form up to four stellar particles. Additionally, a self-consistent dependence of the gas cooling on the local metallicity is included following Wiersma et al. (2009). This simulation follows the gas using a low-viscosity SPH scheme to properly track turbulence (Dolag et al., 2005; Beck et al., 2015), and thermal conduction according to Dolag et al. (2004). Black hole physics and feedback are included according to Springel et al. (2005b); Fabjan et al. (2010); Hirschmann et al. (2014). For the identification of substructures, a modified version of SUBFIND (Springel et al., 2001) is used which includes the contribution of the stars (Dolag et al., 2009). For more details, see Remus et al. (2013); Hirschmann et al. (2014); Remus et al. (2015a).

A full overview of the boxes included in this simulation is shown in the Illustration in Fig. 2.6

**Table 2.4:** *Magneticum Pathfinder simulations: An overview*

	Size (Mpc/h)	Resolution	$M_{\text{DM}}^{\text{part}}$ ( $M_{\odot}/h$ )	$M_{\text{Bar}}^{\text{part}}$ ( $M_{\odot}/h$ )	$N_{\text{part}}$ (kpc/h)	$\epsilon_{\text{DM,Gas}}$ (kpc/h)	$\epsilon_*$	Status
Box1	896	mr	$1.3 \times 10^{10}$	$2.6 \times 10^9$	$2 \times 1526^3$	10	5	done
Box2	352	mr	$1.3 \times 10^{10}$	$2.6 \times 10^9$	$2 \times 594^3$	10	5	done
		hr	$6.9 \times 10^8$	$1.4 \times 10^8$	$2 \times 1564^3$	3.75	2	done
Box3	128	mr	$1.3 \times 10^{10}$	$2.6 \times 10^9$	$2 \times 216^3$	10	5	done
		hr	$6.9 \times 10^8$	$1.4 \times 10^8$	$2 \times 576^3$	3.75	2	done
		uhr	$3.7 \times 10^7$	$7.3 \times 10^6$	$2 \times 1536^3$	1.4	0.7	$z = 1.8$
Box4	48	mr	$1.3 \times 10^{10}$	$2.6 \times 10^9$	$2 \times 81^3$	10	5	done
		hr	$6.9 \times 10^8$	$1.4 \times 10^8$	$2 \times 216^3$	3.75	2	done
		uhr	$3.7 \times 10^7$	$7.3 \times 10^6$	$2 \times 576^3$	1.4	0.7	done
		xhr	$1.9 \times 10^6$	$3.8 \times 10^5$	$2 \times 1536^3$	0.45	0.25	—
Box5	18	hr	$6.9 \times 10^8$	$1.4 \times 10^8$	$2 \times 81^3$	3.75	2	—
		uhr	$3.7 \times 10^7$	$7.3 \times 10^6$	$2 \times 216^3$	1.4	0.7	—
		xhr	$1.9 \times 10^6$	$3.8 \times 10^5$	$2 \times 576^3$	0.45	0.25	$z = 2.4$
Box6	12	uhr	$3.7 \times 10^7$	$7.3 \times 10^6$	$2 \times 144^3$	1.4	0.7	—
		xhr	$1.9 \times 10^6$	$3.8 \times 10^5$	$2 \times 384^3$	0.45	0.25	—

The simulations used in this thesis are highlighted in color.

and Tab. 2.4. The largest Box, Box1 ( $(896 \text{ Mpc}/h)^3$ ), is only simulated in the lowest resolution (mr,  $m_{\text{DM}} = 1.3 \times 10^{10} M_{\odot}/h$ ,  $m_{\text{Gas}} = 2.6 \times 10^9 M_{\odot}/h$ ), which is much less than the Eagles or Illustris simulation in resolution, however, the size of the box is unmatched by those other simulations and is comparable with the sizes of the dark-matter-only boxes like MultiDark or Horizon. So far, this is the only available cosmological simulation of this size including baryons, providing unique opportunities for a statistical approach to cosmological studies including the effects of baryons, and it has been included already in the study of the pressure-profiles of galaxy clusters in comparison to the Planck-survey results (Planck Collaboration et al., 2013), and used to study the temperature of the CMB from galaxy clusters detected by their Sunyaev-Zel'dovich signal (Saro et al., 2014) and the impact of baryons on the cluster mass function (Bocquet et al., 2015).

The second largest box, Box2, in the same resolution was the first box to be finished, and has already been used to study velocities and X-ray properties of simulated clusters (Biffi et al., 2013). Fig. 2.7 shows a temperature map of Box2 hr, where the cosmic web is clearly visible. Most gas is still cold (red color), however, in the central areas of the filaments it starts to heat up (yellow colors), and the most massive structures, the galaxy clusters, are clearly visible as cyan spherical structures, the color of the hot gas in this illustration. This is in excellent agreement with observations. Nevertheless, even if the low resolution is sufficient for studying galaxy cluster properties and cosmology, higher resolutions are needed for the analysis of galaxy properties. This has been done using Box3 with the next highest resolution (hr,  $m_{\text{DM}} = 6.9 \times 10^8 M_{\odot}/h$ ,  $m_{\text{Gas}} = 1.4 \times 10^8 M_{\odot}/h$ ) for three massive BCGs by Remus et al. (2013). The same simulation has also been used by Hirschmann et al. (2014) for a detailed study of the growth of black holes and antihierarchical behaviour of the AGN number density evolution.

The Magneticum Pathfinder simulation set is still under construction, and for Box3, the simulation

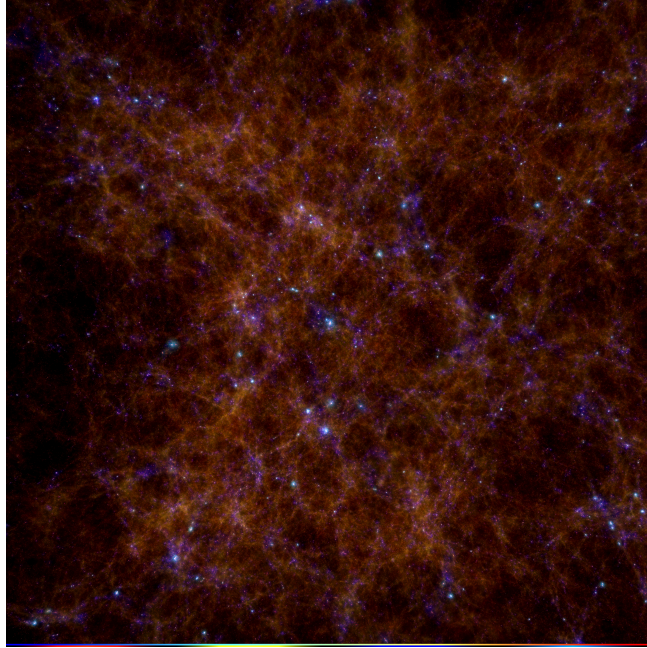


**Figure 2.7:** *Temperature map of Box2/hr of the Magneticum Pathfinder set, with the most massive halos clearly visible as bright bluish objects, since their gas content is very hot, as observed for galaxy clusters (X-ray halos). Image credit: Klaus Dolag and the Magneticum pathfinder team, visualization with the Code Splotch.*

with the even higher resolution uhr is still running, and is currently at a redshift of about  $z = 1.8$ . That box will be slightly larger than the highest resolution Illustris simulation (boxlength of 106.53 Mpc, Vogelsberger et al. 2014), but the mass resolution will be slightly lower. In comparison to the Eagle simulation, Box3 is larger than their largest box (100 Mpc boxlength, Schaye et al. 2015), and the uhr resolution is sufficiently higher at that box size. Box3 hr has a comparable resolution and size as the largest Eagle simulation at its highest resolution.

For a successful analysis of dynamical properties of galaxies, however, the resolution hr is still insufficient. For Box4, the resolution uhr is already available and is extensively used in this work (see blue highlighted simulation in Tab. 2.4). That simulation has a similar size than the second largest box in the Eagle simulation set (50 Mpc boxlength), but the Magneticum uhr resolution is slightly higher ( $m_{\text{bar}}^{\text{Magneticum,uhr}} = 7.3 \times 10^6 M_{\odot}/h$ ,  $m_{\text{bar}}^{\text{Eagle,50 Mpc}} = 1.1 \times 10^7 M_{\odot}/h$ , Schaye et al. 2015). This simulation will be used in several upcoming studies of galaxy properties from Magneticum, of which some are summed up in this thesis (Chap. 4, Chap. 5, App. A.4). Even higher resolutions are planned, however, those high resolution simulations are computationally very challenging due to storage issues and available computational time, and therefore those higher resolutions will only be available for the smallest boxes Box4, Box5 and Box6. Those will be perfect laboratories to study properties of individual galaxies in detail, even if their statistical relevance (apart from Box4) is limited since the two small boxes only contain very few galaxies.

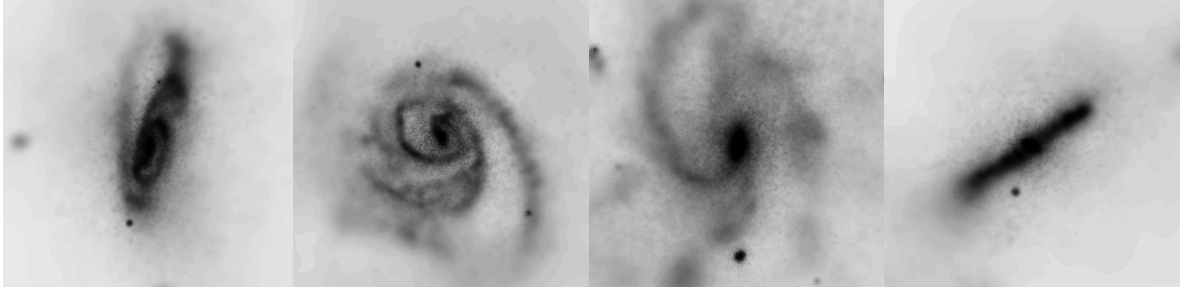


**Figure 2.8:** Four examples for disk galaxies from Box4 uhr. These galaxies are also shown in Remus et al. (2015a).

### 2.4.1 Galaxy Classification

In those simulations where the resolution is high enough to resolve the individual galaxies down to Milky Way mass galaxies, we successfully reproduce a population of disk as well as spheroidal galaxies. This is mostly due to the improvements in the numerical methods, especially the low-viscosity scheme (Dolag et al., 2005; Beck et al., 2015), but the better prescriptions of physical processes also play an important role especially for the gas physics. This is a huge achievement in comparison to earlier cosmological simulations, where the galaxies used to generally be spheroidal, but it also adds an additional challenge to the analysis of the galaxies found in the simulations, namely a proper classification of their morphology. Four examples for disk galaxies found in the Magneticum Pathfinder simulation Box4 uhr are shown in Fig. 2.8 (see also Remus et al. (2015a)).

As a first approximation, we use a classification scheme based on the circularity parameter, similar to Scannapieco et al. (2008): At first, we align each galaxy along its principal axis of inertia of the stars within  $0.1 R_{\text{vir}}$ . The circularity for each gas and star particle within  $0.1 R_{\text{vir}}$  is then calculated as

$$\epsilon = j_z / j_{\text{circ}} \quad (2.4)$$

where  $j_z$  is the specific angular momentum of each particle with respect to the  $z$ -axis and  $j_{\text{circ}}$  is the specific angular momentum expected if the particle would be on a circular orbit. For each galaxy, we now consider the histograms of the circularity parameter. If a galaxy is rotationally supported, that is has a clear rotation around the center of the galaxy on a disk orthogonal to the principal axis of inertia, the majority of the stars (and the gas) particles have a circularity close to  $\epsilon = 1$  (or  $\epsilon = -1$  in case of a counter-rotating (gas) disk). On the other hand, if a galaxy is dispersion-dominated, that is its stars do not have a strong ordered rotation around the principal axis but mostly random spherical orbits around the galaxies center, the majority of the particles have a circularity close to  $\epsilon = 0$ . The upper panels of Fig. 2.9 show an example of the distribution of the circularity parameter for a dispersion dominated spheroidal galaxy (upper left panel) and a rotation-dominated disk galaxy (upper right panel). The differences can also be seen in the lower panels of the same figure, where the radial velocity and line-of-sight velocity dispersion are shown for those example galaxies. The spheroidal is clearly dominated by dispersion, while the disk galaxy has a much lower velocity dispersion in comparison to the spheroidal, and its rotational velocity is higher compared to its velocity dispersion (however, this effect is smaller than in observations, indicating that the disks in the Magneticum simulations are still a bit too thick). In the following studies, we always use the following classifications whenever we talk about different morphologies in the Magneticum simulations (see also Remus et al. 2015a):

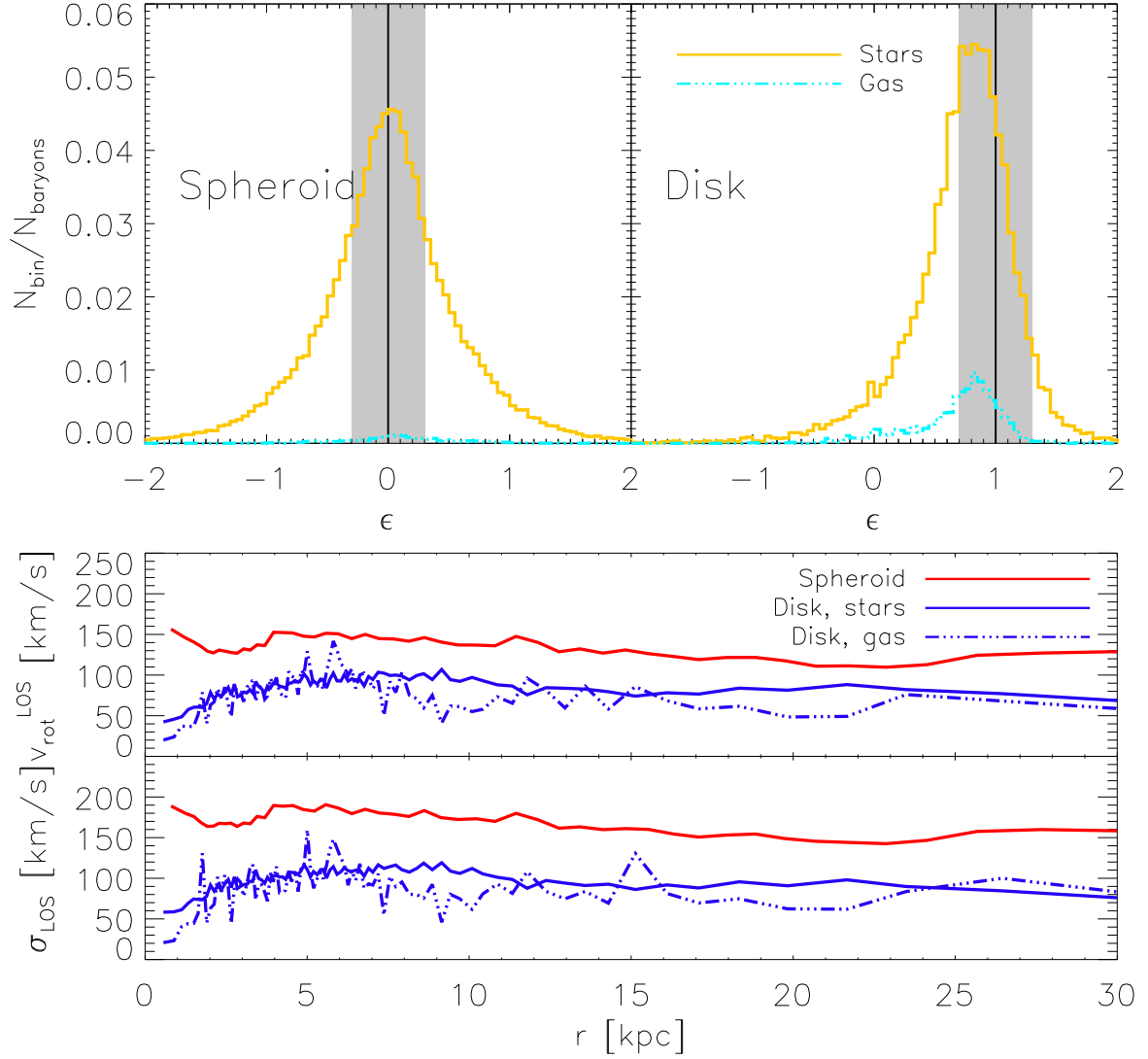


**Figure 2.9:** *Upper panels:* Distribution of the circularity  $\epsilon$  of a spheroidal (left) and a disk galaxy (right) for stars (solid yellow line) and gas (dash-dotted cyan line) within  $0.1 R_{\text{vir}}$ , normalized to the total stellar and gas mass of the galaxy. Gray shaded areas mark the selection criterion for spheroid (left) and disk (right) galaxies used in this work. *Lower panels:* Line-of-sight (LOS) velocity (upper) and LOS velocity dispersion (lower panel) versus radius for the stellar component of the same spheroid (red lines) and disk (blue lines) galaxy as in the upper panels. The gas component of the disk galaxy is shown as dashed blue line. The spheroidal clearly has a higher dispersion relative to its rotation velocity, while for the disk both the stellar and gas component are in very good agreement, as expected from observations. A similar figure including caption is also presented in Remus et al. (2015a).

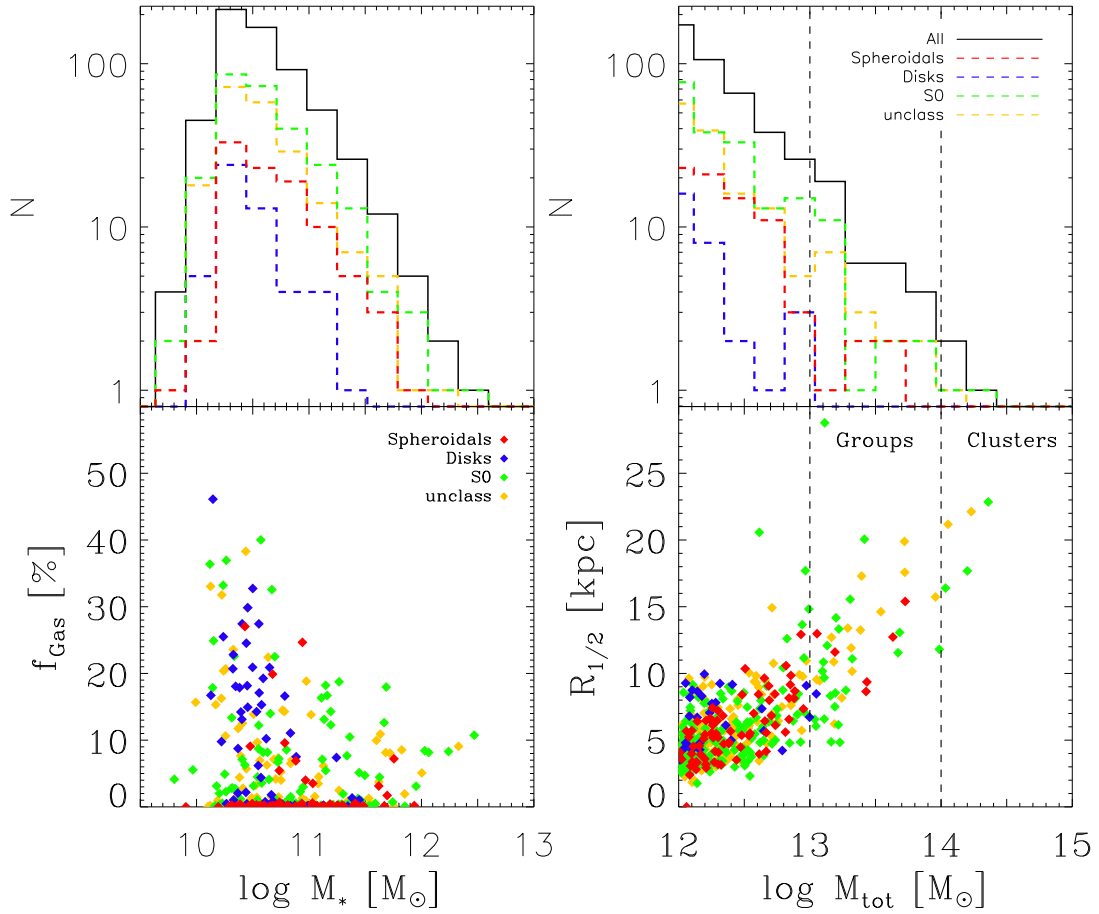


**Figure 2.10:** *Lower left panel:* Fraction of cold gas  $f_{\text{Gas}}$  within the halfmass radius  $R_{1/2}$  of the galaxies versus their stellar mass  $M_*$ . Spheroidals are shown as red, S0 galaxies are shown as green and disk galaxies are shown as blue filled diamonds. Those galaxies that are not classified by our classification scheme are shown in yellow. *Lower right panel:* Stellar halfmass radius versus the total halo mass  $M_{\text{tot}}$ . Colors as in the left panel. *Upper panels:* Histograms of the stellar mass (left panel) and the total mass (right panel). Black lines show the histograms for all galaxies in the simulation, while colors show the histograms according to the classification (colors as in the lower panels).

**Disk Galaxies** A galaxy is classified as disk galaxy, if more than 30% of its stellar particles and more than 40% of its cold gas are within  $0.7 \leq \epsilon \leq 1.3$ .

**Spheroidal Galaxies** A galaxy is classified as elliptical if more than 40% of its stellar particles have circularities within  $-0.3 \leq \epsilon \leq 0.3$  and either 40% of its gas particles also have circularities within  $-0.3 \leq \epsilon \leq 0.3$  or 40% of its gas particles have circularities within  $0.7 \leq \epsilon \leq 1.3$ , and the amount of gas particles is less than 10% of the amount of stellar particles within the half-mass radius (the radius which contains 50% of the stellar content of a galaxy). The former are called gas-less (since their gas is assumed to be hot as it is not within a disk), while the latter are called gas-rich, since they have a gas disk.

**S0 Galaxies** A galaxy is classified as S0 if it has more stars with circularities within  $-0.3 \leq \epsilon \leq 0.3$  than  $-0.3 \leq \epsilon \leq 0.3$  but the amount of stars with circularities within  $-0.3 \leq \epsilon \leq 0.3$  is lower than 40%.

**Unclassified galaxies** A galaxy is not classified if it does not fit in any of the above categories.

Fig. 2.10 shows some basic properties of the galaxies selected from Box4 uhr including our classification. The box contains 621 halos down to a mass of  $5 \times 10^{11} M_{\odot}/h$ , of which five are small clusters and approximately 40 are groups above  $10^{13} M_{\odot}/h$  at redshift  $z = 0$ . The lower panels of Fig. 2.10 show the gas mass fraction versus the stellar mass of each galaxy (left panel) and the stellar half-mass radius versus the total mass of the halo (right panel). We find that our classification scheme works sufficiently well at lower stellar masses, as it identifies several disk galaxies with stellar masses between  $10^{10} M_{\odot} < M_* < 10^{11} M_{\odot}$ , but only three with larger masses. Those disks also only have very little cold gas. For the spheroidals, we find that the scheme identifies galaxies of all stellar mass ranges up to  $M_* = 10^{12} M_{\odot}$ , but all galaxies with larger stellar masses are classified as either S0 galaxies or unclassified. This shows the first flaw in our classification scheme, as it fails to classify any of the brightest cluster galaxies (BCGs) and most of the brightest group galaxies (BGGs) as spheroidals, albeit those most massive galaxies are usually round slow rotators, and therefore clearly are ellipticals. One possible explanation for this problem with the classification due to the circularity could be that there is more gas in those spheroidals than expected due to cooling from the halo. Another possible problem could be counterrotating structures which broaden the ranges of circularities such that there is no small peak around  $\epsilon = 0$  anymore. A second problem with the spheroidal classification becomes apparent in the lower left panel of Fig. 2.10: There are actually four galaxies classified as spheroidals with cold gas mass fractions larger than 10%. Those galaxies “sneaked” in since they have massive cold gas disks which are orientated not perpendicular to the principal axis of the stellar component but along the principal axis. Therefore, their gas circularity seems to be around  $\epsilon = 0$  even though they actually have a rotating disk.

Therefore, we clearly see that the classification due to the circularity is far from successful, however, it identifies the “poster child” galaxies, that is all disk galaxies are clearly undisturbed extended disks, and all spheroidals (but those four misclassifications) are classical spheroidal galaxies. Technically, S0 galaxies would also be spheroidals, but we do not include them in the spheroidal family since the classification due to the circularity is very crude in their case. This classification does not only include classical spheroidal galaxies, but also galaxies with large bulges, ring galaxies, peculiar galaxies and most likely all intermediate stages of thick disks, or barred galaxies which have a circularity peak around  $\epsilon = 0.3$ . The galaxies which are unclassified contain all galaxies currently in the process of merging, and galaxies which have counter-rotating stellar disks and other dynamical or morphological peculiarities. In this work we will mainly focus on the poster child galaxies, but for the future a more detailed study of the classification problem is planned. Part of it is already included in Teklu et al. (2015b) (see also her Master’s Thesis (Teklu, 2014) and App. A.4), where we show that a continuous classification due to the specific angular momentum–stellar mass relation is a much better approach (see Fall 1983; Romanowsky & Fall 2012; Fall & Romanowsky 2013 for the observational motivation for this approach).

**Table 2.5:** *Magneticum BCGs at  $z = 0$  from Box3 hr.*<sup>12</sup>

Model	$M_*^{\text{tot(a)}}$	$M_{\text{Gal}}^{\text{(b)}}$	$M_{\text{DM}}^{\text{(c)}}$	$N_{\text{Gal}}^{\text{(d)}}$	$R_{1/2}^{\text{(e)}}$	$f_{\text{DM}}^{\text{(f)}}$	$f_{\text{DM}}^{0.5\text{(g)}}$
00	174.4	52.2	508.6	142 140	62.68	0.71	0.52
02	178.6	69.4	439.8	163 955	40.47	0.51	0.26
03	152.8	88.3	359.4	182 988	30.98	0.30	0.14

- <sup>a</sup> Total stellar mass within the dark matter virial radius in  $10^{11} M_{\odot}$ ;  
<sup>b</sup> Stellar mass within 10% of the dark matter virial radius in  $10^{11} M_{\odot}$ ;  
<sup>c</sup> Dark Matter mass within 10% of the dark matter virial radius in  $10^{11} M_{\odot}$ ;  
<sup>d</sup> Number of stellar particles within 10% of the dark matter virial radius;  
<sup>e</sup> Effective radius of the stellar component of the galaxy, calculated as three dimensional half-mass radius, in kpc;  
<sup>f</sup> Fraction of dark matter relative to the stellar component within the half-mass radius;  
<sup>g</sup> Fraction of dark matter relative to the stellar component within  $0.5 R_{1/2}$ .

### 2.4.2 Brightest Cluster Galaxies from Box3 hr Used in this Work

Brightest Cluster Galaxies (BCGs) live in the centers of the most massive structures in the universe, namely galaxy clusters. They can contain thousands of galaxies, and the lower limit for their total mass is  $M_{\text{tot}} = 1 \times 10^{14} M_{\odot}$ . The most massive galaxy clusters currently known have masses of several time  $10^{15} M_{\odot}$ , for example the Phoenix cluster, the most X-ray luminous cluster known with a massive, star forming BCG in its center, has a mass of  $M_{\text{Phoenix}} = 2.5 \times 10^{15} M_{\odot}$  (McDonald et al., 2012), “El Gordo”, a massive Bullet-like cluster, has a mass of  $M_{\text{El Gordo}} = 2.16 \times 10^{15} M_{\odot}$  (Menanteau et al., 2012). Our neighbouring cluster, Virgo, with its mass of  $M_{\text{Virgo}} = 1.2 \times 10^{15} M_{\odot}$  (Fouqué et al., 2001) is relatively small in comparison, however, it still contains more than 1000 galaxies.

To find such massive structures in a cosmological simulation, the box has to be relatively large. Our Box4 is too small to contain such massive structures, its most massive halo only has a mass of  $M = 2.3 \times 10^{14} M_{\odot}$  at  $z = 0$ . The next largest box, Box3, has been already available in the hr resolution to be included in the study presented in Remus et al. (2013) (see also Chap. 3), while Box2 hr was still at high redshifts. In hr resolution, however, the resolution of the stellar content of non-BCGs is too low to study dynamical effects. Therefore, we only included BCGs in our analysis.

We selected three BCGs from the most massive clusters present in Box hr, where the BCG contains at least  $10^5$  star particles and is not currently undergoing a merger. We will refer to these massive central cluster galaxies as Magneticum BCGs hereafter, especially in Chap. 3. Table 2.5 summarizes the properties of the three spheroidals from Box3 hr. We did not use a classification for those galaxies, since our classification scheme is flawed for BCGs, as demonstrated before (see Fig. 2.10).

### 2.4.3 Galaxies from Box4 uhr Used in this Work

During most of the studies presented in this thesis we used Box4 uhr from the Magneticum Pathfinder simulation set. This is owed by fact that for all studies large enough numbers of stars are needed in all regions of the galaxies, and thus the galaxies selected from boxes with lower resolutions are not resolved well enough for our needs. As described in Sec. 2.4.1, we find all kinds of morphological

<sup>12</sup> This table has been published in Remus et al. (2013).

types in the galaxies present in Box4 uhr, however, for the analysis performed in Chap. 4 we were only interested in those galaxies that were classified as spheroidals. This includes spheroidals with and without cold gas disks. All our spheroidals from Box4 uhr are listed in Tab. 2.6, with the numbers in the first row the numbers from the catalogue where the galaxies are sorted by their total mass, see Tab. B.1 in App. B.

With our classification scheme we found 97 spheroidals at  $z = 0$  in Box4 uhr covering a stellar mass range of 3 orders of magnitude:  $8.6 \times 10^{11} M_{\odot} > M_* > 8.05 \times 10^9 M_{\odot}$ . Their halfmass radii cover a radius range of  $16 \text{ kpc} > r_{1/2} > 2 \text{ kpc}$ , and their central dark matter fractions within the halfmass radius range from  $f_{\text{DM}} \approx 9\%$  to  $f_{\text{DM}} \approx 60\%$ . About half of our galaxies have a cold gas disk, namely 47. This is a bit on the high end of what is observed in the Atlas<sup>3D</sup> sample, where Young et al. (2013) reported cold gas disks within 40% of their spheroidals, but their detections of gas might still be incomplete due to resolution issues, since they might not detect very tiny gas disks which are still included in our sample. Also, as discussed before, we have included 4 galaxies with massive gas disks in our spheroidal sample by accident since the gas disk is oriented along the short axis of the stellar component and not along the largest axis, and thus their gas disks have been missclassified by the circularity  $\epsilon$ .

In addition to the study presented in Chap. 4, these spheroidal galaxies from Box4 uhr are also used in the analysis presented in Sec. 6.3. A subset of these galaxies is already studied by Remus et al. (2015a) and Remus et al. (2015b), and they are included in the study on fundamental galaxy parameters in the Magneticum Pathfinder simulations shown in App. A.5.

In Chap. 5 we study properties of Milky Way mass halos selected from Box4 uhr. Tab. 2.8 lists all 24 Milky Way mass halos present in this simulation at  $z = 0$ , including properties like the mean formation redshifts of the stars in the galaxy, the total spin parameter (Peebles, 1971; Mo et al., 1998) and the morphology, since in this study we include disk galaxies as well as spheroidals and unclassified systems. All other subsets of galaxies from Box4 uhr used in Chap. 5 are not shown in their own table, but can be found in Tab. B.1 in the Appendix. This is also the case for the study presented in App. A.4.

**Table 2.6:** *Magneticum spheroidals Box4 uhr at  $z = 0$*

$Nr_{\text{Gal}}$	$f_{\text{Cold Disk}}^{(a)}$	$M_{\text{tot}}^{(b)}$	$M_{\text{Gal}}^{(c)}$	$R_{1/2}^{(d)}$	$f_{\text{Gas}}^{(e)}$	$f_{\text{DM}}^{(f)}$	$f_{\text{DM}}^{\text{SR}1/2(g)}$
7	yes	42.94	86.37	13.18	0.18	0.37	0.76
8	no	53.23	49.58	16.23	1.71	0.53	0.84
14	yes	27.20	46.79	9.48	0.16	0.35	0.77
15	no	26.81	56.96	8.71	7.21	0.28	0.73
31	no	15.53	41.73	14.06	3.13	0.38	0.72
45	yes	11.33	30.61	13.24	0.13	0.46	0.82
57	yes	8.93	24.70	7.41	0.10	0.32	0.76
58	yes	8.55	25.73	12.97	0.53	0.51	0.81
69	no	7.68	16.10	8.71	0.22	0.39	0.77

– Continued on next page –

$Nr_{\text{Gal}}$	$f_{\text{Cold Disk}}^{(a)}$	$M_{\text{tot}}^{(b)}$	$M_{\text{Gal}}^{(c)}$	$R_{1/2}^{(d)}$	$f_{\text{Gas}}^{(e)}$	$f_{\text{DM}}^{(f)}$	$f_{\text{DM}}^{5R_{1/2}^{(g)}}$
70	yes	7.57	27.70	8.14	0.11	0.34	0.75
74	yes	7.17	19.91	9.85	0.14	0.41	0.80
75	yes	7.09	17.82	9.24	0.24	0.42	0.76
77	yes	6.93	15.77	8.16	0.19	0.39	0.80
78	no	6.93	7.62	6.57	0.16	0.38	0.82
80	yes	6.58	15.41	10.61	0.40	0.47	0.80
81	yes	6.51	19.71	5.62	0.24	0.20	0.62
90	no	5.45	13.88	6.12	0.04	0.31	0.76
92	no	5.41	20.46	8.46	0.07	0.34	0.76
98	yes	5.09	18.23	6.84	0.14	0.33	0.71
102	yes	4.90	12.75	7.99	0.06	0.38	0.78
104	yes	4.85	11.82	9.06	0.14	0.48	0.81
108	yes	4.65	11.47	5.56	0.14	0.30	0.75
109	no	4.64	10.57	4.34	0.04	0.26	0.70
112	no	4.54	5.10	6.49	0.09	0.44	0.80
113	yes	4.50	10.78	9.65	0.24	0.46	0.79
125	no	4.11	8.16	3.98	0.00	0.18	0.70
128	yes	4.06	13.63	8.43	0.10	0.43	0.76
135	yes	3.73	8.21	7.01	0.17	0.40	0.78
139	yes	3.50	11.72	5.86	0.04	0.26	0.70
143	yes	3.43	10.56	5.34	0.00	0.27	0.72
151	yes	3.21	10.73	10.40	0.58	0.47	0.78
160	no	3.04	10.81	8.43	3.52	0.44	0.77
162	yes	3.02	3.41	5.37	0.28	0.45	0.77
165	yes	2.97	8.81	4.47	0.07	0.22	0.70
172	no	2.76	5.79	3.51	0.00	0.19	0.70
195	no	2.48	8.74	5.97	24.66	0.33	0.68
197	no	1.82	11.88	6.12	0.07	0.33	0.73
198	no	2.42	8.04	4.83	0.03	0.30	0.74
200	yes	2.41	4.74	4.74	0.13	0.31	0.74
213	yes	2.21	4.71	4.73	0.07	0.32	0.78
216	yes	2.17	5.47	7.12	0.67	0.50	0.80
221	no	1.62	9.31	2.92	4.00	0.12	0.55
222	no	2.10	5.05	3.15	0.00	0.17	0.71
235	no	2.01	8.66	4.08	0.50	0.23	0.69
236	no	2.00	7.64	3.44	6.90	0.21	0.61
237	yes	2.00	3.13	5.43	0.48	0.45	0.80
238	no	1.99	3.77	7.25	0.23	0.45	0.82
242	yes	1.97	6.49	7.03	0.27	0.43	0.77
248	no	1.93	4.96	5.49	0.00	0.37	0.80
252	no	1.89	6.39	4.18	0.18	0.24	0.68
255	no	1.87	3.56	3.35	0.00	0.22	0.72
259	no	1.83	4.98	5.19	0.00	0.33	0.76
260	no	1.82	4.75	5.37	19.89	0.36	0.72
261	yes	1.81	4.90	7.43	0.17	0.53	0.84
266	no	1.78	4.55	6.82	0.12	0.41	0.79
270	no	1.74	5.32	6.64	0.17	0.39	0.75

– Continued on next page –

$Nr_{\text{Gal}}$	$f_{\text{Cold Disk}}^{(a)}$	$M_{\text{tot}}^{(b)}$	$M_{\text{Gal}}^{(c)}$	$R_{1/2}^{(d)}$	$f_{\text{Gas}}^{(e)}$	$f_{\text{DM}}^{(f)}$	$f_{\text{DM}}^{5R_{1/2}(g)}$
287	no	1.62	4.59	6.46	0.08	0.45	0.76
289	no	1.61	2.96	3.18	0.00	0.24	0.73
294	no	1.59	4.74	5.42	0.00	0.39	0.81
295	no	1.58	3.75	3.60	0.00	0.25	0.78
306	yes	1.55	4.51	5.10	0.09	0.37	0.77
315	no	1.47	3.76	3.92	0.00	0.26	0.74
321	yes	1.44	3.71	4.59	0.11	0.31	0.73
331	yes	1.39	3.99	6.51	0.26	0.43	0.82
335	yes	1.38	3.46	3.32	0.00	0.24	0.73
340	no	1.36	3.69	3.44	0.06	0.19	0.70
341	yes	1.36	1.93	2.86	0.00	0.27	0.74
352	yes	1.29	3.53	4.55	0.13	0.35	0.74
359	no	1.27	2.35	3.38	0.00	0.30	0.74
363	no	1.26	4.55	5.72	0.07	0.42	0.80
368	no	1.25	2.47	3.97	0.00	0.36	0.78
373	no	1.23	2.29	3.06	0.00	0.26	0.77
381	no	1.21	5.44	2.39	5.45	0.09	0.53
390	yes	1.20	4.94	5.24	0.06	0.30	0.70
399	yes	1.15	3.59	5.40	0.00	0.41	—
401	yes	1.14	4.06	5.67	0.00	0.42	0.77
409	no	0.95	6.09	2.57	9.58	0.12	0.55
424	no	1.05	2.90	3.57	0.08	0.23	0.73
437	yes	1.02	2.91	4.13	0.11	0.36	0.74
452	no	0.99	2.95	3.68	0.00	0.29	0.73
453	no	0.99	3.00	9.52	9.08	0.60	0.85
457	yes	0.97	2.44	6.02	0.40	0.51	0.82
460	no	0.97	3.01	2.86	0.00	0.15	0.65
464	yes	0.96	3.47	4.94	0.07	0.40	0.76
472	no	0.94	2.95	3.15	0.00	0.23	0.75
485	no	0.92	3.54	5.93	0.00	0.47	0.81
494	no	0.90	2.70	4.26	27.03	0.32	0.69
509	no	0.86	3.00	3.55	0.08	0.27	0.70
522	yes	0.85	2.29	4.17	0.14	0.40	0.78
526	no	0.84	3.65	4.12	0.10	0.30	0.72
531	yes	0.83	2.06	3.92	0.26	0.44	0.78
550	no	0.80	3.15	2.82	0.00	0.13	0.66
556	yes	0.79	0.80	2.26	0.00	0.24	0.71
564	yes	0.79	2.61	3.24	0.00	0.28	0.73
569	yes	0.78	2.06	2.99	0.00	0.29	0.75
578	yes	0.77	1.56	4.34	0.00	0.43	0.79
600	no	0.74	2.42	4.04	0.14	0.38	0.75

<sup>a</sup> If a cold gas disk is present in the center of the spheroid, column is “yes”, else “no”;

<sup>b</sup> Total mass of the halo in  $10^{12}M_{\odot}$ ;

<sup>c</sup> Stellar mass within  $2R_{1/2}$  in  $10^{10}M_{\odot}$ ;

<sup>d</sup> Effective radius of the stellar component of the galaxy, calculated as three dimensional half-mass radius, in kpc;

<sup>e</sup> Fraction of the gas mass relative to the stellar mass within the half-mass radius in %;

<sup>f</sup> Fraction of the dark matter relative to the total mass within the half-mass radius;

**Table 2.8:** *Magneticum Box4 uhr Milky Way mass halos at  $z = 0$* 

$Nr_{\text{Gal}}$	Morphology <sup>(a)</sup>	$M_{\text{Gal}}$ <sup>(b)</sup>	$N_{\text{Gal}}$ <sup>(c)</sup>	$M_{\text{Gal}}^{\text{sat}}$ <sup>(d)</sup>	$f_{\text{Cold Gas}}$ <sup>(e)</sup>	$\langle z \rangle$ <sup>(f)</sup>	$\lambda$ <sup>(g)</sup>
438	disk	1.46	7719	3.20	96.40	1.09	0.05
435	disk	4.19	21414	4.21	1.38	1.91	0.02
429	unclass	3.24	14852	3.72	0.00	1.86	0.14
441	unclass	4.12	21050	4.50	0.08	2.07	0.02
443	unclass	5.44	28109	5.44	1.15	1.79	0.06
442	disk	4.89	24814	4.90	7.60	1.23	0.02
447	disk	4.04	19924	4.16	53.27	0.93	0.03
439	unclass	2.50	12906	2.68	11.12	2.20	0.03
450	unclass	3.59	18729	4.23	12.20	1.59	0.07
451	disk	3.86	19353	4.01	30.93	1.50	0.11
430	unclass	4.16	22019	4.28	0.06	2.50	0.02
431	unclass	3.77	19948	3.88	4.14	1.60	0.03
434	disk	1.93	10249	3.69	36.15	1.36	0.20
445	disk	3.90	20133	4.26	0.00	2.91	0.03
437	spheroid	3.19	17153	3.32	10.31	1.89	0.08
440	disk	1.82	9621	2.68	32.77	1.41	0.09
446	unclass	3.52	17846	3.80	0.00	3.17	0.01
428	unclass	2.14	11339	2.98	0.08	2.15	0.06
449	disk	2.69	14191	3.15	22.65	1.69	0.03
433	unclass	3.65	19467	3.65	0.00	2.56	0.02
436	spheroid	2.94	15908	3.37	0.08	3.35	0.02
432	spheroid	2.56	13601	2.82	0.96	2.26	0.02
444	unclass	3.08	16379	3.13	0.00	2.92	0.01
448	spheroid	1.85	10106	2.07	11.22	2.88	0.02

<sup>a</sup> Morphology of the galaxy according to the classification criterion from Sec. 2.4.1;

<sup>b</sup> Stellar mass within the virial radius in  $10^{11}M_{\odot}$ ;

<sup>c</sup> Number of stellar particles within the half-mass radius  $R_{1/2}$ ;

<sup>d</sup> Stellar mass within the virial radius in  $10^{11}M_{\odot}$  including the stars that belong to satellites;

<sup>e</sup> Fraction of the cold gas relative to the stellar content within the half-mass radius in %;

<sup>f</sup> Mean formation redshift of all stars within the main galaxy;

<sup>g</sup> Dimensionless spin parameter according to (Peebles, 1971);

<sup>ng</sup> Fraction of the dark matter relative to the total mass within  $5R_{1/2}$ ;



## Chapter 3

# The Dark Halo – Spheroid Conspiracy and the Origin of Elliptical Galaxies<sup>13</sup>

### 3.1 Introduction

Early-type galaxies are among the most massive and prominent galaxies of the universe, and thus their origin and formation history has been the focus of many observational studies as well as simulations. Since Toomre (1977) proposed that elliptical galaxies can be produced by a merger between two spiral galaxies, several simulations have studied this mechanism in detail, for example White (1978, 1979a,b); Gerhard (1981); Negroponte & White (1983); Barnes (1988), including various gas fractions (Hernquist, 1989; Barnes & Hernquist, 1996; Naab et al., 2006a; Novak et al., 2012) and black hole physics (Springel et al., 2005a; Johansson et al., 2009a,b).

Although major merger simulations of spiral galaxies could explain many observed properties of ellipticals, several problems were also identified. A number of studies have indicated that observations of massive, slowly rotating and spheroidal ellipticals cannot be explained by wet or dry major mergers of disk galaxies (Naab & Burkert, 2003; Cox et al., 2006; Burkert et al., 2008; Bois et al., 2010, 2011). Multiple early-type mergers would be needed in order to form the most massive ellipticals with masses that exceed the mass of spiral galaxies (Naab et al., 2006b; González-García et al., 2006; Khochfar & Silk, 2006). Genel et al. (2010) however demonstrated that the fraction of observed major early-type mergers is not high enough to explain the number of observed giant elliptical galaxies. An additional complication is that the high metallicity and old ages observed in present day massive early-type galaxies cannot be explained by binary mergers between two typical present day spiral galaxies or their progenitors (Naab & Ostriker, 2009, see however Hopkins et al., 2008).

Simulations of the formation of elliptical galaxies in a full cosmological context result in a different overall picture (e.g., Meza et al., 2003; Naab et al., 2007, 2009; González-García et al., 2009; Feldmann et al., 2010, 2011; Oser et al., 2010, 2012; Johansson et al., 2012; Lackner et al., 2012), verifying the idea that elliptical galaxies can be produced by multiple minor mergers, a much more likely evolution of events in the lifetime of a galaxy (see also Bournaud et al., 2007). Mass accretion histories from cosmological simulations (e.g., Gao et al., 2004; Fakhouri & Ma, 2008, 2009) have shown that the most likely process for forming elliptical galaxies is a mixture of both scenarios: most

---

<sup>13</sup> This chapter has been published as Remus et al. (2013), and its scientific part is directly cited from this paper. The discussion of the details of the simulations, however, has been omitted as it is already contained in Chap. 2 of this thesis.

massive halos go through an early dissipative phase of fast accretion, including major merger events, followed by a phase of stellar accretion, during which all kind of mergers and even smooth accretion can be the dominant growth mechanism (e.g., Oser et al., 2010).

There have been several approaches to connect the observed elliptical properties to the different formation scenarios to investigate if we can explain observed features by the evolution history of individual ellipticals. For example, Naab et al. (1999); Bendo & Barnes (2000); Naab & Burkert (2003); Jesseit et al. (2005); Cox et al. (2006) and González-García et al. (2009) studied the kinematics and photometric shapes of simulated spheroidals in order to understand the origin of the shape of the galaxy, the origin of boxy and disk isophotes and the connections between the kinematic properties and the gas fraction of the merger event, Naab et al. (2006a) showed that the line-of-sight velocity dispersions are strongly influenced by gas (see also Hoffman et al., 2009, 2010), while Qu et al. (2010) and Di Matteo et al. (2009) showed that multiple minor mergers slow down the rotation of an elliptical, while major mergers can speed them up.

Recent results from the Atlas<sup>3D</sup> survey (Cappellari et al., 2011a), which uses integral field spectroscopy to study the properties of early-type galaxies, have revealed that the vast majority of all early-type galaxies (82–86 per cent) in their volume-limited local galaxy sample is fast rotating, while only very few early-type galaxies are classified as slow or even non rotating (Emsellem et al., 2011). A significant fraction of the slow rotating ellipticals show special features such as a counter-rotating core. The non rotating early-types are usually found in highly overdense environments (Krajnović et al., 2011). Bois et al. (2011) showed, comparing simulations of isolated merger events to the Atlas<sup>3D</sup> results, that major mergers can reproduce all kinds of elliptical galaxies that are fast rotating as well as population of flat, slow rotating elliptical galaxies with kinematically distinct cores. They fail, however, to reproduce very round, massive, slow or even non-rotating ellipticals that typically live in very dense environments (see also Burkert et al., 2008), supporting the idea that the round slow rotators and the fast rotating systems actually are two distinct families of early-type galaxies with different formation histories.

Elliptical galaxies consist mainly of a stellar and a dark matter component that might provide interesting information about their formation history. For example, it is long known from observations that there exists a dark halo – disk conspiracy for spiral galaxies, i.e., the rotation curves of spiral galaxies are flat (Einasto et al., 1974; Faber & Gallagher, 1979). Detailed dynamical modeling, for example by Kronawitter et al. (2000) and Gerhard et al. (2001), has demonstrated that a similar conspiracy might also exist between the dark halo and the spheroid of massive, slow rotating elliptical galaxies.

Further studies, using planetary nebulae as tracers for the outer dark halo, however have revealed a bimodality in the kinematic structures of the outer regions of elliptical galaxies: Some lower-mass ellipticals show declining velocity dispersion profiles, similar to a Keplerian mass distribution, indicating a constant mass-to-light ratio and thus a shallow dark matter halo (Méndez et al., 2001; Romanowsky et al., 2003), while especially more massive, slow rotating galaxies show flat dispersion profiles as expected for a classical, extended dark matter halo (Napolitano et al., 2001; Peng et al., 2004a). The origin of this bimodality has been discussed, suggesting for example that extremely elongated orbits of stars and planetary nebulae in the outskirts of low-mass ellipticals can mask even a massive dark matter halo (Dekel et al., 2005). A recent study by Deason et al. (2012) investigated dark matter fractions and density and velocity dispersion profiles of 15 elliptical galaxies out to 5 effective radii, using planetary nebulae and globular clusters as tracers.

A more detailed look at the de-projected dark matter component of elliptical galaxies inside the

half-light radius is provided by Thomas et al. (2007, 2009), using Schwarzschild modeling of the observational kinematic and photometric data of early-type galaxies in the Coma cluster. They show that the best fitting models contain 10 to 50 per cent dark matter within the half-light radius. Furthermore, their models without dark matter halos are not able to fit the observations.

Another approach to study the dark matter content of elliptical galaxies comes from strong lensing. Auger et al. (2010), studying 73 early-type galaxies from the SLACS survey, found that the total dark matter plus stellar density profiles of these ellipticals can be described on average by a power law with a slope of  $-2.078$ , with the steepness of the individual slopes correlating with the effective radius and the central density of the stellar component. A similar result was found by Barnabè et al. (2011) for 16 early-type galaxies from SLACS, where they combined the constraints from gravitational lensing with stellar kinematics. Further studies by Ruff et al. (2011) and Bolton et al. (2012) revealed that this is also the case for strong-lensing early-type galaxies at higher redshifts: Ruff et al. (2011) found that their 11 early-type galaxies in a redshift range of  $0.2 \lesssim z \lesssim 0.65$  can be fit on average by a slope of  $-2.16$ , while Bolton et al. (2012) found for their sample of 79 early-type galaxies in the redshift range of  $0.1 \lesssim z \lesssim 0.6$  a density slope of on average  $-2.11$ . Both report a slight trend to flatter slopes at higher redshifts.

An additional method to measure the dark matter content of early-type galaxies is weak lensing, which enables measurements to much larger radii than strong lensing. Gavazzi et al. (2007) showed for 22 early-type galaxies from weak lensing that their total density profiles can be described by a power law with a slope of approximately  $-2$  for radii as large as 300 kpc, which is up to 100 effective radii.

In a recent study Lyskova et al. (2012) investigated a sample of cosmological simulations of massive galaxies presented by Oser et al. (2010) and found a remarkable uniformity of the present day isothermal total stellar mass profiles in good agreement with lensing results. In this work we investigate the structure of dark matter halos (density distribution and kinematics) around simulated ellipticals in more detail and relate it to the formation mechanisms and histories of elliptical galaxies. Using a variety of different simulations allows us to study the effects of the multiple merger evolution in comparison to the major merger scenario as well as the influence of the environment on the resulting dynamical profiles.

In this chapter we analyse spheroidals formed in different scenarios: Isolated binary merger simulations (hereafter Binary Merger), as described in Sec. 2.2.1, hydrodynamical cosmological zoom-in simulations (hereafter CosmoZoom, see Sec. 2.3.1 for the sample included in this chapter) and the three BCGs selected from the Magneticum Pathfinder simulation Box3 hr (hereafter Magneticum Pathfinder, see also Sec. 2.4.2). The details of all simulations are described in Chap. 2 of this thesis<sup>14</sup>.

### 3.2 The Dark Halo – Spheroid Conspiracy

We identify all stars within  $0.1R_{\text{vir}}$  to belong to the central elliptical, similarly to Oser et al. (2010), independent of the simulation type. The galaxy masses used throughout this work are calculated according to these definitions.

For the companion ellipticals from the cosmological simulations, where significant parts of the dark matter have been stripped already and thus the virial radius cannot be obtained from the dark

---

<sup>14</sup> This paragraph was not included in the original paper but added as a replacement for the description of the simulations which was included as a Sec. 2 in Remus et al. (2013).

matter mass of the subhalo, we use the maximum circular velocity  $v_{\max}$  to calculate the virial mass and the virial radius the halo had before the infall into the parent halo, using Equations 2.2 and 2.3 with  $v_{\max}$  as  $v_{\text{vir}}$ . These companion ellipticals are particularly interesting since our observational comparison sample, the elliptical galaxies in the Coma cluster (Thomas et al., 2007), are embedded in the larger Coma cluster environment themselves and thus supposedly have a similar formation scenario to the companion ellipticals.

For most of this work we use the elliptical galaxies at the final output time of 3 Gyr for the binary merger simulations and the ellipticals identified at a redshift of  $z = 0$  for all cosmological simulations. First we calculate the three dimensional stellar half-mass radius  $R_{1/2}$  for all elliptical galaxies in our sample, i.e., the radius which contains 50% of all stars that were identified to belong to the galaxy. Next the intrinsic velocity dispersion and density within spherical equal-mass shells around the center of our simulated galaxies are calculated for stars and dark matter separately as well as for both components combined: within each shell we first calculate the intrinsic velocity dispersion for stars and dark matter separately, as

$$\sigma = \sqrt{\sigma_r^2 + \sigma_\theta^2 + \sigma_\phi^2} \quad (3.1)$$

with  $\sigma_r = \sqrt{\langle v_r^2 \rangle - \langle v_r \rangle^2}$  and  $\sigma_\theta$  and  $\sigma_\phi$  analogous. Since dark matter and stellar particles have different masses within all our simulations, we need to calculate the total intrinsic mass-weighted velocity dispersion for the combined profiles within each shell as

$$\sigma_{\text{tot}} = \sqrt{\frac{m_{\text{DM}}\sigma_{\text{DM}}^2 + m_{\text{S}}\sigma_{\text{S}}^2}{m_{\text{DM}} + m_{\text{S}}}} \quad (3.2)$$

to obtain a total velocity dispersion that is representative for the whole potential. Profiles for three example halos are shown in Figure 3.1, for the density in the upper panels and the velocity dispersion in the lower panels. We choose one example halo for each simulation type, for the Binary (left), the CosmoZoom (central) and the Magneticum (right) Ellipticals.

A power law is fit to these velocity dispersion and density profiles, to stars and dark matter separately as well as to the combined profiles. The fit to the combined profiles is shown as a green dashed line in Figure 3.1 for the three example halos. We were especially interested in the transition area, where the dark matter part becomes dominant in its contribution to the total density and velocity profiles. This transition area is characterized well by the stellar half-mass radius  $R_{1/2}$  for all galaxies, and thus we choose the fitting range to depend on  $R_{1/2}$ . For the Binary Ellipticals and the CosmoZoom Ellipticals the best-fitting power-law index for the velocity dispersions is determined in the radius regime  $0.3R_{1/2}$  to  $2R_{1/2}$ , the power law for the density is fit between  $0.3R_{1/2}$  and  $4R_{1/2}$ . For the CosmoZoom Companions and the Magneticum BCGs the best-fitting power laws are determined with a lower limit of  $0.5R_{1/2}$  instead of  $0.3R_{1/2}$  due to resolution limits. The lower limits are chosen to ensure that the innermost particles included are at least 3 times the smoothing length away from the center. The upper limits are chosen due to comparability with observations of Coma ellipticals by Thomas et al. (2007), where density slopes are available up to  $4R_{\text{eff}}$  while velocity dispersion slopes are only available up to  $2R_{\text{eff}}$ .

Figure 3.2 shows the combined dark matter and baryonic density profiles multiplied by  $r^2$  for all Binary and CosmoZoom Ellipticals normalized to the density at  $0.3R_{1/2}$  and for all CosmoZoom Companions and Magneticum BCGs normalized at  $0.5R_{1/2}$ , illustrating that a power-law fit is actually

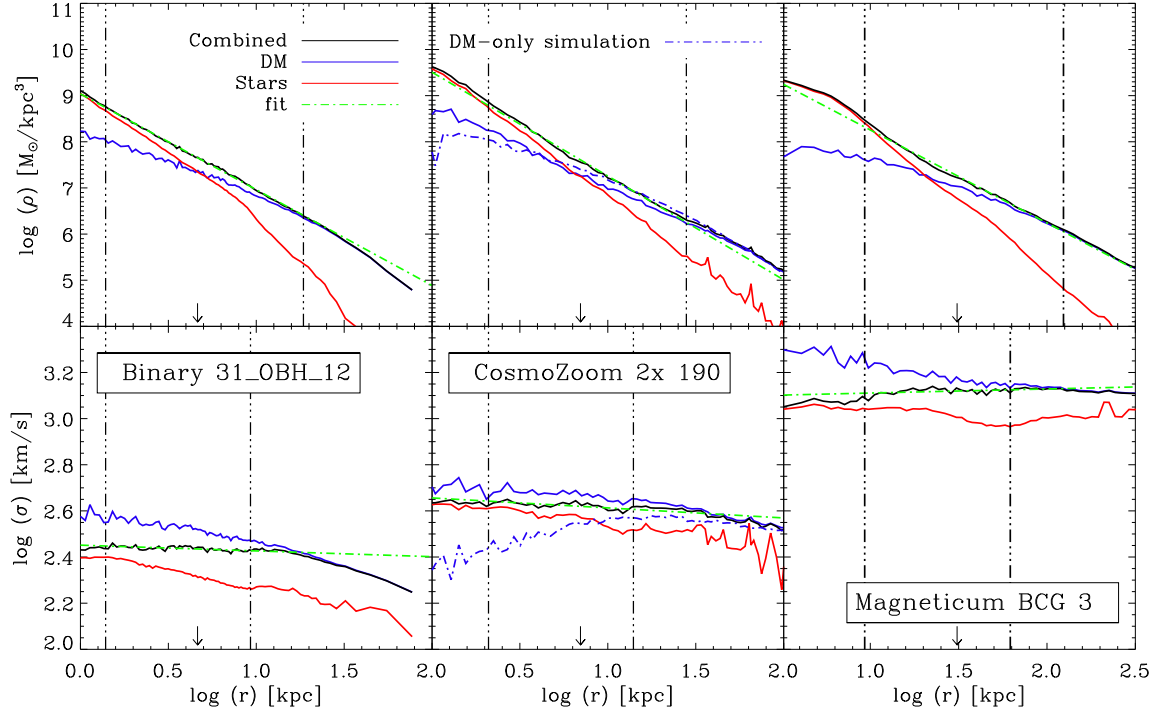


**Figure 3.1:** Density (upper panel) and velocity dispersion (lower panel) profiles for three example halos. Left panels: 3:1 Binary Elliptical 31\_OBH2\_13. Central panel: CosmoZoom Elliptical 190. Right panel: Magneticum BCG 03. Red solid line: stellar profile; blue solid line: dark matter profile; black line: combined profile; green line: power-law fit to the combined profile. Dashed black lines for the left and central panel:  $0.3R_{1/2}$  and  $4R_{1/2}$  for the density,  $0.3R_{1/2}$  and  $2R_{1/2}$  for the velocity; for the right panel:  $0.5R_{1/2}$  and  $4R_{1/2}$  for the density,  $0.5R_{1/2}$  and  $2R_{1/2}$  for the velocity. The arrows mark the position of the half-mass radius. The dash-dotted blue line in the central panel shows the dark matter profile for the dark matter-only re-simulation of CosmoZoom Elliptical 190.

a good approximation for most of our ellipticals. The only exceptions are the halos with an unusually dominant central stellar component, which are the least massive of the CosmoZoom Ellipticals with four times the spatial resolution and some of the CosmoZoom Companions. These halos have slightly curved combined density profiles and the best fitting power laws have generally steeper slopes.

Figure 3.1 and Figure 3.2 also show that the power-law fit to the total density profiles of the CosmoZoom Ellipticals and the Magneticum BCGs is a good approximation to even larger radii than  $4R_{1/2}$ , even though the profiles become less smooth due to the presence of satellite galaxies. This is in agreement with observations from weak lensing by Gavazzi et al. (2007), who found for 22 central elliptical galaxies that their total density profiles can be fit on average by a power law with a slope of  $\gamma \approx -2$  over two decades in radius. A similar behavior can also be seen for the CosmoZoom Companions, although their density profiles break down at about  $10R_{1/2}$  due to the fact that their dark matter halos got stripped during the infall into the larger parent halo. For the Binary ellipticals, the density profiles already break down at about  $5R_{1/2}$  due to the fact that the simulations do not reach further out.

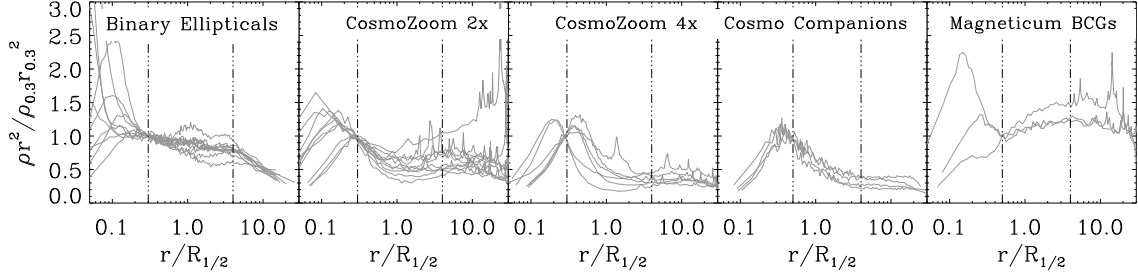


**Figure 3.2:** Combined dark matter and baryonic density profiles for all ellipticals, multiplied by  $r^2$  and normalized to the density value at  $0.3R_{1/2}$  ( $0.5R_{1/2}$  for the CosmoZoom Companions and the Magneticum BCGs). From left to right: Binary Ellipticals, CosmoZoom Ellipticals with twice the spatial resolution, CosmoZoom Ellipticals with four times the spatial resolution, CosmoZoom Companions, and Magneticum BCGs. The dashed lines mark  $0.3R_{1/2}$  and  $4R_{1/2}$  for the first three panels,  $0.5R_{1/2}$  and  $4R_{1/2}$  in the last two panels.

### 3.2.1 Density and Velocity Dispersion Slopes

For a spherical isothermal system the solution of the Jeans Equation is

$$\rho(r) = \frac{\sigma^2}{2\pi G r^2}. \quad (3.3)$$

More generally, under the assumption that both the velocity dispersion and the density can be described by simple power laws, i.e.,  $\rho(r) = Ar^\gamma$  and  $\sigma(r) = Br^\beta$  with  $A$  and  $B$  being constants, the Jeans Equation has the following solution:

$$\rho(r) = \frac{C\sigma(r)^2}{4\pi G r^2} \quad (3.4)$$

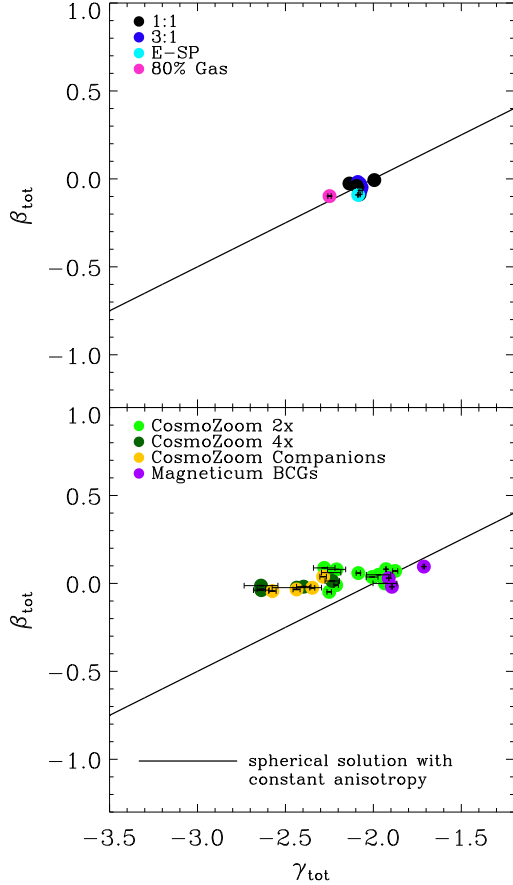
with  $C$  being a dimensionless constant. Thus, the slopes of the dispersion and the density are correlated by

$$\beta = 0.5\gamma + 1. \quad (3.5)$$

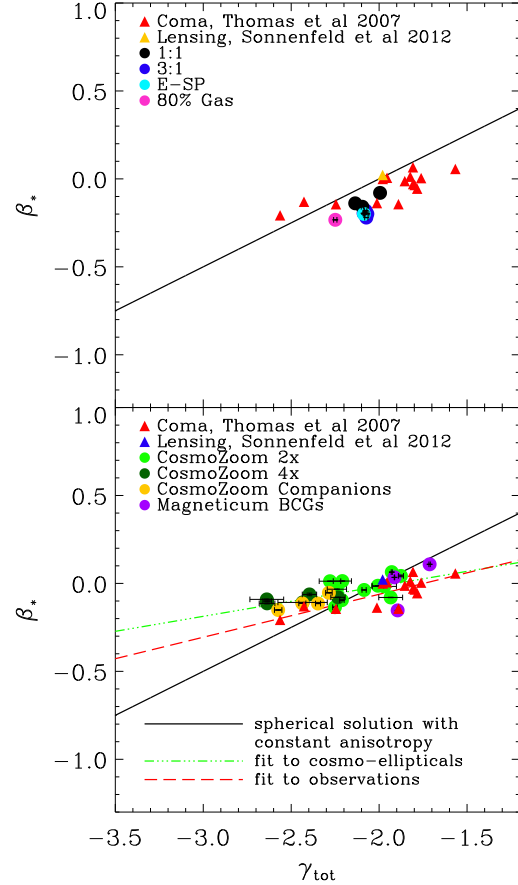
This correlation is shown in both panels of Figure 3.3 and Figure 3.4 as a solid black line and in Figure 3.5 and Figure 3.6 as dotted black line. These relations hold for all systems with constant anisotropy as a function of radius, since different values for the constant anisotropy only change the constant  $C$  and thus Equation 3.5 does not change.

Figure 3.3 shows the total density slopes and total velocity dispersion slopes for all Binary Ellipticals in the upper panel and for all CosmoZoom Ellipticals and Magneticum BCGs in the lower panel. We can clearly see that all total slopes of the Binary Ellipticals lie close to the solution of the Jeans Equation, i.e., they have total density slopes around  $\gamma_{\text{tot}} = -2.1$  and total velocity dispersion slopes around  $\beta_{\text{tot}} = 0$ , implying that these ellipticals are fairly close to spherical systems with constant anisotropy, or even isotropic in some cases.

For our sample, neither the choice of different orbits (G01, G09 or G13) nor the merger type (i.e., if it is a 3:1, a 1:1 or an E-SP merger) or the presence of a Black Hole changes the resulting density slopes significantly, while the variation of the initial gas fraction causes the only significant shift in



**Figure 3.3:** Slopes of the total velocity dispersions  $\beta_{\text{tot}}$  against the slopes of the total density profiles  $\gamma_{\text{tot}}$ . Upper panel: Results from the Binary Ellipticals: 1:1 spiral merger (black), 3:1 spiral merger (blue), Elliptical-spiral merger (cyan) and 3:1 spiral merger with 80% gas (pink). Lower panel: Results from the cosmological simulations: CosmoZoom 2X Ellipticals (bright green), CosmoZoom 4X Ellipticals (dark green), CosmoZoom Companions (yellow) and Magneticum BCGs (violet). For all ellipticals the errors are RMS-deviations to the fit. Black line: analytic solution for a spherical system with constant anisotropy.



**Figure 3.4:** Same as Figure 3.3 but for stellar velocity dispersion slopes versus total density slopes. Red triangles show the total density and stellar velocity dispersion slopes for the Coma early-type galaxies presented in Thomas et al. (2007). The yellow (upper panel) respective blue (lower panel) triangle shows the slopes for the massive strong lensing early-type galaxy studied by Sonnenfeld et al. (2012). Dashed lines: linear fits to the Coma values (red) and all cosmological simulations (green).

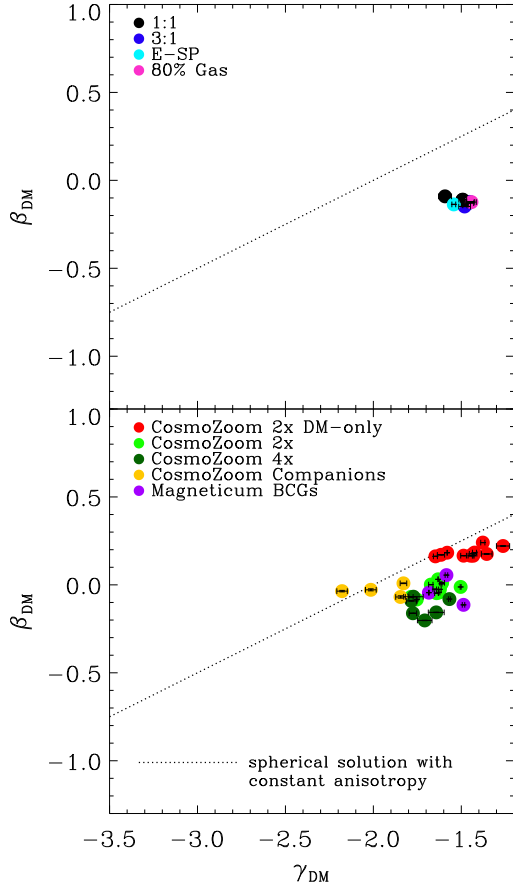


**Figure 3.5:** Same as Figure 3.3 but for both velocity and density slopes of the dark matter alone. Red circles: slopes of the velocity and density from the CosmoZoom dark matter-only re-simulations. Dotted black lines: analytic solution for a spherical system with constant anisotropy. The density slopes cluster in a range of  $-1.8 \lesssim \gamma_{\text{DM}} \lesssim -1.4$  excluding the CosmoZoom Companions (yellow circles) and the dark matter-only re-simulations (red), as explained in the text.

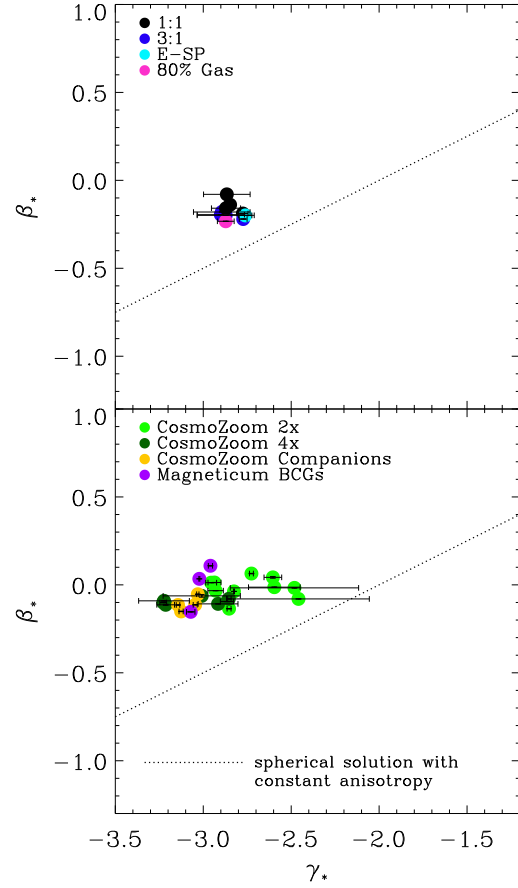


**Figure 3.6:** Same as Figure 3.3 but for both velocity and density slopes of the stellar component alone. Dotted black lines: analytic solution for a spherical system with constant anisotropy. The slopes show no clustering in the density, they are spread over a range of  $-3.25 \lesssim \gamma_* \lesssim -2.4$ .

the density slope. The simulation with 80% initial gas fraction has a significantly steeper total density slope than the comparable simulation with 20% initial gas fraction. At present day, mergers with high gas fractions are unlikely, but at a higher redshift gas-rich major mergers are much more frequent. Still, our 80% gas merger has very large and extended progenitor gas disks, which is unrealistic for high- $z$  disks.

The CosmoZoom Ellipticals show a much larger variety of total density slopes (see the lower panel of Figure 3.3) than the Binary Ellipticals, although they also have flat total velocity dispersion curves, i.e., the slopes of the power-law fits are close to zero. This is in agreement with a detailed

analysis presented in Lyskova et al. (2012), using the same simulation set as Oser et al. (2010). While the CosmoZoom Ellipticals with the flatter density slopes around  $\gamma_{\text{tot}} = -1.9$  and total velocity dispersion slopes around  $\beta_{\text{tot}} = 0.05$  are close to the solution of the Jeans Equation and thus fairly close to spherical systems with constant anisotropy, the CosmoZoom Ellipticals with the steeper density profiles are not. The steeper the total density slopes are, the larger is the deviation from the Jeans solution. This could be due to a combination of gradients in the anisotropy and non-spherical effects that are not included in the simple spherically symmetric approach of this paper. The details will be discussed in a subsequent paper (Remus et al, in preparation). We also find that there is no difference between the behavior of the CosmoZoom Ellipticals and the CosmoZoom Companions. All three Magneticum BCGs are close to the Jeans solution and have relatively flat total density slopes compared to the majority of the CosmoZoom Ellipticals, with their total velocity dispersion slopes are flat as well.

Figure 3.4 shows the stellar velocity dispersion slopes  $\beta_*$  and the total density slopes  $\gamma_{\text{tot}}$  for the Binary Ellipticals in the upper and the CosmoZoom and Magneticum Ellipticals in the lower panel. This figure also includes the stellar velocity dispersion and total density slopes obtained from observations of the Coma ellipticals as presented in Thomas et al. (2007) and the massive, strong-lensing early-type galaxy discussed in detail in Sonnenfeld et al. (2012). The upper panel indicates that our limited sample of Binary Ellipticals cannot reproduce the range of slopes that is seen for the Coma cluster ellipticals, and the observations show no clustering around the values of the Binary Ellipticals. Thus the scenario of a present-day major merger seems unlikely to be the dominant formation scenario for the Coma ellipticals. Binary merger between two high-redshift spirals might produce different results, because the initial conditions for those galaxies would look very different, i.e., they would for example have no large stable gas disks and different dark matter halos, thus we cannot exclude high-redshift binary mergers to be the dominant formation mechanism for the Coma ellipticals.

As can be seen in the lower panel of Figure 3.4, the range of values of the slopes of the CosmoZoom Ellipticals is similar to the range found for the observed Coma cluster ellipticals (Thomas et al., 2007), although there is a slight offset in the velocity dispersion slopes with respect to the observations. The Magneticum BCGs are in good agreement with the slopes found for the more massive Coma Ellipticals, although the observational sample does not include the BCGs since the data of the Coma BCGs reach out to only  $0.5R_{1/2}$ .

Interestingly, if we look at the density slopes against the velocity slopes for the dark matter component only, the values cluster around  $\gamma_{\text{DM}} = -1.5$  for the Binary Ellipticals and around  $\gamma_{\text{DM}} = -1.67$  for the CosmoZoom Ellipticals and the Magneticum BCGs, as shown in Figure 3.5. This is in agreement with the observational results presented by Sonnenfeld et al. (2012), who found a dark matter density slope of  $\gamma_{\text{DM}} = -1.7 \pm 0.2$  for their massive strong-lensing early-type galaxy. Only the CosmoZoom Companions show different values, which is most likely due to the fact that the outer parts of their dark matter halos have been stripped significantly during the infall in the parent halo, causing a steeper slope.

We also include in the lower panel of Figure 3.5 the slopes from the fits to the profiles of the dark matter only re-simulations of the CosmoZoom-2x Ellipticals, to study the influence of the stellar component on the dark matter halos directly. As can be seen, the density slopes of the dark matter only re-simulations are slightly flatter (around  $\gamma_{\text{DM only}} = -1.46$ ) than for the dark halos that contain a stellar component, and both their density and velocity dispersion slopes are closer to the theoretical solution for an isothermal sphere. This can also be seen in the central panels of Figure 3.1, which shows the density and velocity dispersion curves of the dark matter component for an example Cos-

moZoom Elliptical as solid blue line and the corresponding curves for the dark matter only simulation of the same halo as the blue dashed line. These values for the slopes of dark matter halos from dark matter only simulations are in agreement with results for the slopes of the central density of dark matter halos from high resolution dark matter only simulations presented by Moore et al. (1999), who found slopes of  $\gamma_{\text{DM only}} \approx -1.5$ , which is the same as what would be expected for NFW-profiles (Navarro et al., 1996) in this radius range.

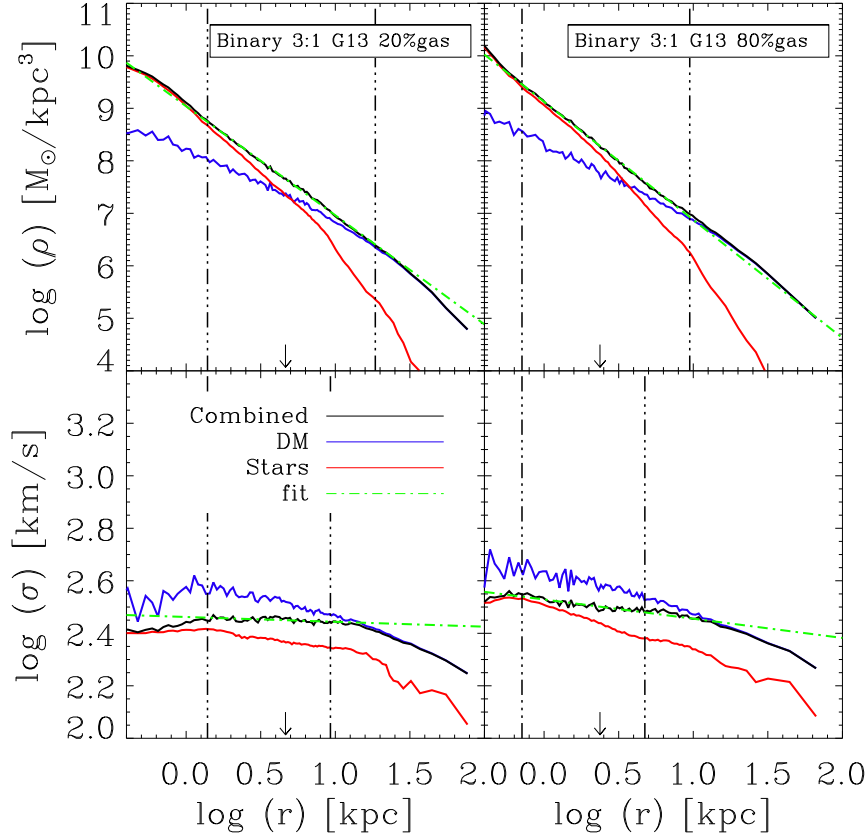
We see that the presence of the stellar component significantly alters the distribution of the dark matter. If the baryonic component is included in the simulation, the dark matter halo is denser in the center and thus the dark matter density slope is steeper, although for both the simulation with and without baryons the density converges to the same values at large radii beyond approximately  $5R_{1/2}$ . This is in agreement with results presented for example by Oñorbe et al. (2007) and Johansson et al. (2012), and is due to the well-known effect of adiabatic contraction, i.e., the dark matter particles are pulled inward due to the condensation of the gas in the center of the halo (e.g., Jesseit et al., 2002; Blumenthal et al., 1986; Gnedin et al., 2004, 2011, see however Dutton et al., 2007 and, regarding the effects of expansion due to sudden outflows driven by supernovae, Pontzen & Governato, 2012). An even stronger effect caused by the presence of baryons can be seen for the velocity dispersion profile in the lower panel of Figure 3.1. While the velocity dispersion of the dark matter component of the simulation with baryons slightly decreases with larger radii, the dark matter-only simulation shows a velocity dispersion that is strongly increasing with larger radii up to approximately  $2R_{1/2}$  and thus the power-law fit has a positive slope.

Figure 3.6 shows the density and velocity dispersion slopes for the stellar component, with the Binary Ellipticals in the upper and the CosmoZoom and Magneticum BCGs in the lower panel. For all ellipticals, the density slopes of the stellar component are generally steeper than the slopes of the dark matter component. While the slopes of the stellar component for the Binary Ellipticals are all around  $\gamma_* = -2.9$ , the slopes of the stellar component of the CosmoZoom Ellipticals and the Magneticum BCGs show a different behavior: In contrast to the dark matter component, which has a small range of density slopes from  $-1.8 \lesssim \gamma_{\text{DM}} \lesssim -1.4$  excluding the Companion ellipticals, the stellar component covers a larger range of slopes ( $-3.25 \lesssim \gamma_* \lesssim -2.4$ ) and there is no correlation between the stellar slope and the type of simulation. This implies that the stellar component is responsible for the steepness of the total density slope, namely a more dominant stellar component in the center of a galaxy leads to a steeper total density slope.

### 3.2.2 The Influence of Gas and Star Formation on the Density Slope

Unlike the stellar and dark matter particles, which are collisionless, the gas particles can dissipate their energy and thus condense in the center of the galaxy. Thus, new stars are mostly formed in the central area of the galaxy. The more gas that is present in a merger event, the more dominant is this newly formed stellar component in the center.

This effect is nicely demonstrated in the comparison between the two Binary Ellipticals which have identical initial conditions apart from the initial gas fraction of 20% respective 80%. Figure 3.7 shows the density and velocity dispersion profiles for both ellipticals. In case of the merger with 80% gas fraction we see two effects that change the stellar density profile compared to the case of the merger with a gas fraction of 20%: First, we see that the overall density is generally higher since more stars have been formed over the whole radius, i.e., the normalization  $A$  in the profile  $\rho(r) = Ar^\gamma$  is larger, while the dark matter profile for both halos did not change significantly. Second, the central



**Figure 3.7:** Same as Figure 3.1 for the 3:1 Binary Elliptical with 20% initial gas fraction (left panel) and the 3:1 Binary Elliptical with 80% initial gas fraction (right panel).

part of the elliptical is much more compact, as a large amount of stars has been formed there. Both effects together cause the total density profile to be much steeper in case of the 80% gas merger. The half-mass radius of the 80% gas merger is with  $R_{1/2} = 2.4$  kpc just half as large as the half-mass radius of the 20% gas merger, while the fraction of stars that are formed during the merger is with  $f_*^{\text{new}} = 51\%$  much higher than in the 20% gas merger ( $f_*^{\text{new}} = 9\%$ ), as can be seen in Table 2.1.

This correlation between the steepness of the total density slope and the half-mass radius can also be seen for the CosmoZoom Ellipticals and Companions, as shown in the left panel of Figure 3.8. The steeper the total density slope of an elliptical, the smaller the half-mass radius. We also find a (weaker) correlation between the stellar mass of an elliptical galaxy and its total density slope  $\gamma_{\text{tot}}$ , as shown in the right panel of Figure 3.8, and a correlation between the total density slope and the dark matter fraction within the half-mass radius, as shown in Figure 3.9. As expected, the total density slope is steeper the more dominant the stellar component is compared to the dark matter in the inner part of the galaxy, i.e., the smaller the fraction of dark matter within the half-mass radius.

In these figures we included the results for the Coma ellipticals by Thomas et al. (2007) as well as the results from the SLACS strong lensing survey presented by Auger et al. (2010), Barnabè et al.

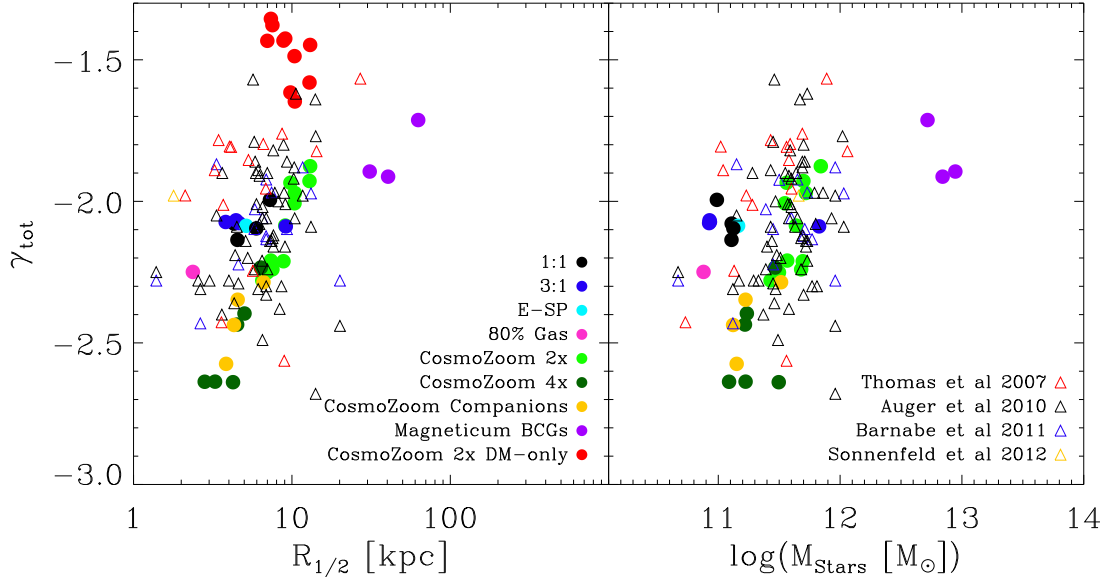


**Figure 3.8:** *Left: total density slope against the half-mass radius for all our ellipticals. Right: total density slope against the stellar mass within  $R_{1/2}$ . Colors are the same as in Figure 3.5. Red triangles are observations of Coma ellipticals from Thomas et al. (2007), blue open triangles are lensing results from (Barnabè et al., 2011), black open triangles are lensing results from (Auger et al., 2010) and the yellow open triangle represents the results from Sonnenfeld et al. (2012). We use the effective radius as half-mass radius for the observed galaxies.*

(2011) and Sonnenfeld et al. (2012), and we see that our results are in good agreement with the observations. The only exceptions are the Magneticum BCGs for which we have no observational counterparts, neither in mass nor in half-mass radius.

Also shown in the left panel of Figure 3.8 are the total density slopes against the half-mass radii for the CosmoZoom dark matter-only simulations. As seen before, the dark matter-only simulations show much flatter density slopes than the simulations including baryon physics, i.e., adding the baryons steepens the total density profile of the halos. We find that the observations clearly favor the slopes given by simulations with baryon physics.

There are a few early-type galaxies in the Coma observational sample that have a slope around  $\gamma_{\text{tot}} \approx -2$  and a very low dark matter fraction (see the upper panel of Figure 3.9). This kind of ellipticals with very low dark matter fractions are also present in the strong lensing sample of Auger et al. (2010) (see the lower panel of Figure 3.9), but not in the strong lensing sample of Barnabè et al. (2011). We cannot reproduce these early-type galaxies with any of our simulated scenarios, not even with the CosmoZoom Companions. Those early types seem to have a dominant stellar component, but a relatively flat density slope.

In case of the Coma Cluster ellipticals we know from Thomas et al. (2011) that these ellipticals with low dark matter fractions have large dynamical mass-to-light ratios in the case of the Coma Cluster ellipticals compared to a Kroupa IMF. This means that these ellipticals either have a bottom-

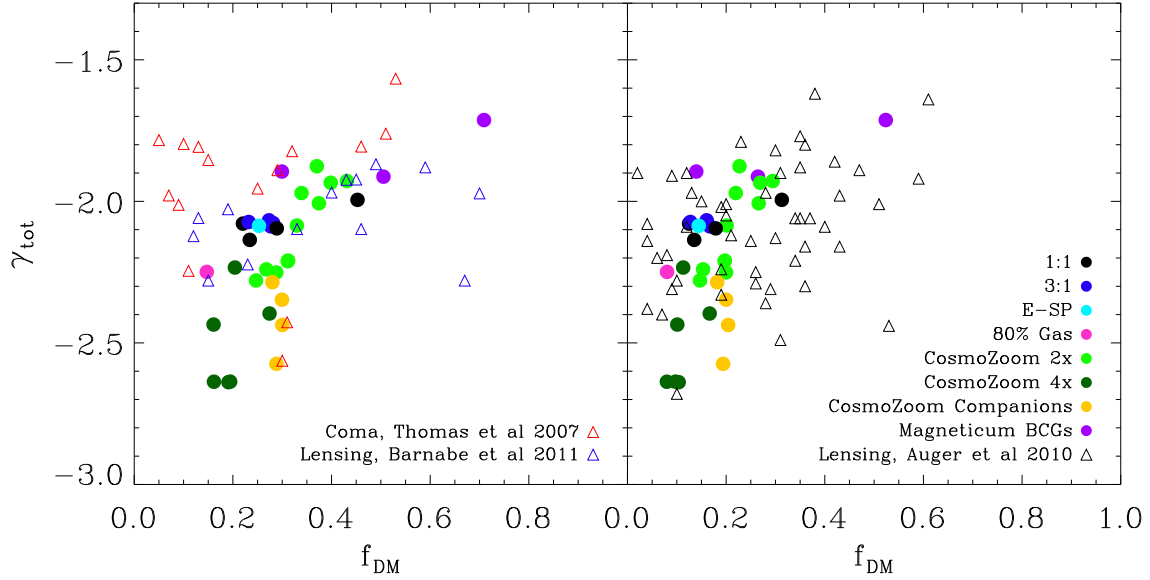


**Figure 3.9:** Total density slope against the fraction of dark matter within  $R_{1/2}$  (upper panel) or within  $0.5R_{1/2}$  (lower panel). The red triangles are observations of Coma ellipticals from (Thomas et al., 2007), the blue open triangles are lensing results from (Barnabè et al., 2011), the black open triangles are lensing results from (Auger et al., 2010).

heavy stellar initial mass function or that their dark matter density is nearly identical to the density of the stellar component.

There have been several recent papers indicating especially in case of massive early-type galaxies, that the IMF is not universal but variable (Cappellari et al., 2012; Ferreras et al., 2013; van Dokkum & Conroy, 2011; Conroy & van Dokkum, 2012; van Dokkum & Conroy, 2012; Treu et al., 2010). This is interesting since the predicted dark matter fractions strongly depend on the assumed IMF. For example, in case of an IMF like Kroupa, the observed dark matter fractions for the Coma Cluster ellipticals would be much higher (between 40% and 70%, see Thomas et al., 2011) and thus fit quite well to our results from the simulations. However, as shown by Conroy & van Dokkum (2012) and Wegner et al. (2012), not even a variable stellar IMF can always explain the high dynamical mass-to-light ratios that are observed.

On the other hand, if the dark matter density follows the stellar component closely enough, both components become indistinguishable from each other and thus the stellar mass becomes overestimated in the Schwarzschild modeling. This is explained in detail for the early-type galaxies in the Abell 262 cluster in Wegner et al. (2012). One possible way to explain an increase of the dark matter is by adiabatic contraction, as discussed beforehand. Nevertheless, the contraction would have to be very strong, stronger than what is seen in our simulations. Another process that could cause similar stellar and dark matter densities is violent relaxation, which has been discussed in Wegner et al. (2012) as well.

It is also possible that our simulations simply do not include ellipticals that are the equivalents

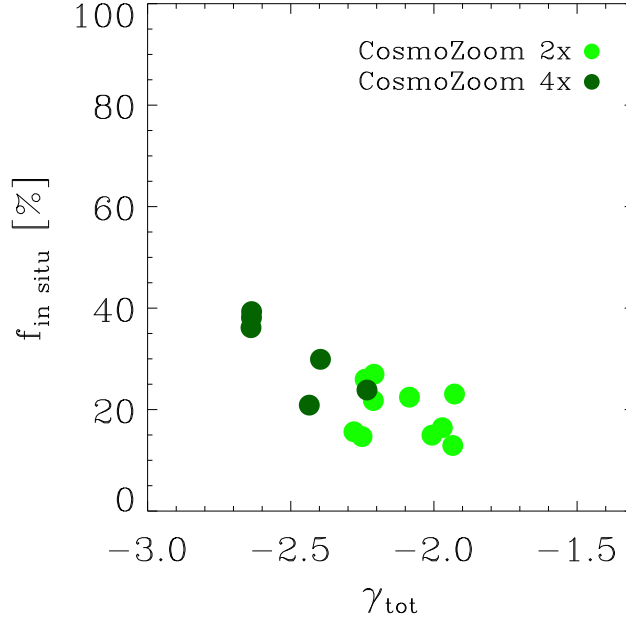


**Figure 3.10:** Fraction of stars formed in situ taken from Oser et al. (2012) versus the total density slope of the halos for the ellipticals taken from the re-simulations with twice (four times) the spatial resolution in bright green (dark green) circles.

to those observed early types. It is possible that these early-type galaxies are actually spirals that suffered from tidal and gas stripping while they entered a dense environment like, for example, the Coma cluster. Gunn & Gott (1972) already suggested ram pressure stripping to be an efficient way to form S0 early-type galaxies in dense environments, and ongoing stripping has been recently observed for the Virgo Cluster by (Abramson et al., 2011), but we have no simulations of such an event in our sample.

For the CosmoZoom Ellipticals that have been studied in Oser et al. (2012) we found that the slope of the total density correlates with the fraction of stars formed in situ, see Figure 3.10. The more stars have been formed within the galaxy itself the steeper the slope of the total density, while the accretion of stars by merger events flattens the slope. This is in agreement with the fact that for the Binary Ellipticals the steepest slope can be found for the 80% gas merger, as discussed above.

### 3.2.3 Evolution of the Slopes

To understand the origin of the total density slopes we study the time evolution of the total slopes. In the upper panel of Figure 3.11 we show the evolution of the density and velocity dispersion slopes for all our Binary Ellipticals, at the time-steps  $t = 0$  Gyr (initial condition time-step),  $t = 0.58$  Gyr,  $t = 1.75$  Gyr,  $t = 2.32$  Gyr and  $t = 2.9$  Gyr. Before the merger event occurs we fit the slopes to one of the spiral galaxies, in case of an unequal mass merger to the more massive spiral. As soon as the galaxies are merged we fit the slopes to the remnant elliptical. The first passage usually takes

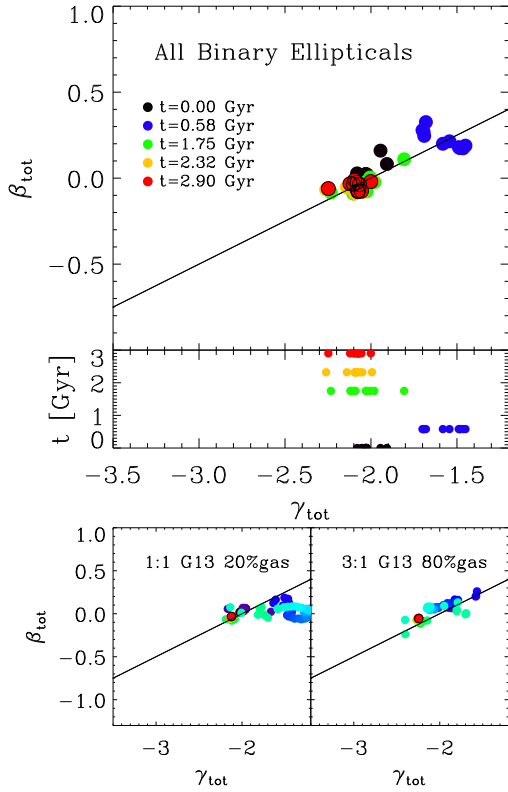


**Figure 3.11:** Total velocity dispersion slopes versus total density slopes for all binary merger ellipticals. Upper panel: Slopes at different time-steps for all ellipticals at  $t = 0$  Gyr (black circle),  $t = 0.58$  Gyr (blue circle),  $t = 1.75$  Gyr (green circle),  $t = 2.32$  Gyr (orange circle) and  $t = 2.9$  Gyr (red circle), with the merger event occurring around 1.5 Gyr. Central panel: Total velocity slopes versus time in Gyr. The colors are the same as in the upper panel. Lower left panel: Isolated full evolution track from  $t = 0$  Gyr to  $t = 3$  Gyr for the 1:1 spiral merger on the G13 orbit with 20% initial gas fraction. Lower right panel: Isolated full evolution track from  $t = 0$  Gyr to  $t = 3$  Gyr for the 3:1 spiral merger on the G13 orbit with 80% initial gas fraction. The black lines in all figures show, like in Figure 3.3, the analytic solution for a spherical system with constant anisotropy.

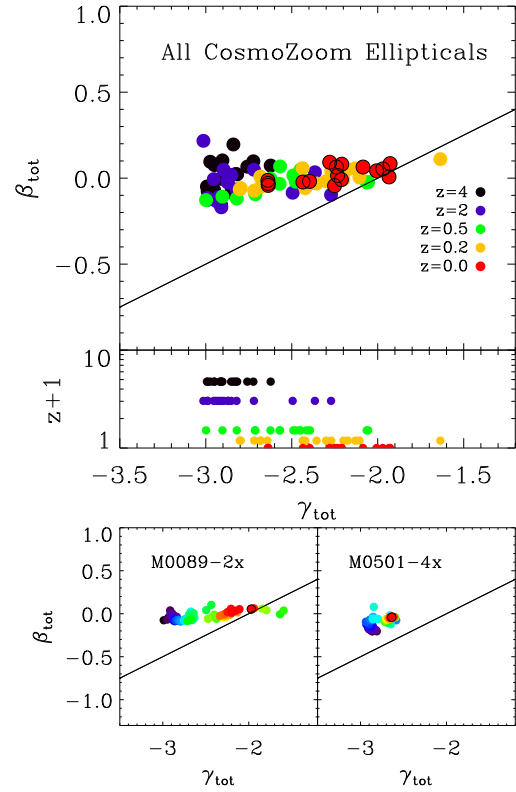


**Figure 3.12:** Total velocity slopes versus total density slopes for all ellipticals selected from the cosmological re-simulations. Upper panel: Slopes at different redshifts for all ellipticals:  $z = 4$  (black circle),  $z = 2$  (blue circle),  $z = 0.5$  (green circle),  $z = 0.2$  (orange circle) and  $z = 0$  (red circle). Central panel: Total velocity slopes versus redshift. The colors are the same as in the upper panel. Lower left panel: Isolated evolution track for the halo M0089-2x, a massive elliptical which is growing through multiple mergers. Lower right panel: Isolated evolution track for the halo M0501-4x, a low-mass elliptical with only minor mergers and smooth accretion. The black lines in all figures show, like in Figure 3.3, the analytic solution for a spherical system with constant anisotropy.

place between  $t = 0.5$  Gyr and  $t = 0.6$  Gyr, the merger event around  $t = 1.5$  Gyr, thus only for the initial condition time  $t = 0$  Gyr and the time-step  $t = 0.58$  Gyr we actually fit the slopes to the spiral progenitor galaxies.

Since we set the initial conditions for the Binary Ellipticals to fit present-day spirals, they are already isothermal systems at  $t = 0$  Gyr, i.e., the initial condition slopes are around  $\gamma_{\text{tot}} = -2.0$  and

$\beta_{\text{tot}} = 0$ . During the merger event, between  $t = 0.5$  Gyr and  $t = 1.5$  Gyr, both the total density and velocity dispersion slopes are disturbed and not in equilibrium, with flatter slopes for the density and slightly positive slopes for the velocity dispersion. This shows clearly that the flat density profiles during the merger are due to non-equilibrium effects, and that, as soon as the central parts of the spirals have merged and the central part of the elliptical has formed, both slopes return to the isothermal solution and stay (nearly) constant.

Detailed examples for two evolution tracks from  $t = 0$  Gyr to  $t = 3$  Gyr are shown in the lower two panels of Figure 3.11. The left panel shows the 1:1 spiral merger with 20% initial gas fraction on a G13 orbit. The right panel shows the 3:1 spiral merger with 80% initial gas fraction on a G13 orbit, the one elliptical from the binary simulations that has a significantly steeper total density slope at 3 Gyr than all others.

The 1:1 spiral merger with 20% initial gas fraction shows the typical behavior described above: The merger event strongly disturbs the total density slope toward flatter slopes, while the velocity dispersion slope only changes slightly, and after the merger event takes place the slopes return to the initial configuration of an isothermal sphere. The merger with an initial gas fraction of 80% is the only merger event in our sample that behaves differently: It evolves along the black line showing the isothermal solutions of the Jeans Equation, and the slope of the density never reaches equally flat values as the merger with 20% initial gas fraction. Even more importantly, after the merger event takes place the final elliptical does not have the same total density and velocity dispersion slopes as the initial setup. Caused by a strong star formation due to gas condensation in the center of the newly formed elliptical, as discussed above, the final density slope is steeper than the density slope of the initial setup. We conclude that a high gas fraction which causes a significant amount of star formation in the central part of the galaxy by condensing gas in the galaxies center, is needed for a merger event to cause a steeper total density slope once the progenitor system has reached an isothermal configuration.

Figure 3.12 shows in the upper panel the evolution of all the CosmoZoom Ellipticals, at redshifts  $z = 4$ ,  $z = 2$ ,  $z = 0.5$ ,  $z = 0.2$  and  $z = 0$ . We always fit the slopes of the most massive progenitor of the present-day elliptical at the given redshift. The lower two panels show the full evolution tracks from  $z = 4$  to present day for two example ellipticals, one with a multiple merger history (left panel) and one with a smooth accretion history, where the merger only occur at high redshifts (right panel).

We see that the progenitors of the CosmoZoom Ellipticals have much steeper density profiles at high redshifts, evolving toward the isothermal spherical system case with every merging event, while the velocity dispersion slopes only change slightly during merger events and otherwise stay constant. Between  $z = 4$  and  $z = 2$  the total density slopes do not change much, they are all about  $\gamma_{\text{tot}} \approx -3$ , and they do not show an equally broad range of values, especially at  $z = 4$ , than their present-day counterparts. After  $z = 2$  the total density slopes of all progenitors become flatter and the range of slopes broadens. This can be explained by the two-phase formation of galaxies that was introduced by Oser et al. (2010): at redshifts  $z \gtrsim 2$  the formation of the galaxies is dominated by the accretion of gas and the in situ star formation followed by a formation phase in which most of the mass growth of the galaxies is due to the accretion of stars in the form of satellite systems.

This also explains the correlation between the total density slopes and the fraction of stars formed in situ (see Figure 3.10) and the correlation between the total density slope and the half-mass radius  $R_{1/2}$  (see Figure 3.8). The CosmoZoom Ellipticals which have a steep density slope have a less dominant mass accretion by mergers in the second phase of their formation than those which have relatively flat total density slopes, i.e., their in situ fraction is higher and they are more compact.

CosmoZoom Elliptical M0501-4x in the lower right panel of Figure 3.12 is an example for such a merger poor second phase of formation. Its total density slope hardly changes from  $z = 4$  to present day, and it has no really massive merger event in its formation history.

The opposite case is shown in the lower left panel of Figure 3.12. CosmoZoom Elliptical M0089-2x has several minor merger events with mass ratios between 10:1 and 3:1 between  $z = 2$  and  $z = 0.8$  and even a major merger around  $z = 0.65$ . The effect of this major merger event can be seen in the lower left panel of Figure 3.12 as the green circles with the flattest total density slopes. As for our Binary Ellipticals, the major merger event disturbs the total density slope even beyond  $\gamma_{\text{tot}} = -2$ . As for the Binary mergers, we also see for the CosmoZoom ellipticals that density slopes lower than  $\gamma_{\text{tot}} \approx -2$  are due to distortions and non-equilibria during massive merging events.

From both elliptical formation scenarios studied in this paper we conclude that merger events, other than in situ star formation, flatten the total density slopes toward the isothermal solution with a density slope of  $\gamma_{\text{tot}} \approx -2$ . Once the ellipticals have reached this configuration, they stay at this density distribution and, when disturbed, evolve back to a density distribution with a slope of  $\gamma_{\text{tot}} \approx -2$ , even though the stellar and the dark matter component themselves might have changed. We therefore conclude that total density distributions with a slope of  $\gamma_{\text{tot}} \approx -2$  act as an attractor solution. Only a very gas rich merger event can steepen the slope again once it reached the attractor solution, as during a gas rich merger the gas can condense in the center of the elliptical and cause significant in situ star formation, but in the second phase of elliptical galaxy formation, which is dominated by the accretion and not by the formation of stars, a gas rich merger is not a common event.

### 3.3 Summary and Discussion

We have investigated a set of 35 spheroidal galaxies formed from isolated binary merger events as well as in cosmological (zoom) simulations. The isolated binary merger spheroids are taken from Johansson et al. (2009a) and Johansson et al. (2009b). The spheroids formed in cosmological simulations are selected from two different simulations: The cosmological zoom-in simulation sample is a subset of the sample presented in Oser et al. (2010), while the brightest cluster galaxy (BCG) sample is selected from a new full hydrodynamical cosmological simulation (Dolag et al., in preparation). We analyzed the total intrinsic density and velocity dispersion profiles of the galaxies to investigate the dependence of the profiles on the formation history, mass, size and dark matter fraction.

We find that all our galaxies are close to isothermal, i.e., their total (dark matter plus stellar) velocity dispersion distributions are flat, independent of the individual total, stellar or dark matter density distributions, the mass, the half-mass radius, the dark matter fraction within one half-mass radius, the environment or the formation scenario. The slopes of the total density distribution peak at values of  $\gamma_{\text{tot}} \approx -2.1$ , with a tendency to steeper slopes for less massive, more compact systems with lower dark matter fractions within the half-mass radius. This is in agreement with observational results found for the Coma Cluster ellipticals (Thomas et al., 2007, 2009) as well as from strong-lensing (Auger et al., 2010; Barnabè et al., 2011; Sonnenfeld et al., 2012).

The cosmological simulations show a similar range of values in the density slopes as the observations in agreement with a similar analysis by Lyskova et al. (2012) for the subset of cosmological zoom in simulations. While our isolated binary mergers of present-day galaxies cannot reproduce the observed range of values, binary merger between two high-redshift spirals might be able to achieve better results since the initial conditions for those galaxies would look very different. This provides

evidence to the idea that, at least in a cluster environment like Coma, the elliptical galaxy population has not been formed by recent major mergers but rather at higher redshifts. This is consistent with the fact that elliptical galaxies have higher dark matter densities than spiral galaxies which indicates a higher assembly redshift of about  $z \sim 3$  (see for example Gerhard et al., 2001; Thomas et al., 2009). Additionally, there is strong evidence that massive ellipticals formed a significant amount of their stars at high redshifts (for example Brinchmann & Ellis, 2000), supported by observations of massive compact ellipticals at high redshifts (e.g., van Dokkum et al., 2009; van de Sande et al., 2011).

There is a small fraction of ellipticals from those observations that cannot be reproduced by our simulated elliptical sample. These objects are characterized by small dark matter fractions, relatively flat total density slopes and large dynamical mass-to-light ratios in the case of the Coma Cluster ellipticals (see Thomas et al., 2011). A possible explanation for these ellipticals could be that they have a bottom-heavy stellar IMF. Non-universal stellar IMFs have been widely discussed recently, for example by Cappellari et al. (2012); Ferreras et al. (2013); van Dokkum & Conroy (2011); Conroy & van Dokkum (2012); van Dokkum & Conroy (2012); Treu et al. (2010), especially in the case of massive ellipticals. The predicted dark matter fractions strongly depend on the assumed IMFs, and assuming for example a Kroupa IMF would result in dark matter fractions for the Coma Cluster ellipticals that are much higher and thus are in good agreement with our simulated results. Nevertheless, as shown by Conroy & van Dokkum (2012) and Wegner et al. (2012), not even a variable stellar IMF can explain all high dynamical mass-to-light ratios that are observed.

We also see the effects of adiabatic contraction in case of the cosmological simulations: While the density slopes for the dark matter component of these ellipticals peak around  $\gamma_{\text{DM}} \sim -1.67$ , in good agreement with the results from Sonnenfeld et al. (2012), the dark matter only comparison sample peaks around  $\gamma_{\text{DM only}} \sim -1.46$ . This is consistent with a number of other studies, for example Jesseit et al. (2002); Blumenthal et al. (1986); Gnedin et al. (2004, 2011) and especially Johansson et al. (2012).

The total density slopes correlate with the fraction of stars that are formed in situ: the steeper the slope, the larger the fraction of stars within the galaxy that were formed in situ and the lower the fraction of stars that were accreted. This is in agreement with our result that the gas fraction in the binary merger scenarios is the only component that can significantly alter the slope of the total density distribution of the systems. A higher star formation rate in the center of the newly formed elliptical due to a higher initial gas fraction causes a more prominent contribution from the new born stars to the total density and thus a steeper total density slope.

At higher redshifts, where gas and in situ star formation dominate the galaxies, the ellipticals from cosmological simulations have a total density slope of  $\gamma_{\text{tot}} \approx -3$ , evolving through merger events toward a slope of  $\gamma_{\text{tot}} \approx -2$ , supporting the idea of the two-phase formation of galaxies (Oser et al., 2010). If the in situ fraction of a galaxy at  $z = 0$  is high, then the galaxy has accreted less stars from its environment in the second phase of its formation than a galaxy with a low in situ fraction at  $z = 0$ . Without enough gas-poor accretion in the second phase of formation, the total density slope could not change a lot toward  $\gamma_{\text{tot}} = -2$ , and thus the slope stays close to  $\gamma_{\text{tot}} \approx -3$ . This is in agreement with results presented in Johansson et al. (2012) but in disagreement with observations from strong lensing by Ruff et al. (2011) and Bolton et al. (2012) who find a slight trend indicating that the slopes of the total density profiles of early-type galaxies at higher redshift are slightly flatter. Nevertheless, this observed trend is very weak, and it could be due to a bias in the weak-lensing sample toward merging systems, as reported by Torri et al. (2004), who found that merging systems tend to boost strong lensing. An enhancement in the lensing efficiency reported by Zitrin et al. (2013) for an observed

merging cluster of galaxies also supports this idea. This would be in agreement with our result that merging systems show much flatter density slopes.

Our simple model predicts that the steepness of the slope of present-day galaxies is a measurement for the importance of the mergers the elliptical galaxy went through in its second formation phase. Ellipticals with steep slopes close to  $\gamma_{\text{tot}} \approx -3$  had (nearly) no merger event in this second phase, while ellipticals with slopes around  $\gamma_{\text{tot}} \approx -2$  had a strong, collisionless merger dominated second formation phase. Since our ellipticals with slopes around  $\gamma_{\text{tot}} \approx -2$  have generally higher dark matter fractions, this is consistent with the results presented by Hilz et al. (2012, 2013) who show that the accretion of several small satellite systems strongly increases the dark matter fraction within the half-mass radius. From both, binary merger ellipticals and ellipticals from cosmological framework, we see that, once an elliptical has reached a total density slope of  $\gamma_{\text{tot}} \approx -2$ , further merger events do not change the slope anymore.

We conclude that the density distributions with a slope of  $\gamma_{\text{tot}} \approx -2$  acts as attractors, independent of the individual stellar mass distributions of ellipticals. We suggest that all elliptical galaxies will in time end up in such a configuration. However, the mechanism that leads to this attractor is still unclear. A possible explanation could be that this attractor state is a result of violent relaxation (Lynden-Bell, 1967), although Hilz et al. (2012) showed that violent relaxation is less efficient in minor merger events than in major merger events.

In general, the relaxation times for the elliptical galaxies from cosmological frameworks are much faster than for isolated binary mergers due to the presence of substructures and potential fluctuations. We conclude that, to understand the entire range of elliptical galaxies observed at present day and their complex evolution scenarios, a full cosmological treatment is needed.



## Chapter 4

# The Dark Halo – Spheroid Conspiracy: Evolution with Redshift

### 4.1 Introduction

In Chap. 3 (Remus et al. (2013)) we have demonstrated that the total (stellar plus dark matter) radial density profiles of spheroidal galaxies at  $z = 0$  can be well described by a power law  $\rho \propto r^\gamma$ , with an average slope of  $\gamma \approx -2.1$ . This holds true for a broad radius range  $0.3 r_{1/2} < r < 4 r_{1/2}$ . Similarly, the total radial velocity dispersion profiles also follow a power-law distribution, with  $\sigma \propto r^\beta$ . While for all galaxies studied in this work the slope of the radial velocity dispersion profiles were flat ( $\beta \approx 0$ ), the scatter in the slopes found for the power-law fits to the total radial density profiles had a much larger scatter, ranging between  $-2.7 < \gamma < -1.6$ .

Observationally, the total radial velocity dispersion is difficult to obtain, but for the total radial density profiles, comparisons are possible. As demonstrated in Remus et al. (2013), the values and the scatter found for the density slopes from the simulations are in excellent agreement with observations of Coma cluster ellipticals by Thomas et al. (2007) at  $z \approx 0.02$ . It also is in decent agreement with the results presented by Humphrey & Buote (2010), who studied 10 early-type galaxies (ETGs) in different environments from field to cluster at low redshifts. While Thomas et al. (2007) used Jeans modeling to infer the total density slopes of their galaxies, Humphrey & Buote (2010) modeled the total mass profiles from X-ray measurements of the hot halo surrounding their objects, covering a radius range of  $0.2 r_{\text{eff}} < r < 10 r_{\text{eff}}$ . They find power-law slopes between  $-2 < \gamma < -1.2$ , with a tendency for larger galaxies to have flatter slopes, similar to what has been shown in Fig. 3.8 in Chap. 3. Humphrey & Buote (2010) also found indications for the central dark matter fraction within the effective radius to vary with properties of the galaxy.

As discussed in the previous chapter, the correlation of the size, dark matter and in-situ fractions of the spheroidals with the steepness of their density slopes originates from their different mass accretion histories. Spheroidals which suffered from multiple massive (mostly) dry merger events have lower in-situ fractions, higher dark matter fractions, and larger sizes (see, for example, Oser et al., 2010; Hilz et al., 2012, 2013), but the violent accretion of mostly collisionless material also leads to a reordering of the system towards an isothermal stage. The latter had already been suggested by Humphrey & Buote (2010) from their observations, and has been confirmed by our recent work. Those spheroidals which have steeper slopes, on the other hand, had nearly no or only gas-rich accretion events since

$z \approx 1.5$ , and therefore still have a high in-situ fraction, a more compact size and have low central dark matter fractions. They also tend to be less massive, however, this tendency is much less pronounced than the correlation between slope and size. A similar result has been found very recently by Tortora et al. (2014a), who studied the central total mass density profiles of  $\approx 4300$  ETGs at  $z < 0.1$  from the SPIDER survey (La Barbera et al., 2010b) and 260 ETGs from the Atlas<sup>3D</sup> survey, down to stellar masses as low as  $M_* \approx 10^{10} M_\odot$ . They find a clear correlation between the slope of the total central density profile of the galaxies and their size and mass, with their most massive galaxies having slopes close to isothermal. A correlation of the total density slope within the effective radius and the mass of the ETG has also been reported by Newman et al. (2015), who studied ETGs in group environments.

Using a test set of isolated binary merger simulations, we demonstrated in Chap. 3 that the density profiles become steeper if cold gas is involved in a merger event. In those cases, the gas forms stars in the center of the galaxy. While accretion events through merging mostly add to the outer regions of a galaxy, the in-situ star formation is mostly enhancing the stellar content in the center. Thus, the total density profile which is in the center dominated by the contribution of the stellar component, becomes steeper (see also Fig. 3.7). This also explains the correlation between the in-situ fraction of a galaxy and its slope of the total density profile. A similar correlation between the steepness of the density slopes and the amount of gas involved in a merger event has been presented also by Sonnenfeld et al. (2014).

At higher redshifts, the amount of cold gas present in galaxies is generally believed to be much higher than at present day, which is also supported by many observations. Even spheroidal galaxies show slightly enhanced blue colors (e.g., van de Sande et al., 2014), and there are multiple detections of compact but star forming galaxies (Barro et al., 2013), but the most extended galaxies at high redshifts are very gas-rich, extended disks (e.g., Genzel et al., 2008; Förster Schreiber et al., 2009, 2011). Therefore, as shown in Chap. 3, the fact that the density slopes of our simulated sample of spheroidals are generally steeper at higher redshifts, is in good agreement with the enhanced presence of cold gas in galaxies, even if the galaxies are spheroidals, especially since most structures which are accreted at higher redshifts will also contain significant amounts of gas. Similar trends with redshift have also been reported from simulations of spheroidal galaxies by Johansson et al. (2012).

However, observations of galaxies which are strong lenses have revealed a different picture: while Koopmans et al. (2006) report no evolution in the density slopes of their set of 15 strong lensing ETGs from the SLACS survey but a constant slope of  $\gamma \approx -2$  up to  $z = 1$ , Sonnenfeld et al. (2013b) even find a tendency towards flatter slopes at higher redshifts. Similarly, Treu & Koopmans (2004) report average slopes of  $\gamma \approx -1.75 \pm 0.10$  for their set of 5 ETGs from the LSD survey at redshifts between  $0.5 < z < 1$ . Additional studies of the total density slope of strong lensing ETGs by Ruff et al. (2011) from the SL2S survey and Auger et al. (2010); Bolton et al. (2012); Barnabè et al. (2011) from the SLACS survey find also no steepening of the slope with redshift but either no indications of an evolution of the slope with redshift or a slight flattening at higher  $z$ .

This is a direct contradiction between the observations and the simulations. In our present study we will address this question and analyze the origin of this discrepancy, especially with regard to the consequences on our current view of the formation scenarios of ETGs. Therefore, we will use the same set of spheroidals from the cosmological zoom simulations as in our previous work (see Sec. 2.3.1), in the following called CETGs (Cosmozoom-ETGs), and spheroidals selected from the fully hydrodynamical cosmological simulation Magneticum Box4 uhr (see Sec. 2.4). For the latter, we will use the method described in Sec. 2.4.1 to identify spheroidal galaxies at each redshift included in this study, namely  $z = 0, 0.5, 1, 2$ , and use a lower mass cut of  $M_{\text{tot}} \geq 1 \times 10^{11} M_\odot$  to guarantee

a sufficiently high particle number of stars in the centers of the selected spheroidals. Spheroidals selected from this simulation will in the following be called METGs (Magneticum ETGs). Both simulation samples include different subgrid physics and numerical switches, as described in Chap. 2. Another difference is the selection mechanism: While the CETGs include the same set of galaxies at all redshifts in their different stages of evolution, the METGs are selected from the box at each redshift only due to their properties but not due to their connection with METGs at different redshifts. We also distinguish between METGs with and without cold gas disks. The number of METGs therefore is slightly different at each studied redshift bin, with about 100 METGS at  $z = 0$ . This approach is more closely to an observers approach, even if it is less directly correlated with the formation history of the individual spheroidals.

In Sec. 4.2 we will evaluate the evolution of the mass-size relation of both CETGS and METGs and compare with observations to understand the differences in the behaviour of our two different samples of spheroidals, and in Sec. 4.3 we will discuss their central dark matter fractions. In Sec. 4.4 we will discuss the values and scatter of the total density slopes found in our simulations at different redshifts and their correlations with different parameters like dark matter fraction and stellar mass density, and present a first comparison with the observed sample of ETGs. A more direct comparison with observations is then presented in Sec. 4.5, where we use the same methods as the observer to generate mock observations of our simulated spheroidals. We will conclude our study in Sec. 4.6 with a summary and discussion.

## 4.2 The Mass-Size Relation

Since the aim of this work is to understand the redshift evolution of the total density slopes of ETGs and its implications for their formation scenarios, we first need to ensure that our simulations can successfully reproduce the observed properties of ETGs at higher redshifts. One of the most essential comparisons is the successful reproduction of the observed trends for the mass size relation, which is one of the main tracers of the importance of galactic mass growth through merger events.

As already introduced in Sec. 1.5, the mass of an ETG is closely correlated with its size, as shown for example by Shen et al. (2003) and Baldry et al. (2012), and even holds true for the least dense environments Fernández Lorenzo et al. (2013). However, the results from the SDSS survey (Shen et al., 2003) and the GAMA survey (Baldry et al., 2012) differ at the low mass end, where the results from the GAMA survey show a tilt which is not present in the SDSS data. However, Mosleh et al. (2013) reanalyzed the data from Shen et al. (2003) and found indications of a tilt in the mass-size relation at small masses as well depending on the method used to calculate the sizes of the small galaxies.

For our simulations, we use the half-mass radius  $r_{1/2}$ , that is, the radius which contains half of the mass of the galaxy within 10% of the virial radius  $r_{\text{vir}}$ , to compare to the effective radius  $r_{\text{eff}}$  from observations. This is the same approximation used in Remus et al. (2013) and other similar studies, and it might slightly overestimate the actual size of the galaxy compared to observations. In Fig. 4.1 we show the mass size relations from SDSS by Shen et al. (2003) (left panel) and from GAMA by Baldry et al. (2012) (right panel) for their ETGs in comparison with the results from our simulations. Both our simulations are in good agreement with the SDSS observations at the high mass end, where the GAMA survey does not have any data points. The CETGs (red filled circles) tend to be slightly below the observed relation from SDSS, and are generally more massive at the same sizes than their

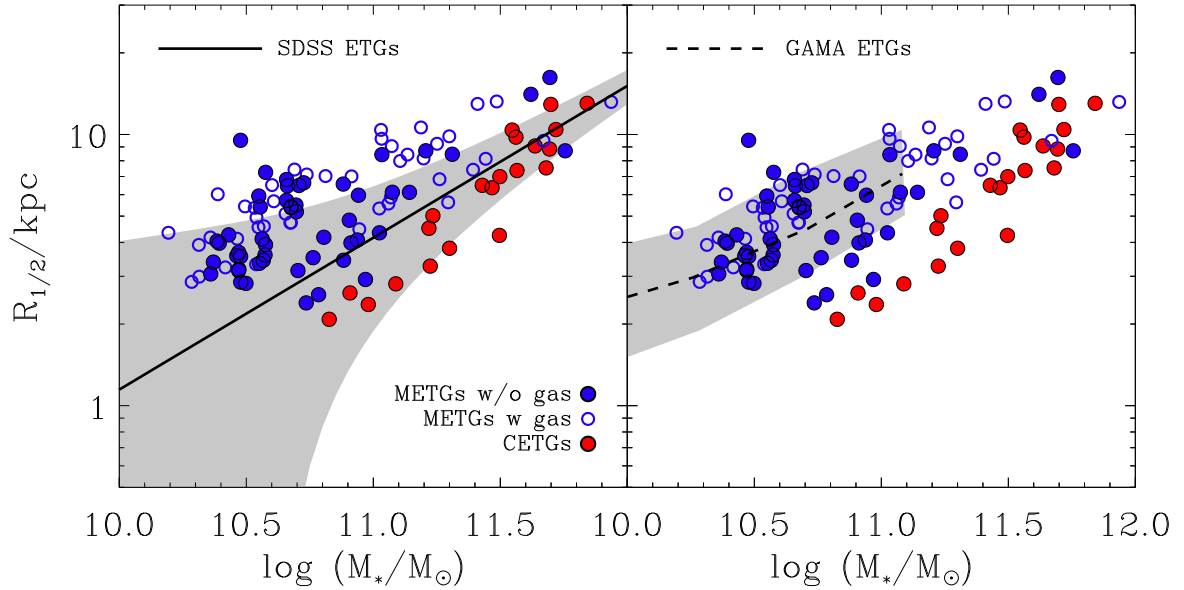


**Figure 4.1:** Mass-size relation at  $z = 0$  for METGs without cold gas disks (filled blue circles), METGs with cold gas disks (open blue circles) and CETGs (filled red circles). **Left panel:** Comparison to the mass-size relations for ETGs from the SDSS survey (Shen et al., 2003, black solid line). **Right panel:** Comparison to the mass-size relation for ETGs from the GAMA survey (Baldry et al., 2012, black dotted line). The shaded areas mark the  $1\sigma$ -deviation.

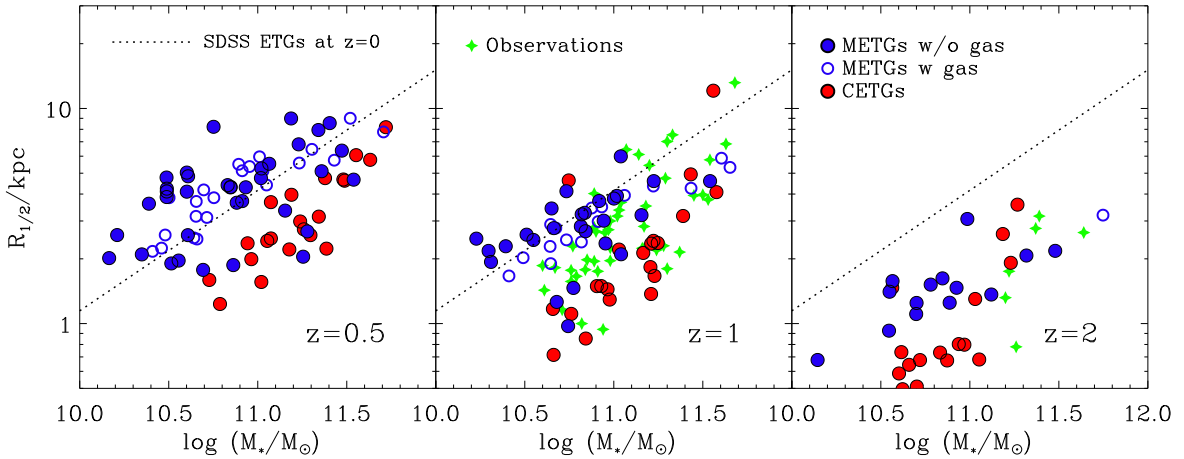


**Figure 4.2:** Same as Fig. 4.1 but at different redshifts. The black dotted line shows the relation from SDSS at  $z = 0$  (Shen et al., 2003) for comparison. **Left panel:** mass-size relation at  $z = 0.5$ . **Middle panel:** mass-size relation at  $z = 1$ . Green filled diamonds show data points at  $0.8 < z < 1.2$  taken from Newman et al. (2010), van der Wel et al. (2008) and Blakeslee et al. (2006), from the compilation of data presented in van de Sande et al. (2013). **Right panel:** mass-size relation at  $z = 1$ . Green filled diamonds show data points at  $1.8 < z < 2.2$  taken from van de Sande et al. (2013), van Dokkum et al. (2009), Onodera et al. (2012) and Toft et al. (2012).

counterparts from the METG (clue circles) sample. This most likely originates from the fact that the simulations of the METGs include black holes and their according feedback, which are not present in the CETG simulations. This feedback regulates the star formation and prevent an over-cooling of the gas, which leads to too large star formation rates, therefore basically suppressing star formation in massive galaxies.

The METGs with stellar masses larger than  $M_* > 6 \times 10^{10} M_\odot$  show the same behaviour as the observations from SDSS, with a slightly larger scatter to larger radii, which could be cause by the uncertainty in the half-mass to half-light relation. For smaller galaxies, the METGs, however, seem to be larger in size than the SDSS galaxies of the same mass. In that mass regime, they are in excellent agreement with the observations from the GAMA survey. At the low mass end we do not have galaxies in the CETG sample, and therefore no sufficient comparison with data from the GAMA survey is possible.

We also see a tendency for those spheroidals in the METG sample which contain small cold gas disks (open blue circles) to be slightly larger than gas-less METGs (filled blue circles) of the same mass. However, cold gas disks are present in METGs of all masses, in about 48% of the spheroidals, which is only slightly larger than the 40% ETGs with gas reported by Young et al. (2013) for the ETG sample of the Atlas<sup>3D</sup> survey. This could originate from the fact that we also detect extremely small gas disks which might not be detectable with the methods used in the Atlas<sup>3D</sup> survey, nevertheless, the difference is very small.

At higher redshifts, observations show that spheroidals tend to be smaller in size than their present-day counterparts of the same mass (e.g., van Dokkum et al., 2009; Williams et al., 2010; Fernández Lorenzo et al., 2011; van de Sande et al., 2011; Onodera et al., 2012; Szomoru et al., 2012; Toft et al., 2012; Bezanson et al., 2013a; Szomoru et al., 2013; van de Sande et al., 2013; van der Wel et al., 2014; Marsan et al., 2015) Fig. 4.2 shows a comparison of our simulated spheroidals with observations at different redshifts of  $z = 0.5$  (left panel),  $z = 1$  (middle panel) and  $z = 2$  (right panel). For the observations, we include those galaxies in the redshift bin of  $0.8 < z < 1.2$  and  $1.8 < z < 2.2$  (middle and right panel, respectively), from different surveys as indicated in the figure caption. To select the galaxies, we used the compilation of high-redshift ETG observations presented in van de Sande et al. (2013).

As can clearly be seen, we find the same shift in size towards more compact galaxies at higher redshifts as seen in the observations, albeit we only have very few galaxies at the high mass end at  $z \approx 2$  in our sample. Both, the CETGs and the METGs show the same behaviour, clearly stating that this is independent of the subgrid models used in the simulations, and thus indicating that the mass growth really is mostly driven by accretion through (mostly dry) merger events at low redshifts, which is the aspect of both simulations which is not different. Nevertheless, both simulations are again shifted compared to each other, with the CETGs slightly below the METGs, already at high redshifts, however, the scatter in both simulations is large, and the number of observations at  $z \approx 2$  is too low to give conclusive results.

On an interesting side note, we see that there is only one single spheroidal in the METG sample at  $z = 2$  which contains a gas disk. This is due to the fact that many spheroidals at high redshifts tend to be rotationally supported, similar to what is observed by van der Wel et al. (2011), and thus not classified as spheroidals in our selection algorithm. Generally, the cold gas fraction in spheroidals from the METG sample at  $z = 2$  is high, as shown by Teklu et al. (2015b), but a less crude classification scheme at high redshift would be needed to properly select all spheroidals at this redshift. This bias, however, has already vanished at  $z = 1$ , where the cold gas fraction in the spheroidals is significantly

lower and much closer to present-day values, which is also shown in Teklu et al. (2015b). Those large cold gas fractions at high redshifts, on the other hand, support the idea of the two-phase growth of galaxies, where in the first phase the mass growth of galaxies is dominated by the accretion of cold gas, possibly through cold streams (Dekel & Birnboim, 2006; Dekel et al., 2009), and the subsequent in-situ star formation (Oser et al., 2010).

### 4.3 Dark Matter Fractions

The fraction of dark matter in the central parts of galaxies has been a matter of debate since many years. Since Navarro et al. (1996) introduced their famous NFW profile for the radial density distributions of dark matter halos in simulations, several attempts have been made to measure the distribution of dark matter through indirect detections: From X-ray measurements of the hot halos in which galaxies are embedded, especially in clusters, and which are assumed to be distributed similarly to the dark matter (e.g., Pratt & Arnaud, 2005; Pointecouteau et al., 2005; Newman et al., 2013; Sereno et al., 2015), via strong lensing measurements, where the total mass content within the lens is measured and the dark matter fraction can be calculated through subtraction of luminous component (e.g., Koopmans et al., 2006; Auger et al., 2010; Barnabè et al., 2011), to dynamical modeling (e.g., Thomas et al., 2007; Tortora et al., 2014b). More recently, with the advent of more advanced methods to measure dynamical properties from tracer populations like planetary nebulae or globular clusters, measurements of the dark matter content of galaxies out to five effective radii have been provided (e.g., Deason et al., 2012; Napolitano et al., 2014, see also Chap. 6 for more details). However, in most of those methods, the choice of the IMF strongly influences the results, leading to a large range of debated dark matter fractions in the literature (e.g., Barnabè et al., 2011; Deason et al., 2012).

We calculated the dark matter fractions within the half-mass radius for all our galaxies, and find a large scatter at  $z = 0$ , from less than  $f_{\text{DM}} \approx 10\%$  up to  $f_{\text{DM}} \approx 60\%$ . This range is similar to the range of dark matter fractions found by Koopmans et al. (2006), however, their measured radii differ slightly from galaxy to galaxy, even though they do not see a strong correlation between the dark matter fraction and the radius. A more direct comparison is possible with the dark matter fractions obtained by Thomas et al. (2007) and Barnabè et al. (2011), who estimate the central dark matter fractions within the effective radius. The upper left panel of Fig. 4.3 shows the stellar mass  $M_*$  of our simulated spheroidals versus the dark matter fraction within the half-mass radius  $f_{\text{DM}}(R_{1/2})$  at  $z = 0$ , with the colors the same as in Fig. 4.2. We do not find a clear correlation between the stellar mass and the central dark matter fraction for the METGs, and only a slight tendency for more massive galaxies to have higher central dark matter fractions for the CETGs. The CETGs show a much smaller scatter in dark matter fractions than the METGs, but there are also much more METGs at  $z = 0$  than CETGs. For comparison, data from Thomas et al. (2007) are shown as yellow stars, data from Barnabè et al. (2011) are shown as green triangles. While there are more observations at the high mass end than at the low mass end, the range of observed dark matter fractions is similar again. Nevertheless, there are several massive ETGs in the Coma sample with relatively low dark matter fractions which have no counterpart in our simulated samples of spheroidals. This has been shown for the CETGs already in Chap. 3 (Remus et al., 2013), but it is still the same for the METGs. Since the METGs are considering a Chabrier IMF while the CETGs use a Salpeter IMF, the differences in the assumed IMFs are most likely not the reason for those massive galaxies with low dark matter fractions. Thus, the more likely explanation is a selection effect in both our simulated spheroidal samples, to only include spheroidals

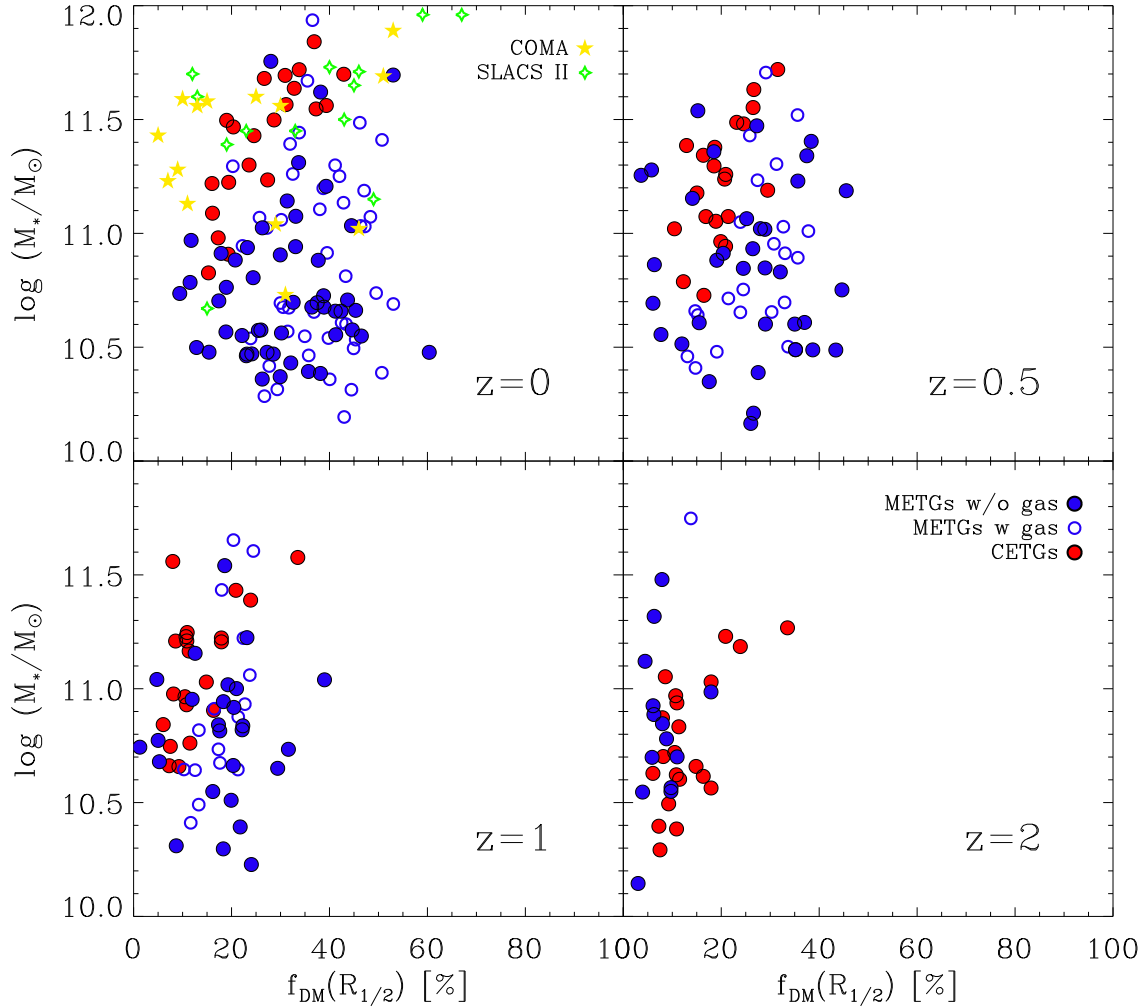


**Figure 4.3:** Dark matter fractions within the half-mass radius for our simulated galaxies. CETGs are shown as red filled circles, METGs without cold gas disks are shown as blue filled circles and METGs with cold gas disks as open blue circles. **Upper left panel:**  $z = 0$ . For comparison, central dark matter fractions from observations are shown, for Coma cluster ETGs as yellow stars (Thomas et al., 2007), and for SLACS lenses (Barnabè et al., 2011), assuming a Chabrier IMF, as green diamonds. **Upper right panel:**  $z = 0.5$ . **Lower left panel:**  $z = 1$ . **Lower right panel:**  $z = 2$ .

which are at the centers of dark matter halos and no subhalos, while all Coma cluster spheroidals in this study are actually substructures within the Coma Cluster host halo. Those substructures will have suffered from processes like tidal stripping and harassment, which could probably reduce the dark matter fractions (Dolag et al., 2009). Unfortunately, the sample of CETGs does not include a galaxy cluster, and the Magneticum Box4 uhr, from which the METGs are selected, only hosts a single massive cluster which is still much smaller than the Coma Cluster, and the substructures are not well enough resolved for a proper comparison study. A larger simulation volume with the same resolution,

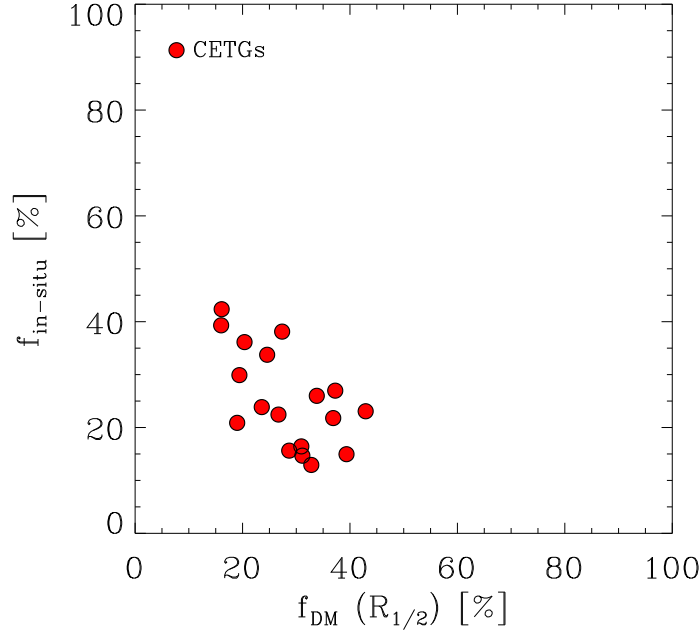


**Figure 4.4:** The fraction of stars formed in-situ versus the fraction of dark matter within the half-mass radius for the CETGs at  $z = 0$ .

however, is currently running, and will include more massive clusters with an according sample of well resolved substructures to test this hypothesis.

The other three panels of Fig. 4.3 show the stellar mass versus central dark matter fractions for our simulated galaxies at different redshifts, for  $z = 0.5$  (upper right panel),  $z = 1$  (lower left panel) and  $z = 2$  (lower right panel). We clearly see that the dark matter fractions within the half-mass radius are significantly smaller at higher redshifts. For the METGs, the highest central dark matter fraction at  $z = 2$  is  $f_{\text{DM}}(R_{1/2}) \approx 20\%$ , for the CETGs there are three galaxies which have higher fractions, but still below  $f_{\text{DM}}(R_{1/2}) < 40\%$ . The majority of spheroidals in both simulation samples have central dark matter fractions of  $f_{\text{DM}}(R_{1/2}) \approx 10\%$  or less, and the scatter is small. The sample of METGs contains slightly more massive galaxies, however, as at  $z = 0$  we see no clear correlation between the stellar mass and the dark matter fraction for the METGs and only a slight correlation for the CETGs. The central dark matter fractions continuously grow with redshift in both samples, which is in agreement with the results from Tortora et al. (2014b) who found for their observed ETGs at redshifts up to  $z \approx 0.8$  that the high-redshift ETGs have significantly smaller central dark matter fractions than their low redshift counterparts.

Most interestingly, the fact that the central dark matter fraction for the CETGs is larger at lower redshifts than at higher redshifts, directly proves that there really is an accretion of dark matter onto the central areas of the galaxies, since the CETGs at high redshifts are the direct progenitors of the low-redshift CETGs. This strongly supports the idea that this is a direct effect of the mass growth of galaxies through (minor) merger events. Hilz et al. (2012) showed that an increase in mass by a factor of 2 through minor merger events enhances the central dark matter fraction by about 80%, while one

equal mass major merger event also increases the dark matter fraction by 25%. Both types of merger can thus explain the observed increase in central dark matter fraction with decreasing redshift, as also indicated by Tortora et al. (2014b). The fact that this increase is seen in both of our simulation samples again indicated that these trends are not caused by numerical facts but due to the underlying physics of accretion through merger events.

This becomes even more clear when we compare the in-situ fraction of the simulated spheroidals at  $z = 0$  with their central dark matter fractions, as shown in Fig. 4.4 for the CETGs, using the in-situ fractions obtained by Oser et al. (2012). As can clearly be seen, the central dark matter fraction is correlated with the in-situ fraction such that galaxies with lower central dark matter fractions have higher in-situ fractions, while spheroidals with high central dark matter fractions have only about  $f_{\text{in-situ}} \approx 20\%$  or less. This is clearly in agreement with the idea that (mostly) dry merging is the main driver of mass growth in early-type galaxies since about  $z \approx 2$ , since dry merging reduces the fraction of stars formed in-situ while simultaneously enhancing the fraction of dark matter in the center. As shown in Fig. 3.10 of Chap. 3 (Remus et al., 2013), the in-situ fraction of the CETGs also is closely correlated with the steepness of the power-law slope which can be fit to the total radial density profiles of the galaxies. Thus, this indicates that the slope evolution is also closely correlated with the mass accretion history of the galaxy, which we will investigate in more detail in the next section.

## 4.4 Conspiracy Evolution with Redshift

In our detailed study of the stellar, dark matter and total (stellar plus dark matter) radial density and velocity dispersion profiles in Chap. 3 we have shown for our sample of CETGs that both the total density and velocity dispersion profiles of spheroidal galaxies can be well described by single power laws with slopes of

$$\gamma = \frac{d \log(\rho)}{d \log(r)} \quad \text{and} \quad \beta = \frac{d \log(\sigma)}{d \log(r)}. \quad (4.1)$$

In Remus et al. (2015b) we also demonstrated that this is also true for a subset of the METGs used in this work.

As already mentioned in the introduction, there is a contradiction between the evolution trends found for the slopes of the total density profiles between observations and simulations, with observations indicating no evolution or, if any, a flattening of the slopes with higher redshifts, while simulations clearly see a general steepening of the slopes with redshift. The flattening of the slope with decreasing redshift found in simulations can be naturally explained from the fact that galaxy growth after about  $z \approx 2$  is dominated by mostly dry merger events, which cause a flattening of the density slope while enhancing the central dark matter fractions. The relatively steeper slopes at high redshifts are, in this picture, also a natural consequence of the fact that galaxies at high redshifts mostly grow in (stellar) mass through the formation of stars from gas which has been accreted onto the galaxy. This gas can efficiently dissipate its energy, therefore leading to star formation at the very centers of the potential wells of the galaxies and therefore increasing the density in the central part where the stellar component is the dominant contributor to the total density profile. While this seems to be a conclusive picture of early-type galaxy formation, the observations disagree. In the following we will investigate in more detail this discrepancy.

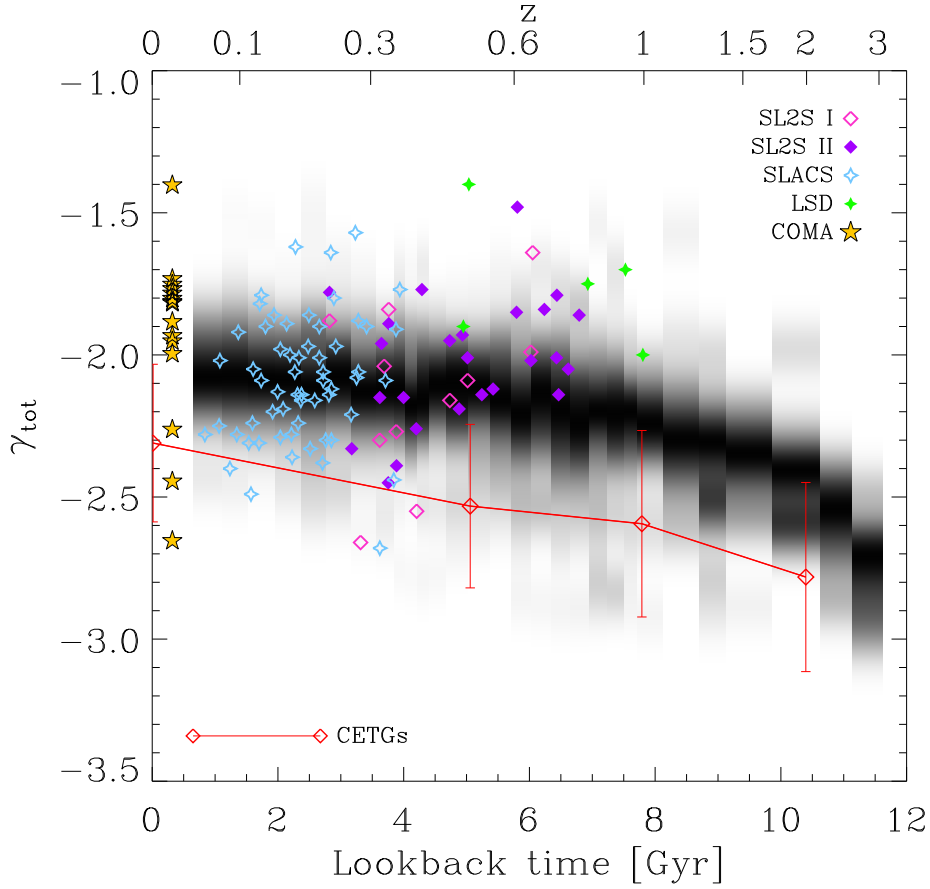


**Figure 4.5:** Total density profile power-law slopes versus lookback time for the spheroidals from the *Magneticum Box4 uhr* simulation, with total masses above  $M_{\text{tot}} \geq 1 \times 10^{11} M_{\odot}$  shown as black histograms at each time-bin. The evolution of the density slope for the CETGs is shown as red open diamonds connected by a red line. The observations are shown as colored symbols: Yellow stars show the observations for the Coma Cluster ETGs from Thomas et al. (2007) at  $z \approx 0.02$ . All other observations are from strong lensing: SLACS lenses (blue open stars, Auger et al., 2010), SL2S lenses (magenta open diamonds: Ruff et al. 2011; and lilac filled diamonds: Sonnenfeld et al. 2013b), and LSD lenses (green filled stars, Treu & Koopmans, 2004).

#### 4.4.1 Slope Evolution with Redshift

Sonnenfeld et al. (2013b) showed that the power-law slopes of the radial density profiles inferred from observations of strong lensing ETGs are flatter at higher redshifts than at low redshifts, and in a subsequent paper, Sonnenfeld et al. (2014) argued that this indicates that merger events at low redshifts must contain a significant amount of cold gas to steepen the slope. While the idea of the gas as the main reason for the existence of slopes which are steeper than isothermal is in agreement with our approach from theory and simulations, the interpretation is not. Fig. 4.5 clearly shows the problem: While both our simulated samples of spheroidals clearly show that at higher redshifts the total density slopes  $\gamma_{\text{tot}}$  were steeper than at lower redshifts (CETGs shown as red line, METGs are

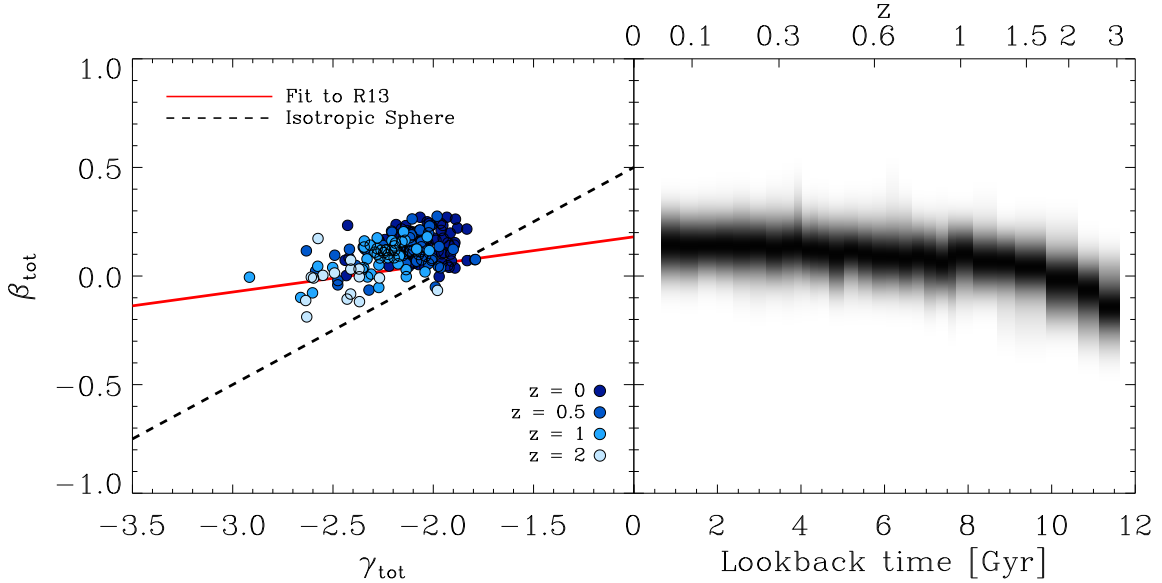


**Figure 4.6:** *Left panel:* Total velocity dispersion slope  $\beta_{\text{tot}}$  versus the total density slope  $\gamma_{\text{tot}}$  for METGs at different redshifts shown as blue circles, with colors as indicated in the legend marking the different redshifts. The black dashed line marks the solution for an isotropic sphere (or a sphere with constant anisotropy), while the red line shows the fit to the values found for the cosmological simulations studied in Chap. 3 (Remus et al., 2013). *Right panel:* The total velocity dispersion slope versus lookback time, shown as histogram for each time bin.

shown as black histograms for the slopes within each redshift bin of the simulation), the observations, which are shown as colored symbols, show the opposite behaviour.

While the total density slopes found for the CETGs at high redshifts are all much steeper than the observed ones, the METG sample actually includes galaxies with total density slopes as flat as the observed ones even at high redshifts. This is mostly due to the fact that the METG sample is selected from a full cosmological box, and thus also includes massive evolved galaxies even as high as  $z = 2$  which are the progenitors of the most massive galaxies at  $z = 0$ . Additionally, we see a clear offset between the distribution of the METGs and the CETGs, with the CETGs having generally steeper slopes than the average METGs. Nevertheless, even if the actual values for the mean total density slopes at each redshift bin for the CETGs are smaller than for the METGs, the general evolution trends are the same. In addition, the evolution trends found for the METGs are similar to those found in Johansson et al. (2012) for their set of re-simulations, which include more physics than our CETGs as well.

While there are spheroidals in the METG sample which show similarly flat slopes than the observations at high redshifts, those are still the outliers. Therefore, there are three possible explanations for this discrepancy: First, it might be possible that, at high redshifts, the most massive galaxies have a higher probability to be a lens galaxy, and thus the observational sample is biased towards massive, more evolved systems. Second, there might be a major problem in our simulations and the underlying theoretical framework. Third, there could be an issue with the calculation of the total density slopes

from observations.

One way to actually test this issue is to test other correlations known to depend on the mass accretion history. The left panel of Fig. 4.6 shows the dark-halo–spheroid conspiracy for the METGs as it was shown for the CETGs in Chap. 3 (Remus et al., 2013), and in Remus et al. (2015b) for a subset of the METGs: the slopes  $\beta_{\text{tot}}$  of the power-law fits to the total velocity dispersion versus the slopes  $\gamma_{\text{tot}}$  of the power-law fits to the total density distributions. We find the same results for both our simulations, and we also clearly see that, while  $\gamma_{\text{tot}}$  flattens with decreasing redshift,  $\beta_{\text{tot}}$  stays nearly the same, around  $\beta_{\text{tot}} \approx 0$ . This is also shown in the right panel of Fig. 4.6, where the evolution of  $\beta_{\text{tot}}$  with redshift is shown for the METGs as histogram.

Thus, we also find the dark-halo–conspiracy for our METG sample of spheroidal galaxies, that is the total density slopes evolve towards the isothermal case of  $\gamma_{\text{tot}} = 2$ , while the total velocity dispersion is flat out to large radii at all redshifts, independent of the total density slope. Only at very high redshifts of  $z > 2$ , the total velocity dispersion profiles steepen slightly. Nevertheless, the origin of this behaviour is still unclear, especially the origin of the constantly flat total velocity dispersion profiles, and remains to be solved in the future.

#### 4.4.2 Correlating Galaxy Properties with the Total Density Slope

As suggested above, since the central dark matter fractions  $f_{\text{DM}}(R_{1/2})$  correlate with the in-situ fractions  $f_{\text{in-situ}}$  of the spheroidals (Fig. 4.4), and the in-situ fractions show a correlation with the total density slope  $\gamma_{\text{tot}}$  (Fig. 3.10), it is self-evident that there should also exist a correlation between the central dark matter fractions and total density slope  $\gamma_{\text{tot}}$ . The upper left panel of Fig. 4.7 shows  $\gamma_{\text{tot}}$  versus  $f_{\text{DM}}(R_{1/2})$ , for the METGs (blue circles) and the CETGs (red circles), including all galaxies which are analyzed in this work, independent of their redshift. The latter is done to enhance the number statistics to see the overall trends, independent of redshift. We find a clear correlation between both quantities for both samples of spheroidals, that is spheroidals with a flatter slope have larger central dark matter fractions, however, the correlations have very different slopes. While the CETGs show a steep, nearly linear increase in  $\gamma_{\text{tot}}$  with increasing  $f_{\text{DM}}(R_{1/2})$ , the METGs show a strong increase in  $\gamma_{\text{tot}}$  for small changes in  $f_{\text{DM}}(R_{1/2})$  at low central dark matter fractions, and a flattening of the correlation above  $f_{\text{DM}}(R_{1/2}) \approx 20\%$ , where the slopes only change slightly, and are on average already close to isothermal. A comparison to observations from strong lensing (SLACS sample, Barnabè et al. 2011) reveals a very good agreement with the correlation found for the METGs, while their match with the CETGs is rather poor. On the contrary, the Coma Cluster ETGs, which show a much larger scatter than both the observations from Barnabè et al. (2011) and our simulated samples, again show deviations from both simulations for a subset of the observed galaxies, which had extremely high masses but low central dark matter fractions. For the other Coma Cluster galaxies, the result is not as clear as for the strong lensing sample, however, the overall agreement with the METG spheroidal sample is better than for the CETGs.

Another interesting quantity to compare to is the stellar mass density:

$$\Sigma_* = \frac{M_*}{2\pi r_{\text{eff}}^2}, \quad (4.2)$$

following Sonnenfeld et al. (2013b), which is basically a measurement of the concentration of the stellar component. The smaller  $\Sigma_*$ , the less concentrated a galaxy. Sonnenfeld et al. (2013b) report for their observations, that ETGs with more concentrated stellar components have steeper total density

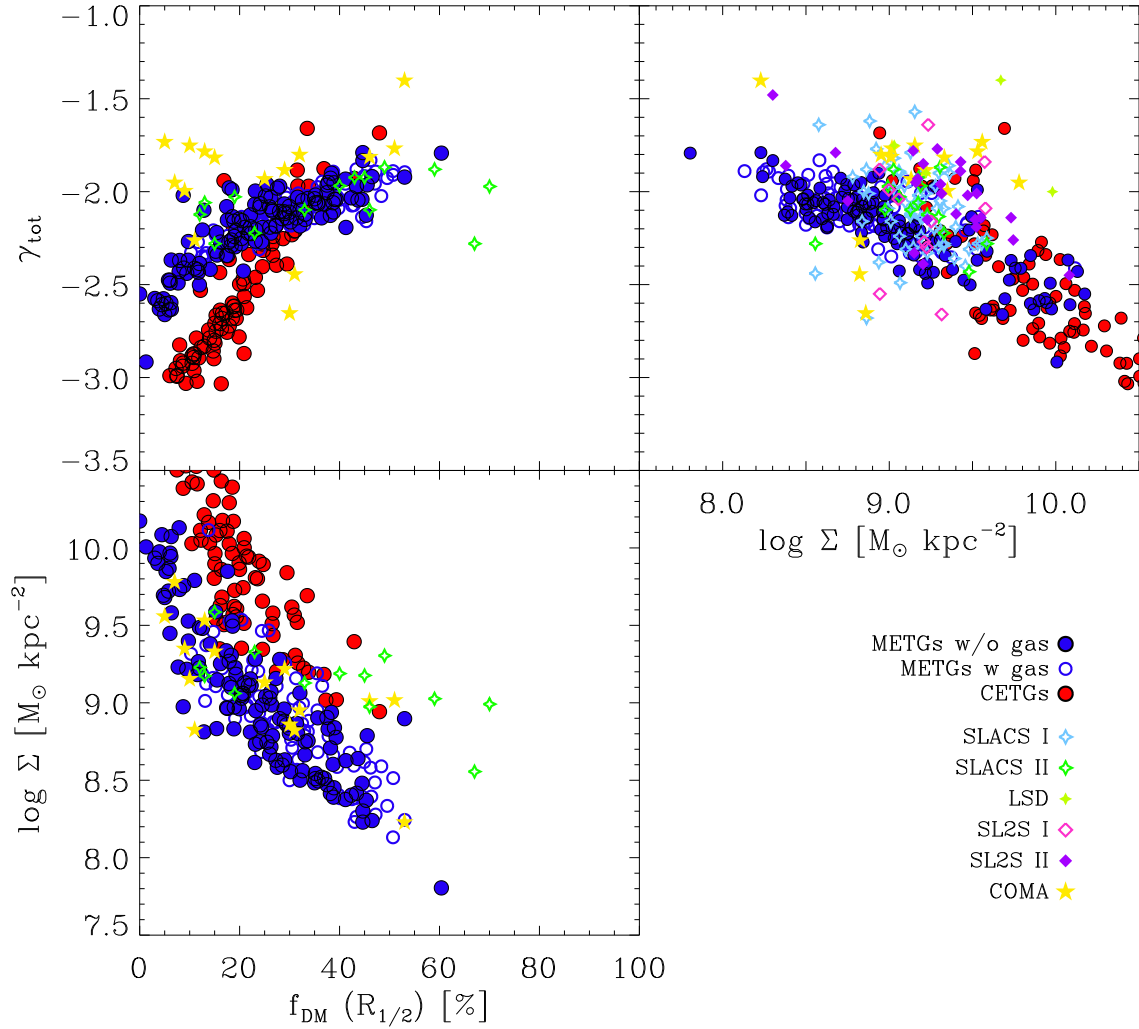


**Figure 4.7:** Correlations between central dark matter fractions  $f_{\text{DM}}(R_{1/2})$ , total density slopes  $\gamma_{\text{tot}}$  and stellar mass density  $\Sigma_*$ . METGs without cold gas disks are shown as filled blue circles, METGs with cold gas disks as open blue circles, and CETGs as red filled circles. Here, all spheroidals at  $z = 0$ ,  $z = 0.5$ ,  $z = 1$  and  $z = 2$  are included in all panels to better see the overall relation between the three parameters. For comparison, observations are included if available, namely Coma Cluster ETGs (yellow stars Thomas et al., 2007), SLACS lens ETGs (blue open stars: Auger et al. 2010; and green open stars: Barnabè et al. 2011), SL2S lens ETGs (magenta open diamonds: Ruff et al. 2011; and lilac filled diamonds: Sonnenfeld et al. 2013b), and LSD lenses (green filled stars, Treu & Koopmans, 2004). **Upper left panel:** Total density slopes  $\gamma_{\text{tot}}$  versus central dark matter fractions  $f_{\text{DM}}(R_{1/2})$ . **Upper right panel:** Total density slopes  $\gamma_{\text{tot}}$  versus stellar mass density  $\Sigma_*$ . **Lower left panel:** Stellar mass density  $\Sigma_*$  versus central dark matter fractions  $f_{\text{DM}}(R_{1/2})$ .

profiles and thus the estimated power-law slopes are steeper, which was also found before by Auger et al. (2010). This is well in agreement with our conclusions from simulations, however, since observations have shown spheroidals to be more compact than their present-day counterparts, this would implicate that the slopes at higher redshifts should also be steeper.

We calculated the stellar mass density for our simulated halos, using the stellar half-mass radius instead of the effective radius in Eq. 4.2. There is a clear correlation between the stellar mass density and the total density slope (see upper right panel of Fig. 4.7), which is the same for both our simulation samples and for the observations, albeit the scatter in the observed total density slopes  $\gamma_{\text{tot}}$  is larger than the scatter found in the simulations at a given stellar mass density. The METGs again match the observations successfully, while most of the CETGs are much more concentrated than the METGs and the observations. This is most likely again due to the missing AGN feedback in the CETG simulations.

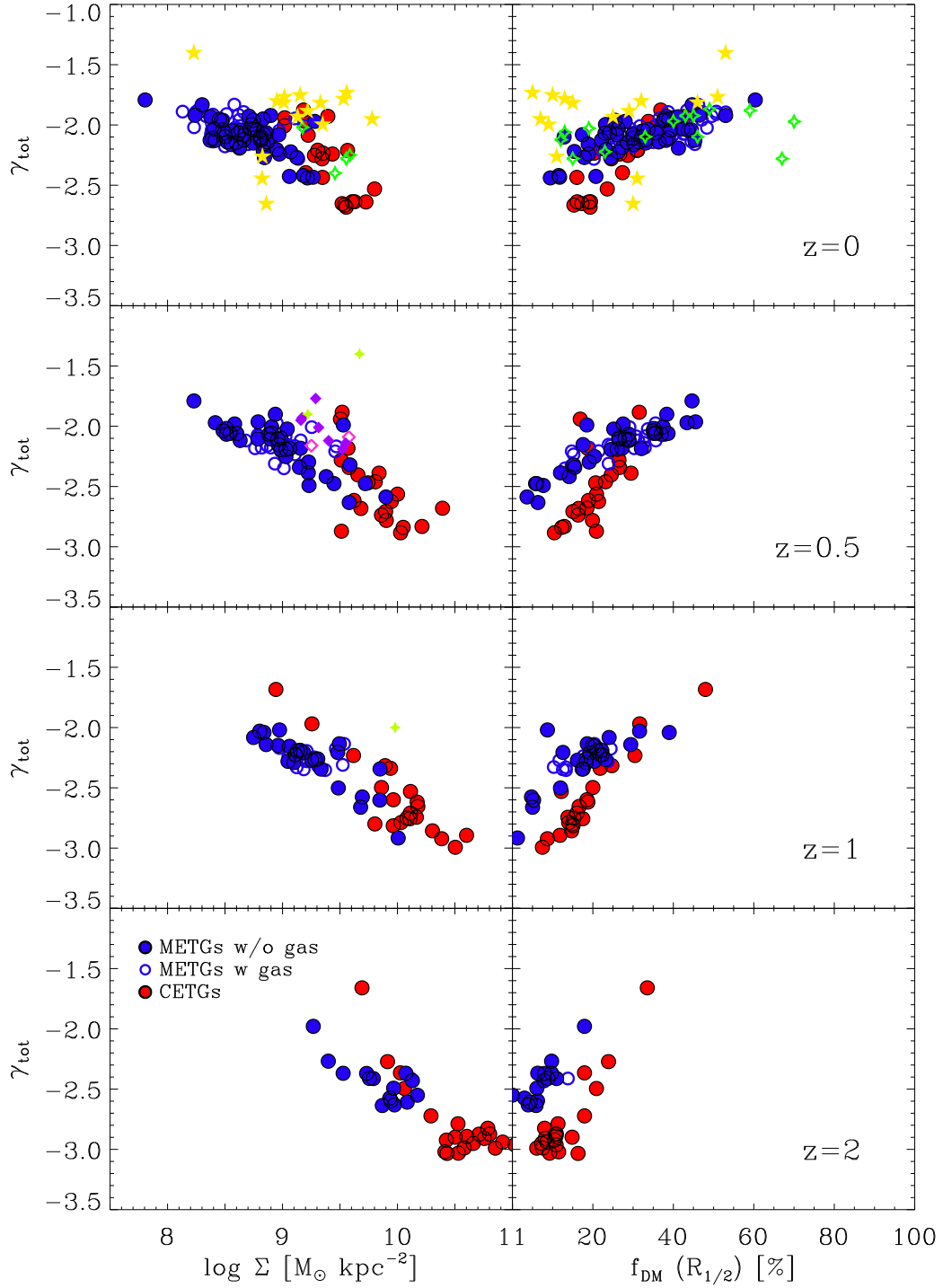
For completeness, we plot in the lower left panel of Fig. 4.7 the stellar mass density  $\Sigma_*$  versus the central dark matter fraction  $f_{\text{DM}}(R_{1/2})$ . As expected, there is a clear tendency for spheroidals with larger  $f_{\text{DM}}(R_{1/2})$  to be less compact, and while this is supported by both simulations, METGs and CETGs, there is a clear offset between the actual values of both simulations. In this case, the simulations and observations do not match too well, albeit the match again is much worse for the CETGs than for the METGs.

Fig. 4.8 shows the relations between the total density slopes  $\gamma_{\text{tot}}$  and the stellar mass densities  $\Sigma_*$  (left columns) and central dark matter fractions  $f_{\text{DM}}(R_{1/2})$  (right columns), at four different redshifts  $z = 0, 0.5, 1$  and  $2$  from top to bottom. There is a clear evolution trend found for the simulations, namely that the central dark matter fractions increase with redshift, while the stellar central concentration is decreasing. These evolution trends are seen in both simulation samples, and support our idea that, after about  $z = 2$ , the evolution of spheroidals is dominated by merger events, which enhance the central dark matter fractions, lead to stronger growth in size than in mass, and evolve the total density slope towards an isothermal solution through dynamical friction and violent relaxation.

## 4.5 Mocking the Slopes: “Observing” our Simulations

Since simulations and observations are in good agreement with the general properties of the spheroidals like mass, dark matter fractions and sizes at different redshifts, but only diverge in the interpretation of the evolution trends for the total density slopes, we wanted to test if this could be explained by a methodical issue. Therefore, A. Sonnenfeld kindly provided his analysis program used to calculate the total density slopes from the observations. This method is based on modeling the total density distribution of the lens as a power law, and the luminous component with a Hernquist profile to mimic a de Vaucouleurs profile with its effective radius according to the observations (see Treu & Koopmans 2002; Sonnenfeld et al. 2013b for more details on the method). For this model, velocity dispersions are calculated using the spherical Jeans equation. This model is then compared to the observed velocity dispersions and the Einstein radius, to identify the free parameter of the model, which is the power-law density slope. In addition, Sonnenfeld et al. (2013b) broadened their models to include also models which use different profiles instead of the de Vaucouleurs profile, and they show that the choice of the base model strongly influences the outcome of the resulting slopes, while the radius of the Einstein lens does not play a crucial role.

For our comparison, we want to use our simulated spheroidals as “fake” lens galaxies and “observe” those galaxies by using the same analysis tools as the observers. The information required



**Figure 4.8:** Same as Fig. 4.7 but split into different redshift bins. **Left panels:** Total density slopes  $\gamma_{\text{tot}}$  versus stellar mass densities  $\Sigma_*$ . **Right panels:** Total density slopes  $\gamma_{\text{tot}}$  versus central dark matter fractions  $f_{\text{DM}}(R_{1/2})$ . **Rows:** From top to bottom:  $z = 0$ ,  $z = 0.5$ ,  $z = 1$ ,  $z = 2$ .

by their method as an input information are: The effective radius  $r_{\text{eff}}$  of the lens galaxy, the Einstein radius of the lens  $r_{\text{Ein}}$ , the projected line-of-sight velocity dispersion  $\sigma_{\text{LOS}}$  within  $0.5 R_{\text{eff}}$ , and the total mass  $M_{\text{tot}}$  within the lens area. To mock observations from our simulations, we use the following inputs to meet the requirements:

- The effective radius  $r_{\text{eff}}$  of the lens galaxy is, as discussed before, approximated by the half-mass radius  $r_{1/2}$ .
- For the Einstein radius of the lens we assume  $r_{\text{Ein}} = 1.5 r_{1/2}$ , according to the ratios between  $r_{\text{Ein}}$  and  $r_{\text{eff}}$  which have been found by Sonnenfeld et al. (2013a) and Ruff et al. (2011) for the SL2S survey. The ratios of the lenses studied in the SLACS (and BELLS) survey were usually smaller, but the ratios for the LSD survey were of similar order. This choice, however, should not strongly influence the results, since Sonnenfeld et al. (2013b) showed that the ratio between effective radius and Einstein radius does not change the resulting slopes significantly. The influence of changes in this ratio on the resulting total density slopes were smaller than the error of the measurements. This is important since there is a tendency for lenses at higher redshifts to have larger ratios between  $r_{\text{Ein}}$  and  $r_{\text{eff}}$  due to geometrical reasons.
- To mimic the projected line-of-sight velocity dispersion  $\sigma_{\text{LOS}}$  within  $0.5 R_{\text{eff}}$ , we rotate our spheroidals on both the face-on and edge-on projection, and calculate the line-of-sight velocity dispersion within half of the half-mass radius for both projections separately. In the following study we will always consider both projections, as they basically are the maximum and minimum values which can be found.
- For the total mass within the lens area we include all star, gas and dark matter particles within the given projected radius of  $r_{\text{Ein}} = 1.5 r_{1/2}$ , for both projections.

The results are shown in Fig. 4.9, for the edge-on (left panels) and face-on (right panels) view, for all galaxies at the four different redshift bins considered in this work ( $z = 0, 0.5, 1, 2$ ). CETGs are again shown as red circles, METGs as blue circles. As can clearly be seen, there is a strong discrepancy between the resulting density slopes taken directly from the simulations,  $\gamma_{\text{sim}}$ , and the mocked density slopes  $\gamma_{\text{mock}}$ . In an ideal case, the resulting values should have been ordered along the dash-dotted line which marks the 1:1 ratio where  $\gamma_{\text{mock}} = \gamma_{\text{sim}}$ . However, in both the edge-on and the face-on view cases, the mocked slopes are closely scattered around  $\gamma_{\text{mock}} = -2.2$  for the edge-on and  $\gamma_{\text{mock}} = -1.9$  for the face-on projections, while the intrinsic slopes from the simulations vary from  $\gamma_{\text{sim}} \approx -3$  to  $\gamma_{\text{sim}} \approx -1.6$ . This is the case for both simulation samples, CETGs and METGs, but the METGs show even flatter mock slopes for the face-on view than the CETGs.

Therefore, we clearly see that there is a discrepancy between the “real” total density slopes and the mocked slopes, which is most prominent at the steeper-slope end. Indications for such a discrepancy between the simulated and observed slopes has already been presented in Sonnenfeld et al. (2014) using a comparison sample of major merger simulations, however, the difference is much larger for our cosmological simulations where we find significantly steeper slopes at high redshifts. In addition, as shown for the major merger sample studied in Chap. 3 (Remus et al., 2013), with the usual present-day configuration for disk galaxies, the initial slopes are also close to isothermal, which is why the effect of the discrepancy between the mocked and intrinsic slopes are less pronounced in those cases. Since the line-of-sight velocity dispersion is one of the major input parameters to calculate the mocked slopes, and actually the most error-prone one, we tested whether the difference between the mocked

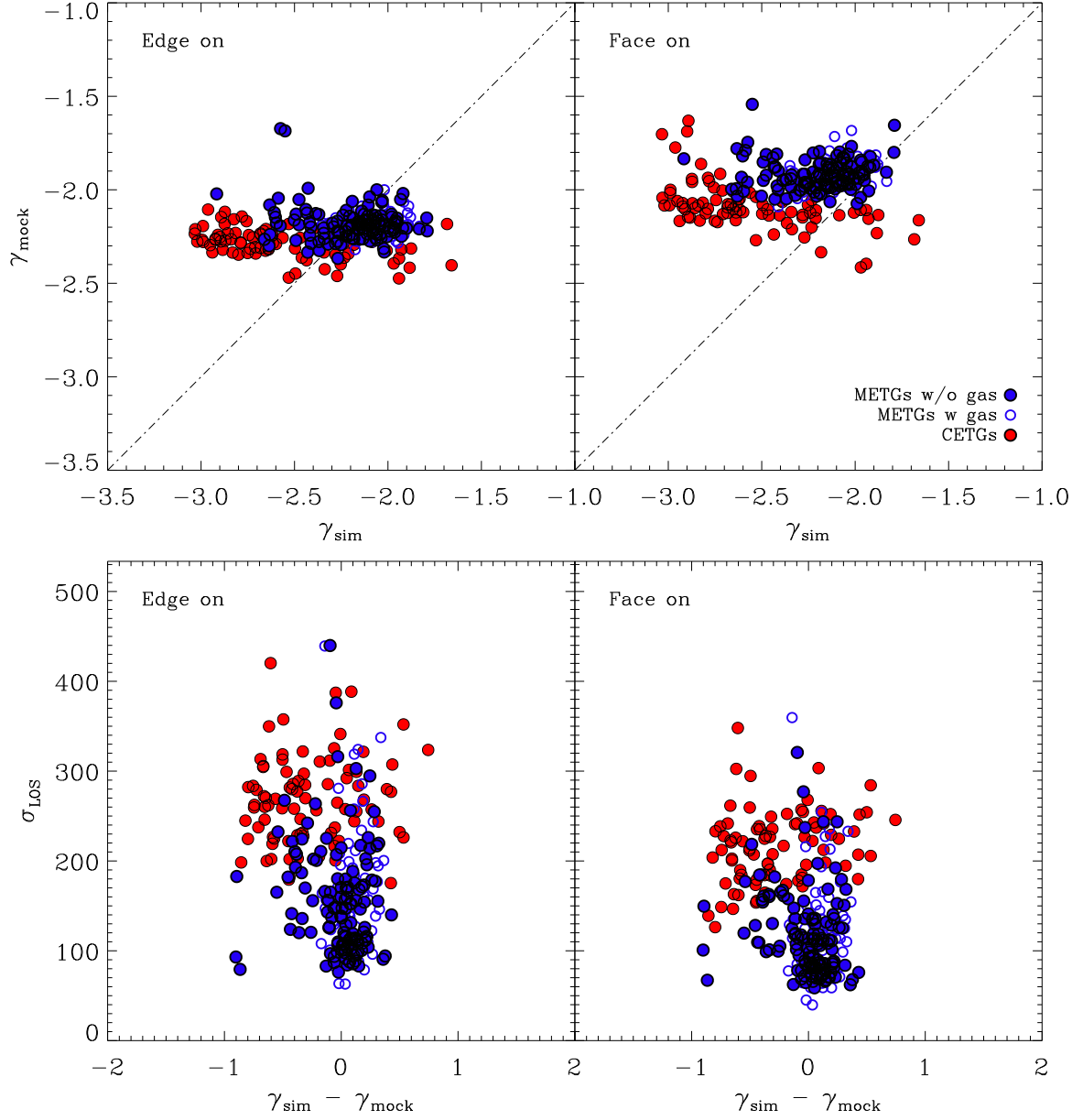


**Figure 4.9:** *Upper panels:* total density slopes from mock observations of our simulated galaxies ( $\gamma_{\text{mock}}$ ) versus the total density slope calculated directly from the simulations ( $\gamma_{\text{sim}}$ ), for CETGs (red circles) and METGs (blue circles). The dash-dotted line shows the 1:1 ratio. *Lower panels:* Line-of-sight velocity dispersion calculated for our spheroidals versus the difference between the two density slopes from mocked observations and simulations ( $\gamma_{\text{sim}} - \gamma_{\text{mock}}$ ). Left and right panels show the  $\gamma_{\text{mock}}$  calculated from edge-on and face-on view of the simulated spheroidal, respectively.

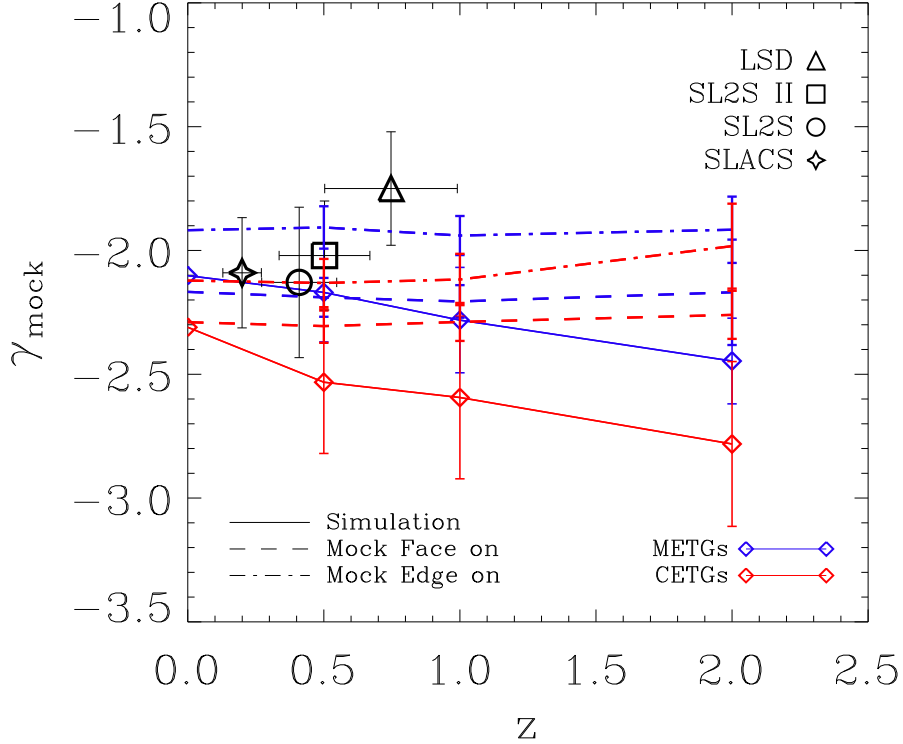


**Figure 4.10:** Evolution of the total density slope obtained from the mock observations of our simulated spheroidals,  $\gamma_{\text{mock}}$ , with redshift. Results for the METGs are shown as blue lines, while those obtained for the CETGs are shown as red lines. Dashed (dash-dotted) lines show the average density slope  $\langle \gamma_{\text{mock}} \rangle$  at each redshift bin for the face-on (edge-on) projections, with the according variance shown as error bars. The solid lines show the mean of the intrinsic slopes obtained directly from the simulations, for comparison, with the error bars showing the variance. For comparison, the mean value of the observed slopes for each of the four comparison samples is shown as large symbols, including the variance error bars, with the LSD data from Treu & Koopmans (2004) (triangle), the SL2S data from Ruff et al. (2011) (circle), the SL2S II data from Sonnenfeld et al. (2013b) (square) and the SLACS data from Auger et al. (2010) (star).

and the intrinsic slopes correlate with the line-of-sight velocity dispersions of our simulated sample. As can be seen in the lower panels of Fig. 4.9, there is no correlation between the deviations of the two slopes and  $\sigma_{\text{LOS}}$ . On a side notice, we also see that the velocity dispersions obtained for the METGs are significantly lower and more realistically spread than those obtained for the CETGs. This is also due to the improved numerical schemes used in the Magneticum simulation sets.

To conclude the results of our study and analysis of the origin of the differences between the evolution tendencies of the total density slopes of spheroidal galaxies seen in simulations and observations, we again plot the evolution of the slopes for simulations and observations, as done in Fig. 4.5, but this time we use the total density slopes obtained from the mock observations. As can clearly be seen in Fig. 4.10, the discrepancy between the observed and the simulated density slopes has vanished for the METGs and is significantly smaller for the CETGs. The dashed lines show the median values obtained for the face-on mocks, the dash-dotted lines show the median values obtained for the edge-on views

at the different redshifts. Those values show the lower and upper median values, and the observations, marked as big black symbols, all but for the LSD sample lie between those median-value-lines for the METGs. For comparison, the solid lines show the intrinsic evolution trends for the METGs (blue) and CETGs (red) as measured directly from the simulations.

Most importantly, all three samples now show the same behaviour, namely that there is basically no evolution of the density slopes with redshift. While this solves the issue of the discrepancies between the evolution trends from observations and simulations, it on the other hand raises the question how to modify the analysis tools used to infer the total density slopes from strong lensing measurements. A more detailed comparison of the observational methods with simulations will hopefully help to solve those issues, and enhance our understanding of the interaction processes between the dark and luminous components as well as the role of the cold gas.

## 4.6 Summary and Discussion

We used spheroidal galaxies selected from two different simulations over a redshift range from  $0 < z < 2$ . The first set of 20 spheroidals at  $z = 0$  was selected from the sample of cosmological zoom simulations presented in Oser et al. (2010) (hereafter CETGs). Those 20 galaxies were traced back in time, and at each timesteps analysed in this work the 20 CETGs were the progenitors of the 20 spheroidals selected at  $z = 0$ . The second set of spheroidals, the METGs, was drawn from the full hydrodynamic cosmological simulation Magneticum Box4 uhr, according to their classification as spheroidal, as described in Sec. 2.4.1. For this second set of galaxies, we selected at each timestep all spheroidals which were more massive than  $M_{\text{tot}} = 1 \times 10^{11} M_{\odot}$ , independent of them being progenitors of spheroidals at other redshifts or not. Both samples, however, are limited to central halo galaxies, excluding spheroidals which are substructures.

For both samples, we studied the evolution of the mass-size relation with redshift. We find a generally good agreement with the observations, at both low and high redshift. At low redshifts, our relation found from the simulated spheroidals is in good agreement with the mass-size relation found for the SDSS sample by Shen et al. (2003), while at the lower mass range our simulations more closely resemble the results from the GAMA survey (Baldry et al., 2012), which is focussed especially on the low mass end of the galaxy mass function. Both our simulated samples of spheroidals show a similar scatter around the relation as well as similar evolution trends for the high redshift spheroidals to have smaller sizes, however, the METGs are less massive than the CETGs of the same size at all redshifts. This is due to the fact that the CETGs do not include a central black hole and the associated AGN feedback, which, in case of the METGs, efficiently prevents the overcooling problem by heating part of the cold gas in the centers of the galaxies during their evolution due to the feedback and thus preventing that too many stars are formed at the centers of the galaxies. Our METGs also show more realistic velocity dispersions compared to the CETGs, which is also a result of more realistic modelling of the underlying physics and the improved numerical schemes.

We also find that about 48% of our spheroidals from the METG sample contain a small cold gas disk at  $z = 0$ . This matches the fraction found by Young et al. (2013) for the spheroidals in the Atlas<sup>3D</sup> survey, who reported a fraction of about 40% of their spheroidals to have cold gas disks. In addition, at  $z = 2$  many spheroidal galaxies actually contain a huge amount of cold gas, as shown by Teklu et al. (2015b), which is also the reason why those galaxies are not classified as spheroidals by our crude selection criterion. Nevertheless, this supports the idea of the two-phase evolution of spheroidal

galaxies, with the high redshift phase at  $z > 2$  dominated by cold gas accretion, gas-rich merger events and in-situ star formation, while the later phase is dominated by more or less gas-poor merger events as the main driver of mass growth. This is in agreement with the results presented by Hilz et al. (2012, 2013), who showed that the observed evolution of the mass-size relation with redshift can be well explained through the accretion of multiple dry minor merger events.

Another aspect of this evolution scenario is the increase of the central dark matter fraction of spheroidal galaxies with decreasing redshift. We find this increase for all galaxies in our sample, independent of the selection method and simulation, in good agreement with recent observational results by Tortora et al. (2014b). While there is only a weak correlation with the mass of the galaxies, we find a strong anti-correlation between the in-situ fraction and the central dark matter fraction of galaxies, with galaxies with high central dark matter fractions having only very little stars formed in situ. This is a natural consequence of the late growth through (dry) merger events.

We had already shown in Remus et al. (2013) that there exists a dark-halo–spheroid conspiracy for the CETGs, that is that, at  $z = 0$ , their total (stellar plus dark matter) radial density profiles can be well described by an isothermal power-law with a slope of  $\gamma_{\text{tot}} \approx -2$ . In this work, we demonstrate that this is also true for the spheroidals from the Magneticum simulations, and that both simulations show a similar scatter in  $\gamma_{\text{tot}}$ , with a tendency towards steeper slopes found at higher redshifts. This trend for steeper slopes at high redshifts is more pronounced for the CETGs than for the METGs, but the overall trend is the same in both simulations, indicating that this is a real evolution trend and not a numerical feature. However, observations from strong lensing (Treu & Koopmans, 2004; Auger et al., 2010; Ruff et al., 2011; Sonnenfeld et al., 2013b) find no changes in the total density slopes with redshift, or, if any, a tendency towards flatter slopes at higher redshifts.

Using mock observations of our simulated spheroidal samples and applying the same analysis tool as for the observed samples, following Sonnenfeld et al. (2013b), we demonstrate that the applied assumptions for the modeling of the density profiles provide good fits for spheroidals with nearly isothermal density profiles, but for those spheroidals with steeper slopes, the slopes obtained from the mocked observations are much flatter than the intrinsic profiles. Using the slopes obtained from the mock observations leads to an excellent match between our simulations and the observations, however, to successfully measure the total density slopes even for the more compact spheroidals with the steeper slopes, a better refinement of the modeling is needed.

Simulations and observations agree in that compact spheroidal galaxies tend to have steeper total density slopes than their more extended counterparts, see Sonnenfeld et al. (2013b), but also Tortora et al. (2014a). Spheroidals with flatter slopes also have larger central dark matter fractions, in agreement with the fact that there are more compact spheroidal galaxies at higher redshifts, where we also find more galaxies with steeper density slopes and smaller dark matter fractions.

In summary, we find clear indications from our new set of simulations for the two-phase evolution scenario for central spheroidal galaxies: At high redshift, gas dominates the mass growth of (spheroidal) galaxies, thus many stars are formed in situ and only few are accreted. The gas dissipates its energy and sinks to the center of the potential well where it forms the stars in a compact central structure, thus the dark matter fractions are small and the total density slopes are steeper. At lower redshifts, (dry) merger events of all mass ratios start to dominate the mass growth of the galaxies, leading to an enhanced growth in size compared to the growth in mass, as mass is mostly added to the outskirts (apart from the rare major merger events which actually mix the whole galaxy). This leads to a growth of the central dark matter fraction, a flattening of the total density slopes and a decrease of the in-situ fraction of stars. Therefore, we conclude that the central dark matter fractions and the

slopes of the total radial density profiles of spheroidal galaxies are good indicators for the amount of dry merging events a galaxy has undergone.



## Chapter 5

# A “Universal” Density Profile for the Stellar Halos of Galaxies

### 5.1 Introduction

In addition to the clearly visible content of a galaxy, every galaxy is surrounded by a diffuse global stellar halo, which usually is assumed to be spherical. This outer halo consists of old and thus not very massive stars, since there is basically no in-situ star formation in the outskirts of a galaxy because the gas density is much too low to form stars. (However, recent studies of extended H I disks indicate that in those disk galaxies there is a constant albeit low star formation rate per unit of gas even at large radii in the metal poor, low density gas disks, see for example Espada et al. (2011).) Therefore, those old populations must (mostly) be accreted through merging events and stripped from the main or the accreted galaxies during the encounters, as suggested for example by observations from Martínez-Delgado et al. (2010), or by the wealth of substructures observed around the Milky Way or Andromeda. The outer stellar halo contains vital information about the formation history of a galaxy, as in these outer regions the stars still remember the violent mass accretion the galaxy has gone through in its lifetime, since the mixing times in the outer halo are much larger than in the inner regions of the galaxy. Measuring densities and velocities of the outer stellar halo could therefore provide a multitude of unique information about the mass accretion history and morphological changes of a galaxy.

However, since these halos are usually made up of very old and thus faint stars, those outer stellar halos are difficult to observe as their surface brightness is very low. The usual method to gain information about the stellar outer halos is to use their brightest objects (or objects that are especially dominant in a certain narrow waveband) as tracers, such as globular clusters (GCs) or planetary nebulae (PNe), or, in nearby galaxies, the brighter classes of stars within those low mass stellar populations. Using stellar population models, it is then possible to calculate the actual total density profiles from the number densities of the tracer populations. However, this approach includes a multitude of assumptions in the models for the different tracers as well as the additional problem of substructures and merger remnants that cause local overdensities and therefore could imply a higher global stellar halo density than the actual one. Thus, it is very important to use as many different tracer populations as possible and carefully subtract substructures from the analysis to ensure that we do not measure the stellar populations of the substructures.

While PNe and GCs are bright enough to be used as tracer populations for galaxies outside the local group (see Chap. 6.1), the resolution of present-day telescopes is not high enough to detect individual stars in massive galaxies other than the Milky Way and Andromeda. Hence, those two galaxies are perfect laboratories to gather information about their stellar halos which might provide insight into the properties of stellar halos of massive galaxies in general, and learn about the significance of the different stellar tracer populations. This has been done for the Milky Way in a multitude of studies, for example Preston et al. (1991) and Kinman et al. (1994) used blue horizontal branch stars in the nearby stellar halo regions, Miceli et al. (2008) used RR Lyrae stars out to 30 kpc from the galactic center, and Carollo et al. (2007) used 10123 stars within 4 kpc around the sun from SDSS Data Release 5 to measure density and metallicity gradients in the stellar halo. They report a dichotomy in the Milky Way halo density, metallicity and net rotation, indicating that the Milky Way has indeed two distinct stellar halo components. Bovy & Rix (2013) obtained the mass of the Galactic stellar disk and the radial profile of the dark halo at small radii from a sample of G-type dwarf stars from the SEGUE survey at radii between  $5 \text{ kpc} < R_{\text{Galactic Plane}} < 12 \text{ kpc}$  and  $0.3 \text{ kpc} < R_z < 3 \text{ kpc}$ . More recently, Kafle et al. (2014) used K giant stars from SEGUE to measure the density of the stellar halo out to  $\approx 160 \text{ kpc}$ , reporting a power-law break in the density at  $\approx 17 \text{ kpc}$  and an exponential cutoff at radii larger than  $97.7 \text{ kpc}$ , while Deason et al. (2014) found a drop in the density profile of the stellar halo at radii larger than  $50 \text{ kpc}$ , changing from a power-law  $\rho \propto r^{\gamma_{\text{out}}}$  with a slope of  $-2 > \gamma_{\text{out}} > -3$  at radii smaller than  $\approx 25 \text{ kpc}$  to a steeper slope of  $-5 > \gamma_{\text{out}} > -6$  at  $\approx 50 \text{ kpc}$ , with indications for an even steeper slope at larger radii. They interpret that this behaviour indicates that the Milky Way had a quiet mass accretion history, with the last accretion into the stellar outer halo about 6 Gyr ago. This interpretation is supported by Bullock & Johnston (2005) who used dark matter merger trees from simulations with semi-analytic stellar components to study Milky Way mass halos and found a steepening in the stellar halo profiles at large radii, with the smooth component accreted much earlier than the structures which are still visible as satellites in the stellar halo. Additionally, Rashkov et al. (2013) also reported a steepening of the density profile at radii larger than  $60 \dots 70 \text{ kpc}$  for the ERIS simulation of a Milky Way type spiral galaxy (Guedes et al., 2011).

For our neighbouring galaxy, Andromeda, the density profile of the stellar outer halo was measured in several studies as well. For example, Tanaka et al. (2010) reported a density profile for the smooth halo component which can be described by a power-law  $\rho \propto r^{\gamma_{\text{out}}}$  with a slope of  $\gamma_{\text{out}} \approx -2.17$  out to  $R \approx 100 \text{ kpc}$ . More recently, Ibata et al. (2014) measured the stellar halo density profile from the RGB stars from the PANDAS-survey and found a power-law fit to the smooth, metal poor halo component with a slope of  $\gamma_{\text{out}} = -3.08$  that stays nearly constant from  $30 \text{ kpc}$  to  $300 \text{ kpc}$ .

Both studies find a much flatter density profile for the outer stellar halo of Andromeda than what has been reported for the Milky Way stellar halo, and they find no indication of a steepening in the density profile. Thus, it was concluded in many papers (e.g., Deason et al. (2014), Pillepich et al. (2014)) that the Milky Way and Andromeda, although both are large spiral galaxies of similar mass, have very different formation histories, in that Andromeda had a much more violent accretion history than the Milky Way, with multiple dwarf galaxy mergers compared to the relatively quiet accretion history assumed for the Milky Way due to its steep outer stellar slope and its low number of satellite galaxies.

In this work we use the Magneticum Pathfinder simulations to address the question of the steepness of the density slopes of the outer halos of Milky Way mass galaxies and its implications for the accretion history of those galaxies. This simulation set provides a statistically relevant sample of galaxies in the Milky Way mass range to address those questions. Additionally, it allows us to broaden

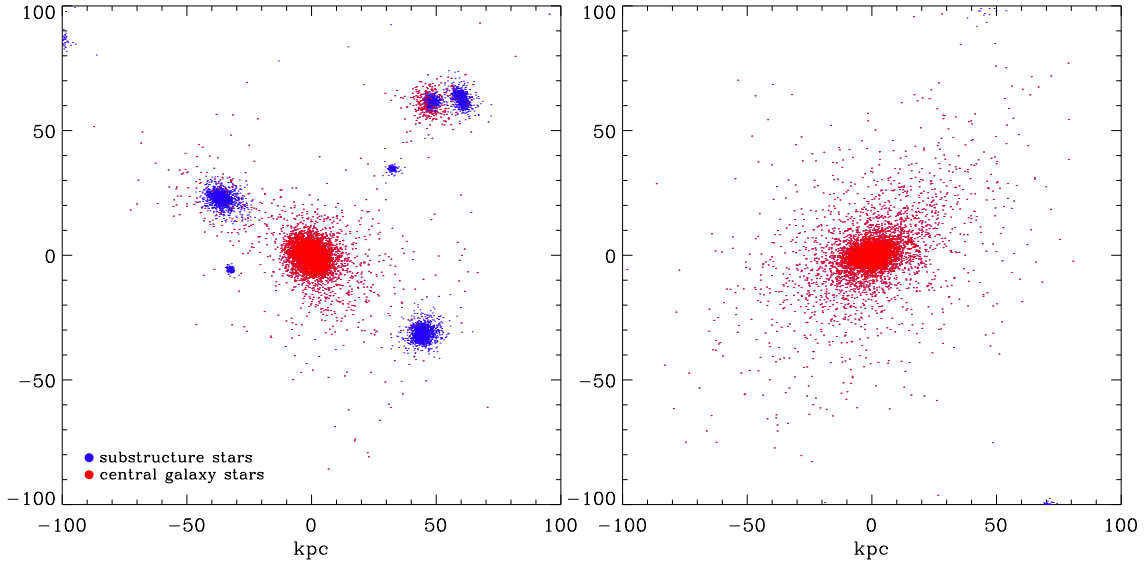


**Figure 5.1:** *Stellar particle plots for two example galaxies selected from the Magneticum Pathfinder Box4 uhr with a total mass of  $M_{\text{tot}} \approx 1 \times 10^{12} M_{\odot}$ , with stars that belong to the central galaxy shown in red and stars associated to a substructure shown in blue, within a radius of 100 kpc around the central galaxy. **Left panel:** Halo containing several substructures around the main central galaxy. The outer stellar halo is clearly disturbed by the presence of the substructures, with stars stripped from the substructures already causing local overdensities in the stellar halo of the main galaxy, see especially the substructure on the upper right. **Right panel:** Halo that contains no substructures. Here, the outer halo of the galaxy is clearly visible as undisturbed shallow spherical object.*

this study to a larger range of total galaxy masses in order to understand whether there is a self-similar behaviour in the outer stellar halos, as is the case for dark matter halos at all mass ranges, or whether the outer stellar halos behave differently depending on the morphological type of the galaxies.

## 5.2 Fitting a Power-Law to the Outer Stellar Halo

We select all halos in the Milky Way mass range of around  $M_{\text{tot}} \approx 1 \times 10^{12} M_{\odot}$ , from the Magneticum Pathfinder Box3 hr (458 halos) and Box4 uhr (24 halos) to provide a statistically relevant sample of galaxies for our analysis of the outer stellar halos of Milky Way type galaxies. This sample of galaxies includes elliptical galaxies as well as disk galaxies and galaxies that cannot be classified by our simple classification algorithm (see Sec. 2.4.1). Since the stellar halo of the galaxy, independent of its morphology, is the region where substructures become important, it is necessary to identify and subtract those structures before we can start our analysis of the outer stellar halos. We use SUBFIND (Springel et al. 2001, Dolag et al. 2009) to identify structures and subhalos in our simulations, as illustrated in Fig. 5.1, where we show as examples a halo which contains multiple substructures (left panel) and a halo which does not (right panel).

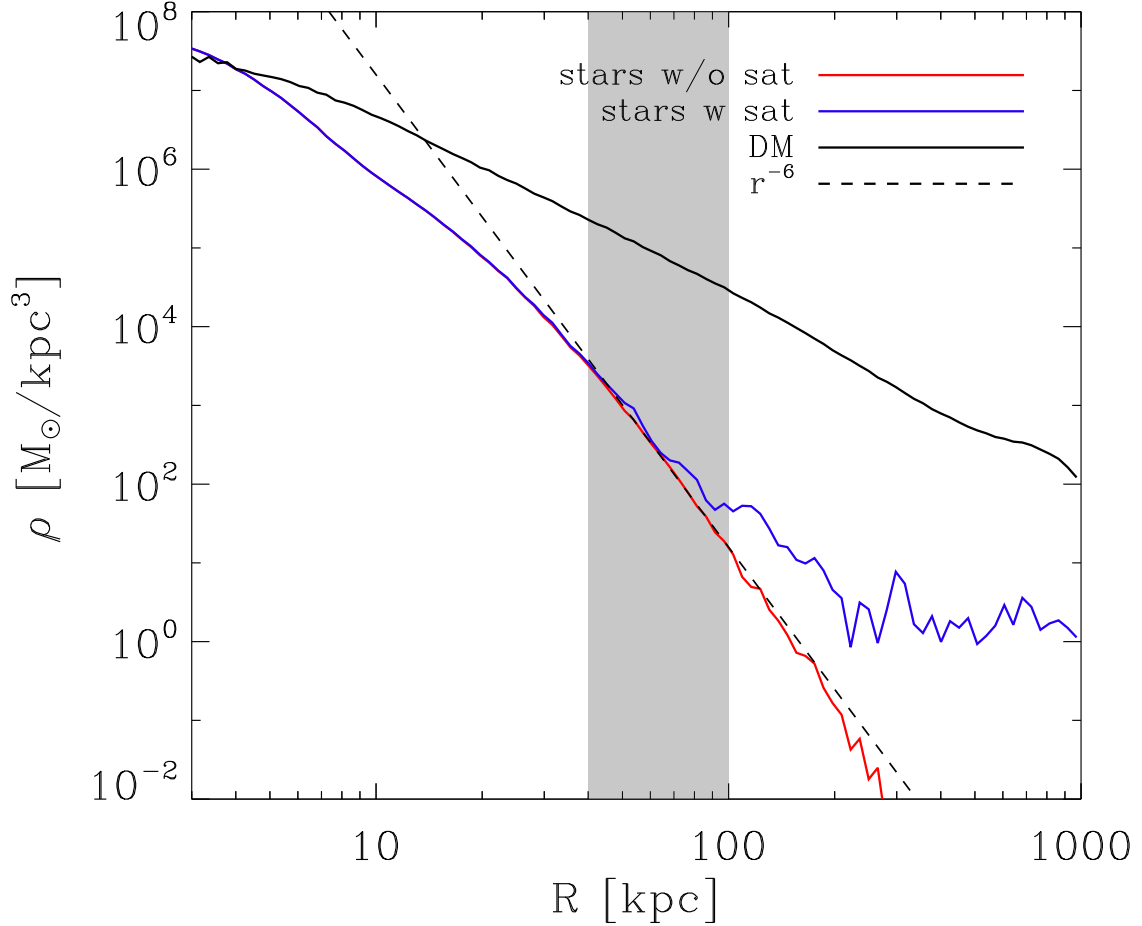


**Figure 5.2:** Stacked density profiles of all 458 halos with  $M_{\text{tot}} = 1 \times 10^{12} M_{\odot}$  from Box3 hr for DM (black), stars with satellites (blue) and stars which belong to the central galaxy (red). The dashed line is a  $\rho \propto r^{-6}$ -fit to the red line within 40 kpc and 100 kpc (shaded area).

### 5.2.1 Milky Way Mass Galaxies

In a first approach we want to understand how well the outer stellar halo of Milky Way mass galaxies can be described by a power law  $\rho \propto r^{\gamma}$ , and which range of slopes those power laws cover. For this purpose, we bin particles in logarithmically evenly spaced radial shells from 3 to 1000 kpc, excluding the innermost part of the galaxies and reaching out far beyond the virial radii of galaxies in the Milky Way mass range ( $\approx 200$  kpc).

Since our mass resolution in Box3 hr is still low, the number of particles in the outer stellar halos is also low; however, if we stack the density profiles of our 458 halos, the resulting profiles are smooth and well resolved, as shown in Fig. 5.2. The stacked dark matter profile is much flatter than the stacked density profile for the stellar halo, and never reaches slopes as steep as the stellar profile, while the

stellar density profile becomes even steeper with larger radii, in agreement with other simulations (e.g., Bullock & Johnston (2005) and Pillepich et al. (2014)). Comparing the stacked stellar density profiles with and without satellites (blue and red curves in Fig. 5.2, respectively), we clearly see that the substructures become important only in the far outskirts of the halo, while both profiles are identical for smaller radii. For radii around the virial radius the substructures dominate the stellar density profile and the density of the stellar halo of the central galaxy becomes negligible.

Following Deason et al. (2014), we fit a power law to the stellar density profile within the radius range of 40 kpc to 100 kpc. We find that in this range the stacked stellar density profile can be described very well by a power law with a slope of  $\gamma_{\text{out}} = -6$ , as shown by the dashed line in Fig. 5.2, while the stellar profile gets steeper for larger radii. This is in very good agreement with the measurement from Deason et al. (2014) for the Milky Way halo; however, it is in contradiction to the observations for the Andromeda galaxy, where  $-2 \gtrsim \gamma_{\text{out}} \gtrsim -3$ . The fact that the substructures do not strongly dominate the stellar profile in the radius range of 40 kpc to 100 kpc is also in good agreement with the results from (Deason et al., 2014), who find that their observed density slope is the same whether they include the substructures or not.

Since the mass resolution of Box3 hr is too low to study the outer stellar density profiles of the individual galaxies, we cannot use this simulation for a detailed study of the scatter of stellar density slopes around the mean value of  $\gamma_{\text{out}} = -6$ . Therefore, albeit reducing the number of halos significantly, we use Box4 uhr to address this question. In the Milky Way mass range of  $M_{\text{tot}} \approx 1 \times 10^{12} M_{\odot}$  we find 24 halos at  $z = 0$ . As shown in the left panel of Fig. 5.3, the stacked profiles for these halos provide similar results as the stacked profiles from the larger box despite the smaller number of galaxies. However, the curves are less smooth and more strongly influenced by the residuals of the substructures, as can be seen in the small excess around 100 kpc in the stacked stellar density profile without satellites, which corresponds to a large density peak in the stacked stellar plus satellite density profile with a strong drop at 100 kpc visible in both profiles.

The right panel of Fig. 5.3 shows the individual stellar density profiles of the 24 galaxies, including the substructures (blue lines). As can clearly be seen from this figure, the stacked stellar density profile excluding the substructures (red solid line) is a very good overall approximation of the general behaviour of these individual stellar density profiles, since each galaxy only has very few (or even no) substructures which show up as a very localised peak in the density profile, without changing the global behaviour of the stellar density profile. Thus, excluding the substructures, the individual stellar density profiles of all our 24 galaxies in the Milky Way mass range are similar to each other.

A histogram of the outer stellar density slope  $\gamma_{\text{out}}$  at  $z = 0$  of our galaxies is shown in the upper left panel of Fig. 5.4, where we also see the similarity of the individual stellar density profiles if the substructures are excluded from the fit (red line). We clearly see a maximum for values of the slope of  $-5 > \gamma_{\text{out}} > -6$ , with only very few halos scattering towards flatter slopes of  $-2 > \gamma_{\text{out}} > -3$ . However, this scatter covers the slope observed for Andromeda, indicating that, while the Milky Way behaves more like the average galaxy in this mass range, the values for Andromeda are still within the expected range of slopes.

This figure also shows that the slopes become strongly disturbed towards both steeper and flatter slopes when the substructures are not subtracted, depending on the radial position of the substructure and the radial range of the fit. If the power-law fit catches the tail of the peak of the substructure, the resulting slope is much steeper than the actual slope of the outer stellar halo of the central galaxy. If the power-law fit catches the rising part of the substructure peak, the resulting slope can even become positive if the substructure is very massive.

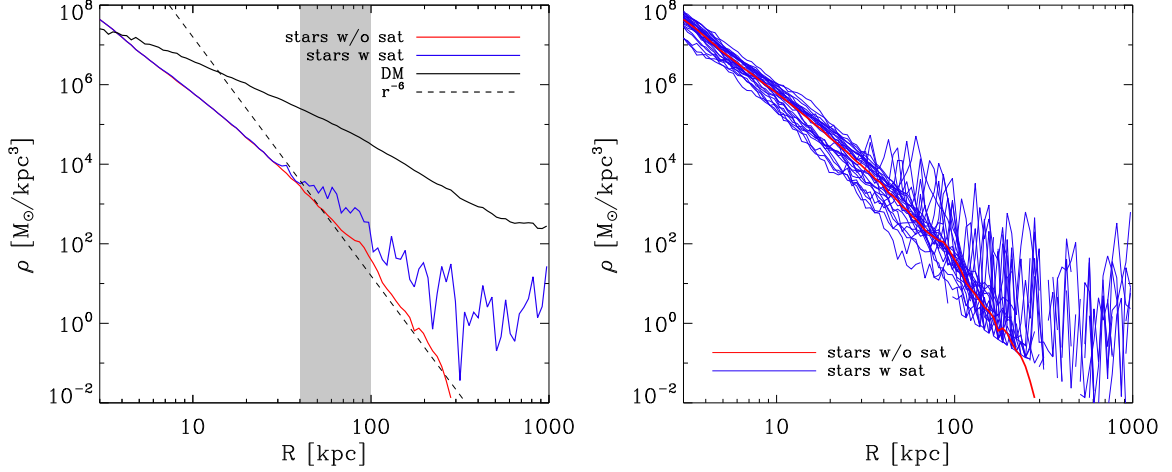


**Figure 5.3:** *Left panel:* Same as Fig. 5.2 but for all 24 halos with  $M_{\text{tot}} \approx 1 \times 10^{12} M_{\odot}$  from Box4 uhr. *Right panel:* Stellar density profiles for the 24 individual galaxies with  $M_{\text{tot}} \approx 1 \times 10^{12} M_{\odot}$  from Box4 uhr including substructures (blue lines). The red curve shows the same stacked density profile of the stars without substructures as in the left panel. The cut-off on the lower part of the blue curves shows the one particle per bin limit of the individual halos (resolution limit). We see that, even if the stacked profile with satellites does not follow the red curve, the individual curves scatter around the red curve, since the satellites only cause peak-like features in the individual profiles which otherwise follow approximately the red stacked curve.

As shown in the other three panels of Fig. 5.4, this is true for halos with total masses of  $M_{\text{tot}} \approx 1 \times 10^{12} M_{\odot}$  at all redshifts. At  $z = 0.5$  (upper right panel),  $z = 1$  (lower left panel) and  $z = 2$  (lower right panel), the distribution of stellar density slopes at radii of 40 kpc to 100 kpc always peaks around  $-5 > \gamma_{\text{out}} > -6$ , with a broadening of the distribution for the slopes when the substructures are not subtracted. The halos at those redshifts are, as for  $z = 0$ , solely selected according to their total mass, independent of their morphology or their present-day properties. This indicates that the outer stellar halos of galaxies of Milky Way mass are very similar, independent of the redshift, and thus there must be a universal mechanism assembling those stellar halos which is independent of the redshift and thus also of the star formation (which is enhanced at higher redshifts in both simulations and observations, see for example Steinborn et al. 2015 and references therein for a compilation of simulated and observed data) and only dependent on the mass. This is also visible in the stacked density profiles at different redshifts, shown in Fig. 5.5.

While the total mass of the selected halos is always  $M_{\text{tot}} \approx 1 \times 10^{12} M_{\odot}$ , the properties of the central galaxies can be very different. It is therefore interesting to investigate whether the outer stellar slopes  $\gamma_{\text{out}}$  are correlated with the properties of the individual galaxies in the center or not. We tested several properties, with the four most interesting results shown in Fig. 5.6. For all galaxies, we use the classification based on the circularity of the stars with an additional cut in the cold gas fraction, as described in Sec. 2.4.1. Disk galaxies are shown in blue, spheroidals in red, and galaxies which cannot be classified with this crude criterion are colored in green. The upper left panel of Fig. 5.6 shows the average age  $\langle z_* \rangle$  of the stellar content of the central galaxy. While we see no real correlation between the outer stellar slope  $\gamma_{\text{out}}$  and  $\langle z_* \rangle$  for the spheroidals and the unclassified galaxies, the disks have

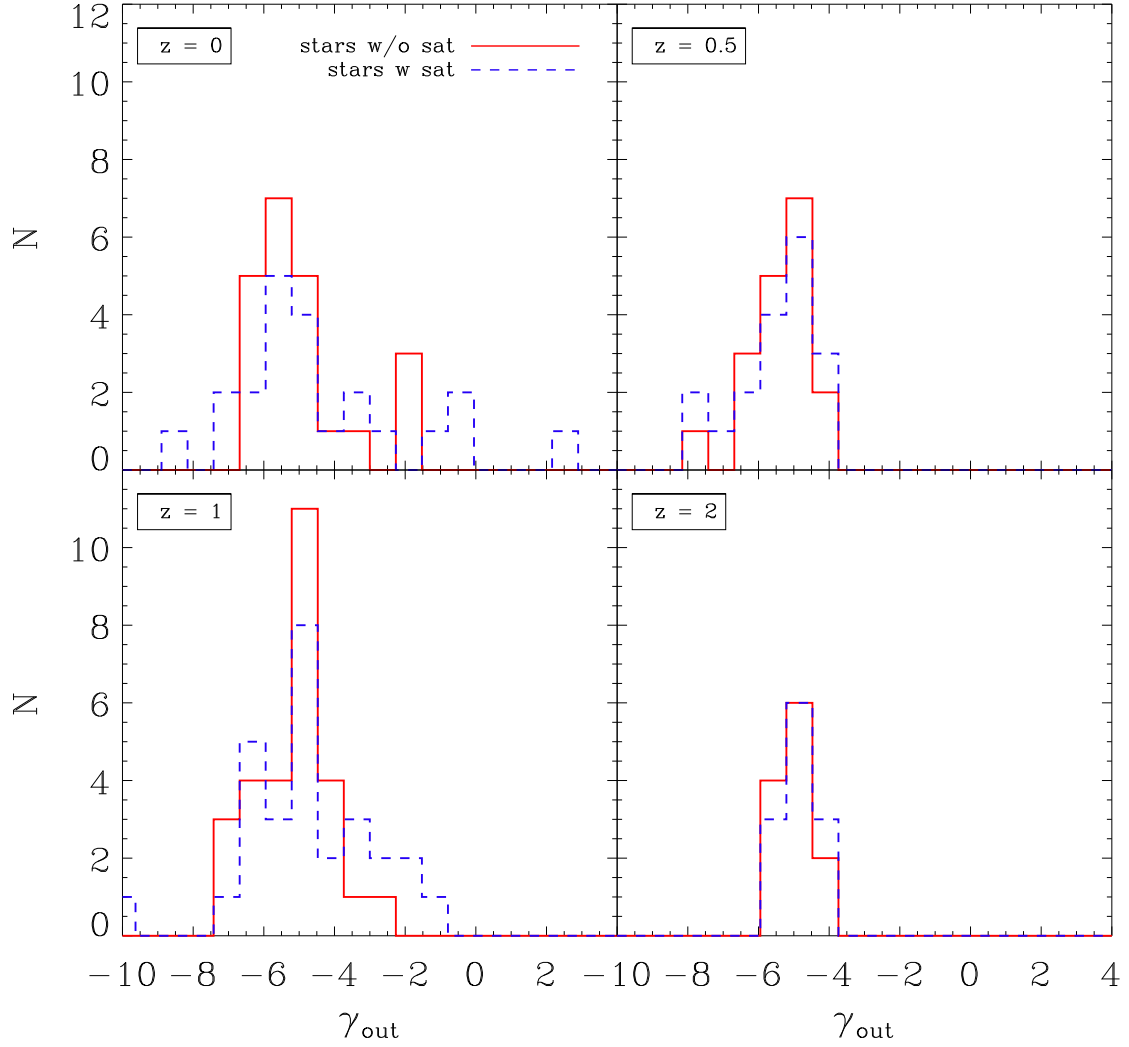


**Figure 5.4:** Histograms of the power-law slopes  $\gamma_{\text{out}}$  fitted to the stellar density at 40 kpc to 100 kpc of the individual halos with  $M_{\text{tot}} \approx 1 \times 10^{12} M_{\odot}$  from Box4 uhr both including satellites (blue dashed lines) and excluding the satellite structures (red solid lines). **Upper left panel:** for 24 halos at  $z = 0$ . **Upper right panel:** for 18 halos at  $z = 0.5$ . **Lower left panel:** for 28 halos at  $z = 1$ . **Lower right panel:** for 12 halos at  $z = 2$ .

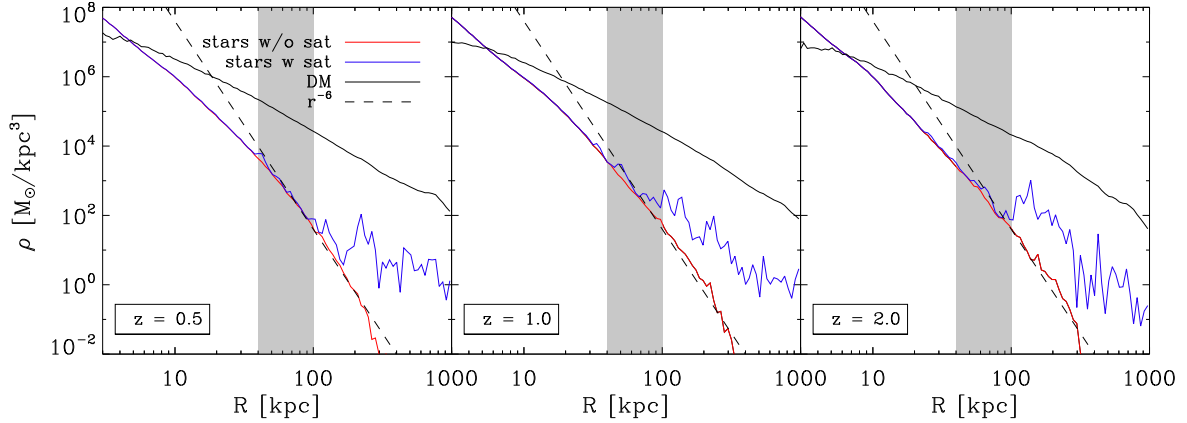


**Figure 5.5:** Same as the left panel of Fig. 5.3 but for  $z = 0.5$  (left panel, 18 halos),  $z = 1$  (middle panel, 28 halos) and  $z = 2$  (right panel, 12 halos).

a generally younger average stellar population, indicating ongoing star formation in good agreement with observations. However, the flatter slopes of  $-2 > \gamma_{\text{out}} > -3$  all belong to halos surrounding a disk galaxy, although the reverse is not true since there are also disk galaxies that exhibit steep slopes of  $-5 > \gamma_{\text{out}} > -6$ .

This is in agreement with the results shown in the lower left panel of Fig. 5.6, where the fraction of cold gas compared to the stellar mass is shown: All galaxies with large cold gas fractions are also disk galaxies, which proves that the cold gas properties are simulated well within the Magneticum Pathfinder simulation set due to better sub-grid models for the gas physics (e.g., Beck et al., 2015, see also Appendix A.8) and feedback models. The unclassified galaxies and the spheroidals show much lower fractions of cold gas, in agreement with the mean age of the stellar population as discussed in the previous paragraph. This is an improvement in comparison to previous simulations with GADGET and one of the reasons why the Magneticum Simulations produce both disk-like and spheroidal galaxies.

While the total mass of the halos is the same, the galaxies in their centers cover a much broader stellar mass range from about  $M_* \approx 1 \times 10^{10} M_\odot$  to nearly  $M_* \approx 1 \times 10^{11} M_\odot$ . However, there is no clear correlation between stellar mass and the stellar outer slope  $\gamma_{\text{out}}$ , as shown in the lower right panel of Fig. 5.6, with the exception of the three galaxies with the flattest slopes. These galaxies are all in the low mass range and have a disk-like morphology, while the disk galaxies with steeper slopes are more massive. This is due to the fact that those halos which host central galaxies of nearly two magnitudes lower stellar mass are highly disturbed by several gas-rich substructures inside the dark matter halo which are currently in the process of merging, causing stripping of the stars into the stellar halo of the central galaxy, and especially actively forming stars. One of these three galaxies is shown in the left panel of Fig. 5.1 as an example halo that contains multiple substructures. Here, in addition to the stripping, the star formation in the outer areas of the galaxy increases the stellar density in the outskirts and therefore flattens the slope. This is a very interesting result considering that the Andromeda galaxy also exhibits a flatter slope, and its outer halo similarly overlaps with the outer halo of M33, with numerous other substructures visible in the observed density distribution (see,

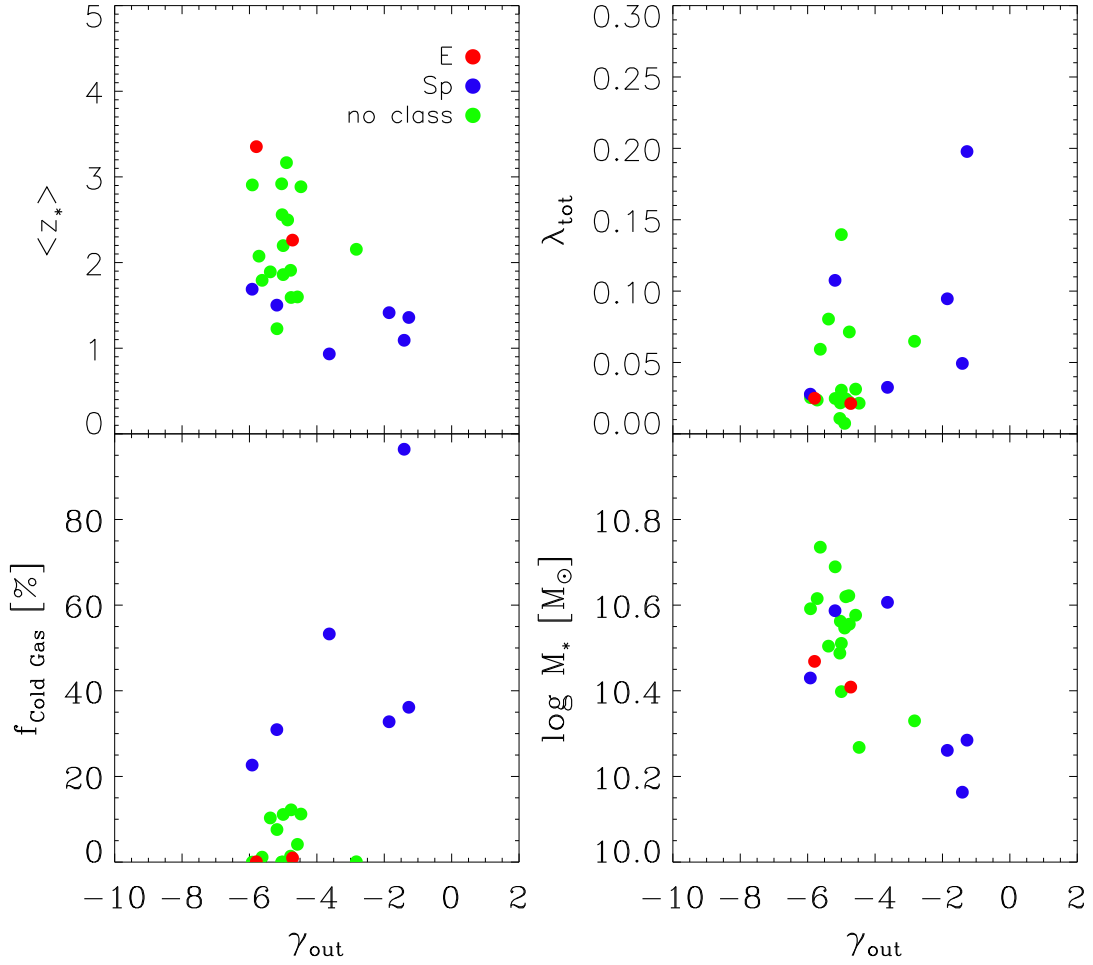


**Figure 5.6:** Properties of the 24 individual galaxies with  $M_{\text{tot}} \approx 1 \times 10^{12} M_{\odot}$  from Box4 uhr at  $z = 0$  versus the slope  $\gamma_{\text{out}}$  of the power-law fit to their stellar density at 40 kpc to 100 kpc. Filled circles show disks (blue), spheroidals (red) and unclassified galaxies (green) according to the morphological classification from Sec. 2.4.1. **Upper left panel:** Mean age  $\langle z_* \rangle$  of the stellar content of the central galaxy versus  $\gamma_{\text{out}}$ . **Upper right panel:** Spin parameter  $\lambda_{\text{tot}}$  for the total halo within the virial radius versus  $\gamma_{\text{out}}$ . **Lower left panel:** Fraction of cold gas with respect to the stellar mass of the central galaxy within the halfmass radius versus  $\gamma_{\text{out}}$ . **Lower right panel:** Stellar mass within  $10\%R_{\text{vir}}$  of the central galaxy versus  $\gamma_{\text{out}}$ .

e.g., Ibata et al. 2014). We note that the mean stellar density profile including the substructures shows a much flatter slope out to large radii, in contrast to the profile without substructures (left panel of Fig. 5.3, blue versus red curve), supporting the idea that the flat slope of the Andromeda stellar halo is related to its richness in substructures.

We conclude that the outer stellar slope  $\gamma_{\text{out}}$  is basically independent of the properties of the central galaxy. Nevertheless, we know that the spin parameter of the total halo is an important quantity (see Appendix A.4 for more details on the spin parameter and the angular momentum in Magenticum galaxies). However, as shown in the upper right panel of Fig. 5.6, there is no correlation between the total spin  $\lambda_{\text{tot}}$  and the outer stellar slope  $\gamma_{\text{out}}$ . This is in agreement with our previous conclusion that there is a universality to the properties of the outer stellar halo of all galaxies of Milky Way mass, similar to what is known about the density profiles of dark matter halos, independent of central galaxy properties or the global spin parameter as well as the redshift.

## 5.2.2 Including other Mass Ranges

From our previous analysis the question arises whether there might be a universality in the density profiles for all outer stellar halos independent of the total mass, or whether this universality is a feature purely of galaxies in the Milky Way mass range. The resolution of the Magenticum Simulation Box4 uhr is not sufficient to investigate this for halos of lower total mass, but the upper mass range can be tested. Therefore, we select all halos with a total mass around  $M_{\text{tot}} \approx 3 \times 10^{12} M_{\odot}$  and  $M_{\text{tot}} \approx 1 \times 10^{13} M_{\odot}$  at  $z = 0$ , resulting in a sample of 25 and 15 halos, respectively. The resulting stacked density profiles are shown in the left panels of Fig. 5.7, for the  $M_{\text{tot}} \approx 3 \times 10^{12} M_{\odot}$  mass sample in the upper and the  $M_{\text{tot}} \approx 1 \times 10^{13} M_{\odot}$  sample in the lower panel. We find that the general shapes of the density profiles for dark matter, stars, and stars including satellites show similar shapes as for the Milky Way mass halos, however, the profiles are shifted towards larger radii. Thus, a power law of  $\rho \propto r^{-6}$  is not a good fit to the stellar halo without satellites at a radius range of 40 kpc to 100 kpc anymore, but there is a radius range at larger radii where this power law is a good fit. This range is shifted to even larger radii for the most massive galaxy sample.

This is also reflected in the histograms of the outer stellar slopes, as shown in the right panels of Fig. 5.7. For halos with a total mass of  $M_{\text{tot}} \approx 3 \times 10^{12} M_{\odot}$ , the outer density slopes  $\gamma_{\text{out}}$  peak around  $-4$  to  $-5$ , while for the galaxies with a total mass of  $M_{\text{tot}} \approx 1 \times 10^{13} M_{\odot}$  this peak is clearly at  $\gamma_{\text{out}} \approx -4$  with a slight tendency towards flatter slopes. As for the Milky Way mass sample, both samples show a larger scatter in  $\gamma_{\text{out}}$  when the substructures are included. However, the scatter for the more massive galaxies is smaller due to the fact that the mass ratios between the satellites and the central galaxy are smaller than for Milky Way mass galaxies, even if the individual masses of the satellites are comparable. Halos of  $M_{\text{tot}} \approx 1 \times 10^{13} M_{\odot}$  usually host the most massive individual elliptical galaxies and are called fossil groups.

Interestingly, Rejkuba et al. (2014) recently reported an observation of the outer stellar density of the massive ( $M_{\text{tot}} \approx 9.2 \times 10^{12} M_{\odot}$  including substructures, Woodley 2006) elliptical galaxy NGC 5128 (Cen A) out to radii larger than 100 kpc. As shown in their Fig. 5, they find that the surface density between 40 kpc and 100 kpc can be well described by a power law with a slope of  $\Gamma_{\text{out}} \approx -2.6$ , which corresponds to a density slope of  $\gamma_{\text{out}} \approx -3.6$ . This agrees well with our result for the halos with  $M_{\text{tot}} \approx 1 \times 10^{13} M_{\odot}$ .

In summary, we find that the outer radial density profiles of stellar halos can be locally approximated by power laws. The slopes of those power-laws have a broad distribution, ranging from

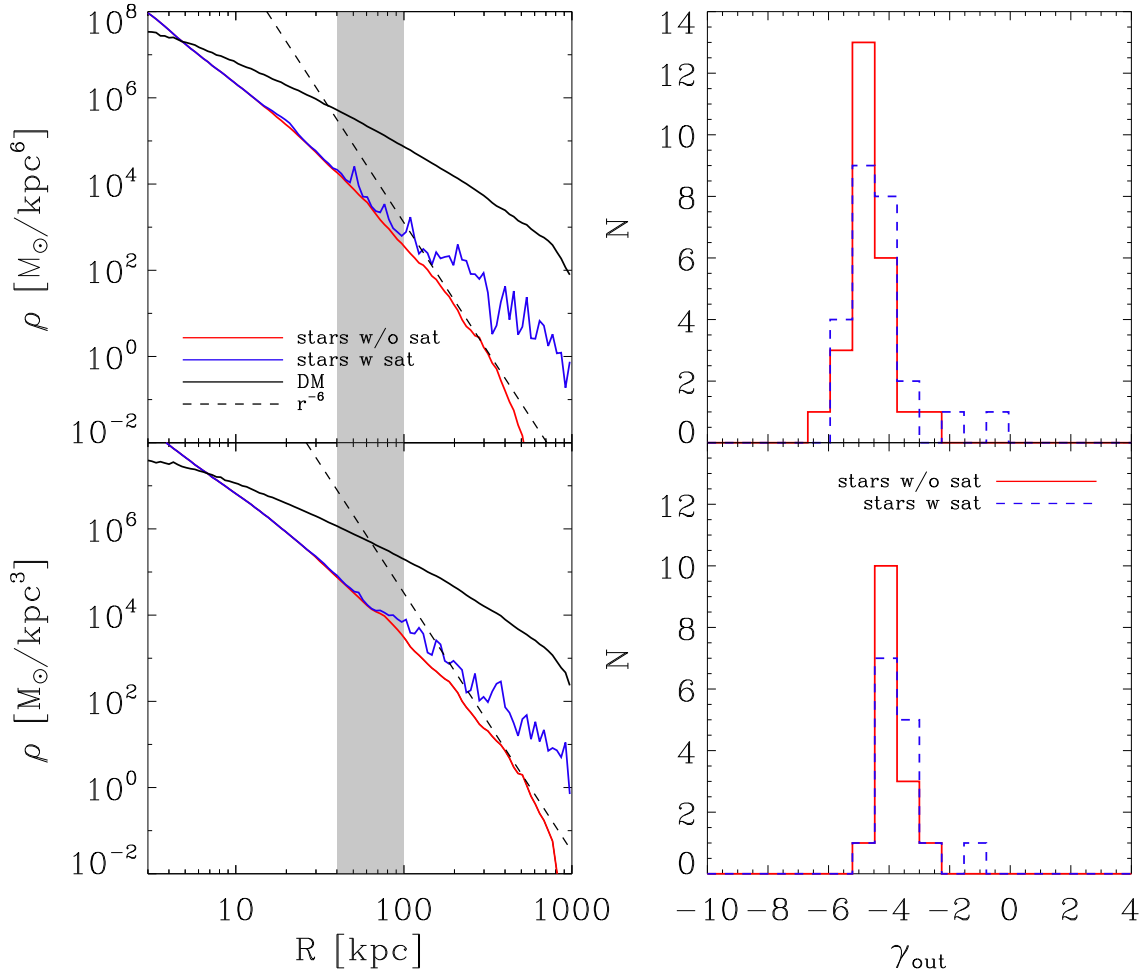


**Figure 5.7:** *Left panels:* Same as left panel of Fig. 5.3 but for halos with  $M_{\text{tot}} \approx 3 \times 10^{12} M_\odot$  (upper panel) and halos with  $M_{\text{tot}} \approx 1 \times 10^{13} M_\odot$  (lower panel) from Box4 uhr at  $z = 0$ . The stellar density profiles do not follow a  $\rho \propto r^{-6}$  law anymore at 40 kpc to 100 kpc, since they are flatter in this region, however, at larger radii for both mass ranges there is a radius range where the  $\rho \propto r^{-6}$  law fits the density slope well (dashed lines). *Right panel:* Histograms of the slopes  $\gamma_{\text{out}}$  of power-law fits at 40 kpc to 100 kpc for the individual halos within  $M_{\text{tot}} \approx 3 \times 10^{12} M_\odot$  (upper panel, 25 halos) and  $M_{\text{tot}} \approx 1 \times 10^{13} M_\odot$  (lower panel, 15 halos). Blue dashed lines show the distribution of  $\gamma_{\text{out}}$  for the stellar density profiles including substructures, red solid lines show  $\gamma_{\text{out}}$  for the stellar density profiles without substructures.

$-1 \gtrsim \gamma_{\text{out}} \gtrsim -9$ , which spans the range of slopes found in observations, even though that sample is small. This invites the question whether there might exist a universal density profile similar to the NFW profile found for dark matter halos, and whether the properties of this profile might be correlated with individual galaxy properties. In the following section we will investigate this in more detail.

### 5.3 A “Universal” Density Profile for the Stellar Halo of Galaxies: the Einasto Profile

Since Navarro et al. (1996, 1997) showed from numerical cosmological dark-matter-only simulations that the density profiles of dark matter halos are similar to each other with only little dependence of mass (see also Navarro et al. 2004), the broken power law that they introduced to describe the shape of those dark matter halos (see Sec. 1.4.2 for more details on the profile) has been used in a multitude of studies on the dark matter content of galaxies, from cluster environments down to isolated galaxies. The so called NFW-profile,

$$\rho_{\text{NFW}}(r) = \frac{\rho_0}{(r/r_s)(1 + r/r_s)^2}, \quad (5.1)$$

where  $r_s$  is the characteristic scale radius and  $\rho_0$  is the characteristic density (see also Eq. 1.30), increases monotonically towards the center as  $d \ln \rho / d \ln r \approx -1$  and is thus shallower than isothermal, while in the outskirts it follows  $d \ln \rho / d \ln r \approx -3$ . In simulated halos, however, the two “free” parameters of this profile,  $r_s$  and  $\rho_0$ , are not uncorrelated, in fact they reflect the accretion history of the individual halos, with more concentrated halos living in denser environments (e.g., Bullock et al., 2001). In other words, the earlier a halo starts to assemble, the higher its central density.

For stellar systems, there exists a number of density profiles in the literature that are used to analytically describe collisionless systems: the Hernquist profile (see Eq. 1.29) and the Jaffe profile (see Eq. 1.27), for example, are often used to describe the bulges of spiral galaxies and ellipticals, as they reproduce successfully the de Vaucouleur profile (see Eq. 1.17) when projected; the Plummer profile (see Eq. 1.26) is often used to describe the stellar distributions within globular clusters. Less accurate, however still used for its simplicity, is the density profile of an isothermal sphere (see Eq. 1.22).

As a first approach to find a universal description for the density profile of the stellar halos of galaxies, we fit these profiles to our stacked density profiles in the entire radius range, as shown in Fig. 5.8. For the dark matter density (upper left panel), we find that the NFW-profile (dash-dotted line) is a good approximation to our density profile, as expected, and the power-law (short-dashed black line) and the isothermal sphere (dotted black line) profiles fit parts of the profile but show strong deviations in the inner and outer parts. While the Jaffe profile (dash-dot-dot-dotted line) provides a rather good fit to the dark matter density, the Hernquist (long-dashed line) and the Plummer (solid thin black line) profiles both fail to fit the dark matter density profiles properly.

For the stellar halo density profiles with (upper right panel) and without (lower left panel) substructures, none of these standard profiles works. The closest approximation to the stellar halo density with substructures is a Jaffe profile, and the stellar halo without substructures is best represented by a Plummer profile, but both fits are crude and do not mirror the curved behaviour of the stellar halo. The crudeness of those fits originates from the fact that all models have two or even only one free parameter, and none of them has a continuous change of slope with radius from a flat inner profile to a very steep outer profile, as needed for a successful description of the stellar halo density profile.

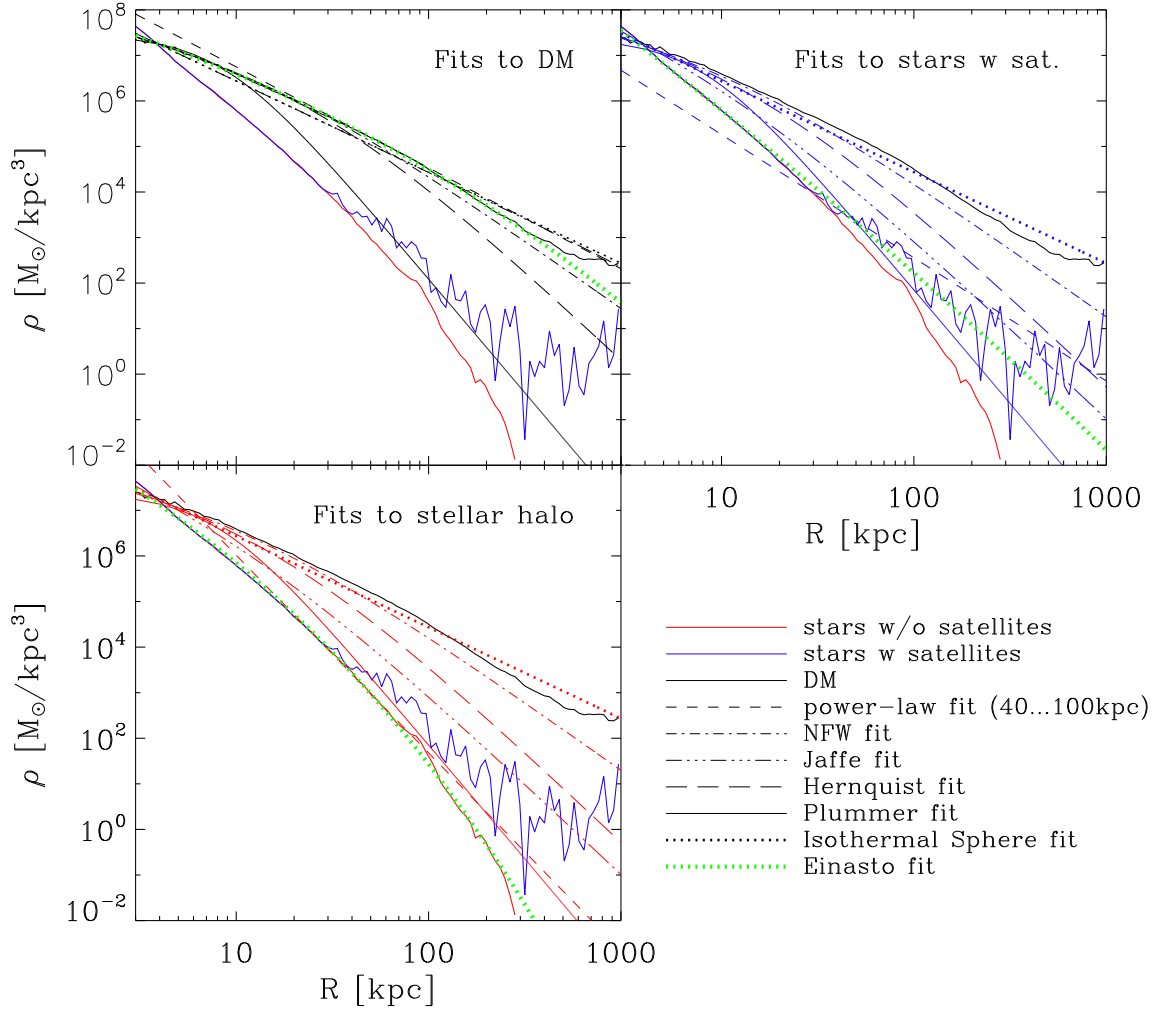


**Figure 5.8:** Fits of different density profiles to the stacked dark matter (black solid lines) and stellar density profiles including satellites (blue solid lines) and without satellites (red solid lines) for halos with  $M_{\text{tot}} \approx 1 \times 10^{12} M_{\odot}$  from Box4 uhr at  $z = 0$ : power-law fits at 40 kpc to 100 kpc radius (short-dashed lines), NFW profile fits (dash-dotted lines), Jaffe profile fits (dash-dot-dot-dotted lines), Hernquist profile fits (long-dashed lines), Plummer profile fits (thin solid lines), isothermal sphere density fits (dotted lines) and Einasto profile fits (green dotted lines). **Upper left panel:** Fits to the stacked dark matter density profile. **Upper right panel:** Fits to the stacked stellar density profile including satellites. **Lower panel:** Fits to the stacked stellar density profile without satellites.

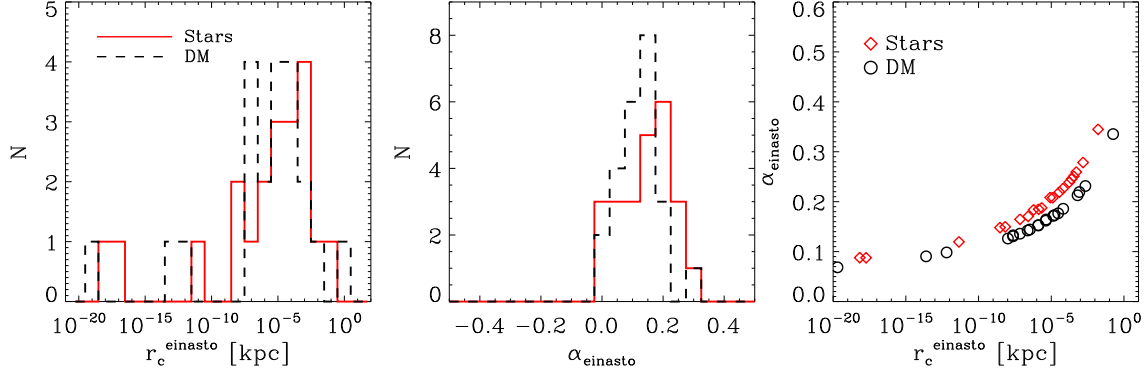


**Figure 5.9:** Parameters resulting from fits of the Einasto profile to the individual density profiles for the 24 halos with  $M_{\text{tot}} \approx 1 \times 10^{12} M_{\odot}$  from Box4 uhr for dark matter (black dashed line/open circles) and stars without substructures (red solid line/open diamonds) **Left panel:** Histogram of the scale radii  $r_c^{\text{Ein}}$ . **Middle panel:** Histogram of the slope  $\alpha_{\text{Ein}}$  of the fits of the Einasto profile. **Right panel:**  $\alpha_{\text{Ein}}$  versus  $r_c^{\text{Ein}}$ .

Thus, we need a profile with an additional free parameter to represent the curvature of the stellar halo density profile. One such profile is the Einasto profile, first introduced by Einasto (1965) and used to fit stellar profiles of nearby galaxies like the Milky Way and Andromeda (Einasto, 1974), which is characterised by its power-law logarithmic slope:

$$\rho(r) = \rho_{-2} \exp \left\{ -\frac{2}{\alpha_{\text{Ein}}} \left[ \left( \frac{r}{r_{-2}} \right)^{\alpha_{\text{Ein}}} - 1 \right] \right\}, \quad (5.2)$$

where  $\alpha_{\text{Ein}}$  controls the curvature,  $\rho_{-2}$  is the density and  $r_{-2}$  the radius at which  $\rho(r) \propto r^{-2}$ , see Retana-Montenegro et al. (2012) and Sec. 1.4.2 for more details. This profile can equivalently be written as

$$\rho_{\text{Ein}}(r) = \rho_0 \exp \left\{ -\left( \frac{r}{r_c^{\text{Ein}}} \right)^{\alpha_{\text{Ein}}} \right\}, \quad (5.3)$$

where  $\rho_0 = \rho_{-2}(r) e^{2/\alpha_{\text{Ein}}}$  is the central density and

$$r_c^{\text{Ein}} = \frac{r_{-2}^{\text{Ein}}}{\left( \frac{2}{\alpha_{\text{Ein}}} \right)^{1/\alpha_{\text{Ein}}}} \quad (5.4)$$

is the scale length (i.e., the radius at which the density has decreased to  $1/e$  of its central value), as shown by Retana-Montenegro et al. (2012).

As demonstrated in Fig. 5.8, the Einasto profile is a much more accurate fit to all three stacked density profiles (see green dotted lines), and even for the dark matter density it provides a better fit than the commonly used NFW profile. For the dark matter density it has already been shown that there are systematic deviations from the NFW profile in several different simulations, and that the Einasto profile is a much better fit (Navarro et al. (2004), Merritt et al. (2006), Gao et al. (2008), Stadel et al.

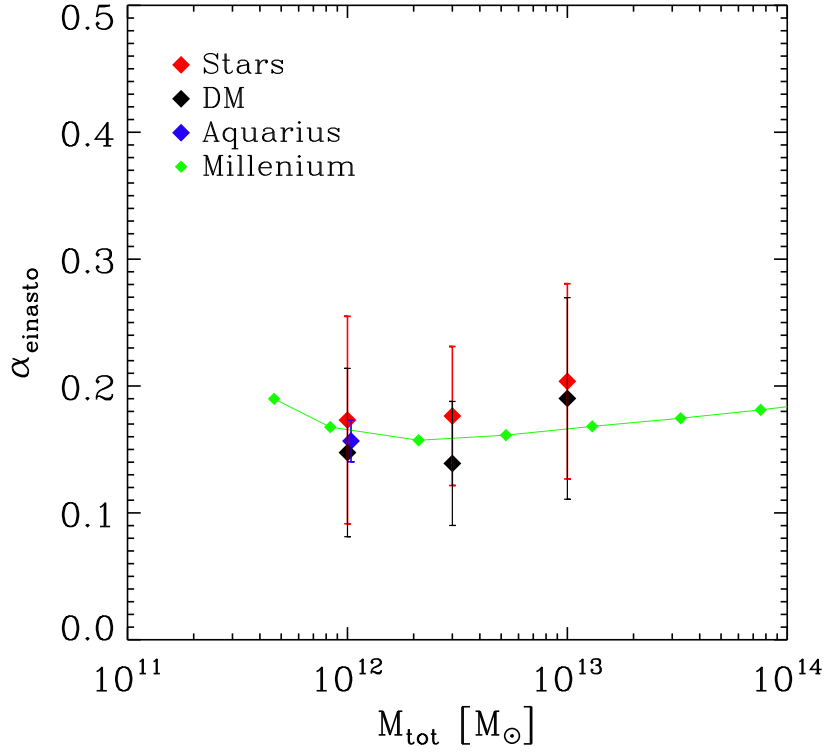


**Figure 5.10:** Mean value of the slope  $\alpha_{\text{Ein}}$  of the Einasto profile fits within the three halo mass ranges studied in this work versus the total mass  $M_{\text{tot}}$ , for the dark matter fits (black diamonds) and the stellar halo fits (red diamonds). Error bars show the standard deviations within our sample. For comparison, the mean values for the six dark-matter-only Aquarius halos from Navarro et al. (2010) are shown as blue diamond, and the values presented in Gao et al. (2008) for the Millenium simulation dark matter halos are shown as green diamonds (for  $z = 0$ ).

(2009), Navarro et al. (2010) & Klypin et al. (2014)). Navarro et al. 2004, 2010 showed that the NFW profile underestimates the dark matter density in the inner regions, and especially for massive halos it is far off the true profile (Klypin et al., 2014), causing a systematic bias in the concentration measurements (Gao et al., 2008). In contrast, the Einasto profile is more successful in describing the density profiles of the dark matter halos, even if the slope  $\alpha_{\text{Ein}}$  is kept at a constant average value, i.e., the profile is effectively reduced to two free parameters, see Navarro et al. (2010).

As mentioned by Merritt et al. (2006) and Retana-Montenegro et al. (2012), the Einasto profile mimics the Sersic profile. Thus, one might expect it to be a good fit to the stellar halo of galaxies as well. We fitted the dark matter and stellar halos for our galaxies of Milky Way mass ( $M_{\text{tot}} \approx 1 \times 10^{12} M_{\odot}$ ) with Einasto profiles, using the same logarithmic binning as before. The resulting distributions of the fitted parameters  $r_{\text{c}}^{\text{Ein}}$  and  $\alpha_{\text{Ein}}$  are shown in the left respective the middle panel of Fig. 5.9, while the right panel shows the correlation between both parameters.

We find that the values for both parameters are similar for the dark matter and the stellar halo, with slight trends to larger values for both parameters for the stellar component. The slope-parameter  $\alpha_{\text{Ein}}^*$

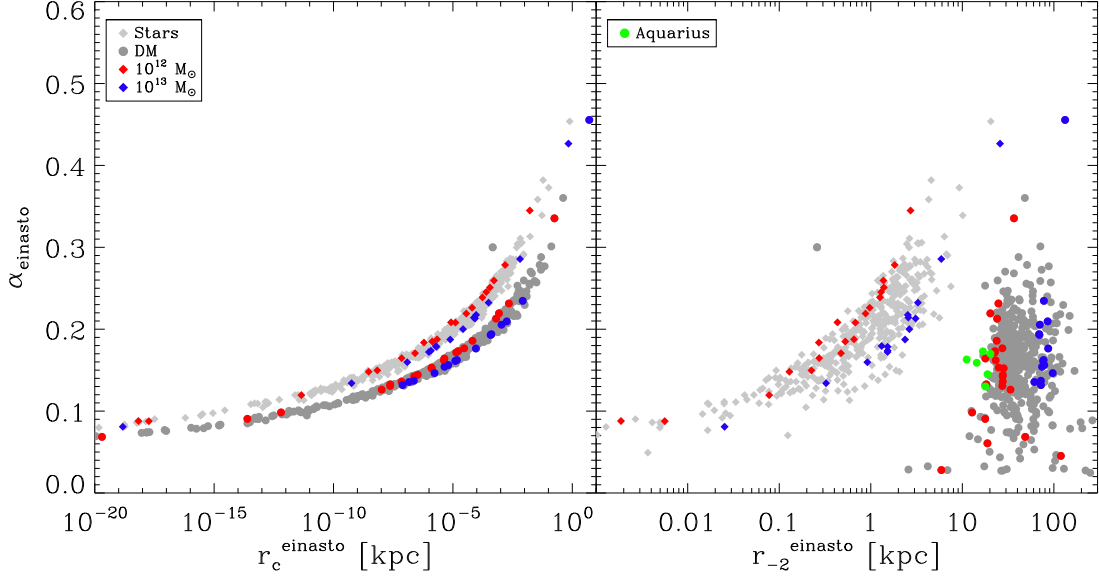


**Figure 5.11:** *Left panel:* Slope  $\alpha_{\text{Ein}}$  versus scale radius  $r_c^{\text{Ein}}$  of the Einasto profile fits to the DM (filled circles) and stellar (filled diamonds) density profiles of all 449 halos with total masses between  $M_{\text{tot}} \approx 1 \times 10^{12} M_{\odot}$  and  $M_{\text{tot}} \approx 1 \times 10^{14} M_{\odot}$  from Box4 uhr (DM dark grey, stars light grey). Red and blue symbols are the parameters for the fits to the halos with total mass of  $M_{\text{tot}} \approx 1 \times 10^{12} M_{\odot}$  and  $M_{\text{tot}} \approx 1 \times 10^{13} M_{\odot}$ , respectively. *Right panel:* Slope  $\alpha_{\text{Ein}}$  versus the radius  $r_{-2}^{\text{Ein}}$  where the fitted Einasto profile has the value of  $\rho_{-2}(r) \approx r^{-2}$ . Colors and symbols as in the left panel. Green circles show the values for the six dark matter Aquarius halos presented in Navarro et al. (2010).

peaks around  $\alpha_{\text{Ein}}^* \approx 0.20$ , with a mean value of  $\alpha_{\text{Ein}}^* = 0.17 \pm 0.08$ , and for the dark matter we find a peak at  $\alpha_{\text{Ein}}^{\text{DM}} \approx 0.15$  with a mean value of  $\alpha_{\text{Ein}}^{\text{DM}} = 0.15 \pm 0.07$ . Our values for the dark matter are in excellent agreement with the results presented by Navarro et al. (2010) for the Aquarius simulations (Springel et al., 2008), where they analysed the density profiles for six high-resolution dark matter re-simulations of Milky-Way like galaxies, and found values for the Einasto slope parameters of  $0.130 \pm 0.0200 < \alpha_{\text{Ein}}^{\text{DM}} < 0.173 \pm 0.0123$ .

Similar results for halos in the Milky-Way mass range were also found by Gao et al. (2008) who fitted Einasto profiles to dark matter halos selected from the Millenium Simulation (Springel et al., 2005c). They also found an interesting trend of the slope  $\alpha_{\text{Ein}}^{\text{DM}}$  with the total mass of a halo: for halos with larger masses, the slope  $\alpha_{\text{Ein}}^{\text{DM}}$  tends to be generally larger than for less massive halos. These systematic variations of the density profiles with the total halo mass had already been found by Merritt et al. (2006) from a study of six cluster mass halos and four galaxy mass halos, and have been recently confirmed by Klypin et al. (2014) for halos selected from the MultiDark simulations (Prada et al., 2012).

As shown in Fig. 5.10, we find a similar trend with mass if we include the halos from the other two mass ranges studied in the previous section, namely  $M_{\text{tot}} \approx 3 \times 10^{12} M_{\odot}$  and  $M_{\text{tot}} \approx 1 \times 10^{13} M_{\odot}$ , see the black diamonds. Error bars show the standard deviations within our sample. In addition, we included the mean value for the six Aquarius halos (blue diamond) and the values from the Millenium

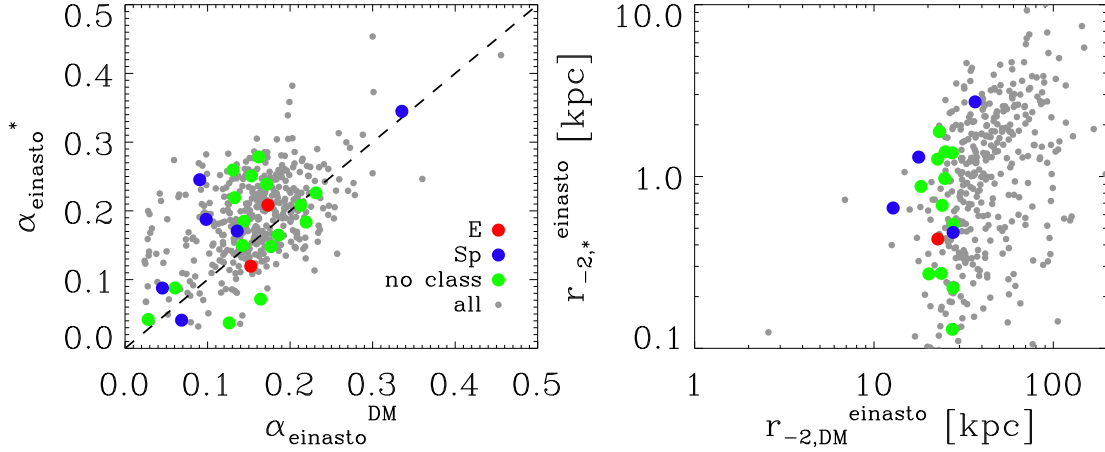


**Figure 5.12:** *Left panel:* Slopes  $\alpha_{\text{Ein}}^*$  from Einasto profile fits to the stellar halos versus those from fits to the dark matter halos,  $\alpha_{\text{Ein}}^{\text{DM}}$ . Halos in the Milky Way mass range are shown as large symbols, with colors according to their morphology as in Fig. 5.6. The full sample of Magneticum halos with more than  $M_{\text{tot}} \approx 1 \times 10^{12} M_{\odot}$  is shown as filled small grey circles. The dashed line marks the 1:1 correlation. *Right panel:* Same as the left panel but for the radii  $r_{-2}^{\text{Ein}}$ .

halos at  $z = 0$  as presented in the left panel of Fig. 2 of Gao et al. (2008) (green diamonds). The dark matter halos from Magneticum agree very well with the previous results. In addition, we show the mean values of  $\alpha_{\text{Ein}}^*$  for our three halo mass ranges as red diamonds. We clearly see that for all three mass ranges  $\alpha_{\text{Ein}}^*$  is larger than  $\alpha_{\text{Ein}}^{\text{DM}}$ , indicating that the stellar halo profiles are curved more strongly than their dark matter counterparts.

While the slope parameters of the Einasto profile have been discussed in the literature in some detail (at least for dark matter halos due to the lack of sufficiently large simulations including baryons with high enough resolution to study the stellar density profiles), less attention has been given to the scale radii. As already shown in the right panel of Fig. 5.9 for our halos in the Milky Way mass range, there is a correlation between the scale radius  $r_c^{\text{Ein}}$  and the slope  $\alpha_{\text{Ein}}$  for both dark matter and stellar halos, i.e., for larger values of  $\alpha_{\text{Ein}}$  the scale radius is larger. The correlation is the same for dark matter and stars, but the values for  $\alpha_{\text{Ein}}$  are larger for the stars, as discussed before, while the values for the scale radii cover nearly the same range for both components.

This behaviour can also be seen in the left panel of Fig. 5.11, where we show  $\alpha_{\text{Ein}}$  and  $r_c^{\text{Ein}}$  for all halos selected from Magneticum with a total mass  $M_{\text{tot}} > 1 \times 10^{12} M_{\odot}$  as light grey diamonds (stellar halo fits) and dark grey circles (dark matter halo fits). The halos with a total mass of  $M_{\text{tot}} \approx 1 \times 10^{12} M_{\odot}$  are shown in red, the halos with a total mass of  $M_{\text{tot}} \approx 1 \times 10^{13} M_{\odot}$  are shown in blue. We find a clear trend with the total halo mass in the correlation of the two parameters as well, with more massive stellar and dark matter halos having smaller values of  $\alpha_{\text{Ein}}$  at a given  $r_c^{\text{Ein}}$  than their less massive counterparts.

As the scale radii of the Einasto profiles are far inside the centers of the galaxies and thus not clearly part of the visible halos, it is more useful for the understanding of its meaning to use Eq. 5.4 and calculate  $r_{-2}^{\text{Ein}}$ , the radius at which the fitted Einasto profile has a slope of  $\rho(r) \propto r^{-2}$ . The result

is shown in the right panel of Fig. 5.11, using the same colors as before. While the correlation was rather narrow for slope versus scale radius, the scatter in  $r_{-2}^{\text{Ein}}$  for both dark matter and stellar halo is much larger. But despite the larger scatter, we still see that there is an obvious trend for stellar halos with larger  $r_{-2}^{\text{Ein}}$  to have larger slopes, and for less massive halos to have smaller  $r_{-2}^{\text{Ein}}$ . This implies that the less massive galaxies have less extended stellar halos, and more compact stellar halos have generally smaller slopes.

While we see a trend with halo mass for the dark matter, in that more massive halos have larger  $r_{-2}^{\text{Ein}}$ , there is no clear trend with the slope. For comparison, we again included the values of the six Aquarius halos from Navarro et al. (2010), and we again find a good agreement with our results. Thus we conclude that for the dark matter halos the halo mass is the most important quantity in determining the radial extension of the halo, while the whole range of curvatures is covered. For the stars, however, there must be an additional mechanism that causes more compact halos to have smaller  $\alpha_{\text{Ein}}$  and thus be less curved, and we suspect that the gas content during accretion might be the critical ingredient, since gas dissipates energy and thus can reach the galaxy centers, causing star formation there, but thereby “starving” the outer halos compared to the dark matter halos. In this picture, only dry mergers would cause the stellar halo to grow like the dark matter halo, while wet merging would cause the inner core of the galaxy to grow in situ, while growing the stellar halo only slightly.

To understand the correlation between the shape of the density profiles of stellar and dark matter halo, we investigate the correlations between  $\alpha_{\text{Ein}}^{\text{DM}}$  and  $\alpha_{\text{Ein}}^*$ , and  $r_{-2,\text{DM}}^{\text{Ein}}$  and  $r_{-2,*}^{\text{Ein}}$ . As expected, there is no clear correlation between  $r_{-2,\text{DM}}^{\text{Ein}}$  and  $r_{-2,*}^{\text{Ein}}$  (right panel of Fig. 5.12). Within a given total mass range,  $r_{-2,\text{DM}}^{\text{Ein}}$  is approximately constant independent of  $r_{-2,*}^{\text{Ein}}$ , which can clearly be seen from the colored round symbols in that panel which mark the galaxies with  $M_{\text{tot}} \approx 1 \times 10^{12} M_{\odot}$ . We also do not find any correlation in  $r_{-2,\text{DM}}^{\text{Ein}}$  and  $r_{-2,*}^{\text{Ein}}$  depending on the galaxy morphology. The only slight trend can be found for the dark matter halos, where  $r_{-2,\text{DM}}^{\text{Ein}}$  correlates with the total mass of the halo: the small grey circles show all halos with  $M_{\text{tot}} > 1 \times 10^{12} M_{\odot}$ , and since most of the grey symbols are at larger values of  $r_{-2,\text{DM}}^{\text{Ein}}$  than the large colored symbols that mark the Milky-Way mass halos, this indicates that  $r_{-2,\text{DM}}^{\text{Ein}}$  increases slightly with total halo mass.

For the slopes of the Einasto profiles, we see a different behaviour, shown in the left panel of Fig. 5.12: stellar halos with a smaller slope seem to reside in dark matter halos with relatively small slopes as well, while large stellar slopes usually coexist with larger dark matter slopes. This indicates that there is, indeed, a correlation between the shapes of both halos. While there is a slight trend for stellar halos to have larger slope values than their dark matter counterparts, there are also several halos which lie on the 1:1 relation for the slope parameters. As indicated by the large filled circles, we do not find any correlation between the mass or morphology of a galaxy and its correlation of slopes  $\alpha_{\text{Ein}}^{\text{DM}}$  and  $\alpha_{\text{Ein}}^*$ .

Since we found no other correlations than with total halo mass for the Einasto profile parameters of the dark matter halos, whereas those of the stellar halos do appear correlated, we checked whether  $\alpha_{\text{Ein}}^*$  and  $r_{-2,*}^{\text{Ein}}$  correlate with other properties of the central galaxies as well. We tested the outer power-law slope  $\gamma_{\text{out}}$ , the stellar mass  $M_*$  and the mean age  $\langle z_* \rangle$  for our sample of galaxies with  $M_{\text{tot}} \approx 1 \times 10^{12} M_{\odot}$ . The results are shown in Fig. 5.13. For the outer slopes we find a slight correlation for galaxies with steeper outer slopes to also have larger Einasto slopes and larger  $r_{-2,*}^{\text{Ein}}$ , however, there is no obvious trend with morphology (upper panels). This agrees well with our conclusion that the galaxies with the larger Einasto slopes are more compact and thus most likely have had a smaller amount of recent merging.

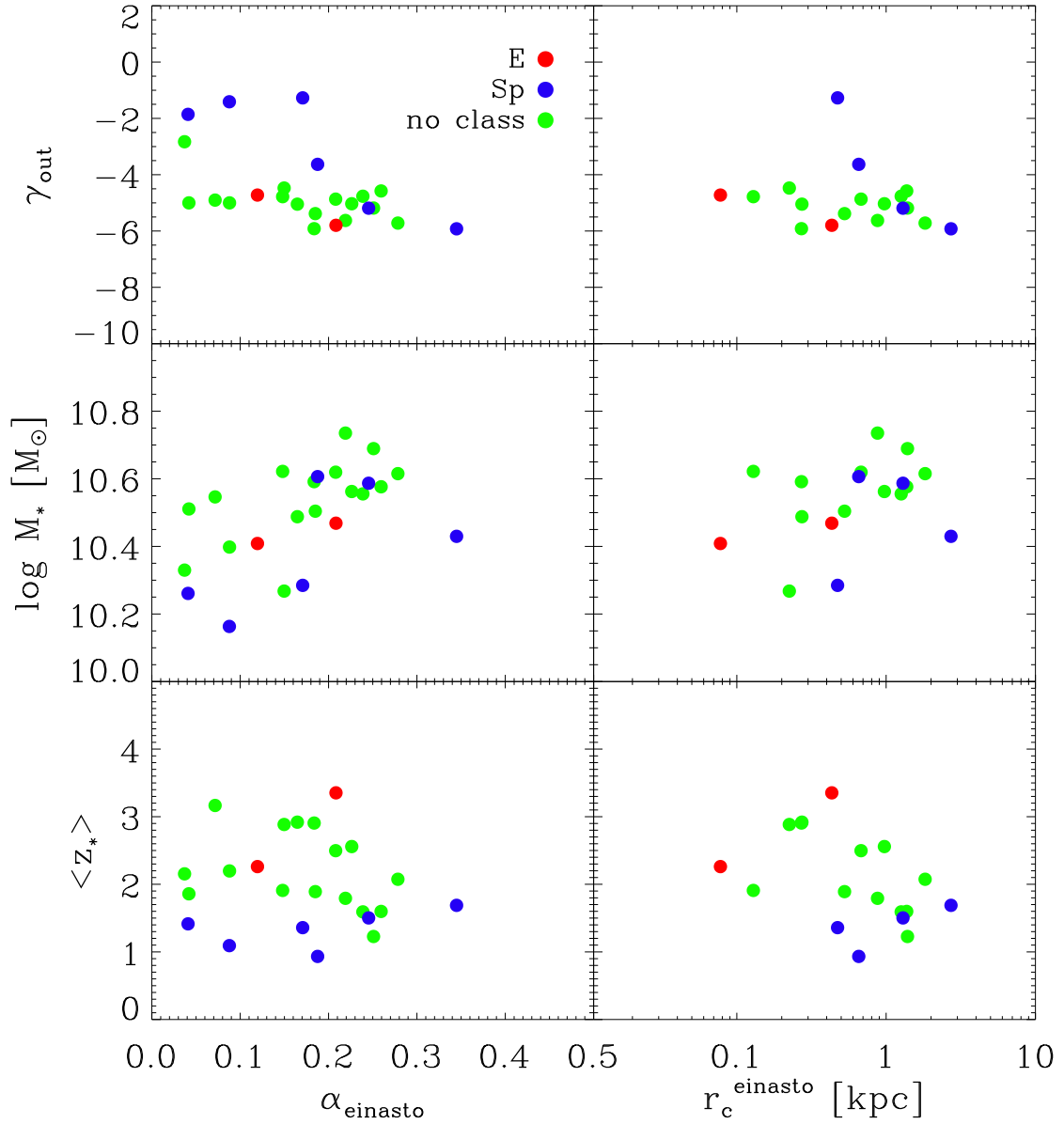


**Figure 5.13:** Different Galaxy properties versus the slopes  $\alpha_{\text{Ein}}^*$  (left panels) and radii  $r_{\text{c}}^{\text{Ein}}$  (right panels) of the Einasto profile fits for the 24 individual halos with  $M_{\text{tot}} \approx 1 \times 10^{12} M_{\odot}$  from Box4 uhr: **Upper panels:** versus the slopes  $\gamma_{\text{out}}$  of the power-law fits. **Middle panels:** Versus the stellar mass  $M_*$  of the Galaxies. **Lower panels:** Versus the mean age of the stellar population  $\langle z_* \rangle$ . Colors show the morphological classification according to Sec. 2.4.1 with disks, spheroidals and unclassified galaxies in blue, red and green, respectively.

For the stellar mass, we also find a slight trend for more massive galaxies to have larger Einasto parameters, but this trend is very weak and could be a bias due to the low number of studied galaxies within this mass range. We also find that there is no trend at all of the mean age  $\langle z_* \rangle$  with either of the Einasto parameters, see lower panels of Fig. 5.13.

## 5.4 Summary and Discussion

We studied the stellar halos of galaxies with total masses larger than  $M_{\text{tot}} \approx 1 \times 10^{12} M_{\odot}$  selected from the Magneticum Pathfinder Simulations. We used halos from two different simulation boxes: from Box3 hr, a larger box with medium resolution, we selected 458 halos with total masses of  $M_{\text{tot}} \approx 1 \times 10^{12} M_{\odot}$  to investigate the properties of the stacked outer halo since the resolution is not high enough to study individual outer stellar halos. For the detailed analysis we used Box4 uhr, a small box with much higher resolution. We chose halos within three different mass bins, namely 24 halos with  $M_{\text{tot}} \approx 1 \times 10^{12} M_{\odot}$ , 25 halos with  $M_{\text{tot}} \approx 3 \times 10^{12} M_{\odot}$  and 15 halos with  $M_{\text{tot}} \approx 1 \times 10^{13} M_{\odot}$ .

In the first part we fitted power-laws to the stacked and individual stellar halos of our samples of galaxies with  $M_{\text{tot}} \approx 1 \times 10^{12} M_{\odot}$ , in a radius range of 40 kpc to 100 kpc. This radius range was chosen following Deason et al. (2014), who measured the power-law slope of the Milky Way in this radius range, and the study by Ibata et al. (2014) from the PANDAS survey, who also cover this radius range with their measurement of the slope of the stellar halo of the Andromeda galaxy. The mass range was chosen to reflect the total mass range of our Milky Way galaxy and Andromeda.

We find that the power-law slopes  $\gamma_{\text{out}}$  of our stacked profiles for both simulation boxes converge on a value of  $-5 > \gamma_{\text{out}} > -6$  in the radius range of 40 kpc to 100 kpc. In agreement with simulations by Bullock & Johnston (2005) and Pillepich et al. (2014) we find that the density profiles of the stellar outer halos are always steeper than the corresponding dark matter halos. For the individual galaxies, the slopes  $\gamma_{\text{out}}$  of our 24 galaxies scatter around  $\gamma_{\text{out}} \approx -5$ , with the values for the Milky Way ( $\gamma_{\text{out}}^{\text{MW}} \approx -6$  or steeper at larger radii, Deason et al. 2014) and Andromeda ( $\gamma_{\text{out}}^{\text{And}} \approx -3$ , no steepening until at least 300 kpc, Ibata et al. 2014) both within the possible parameter space, however, the value found for Andromeda is at the upper range of slopes found in our simulations. The presence of satellite galaxies and other substructures like stellar streams causes a larger scatter in the slope distribution when included, however, for some halos with only small substructures there is no difference in the resulting slope  $\gamma_{\text{out}}$ . This agrees with the result from Deason et al. (2014) that there is no difference between the outer power-law slope of the Milky Way including and excluding the Milky Way satellites, respectively, and also with the observation by Ibata et al. (2014) for Andromeda, who find no steepening of the stellar halo slope with radius, but also find a flatter slope since Andromeda has multiple shells, streams and satellites.

We broadened our study to larger redshifts and studied the stacked and individual power-law slopes at a radius range of 40 kpc to 100 kpc for 18 galaxies at  $z = 0.5$ , 28 galaxies at  $z = 1$  and 12 galaxies at  $z = 2$ , all with  $M_{\text{tot}} \approx 1 \times 10^{12} M_{\odot}$  corresponding to the Milky Way mass at present day. Although our number statistics are still small, we conclusively show that profiles and slope distributions behave similarly to those found at  $z = 0$ , leading us to the conclusion that there is some universal process that builds up the outer stellar halos of Milky Way mass galaxies independent of the redshift. The same is true for halos at the other two mass ranges at  $z = 0$ . Their stacked profile shows a similar behaviour to what we found for Milky Way mass galaxies, albeit shifted to larger radii. Thus, at the tested radius range the power-law slopes are systematically flatter, however there is always a

radius range where a power-law with a slope of  $-6$  is a good fit to the density profile.

Within the Milky Way mass range, we find a correlation of the outer stellar slope  $\gamma_{\text{out}}$  with the stellar mass of the central galaxy, in that less massive galaxies have flatter slopes. This is due to the fact that there are more substructures within the halo, which have been stripped beyond the threshold where our subhalo finder can subtract them. This is the same effect observed for Andromeda, even though it is more massive than the Milky Way, but its multitude of streams cannot easily be subtracted from the global stellar halo. There is also a correlation of the stellar slope  $\gamma_{\text{out}}$  with the mean age of the stellar population of the central galaxy: galaxies with younger stellar populations have flatter slopes than galaxies with older stellar populations. This originates from the same phenomenon, as younger systems had more recent merging activity, causing starbursts and streams. In the same picture, a flatter slope indicates that the galaxy has more cold gas, with extended gas disks, bridges between merging galaxies and ongoing star formation. However, the opposite is not true: there are equally many gas rich systems with steep slopes (e.g., the Milky Way). We do not find any correlation with the spin parameter at all.

Our results agree with the results from the Illustris simulation (Vogelsberger et al., 2014; Pillepich et al., 2014) in that galaxies with larger stellar masses within a certain total mass range have steeper slopes than their lighter counterparts. Also, both studies see a tendency for halos with larger total mass to host galaxies with flatter slopes, however our results indicate that this is due to the fact that the stellar halos simply extend to larger radii and thus the probed range is relatively farther inside. We disagree with Pillepich et al. (2014) that there is a clear correlation for disk-like, younger galaxies to have steeper stellar halos. On the contrary, we find the opposite trend within a total mass range. The origin of these differences remains to be investigated in detail and could also originate from the small sample of objects included in our detailed study.

In the second part we attempt to understand the nature of the “universality” of the density profile of the outer stellar halos. As discussed before, a power-law is an approximation of the compactness of the stellar halo, but not a sufficient description of the density profile since its shape is more curved. We tested different density profiles from the literature and find that none of the classical double power-law profiles can fit the stellar outer halo. However, the Einasto profile, which is an exponential law, turns out to be a very good fit to both the dark matter and the stellar halos. For the dark matter halos, this has been shown before in several studies (for example Gao et al. (2008) & Navarro et al. (2010)), and our results are in good agreement their results.

For the stellar halo, this has never been tested before due to the lack of sufficiently large and well resolved samples of simulated galaxies from hydrodynamical cosmological simulations. We find that an Einasto profile is a good description of the density profiles of the outer stellar halos of all galaxies in our sample. Although the Einasto profile contains one more free parameter than the double power law profiles, the parameter fits to the profiles from the simulations show a strong correlation between the scale radius and the curvature parameter of the Einasto profile, indicating that these two parameters effectively represent only one free parameter, which is in fact dependent only on the total mass. While the Einasto profile is a good fit to both stellar and dark matter halo, the individual parameters between stellar and dark matter halo appear mostly uncorrelated. For a given total mass range, we find a slight correlation between the Einasto slope parameter and the stellar mass of the galaxy as well as the slope of the power-law fit to the outer stellar halo, indicating that more compact stellar halos have a larger curvature of the profile and are slightly more massive.

While we find that the Einasto profile is an excellent description for stellar and dark matter halos, there are a few critical issues about the Einasto profile that are problematic in the interpretation: As

discussed by Klypin et al. (2014),  $R_{\text{vir}}/r_{-2}$  of the Einasto profile cannot be used as measurement for the concentration, as it can be done for other profiles like the NFW, because for the same value of  $R_{\text{vir}}/r_{-2}$ , halos with a larger slope  $\alpha_{\text{Ein}}$  are more concentrated than halos with the same  $R_{\text{vir}}/r_{-2}$  ratio but smaller slopes (see Fig. 1.11). Thus, measuring the concentration of a stellar halo is less straightforward than for the double power-law profiles. Also, Diemer & Kravtsov (2014) find from their dark matter simulations that the density profiles deviate from Einasto profiles, since massive and strongly accreting halos have much steeper profiles than expected.

We conclude that there exists a universal profile for the stellar halo density, and it can be well described by an Einasto profile. More compact halos have flatter Einasto slopes as well as steeper outer power-law slopes, usually are a bit more massive and their  $r_{-2}$  is shifted to larger radii. We suggest that this indicates that those galaxies have only small substructures within their halos and no massive recent merging. However, the implications of the Einasto-profile fits on the galaxy properties, their mass accretion histories and especially their evolution with redshift need to be investigated in a further study, preferably with an even larger set of galaxies at this high resolution.

## Chapter 6

# Tracing the Outer Halo

### 6.1 Introduction

As discussed in the previous chapter, tracers are needed to probe the dynamical properties of the faint outskirts of galaxies where the stellar populations are so thin that the light is too faint to be measured directly (without using very long exposures, which are extremely costly). Those tracers must be either very bright or dominant at a certain wavelength to be detectable even at distances of several Mpc, and they have to be present in a sufficient amount around the galaxies. Supernovae, for example, would be bright enough to be easily detectable, but they are far too rare to be used as tracers for the extended outskirts of galaxies.

Currently, two different kinds of tracers are used: Planetary Nebulae (PNe) and Globular Clusters (GCs). Both are bright enough to be detected with ground-based telescopes in the nearby universe: GCs shine as relatively bright objects due to their numerous stars concentrated in a small volume of space, thus enhancing the observed luminosity significantly even if the individual stars of the GCs are not very luminous themselves since GCs are very old and their stellar content is thus very old as well. PNe, however, even if they are not very bright by themselves, emit strongly in the oxygen [O III] emission line ( $\lambda = 5007 \text{ \AA}$ ) and thus they are easily detectable out to large distances (see, for example, Méndez et al. 2001; Coccato et al. 2009; Shih & Méndez 2010 and Master's Thesis by Schauer 2014a).

Studies of dynamical properties of galaxies use these objects as tracer populations for all kinds of galaxies, especially to probe the faint outskirts of early-type galaxies (e.g., for PNe: Méndez et al., 2001; Romanowsky et al., 2003; Napolitano et al., 2001; Coccato et al., 2009; Napolitano et al., 2009; Méndez et al., 2009; Napolitano et al., 2011; Cortesi et al., 2013; and for GCs: Peng et al., 2006; Romanowsky et al., 2009; Pota et al., 2013; Arnold et al., 2014), where the tracers are easier to observe since no dust or star formation obscures them (Blom et al., 2012a). However, when using tracers to estimate the dynamical properties of a distant population of stars, several questions arise that are crucial to the interpretation of the observed results: how many tracers are needed to accurately estimate the true underlying population? What part of the underlying distributions do the different types of tracers mirror? And which features can be detected with the sensitivity available?

In this chapter, we will address those questions. In Sec. 6.2 we use a final spheroidal from our high-resolution binary merger simulations and an initial spiral galaxy for a statistical analysis of the amount of tracers needed to accurately represent velocity and density distributions of the outskirts of galaxies to measure scale heights and density slopes. To answer the question which parts of the

galaxies are traced by the different kinds of tracer populations we use spheroidal galaxies from the Magneticum Pathfinder Simulations Box4 uhr in Sec. 6.3. We will discuss velocity features that can be detected by observations of the tracer populations and the possible implications of those features for the formation history of a galaxy in Sec. 6.4. Finally, we conclude this chapter with a short summary and discussion in Sec. 6.5.

## 6.2 Number Statistics

Tracer populations are the best source of information about the dynamical properties in the outskirts of galaxies, but their number is usually limited. While in some cases there are hundreds of confirmed tracers (for example, for NGC 5128, also known as Cen A, 1267 PNe have been detected (Walsh et al., 2015), and for M87 Peng et al. (2009) studied a sample of 2250 GCs), in most cases there are only about 100 PNe or GCs to estimate the dynamical properties, and sometimes the number of confirmed tracers can be as low as 20 objects. Therefore, it is legitimate to ask how well the dynamical properties are represented by the tracers, and how much this depends on the number of tracers available.

In a first approach to this question, we use a simulated spiral galaxy from our initial conditions for binary spiral–spiral mergers (see Sec. 2.2.1 for more details), in an edge-on view, and randomly draw stars from the full sample of stars to use as “tracer” populations. Since we want to test the impact of the number of tracers on the accuracy of the predicted properties, we use five different numbers of randomly drawn tracers:  $N = 20$ ,  $N = 50$ ,  $N = 100$ ,  $N = 500$  and  $N = 1000$ . For each number of tracers we repeat the experiment of randomly drawing stars from the full stellar sample of the simulation 100 times, thus estimating each quantity 100 times with the same amount of tracer stars. The stars are drawn from within a sphere of radius 20 kpc around the center of the spiral galaxy, and all stars have the same probability to be selected. However, we mask the central disk plane of the galaxy, i.e., 0.4 kpc above or below the disk plane, since in this region the stellar brightness is so large that neither PNe nor GCs would be detectable.

Two examples for this experiment with  $N = 100$  are shown in the left panels of Fig. 6.1. These two examples clearly show that the random drawing can lead to very different spatial distributions of the tracers. While in the case shown in the upper panel there are several tracers in the stellar halo around the galaxy, in the case shown in the lower panel there are no tracers at all detected within the halo. Since our spiral galaxy is an idealised set-up of such a galaxy and thus does not have any streams or substructures around it, the clustering of the tracers is by no means a result of a real substructure but purely an effect of the random selection of stars. However, the lower case shows a clear clustering of three tracers slightly above the plane, while in the upper case there are several small groupings of tracers that could be interpreted as detection of shells or substructures. This demonstrates how difficult the interpretation of clustering of tracers or the absence of tracers can be. In addition, we also had one case in our sample of 100 repetitions of random drawings of 100 tracers where there were several tracers in the halo above the plane, but none in the halo below the plane.

In the rare cases of spiral galaxies that can be observed exactly edge-on, for example NGC 891 (Shih & Méndez, 2010), there have been studies of the dynamics using PNe as tracer populations. NGC 891 is such a case where the detected PNe are distributed very asymmetrically, which has been interpreted as possible markers of streams. However, confirmation by stellar light detection is still missing. Another example of such an edge-on spiral is NGC 4244 (private communication with R. Méndez, see also Master’s Thesis of A. Schauer (2014a)), where all but 2 PNe are detected close

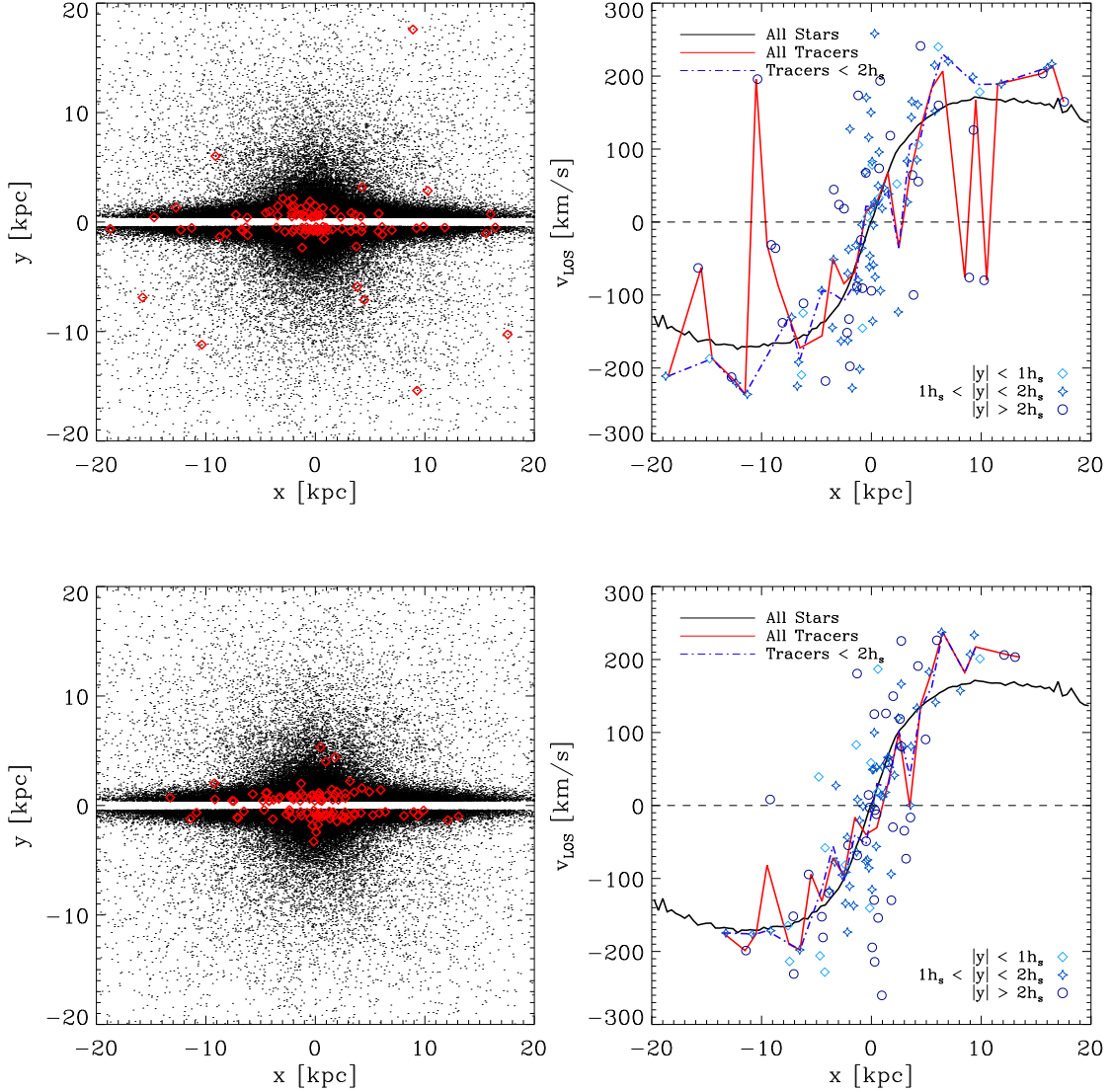


**Figure 6.1:** Two examples for the Line-of-Sight (LOS) velocity profiles measured by a random selection of 100 tracer stars from a simulation of a spiral galaxy. **Upper left panel:** Edge-on view on the simulated spiral galaxy, with stars marked as black dots. The central disk lane is masked due to the fact that observers would not be able to detect tracers in this region because of the high luminosity. Red open diamonds mark the 100 randomly chosen stars that are used as tracers. **Upper right panel:** LOS-velocity profiles calculated from all stars (black solid line), from all 100 tracer stars shown in the upper left panel (red solid line), and only from the tracer stars that are less than two times the scale height  $h_s$  away from the disk lane (blue dash-dotted line). The blue symbols show the LOS-velocities of the individual tracer stars colored according to their distances from the disk lane: within  $1 h_s$  (light blue diamonds), between  $1 h_s$  and  $2 h_s$  (medium blue stars) and farther away than  $2 h_s$  (dark blue circles). **Lower left panel:** Same as upper left panel but for a different set of randomly chosen tracers. **Lower right panel:** Same as upper right panel but for the tracer set shown in the lower left panel.

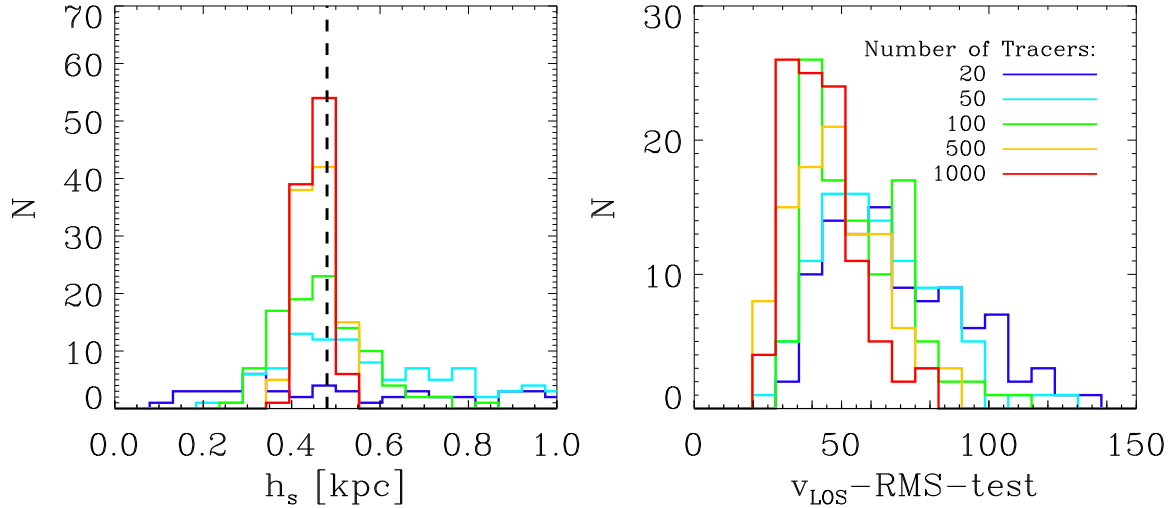


**Figure 6.2:** *Left panel:* Histograms for the scale heights  $h_s$  calculated from the 100 repetitions of  $N$  randomly drawn tracer stars, with  $N = 20$  tracers (blue line),  $N = 50$  tracers (cyan line),  $N = 100$  tracers (green line),  $N = 500$  tracers (yellow line) and  $N = 1000$  tracers (red line). *Right panel:* Histogram of the LOS-velocity-RMS-test for the same sets of 100 repetitions of  $N$  randomly drawn tracers as in the left panel. The smaller the values, the better does the LOS-velocity profile estimated from the  $N$  tracers represent the true profile (see right panels of Fig. 6.1, red and black lines respectively).

to the galaxy’s plane, similar to the case shown in the lower panel of Fig. 6.1.

Tracers are often used to estimate velocity profiles for the galaxies, as long as these are not seen face-on. For a spiral galaxy, for example, a face-on view would not provide any information about the rotational velocity since the ordered motion of rotation in those cases is orthogonal to the line-of-sight (however, Herrmann et al. (2008) and Herrmann & Ciardullo (2009) studied the PN systems of 6 face-on disk galaxies to test if the mass-to-light ratio is really constant in spiral disk galaxies). For each of our tracer drawing events we calculate the resulting LOS-velocity profile and compare it to the LOS-velocity profile calculated from all stars within the studied area of our simulation. For both profiles we bin the LOS-velocities in 40 equal-distance bins of 1 kpc each along the x-axis, independently of the number of objects included in each bin. The results for the two examples discussed above are shown in the right panels of Fig. 6.1, with the “real” LOS-velocity profile shown as black solid line and the estimated profile from the 100 tracer stars shown as red solid line. The positions and LOS-velocities of the individual tracers are shown as blue open symbols, with different symbols and shades of blue according to the distance of the tracer from the galaxy’s disk plane. As can be seen in the upper panel, the tracers within the halo have significantly different velocities from the tracers that are part of the disk structures. This is due to the fact that the halo stars have non-ordered, spherical orbits, while the disk stars have ordered rotation on circular orbits around the galaxy’s center within the disk plane. Thus, excluding the tracers within the halo from the calculation of the LOS-velocity profiles give smoother and more accurate profiles in general (see the blue dash-dotted line in the upper right panel of Fig. 6.1), however, at the cost of lower number statistics.

We investigate the accuracy of the estimated profiles from the randomly drawn tracers compared to the “real” LOS-velocity profile using an RMS-test, by calculating the mean deviations of the tracer-profile from the real profile for each experiment. The right panel of Fig. 6.2 shows the results of these tests as histograms for the 100 experiments performed for each of the five different numbers of tracers  $N$  ( $N = 20$  (blue line),  $N = 50$  (cyan line),  $N = 100$  (green line),  $N = 500$  (yellow line) and  $N = 1000$  (red line)). The histogram clearly shows that, the more tracers are available to calculate the LOS-velocity profiles, the better the representation of the underlying general rotational velocity profile, i.e., the experiments with  $N = 20$  tracers (blue line) exhibit generally larger RMS-deviations than the experiments with  $N = 1000$  tracers (red line).

For those disk galaxies which are seen edge-on, the tracer density perpendicular to the disk can be used to estimate the scale height of the disk by fitting an exponential to the density (as has been done by Shih & Méndez (2010)). We estimated the scale height  $h_s$  for all our experiments as well, with the resulting histograms shown in the left panel of Fig. 6.2. While the 100 experiments with  $N = 20$  tracers drawn from the full sample cover the whole range of resulting scale heights from  $0.05 \text{ kpc} < h_s < 1.2 \text{ kpc}$  (blue line), the 100 experiments with  $N = 1000$  converge on values of  $0.4 \text{ kpc} < h_s < 0.6 \text{ kpc}$  (red line), with the real scale height  $h_s = 0.48 \text{ kpc}$  (black dashed line, calculated from all stars within the simulation). In general, for  $N = 500$  and  $N = 1000$  the probability of getting a good approximation of the scale height is very high, while for  $N = 20$  and  $N = 50$  the likelihood for a good representation of the real scale height is rather low. In the case of  $N = 100$  tracers (green line), the resulting scale heights will most likely be a good approximation of the true value, yet there is still a high probability of too low or too high values (from 100 experiments, 68 have a scale height within  $h_s = 0.48 \pm 0.1 \text{ kpc}$ , and only nine have a scale height outside of  $h_s = 0.48 \pm 0.2 \text{ kpc}$ ).

Most of the currently ongoing surveys using PNe or GCs as tracer populations, however, are studying early-type galaxies and not disk galaxies, since those systems are approximately spheroidal and thus the resulting kinematic information is less strongly dependent on the inclination angle under which the galaxy can be observed. Also, as mentioned before, the obscuration due to dust and star formation is much lower in early-type galaxies than in late-type galaxies, which facilitates the detections of the tracers (Blom et al., 2012a). These observations can be used together with kinematic surveys studying the innermost areas of ETGs, like Atlas<sup>3D</sup> (Cappellari et al. (2011a), see also Sec. 1.2.3 for more details on this survey) to detect kinematic twists between the inner, bright parts of ETGs and their faint outskirts that might provide informations about the formation scenarios of the ETGs (see Foster et al. (2013) and Brodie et al. (2014) for first comparisons).

Therefore, we repeat our experiments of drawing 100 times  $N$  tracers, with  $N = 20$ ,  $N = 50$ ,  $N = 100$ ,  $N = 500$  and  $N = 1000$ , from a parent sample of stars, this time using a spheroidal galaxy. We use a spheroidal from a binary merger simulation, 11 OBH2 13 (see Sec. 2.2.1), which we evolved for about 8.5 Gyr after the first encounter, ensuring that the system could relax properly and shell and stream structures have vanished by the time we conduct our experiment. This time, we include all stars within a sphere of radius  $r_{\text{max}} = 100 \text{ kpc}$  as parent population of tracers. We exclude stars within a sphere of  $1.5 R_{1/2}$  (6.3 kpc) from the parent sample to mask the innermost area where the galaxy is too bright for PNe and GCs to be detected. One example of such an experiment with  $N = 100$  tracers is shown in the upper left panel of Fig. 6.3, with all stars of the parent population shown as black points. The 100 tracers chosen in this experiment are shown as open diamonds, with colors according to their individual LOS-velocity. Here, the blue/cyan parts of the galaxy move away from the observer, while the red/orange tracers move towards the observer. This is similar to what has been shown for example by Coccato et al. (2009) and Coccato et al. (2013).

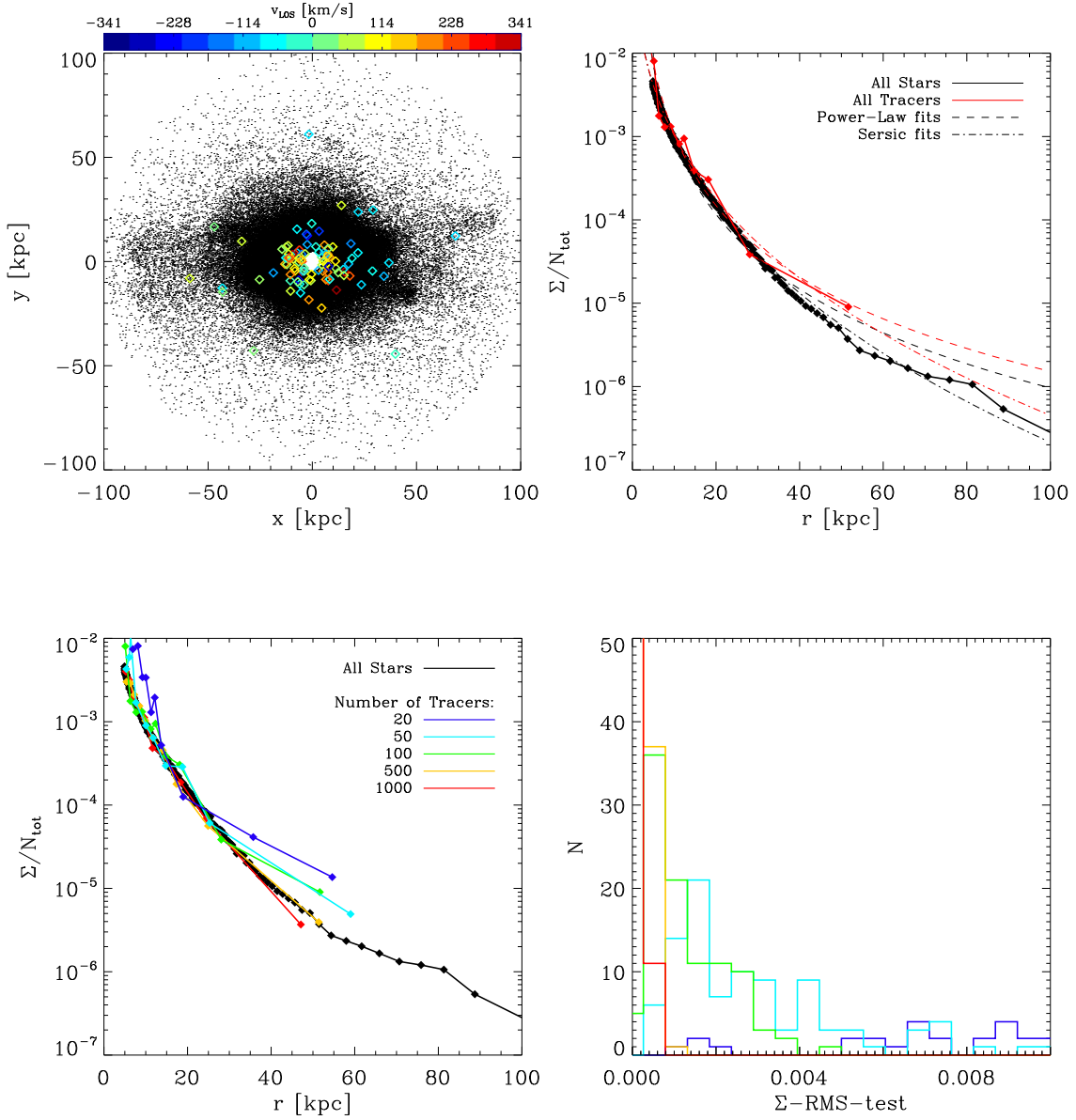


**Figure 6.3:** *Upper left panel:* Edge-on view of a simulated spheroidal from a binary merger (11 OBH2 13, see Sec. 2.2.1), at a relaxed state at about 7.5 Gyr after the merger event, with the major axis calculated within 2 times the halfmass radius ( $r_{1/2} \approx 4.2$  kpc). The galaxy has a slight twist in its density at the outskirts, causing the tilt of the major axis. The 100 randomly drawn tracers are shown as open diamonds, with their colors according to their LOS-velocity, revealing the slight rotation of the spheroidal around its minor axis. **Upper right panel:** Surface density profiles calculated from all stars (black solid line) and from the 100 tracer stars (red solid line). Dashed lines show the power-law fits to the density of the total (black) and the tracer (red) profile, dash-dotted lines show the respective Sérsic fits. **Lower left panel:** Surface density profiles calculated from all stars (black solid line) and from one experiment of  $N$  tracers each, with  $N = 20$  tracers (blue line),  $N = 50$  tracers (cyan line),  $N = 100$  tracers (green line),  $N = 500$  tracers (yellow line) and  $N = 1000$  tracers (red line). The line for  $N = 100$  is the same as in the upper right panel. **Lower right panel:** RMS-test for the deviations between the surface density profiles estimated from the tracer populations and the true profile, for 100 repetitions each.

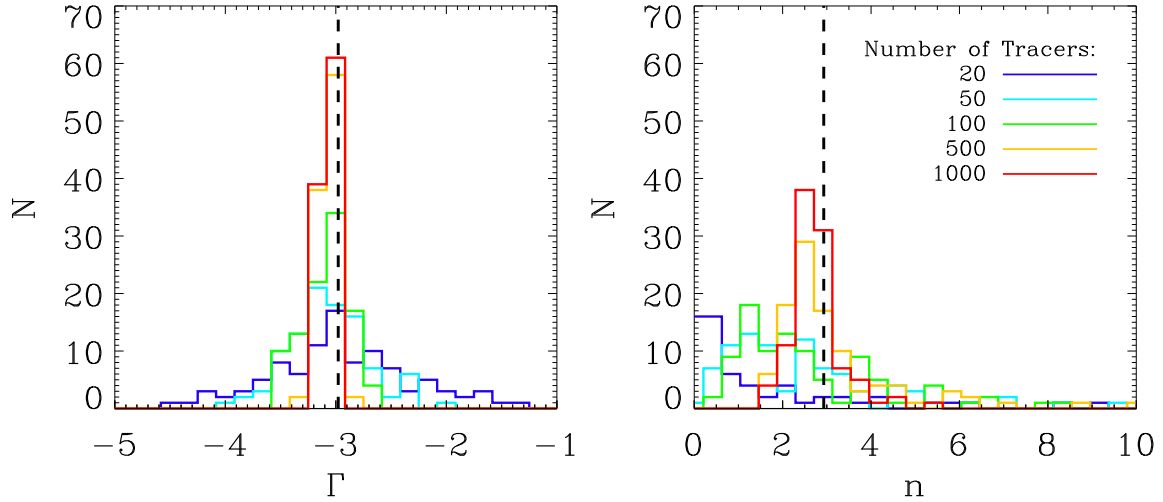


**Figure 6.4:** *Left panel:* Histograms for the slopes  $\Gamma$  of the power-law fits to the surface density profiles calculated from the 100 repetitions of  $N$  randomly drawn tracer stars, with  $N = 20$  tracers (blue line),  $N = 50$  tracers (cyan line),  $N = 100$  tracers (green line),  $N = 500$  tracers (yellow line) and  $N = 1000$  tracers (red line). *Right panel:* Histograms for the Sérsic indices  $n$  of the Sérsic fits to the surface density profiles calculated from the 100 repetitions of  $N$  randomly drawn tracer stars, with colors as in the left panel.

From the tracer samples, we calculate surface density profiles using 10 radial bins of equal number of particles for the 100 experiments of a given number of tracers  $N$ , i.e.,  $0.1N$  particles per bin, with the maximum radius  $R_{\max}$  the largest radius at which a tracer has been drawn for each experiment. The upper right panel of Fig. 6.3 shows the resulting surface density profile for one experiment with  $N = 100$  tracers (the same one for which the spatial distribution of the tracers is shown in the upper left panel of the same figure) as solid red line. The surface density calculated from all stars of the parent population is shown as solid black line. The lower left panel shows the resulting surface density profiles for one experiment of each number of tracers ( $N = 20$ : blue line,  $N = 50$ : cyan line,  $N = 100$ : green line (same as the red one in the upper right panel),  $N = 500$ : yellow line,  $N = 1000$ : red line) on top of the surface density calculated from all stars of the parent population (black solid line). As can be seen, for all numbers of tracers the binned surface density profiles are in good agreement in the inner parts, however, the larger radii are poorly fitted in all cases. This is due to the fact that we use equal numbers of bins, and thus lose the information in the outskirts by binning 50 or 100 tracers in one bin for  $N = 500$  or  $N = 1000$ , respectively. The deviations from the “true” underlying surface density are much larger for the smaller samples of tracers, as is also shown in the lower right panel of the same figure where we show histograms of the RMS-deviations between the true profile and those calculated from the tracer distributions.

Since we want to get as much information from the tracers as possible, it is more natural to use larger numbers of bins when larger numbers of tracers are available, but then the RMS-errors cannot be compared between the different experiments anymore. Nevertheless, if we use equal-particle bins of 10 particles per bin, we find that the profiles are fitted generally much better the more tracers are

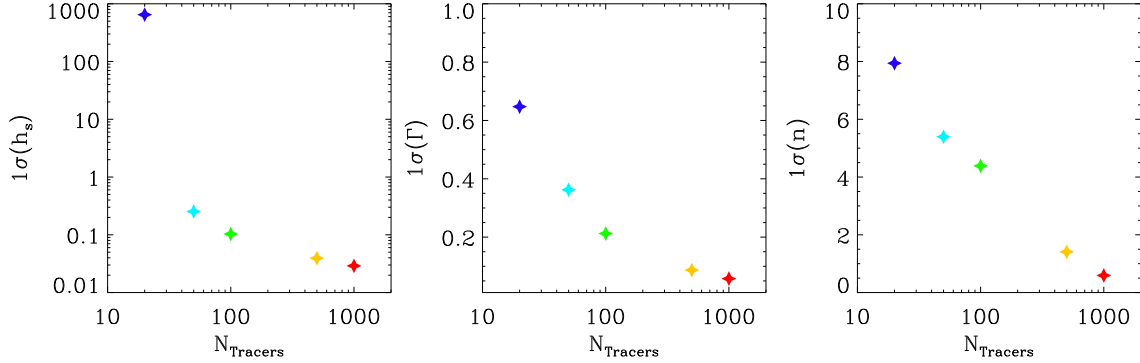


**Figure 6.5:** *Left panel:*  $1\sigma$ -deviations from the scale height  $h_s$  for the 100 experiments with each  $N = 20$  (blue),  $N = 50$  (cyan),  $N = 100$  (green),  $N = 500$  (yellow) and  $N = 1000$  (red) versus the number of tracers  $N$ . *Middle panel:*  $1\sigma$ -deviations from the slope of the single-power-law fit  $\Gamma$  to the radial surface density profiles for the 100 experiments versus the number of tracers  $N$  (colors as in the left panel). *Right panel:*  $1\sigma$ -deviations from the Sérsic index  $n$  of the Sérsic fits to the radial surface density for the 100 experiments versus the number of tracers  $N$  (colors as in the left panel).

available, since the outskirts are reconstructed much more accurately. For the following analysis, we therefore use equal-particle bins of 10 tracers per bin to reconstruct the underlying information from the tracer population instead of an equal number of bins for all experiments.

Usually, surface density profiles of spheroidals are fitted by either a power-law

$$\Sigma(r) \propto r^\Gamma \quad (6.1)$$

or by a Sérsic profile

$$\Sigma(r) \propto e^{-kr^{1/n}} \quad (6.2)$$

with  $n$  the so-called Sérsic index (see Sec. 1.4.1 for more details). We fit all our surface density profiles given by the different tracer populations with both theoretical profiles, as shown in the upper right panel of Fig. 6.3 for the example with  $N = 100$  tracers as red dashed (power-law fit) and red dash-dotted (Sérsic fit) lines. The fits for the underlying parent population of stars is shown as black dashed (power-law fit) and black dash-dotted (Sérsic fit) lines.

The results for the power-law slope  $\Gamma$  and the Sérsic index  $n$  are shown in the left and the right panel of Fig. 6.4, respectively. The colors are coded as before for the 100 experiments with  $N$  tracers ( $N = 20$ : blue line,  $N = 50$ : cyan line,  $N = 100$ : green line,  $N = 500$ : yellow line,  $N = 1000$ : red line). Both the power-law slope  $\Gamma$  and the Sérsic index  $n$  from the fits to the surface density profiles with large numbers of tracers ( $N = 500$  and  $N = 1000$ ) are very close to the values for the “true” profile, for all 100 experiments, while the values for  $\Gamma$  and  $n$  scatter strongly for the experiments with the small numbers of tracers ( $N = 20$ ,  $N = 50$ ), even if their mean values agree with the values for the true profile. The case of  $N = 100$  is on average a good fit, but strong deviations are still possible.

Unsurprisingly, we find that the surface density profiles for the spheroidals are represented better when more tracers are available. As for the experiments with the LOS-velocity dispersion profiles for the spiral galaxy we find that a number of  $N = 100$  tracers already has a sufficiently high probability

to properly represent the true underlying profiles of a spheroidal galaxy. This is illustrated in Fig. 6.5 where we show the  $1\sigma$ -deviations for the histograms of the scale-heights (see left panel of Fig. 6.2), the slopes  $\Gamma$  of the single-power-law fits to the radial surface density profiles (see left panel of Fig. 6.4) and Sérsic index  $n$  of the Sérsic fits to the radial surface density (see right panel of Fig. 6.4), calculated for the 100 drawing experiments for each of the five numbers of tracers tested. We clearly see that 20 or even 50 tracers are not enough to converge sufficiently for all three parameters throughout our experiments and the deviations are quite large, while for the large numbers of tracers (500 or 1000) the  $1\sigma$ -deviations are very small and the uncertainties are low. From our experiment we conclude that a number of  $N = 100$  is sufficient for obtaining trustworthy results for density and velocity profiles, but with fewer tracers than this there is a large chance for over- or underestimating the profiles and the fits to them.

However, this is only true in case of a discrete sample of tracers which follow the same spatial and kinematic distribution as the underlying stellar population. For the PNe, this is a valid assumption as shown by Coccato et al. (2009) and Cortesi et al. (2013). However, it might not be valid for GCs since there exist two different populations of GCs in most observed early-type galaxies: The metal-rich, red GCs (RGCs) seem to follow the stellar distributions, while the metal-poor, blue GCs (BGCs) are distributed farther in the outskirts of the galaxy (e.g., Pota et al. (2013)). This could indicate an external origin of the latter class of GCs, brought to the galaxy through merging and accretion events. In that case, our experiments of randomly drawing stars as tracers from all areas of the galaxy with the same likelihood for each star to be drawn would not be representative, since stars in the outskirts should be more likely to be selected as tracers.

### 6.3 What do the Different Kinds of Tracers Trace?

Planetary Nebulae and Globular Clusters, although both used as tracers for the outer faint components of galaxies, are very different objects. GCs are among the oldest remaining structures in the universe, and PNe are the remnants of stars with masses between  $1 M_{\odot}$  and  $8 M_{\odot}$  (Badenes et al., 2015, and references therein; these authors also present observational evidence for two distinct formation scenarios for PNe depending on the mass of the progenitor stars). PNe can therefore occur anywhere in a galaxy where stars of the given mass end their lives, i.e., in the bulges, disks and the stellar halos, with their number density higher wherever higher numbers of those stars are present. Assuming that the IMF is universal (e.g., Padoan et al., 1997b) and the stellar populations are similar for every galaxy in the universe, the number of PNe should always be a good representative for the underlying stellar population (see, for example, Coccato et al. 2009, Coccato et al. 2013 and Cortesi et al. 2013 and references therein, but also Cappellari et al. 2012; Ferreras et al. 2013; van Dokkum & Conroy 2011, 2012; Tortora et al. 2013, and references therein for indications on a variable IMF). Thus, PNe can be used to trace the stellar content independent of whether it is accreted or not, and therefore all kinds of structures should be detectable as long as they are on average dense enough to enhance the number of expected PNe.

GCs, however, are not found in the inner parts of galaxies, but usually in the outskirts where the stellar halo of a galaxy dominates the stellar component, and the dark matter becomes the dominant part of a galaxy (e.g., Pota et al., 2013). Their formation mechanisms are still unknown and a matter of heavy debate within the literature: An external origin outside the galaxies they are found in at present day, as products of the gravitational collapse of single gas clouds in the early universe at the cores of

small dark matter halos has been suggested, for example, by Peebles & Dicke (1968); Peebles (1984); Rosenblatt et al. (1988); Padoan et al. (1997a), assuming that they lose all their dark matter during the accretion into their present-day host galaxies. An internal formation scenario within their host galaxies has been proposed by Fall & Rees (1985), with the GCs being formed in fragments of the protogalactic clouds due to the compression of the cold gas induced by the hot gas components. A third mechanism was introduced by Ashman & Zepf (1992), where the formation of the GCs is induced by shocks during merging events of massive structures. GCs (mostly) contain multiple stellar populations (see, for example, the review by Gratton et al. (2012) and references therein). To account for these multiple stellar populations, Trenti et al. (2015) recently suggested another formation scenario, where GCs are formed in high-redshift mergers of atomic cooling halos.

Their formation usually occurred at very high redshifts (about 10 Gyr ago) with only a small fraction of GCs younger than 5 to 6 Gyr (Brodie & Strader, 2006). Additionally, the number of GCs detected in a galaxy is known to correlate with the mass of its central black hole (Berkert & Tremaine, 2010), and this correlation is tighter than the well-known black-hole- $\sigma$  relation. There is strong observational evidence from recent studies of the colors of GCs that there actually exist two distinct populations of GCs (red and blue, see for example Peng et al. (2006) and Richtler et al. (2015), and Blom et al. (2012b,a) for NGC 4365 which even exhibits hints of a third population of GCs). A bimodality is also found in the metallicity (e.g., Zinn, 1985, for the Milky-Way GCs), with indications that the red GCs (RGCs) might have higher metallicities than the blue GCs (BGCs) (see Usher et al., 2012).

The RGCs have been shown to trace the light of the central stellar component, similarly to the PNe (Peng et al. 2004b; Schubert et al. 2010; Pota et al. 2013; however, Coccato et al. (2013) find indications that PNe and RGCs might actually trace different stellar populations), while the BGCs show a different behaviour (e.g., Forbes et al., 1997; Schubert et al., 2010). This led to the assumption that RGCs might have formed in-situ in the main galaxy, while the BGCs have been accreted onto the halo in violent merging events with other galaxies (Côté et al. 1998; Schubert et al. 2010). Thus, it has been proposed by Forbes et al. (2012) who compared the X-ray halos with the surface density of BGCs and found a good agreement, that the BGCs could be effectively tracing the dark matter component of galaxies (see also Forte et al. 2005; Brodie & Strader 2006). However, the question remains whether BGCs really can be used to trace the dark matter properties of galaxies or not.

Deason et al. (2012) used PNe and GCs from the literature detected in 15 nearby early-type galaxies to probe their dark matter halos, without splitting the GCs into two populations. They fitted single power-laws  $\rho \propto r^\gamma$  to the radial density profiles of those galaxies in the radius range from  $2 R_{\text{eff}}$  to  $R_{\text{max}}$  (the largest radius at which a tracer has been detected). Whenever three dimensional densities had been provided for the density, they used those densities for their fits, while they increased the power-law index by 1 whenever only two-dimensional surface densities had been provided. For all galaxies, they used the density and velocity profiles constructed from the tracers to calculate the potentials and the dark matter fractions of the galaxies within five effective radii ( $5 R_{\text{eff}}$ ).

We use those dark matter fractions and density slopes to compare the observations with our simulations, with the aim of understanding whether the tracers really provide information about the dark matter densities of early-type galaxies. To broaden the analysis in order to understand if the BGCs might be tracing the dark matter component, we also included NGC 5846 in our analysis, whose dark matter fraction at  $5 R_{\text{eff}}$  is given by Napolitano et al. (2014). We used the number-density profiles for BGCs and RGCs from that work to perform single-power-law fits to both profiles, as well as Sérsic fits. The result is shown in the right panel of Fig. 6.6, with the data for the BGCs shown as blue

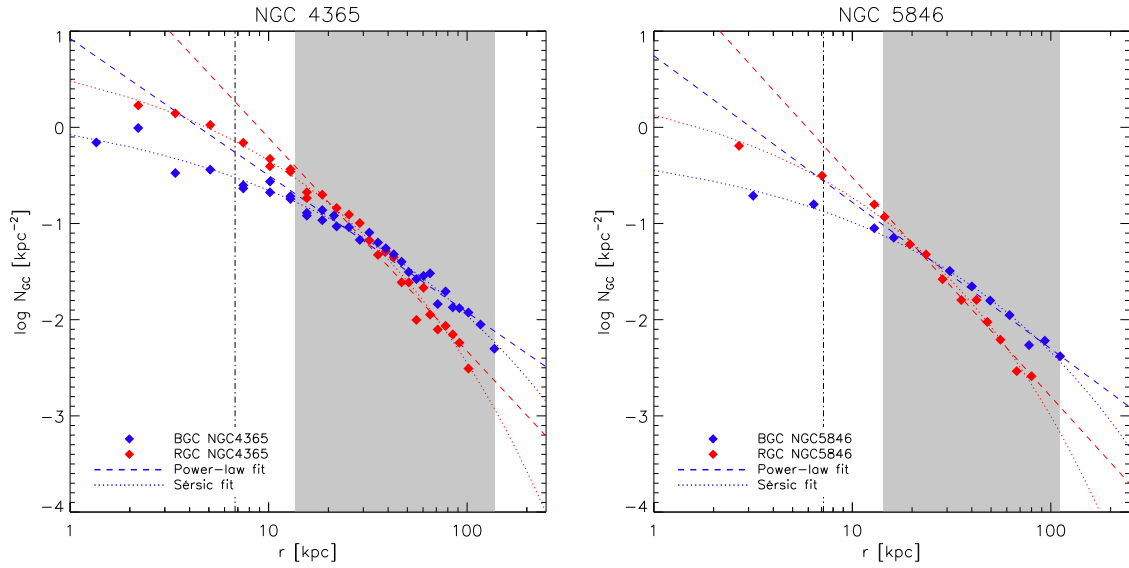


**Figure 6.6:** Number density profiles of the RGC (red diamonds) and BGC populations (blue diamonds) of the elliptical galaxies NGC 4365 (left panel) and NGC 5846 (right panel). Power law fits to the profiles in a radius regime of  $2 R_{\text{eff}}$  to the maximum radius at which there are still GCs detected (gray shaded areas) are shown as dashed lines, Sérsic fits to the whole profiles are shown as dash-dotted lines. The solid black line marks the effective radius. Data points are taken from Pota et al. (2013) for NGC 4365 and from Napolitano et al. (2014) for NGC 5846.

diamonds and the data for the RGCs shown as red diamonds. The dashed lines are the power-law fits between  $2 R_{\text{eff}}$  and  $R_{\text{max}}$  (shaded gray areas), while the dotted lines show the Sérsic fits (colors red and blue for RGCs and BGCs respectively).

In addition, we also included three galaxies in the analysis where the dark matter fractions within  $5 R_{\text{eff}}$  are given by Deason et al. (2012) and took the number-density profiles for BGCs and RGCs from Pota et al. (2013). As for NGC 5846 we performed single-power-law fits to both the RGC and BGC number density profiles as well as Sérsic fits, with the results shown in Fig. 6.7 for NGC 821 (left panel), NGC 1407 (middle panel) and NGC 3377 (right panel). However, NGC 821 only has 61 tracers which is a very low number to perform the fits, and we clearly see that the behaviour of RGCs to BGCs differs from the other two cases, i.e., the RGCs become dominant in the outskirts. NGC 3377 has 126 GCs as tracers, which would generally be enough for a good analysis, however, since the tracers are split into two populations the profiles found for this galaxy could also be suffering from low-number statistics. NGC 1407 has a total number of 369 GCs, and the fits are clearly the best. Nevertheless, we also see that a power-law is not a very good fit to both the RGC and the BGC profiles for this galaxy, as both profiles are strongly curved and much better represented by a Sérsic fit.

The left panel of Fig. 6.6 shows the same fits but for NGC 4365, with the data taken from Pota et al. (2013) as well. Here, both the power-law fits and the Sérsic fits are a very good approximation to the radial profile between  $2 R_{\text{eff}}$  and  $R_{\text{max}}$ . Unfortunately, we could not find dark matter fractions within  $5 R_{\text{eff}}$  for this galaxy in the literature, and thus we cannot include NGC 4365 in the following

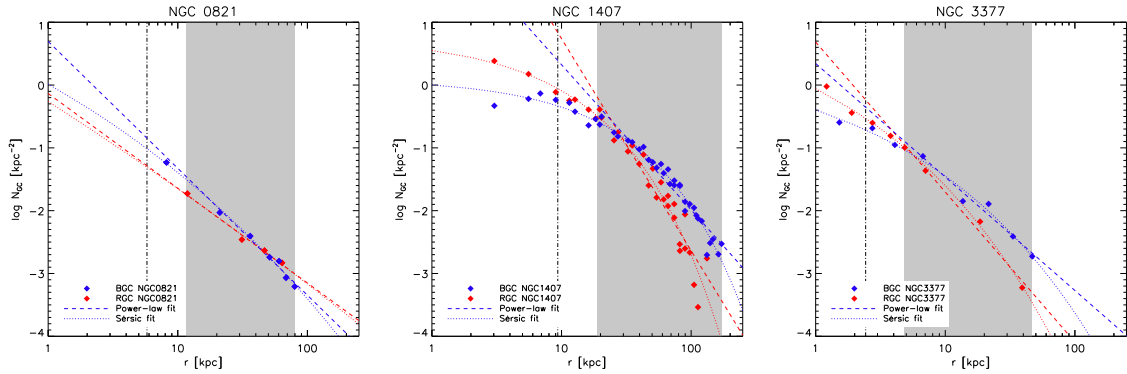


**Figure 6.7:** Same as Fig. 6.6 but for NGC 821 (left panel), NGC 1407 (middle panel) and NGC 3377 (right panel). Data points are taken from Pota et al. (2013).

analysis, although it would be a very interesting candidate since this galaxy exhibits strong indications of having even a third GC component, as mentioned above.

In order to obtain approximations to the slopes of the three-dimensional number densities from our fits to the two-dimensional number densities, we followed Deason et al. (2012) and incremented the power-law exponents by 1. Fig. 6.8 shows the resulting density slopes for the 15 galaxies from Deason et al. (2012) (green circles for PNe, cyan circles for GCs), the galaxy from Napolitano et al. (2014) (NGC 5846, red (RGC) and blue (BGC) filled diamonds) and the three galaxies with density slopes estimated from data taken from Pota et al. (2013) (red and blue bow-tie, stars and hourglass for NGC 821, NGC 1407 and NGC 3377, respectively) versus the dark matter fraction  $f_{\text{DM}}$  within  $5 R_{\text{eff}}$  in all three panels.

To address our question which parts of the galaxies are represented by the different tracer populations, we included the density slopes calculated between  $2 R_{1/2}$  and  $5 R_{1/2}$  for the spheroidals from the Magneticum simulation Box4 uhr (see Sec. 2.4) with total masses larger than  $M_{\text{tot}} = 5 \times 10^{11} M_{\odot}$  as small grey circles (dark grey for spheroidals without any cold gas, light grey for spheroidals with small cold gas disks) in all panels of Fig. 6.8. In the left panel, we show the density slopes  $\gamma_{\text{tot}}$  obtained from single power-law fits to the total combined stellar and dark matter density profiles (see Chap. 3 for more details on the total density profiles), in the middle panel we show the density slopes  $\gamma_{*}$  from single power-law fits to the stellar component of the spheroidals (in this region we basically fit the stellar halo component, see Chap. 5 for more details), and in the right panel we show the density slopes  $\gamma_{\text{DM}}$  for the dark matter alone. As can be seen from this figure, the range of observed dark matter fractions within  $5 R_{\text{eff}}$  agrees well with the dark matter fractions of the Magneticum spheroidals within  $5 R_{1/2}$ , however, the power-law slopes of the density from the observations do not agree at all with the total power-law slopes  $\gamma_{\text{tot}}$  or the dark matter power-law slopes  $\gamma_{\text{DM}}$ . Both the total (around  $\gamma_{\text{tot}} \approx -2$ ) and the dark matter slopes (around  $\gamma_{\text{DM}} \approx -1.7$ ) are much too large in comparison to the observed values, independent of the tracers used for estimating the observed profiles.

However, the observed density slopes are all in excellent agreement with the density slopes found for the stellar (halo) component for the Magneticum spheroidals, as can be clearly seen in the middle panel of Fig. 6.8. Thus, we conclude that all tracers do actually trace the densities of the stellar components of the galaxies. Nevertheless, the observations clearly show a difference between the density slopes estimated for the different types of tracer, which can best be seen in the case of NGC

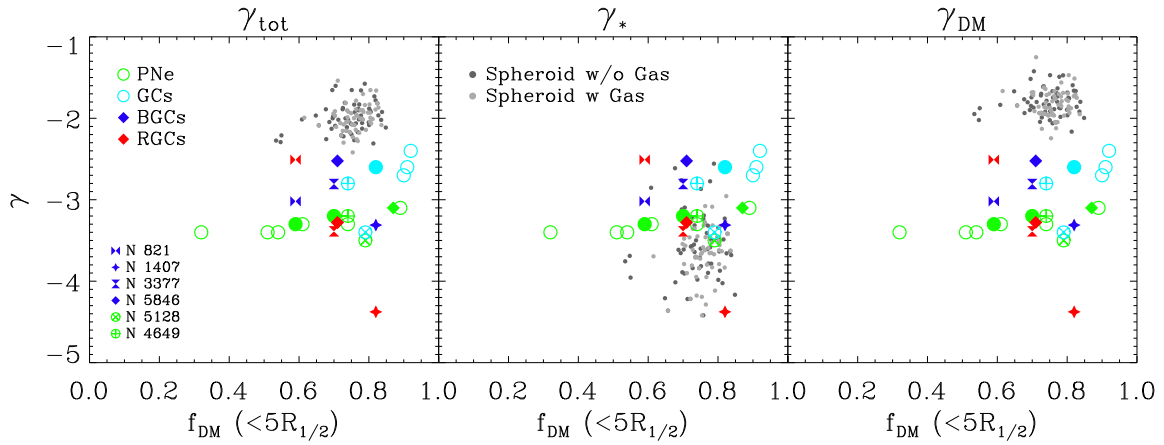


**Figure 6.8:** Density slopes from power-law fits to the density profiles between  $2R_{1/2}$  and  $5R_{1/2}$  for the spheroidals from the Magneticum simulation Box4 uhr, shown as small grey circles (dark grey for spheroidals without any cold gas, light grey for spheroidals with small cold gas disks). **Left panel:** density slopes  $\gamma_{\text{tot}}$  obtained from single power-law fits to the total combined stellar and dark matter density profiles. **Middle panel:** density slopes  $\gamma_*$  from single power-law fits to the stellar component. **Right panel:** density slopes  $\gamma_{\text{DM}}$  for the dark matter. In all three panels, the density slopes from power-law fits to the tracer densities from observations in the radius range  $2R_{\text{eff}}$  and  $R_{\text{max}}$  versus the dark matter fractions  $f_{\text{DM}}$  within  $5R_{\text{eff}}$  are shown as well, for the 15 galaxies from Deason et al. (2012) (green circles for PNe, cyan circles for GCs), the galaxy from Napolitano et al. (2014) (NGC 5846, red (RGC) and blue (BGC) filled diamonds) and the three galaxies with density slopes estimated from data taken from Pota et al. (2013) (red and blue bow-tie, stars and hourglass for NGC 821, NGC 1407 and NGC 3377, respectively). We used the dark matter fractions from a Chabrier IMF for the values from Deason et al. (2012). Filled circles mark the values from Deason et al. (2012) for the galaxies included also in the sample of Pota et al. (2013), while open circles with crosses or pluses mark galaxies where there have been GCs and PNe used separately to estimate densities and dark matter fractions within the work by Deason et al. (2012). For NGC 5846, Deason et al. (2012) provided a measurement from PNe independent of the RGC and BGC measurements from Napolitano et al. (2014), and the value from Deason et al. (2012) is shown as filled green diamond.

5846 where we have three density slopes for all three different tracers:  $\gamma_{\text{PNe}} = -3.1$  from Deason et al. (2012), and  $\gamma_{\text{RGCs}} = -3.28$  and  $\gamma_{\text{BGCs}} = -2.52$  from our fits to the data from Napolitano et al. (2014) for RGCs and BGCs, respectively. The slopes for the PNe and the RGCs are very similar, supporting the idea that RGCs and PNe might actually both trace the main stellar component of their host galaxies. The slope obtained for the BGCs, however, is much flatter. This is true for NGC 3377 and NGC 1407 as well, even if the fits for NGC 1407 give much steeper slopes than for the other galaxies since the density profiles are curved so much (middle panel of Fig. 6.7). Only NGC 821 shows an opposite behaviour, but this might be due to the low numbers of the GCs found in this galaxy. We conclude that a more detailed analysis of the simulations, including metallicities and decompositions of the different galaxy components is needed to give a final answer to the question what the different kinds of tracers actually trace, but we also find clear evidence that none of the tracers actually trace the density profiles of either the dark matter or the total density profile.

On a last note to this section, we tested the dependence of the density slopes found for the observations on the largest radius at which a tracer is observed, and whether there is a correlation between

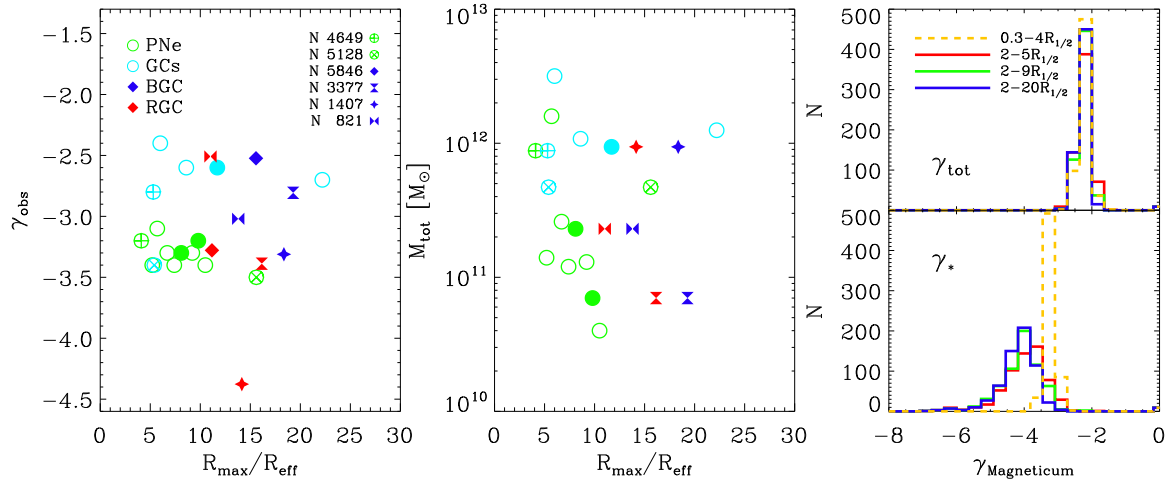


**Figure 6.9:** *Left panel:* Observed density slopes  $\gamma_{\text{obs}}$  versus the maximum radius of the fit in units of the effective radius,  $R_{\text{max}}/R_{\text{eff}}$ , for the same galaxies as in Fig. 6.8 (PNe from Deason et al. (2012), NGC 5846 from Napolitano et al. (2014), and  $R_{\text{max}}/R_{\text{eff}}$  and  $\gamma_{\text{obs}}$  from our analysis of the data presented in Pota et al. (2013) for NGC 821, NGC 3377 and NGC 1407). Colors and symbols also as in Fig. 6.8. *Middle panel:* Stellar mass of the same observed galaxies versus  $R_{\text{max}}/R_{\text{eff}}$ . *Right panel:* Histograms for the slopes of the fits to the total density profiles (upper panel) and the slopes of the fits to the stellar density profiles (lower panel) of the Magneticum spheroidals, fitted at different radius ranges of  $2 R_{1/2}$  to  $5 R_{1/2}$  (red lines),  $2 R_{1/2}$  to  $9 R_{1/2}$  (green line),  $2 R_{1/2}$  to  $20 R_{1/2}$  (blue line) and  $0.3 R_{1/2}$  to  $4 R_{1/2}$  (yellow dashed line).

this largest radius  $R_{\text{max}}$  and the stellar mass of the galaxy. The results are shown in the left and the middle panel of Fig. 6.9, respectively, with the colors and symbols of the observations as in Fig. 6.8. For the PNe we see a slight dependence of the observed density slope  $\gamma_{\text{obs}}$  on the maximum radius of the fit in units of the effective radius,  $R_{\text{max}}/R_{\text{eff}}$ , with the slopes being slightly smaller for larger  $R_{\text{max}}/R_{\text{eff}}$  (see left panel of Fig. 6.9). However, this could also be an effect of galaxies with smaller stellar masses having slightly steeper slopes, as already discussed in Deason et al. (2012), since we also find  $R_{\text{max}}/R_{\text{eff}}$  to be generally larger for galaxies of less stellar mass. We do not see a similar behaviour for the GCs, neither red nor blue, in fact neither the slope nor the stellar mass seem to correlate with  $R_{\text{max}}/R_{\text{eff}}$ . This could be an effect of the different nature of GCs and PNe; however, if the red GCs really follow the same stellar component as the PNe there should be a similar behaviour and only the blue GCs should behave differently. This is supported by Kartha et al. (2014) who find a correlation between the spatial extent of GCs and the stellar mass of the host galaxy for a sample of 40 galaxies, including spirals, ellipticals and lenticulars. For the lenticulars and the ellipticals they also find that the spatial extent of the GC systems is proportional to the effective radius, which agrees with the mass-size relation seen for ETGs at present day (e.g., Shen et al., 2003, and Chap. 4). With the currently available data sets a conclusive interpretation of this problem is not possible and thus further studies are needed.

Nevertheless, from our simulations we find that the stellar slopes calculated for our spheroidals from the Magneticum simulation actually do depend slightly on the radius range in which the fit is performed, as demonstrated in the lower right panel of Fig. 6.9. The blue histogram shows the stellar slopes for our spheroidals fitted from  $2 R_{1/2}$  to  $20 R_{1/2}$ , while the red histogram shows the distribution

of the slopes of the same spheroidals but fitted in a radius range of  $2 R_{1/2}$  to  $5 R_{1/2}$ . Although the trend is very weak, we still find that the slopes tend to be steeper on average for larger maximal radii of fitting. This is due to our result shown in Chap. 5, that the outer stellar halos of galaxies are curved like an exponential (and best fitted by an Einasto profile) and therefore the power-law fit is only an approximation which varies towards steeper slopes the farther outside the fit is made, since different tangents with different slopes at different radii can always be fitted to a curved profile. This is also supported by the power-law fit to the stellar density component at radii between  $0.3 R_{1/2}$  to  $4 R_{1/2}$ , which is the range where we fitted the power-laws in Chap. 3 and Chap. 4 (see also Remus et al. 2013), and where the slopes are all much flatter (around  $\gamma_* \approx -3$ , yellow dashed histogram).

However, for the slopes of the total density profile,  $\gamma_{\text{tot}}$ , we do not find this behaviour: interestingly, the slope remains around  $\gamma_{\text{tot}} \approx -2$  independent of the radii used for the fit, see upper right panel of Fig. 6.9. This supports our results from Chap. 3 and Remus et al. (2013), where we showed that the total density can be very well represented by a power-law with a slope around  $\gamma_{\text{tot}} \approx -2$ , and that this behaviour holds for a large radius range. This is in agreement with results from weak lensing by Gavazzi et al. (2007), who showed that the total density profiles can be described by a power law with a slope of approximately  $-2$  for radii up to 100 effective radii.

## 6.4 Surveying the Outer Halo: Shells, Streams and other Features

In a universe with a hierarchical growth of structures, tidal disruptions and stripping of smaller structures within larger structures is a common, natural process. While the gas content involved in those merging and accretion events can dissipate its energy through heating and cooling, and thus fall into the center of the main halo or get shock heated in the outskirts, losing the dynamical information about its origin in this process, the collision- and dissipationless components of those events still remember the kinematic features of the event itself and might even keep information about the stages of the structures before the event. The dynamical timescales on which those structures can relax through gravitational violent relaxation and phase mixing are much larger the farther away those structures are from the central areas of the main halos. However, those structures, such as streams resulting from a stripping event where a satellite is disrupted in the outskirts of the stellar halo of a larger host galaxy, or shell-like structures that are caused by the disruption of a satellite that is merging into the central structure, are much less dense than the main galaxy in the center and therefore less bright.

Therefore, in order to detect these structures directly, photometric ultra-deep imaging is needed. This has been done extensively for the Milky Way and Andromeda, revealing that Andromeda actually exhibits a stellar halo which is very rich in streams and shells (e.g., Ibata et al., 2014), leading to the conclusion that Andromeda suffered several recent minor merger events (see also Chap. 5 for more details on the stellar halo properties of the Milky Way and Andromeda).

For other spiral galaxies, this has been done, for example, by Martínez-Delgado et al. (2010) for a set of 8 spiral galaxies where they systematically mapped the faint outskirts of those galaxies and detected a multitude of structures, from circular features, similar to the Sagittarius stream around the Milky Way (Lynden-Bell & Lynden-Bell 1995; Newberg et al. 2002), to jetlike arms and remote shells, or by Martínez-Delgado et al. (2014) for the Whale Galaxy. Recently, Duc et al. (2015) published ultra-deep imaging for a sample of 92 early-type galaxies in low to medium dense environments, revealing that those faint structures are actually common in the outskirts of all kinds of galaxies. One example of an ETG from this survey is shown in the left panel of Fig. 6.11. Another example of an

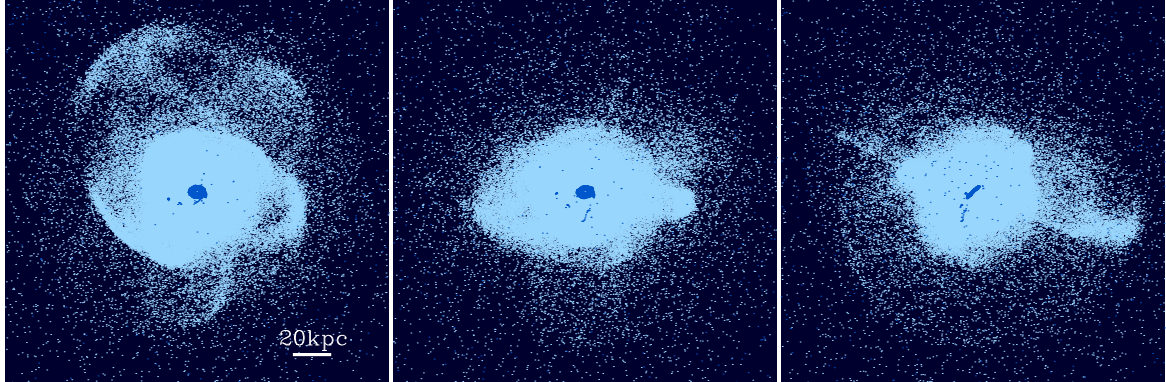


**Figure 6.10:** Visualization of the outer halo shell structures found about 2.5 Gyr after the first encounter in a 1:1 binary merger of two spiral galaxies from the sample of Johansson et al. 2009a,b, see also Sec. 2.2.1. Stars are shown in light blue, while the cold gas is shown in darker blue. The three panels show the galaxy from three different viewing angles. The halfmass radius of the galaxy is about the size of the cold gas disk in the center ( $R_{1/2} = 4.2$  kpc).



**Figure 6.11:** Observations of two early-type galaxies with extended shell structures, remnants of recent merging events. **Left panel:** NGC 474. Image credit: P.-A. Duc and the Atlas<sup>3D</sup>-Team (Duc et al., 2015). **Right panel:** NGC 7252, also called Arp 226 or “Atoms-for-peace”-Galaxy. Image credit: ESO

ETG, where the remnant tidal arms and shells from a very recent merging event are still very bright, is NGC 7252, the “Atoms-for-peace” galaxy, which was already classified as a peculiar galaxy by Halton Arp in his “Atlas of peculiar galaxies” (Arp, 1966) as Arp 226 (see also Kanipe & Webb 2006). A beautiful image of this galaxy provided by the ESO is shown in the right panel of Fig. 6.11.

Those observations have remarkable resemblance with the results of binary merger simulations, as shown for example for one of our binary major mergers (11 OBH2 13, see Sec. 2.2.1 and Johansson et al. 2009a,b) in Fig. 6.10 for three different projection angles. Especially, the umbrella-like structure in the upper left corner of the left panel is very similar to the umbrella-like structure found for NGC 474 by Duc et al. (2015). The similarities between (heavily) distorted galaxies like those collected in the Arp Atlas, the Mice Galaxies, the Antennae system or Hoag’s Object and the results of simulated isolated binary minor or major merger events has been discussed widely in the literature, starting with simple simulations of merging disks with only very few particles (e.g., Toomre & Toomre (1972) showed that bridges and tails can be remnants of encounters between two galaxies), to detailed studies of individual systems (for example Karl et al. 2010, 2013 studied the formation of the Antennae system, Bournaud & Combes (2003) studied different mechanisms to form polar ring galaxies like Hoag’s Object) and general comparisons of merger remnant features with observed peculiar structures (e.g., Martínez-Delgado et al. (2010) and references therein, or Amorisco (2014) for a detailed dynamical analytical analysis of stream features).

However, to gain detailed information about the kinematic properties of these faint structures, photometry is not sufficient. As discussed in the previous sections, tracer populations can be used to provide this additional information on top of the photometric detection. This has been done for example for the Umbrella galaxy by Foster et al. (2014), who used PNe, GCs, and H II regions as tracers to map the kinematics of the streams and shells caused by a disrupted satellite. With those kinematics it is possible to get constraints on the mass, kinematic properties, and orbits of encounters of the progenitor satellite with the main galaxy, as has been done in that remarkable work. As new instruments become available, more detailed studies about the kinematics of those remnant structures of merging events in the outer halos will be possible and can provide, together with new, large sets of cosmological simulations, new insights into the formation history of all types of galaxies.

### 6.4.1 Shells

Faint shell structures are observed around many galaxies nowadays, but one prominent example of such a shell galaxy is NGC 3923, which actually has 22 symmetric shells in its outskirts (Prieur, 1988). Those shells are interpreted as remnants of a merging event between two galaxies on a nearly radial trajectory, mostly in the context of a small satellite merger into a large structure. The faint concentric arcs consist of the stars of the intruder galaxy that got disrupted in the larger and deeper potential of the bigger galaxy. These stars now oscillate within the potential, and cause the shell-like structures due to the fact that they spend most of the time close to the apocenter of their orbits, where they “pile up” and cause the symmetric arcs (see, for example, Quinn 1984; Hernquist & Quinn 1989; Ebrova et al. 2010; Cooper et al. 2011; Torrey et al. 2015; and the review by Athanassoula & Bosma (1985)). They usually form incomplete (rarely full) circles, with the next outermost shell usually on the opposite side of the previous shell (Quinn, 1984), and can reach out to large radii. The outermost shell indicates the time of the first encounter, while each new passage of the satellite through the main galaxy causes a new shell on the opposite site of the previous one (see, e.g., Quinn (1984), Ebrova et al. (2010)).

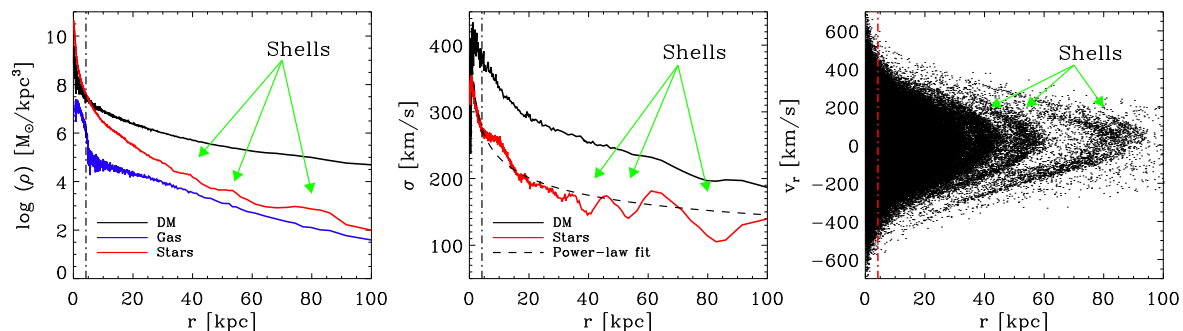


**Figure 6.12:** The different signatures of shell structures in the binary merger 11 OBH2 13 (see Sec. 2.2.1). **Left panel:** Density profiles for the dark matter (black), the stars (red) and the gas (blue). **Middle panel:** Velocity dispersion profiles of the dark matter (black solid line) and the stars (red solid line), with a power-law fit to the stellar component shown as dashed black line. **Right panel:** Phase-space diagram of the radial velocity versus the radius. The halfmass radius of the galaxy ( $R_{1/2} = 4.2$  kpc) is shown as dash-dotted line in all three panels. The shell structures are indicated by green arrows in all three panels, however, in the right-hand panel the innermost shell is barely visible due to the particle density in that area.

While they are mostly associated with minor merger events, we find those faint shells in the outskirts of the remnants of our major mergers as well, as shown in Fig. 6.12 (again we use the galaxy 11 OBH2 13, at the same time-step as in Fig. 6.10). We find signatures of those shells in the intrinsic stellar density profiles of our merger remnant (left panel, red solid curve) in the form of small density enhancements (green arrows). They are, however, not present in the dark matter (black solid line) or the gas (blue solid line) density profiles. The shells also leave signatures in the velocity dispersion profile of the stars (middle panel of Fig. 6.12, red solid line), but here they are visible as diminishments (green arrows) instead of enhancements, due to the more ordered radial motions compared to the random distribution of orientations in the smooth stellar halo. This can clearly be seen in the right panel of Fig. 6.12, which shows a phase space diagram of our binary merger. The shells are clearly visible as dense areas in the  $v_r$ - $r$  plane. Similar phase-space diagrams are found by Quinn (1984) for their mergers of small substructures into larger galaxies. Like for the density, we do not find signatures of the shells in the dark matter velocity dispersion profile (middle panel, black curve).

With time, dynamical friction and dispersion cause the shell structures to become less prominent and finally, when the system relaxes, vanish completely. This happens on timescales of the ratio of the velocity dispersions of the main galaxy and that of the shell, multiplied by the typical orbital time in the potential (Quinn, 1984), i.e., within about 1 Gyr. Thus, the outermost shell keeps a record of the time since the last merger event, however, when the outermost shell has decayed already the real timespan might be underestimated. Therefore, the “outermost” shell currently observed can only give a lower limit for the time since the merger event. Additionally, multiple mergers might cause multiple shells from different events that overlap, and disentangling those remnants can be very difficult and require detailed data on velocities, metallicities and other possible indicators for the stellar populations of the different intruders.

On the modeling side, both detailed simulations of individual merger events as well as cosmological simulations with sufficiently high spatial and temporal resolution are needed to analyse those

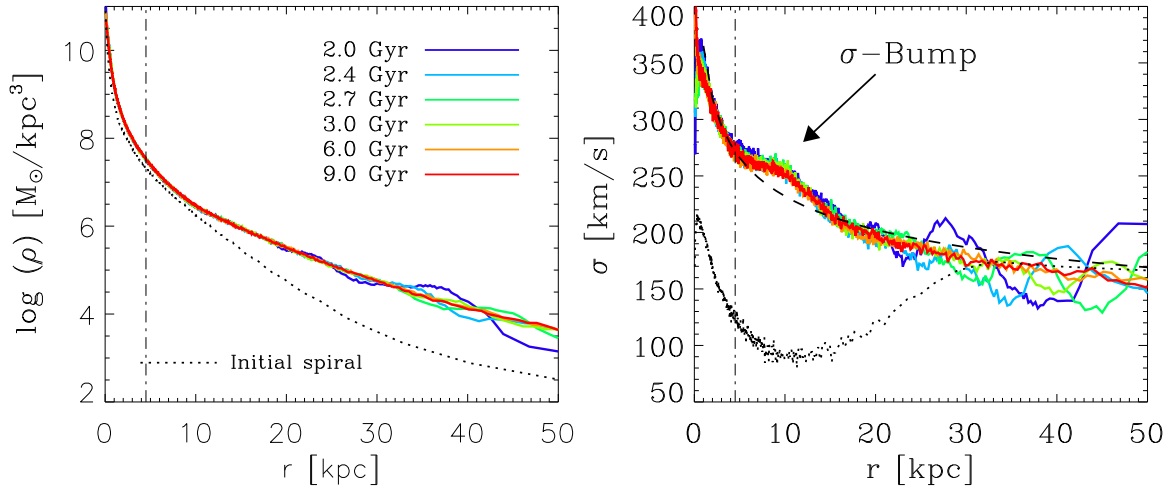


**Figure 6.13:** Radial profiles of the binary merger 11 OBH2 13. **Left panel:** Logarithmic radial density profile for the merger remnant at different timesteps of the simulation. The merger event happens at about 1.5 Gyr after the beginning of the simulation, and the first density profile is shown at 2 Gyr (blue line). The last timestep included is at 9 Gyr, i.e., 8.5 Gyr after the first encounter and 7.5 Gyr after the final merging took place. At larger radii, the density distortions caused by the shell structures are visible in the first timesteps, the last profile is very smooth as the shells have dispersed. The density profile of the initial spiral galaxy is shown as dotted black line, the halfmass radius of the final spheroidal is shown as dash-dotted line. **Right panel:** Total velocity dispersion profiles at the same timesteps as in the left panel. At early timesteps, the wiggles in the profiles caused by the shell structures can clearly be seen, in the last two timesteps those shells have dispersed. The  $\sigma$ -bump (black arrow) however can be seen at all timesteps and stays constant with time. The power-law fit to the velocity dispersion profile at 9 Gyr is shown as dashed black line, the total velocity dispersion profile of the initial spiral galaxy is shown as dotted black line, the halfmass radius of the final spheroidal is shown as dash-dotted line.

complex systems: While the isolated merger simulations can provide detailed information on the kinematics of mergers, the cosmological simulations provide statistical information on the amount of shell galaxies at a given redshift and the likelihood of certain configurations (mass ratios and orbit parameters). In addition, only cosmological simulations can provide realistic results of multiple merging events to compare to observations, since the full range of cosmological formation histories is included.

### 6.4.2 The $\sigma$ -Bump

Another feature in the outskirts of merger remnants is the so-called  $\sigma$ -bump, which we presented in a recent paper (Schauer, Remus, et al., 2014). The  $\sigma$ -bump is a deviation of the velocity dispersion profile from the power-law fit at a radius of about  $2R_{1/2}$ , similar to the signatures left by the shell structures discussed in the previous subsection. While the shells cause local decreases in the velocity dispersion profiles, the  $\sigma$ -bump is an area where the velocity dispersion stays constant and which thus has an enhanced velocity dispersion compared to the velocity dispersion expected from the power-law fit. An example of this  $\sigma$ -bump is shown in the right panel of Fig. 6.13 (black arrow).

In contrast to the shells, this  $\sigma$ -bump cannot be seen as a feature in the density profile of the stars (left panel of Fig. 6.13). While the shells can be seen as wiggles at radii from 20 kpc outwards at the timesteps shortly after the merger event (at 1.5 Gyr), with their intensity decreasing with time, the density profile is completely smooth at the last timestep of the simulation where the merger remnant is completely relaxed.

This also holds for the shells in the velocity dispersion profiles (right panel of Fig. 6.13), where the shells appear as strong wiggles in the profile at  $t = 2$  Gyr (blue line) and subside until they are completely gone at  $t = 6$  Gyr (yellow line). 1.5 Gyr after the first encounter, the shells are still clearly visible (see blue line), and even 1.5 Gyr after the merger even took place the shells are still visible (green line). Thus, the shells in our simulations do not vanish as quickly as predicted for the shells from minor merger events by Quinn (1984). The  $\sigma$ -bump, however, stays constant during all timesteps of the simulation after the merger took place, and thus is clearly not a shell feature. It has not been present in the velocity dispersion profile of the spiral galaxy at the beginning (see dotted black line), and thus is not a remnant of our initial conditions. We found this bump in all our binary merger simulations (see Johansson et al. 2009a,b and Sec. 2.2.1), including those without gas and without bulge components, independently of the parabolic orbit chosen for the initial spirals, see Master's Thesis by Schauer (2014b).

A similar feature seen in equal-mass binary merger simulations has been presented by Jesseit et al. (2007), who found a depression in the velocity dispersion at  $0.5 R_{\text{eff}}$ . However, apart from the fact that this depression is much farther inside the galaxy than the  $\sigma$ -bump, Jesseit et al. (2007) do not find the depression in their gasless mergers and conclude that this depression is caused by the gas component, while we find the  $\sigma$ -bump in our gas-less mergers as well (Schauer, 2014b). Also, the depression has been found mostly in face-on view, while the  $\sigma$ -bump can clearly be seen under edge-on as well as face-on view (see Schauer, Remus, et al. (2014) and Fig. A.1 in App. A.1). Therefore, it appears unlikely that both the depression and the  $\sigma$ -bump have the same origin, but further analysis will be needed to conclusively confirm this.

The  $\sigma$ -bump can also be seen in observations, as demonstrated by Schauer, Remus, et al. (2014) for galaxies where the outer velocity dispersion is probed with PNe or GCs (data from Pota et al. (2013) and Coccato et al. (2009), see also Master's Thesis by Schauer (2014a)) and afterwards reported from kinematics measured directly from the stellar light by Lane et al. (2015). However, as it is only possible to measure the velocity dispersion profile for an observed galaxy at a single instant in its life, it is not clear whether the measured velocity dispersion "bumps" are caused by shells or whether they actually are observations of the  $\sigma$ -bump-feature. For the future, it will therefore be important to understand the origin of the  $\sigma$ -bump to find a better way to distinguish between shells and the  $\sigma$ -bump for observational purposes.

The origin of the  $\sigma$ -bump is still unknown. So far, we have only been able to investigate the  $\sigma$ -bump in idealized binary major merger events. Finding the  $\sigma$ -bump in the context of a cosmological high resolution (zoom) simulation would help in understanding whether the  $\sigma$ -bump really is a feature only seen in (nearly) equal-mass merger events; this is work currently in progress (see App. A.2 for high-resolution zoom simulations performed in our group, and Sec. 2.4 for details on the high resolution simulations in *Magneticum*). In addition, a proper orbital analysis will hopefully shed light on the reason why the  $\sigma$ -bump is not visible in the density, and which kind of stellar configurations are accountable for it.

## 6.5 Summary and Discussion

In this chapter we have addressed the following three questions: First, how many tracers are needed to successfully and reliably reproduce the underlying stellar distribution of galaxies, their densities and velocity dispersions? Second, can blue globular clusters (BGCs) really be used to trace the dark matter content of a spheroidal galaxy? Third, which structures can be detected in the faint outskirts of galaxies and what information is encoded in these structures about the formation history of a galaxy?

To answer the first question, we used the initial and the final stage of one of our binary merger simulations (11 OBH2 13, see Sec. 2.2) presented by Johansson et al. (2009a), Johansson et al. (2009b) and Remus et al. (2013). The initial stage, an artificially set up spiral galaxy, has been used to test how well the tracers can reproduce the scale-height of a disk galaxy and its line-of-sight velocity distribution. The final stage, a relaxed spheroidal as the end-product of the merger between two equal-mass spiral galaxies, was utilised to test how well the tracers can reproduce the surface density profiles of spheroidal galaxies and how well the power-law and Sérsic fits to the tracer populations represent the respective fits to the real underlying surface density profiles. For these tests, we randomly drew five different numbers of stars,  $N = 20, 50, 100, 500,$  and  $1000$ , from the parent sample to be used as tracers and repeated the experiment 100 times for each of the five numbers of tracers. For those 100 experiments for each of the five different numbers  $N$  of tracer particles, we performed the fits and compared the resulting scale heights, power-law slopes and Sérsic indices to the “true” results found from the fits to the total sample of stars.

We find that a number of  $N = 20$  tracers is not sufficient at all to adequately reproduce any of those three quantities, and that with  $N = 50$  tracers the probability is still high to obtain strongly over- or underestimated results. For  $N = 500$  or more tracers we find a generally very good agreement of the quantities calculated from the tracers with those calculated from the full stellar samples. For  $N = 100$  tracers, the likelihood for good results for the scale height and the power-law slopes is already very good, while the probability for a misfit of the Sérsic index compared to the real value is still high, but the fit is better whenever tracers at larger radii are present. This is due to the fact that the Sérsic profile is curved and thus needs tracers in a broad range of radii to successfully reproduce the curvature. Thus, the more tracer particles that can be used, the higher the likelihood for good representations of the underlying profiles;  $N = 100$  tracers is already sufficient in most cases to obtain a reliable result. However, we caution that the distribution of the tracers can lead to misinterpreting an aggregation of tracers as representing a substructure, since we several times found a number of tracers in close proximity to each other in the halo, even though our test-galaxies do not have any substructures in the outskirts.

To investigate the second question, we used the spheroidals from the Magneticum simulation Box4 uhr (see Sec. 2.4) with total masses larger than  $M_{\text{tot}} = 5 \times 10^{11} M_{\odot}$ . For those spheroidals, we calculated the dark matter fraction  $f_{\text{DM}}$  within  $5 R_{1/2}$  and fitted a power-law to the radial density profile in a radius range from  $2 R_{1/2}$  to  $5 R_{1/2}$ , for the stellar component, the dark matter component, and the combined stellar and dark matter profile. We compared the slopes of those power-law fits,  $\gamma_{\text{tot}}, \gamma_{*}$  and  $\gamma_{\text{DM}}$ , and the dark matter fractions with the dark matter fractions and power-law slopes calculated from the observed tracer populations by Deason et al. (2012) for the same radial ranges. In addition, we calculated the power-law slopes of the surface density profiles for three galaxies presented by Pota et al. (2013) and the galaxy presented by Napolitano et al. (2014), and included those galaxies in the comparison. To obtain the density fits from the surface density, we added  $-1$  to the slope calculated for the surface density profiles.

Our analysis clearly showed that none of the tracers, neither PNe nor RGCs or BGCs, actually represent the surface density profile of the dark matter component, and that they also do not trace the total density profiles. Instead, we show that all tracers actually do represent the stellar density profiles, with the observed values covering the whole range of stellar density slopes found for our Magellanic spheroidals. To understand which components of the stellar content of a spheroidal the different tracers actually trace, especially in the light of new studies like SLUGGS (Brodie et al., 2014) and comparison studies between the different tracers (e.g., Coccato et al., 2013), a decomposition of the stellar components in our simulations including metallicity, color and age gradients for the stars would be needed. We speculate that the BGCs, which have been shown from observations to clearly behave differently than PNe and RGCs (e.g., Peng et al. 2006; Schuberth et al. 2010; Blom et al. 2012b,a; Pota et al. 2013; Richtler et al. 2015), might actually be excellent tracers for the density profiles of the (accreted) stellar halo of their host galaxies, while the PNe and the RGCs trace the central bulge components. Nevertheless, we cannot disprove that the BGCs could actually trace the kinematics of the dark matter halo, as a much more detailed study of the potential and the velocity profiles would be needed, which is clearly beyond the scope of this work. In any case, further studies on this topic are needed especially in view of upcoming large tracer surveys like SLUGGS.

The last question was explored using the same binary simulation as for the first question, but this time we used a timestep of about 1.5 Gyr after the spiral-spiral merger event (i.e., 2.5 Gyr after the first encounter). At this timestep, the central part of the galaxy has already relaxed, while the outskirts still show several residuals of the merger event, most dominantly the shell-structures. The structures in the outskirts of the remnant clearly resemble observed spheroidals surrounded by shells (e.g., Arp 1966; Duc et al. 2015), however, our shells are formed in a major merger and not in a minor merging event as investigated in previous studies (e.g., Quinn 1984; Athanassoula & Bosma 1985; Ebrova et al. 2010). The signatures of the shells can be found in the stellar density and velocity dispersion profiles of our spheroidals as enhancements and depressions respectively, and in the phase-space diagram. Those shells are expected to disperse on timescales of 1 . . . 2 Gyr (Quinn, 1984) after the first encounter of the galaxies, however, the shells formed in our merger event still are prominent at 3 Gyr after the first encounter. A more detailed analysis of the lifetimes and morphologies of these shells is therefore needed to understand the information about the merger history encoded in the outskirts of galaxies.

Additionally, we report a new feature found in the velocity dispersion profiles of our merger remnants, the  $\sigma$ -bump (Schauer, Remus, et al. (2014), see also App. A.1 and Master’s Thesis of Schauer (2014b)). The  $\sigma$ -bump is an area of constant velocity dispersion at 1 . . . 3  $R_{1/2}$  in the stellar radial velocity dispersion profile, which does not have a counterpart visible in the stellar density profile. It can be found in all merger remnants presented by Johansson et al. (2009a) and Johansson et al. (2009b), even in the gasless or bulgeless setups, and stays unchanged in time once it is formed, which proves that it is of a nature distinct from the shells. This feature, whose origin is still unknown, is clearly different from the  $\sigma$ -depression reported by Jesseit et al. (2007), and its origin needs to be investigated in future studies. Schauer, Remus, et al. (2014) showed that features similar to the  $\sigma$ -bump can be found in observations of stellar radial velocity dispersions using tracer populations (Coccato et al. 2009; Pota et al. 2013), and recently Lane et al. (2015) reported a similar feature found in an observation of stellar light at the outskirts of an elliptical galaxy. However, it is observationally difficult to distinguish between a shell and the  $\sigma$ -bump, as long as the stellar light cannot be mapped in detail and only tracers can be used. Therefore, more advanced cosmological zoom-simulations are needed, including metals and winds, to test whether the  $\sigma$ -bump can be found in the metallicity gradients or other observables and to understand whether it really is a feature indicating a major

merging event or whether it can be caused by minor mergers as well.

We conclude that the outer stellar halos and the information that is encoded in them about the formation history of their host galaxies is an important field of research, which is still in its infancy. Tracers like PNe and GCs, if present in sufficient numbers, can give valuable insight into those otherwise difficult to observe parts of a galaxy, but more effort is needed to understand which parts of a galaxy the different tracers actually map. Detailed comparisons between observations and simulations along with a close collaboration between observers and theorists are needed to decipher the rich information encoded in those beautiful but faint structures, and will be an interesting field of work for the future.



## Chapter 7

# Summary, Discussion and Conclusions

This dissertation was dedicated to understanding the information that is encoded in the outer regions of massive galaxies, with the main focus on early-type galaxies. To reach this goal, we analysed galaxies from different sets of simulations: We used isolated binary merger simulations to study the impact of physical processes in idealized setups, fully hydrodynamical cosmological zoom-simulations of selected galaxies from a large cosmological dark-matter-only parent simulation to study galaxy formation in a cosmological context in high resolution, and also a fully hydrodynamical cosmological box with a statistically significant amount of all morphological kinds of galaxies.

In the course of this work we addressed two big questions: First, we studied the total radial density and velocity dispersion profiles of spheroidal galaxies at present day to infer what we can learn from these profiles about the interplay between the dark matter and stellar components and the amount and kind of merger events and their correlation with basic properties like mass, size, and dark matter fractions. The results were presented in Chap. 3 (Remus et al., 2013) and Chap. 4. Second, we analysed the stellar outer halos of massive galaxies in detail in order to extract the information about the formation processes that is stored in the outskirts of galaxies, since at the outskirts the relaxation timescales are the longest and thus they best preserve the information about the history of a galaxy. The studies centered around this question are presented in Chap. 5 and Chap. 6.

Regarding the first question, we find that all spheroidal galaxies from our simulations, regardless of the implemented physics, are close to isothermal, that is their total (combined stellar and dark matter) radial velocity dispersion profiles are flat. This holds true at least for  $z \lesssim 2$ . The total radial density profiles of spheroidals at present day can be well described by a power law  $\rho \propto r^{\gamma_{\text{tot}}}$  with  $\gamma_{\text{tot}} = -2$  over a large radius range, as expected from hydrostatic equilibrium, in good agreement with observations from dynamical modeling of Coma cluster early-type galaxies (Thomas et al., 2007) and strong lensing measurements (Auger et al. 2010; Barnabè et al. 2011; Ruff et al. 2011; Sonnenfeld et al. 2013b). However, there is a tendency towards steeper slopes for less massive, compact galaxies.

We also see the effect of adiabatic contraction of the dark matter: in comparison to the simulations with the same initial conditions including baryons, the halos from the dark-matter-only simulations always have flatter slopes than their counterparts with baryons. Therefore we conclude that the baryons play an important role in reordering the global structures of the dark matter halos, since the gas can cool into the center of the halos and form stars, and in the process steepen the total potential in the center. This forces the dark matter particles to “reorder” their orbits and adjust to the new potential, since the dark matter cannot radiate away its energy.

We used the isolated binary merger simulations to understand the influence of (cold) gas on the

slope of the total density profile and found that the presence of gas during merging events clearly causes a steepening of the density slopes. This is due to the fact that the gas falls into the center, where it forms stars and thus enhances the amount of stars mostly in the inner regions of the galaxies, which leads to a steepening of the total density profile mostly in its inner regions. The less gas is involved in a merger event, the less star formation is induced in the central regions and the more important is the contribution of stars that are accreted in the outskirts without enhancing the inner parts of the galaxy. Thus, dry mergers tend to flatten the slopes of the total density profiles. This idea is supported by the fact that we find clear correlations between the steepness of the total density slopes, the central dark matter fractions, and the fractions of stars formed in-situ (i.e., inside the host galaxy, in comparison to stars which form inside other galaxies and are later accreted onto the host galaxy). The more stars are formed in-situ, the smaller are the central dark matter fractions and the steeper is the total density slope. Therefore, the mass accretion history of a galaxy determines its central dark matter fraction, its in-situ fractions, and the steepness of the slope of the total density profile of the galaxy. We find only a very weak correlation between the central dark matter fraction and the stellar mass of a galaxy, which supports the idea that not the mass but the mass accretion history is the most important ingredient.

We find that dry merging drives the slopes of the total density profiles towards  $\gamma_{\text{tot}} = -2$ . Once the slope reaches  $\gamma_{\text{tot}} = -2$  additional merging changes the slope only temporarily and it returns to  $\gamma_{\text{tot}} = -2$  after relaxation. Therefore, we conclude that a total density profile with a slope of  $\gamma_{\text{tot}} = -2$  is an attractor state, which is independent of the mass of a galaxy, and suggest that all spheroidal galaxies will end up in such a state at some point in their lives. Spheroidals which have a steep total density slope at present day therefore did not have much (dry) merging in the second phase of their evolution (Oser et al., 2010) and thus the present-day total density slope of spheroidals can be used as a measurement of the importance of mergers during the second phase of a spheroidals formation history.

In the observational sample of Coma cluster early-type galaxies, a few of the observed galaxies cannot properly be described by the spheroidals selected from our simulations, namely those that have a small dark matter fraction but a flat total density slope. There are two possible explanations for this inability to reproduce those galaxies: The first reason could be that we simply did not include those galaxies in our analysis, since we only used spheroidals which sit in the centers of their halo potentials and did not analyse satellite galaxies, while all of the galaxies from the observational study are satellites inside the cluster potential. We would expect those galaxies to have lost a significant amount of their dark matter already due to stripping in the cluster potential, and this might explain the low dark matter fractions. Their flat slopes could be explained by the fact that their total density slope in the outskirts is dominated by the cluster potential and not by the galaxies' own halos, as normally we would expect the profiles to become steeper due to stripping. The second possible cause for this difference between simulations and observations could be that the IMF is not constant. This would change the results of the measured dark matter fractions from observations significantly, and could shift those galaxies into the range of dark matter fractions found in the simulated sample. Nevertheless, at the current stage we cannot tell which explanation is the right one, or whether it may even be a combination of both.

At higher redshifts, we generally find steeper slopes than  $\gamma_{\text{tot}} = -2$ , which we would expect since the available amount of gas is much higher and thus the star formation even in spheroidals is still higher than at present day. However, our result is in contradiction with observational results from strong lensing. To understand this discrepancy, we used the same technique that the observers

use for their analysis (kindly provided by A. Sonnenfeld) to produce “mock” observations from our simulations. We find that this technique provides slopes that tend to be much flatter than the real slopes measured from the simulations in case of spheroidals which have a steep slope, that is the technique usually provides total density slopes of about  $\gamma_{\text{tot}} = -2$  for our simulated galaxies seemingly independent of the real slope. To understand the reason for this result we are currently working closely with the observers to solve this problem.

Regarding the second question of this thesis, we find that the outer stellar density profiles of all galaxies independent of their individual morphology generally have a universal, curved exponential shape which can be well described by an Einasto profile (Einasto, 1965). This has been studied for the first time in the course of this work due to the previous lack of full baryonic simulations with the proper resolution and a statistically meaningful number of galaxies. While for the dark matter it has been known for some time that the density profile is better described by an Einasto profile than a NFW profile, this result is new for the stellar halo. We find the density profiles of the stellar halos to always be curved more strongly than their dark matter counterparts, and there is no correlation between the free parameters of the Einasto profile fits to the dark matter and those of the fits to the stellar halo. For the free parameters of the Einasto profile fits to the stellar halo, however, we find a tight correlation between the scale radius and the curvature parameter, indicating that the parameters actually are not independent but correlated through the mass accretion history, where the exact shape of the correlation depends only on the total mass of the system. The profiles of more compact stellar halos are curved more strongly, and we interpret this to be an indication for the amount of stellar mass accreted onto the outskirts of a galaxy: similar to the total halo, the stellar halo mostly grows through accretion, since the star formation only feeds the central part of the galaxy. This also explains why the outer stellar halo always has the same shape independent of the morphology of the galaxy in its center. The more accretion happens in the outskirts, and the more satellites or streams are present, the less curved is the density profile of the outer stellar halo, similar to our results for the total stellar and dark matter density profiles of spheroidal galaxies. We conclude that the outer stellar halo “knows” a lot about the formation and mass accretion history of a galaxy. Unfortunately, the Einasto profile does not offer a clear-cut way to uniquely define a concentration of the (stellar) halo because for the same scale radius, different curvatures are possible. Therefore, in order to get the concentration information, the correlation between the two parameters has to be understood in more detail to construct concentration information directly from the profiles.

Since the density profile of the stellar halo is curved, especially in the outskirts, any small enough region of the profile can be well approximated by a power-law fit but with different slopes. Those power-laws become steeper the further outside the fit is performed. For Milky Way mass halos at a radius range of 50 to 100 kpc those power-laws usually have slopes of  $-5 > \gamma_{\text{stellar halo}} > -6$ , which agrees well with the results found for the Milky Way (Deason et al., 2014), but flatter slopes are possible in the presence of substructures like streams or satellites. This is the case for Andromeda, and we also find Andromeda-like slopes in our range of slopes of power-law fits to our simulated spheroidals of Milky Way mass.

To decode the information included in the stellar halos, the analysis of “wiggles” in the stellar density and velocity dispersion profiles is a helpful tool, since structures like shells or features like the  $\sigma$ -bump (Schauer, Remus, et al., 2014) leave clear signatures in at least one of those profiles. However, those profiles are observationally very difficult to measure since the outer stellar halos have very low luminosities and densities, and (nearly) no star formation, that is they consist mostly of old stars. Therefore, tracers like planetary nebulae or globular clusters are needed to measure the

profiles, but we showed that the number of tracers must be high (100 tracers is the lower limit) to detect the “wiggles” with sufficient significance. Also, the question needs to be answered which part of the galaxies the different tracers actually represent, since this is crucial for the interpretation of the resulting density and velocity dispersion profiles. We found that none of the tracers, not even the blue globular clusters, trace the dark matter density content of the galaxies, but they all clearly trace different parts of their stellar content.

In case of a sufficient amount of tracers, shells can be detected. However, shells can result from minor as well as major merger events. To extract the information about the merger history that is contained in the observed shells, more detailed studies of the shells are needed before it is possible to distinguish between their different formation scenarios. With the  $\sigma$ -bump we have introduced a feature which indicates a major merger event, although this feature is observationally difficult to distinguish from shells if no confirmation from direct observations of the stellar content is possible. We find that the stellar halos of galaxies contain a multitude of information about the mass accretion and formation histories of galaxies, however, more detailed studies of this matter are needed to disentangle the information originating from the different mechanisms and successfully interpret the observations.



From the studies presented in this thesis we conclude that early-type galaxies are generally isothermal and that there exists a universal attractor state for the total radial density distribution of early-type galaxies, namely a profile where  $\rho \propto r^{\gamma_{\text{tot}}}$  with  $\gamma_{\text{tot}} = -2$  over a large radial range independent of the individual stellar mass distribution of the galaxies. At higher redshifts, the slopes of the total density distributions are generally flatter than  $\gamma_{\text{tot}} = -2$ . The attractor state of  $\gamma_{\text{tot}} = -2$  is reached through dry merging events, since each dry merging event flattens the slope until it reaches  $\gamma_{\text{tot}} = -2$ , while gas rich merger events steepen the slope due to the induced in-situ star formation in the center of the remnant galaxy. Therefore, the merger history of an early-type galaxy is encoded in its total density slope. Flat slopes imply high central dark matter fractions and low amounts of stars formed in-situ, and steep slopes vice versa.

Generally, this is independent of the mass of a galaxy, however, since multiple dry mergers are needed to reach the attractor state, the systems with more mass tend to be more evolved. This is true for all redshifts, but since there is much more gas available at high redshifts, the slopes of the early-type galaxies tend to be generally steeper, their central dark matter fractions are lower and their amount of stars formed in-situ is larger. This proves that the systems evolve to this attractor state automatically in a  $\Lambda$ CDM universe. This would not be the case if gravity was not constant for all masses and distances. Therefore, our result provides an excellent test case for  $\Lambda$ CDM, which already has strong support from strong lensing observations.

We also found that there exists a universal radial density profile for the stellar outer halos of all galaxies independent of the morphology of the central galaxy. Its shape can be well described by the Einasto profile, i.e., it follows a curved exponential instead of a power-law. We suggest that the amount of curvature is due to the amount of dry merging and substructures present in the outskirts, namely the more dry mergers and substructures there are, the less curved the profile.

The outskirts of galaxies encode much more information about the individual galaxy formation history, and need to be studied more extensively in the future, especially emphasizing the different characteristics of major and minor merger events as well as smooth accretion, and understanding the impact of gas-rich or gas-poor accretion events. Also, the origin of the total density profile attractor for early-type galaxies needs to be understood as well as the mechanisms that are causing the correla-

tion of the parameters in the Einasto profile for the outer stellar halos, since there might be important information about the mass accretion history of galaxies of all morphological types encoded in this correlation. Additionally, metallicity gradients could provide significant information about the evolution of the galaxies, and with new simulations like *Magneticum* it has become possible to study this in detail in the future. This can also help to answer the question what the different kinds of observed tracers really trace and what kind of information can be gained from them, on our journey of understanding the formation and evolution of galaxies through cosmic time, their morphological changes and their interplay with the environments they are living in.



# Appendix A

## Additional work

This Appendix is a compilation of studies I have been involved in during the course of my PhD. Some of those studies are already published, some are to be submitted soon, as indicated in the footnote to each section.

The first four studies are connected to the Master's Theses of A. T. P. Schauer (Sec. A.1), D. P. Schlachtberger (Sec. A.2), F. Schulze (Sec. A.3) and A. F. Teklu (Sec. A.4), where I directly supervised the work. I am second author on the publications in the first and the last case, and in case of the second study I will be the first author of the publication since the student left the field without writing up his results for a refereed journal article, and since the topic of his work was taken directly from the main body of my own thesis subject. I will also briefly present four other studies where I have been involved in the parts that focus on galaxy evolution and dynamics. The short presentation of these studies provided in this work will mostly be centered around those aspects.

The studies are ordered starting with those closest to the main topic of my work, namely dynamics of elliptical galaxies. The first study analyses a dynamical feature in simulated spheroidals formed in major merger events (Sec. A.1), the second is dedicated to the question of the origin of the cold gas content that has been observed in many elliptical galaxies lately (Sec. A.2), the third is concerned with a detailed analysis of the origin of kinematic features of spheroidal galaxies (Sec. A.3), and the fourth study is focussed on the connection between the spin parameter of the host halo and the dynamical properties of its central galaxy (Sec. A.4). In Sec. A.5 I present an overview of the properties of the galaxies found in the new Magneticum Pathfinder simulations. The technical details of this set of simulations are described in detail in Sec. 2.4 of this thesis and thus I will only present the scientific results here, similar to what I have presented in my contribution to the proceedings of the IAU symposium 309 (Remus et al., 2015a). Sec. A.6 presents a modified sub-grid model for black holes in simulations and its effect on the star formation properties of the galaxies, and in Sec. A.7 the question of the origin of the magnetic fields in voids is addressed. In the final section, Sec. A.8, a new modified SPH treatment is presented with the focus on the influence of the modifications to the simulation code on the dynamical properties of galaxies.

## A.1 The Mystery of the $\sigma$ -Bump\*

In general, the radial stellar velocity dispersion profile of a spheroidal galaxy can be described by a single power law  $\sigma \propto r^\beta$ . This has been shown in observations to usually be a good approximation out to large radii, nevertheless, deviations from this power-law profile have been observed as well. Those could be caused by shell-structures, as observed for example by Malin & Carter (1980), originating from recent merger events (Quinn, 1984). Another possible interpretation of such a deviation could be the  $\sigma$ -bump which is introduced by Schauer, Remus, et al. (2014), where we used 10 spheroidal galaxies formed in isolated binary merger simulations presented in Johansson et al. (2009a) and Johansson et al. (2009b) to study the radial velocity dispersion profiles of spheroidal galaxies.

The  $\sigma$ -bump, as also shown in Sec. 6.4.2 of this PhD thesis, is a deviation of the radial stellar velocity dispersion from the power-law behaviour in form of a constant plateau or slight enhancement at radii around  $2 R_{1/2}$ . This is shown in the upper right panel of Fig. A.1 for one example galaxy from our simulations as black solid line with the best-fitting power-law to the radial velocity dispersion profile included as black dashed line. In contrast to the shell structures, which can also be seen in this figure as wiggles at the outer part of the velocity dispersion profile, the  $\sigma$ -bump does not change in time (see also Fig. 6.13 and Sec. 6.4.2) but remains constant in strength and place, as shown in Fig. 3 of Schauer, Remus, et al. (2014).

In addition, it is long lived and solely visible in the stellar component (see Fig. 1 of Schauer, Remus, et al. (2014)), i.e., no comparable feature can be found in the velocity dispersion profiles of the dark matter or the gas. As shown in Sec. 6.4.2 of this PhD thesis, the  $\sigma$ -bump has no counterpart in the radial stellar density profiles of our simulated spheroidal. It can be seen in the line-of-sight velocity dispersion under all projections, being the weakest if seen face-on and strongest if seen edge-on, however, the changes in prominence are only very small, as shown in the upper left panel of Fig. A.1 as colored lines. Even under projections, the  $\sigma$ -bump still is clearly identifiable.

We find this feature in all our simulations to different extents, with the  $\sigma$ -bump being most prominent in mergers of equal mass, and less prominent in the remnants of 3:1 mass mergers. Nevertheless, the feature is present in all 10 simulations, including those without gas or bulge components. We therefore concluded in Schauer, Remus, et al. (2014) that the  $\sigma$ -bump is a purely stellar feature, and most likely the characteristic of a major merger event.

Since we found the  $\sigma$ -bump to be prominent in radial line-of-sight velocity dispersion profiles as well, we investigated observations from Pota et al. (2013) who presented radial line-of-sight velocity dispersion profiles out to large radii for observed galaxies, measured from stellar light at the central parts and red and blue globular clusters at the outskirts. Since the  $\sigma$ -bump is a feature in the outskirts of galaxies, our comparison sample was limited to those spheroidals where the tracers are available at large radii in sufficient numbers to construct the velocity dispersion profiles, as it is critical to not only see the plateau of the  $\sigma$ -bump but also its decline at radii of at least  $3-4 R_{\text{eff}}$ .

We found a  $\sigma$ -bump in 4 of the 12 galaxies studied by Pota et al. (2013), as shown in the upper right and both lower panels of Fig. A.1 for the three most prominent examples, while 3 of those 12 galaxies clearly have no  $\sigma$ -bump. For the other 5 galaxies of that work we cannot draw any conclusions since the number of tracers is too low to get a clear result. If possible, we included the measurements from planetary nebulae tracers in the analysis, as done for NGC 821 (see lower left panel of Fig. A.1

---

\* The results of this Master's Thesis by Schauer (2014b) have been published as *The Mystery of the  $\sigma$ -Bump – A New Signature for Major Mergers in Early-type Galaxies?* by A. T. P. Schauer, **R.-S. Remus**, A. Burkert & P. H. Johansson, ApJ Letters 783, 32.

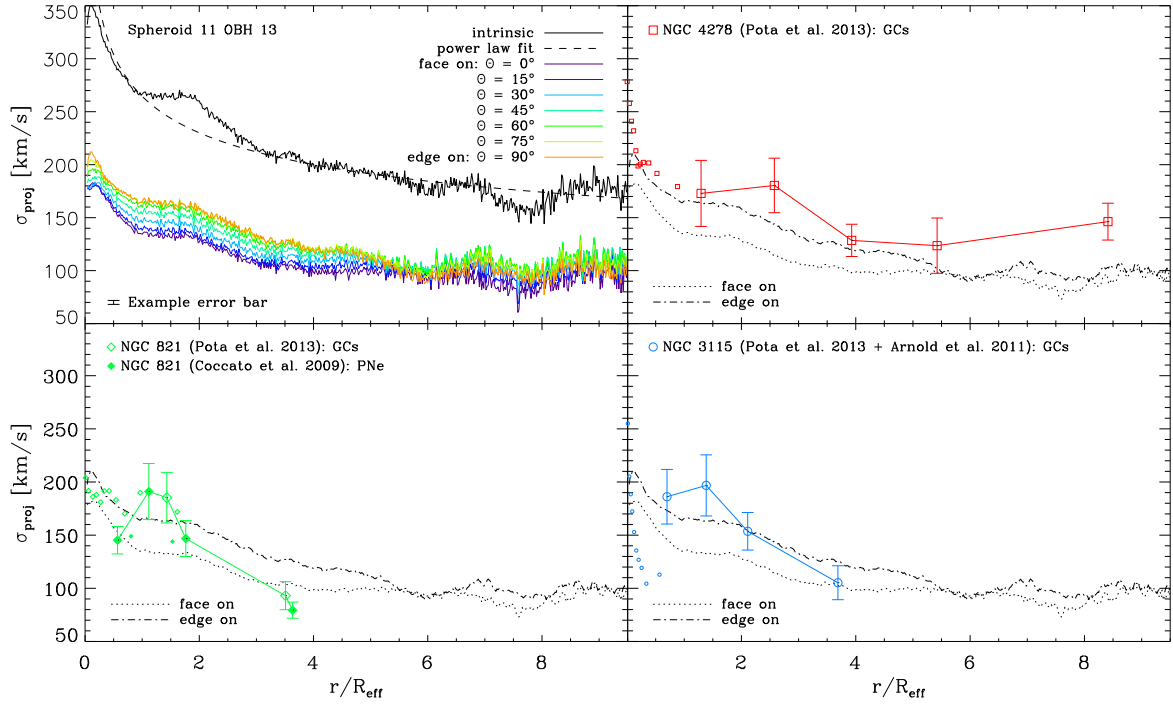


**Figure A.1:** Fig. 4 from Schauer, Remus, et al. (2014). Stellar velocity dispersion versus radius in units of the halfmass radius  $R_{\text{eff}}$ . **Upper left panel:** For the Binary Merger elliptical 11 OBH 13, at different projection angles (from face on (violet line) to edge on (orange line)). The black line is the intrinsic stellar velocity dispersion profile, with the dashed black line the power-law fit to the intrinsic profile. **Other panels:** For three different observed galaxies where a  $\sigma$ -bump might be detected from GCs (large open symbols) surveys, with additional stellar data shown as open small symbols, see Schauer, Remus, et al. (2014) for more details. Black dash-dotted lines show the edge- and face-on projections from the left panel. **Upper right panel:** for NGC 4278, GC data from Pota et al. (2013). **Lower left panel:** for NGC 821, GC data from Pota et al. (2013), with additional PNe data from Coccato et al. (2009) (large filled diamonds). **Lower right panel:** for NGC 3115, GC data from Pota et al. (2013) and Arnold et al. (2011).

with PNe data from Coccato et al. (2009)). Interestingly, the  $\sigma$ -bump could never be found in the radial line-of-sight velocity dispersion profiles from blue globular clusters, but only for the profiles from red globular clusters. However, from this analysis we cannot doubtlessly declare those observed bumps to be identical with our  $\sigma$ -bump, since shell structures would cause signatures in the radial velocity dispersion profiles, albeit the shell-induced signatures should also show depressions in the line-of-sight velocity dispersion and not only enhancements.

We conclude that the  $\sigma$ -bump is a signature left by major merger events in the radial velocity dispersion profiles of spheroidal galaxies and therefore could be used to identify those spheroidals formed in major merger scenarios in comparison to those formed through multiple minor merger events. However, the origin of the  $\sigma$ -bump remains to be investigated in more detail in the future.

## A.2 The Origin of the Cold Gas in Isolated Elliptical Galaxies<sup>†</sup>

Early-type galaxies are known to be mostly “red and dead”, meaning their cold gas content is relatively low compared to disk galaxies, and most of their gas mass is inside their surrounding hot halo. Some early-type galaxies have a small fraction of cold, even star forming gas, but the star formation rates are usually low (e.g., Knapp, 1999). Recently, new detailed observations in the context of the Atlas<sup>3D</sup> survey (Cappellari et al., 2011a) have show that between 22% (Young et al., 2011) and 40% (Young et al., 2013) of all early-type galaxies in the survey host a cold gas disk. These cold gas disks usually contain  $M_{\text{Cold gas}} = 10^7 \dots 10^9 M_{\odot}$ , (for comparison, the Milky Way has  $M_{\text{Cold gas}}^{\text{MW}} \simeq 10^9 M_{\odot}$ ) and the presence is independent of other internal dynamical properties tested in the survey (Krajnović et al. 2011; Emsellem et al. 2011). Usually, the early-type galaxies that host the largest cold gas masses live in environments with low densities (Young et al. 2011, 2013). The angular momentum vectors of the stellar and cold-gas components of galaxies in dense environments (for example in the Virgo cluster) generally are aligned, while 50% of all field early-type galaxies show a misalignment between those angular momentum vectors (Davis et al., 2011), similar to the result found for the alignment of the angular momentum vectors of stars and cold gas for the Magneticum spheroidals (see Sec. A.4). This indicates that the cold gas in early-type galaxies in dense environments could have an internal origin, e.g., from cooling from the halo as seen for example in the Phoenix cluster BCG (McDonald et al. 2012, 2014) or the Perseus Cluster galaxy NGC 1275 (e.g., Lim et al., 2008), probably enhanced due to dusty ejections from the stars (Mathews & Brighenti, 2003). In contrast, the misalignment of the angular momentum vectors of the stars and the gas suggests an external origin through merging and/or smooth accretion (e.g., cold streams, Dekel et al. (2009)). With more advanced observational instruments and methods, even the mapping of the individual clouds inside the gas disks of spheroidals becomes possible (Utomo et al., 2015), and therefore the question of the origin of the cold gas in spheroidal galaxies becomes important.

To investigate the origin of the cold gas in field galaxies, we selected four isolated massive galaxies ( $M_{\text{tot}} \approx 1 \times 10^{13} M_{\odot}$ ) in a void environment from the dark-matter-only cosmological simulation Dianoga (Borgani & Viel, 2009) at  $z = 0$  and performed full baryonic zoom-simulations (see Sec. 2.3) with very high resolutions ( $M_{\text{part}}^{\text{DM}} = 4 \times 10^6 h^{-1} M_{\odot}$  and  $M_{\text{part}}^{\text{Gas}} = 6.2 \times 10^5 h^{-1} M_{\odot}$ ) using a modified version of GADGET-3. We adapted a  $\Lambda$ CDM cosmology with  $h = 0.72$ ,  $\Omega_{\Lambda} = 0.76$  and  $\Omega_{\text{m}} = 0.24$  with a baryon fraction of  $f_{\text{bar}} = 0.04$ . The selection was made such that the galaxies hosted inside these halos have to be spheroidals due to the mass range, and due to the isolation criterion the computational time for the zoom-simulations was manageable.

All four simulated galaxies are spheroidals at  $z = 0$ , but have very different formation histories. One is formed in a classical major merger scenario (merger at  $z = 0.5$ ), another one is formed only through continuous minor merging until present day. The third galaxy has accreted most of its mass already at a redshift of about  $z = 1.5$  with a quiet, nearly merger-less history afterwards, while the last galaxy has just recently finished a massive merger event. One example of our galaxies at  $z = 0$  is shown in the left panel of Fig. A.2 in an edge-on projection as density map, colored according to the stellar density. In all four galaxies we find gas disks, ranging from  $M_{\text{Cold Gas}} = 0.4 \times 10^9 M_{\odot}$  to  $M_{\text{Cold Gas}} = 1.2 \times 10^9 M_{\odot}$ , independent of the individual formation scenarios. The stellar-mass to gas-mass fractions agree well with the values for massive red-sequence galaxies presented in Wei et al. (2010). In three of the four cases, we see a misalignment between the orientation of the stellar structure

<sup>†</sup> The results of this Master’s Thesis by Schlachtberger (2014) will be submitted as *The Origin of the Cold Gas in Isolated Elliptical Galaxies* by **R.-S. Remus**, D. P. Schlachtberger & K. Dolag

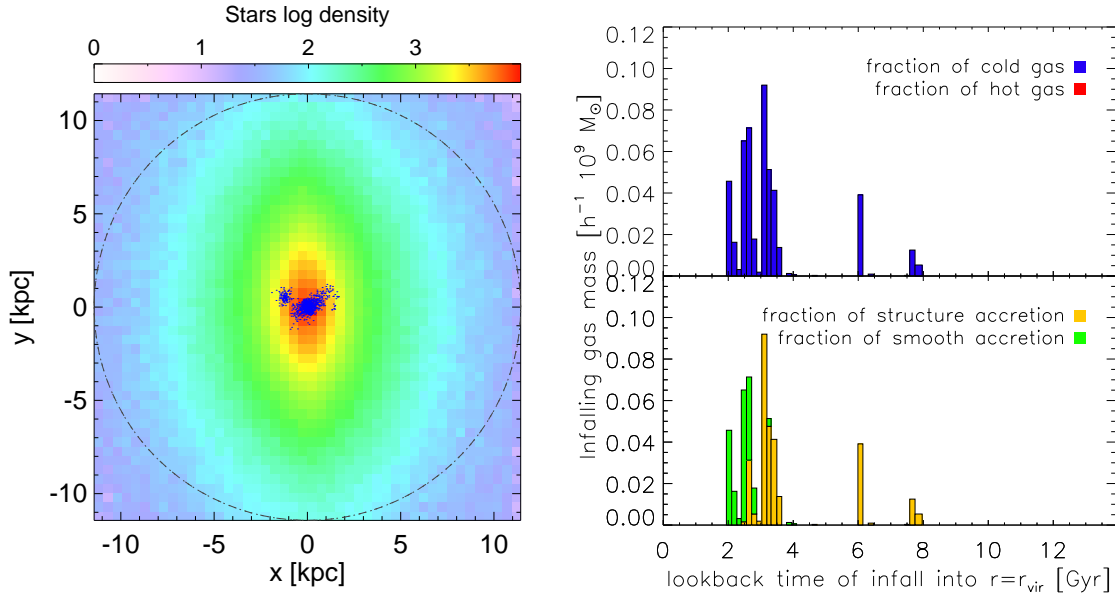


**Figure A.2:** *Left panel:* Projection of the mass weighted stellar density distribution of one example from our four zoom-simulations. The cold gas particles are shown as blue dots, and the dashed circle marks the halfmass radius. *Right panels:* Infall time of the cold gas that is present in the gas disk of the spheroidal galaxy shown in the left panel into the virial radius  $r_{\text{vir}}$  (lookback time). In the upper panel, the color indicates if the gas is cold ( $T_{\text{Gas}} < 5 \times 10^5$  K, blue) or hot ( $T_{\text{Gas}} > 5 \times 10^5$  K, red) at the time of infall. In the lower panel, the color indicates if the gas was accreted bound to a substructure (yellow) or smoothly (green).

and the gas disk, as shown in the left panel of Fig. A.2 (gas particles are shown as blue points), in agreement with the observations. This supports the idea of an external origin of the (misaligned) cold gas in field early-type galaxies and is in agreement with the results from semi-analytic models presented in Lagos et al. 2014, 2015.

To investigate the origin of the cold gas we traced all cold gas particles inside the galaxies at  $z = 0$  back in time to find the time of their accretion into the virial radius  $r_{\text{vir}}$ . If the temperature of the gas particle is  $T_{\text{Gas}} < 5 \times 10^5$  K then we call it cold, if  $T_{\text{Gas}} > 5 \times 10^5$  K we call it hot. As can be seen in the upper right panel of Fig. A.2 all of the gas that is in the cold disk at  $z = 0$  was already cold at its time of accretion. In the lower panel we show the results from the test if the gas was accreted while bound to an infalling substructure (yellow) or as part of a smooth cold stream (green). We find that both feeding mechanisms are present in our galaxy. No gas which is inside the gas disk at  $z = 0$  has fallen into the halo less than 2 Gyr ago, which is simply due to the fact that the gas that fell into the halo more recently did not have enough time to reach the center (the free-fall time in our galaxies is approx.  $t_{\text{ff}} \approx 2.6$  Gyr, Binney & Tremaine 2008, p.268). Generally, most of this cold gas was accreted relatively late, namely around the free-fall time, and only a small fraction is inside the halos longer than  $2 t_{\text{ff}}$ . Those gas particles, that have been inside the halo for the longest time where usually accreted in the vicinity of a substructure. Tracing the temperature of those gas particles during their lifetime inside the halo reveals that they never got heated up to high temperatures, proving that, at least for our four examples of isolated spheroidals, the hot mode accretion and cooling from the halo

do not play a role.

In summary, we find no cooling from the halo, but only accretion of cold gas from both streams and merging satellites with similar likelihood. In case of cold gas accretion through merging substructures, the main sources interestingly are not the most massive satellites accreted during the late formation history of the galaxy but small substructures which do not contribute strongly to the mass growth. In case of cold gas accreted from streams, we find, in disagreement with the work presented by Dekel & Birnboim (2006), that the cold streams can still penetrate the hot halo and reach the central galaxy, although the halo masses of all our galaxies are well above  $M_{\text{tot}} > 10^{12} M_{\odot}$ . However, the amount of cold gas accreted through those streams is much smaller than for less massive galaxies. We conclude that the gas in isolated galaxies is most likely of external origin, and that this explains the random orientations of the gas disks with respect to the main stellar body. The environment seems to be the most important driver of the feeding mechanisms, while the formation scenario does not have an impact on the existence of a cold gas disk. Nevertheless, these simulations were performed without black holes and AGN feedback, metal cooling or stellar feedback and winds, and thus the behaviour might change if those physics are included. We therefore are currently performing the same simulations including these models, and that analysis will be included in the forthcoming paper.



### A.3 The Dynamics of Spheroidal Galaxies from Cosmological Simulations<sup>‡‡</sup>

One of the main results from the study of the two-dimensional velocity maps of early-type galaxies in the Atlas<sup>3D</sup> survey is the classification of spheroidal galaxies in fast and slow rotators, and the recognition that the fast rotators have similar velocity and velocity dispersion properties as disk galaxies (Emsellem et al., 2011; Cappellari et al., 2011b). The survey is accompanied by comparison studies of simulated spheroidal galaxies, namely spheroidals from isolated binary merger simulations (Bois et al., 2011) and spheroidals from zoom-simulations (Naab et al., 2014).

For the isolated binary mergers, Bois et al. (2011) showed that they can successfully reproduce fast rotators with high ellipticities in disc mergers with mass ratios of 3 : 1 or larger, and fast rotators with intermediate ellipticities in major merger events. They can also produce slow rotators in binary disk major merger events; however, those are usually of high ellipticities and exhibit kinematically distinct cores. Therefore, those binary major mergers can explain the origin of the observed class of  $2\sigma$ -galaxies (see Krajnović et al. 2011 and Sec. 1.2.3), but they cannot reproduce the other types of slow rotators. Binary remergers of spheroidal galaxies can form round fast rotators and those slow rotators with the highest  $\lambda_R$  (see Eq. 1.7), but they also fail to reproduce the extremely round, basically non-rotating, most massive spheroidals. In addition, Bois et al. (2011) showed that the fastest rotators in the Atlas<sup>3D</sup> survey have similar properties as their initial spiral galaxies.

While the isolated binary merger simulations provide information about the formation of spheroidals from controlled initial conditions, they cannot encompass the full evolution history of a galaxy. For this, cosmological simulations are needed. Naab et al. (2014) already studied a sample of spheroidals from re-simulations (see Sec. 2.3.1 and Oser et al. 2010), and could successfully reproduce both slow and fast rotating spheroidals in their limited sample of galaxies. They showed that major mergers are of high importance in reproducing the observed ellipticities and  $\lambda_R$  values, and that the gas-fraction and time of the merger event play a crucial role. Most interestingly, they also find non-rotating, massive spheroidals, in contrast to Bois et al. (2011), because those non-rotators were formed by gas-poor minor mergers alone, which was not included in the study presented by Bois et al. (2011). Nevertheless, they still do not find the extremely fast rotating spheroidals, indicating that there might be a different formation channel important for the evolution of those objects. To test this, a more statistically complete sample of spheroidals is required.

We use spheroidals selected from the Magneticum Pathfinder simulation Box4 uhr (see Sec. 2.4.1) to perform an analysis similar to that presented in the Atlas<sup>3D</sup> study and analyse the kinematic features present in our simulation. The left panel of Fig. A.3 shows the resulting  $\lambda_R$ -ellipticity values from our simulations for the spheroidals (blue circles) and the S0 galaxies (red circles), with the S0 being disk-like, puffed-up but gas-poor galaxies. We find that our simulation successfully reproduces a population of slow and fast rotators similar to the observations (see right panel of Fig. A.3 for the observations taken from Emsellem et al. (2011)), and that our S0 galaxies clearly tend to be fast rotators, similar to what is shown by Emsellem et al. (2011). However, although we find a few very fast rotating S0 galaxies, we also do not see as many spheroidals with very high  $\lambda_R$  values. One possible explanation for this could be that, at the current state of the study, we have only included central galaxies in our sample and ignored the satellite galaxies. While this is not important for field galaxies, there is large number of massive satellites in the cluster and group environments of our simulation. Those

---

<sup>‡‡</sup> The results of this work are part of the Master's Thesis by F. Schulze, supervised by **R.-S. Remus** and K. Dolag

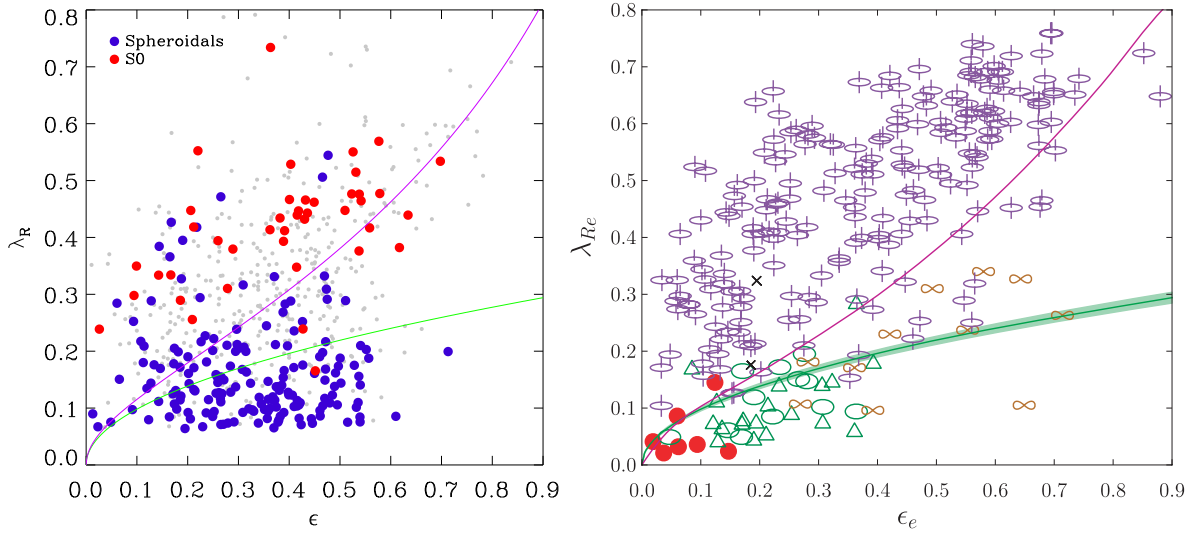


**Figure A.3:** *Left panel:* The  $\lambda_R$  parameter versus ellipticity for spheroidals in Magneticum Box4 uhr. The spheroidals are not rotated to their principal axes but are viewed at a random inclination angle. The spheroidals are shown as blue circles, the S0 galaxies as red circles. Grey small circles mark the positions of all other galaxies with  $M_{\text{tot}} > 1 \times 10^{11} M_{\odot}$  in the simulation. *Right panel:* Fig. 7 from Emsellem et al. (2011), showing the  $\lambda_R$  parameter versus ellipticity for the early-type galaxies from the Atlas<sup>3D</sup> sample. Lilac symbols indicate fast rotating early-types, green symbols mark slow rotating galaxies, with the symbol type according to their kinematic features (see Sec. 1.2.3 for more details). Red circles show the massive, round galaxies without any signs of rotation, while brown infinity-symbols mark galaxies with counter-rotating cores. In both panels, the green line indicates the division between slow and fast rotators, as introduced by Emsellem et al. (2011). The magenta line is a theoretical curve for galaxies viewed edge-on with an intrinsic anisotropy of  $0.65 \times \epsilon$ .

satellites which are spheroidals partially have a formation scenario very different from the merger scenarios discussed in the previous studies: They suffered from ram-pressure stripping and starvation in the hot environment of the intra-cluster medium, similar to what is observed in the Virgo cluster (Abramson et al., 2011; Vollmer et al., 2012; Boissier et al., 2012). As shown by Jaffé et al. (2015) and discussed in the introduction (Chap. 1), this ram-pressure stripping leads to the formation of gas-poor, flat spheroidals, which still have the dynamical properties of the original disk galaxies. This would also be in agreement with the result of Bois et al. (2011) who found that their initial spiral galaxies have properties similar to the high- $\lambda_R$  spheroidals found in the Atlas<sup>3D</sup> sample. These spheroidals are very likely to populate the high- $\lambda_R$  range, and including those objects in our analysis will be the next step in our analysis, especially since the Atlas<sup>3D</sup> sample also includes spheroidals from the Virgo cluster.

This clearly shows the need of a full cosmological sample of spheroidals to understand all formation channels of early-type galaxies. With our full sample of spheroidals we will be able to study the kinematic families or early-type galaxies identified in the Atlas<sup>3D</sup> sample in great detail, and also study the connection between the kinematic properties in central areas with those in the outskirts of galaxies, especially in the light of new upcoming surveys of the outer halos like SLUGGS (see Arnold et al., 2014, for a first observational approach to this question).

## A.4 Connecting Angular Momentum and Galactic Dynamics<sup>‡</sup>

The connection between the angular momentum of a dark matter halo and its galaxy has been discussed in several studies since more than 20 years. In a hierarchical  $\Lambda$ CDM universe, structures grow through accretion of smaller substructures, but at the very beginning the gas cools and collapses into the dark matter halos to form the stars and galaxies at their centers. In this process, both components, gas and dark matter, gain a similar amount of angular momentum through tidal torques (Peebles, 1969), albeit the gas can transport the angular momentum to the center of the halo. Since the angular momentum is conserved, the spin of the gas component in the center, namely the spin of the disk in the case of spiral galaxies, should be the same as the spin of the total dark matter halo (e.g., Fall & Efstathiou 1980; Fall 1983; Mo et al. 1998). Additionally, Fall (1983) (hereafter F83) showed that the specific stellar angular momentum  $j_*$  of disk and spheroidal galaxies is correlated with the stellar mass of the galaxy, but the correlation is different for the different types of galaxies. He showed that the  $j_*$  is higher for disk galaxies than for ellipticals of the same mass. This study was reviewed and extended by Romanowsky & Fall (2012) (RF12) and Fall & Romanowsky (2013) (FR13), who included S0 galaxies in the study and found them to have  $j_*$  lower than those of disks and higher than those of spheroidals for the same mass. Thus, they concluded that the mass and the angular momentum determine the morphology of the galaxy.

In this work we analyse the connection between the angular momentum of dark matter halos and the properties of the galaxies in their centers and test the conclusions drawn from observations. We use elliptical and disk galaxies selected from the Magneticum Pathfinder simulation Box4 uhr (see Sec. 2.4 for more information on the simulation) and calculate their specific angular momentum for the central stellar component (within  $10\%R_{\text{vir}}$ ) as

$$j_* = \frac{\sum_i m_{*,i} r_{*,i} \times v_{*,i}}{\sum_i m_{*,i}} \quad (\text{A.1})$$

with  $m_{*,i}$  the mass,  $r_{*,i}$  the radial distance to the center of the galaxy and  $v_{*,i}$  the velocity of the  $i$ th stellar particle. We find the same correlation between  $j_*$  and the stellar mass of our galaxies as F83, RF12 and FR13, as shown in Fig. A.4.

In addition, we find that the unclassified galaxies from this simulation, i.e., the S0, irregular and peculiar galaxies, cover the space between the “poster-child” disk and spheroidal galaxies, in agreement with what is shown for S0 galaxies in RF12 and FR13. In fact, for the same mass we find that the galaxies with higher peaks of the  $\epsilon$ -parameter (a measurement of the circularity, see Sec. 2.4.1) have larger  $j_*$  than their low- $\epsilon$  counterparts, Nevertheless, some spheroidals can even have  $j_*$  similar to those of the disks. We also calculated the specific angular momentum for the cold gas  $j_{\text{Gas}}$ , and we find  $j_* \approx j_{\text{Gas}}$  for the disk galaxies, while  $j_* < j_{\text{Gas}}$  is always true for the spheroidals, in agreement with observational results presented in Obreschkow & Glazebrook (2014).

The total angular momentum vectors of gas and stars tend to be aligned for the disks, but for the spheroidals we find a random distribution of the angle between the two vectors over the whole  $180^\circ$  range. This agrees with observations of the alignment between gas disks in spheroidals and the stellar major axis presented in Davis et al. (2011) and the results shown in Schlachtberger (2014)

<sup>‡</sup> The results of this Master’s Thesis by Teklu (2014) have been submitted as *Connecting Angular Momentum and Galactic Dynamics: The complex Interplay between Spin, Mass and Morphology* by A. F. Teklu, **R.-S. Remus**, K. Dolag, A. M. Beck, A. Burkert, A. S. Schmidt, F. Schulze & L. K. Steinborn, ArXiv 1503.03501

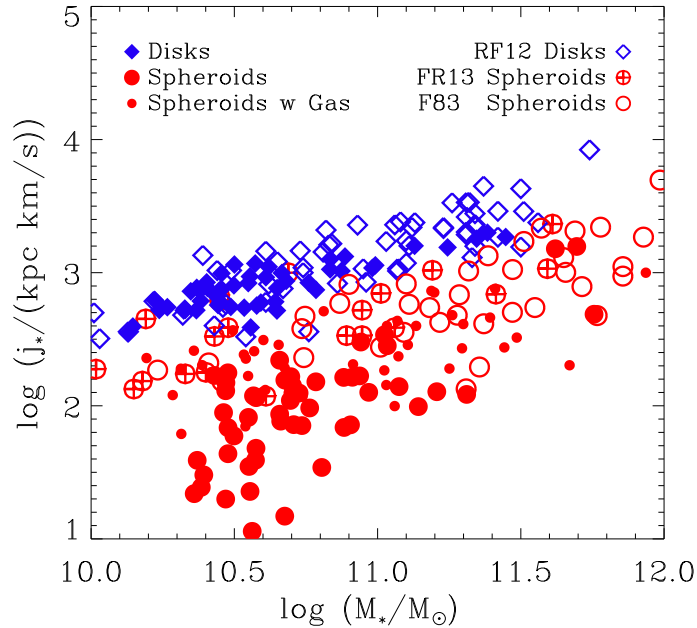


**Figure A.4:** Specific stellar angular momentum  $j_*$  versus stellar mass  $M_*$ , for the galaxies from the *Magneticum Pathfinder* simulation *Box4 uhr* with disk galaxies as blue filled diamonds, gas less spheroidals as big red filled circles and spheroidals with maximal 10% cold gas fraction as small red filled circles. Open symbols represent the observations of disk galaxies from Romanowsky & Fall 2012 (RF12, blue diamonds) and for ellipticals from Fall & Romanowsky 2013 (FR13, red plussed circles) and Fall 1983 (F83, red open circles). Figure similar to the right panel of Fig. 3 by Remus et al. (2015a).

(see Sec. A.2). This is true for all redshifts tested in this work (up to  $z = 2$ ). For the total angular momentum of the dark matter  $J_{\text{DM}}$  and  $J_*$  we do not find a general alignment of the vectors, albeit it is slightly more significant for the disks than for the spheroidals. This indicates that merging could destroy the alignment between the angular momentum vectors of dark matter and stars.

In addition, we tested the total spin parameter (Peebles, 1971) and the component-wise spin in the form presented by van den Bosch et al. (2002), and find that disk galaxies tend to live in halos with slightly higher total spin parameter than ellipticals, albeit both galaxy types can occur at all spin-values (see also Teklu et al. (2015b)). This is due to the fact that the spin of the cold gas component is noticeably larger than the spin of the dark matter component (the spin of the stellar component is negligible) since the gas can redistribute the angular momentum and transport it to the galaxies center. Therefore the total spin of the gas-rich disk galaxies tends to be larger than that of the relatively gas-poor spheroidals.

We conclude that galaxies cover the whole range in the  $j_*$ - $M_*$  space with the “poster-child” disk and spheroidals as upper and lower limits. Merging can destroy the alignment between the angular momentum vectors of gas disk and stellar component, causing the cold gas disks in spheroidals to be more often misaligned with the stellar main axis. The total spin parameters of spheroidals tend to be lower than for disks, indicating that the total spin of a structure and its morphology are driven by the same physical processes.

## A.5 Testing Fundamental Galaxy Properties in the Magneticum Simulations\*\*

From observations, there are several fundamental scaling relations known for galaxies, and due to the large surveys with tens of thousands of classified and characterized galaxies, those relations are known in great detail. Therefore, it is crucial for a successful simulation of galaxies in a cosmological environment to reproduce these scaling relations.

Until recently, fully cosmological hydrodynamical simulations had grave issues in producing both spheroidal galaxies and disk galaxies within the same simulation. For SPH codes like GADGET (see Sec. 2.1), this was mostly due to problems in the numerical setups of the subgrid-physics used in SPH to model the galaxies and the issue of SPH not being able to properly solve phase mixing between two fluids of different temperature and velocity (Agertz et al., 2007). The most significant enhancement that has led to a change in this issue was the implementation of the low-viscosity scheme (Dolag et al., 2005), and with additional physics like stellar winds, metal cooling and AGN feedback the properties of the resulting disks become even more realistic (see Sec. 2.1). In our new Magneticum Pathfinder Simulations (see Sec. 2.4), those improved implementations have been included, and we find both disk and spheroidal galaxies in the simulation boxes with high enough resolution (namely uhr) at all redshifts.

For the stellar mass functions this has been already presented by Hirschmann et al. (2014), and by Remus et al. (2015a) especially for the Box4 uhr, which is studied extensively in this PhD thesis. We find a generally good agreement with observations. The mass-size relation, another fundamental relation for galaxies, has been shown for the spheroidals in detail in Chap. 4 of this thesis, and for both the disk and the spheroidal populations of the Magneticum Simulation Box4 uhr it is shown in Fig. A.5 (as open blue or filled red circles, respectively) for galaxies at present day ( $z = 0$ ). We compare the simulations with observations from the SDSS survey (Shen et al., 2003, left panel of Fig. A.5) and the GAMA survey (Baldry et al., 2012, right panel of Fig. A.5). On average, the Magneticum galaxies tend to be slightly larger than the observed galaxies from SDSS, but they are in excellent agreement with the GAMA results. As for the observations, we find the Magneticum disk galaxies to be more extended than the Magneticum spheroidals at a given mass, which is a big step forward compared to previous simulations. The results are similar to those found for the EAGLE simulation (Fig. 9 in Schaye et al., 2015).

The Magneticum Simulations also include luminosities in 12 different wavebands (u,V,G,r,i,z,Y,J,H,K,L,M), enabling a direct comparison with observations. This allows us to study additional fundamental scaling relations for galaxies, as for example the fundamental plane for spheroidal galaxies (Jorgensen et al., 1996):

$$\log r_{\text{eff}} = 1.24 \log \sigma - 0.82 \log \langle I \rangle_e \quad (\text{A.2})$$

with  $r_{\text{eff}}$  the effective radius,  $\sigma$  the central velocity dispersion and  $\langle I \rangle_e$  the mean surface brightness within the effective radius (in flux units, see also La Barbera et al. 2010a and Eq. 1.33). This relation correlates the size, central velocity dispersion and luminosity of spheroidals, and the relation is very narrow. It includes the well-known Faber-Jackson relation (Faber & Jackson, 1976) for spheroidal

---

\*\* The results of this work will be part of the following paper submitted soon as *The Magneticum Pathfinder Simulation* by K. Dolag et al.

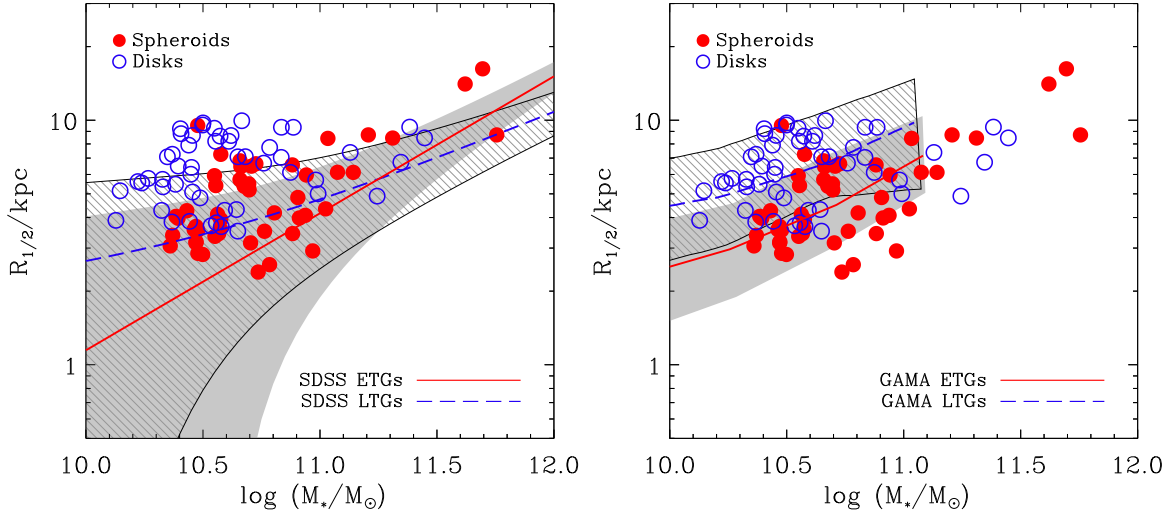


**Figure A.5:** Mass-Size Relation for the Magneticum Pathfinder Simulation Box4 uhr for disks (blue open circles) and spheroidals (red filled circles) in comparison to SDSS (left panel, Shen et al. 2003) and GAMA (right panel, Baldry et al. 2012) observations. Grey shaded areas show the  $1\sigma$  deviations from the mean fits to the data (red solid lines) for the spheroidals, diagonally striped areas show the  $1\sigma$  deviations from the mean fits to the data (blue dashed lines) for the disk galaxies.

galaxies:

$$L \propto \sigma^4 \quad (\text{A.3})$$

which correlates the luminosity  $L$  of the spheroidals with their velocity dispersion  $\sigma$ . However, the scatter is larger than that of the Fundamental Plane, since it represents just a two-dimensional projection of the Fundamental Plane, similar to the Kormendy Relation (Kormendy 1977,  $\langle I \rangle_c = r_{\text{eff}}^\gamma$ , which is another projection of the Fundamental Plane direction and a fairly natural result of the merger scenario (Mo et al., 2010, p. 606)).

La Barbera et al. (2010a) studied the Fundamental Plane and the Faber-Jackson Relation in detail for 39993 early-type galaxies in 8 different luminosity bands. We compared the results from their Faber-Jackson relations at the different wavebands with the results from our Magneticum simulation spheroidals, and find a very good agreement. A similar relation, called Tully-Fisher Relation (Tully & Fisher 1977,  $L \propto v_{\text{max}}^\beta$ , with  $\beta$  depending on the observed waveband) is also known for disk galaxies, and with the Magneticum simulations we can now also compare the observed relations to the simulated.

We conclude that the Magneticum Pathfinder simulation in its high resolution boxes is able to successfully reproduce disk and spheroidal galaxies which satisfy the fundamental scaling relations known from observations at  $z = 0$ . Therefore, it is an excellent tool to study galaxy formation and evolution for the different morphological classes of galaxies, the impact of merger events as well as secular evolution, and it will provide interesting new insights into the differences and similarities between those different types of galaxies.

## A.6 A Refined Sub-Grid Model for Black Hole Accretion and AGN Feedback<sup>¶</sup>

In fully hydrodynamical, cosmological simulations like Magneticum Pathfinder (see Sec. 2.4), physical properties like winds, stellar feedback and metal cooling are implemented as simple sub-grid models, usually containing free parameters to approximate the analytical solutions. This is necessary since it is impossible to resolve the processes directly in cosmological simulations. However, the free parameters needed to describe the sub-grid models are not well constrained. Another important property which is usually described by such a sub-grid model is the AGN feedback from the central black holes (BHs) in galaxies. This feedback has significant influence on the star formation history of galaxies, since the feedback from the BH is thought to be one of the main reasons for the shut-off of star formation in massive galaxies: the feedback is heating up the cold gas, feeding the hot halo around massive galaxies and thus switching off cold streams Dekel & Birnboim (2006) and suppressing cooling from the halo (Churazov et al., 2005).

In Steinborn et al. (2015) we present a more detailed sub-grid model for BH accretion and AGN feedback: *i.*) Due to the limited resolution, the Bondi accretion rate has to be multiplied with a so-called boost-factor (Springel et al., 2005b). In our new model we use different boost-factors depending on whether the gas that is accreted is cold (higher boost-factor) or hot (lower boost-factor) due to the result from Gaspari et al. (2013). *ii.*) Although we implement the feedback as thermal feedback, we consider both mechanical and radiative feedback for the calculation of the feedback energy. This split is oriented on Churazov et al. (2005) and supported by recent observations by Russell et al. (2013). Both feedbacks have different efficiencies. Furthermore, the radiative efficiency depends on the BH mass, as found in observations by Davis & Laor (2011) and Chelouche (2013), and we include this dependence in our model. While the old model has three free parameters, our new model now only has one free parameter, namely  $\epsilon_r$ , the efficiency with which the radiative feedback couples to the surrounding medium.

We simulate the same cosmological box with the same initial conditions, namely Box3 hr, with the old feedback model (Fabjan et al., 2010) and our new model to study the impact of our new feedback on the BH and galaxy properties. As a result of those modifications, we find no over-accretion of mass onto the BHs anymore, leading to an BH- $M_*$  relation that fits better to the observations. In addition, the suppression of star formation in the massive galaxies is slightly more efficient than in the old models, which leads to an increase in the number of quiescent galaxies especially at high redshifts, as can be seen in Fig. A.6 (red dashed lines for quiescent galaxies in simulations with the in the new model, blue dashed lines for quiescent galaxies in the simulations with the old model). Although discrepancies remain, those larger numbers of quiescent galaxies are in better agreement with observations (e.g., Muzzin et al., 2013, black dashed lines and dark gray shaded areas in Fig. A.6). At low redshifts, we do not see any changes of the fraction of quiescent and star forming galaxies between the old and the new model, i.e., the fraction of star forming galaxies at low redshifts is too low. The baryon conversion efficiency in our new model is consistent with observations over the whole mass range resolved in our simulation, except for the very high mass end.

In general, we find that the modifications to the BH sub-grid model enhance the agreement with observations for both BH and galaxy properties in comparison to other models. Nevertheless, there

<sup>¶</sup> The results of this work have been published as *A refined sub-grid model for black hole accretion and AGN feedback in large cosmological simulations* by L. K. Steinborn, K. Dolag, M. Hirschmann, M. A. Prieto, & **R.-S. Remus**, MNRAS 448, 1504.

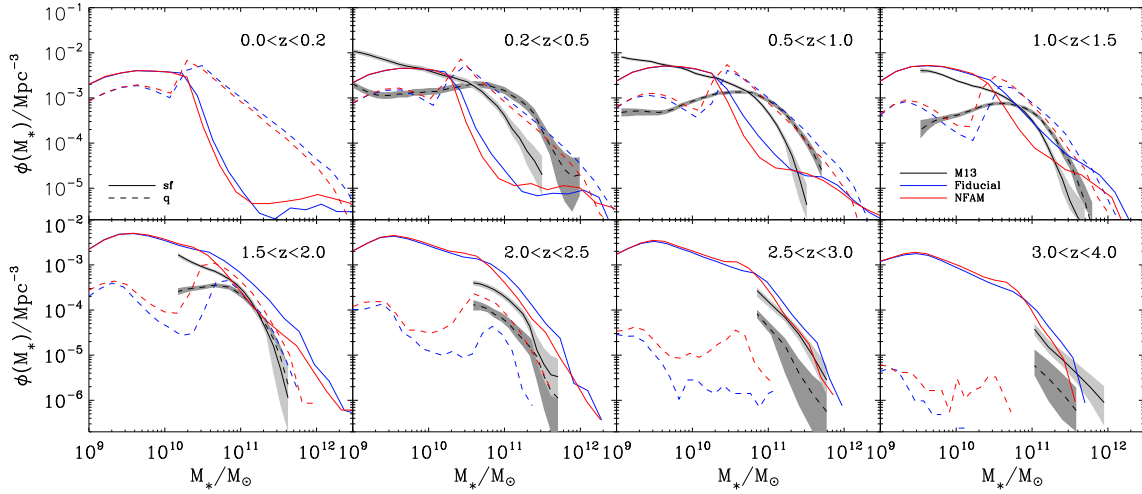


**Figure A.6:** Fig. 9 from Steinborn et al. (2015). Stellar mass functions of star forming (solid lines) and quiescent (dashed lines) galaxies at different redshifts for the old BH-subgrid model (blue lines) and the new BH-subgrid model (red lines) introduced in Steinborn et al. (2015). Black lines show the observations from Muzzin et al. (2013), with shaded areas their Poisson-errors (light gray for star forming galaxies, dark gray for quiescent galaxies).

are still deviations from observations, namely at the fraction of star forming galaxies at low redshifts or the luminosity function at the low-mass end. We conclude that more advanced models are needed for other sub-grid quantities like star formation, stellar feedback or metal cooling to improve the properties of the simulated galaxies in cosmological hydrodynamical simulations.

## A.7 On the Magnetic Fields in Voids<sup>§</sup>

In our universe, it is well known that most galaxies do not live in isolation but in groups of a few up to thousands of galaxies, embedded in much more massive dark matter structures. These structures are ordered along filaments, and at the crossings of such filaments the most massive structures in the universe, namely galaxy clusters, are formed. Nevertheless, at the very beginning of the universe, all matter, dark and baryonic, was distributed nearly homogeneously, apart from those small-scale distortions in the dark matter density that were caused by the initial fluctuations in the quantum field before inflation. Thus, as the matter condensed in those small potential wells, growing into more and more massive, over-dense structures, the initial small potential hills grew larger as well, forming large under-dense regions in space, which are called cosmic voids (see Chap. 1 for more details).

However, even if voids are under-dense regions, they still contain matter in form of galaxies, as shown in several studies, for example by Szomoru et al. (1996); Lindner et al. (1996); Grogin & Geller (1999); Pan et al. (2012); Kreckel et al. (2012); Ricciardelli et al. (2014). These galaxies are small, gas-rich and star forming, and often aligned along small filaments (e.g., Szomoru et al. 1996; Kreckel et al. 2012; Alpaslan et al. 2014), but their properties are similar to comparable galaxies in denser environments. Many of those galaxies also show signs of interactions, indicating an ongoing assembly (Kreckel et al., 2014).

Recent observations have indicated that there exist magnetic fields of about  $10^{15}$ G in voids (Neronov & Vovk, 2010). In Beck et al. (2013) we discuss the void galaxies as a possible source of such magnetic fields in voids: Galaxies which are in the process of assembly and have (strong) star formation are known to build and amplify magnetic fields, supported by the cosmic rays produced in supernovae events (see Beck et al., 2013, and references therein). Turbulence and small scale dynamos can amplify the strength of such seed magnetic fields to a global galactic magnetic field (Lesch & Hanasz, 2003; Beck et al., 2012), and cosmic rays can drive winds from the galaxies, effectively transporting magnetic field into the surrounding environment (Breitschwerdt, 2008; Longair, 2011). In addition, even if the galaxies in voids are small, they are likely to contain intermediate mass central black holes, which are known to transport charged particles as feedback from the galaxy to the surroundings.

The escape velocity of the cosmic rays depends on the mass of a galaxy. Since void galaxies are relatively small and the potential wells in which they reside a relatively shallow, cosmic rays emitted from void galaxies can travel much farther into the surroundings in a void environment than in denser environments like filaments and galaxy clusters. A schematic view of this transport of magnetic fields into the surrounding environment is shown in Fig. A.7. According to Kreckel et al. (2012), an average void galaxy has a radius of  $R_{\text{Gal}} \approx 3$  kpc, a mass of less than  $M_{\text{Gal}} < 10^{11} M_{\odot}$  and, assuming constant star formation rates, an age of about 7.5 Gyr. This leaves about 6 Gyr for the cosmic rays to expand into the void. In this time, we find the cosmic rays to be able to travel distances of about 10 Mpc. Thus, we find the strength of the magnetic field that can be caused by the cosmic rays emitted from a void galaxy into a surrounding bubble of radius  $R_{\text{Bub}}$  to be

$$B_{\text{Bub}} = \epsilon \sqrt{N} B_{\text{Gal}} \left( \frac{V_{\text{Gal}}}{V_{\text{Bub}}} \right)^{\frac{2}{3}} \quad (\text{A.4})$$

<sup>§</sup> The results of this work have been published as *On the magnetic fields in voids* by A. M. Beck, M. Hanasz, H. Lesch, R.-S. Remus, & F. A. Stasyszyn, MNRAS Letters 429, 60.

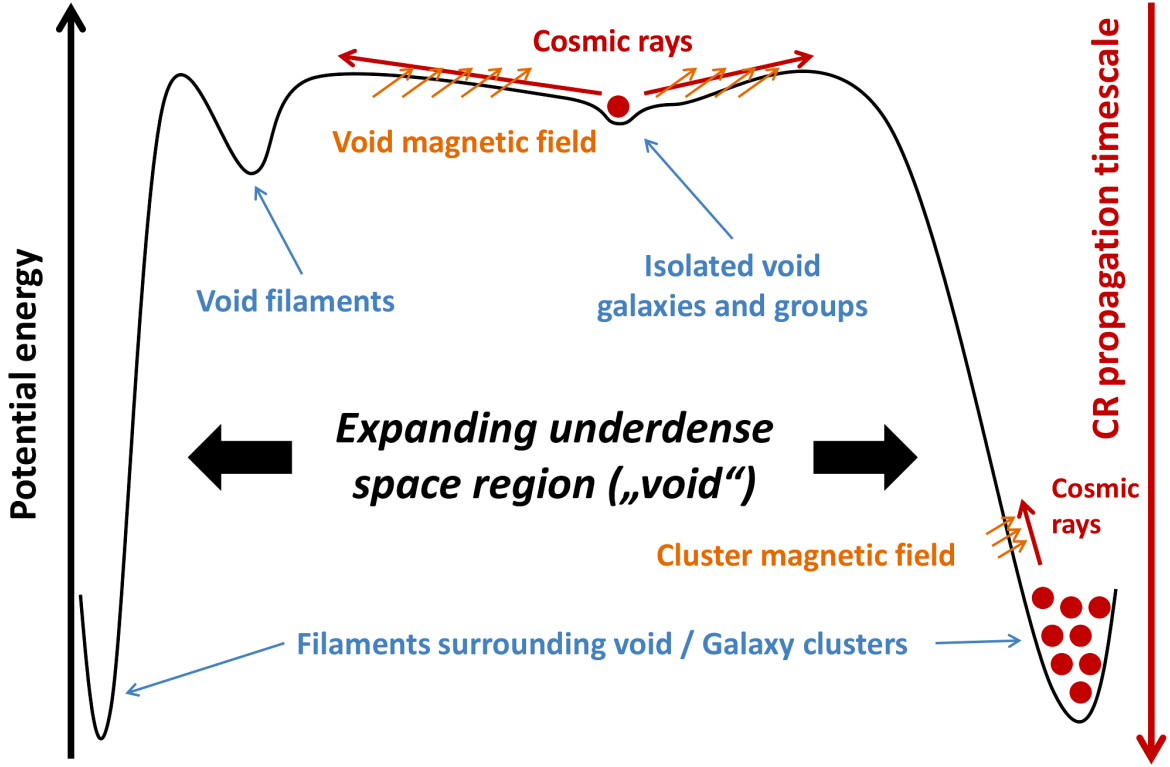


**Figure A.7:** Fig. 2 from Beck et al. (2013): Schematic view of a void environment, surrounded by filaments and cluster structures, and the magnetization due to cosmic rays emitted from the void galaxies.

with  $N$  the number of galaxies inside the void and the fraction of magnetic energy that is transported into the bubble and  $V$  the volumes. The volume filling factor  $f$  of the  $N$  bubbles in the void of radius  $R_{\text{Void}}$  is

$$f = \sqrt{N} \left( \frac{R_{\text{Bub}}}{R_{\text{Void}}} \right)^3. \quad (\text{A.5})$$

Following Pan et al. (2012), a typical void has a radius of about 20 Mpc and approximately  $N = 10$  galaxies inside the void. Thus, for such a void the averaged magnetic field strength caused by the void galaxies is already enough to account for the lower limit observed within the void if we assume only a very low fraction of magnetic energy  $\epsilon = 0.001$ . In addition, galaxies within the filaments at the borders of the voids can contribute to the magnetic fields inside the void as well. We therefore conclude that the low number of young, active galaxies inside the voids is enough to magnetize the average void.

## A.8 Disk Properties in the New Modified SPH<sup>||</sup>

One of the most commonly used numerical methods in simulating the formation of galaxies in the universe is  $N$ -body/SPH. The collisionless gravitational components like dark matter and stars are accurately modeled by the  $N$ -body part of the method (Hernquist & Quinn, 1989), while the hydrodynamic components are treated by the SPH part of the code, where the fluid equations are solved ensuring Galilean invariance and the conservation of mass, momentum, angular momentum, energy and entropy by modeling the fluid as a Lagrangian mass-discretized particle fluid. This treatment of the fluid has several computational benefits, however, it has some downsides which strongly influence the outcome of simulations of galaxy formation in a cosmological context: Due to its particle treatment of the fluid, SPH fails to successfully mix different fluid phases as it cannot treat the contact discontinuities properly, which introduces a completely numerical artificial surface tension between fluid phases and thus instabilities like Kelvin-Helmholtz and Rayleigh-Taylor which normally lead to the mixing of the gas phases are suppressed (e.g., Agertz et al., 2007; Junk et al., 2010). In addition, this suppression of phase mixing leads to a transport of gas with low-entropy to the centers of galactic halos, which is not found in Eulerian codes. Another big issue of standard SPH is caused by its inability to treat subsonic turbulence, which leads to problems in the treatments of shocks and turbulent cosmic plasmas.

However, gas physics is highly important for the formation of galaxies, especially regarding the populations of spirals and irregulars, but also for spheroidals and the group and cluster environments. In particular, the correct treatment of shocks, introduced by stars, AGNs and merger events, is crucial regarding the physics of (in-situ) star formation properties and the hot halo interactions (or cooling from the halo), as known from observations. Thus, to successfully perform cosmological simulations with baryons with  $N$ -Body-SPH, these problems need to be solved.

In our new improved SPH scheme we implement artificial conduction of internal energy (e.g., Price, 2008) to enable better treatment of the mixing between fluid phases, artificial viscosity (e.g., Dolag et al., 2005) where the particle velocity distributions are regulated in case of a shock event, the Wendland Kernel (Dehnen & Aly, 2012), and use a timestep limiter for strong shocks. Artificial viscosity and conduction are included in a time-dependent scheme, as well as a flow limiter for shearing flows.

In Fig. A.8 we show the impact of those new modifications on the properties of a “galaxy” formed from a cooling gas cloud inside a rotating dark matter halo of Milky Way like mass, including only a simple model for cooling, star formation and supernova feedback by Springel & Hernquist (2003). In this test case, we ignore the influence of a cosmological context (i.e., the mass accretion history through merger events and accretion of gas from the surroundings). Similar to a cosmological context, stars are formed only from the gas and are not present at the beginning of the simulation. The simulation was performed once without our modifications and once including those modifications.

The resulting galaxy in both cases exhibits a bulge-like structure in the center surrounded by a gas disk, that also contains stars, however, the individual properties of those test galaxies are significantly different: The bulge formed in the new scheme is significantly smaller, the resulting disk is much more symmetrical and extended, and shows more pronounced spiral arms than in the old scheme. This is caused by the combined effect of the artificial viscosity and conduction, which solve the problem of

---

<sup>||</sup> The results of this work have been submitted to MNRAS as *An improved SPH scheme for cosmological simulations* by A. M. Beck, G. Murante, A. Arth, **R.-S. Remus**, A. F. Teklu, J. M. F. Donnert, S. Planelles, M. C. Beck, P. Förster, M. Ingrund, K. Dolag, S. Borgani, ArXiv 1502.07358

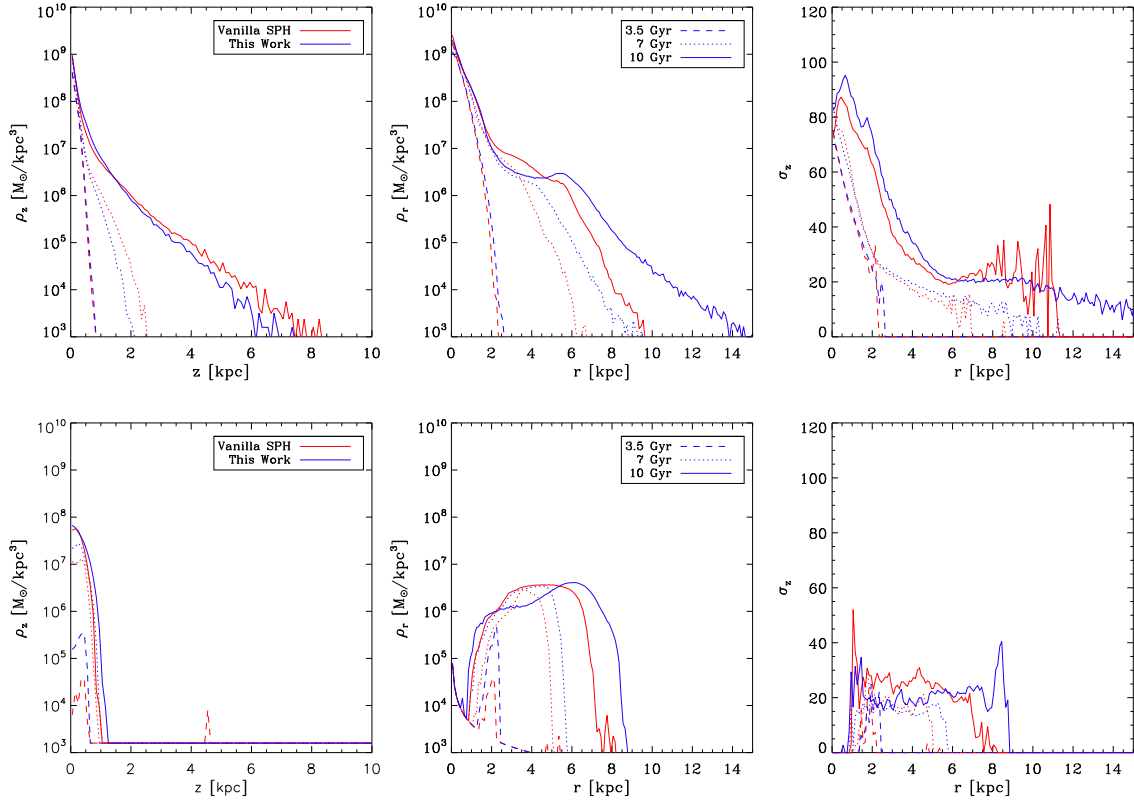


**Figure A.8:** Galaxy properties test for the new SPH scheme presented by Beck et al. (2015) (Fig. 17 therein). **Upper panels:** Vertical (left) and radial (middle) density profiles as well as the vertical velocity dispersion (right) profiles of the stellar component at different timesteps (after 3.5 Gyr (dashed lines), 7 Gyr (dotted lines) and 10 Gyr (solid lines)) for standard (blue) SPH and the new scheme (red). **Lower panels:** Same as upper panels but for the cold gas component ( $T_{\text{Gas}} < 1 \times 10^5$  K).

the numerical surface tension due to the mixing inability, which usually lead to the conversion of cold clumps in the gas disks, which lead to enhanced star formation causing the unphysically fast growth of the bulge. Fig. A.8 shows a more quantitative analysis of the effects of the improved SPH scheme: The density in vertical and radial direction as well as the vertical velocity dispersion are shown for the stellar (upper panels) and gaseous (lower panel) components for both schemes at different timesteps of the simulation. The galaxy simulated with the new scheme has a thinner and much more radially extended stellar disk, and a more extended gas disk, which is significantly colder than the gas disk formed in the simulation with the old scheme, as seen in vertical velocity dispersion (lower left panel).

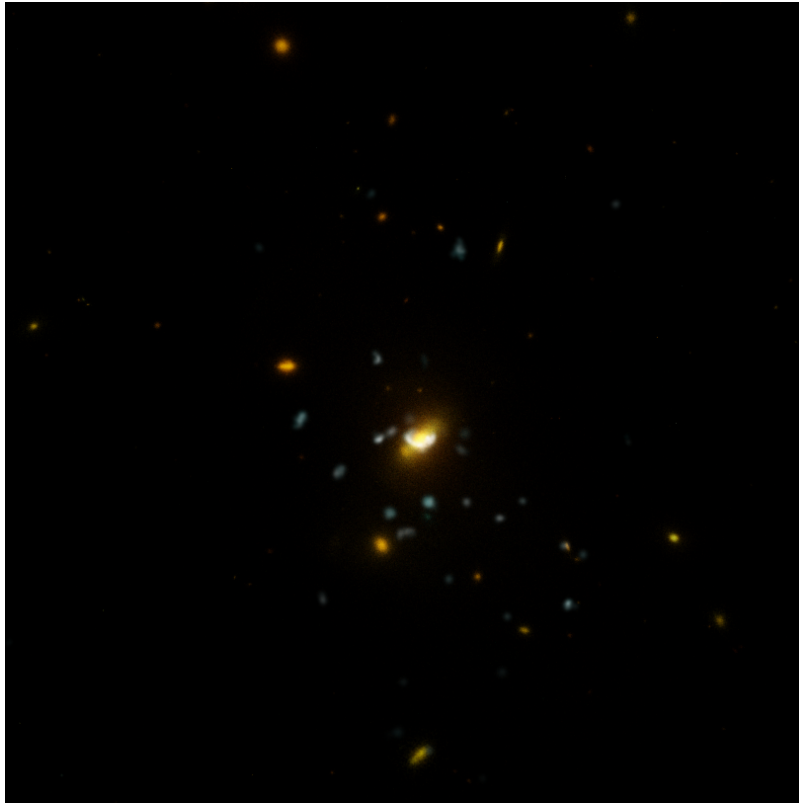
We conclude that our new SPH scheme including reduced artificial viscosity and conduction is significantly improving the treatment of gas physics in simulations of galaxies using SPH. Thus, it is an advanced treatment of the interactions between different fluid phases, resulting in a more realistic presentation of shocks and turbulence and the mixing of gas phases, which are crucial for star formation properties. This will, in the future, enhance our understanding of galaxy formation especially with regard to disk-dominated galaxies.



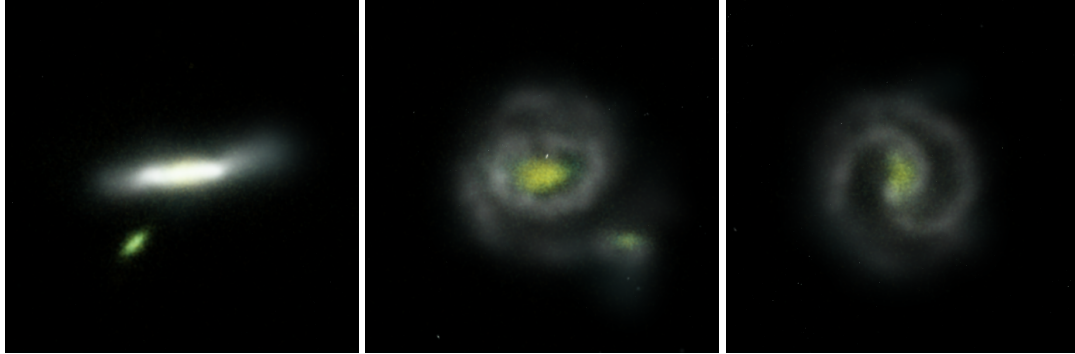
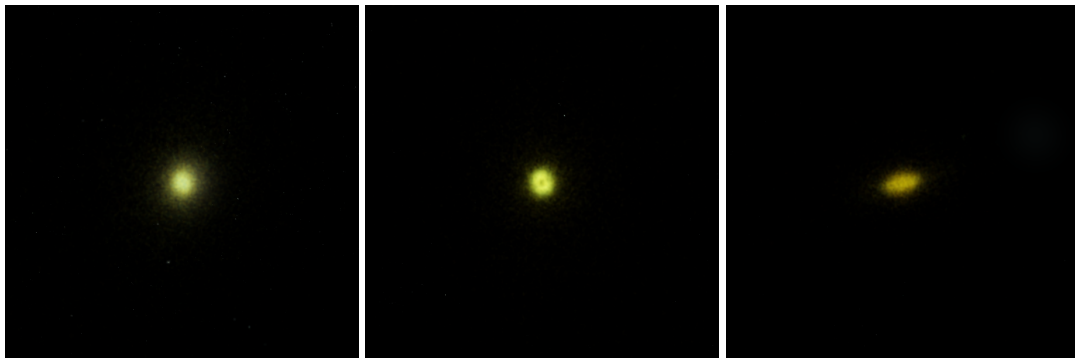
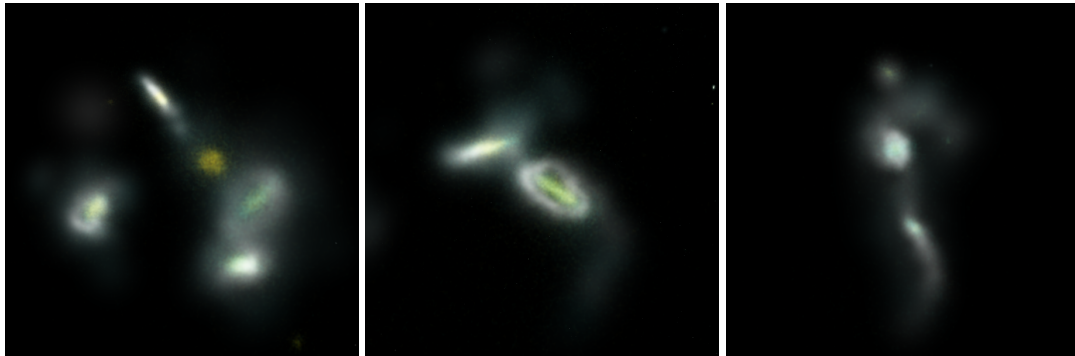
## Appendix B

# Magneticum Box4 uhr Galaxies

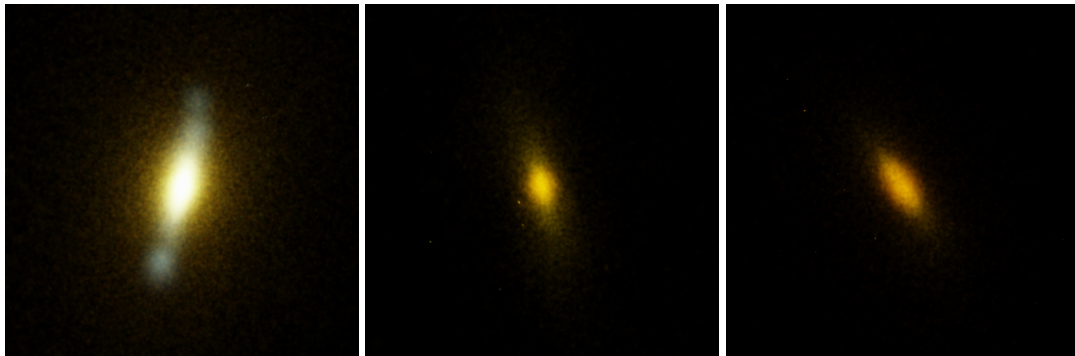
**Figure B.1:** *The most massive galaxy cluster in Magneticum Box4 uhr at  $z = 0.38$*



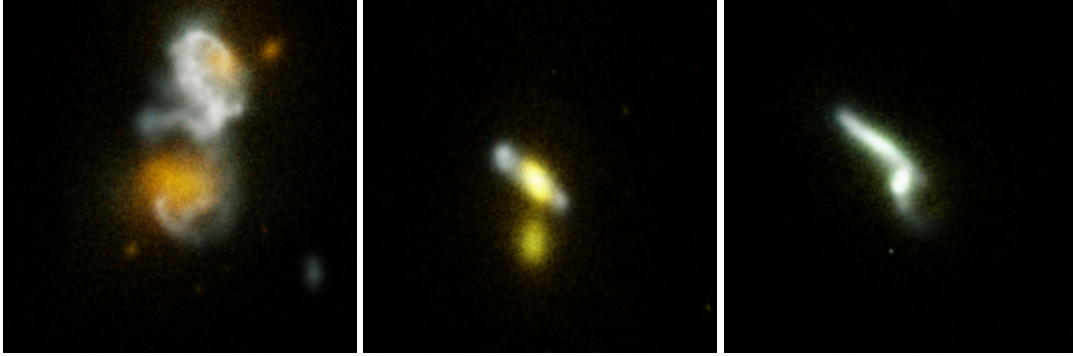
*This image shows the most massive cluster within Box4 uhr, with its total mass of  $M_{\text{tot}} \approx 2.3 \times 10^{14} M_{\odot}$  still a dwarf compared to the most massive clusters seen in the universe, which are roughly an order of magnitude more massive. Nevertheless, as in real clusters, our cluster has an extremely massive BCG in the center, surrounded by several smaller spheroidal and disk galaxies (stars in yellow (young) to red (old), gas in blue). However, those “small” spheroidal galaxies still have stellar masses comparable to the Milky Way, and as such are not at all “dwarfs”. Distance to the BCG from the observer’s point of view is 500 kpc.*

**Figure B.2:** *Galaxies in Magneticum at  $z = 2.33$* *Disk galaxies**Spheroidal galaxies**Merging galaxies*

*A selection of galaxies from Magneticum Box4 uhr at a redshift of  $z = 2.33$ , shown at the correct relative sizes. Spheroidals are much more compact and concentrated than the disk galaxies, and the disk galaxies shown here have pronounced spiral patterns. Most galaxies at this redshift, however, are currently undergoing wet mergers, most of them with small substructures that support the formation of the spiral patterns (upper central panel), and some even have spectacular interactions showing tidal arms, but since they are so gas rich their final state will most likely still be a disk galaxy, different than at present day where such encounters involve only a small fraction of gas and the collisionless stars dominate the outcome of the merger event.*

**Figure B.3:** *Galaxies in Magneticum at  $z = 0.38$* *Disk galaxies**Spheroidal galaxies**S0 galaxies*

A selection of galaxies from Magneticum Box4 uhr at a redshift of  $z = 0.38$ , also shown at the correct relative sizes. The disks tend to have more massive bulges than at  $z = 2.33$ , and their relative number has decreased. The spheroidals are also much more massive than at  $z = 2.33$ , and their stellar components are much older (thus the red hue that indicates the age of the stars). While we basically did not find any S0-like galaxies (flattened spheroidals) at  $z = 2.33$ , at  $z = 0.38$  they are now present, some of them still having gas similar to the Sombrero galaxy (lower left panel).

**Figure B.3:** *continued**Merging galaxies**Peculiar galaxies*

*Mergers at  $z = 0.38$  are rare, but they still occur, as shown in the three upper panels. Most of them involve only small amounts of gas compared to the merger events at  $z = 2.33$ , but a small amount of gas is often present and completely dry mergers are rare. At low redshifts, there are many peculiar galaxies, still exhibiting signs of recent merger events. Their bulges are twisted compared to the gas plane, similar to the galaxy NGC 3718 and other peculiar galaxies presented in the Arp Atlas (Arp, 1966). We also see galaxies with gas rings around a central bulge, similar to Hoag's Object or other deformed ring galaxies.*

**Table B.1:** All galaxies with  $M_{\text{tot}} > 1 \times 10^{11} M_{\odot}$  from Magneticum Box4 uhr at  $z = 0$ 

$Nr_{\text{Gal}}$	Morphology <sup>(a)</sup>	$M_{\text{tot}}$ <sup>(b)</sup>	$M_{\text{Gal}}$ <sup>(c)</sup>	$R_{1/2}$ <sup>(d)</sup>	$f_{\text{Gas}}$ <sup>(e)</sup>	$f_{\text{DM}}$ <sup>(f)</sup>	$f_{\text{DM}}^{\text{SR}1/2}$ <sup>(g)</sup>
0	S0	228.85	294.94	22.85	10.73	0.38	0.79
1	unclass	169.74	213.80	22.12	9.08	0.54	0.82
2	S0	158.58	174.17	17.68	8.30	0.47	0.81
3	unclass	113.02	66.81	21.17	8.54	0.60	0.86
4	S0	108.07	116.00	16.40	8.16	0.46	0.77
5	S0	96.96	106.98	11.81	8.42	0.36	0.67
6	unclass	90.63	52.51	15.73	8.06	0.46	0.77
7	spheroid	42.94	86.37	12.73	0.18	0.37	0.76
8	spheroid	53.23	49.58	15.39	1.71	0.53	0.84
9	unclass	52.86	41.80	17.58	3.76	0.54	0.87
10	unclass	52.59	100.70	19.89	5.09	0.51	0.84
11	S0	48.32	89.61	13.07	3.09	0.58	0.80
12	S0	46.97	71.27	11.55	0.10	0.40	0.80
13	unclass	34.72	70.92	14.63	1.93	0.41	0.79
14	spheroid	27.20	46.79	9.36	0.16	0.35	0.77
15	spheroid	26.81	56.96	8.65	7.21	0.28	0.73
16	S0	26.04	46.57	20.06	12.62	0.55	0.83
17	unclass	24.76	43.12	17.30	10.91	0.48	0.82
18	unclass	24.30	56.59	13.25	0.09	0.45	0.80
19	S0	21.04	27.23	11.10	1.26	0.45	0.82
20	unclass	20.98	37.31	10.16	0.17	0.39	0.77
21	unclass	20.63	25.52	11.91	0.43	0.45	0.81
22	S0	20.28	38.87	15.56	0.50	0.53	0.82
23	unclass	19.44	39.76	13.40	9.96	0.40	0.78
24	S0	18.80	48.65	8.73	17.96	0.61	0.72
25	unclass	17.51	18.51	8.16	2.48	0.37	0.73
26	S0	16.93	42.45	4.83	4.45	0.14	0.56
27	S0	16.63	27.92	13.33	5.14	0.55	0.81
28	S0	16.48	12.96	6.15	0.23	0.28	0.69
29	S0	15.82	55.50	14.17	0.73	0.38	0.79
30	S0	15.64	14.09	8.54	5.44	0.35	0.76
31	spheroid	15.53	41.73	11.60	3.13	0.38	0.72
32	S0	15.50	29.69	7.51	0.26	0.29	0.71
33	unclass	15.39	48.10	6.22	8.14	0.19	0.59
34	unclass	15.20	34.03	10.87	1.28	0.38	0.78
35	unclass	14.62	34.95	12.70	0.61	0.45	0.79
36	S0	14.52	29.58	4.87	0.06	0.15	0.59
37	S0	14.35	34.34	8.32	0.19	0.30	0.70
38	S0	12.97	15.64	28.78	12.29	0.76	0.90
39	S0	13.55	38.57	12.09	0.41	0.45	0.77
40	S0	12.87	21.35	9.68	0.12	0.45	0.80
41	S0	12.87	31.37	6.59	4.72	0.22	0.65
42	S0	12.68	28.97	10.85	0.97	0.44	0.76

Continued on next page

$Nr_{\text{Gal}}$	Morphology <sup>(a)</sup>	$M_{\text{tot}}$ <sup>(b)</sup>	$M_{\text{Gal}}$ <sup>(c)</sup>	$R_{1/2}$ <sup>(d)</sup>	$f_{\text{Gas}}$ <sup>(e)</sup>	$f_{\text{DM}}$ <sup>(f)</sup>	$f_{\text{DM}}^{5R_{1/2}}$ <sup>(g)</sup>
43	S0	12.46	26.50	10.17	0.94	0.39	0.79
44	unclass	11.84	15.65	9.44	0.19	0.47	0.87
45	spheroid	11.33	30.61	12.98	0.13	0.46	0.82
46	unclass	11.27	23.21	9.54	0.60	0.43	0.80
47	disk	11.20	28.00	8.47	1.05	0.37	0.73
48	S0	11.13	25.34	6.05	0.13	0.19	0.67
49	S0	10.88	15.33	6.56	0.38	0.42	0.76
50	disk	9.94	22.17	6.72	0.12	0.33	0.70
51	S0	9.81	21.76	14.83	7.66	0.52	0.86
52	disk	9.40	24.18	9.09	1.33	0.37	0.74
53	unclass	9.39	23.48	10.95	0.14	0.44	0.82
54	S0	9.29	23.06	6.99	10.48	0.24	0.63
55	S0	9.24	23.63	17.70	0.82	0.54	0.84
56	S0	9.00	19.56	11.16	0.42	0.46	0.79
57	spheroid	8.93	24.70	7.34	0.10	0.32	0.76
58	spheroid	8.55	25.73	12.92	0.53	0.51	0.81
59	S0	8.84	17.89	7.25	0.12	0.34	0.75
60	unclass	8.82	23.87	9.78	0.08	0.42	0.80
61	S0	8.74	18.52	13.65	18.75	0.51	0.86
62	unclass	8.66	20.42	5.73	0.10	0.25	0.68
63	S0	8.50	20.10	4.85	1.93	0.16	0.57
64	unclass	8.32	13.54	9.91	0.17	0.42	0.82
65	S0	8.15	15.62	8.47	14.29	0.40	0.78
66	S0	8.03	31.82	6.92	0.04	0.24	0.69
67	S0	7.77	18.37	8.14	0.38	0.38	0.76
68	unclass	7.74	19.66	8.35	0.18	0.44	0.79
69	spheroid	7.68	16.10	8.68	0.22	0.39	0.77
70	spheroid	7.57	27.70	8.14	0.11	0.34	0.75
71	S0	7.45	21.00	6.43	0.28	0.29	0.72
72	unclass	7.38	19.28	7.89	0.06	0.43	0.79
73	unclass	7.17	22.27	7.60	0.93	0.30	0.71
74	spheroid	7.17	19.91	9.85	0.14	0.41	0.80
75	spheroid	7.09	17.82	9.16	0.24	0.42	0.76
76	S0	7.02	18.40	4.78	0.03	0.15	0.61
77	spheroid	6.93	15.77	8.15	0.19	0.39	0.80
78	spheroid	6.93	7.62	6.56	0.16	0.38	0.82
79	S0	6.69	16.41	12.61	0.33	0.53	0.86
80	spheroid	6.58	15.41	10.58	0.40	0.47	0.80
81	spheroid	6.51	19.71	5.60	0.24	0.20	0.62
82	S0	6.26	13.62	10.43	13.12	0.35	0.76
83	S0	6.22	8.45	8.75	0.63	0.51	0.83
84	disk	6.16	17.55	4.22	7.39	0.17	0.57
85	unclass	6.12	10.51	7.51	0.17	0.44	0.81
86	unclass	5.75	5.52	6.43	0.29	0.41	0.79
87	S0	5.62	14.07	7.33	18.22	0.34	0.69
88	S0	5.60	11.50	6.83	0.19	0.35	0.73
89	S0	5.55	15.28	6.18	0.05	0.31	0.75

*Continued on next page*

$Nr_{\text{Gal}}$	Morphology <sup>(a)</sup>	$M_{\text{tot}}$ <sup>(b)</sup>	$M_{\text{Gal}}$ <sup>(c)</sup>	$R_{1/2}$ <sup>(d)</sup>	$f_{\text{Gas}}$ <sup>(e)</sup>	$f_{\text{DM}}$ <sup>(f)</sup>	$f_{\text{DM}}^{5R_{1/2}}$ <sup>(g)</sup>
90	spheroid	5.45	13.88	6.12	0.04	0.31	0.76
91	S0	5.45	11.68	5.00	0.24	0.26	0.71
92	spheroid	5.41	20.46	8.46	0.07	0.34	0.76
93	unclass	5.14	9.48	14.92	18.84	0.72	0.90
94	unclass	5.30	12.22	8.44	4.51	0.48	0.78
95	unclass	5.28	9.37	10.75	0.94	0.56	0.85
96	S0	5.15	14.51	4.72	16.70	0.20	0.62
97	unclass	5.12	12.75	6.95	0.07	0.35	0.81
98	spheroid	5.09	18.23	6.84	0.14	0.33	0.71
99	unclass	5.09	15.95	5.30	0.00	0.28	0.71
100	unclass	5.05	14.72	4.83	0.00	0.23	0.70
101	unclass	4.95	16.79	6.46	0.08	0.34	0.74
102	spheroid	4.90	12.75	7.99	0.06	0.38	0.78
103	S0	4.86	7.86	6.38	0.30	0.23	0.68
104	spheroid	4.85	11.82	9.06	0.14	0.48	0.81
105	unclass	4.71	8.20	4.75	0.00	0.26	0.75
106	S0	4.70	15.28	9.05	0.19	0.44	0.80
107	S0	4.44	9.04	3.85	0.08	0.32	0.67
108	spheroid	4.65	11.47	5.56	0.14	0.30	0.75
109	spheroid	4.64	10.57	4.16	0.04	0.26	0.70
110	S0	3.52	13.14	4.07	7.13	0.18	0.58
111	unclass	4.56	11.22	9.50	0.25	0.48	0.82
112	spheroid	4.54	5.10	6.43	0.09	0.44	0.80
113	spheroid	4.50	10.78	9.65	0.24	0.46	0.79
114	disk	4.45	9.59	5.70	0.09	0.32	0.74
115	S0	4.43	7.99	4.99	0.07	0.30	0.76
116	S0	4.38	6.82	6.03	0.20	0.37	0.76
117	unclass	3.35	4.86	4.80	0.13	0.34	0.74
118	disk	4.31	13.47	7.36	0.24	0.45	0.77
119	unclass	4.28	12.09	8.43	3.48	0.47	0.79
120	S0	4.25	11.20	5.80	0.00	0.36	0.76
121	S0	4.24	12.80	7.97	0.10	0.38	0.80
122	S0	4.17	9.30	4.82	0.04	0.25	0.70
123	S0	4.16	11.68	7.35	0.05	0.36	0.77
124	S0	4.12	3.73	20.57	40.02	0.65	0.91
125	spheroid	4.11	8.16	3.95	0.00	0.18	0.70
126	unclass	4.10	6.47	3.44	0.00	0.24	0.76
127	unclass	4.06	10.37	8.96	0.39	0.42	0.78
128	spheroid	4.06	13.63	8.43	0.10	0.43	0.76
129	unclass	3.95	10.58	6.40	0.00	0.37	0.79
130	unclass	3.90	5.64	9.31	4.00	0.50	0.80
131	S0	3.89	9.06	6.70	0.19	0.39	0.73
132	unclass	3.89	12.37	9.82	0.15	0.49	0.81
133	S0	3.81	14.46	5.46	0.00	0.28	0.73
134	unclass	3.77	8.71	9.39	1.29	0.40	0.78
135	spheroid	3.73	8.21	7.01	0.17	0.40	0.78
136	S0	3.61	14.70	5.14	0.10	0.26	0.67

Continued on next page

$Nr_{\text{Gal}}$	Morphology <sup>(a)</sup>	$M_{\text{tot}}$ <sup>(b)</sup>	$M_{\text{Gal}}$ <sup>(c)</sup>	$R_{1/2}$ <sup>(d)</sup>	$f_{\text{Gas}}$ <sup>(e)</sup>	$f_{\text{DM}}$ <sup>(f)</sup>	$f_{\text{DM}}^{5R_{1/2}}$ <sup>(g)</sup>
137	S0	3.58	6.37	3.75	0.00	0.19	0.67
138	S0	3.50	8.36	6.37	0.13	0.31	0.76
139	spheroid	3.50	11.72	5.52	0.04	0.26	0.70
140	S0	3.49	12.74	2.31	0.00	0.03	0.43
141	unclass	3.45	12.79	6.09	0.06	0.35	0.75
142	unclass	3.45	11.26	10.04	1.56	0.52	0.79
143	spheroid	3.43	10.56	5.34	0.00	0.27	0.72
144	unclass	3.40	4.61	5.90	0.68	0.43	0.77
145	S0	3.38	7.40	3.44	0.00	0.20	0.67
146	S0	3.36	4.53	4.26	13.98	0.31	0.69
147	S0	3.33	7.62	6.35	0.55	0.41	0.76
148	S0	3.33	11.65	7.48	0.04	0.33	0.75
149	S0	3.29	11.83	6.21	0.03	0.28	0.69
150	S0	3.23	12.90	6.08	16.34	0.64	0.76
151	spheroid	3.21	10.73	10.35	0.58	0.47	0.78
152	unclass	3.20	6.28	4.44	0.00	0.27	0.75
153	S0	3.19	8.30	3.09	0.00	0.16	0.66
154	S0	3.17	6.31	4.07	8.57	0.22	0.62
155	S0	3.14	11.01	8.55	0.22	0.44	0.79
156	S0	3.13	8.91	3.93	0.00	0.15	0.64
157	S0	3.08	9.72	3.45	0.00	0.21	0.68
158	S0	3.07	7.55	5.69	0.28	0.40	0.78
159	S0	3.07	10.10	4.44	0.06	0.19	0.65
160	spheroid	3.04	10.81	8.41	3.52	0.44	0.77
161	unclass	3.03	10.43	4.40	13.81	0.23	0.59
162	spheroid	3.02	3.41	5.37	0.28	0.45	0.77
163	S0	2.98	6.99	3.68	0.07	0.22	0.71
164	unclass	2.98	13.46	3.45	6.14	0.08	0.51
165	spheroid	2.97	8.81	4.47	0.07	0.22	0.70
166	S0	2.94	6.21	6.01	0.20	0.37	0.76
167	S0	2.92	6.30	3.72	0.00	0.20	0.69
168	S0	2.88	6.94	5.74	0.21	0.29	0.74
169	unclass	2.83	8.15	7.61	0.15	0.47	0.84
170	unclass	2.82	8.27	8.07	0.20	0.51	0.83
171	S0	2.81	6.70	7.91	1.25	0.52	0.83
172	spheroid	2.76	5.79	3.51	0.00	0.19	0.70
173	S0	2.75	4.41	6.35	4.11	0.47	0.74
174	unclass	2.73	5.65	4.42	0.02	0.27	0.73
175	unclass	2.73	5.35	4.66	0.05	0.31	0.76
176	unclass	2.71	9.04	5.28	0.00	0.28	0.72
177	unclass	2.69	6.02	5.61	0.00	0.37	0.80
178	unclass	2.69	5.79	6.18	0.06	0.37	0.78
179	S0	2.68	11.60	4.26	0.00	0.19	0.69
180	S0	2.67	7.63	3.00	0.00	0.16	0.65
181	unclass	2.63	3.34	5.95	0.11	0.48	0.82
182	unclass	2.62	8.48	4.20	0.00	0.21	0.71
183	unclass	2.62	6.86	6.75	0.11	0.39	0.78

*Continued on next page*

$Nr_{\text{Gal}}$	Morphology <sup>(a)</sup>	$M_{\text{tot}}$ <sup>(b)</sup>	$M_{\text{Gal}}$ <sup>(c)</sup>	$R_{1/2}$ <sup>(d)</sup>	$f_{\text{Gas}}$ <sup>(e)</sup>	$f_{\text{DM}}$ <sup>(f)</sup>	$f_{\text{DM}}^{5R_{1/2}}$ <sup>(g)</sup>
184	unclass	2.60	3.26	6.57	0.04	0.50	0.83
185	S0	2.58	8.91	4.83	0.10	0.44	0.75
186	disk	2.57	6.84	9.17	11.06	0.51	0.79
187	unclass	2.55	6.17	6.23	0.04	0.39	0.80
188	unclass	2.55	4.84	6.21	0.11	0.42	0.83
189	S0	2.54	7.85	8.68	0.31	0.48	0.80
190	unclass	2.53	8.13	6.59	0.07	0.41	0.78
191	S0	2.53	7.02	4.80	0.00	0.30	0.73
192	S0	2.53	9.54	4.84	0.08	0.36	0.66
193	disk	2.51	9.82	5.00	0.19	0.23	0.64
194	unclass	2.49	7.58	3.76	0.00	0.24	0.71
195	spheroid	2.48	8.74	5.67	24.66	0.33	0.68
196	unclass	2.47	7.89	7.35	0.00	0.47	0.78
197	spheroid	1.82	11.88	6.12	0.07	0.33	0.73
198	spheroid	2.42	8.04	4.83	0.03	0.30	0.74
199	S0	2.42	8.17	4.79	0.00	0.27	0.74
200	spheroid	2.41	4.74	4.74	0.13	0.31	0.74
201	S0	2.40	8.37	9.00	2.27	0.50	0.77
202	unclass	2.40	8.37	3.93	0.00	0.20	0.67
203	unclass	1.82	5.20	5.61	0.00	0.38	0.83
204	unclass	2.34	6.07	3.73	0.00	0.20	0.68
205	S0	2.30	9.69	4.07	0.00	0.22	0.65
206	disk	2.29	7.48	6.12	0.25	0.35	0.76
207	unclass	2.28	5.88	3.40	0.00	0.16	0.63
208	unclass	2.26	3.28	5.93	0.12	0.46	0.81
209	unclass	2.25	9.83	6.11	0.07	0.33	0.73
210	S0	2.23	5.73	4.30	0.06	0.27	0.74
211	unclass	2.22	4.80	5.71	0.14	0.42	0.78
212	S0	2.21	7.95	5.94	0.00	0.37	0.80
213	spheroid	2.21	4.71	4.72	0.07	0.32	0.78
214	S0	2.19	4.40	4.96	0.00	0.33	0.76
215	unclass	2.17	2.49	4.64	0.13	0.46	0.79
216	spheroid	2.17	5.47	6.83	0.67	0.50	0.80
217	S0	2.17	5.12	8.09	0.19	0.56	0.86
218	S0	2.16	5.57	3.43	0.00	0.23	0.71
219	S0	2.12	5.38	3.14	0.00	0.15	0.68
220	unclass	2.12	5.32	3.97	0.00	0.21	0.75
221	spheroid	1.62	9.31	2.92	4.00	0.12	0.55
222	spheroid	2.10	5.05	3.15	0.00	0.17	0.71
223	S0	2.10	5.09	4.87	0.10	0.34	0.76
224	S0	2.09	7.14	8.49	0.63	0.52	0.78
225	S0	2.08	7.46	5.61	0.00	0.32	0.75
226	S0	2.07	6.34	5.04	0.00	0.29	0.72
227	unclass	2.07	5.40	4.99	0.00	0.33	0.76
228	disk	2.06	7.70	9.24	7.51	0.45	0.75
229	S0	2.06	6.18	4.22	0.00	0.25	0.73
230	S0	2.06	5.02	4.24	0.00	0.26	0.77

Continued on next page

$Nr_{\text{Gal}}$	Morphology <sup>(a)</sup>	$M_{\text{tot}}$ <sup>(b)</sup>	$M_{\text{Gal}}$ <sup>(c)</sup>	$R_{1/2}$ <sup>(d)</sup>	$f_{\text{Gas}}$ <sup>(e)</sup>	$f_{\text{DM}}$ <sup>(f)</sup>	$f_{\text{DM}}^{5R_{1/2}}$ <sup>(g)</sup>
231	S0	2.05	6.71	3.51	0.12	0.17	0.62
232	unclass	2.04	5.01	6.57	0.05	0.41	0.81
233	unclass	2.03	7.24	4.59	0.00	0.25	0.72
234	unclass	2.01	7.13	3.33	0.00	0.18	0.62
235	spheroid	2.01	8.66	4.08	0.50	0.23	0.69
236	spheroid	2.00	7.64	3.20	6.90	0.21	0.61
237	spheroid	2.00	3.13	5.21	0.48	0.45	0.80
238	spheroid	1.99	3.77	7.20	0.23	0.45	0.82
239	unclass	1.99	4.62	7.45	1.51	0.54	0.79
240	S0	1.97	8.10	4.96	0.15	0.35	0.73
241	S0	1.97	8.88	3.15	3.00	0.14	0.59
242	spheroid	1.97	6.49	6.47	0.27	0.43	0.77
243	unclass	1.96	4.66	3.97	0.00	0.27	0.75
244	S0	1.96	6.09	5.68	0.11	0.36	0.74
245	S0	1.95	6.61	7.30	0.08	0.47	0.79
246	S0	1.94	3.66	6.70	0.11	0.53	0.83
247	S0	1.93	4.38	4.81	0.02	0.39	0.79
248	spheroid	1.93	4.96	5.49	0.00	0.37	0.80
249	unclass	1.93	7.56	3.41	0.14	0.17	0.63
250	unclass	1.92	5.49	3.00	0.00	0.13	0.60
251	disk	1.91	3.58	7.81	27.43	0.49	0.75
252	spheroid	1.89	6.39	4.16	0.18	0.24	0.68
253	S0	1.89	5.41	6.29	0.16	0.41	0.79
254	unclass	1.87	4.06	5.50	0.00	0.45	0.79
255	spheroid	1.87	3.56	3.35	0.00	0.22	0.72
256	unclass	1.86	4.23	4.20	6.27	0.29	0.69
257	S0	1.86	6.40	3.36	0.00	0.20	0.70
258	S0	1.84	5.11	5.00	0.08	0.35	0.79
259	spheroid	1.83	4.98	5.19	0.00	0.33	0.76
260	spheroid	1.82	4.75	5.34	19.89	0.36	0.72
261	spheroid	1.81	4.90	7.43	0.17	0.53	0.84
262	unclass	1.80	7.58	5.24	0.06	0.30	0.73
263	disk	1.79	6.10	7.74	16.61	0.45	0.78
264	unclass	1.79	6.84	9.17	0.47	0.50	0.81
265	S0	1.78	6.66	3.99	0.00	0.20	0.66
266	spheroid	1.78	4.55	5.55	0.12	0.41	0.79
267	S0	1.77	4.97	3.29	0.06	0.21	0.72
268	unclass	1.76	3.47	5.05	0.18	0.37	0.72
269	unclass	1.76	6.07	4.82	0.09	0.32	0.72
270	spheroid	1.74	5.32	6.64	0.17	0.39	0.75
271	disk	1.74	5.75	6.55	0.46	0.42	0.77
272	S0	1.73	4.62	2.63	0.33	0.14	0.59
273	disk	1.73	6.83	7.05	0.17	0.45	0.76
274	unclass	1.62	4.43	4.64	0.00	0.33	0.78
275	S0	1.71	5.30	7.17	6.69	0.51	0.75
276	unclass	1.70	4.73	3.11	0.00	0.19	0.64
277	unclass	1.69	3.84	6.15	0.00	0.42	0.84

Continued on next page

$Nr_{\text{Gal}}$	Morphology <sup>(a)</sup>	$M_{\text{tot}}$ <sup>(b)</sup>	$M_{\text{Gal}}$ <sup>(c)</sup>	$R_{1/2}$ <sup>(d)</sup>	$f_{\text{Gas}}$ <sup>(e)</sup>	$f_{\text{DM}}$ <sup>(f)</sup>	$f_{\text{DM}}^{5R_{1/2}}$ <sup>(g)</sup>
278	S0	1.68	5.39	2.84	7.21	0.16	0.54
279	S0	1.68	4.69	3.60	0.02	0.23	0.73
280	unclass	1.65	2.24	5.65	0.45	0.53	0.84
281	S0	1.65	3.89	3.67	0.00	0.22	0.74
282	unclass	1.64	4.43	5.56	0.31	0.41	0.77
283	S0	1.64	6.88	7.83	1.51	0.48	0.76
284	unclass	1.63	5.25	5.38	0.00	0.36	0.77
285	unclass	1.62	2.78	6.50	5.72	0.51	0.81
286	S0	1.62	5.42	5.22	0.00	0.32	0.78
287	spheroid	1.62	4.59	6.46	0.08	0.45	0.76
288	S0	1.62	3.50	5.29	0.00	0.45	0.80
289	spheroid	1.61	2.96	3.18	0.00	0.24	0.73
290	S0	1.60	7.93	3.28	0.00	0.16	0.59
291	unclass	1.60	5.14	5.91	0.10	0.46	0.79
292	unclass	1.60	5.57	4.33	0.07	0.25	0.73
293	S0	1.59	2.84	5.89	0.10	0.43	0.85
294	spheroid	1.59	4.74	5.42	0.00	0.39	0.81
295	spheroid	1.58	3.75	3.60	0.00	0.25	0.78
296	unclass	1.58	4.87	8.04	7.12	0.55	0.83
297	unclass	1.58	5.82	6.26	0.14	0.46	0.80
298	unclass	1.58	5.62	9.74	5.23	0.54	0.80
299	disk	1.57	4.63	9.95	1.81	0.63	0.85
300	S0	1.56	1.32	7.77	36.37	0.60	0.79
301	unclass	1.56	2.67	7.03	0.36	0.55	0.85
302	S0	1.56	5.99	4.86	0.00	0.31	0.74
303	S0	1.56	4.07	4.27	0.09	0.28	0.74
304	S0	1.55	3.47	3.76	0.00	0.28	0.79
305	unclass	1.55	5.54	7.98	0.14	0.50	0.82
306	spheroid	1.55	4.51	5.10	0.09	0.37	0.77
307	unclass	1.54	3.44	9.04	1.43	0.58	0.81
308	unclass	1.52	3.65	5.19	6.96	0.41	0.79
309	S0	1.52	2.77	3.39	0.08	0.25	0.75
310	S0	1.52	4.57	3.92	0.00	0.27	0.76
311	disk	1.50	3.74	8.30	4.39	0.60	0.78
312	unclass	1.49	6.86	2.72	6.50	0.12	0.53
313	unclass	1.49	2.45	5.10	0.00	0.54	0.82
314	S0	1.49	3.81	3.25	0.00	0.19	0.73
315	spheroid	1.47	3.76	3.92	0.00	0.26	0.74
316	unclass	1.47	3.37	5.83	3.24	0.41	0.74
317	disk	1.45	3.91	4.28	19.26	0.29	0.64
318	S0	1.46	4.45	5.27	0.16	0.37	0.77
319	unclass	1.45	2.86	3.49	0.25	0.26	0.71
320	disk	1.45	1.40	4.76	46.12	0.39	0.70
321	spheroid	1.44	3.71	4.57	0.11	0.31	0.73
322	unclass	1.43	3.26	3.22	0.00	0.19	0.67
323	unclass	1.42	2.58	3.49	0.00	0.29	0.81
324	unclass	1.42	4.06	5.72	0.65	0.12	0.52

Continued on next page

$Nr_{\text{Gal}}$	Morphology <sup>(a)</sup>	$M_{\text{tot}}$ <sup>(b)</sup>	$M_{\text{Gal}}$ <sup>(c)</sup>	$R_{1/2}$ <sup>(d)</sup>	$f_{\text{Gas}}$ <sup>(e)</sup>	$f_{\text{DM}}$ <sup>(f)</sup>	$f_{\text{DM}}^{5R_{1/2}}$ <sup>(g)</sup>
325	unclass	1.41	5.37	6.14	1.48	0.43	0.77
326	S0	1.41	4.18	8.21	0.42	0.54	0.81
327	S0	1.41	1.70	4.27	0.54	0.38	0.81
328	S0	1.40	2.94	5.11	0.00	0.50	0.82
329	S0	1.39	2.16	3.00	22.58	0.25	0.57
330	disk	1.39	4.17	8.66	10.21	0.55	0.80
331	spheroid	1.39	3.99	6.41	0.26	0.43	0.82
332	disk	1.38	4.80	6.71	0.86	0.50	0.79
333	S0	1.38	1.60	3.68	2.02	0.42	0.71
334	S0	1.38	2.55	1.76	7.11	0.06	0.49
335	spheroid	1.38	3.46	3.32	0.00	0.24	0.73
336	unclass	1.38	4.59	3.71	0.00	0.23	0.73
337	S0	1.38	5.35	3.59	0.00	0.20	0.71
338	S0	1.37	3.16	3.95	0.07	0.34	0.77
339	unclass	1.37	4.34	8.83	22.43	0.54	0.80
340	spheroid	1.36	3.69	3.37	0.06	0.19	0.70
341	spheroid	1.36	1.93	2.81	0.00	0.27	0.74
342	S0	1.36	4.87	3.50	0.09	0.18	0.69
343	S0	1.35	4.55	4.40	0.00	0.32	0.76
344	unclass	1.34	1.66	6.64	16.27	0.55	0.82
345	unclass	1.34	4.42	3.66	0.00	0.19	0.69
346	S0	1.33	6.06	3.09	0.57	0.16	0.60
347	S0	1.33	3.09	4.99	0.00	0.41	0.81
348	S0	1.33	4.11	5.00	0.00	0.35	0.75
349	unclass	1.33	5.07	1.97	4.16	0.06	0.47
350	unclass	1.31	3.58	4.26	0.44	0.34	0.73
351	S0	1.30	2.45	5.83	1.18	0.55	0.84
352	spheroid	1.29	3.53	4.54	0.13	0.35	0.74
353	S0	1.29	4.15	3.84	0.09	0.21	0.73
354	S0	1.29	3.38	3.50	0.04	0.24	0.66
355	S0	1.28	2.06	9.16	13.36	0.61	0.91
356	S0	1.28	4.67	5.01	0.00	0.36	0.76
357	unclass	1.27	2.83	4.89	29.83	0.38	0.72
358	unclass	1.27	3.19	4.12	0.00	0.30	0.76
359	spheroid	1.27	2.35	3.38	0.00	0.30	0.74
360	unclass	1.27	5.82	1.84	14.49	0.10	0.43
361	disk	1.27	2.55	8.75	27.44	0.51	0.83
362	unclass	1.27	3.15	5.16	0.00	0.40	0.81
363	spheroid	1.26	4.55	5.72	0.07	0.42	0.80
364	S0	0.94	3.34	3.94	0.00	0.28	0.76
365	S0	1.26	3.89	6.23	0.17	0.42	0.81
366	disk	1.26	2.10	4.28	20.70	0.39	0.68
367	S0	1.26	4.09	3.07	0.07	0.19	0.70
368	spheroid	1.25	2.47	3.97	0.00	0.36	0.78
369	S0	1.25	3.14	4.96	0.05	0.50	0.82
370	unclass	1.24	5.27	8.44	0.19	0.55	0.82
371	S0	1.24	4.43	5.37	0.12	0.40	0.77

Continued on next page

$Nr_{\text{Gal}}$	Morphology <sup>(a)</sup>	$M_{\text{tot}}$ <sup>(b)</sup>	$M_{\text{Gal}}$ <sup>(c)</sup>	$R_{1/2}$ <sup>(d)</sup>	$f_{\text{Gas}}$ <sup>(e)</sup>	$f_{\text{DM}}$ <sup>(f)</sup>	$f_{\text{DM}}^{5R_{1/2}}$ <sup>(g)</sup>
372	unclass	1.23	6.05	3.24	14.29	0.22	0.57
373	spheroid	1.23	2.29	3.06	0.00	0.26	0.77
374	S0	1.23	4.96	7.21	22.51	0.46	0.72
375	unclass	1.23	2.56	6.99	12.53	0.50	0.76
376	S0	1.23	2.11	3.08	0.09	0.29	0.73
377	S0	1.22	5.13	7.47	0.07	0.53	0.81
378	disk	1.22	4.07	8.20	0.76	0.58	0.85
379	S0	1.22	4.68	2.53	32.57	0.14	0.49
380	S0	1.21	2.86	3.37	0.00	0.24	0.73
381	spheroid	1.21	5.44	2.39	5.45	0.09	0.53
382	S0	1.21	2.86	4.22	0.00	0.31	0.76
383	unclass	1.21	4.67	5.44	0.15	0.44	0.79
384	S0	1.21	2.40	4.46	0.00	0.42	0.79
385	S0	1.21	5.09	8.34	1.14	0.52	0.82
386	unclass	1.21	3.22	5.44	13.89	0.34	0.71
387	disk	1.21	4.46	6.80	20.89	0.41	0.73
388	S0	1.20	1.83	3.69	2.27	0.32	0.66
389	unclass	1.20	3.10	9.64	1.36	0.63	0.87
390	spheroid	1.20	4.94	5.24	0.06	0.30	0.70
391	unclass	1.19	3.79	2.99	0.09	0.18	0.69
392	unclass	1.16	2.15	2.99	0.06	0.30	0.74
393	S0	1.19	3.28	4.30	0.07	0.35	0.71
394	S0	1.18	2.62	4.26	0.09	0.45	0.81
395	disk	1.16	2.81	4.67	0.45	0.50	0.76
396	S0	1.16	3.58	3.40	12.22	0.24	0.68
397	S0	1.15	3.28	3.80	0.00	0.24	0.75
398	S0	1.15	1.93	2.80	0.00	0.27	0.74
399	spheroid	1.15	3.59	0.00	0.00	0.41	—
400	unclass	1.12	2.16	3.49	0.00	0.38	0.78
401	spheroid	1.14	4.06	5.67	0.00	0.42	0.77
402	S0	1.14	4.17	6.44	0.42	0.45	0.72
403	S0	1.13	3.44	3.12	0.00	0.22	0.70
404	disk	1.13	3.07	4.80	0.16	0.39	0.80
405	disk	1.13	3.54	9.27	6.19	0.55	0.85
406	S0	1.13	4.86	3.58	0.06	0.20	0.63
407	unclass	1.12	4.17	4.99	0.00	0.32	0.76
408	unclass	1.12	7.08	2.26	7.05	0.06	0.45
409	spheroid	0.95	6.09	2.57	9.58	0.12	0.55
410	unclass	1.10	5.33	4.37	7.33	0.24	0.65
411	S0	1.09	4.43	5.10	0.00	0.39	0.78
412	S0	1.09	2.05	3.57	0.00	0.25	0.78
413	S0	1.09	1.39	8.57	17.86	0.59	0.89
414	disk	1.07	4.39	4.28	0.00	0.27	0.71
415	S0	1.07	4.10	6.00	0.22	0.49	0.77
416	S0	1.07	4.09	4.55	0.13	0.25	0.69
417	unclass	1.07	2.12	3.21	23.58	0.25	0.63
418	unclass	1.07	4.52	4.40	0.00	0.28	0.73

Continued on next page

$Nr_{\text{Gal}}$	Morphology <sup>(a)</sup>	$M_{\text{tot}}$ <sup>(b)</sup>	$M_{\text{Gal}}$ <sup>(c)</sup>	$R_{1/2}$ <sup>(d)</sup>	$f_{\text{Gas}}$ <sup>(e)</sup>	$f_{\text{DM}}$ <sup>(f)</sup>	$f_{\text{DM}}^{5R_{1/2}}$ <sup>(g)</sup>
419	S0	1.07	3.90	4.76	0.15	0.40	0.77
420	unclass	1.06	2.95	6.17	0.94	0.48	0.78
421	S0	1.06	1.47	5.49	0.17	0.56	0.87
422	unclass	1.06	2.47	4.75	0.22	0.42	0.76
423	unclass	1.05	2.64	4.70	0.00	0.45	0.76
424	spheroid	1.05	2.90	3.57	0.08	0.23	0.73
425	S0	1.05	2.67	2.58	0.11	0.16	0.67
426	unclass	1.05	5.17	4.43	0.05	0.31	0.70
427	S0	1.05	3.56	3.43	8.72	0.27	0.63
428	S0	1.04	2.02	2.68	0.00	0.24	0.68
429	S0	1.04	3.20	2.70	0.00	0.12	0.61
430	S0	1.04	3.82	3.72	0.00	0.24	0.73
431	S0	1.04	3.46	4.25	0.07	0.33	0.73
432	unclass	1.04	2.36	2.77	0.00	0.24	0.70
433	S0	1.04	3.29	3.90	0.00	0.31	0.76
434	unclass	1.03	1.81	5.44	10.63	0.58	0.82
435	S0	1.03	3.97	2.66	0.12	0.10	0.57
436	unclass	1.02	2.83	3.65	0.00	0.33	0.78
437	spheroid	1.02	2.91	4.07	0.11	0.36	0.74
438	unclass	1.02	1.33	4.43	33.05	0.44	0.71
439	S0	1.02	2.45	3.20	0.00	0.28	0.72
440	S0	1.02	1.74	2.83	0.18	0.28	0.71
441	S0	1.02	3.79	2.93	0.00	0.14	0.66
442	disk	1.02	4.45	3.52	0.00	0.20	0.64
443	S0	1.01	4.91	4.48	0.00	0.30	0.71
444	S0	1.02	2.89	3.05	0.00	0.19	0.73
445	S0	1.01	3.76	3.78	0.00	0.25	0.76
446	S0	1.01	3.39	3.50	0.00	0.27	0.75
447	disk	1.01	3.61	3.77	17.09	0.30	0.64
448	unclass	1.00	1.71	2.80	0.00	0.25	0.76
449	disk	1.00	2.53	9.26	13.12	0.60	0.87
450	S0	1.00	3.21	5.19	3.16	0.45	0.77
451	S0	1.00	3.58	2.66	0.00	0.10	0.61
452	spheroid	0.99	2.95	3.68	0.00	0.29	0.73
453	spheroid	0.99	3.00	9.52	9.08	0.60	0.85
454	unclass	0.99	2.55	3.11	0.00	0.24	0.73
455	unclass	0.98	3.52	4.22	0.11	0.36	0.78
456	S0	0.98	3.26	4.48	0.18	0.44	0.78
457	spheroid	0.97	2.44	6.02	0.40	0.51	0.82
458	unclass	0.97	3.37	6.09	0.77	0.49	0.78
459	S0	0.97	2.96	2.87	0.00	0.14	0.69
460	spheroid	0.97	3.01	2.86	0.00	0.15	0.65
461	S0	0.96	4.50	2.58	0.00	0.09	0.59
462	S0	0.96	1.66	2.83	0.00	0.27	0.75
463	unclass	0.96	2.44	4.93	0.08	0.43	0.80
464	spheroid	0.96	3.47	4.94	0.07	0.40	0.76
465	S0	0.96	3.09	6.20	0.23	0.53	0.82

Continued on next page

$Nr_{\text{Gal}}$	Morphology <sup>(a)</sup>	$M_{\text{tot}}$ <sup>(b)</sup>	$M_{\text{Gal}}$ <sup>(c)</sup>	$R_{1/2}$ <sup>(d)</sup>	$f_{\text{Gas}}$ <sup>(e)</sup>	$f_{\text{DM}}$ <sup>(f)</sup>	$f_{\text{DM}}^{5R_{1/2}}$ <sup>(g)</sup>
466	unclass	0.96	3.31	3.24	0.00	0.22	0.73
467	S0	0.96	2.72	2.81	0.00	0.19	0.71
468	unclass	0.95	5.26	3.63	0.00	0.23	0.66
469	disk	0.95	3.15	9.64	20.92	0.53	0.84
470	S0	0.94	4.68	6.03	0.30	0.42	0.76
471	unclass	0.94	2.99	5.18	0.14	0.42	0.78
472	spheroid	0.94	2.95	3.15	0.00	0.23	0.75
473	S0	0.93	3.07	2.70	0.00	0.13	0.67
474	unclass	0.93	2.29	2.92	0.00	0.27	0.74
475	S0	0.93	3.49	4.53	4.50	0.37	0.74
476	S0	0.93	3.05	5.60	0.00	0.52	0.82
477	unclass	0.93	4.55	5.26	0.19	0.39	0.80
478	unclass	0.93	3.55	5.22	0.09	0.45	0.81
479	unclass	0.93	2.28	6.55	1.51	0.58	0.82
480	S0	0.92	2.80	4.00	0.00	0.39	0.77
481	unclass	0.92	2.88	4.87	0.10	0.39	0.77
482	unclass	0.92	2.10	3.72	0.00	0.37	0.76
483	unclass	0.92	2.06	3.07	0.00	0.29	0.77
484	S0	0.92	3.23	5.84	0.31	0.46	0.80
485	spheroid	0.92	3.54	5.93	0.00	0.47	0.81
486	S0	0.92	2.29	4.39	0.00	0.43	0.80
487	S0	0.92	2.79	3.35	0.15	0.33	0.75
488	unclass	0.92	1.26	2.40	0.00	0.22	0.70
489	S0	0.91	3.28	4.20	0.00	0.38	0.76
490	unclass	0.91	2.74	4.90	38.30	0.40	0.69
491	S0	0.91	3.43	2.69	0.15	0.15	0.62
492	S0	0.91	1.73	0.00	33.21	0.47	—
493	unclass	0.90	1.73	2.82	0.00	0.24	0.73
494	spheroid	0.90	2.70	4.26	27.03	0.32	0.69
495	S0	0.90	3.83	2.64	0.00	0.14	0.62
496	S0	0.90	2.42	4.78	1.22	0.33	0.73
497	unclass	0.89	2.47	10.06	7.66	0.66	0.88
498	S0	0.89	0.93	3.14	5.55	0.41	0.70
499	unclass	0.89	2.13	4.49	0.07	0.37	0.78
500	unclass	0.88	0.98	3.09	15.67	0.44	0.62
501	S0	0.88	3.90	3.78	8.16	0.28	0.64
502	S0	0.88	3.71	3.55	0.00	0.25	0.73
503	disk	0.87	2.12	5.73	22.82	0.45	0.75
504	S0	0.87	2.84	3.73	0.14	0.29	0.76
505	disk	0.87	3.16	9.73	32.73	0.54	0.83
506	unclass	0.86	3.07	3.66	0.00	0.29	0.74
507	S0	0.86	3.80	4.08	3.57	0.32	0.70
508	unclass	0.86	4.15	5.86	0.00	0.51	0.81
509	spheroid	0.86	3.00	3.55	0.08	0.27	0.70
510	S0	0.86	3.02	3.14	0.00	0.20	0.74
511	S0	0.86	2.31	3.97	0.07	0.44	0.79
512	unclass	0.86	3.11	6.93	0.20	0.56	0.82

Continued on next page

$Nr_{\text{Gal}}$	Morphology <sup>(a)</sup>	$M_{\text{tot}}$ <sup>(b)</sup>	$M_{\text{Gal}}$ <sup>(c)</sup>	$R_{1/2}$ <sup>(d)</sup>	$f_{\text{Gas}}$ <sup>(e)</sup>	$f_{\text{DM}}$ <sup>(f)</sup>	$f_{\text{DM}}^{5R_{1/2}}$ <sup>(g)</sup>
513	S0	0.86	2.28	6.36	0.37	0.52	0.84
514	unclass	0.86	2.50	3.48	0.00	0.30	0.74
515	S0	0.86	4.16	5.13	0.19	0.37	0.74
516	unclass	0.78	2.59	6.27	0.00	0.53	0.83
517	unclass	0.86	1.68	3.83	31.77	0.42	0.60
518	S0	0.86	2.43	3.38	0.00	0.32	0.77
519	S0	0.85	2.23	2.83	0.00	0.26	0.69
520	unclass	0.85	2.76	3.04	0.11	0.19	0.73
521	unclass	0.85	1.82	3.26	0.00	0.36	0.77
522	spheroid	0.85	2.29	4.17	0.14	0.40	0.78
523	S0	0.85	4.28	2.12	8.18	0.12	0.47
524	S0	0.84	2.20	5.02	2.74	0.45	0.75
525	unclass	0.84	2.94	4.04	0.00	0.33	0.75
526	spheroid	0.84	3.65	4.12	0.10	0.30	0.72
527	S0	0.00	0.00	0.00	—	—	—
528	unclass	0.84	2.46	2.85	0.00	0.23	0.74
529	unclass	0.84	3.59	4.33	0.13	0.38	0.75
530	unclass	0.84	3.10	3.55	0.00	0.42	0.78
531	spheroid	0.83	2.06	3.92	0.26	0.44	0.78
532	S0	0.83	2.57	3.51	0.00	0.32	0.74
533	S0	0.83	2.72	3.17	0.00	0.24	0.73
534	unclass	0.83	1.74	2.92	20.38	0.35	0.67
535	disk	0.83	2.85	5.09	29.86	0.35	0.71
536	unclass	0.83	4.29	4.23	0.20	0.30	0.72
537	S0	0.82	3.17	2.91	0.00	0.20	0.71
538	unclass	0.82	2.35	6.30	11.75	0.50	0.80
539	unclass	0.82	1.53	3.87	0.40	0.41	0.77
540	S0	0.82	2.53	2.99	0.00	0.32	0.71
541	S0	0.82	1.51	4.58	3.14	0.50	0.73
542	unclass	0.82	1.32	0.00	0.20	0.34	—
543	S0	0.81	2.36	3.37	0.46	0.32	0.74
544	S0	0.81	1.73	2.50	0.00	0.25	0.70
545	S0	0.81	2.04	3.11	0.00	0.34	0.77
546	S0	0.81	1.42	5.42	24.90	0.53	0.78
547	S0	0.81	1.75	0.00	0.18	0.35	—
548	unclass	0.81	1.84	4.22	0.08	0.47	0.81
549	disk	0.80	2.85	8.67	14.94	0.57	0.77
550	spheroid	0.80	3.15	2.82	0.00	0.13	0.66
551	unclass	0.80	1.98	3.01	0.09	0.28	0.74
552	S0	0.80	0.63	0.00	4.14	0.35	—
553	unclass	0.80	2.95	6.00	0.11	0.48	0.82
554	disk	0.79	2.48	6.47	14.22	0.45	0.76
555	disk	0.79	2.34	7.17	8.74	0.60	0.77
556	spheroid	0.79	0.80	2.26	0.00	0.24	0.71
557	unclass	0.79	1.99	2.85	0.00	0.29	0.73
558	S0	0.79	2.14	2.96	0.00	0.31	0.73
559	unclass	0.79	3.60	4.21	0.05	0.28	0.70

Continued on next page

$Nr_{\text{Gal}}$	Morphology <sup>(a)</sup>	$M_{\text{tot}}$ <sup>(b)</sup>	$M_{\text{Gal}}$ <sup>(c)</sup>	$R_{1/2}$ <sup>(d)</sup>	$f_{\text{Gas}}$ <sup>(e)</sup>	$f_{\text{DM}}$ <sup>(f)</sup>	$f_{\text{DM}}^{5R_{1/2}}$ <sup>(g)</sup>
560	disk	0.79	2.41	5.47	17.87	0.45	0.71
561	unclass	0.79	3.42	4.18	0.00	0.31	0.72
562	unclass	0.79	2.08	4.16	0.00	0.49	0.79
563	disk	0.79	1.85	5.44	0.48	0.46	0.75
564	spheroid	0.79	2.61	3.24	0.00	0.28	0.73
565	S0	0.78	2.04	2.97	0.14	0.30	0.72
566	S0	0.78	2.56	5.20	0.00	0.43	0.83
567	S0	0.78	3.49	4.36	0.00	0.36	0.75
568	unclass	0.78	1.40	2.54	0.00	0.29	0.68
569	spheroid	0.78	2.06	2.99	0.00	0.29	0.75
570	S0	0.78	2.09	6.86	2.84	0.57	0.87
571	unclass	0.78	2.58	7.56	2.79	0.60	0.84
572	unclass	0.78	2.80	3.72	0.00	0.33	0.75
573	S0	0.77	2.76	3.47	0.00	0.26	0.71
574	S0	0.77	1.44	2.42	0.00	0.21	0.72
575	S0	0.77	2.06	2.68	0.00	0.18	0.71
576	disk	0.77	2.82	6.41	18.16	0.49	0.69
577	S0	0.77	2.84	3.45	0.00	0.32	0.74
578	spheroid	0.77	1.56	4.28	0.00	0.43	0.79
579	unclass	0.77	2.93	4.42	0.04	0.36	0.77
580	disk	0.77	1.34	0.00	16.71	0.47	—
581	unclass	0.77	1.48	5.61	15.33	0.52	0.77
582	S0	0.77	2.75	3.15	0.00	0.23	0.70
583	S0	0.76	2.96	3.21	0.00	0.24	0.71
584	unclass	0.76	3.47	4.78	0.00	0.43	0.79
585	S0	0.76	2.05	0.00	2.79	0.43	—
586	S0	0.76	1.86	3.22	0.16	0.31	0.77
587	S0	0.76	2.69	6.23	6.27	0.50	0.74
588	disk	0.76	2.13	5.34	1.02	0.48	0.76
589	unclass	0.76	1.81	8.79	20.68	0.57	0.87
590	disk	0.76	3.42	3.47	14.27	0.27	0.62
591	disk	0.76	3.78	3.67	15.30	0.26	0.61
592	unclass	0.74	3.01	3.86	0.00	0.36	0.74
593	disk	0.75	2.33	0.00	2.06	0.38	—
594	disk	0.75	2.75	7.91	2.18	0.50	0.78
595	S0	0.75	3.48	7.70	1.02	0.57	0.81
596	unclass	0.75	3.23	3.47	0.00	0.21	0.69
597	S0	0.75	2.55	4.40	0.00	0.35	0.81
598	unclass	0.75	1.54	2.72	0.97	0.24	0.64
599	unclass	0.75	2.24	5.17	0.93	0.44	0.75
600	spheroid	0.74	2.42	3.99	0.14	0.38	0.75
601	unclass	0.74	3.18	3.47	0.00	0.20	0.70
602	S0	0.74	1.84	9.18	36.95	0.60	0.84
603	unclass	0.74	2.41	7.60	4.42	0.56	0.82
604	unclass	0.74	3.47	2.46	9.68	0.15	0.55
605	S0	0.73	3.39	3.61	0.00	0.24	0.71
606	S0	0.73	2.20	4.20	0.00	0.36	0.78

Continued on next page

$Nr_{\text{Gal}}$	Morphology <sup>(a)</sup>	$M_{\text{tot}}$ <sup>(b)</sup>	$M_{\text{Gal}}$ <sup>(c)</sup>	$R_{1/2}$ <sup>(d)</sup>	$f_{\text{Gas}}$ <sup>(e)</sup>	$f_{\text{DM}}$ <sup>(f)</sup>	$f_{\text{DM}}^{5R_{1/2}}$ <sup>(g)</sup>
607	S0	0.73	3.88	5.01	0.13	0.42	0.77
608	S0	0.73	2.27	5.16	0.39	0.54	0.81
609	unclass	0.73	2.77	3.75	0.00	0.34	0.75
610	S0	0.73	2.19	5.12	0.23	0.49	0.82
611	disk	0.73	2.77	3.86	24.54	0.31	0.60
612	S0	0.73	2.21	2.74	0.00	0.24	0.68
613	unclass	0.73	3.23	6.27	0.21	0.57	0.81
614	unclass	0.72	2.84	5.13	0.15	0.41	0.80
615	disk	0.72	1.67	5.89	9.78	0.57	0.73
616	S0	0.72	1.59	3.39	0.28	0.30	0.72
617	disk	0.72	1.73	5.54	25.50	0.48	0.71
618	S0	0.71	2.57	5.12	0.06	0.46	0.79
619	S0	0.71	3.43	4.48	0.00	0.32	0.75
620	S0	0.71	1.78	7.76	4.91	0.57	0.84
621	disk	0.71	2.23	7.14	18.06	0.54	0.76

- <sup>a</sup> Morphology of the galaxy according to the classification criterion from Sec. 2.4.1;
- <sup>b</sup> Total mass of the halo in  $10^{12}M_{\odot}$ ;
- <sup>c</sup> Stellar mass within  $2R_{1/2}$  in  $10^{10}M_{\odot}$ ;
- <sup>d</sup> Effective radius of the stellar component of the galaxy, calculated as three dimensional half-mass radius, in kpc;
- <sup>e</sup> Fraction of the gas mass relative to the stellar mass within the half-mass radius in %;
- <sup>f</sup> Fraction of the dark matter relative to the total mass within the half-mass radius;
- <sup>g</sup> Fraction of the dark matter relative to the total mass within  $5R_{1/2}$ ;

# Bibliography

- Abramson A., Kenney J. D. P., Crowl H. H., Chung A., van Gorkom J. H., Vollmer B., & Schiminovich D.: *Caught in the Act: Strong, Active Ram Pressure Stripping in Virgo Cluster Spiral NGC 4330*. *Astronomical Journal* **141**, 164 (2011)
- Agertz O., Moore B., Stadel J., Potter D., Miniati F., Read J., Mayer L., Gawryszczak A., Kravtsov A., Nordlund Å., et al.: *Fundamental differences between SPH and grid methods*. *Monthly Notices of the Royal Astronomical Society* **380**, 963 (2007)
- Alcock C., Allsman R. A., Alves D. R., Axelrod T. S., Becker A. C., Bennett D. P., Cook K. H., Dalal N., Drake A. J., Freeman K. C., et al.: *The MACHO Project: Microlensing Results from 5.7 Years of Large Magellanic Cloud Observations*. *The Astrophysical Journal* **542**, 281 (2000)
- Alcock C.: *Bohdan Paczyński, Cosmic Dark Matter, and Gravitational Microlensing*. In: Stanek K. Z. (ed.): *The Variable Universe: A Celebration of Bohdan Paczynski*. *Astronomical Society of the Pacific Conference Series* **403**, 71 (2009)
- Alpaslan M., Robotham A. S. G., Obreschkow D., Penny S., Driver S., Norberg P., Brough S., Brown M., Cluver M., Holwerda B., et al.: *Galaxy and Mass Assembly (GAMA): fine filaments of galaxies detected within voids*. *Monthly Notices of the Royal Astronomical Society* **440**, L106 (2014)
- Amorisco N. C.: *On feathers, bifurcations and shells: the dynamics of tidal streams across the mass scale*. *ArXiv e-prints* **1410.0360** (2014)
- Arnold J. A., Romanowsky A. J., Brodie J. P., Chomiuk L., Spitler L. R., Strader J., Benson A. J., & Forbes D. A.: *The Fossil Record of Two-phase Galaxy Assembly: Kinematics and Metallicities in the Nearest S0 Galaxy*. *The Astrophysical Journal Letters* **736**, L26 (2011)
- Arnold J. A., Romanowsky A. J., Brodie J. P., Forbes D. A., Strader J., Spitler L. R., Foster C., Blom C., Kartha S. S., Pastorello N., et al.: *The SLUGGS Survey: Wide-field Stellar Kinematics of Early-type Galaxies*. *The Astrophysical Journal* **791**, 80 (2014)
- Arp H.: *Atlas of Peculiar Galaxies*. *The Astrophysical Journal Supplement* **14**, 1 (1966)
- Ashman K. M. & Zepf S. E.: *The formation of globular clusters in merging and interacting galaxies*. *The Astrophysical Journal* **384**, 50 (1992)
- Athanassoula E. & Bosma A.: *Shells and rings around galaxies*. *Annual review of astronomy and astrophysics* **23**, 147 (1985)

- Auger M. W., Treu T., Bolton A. S., Gavazzi R., Koopmans L. V. E., Marshall P. J., Moustakas L. A., & Burles S.: *The Sloan Lens ACS Survey. X. Stellar, Dynamical, and Total Mass Correlations of Massive Early-type Galaxies*. *The Astrophysical Journal* **724**, 511 (2010)
- Badenes C., Maoz D., & Ciardullo R.: *The Progenitors and Lifetimes of Planetary Nebulae*. ArXiv e-prints **1502.01015** (2015)
- Baldry I. K., Driver S. P., Loveday J., Taylor E. N., Kelvin L. S., Liske J., Norberg P., Robotham A. S. G., Brough S., Hopkins A. M., et al.: *Galaxy And Mass Assembly (GAMA): the galaxy stellar mass function at  $z < 0.06$* . *Monthly Notices of the Royal Astronomical Society* **421**, 621 (2012)
- Bamford S. P., Nichol R. C., Baldry I. K., Land K., Lintott C. J., Schawinski K., Slosar A., Szalay A. S., Thomas D., Torri M., et al.: *Galaxy Zoo: the dependence of morphology and colour on environment*. *Monthly Notices of the Royal Astronomical Society* **393**, 1324 (2009)
- Barnabè M., Czoske O., Koopmans L. V. E., Treu T., & Bolton A. S.: *Two-dimensional kinematics of SLACS lenses – III. Mass structure and dynamics of early-type lens galaxies beyond  $z \approx 0.1$* . *Monthly Notices of the Royal Astronomical Society* **415**, 2215 (2011)
- Barnes J. E.: *Encounters of disk/halo galaxies*. *The Astrophysical Journal* **331**, 699 (1988)
- Barnes J. E. & Hernquist L.: *Transformations of Galaxies. II. Gasdynamics in Merging Disk Galaxies*. *The Astrophysical Journal* **471**, 115 (1996)
- Barro G., Faber S. M., Pérez-González P. G., Koo D. C., Williams C. C., Kocevski D. D., Trump J. R., Mozena M., McGrath E., van der Wel A., et al.: *CANDELS: The Progenitors of Compact Quiescent Galaxies at  $z \sim 2$* . *The Astrophysical Journal* **765**, 104 (2013)
- Bartelmann M. & Steinmetz M.: *A Comparison of X-ray and Strong Lensing Properties of Simulated X-ray Clusters*. *Monthly Notices of the Royal Astronomical Society* **283**, 431 (1996)
- Beck A. M., Lesch H., Dolag K., Kotarba H., Geng A., & Stasyszyn F. A.: *Origin of strong magnetic fields in Milky Way-like galactic haloes*. *Monthly Notices of the Royal Astronomical Society* **422**, 2152 (2012)
- Beck A. M., Hanasz M., Lesch H., Remus R.-S., & Stasyszyn F. A.: *On the magnetic fields in voids*. *Monthly Notices of the Royal Astronomical Society* **429**, L60 (2013)
- Beck A. M., Murante G., Arth A., Remus R.-S., Teklu A. F., Donnert J. M. F., Planelles S., Beck M. C., Foerster P., Imgrund M., et al.: *An improved SPH scheme for cosmological simulations*. ArXiv e-prints **1502.07358** (2015)
- Bendo G. J. & Barnes J. E.: *The line-of-sight velocity distributions of simulated merger remnants*. *Monthly Notices of the Royal Astronomical Society* **316**, 315 (2000)
- Bennett C. L., Halpern M., Hinshaw G., Jarosik N., Kogut A., Limon M., Meyer S. S., Page L., Spergel D. N., Tucker G. S., et al.: *First-Year Wilkinson Microwave Anisotropy Probe (WMAP) Observations: Preliminary Maps and Basic Results*. *The Astrophysical Journal Supplement* **148**, 1 (2003)

- Bernardi M., Sheth R. K., Annis J., Burles S., Eisenstein D. J., Finkbeiner D. P., Hogg D. W., Lupton R. H., Schlegel D. J., SubbaRao M., et al.: *Early-Type Galaxies in the Sloan Digital Sky Survey. III. The Fundamental Plane*. *Astronomical Journal* **125**, 1866 (2003)
- Bertschinger E.: *Multiscale Gaussian Random Fields and Their Application to Cosmological Simulations*. *The Astrophysical Journal Supplement* **137**, 1 (2001)
- Beygu B., Kreckel K., van de Weygaert R., van der Hulst J. M., & van Gorkom J. H.: *An Interacting Galaxy System along a Filament in a Void*. *Astronomical Journal* **145**, 120 (2013)
- Beygu B., Kreckel K., van der Hulst J. M., Peletier R., Jarrett T., van de Weygaert R., van Gorkom J. H., & Aragón-Calvo M.: *The Void Galaxy Survey: Morphology and Star Formation Properties of Void Galaxies*. *ArXiv e-prints* **1501.02577** (2015)
- Bezanson R., van Dokkum P. G., van de Sande J., Franx M., Leja J., & Kriek M.: *Tight Correlations between Massive Galaxy Structural Properties and Dynamics: The Mass Fundamental Plane was in Place by  $z \sim 2$* . *The Astrophysical Journal Letters* **779**, L21 (2013a)
- Bezanson R., van Dokkum P., van de Sande J., Franx M., & Kriek M.: *Massive and Newly Dead: Discovery of a Significant Population of Galaxies with High-velocity Dispersions and Strong Balmer Lines at  $z \sim 1.5$  from Deep Keck Spectra and HST/WFC3 Imaging*. *The Astrophysical Journal Letters* **764**, L8 (2013b)
- Bezanson R., Franx M., & van Dokkum P. G.: *One Plane for All: Massive Star-forming and Quiescent Galaxies Lie on the Same Mass Fundamental Plane at  $z \sim 0$  and  $z \sim 0.7$* . *The Astrophysical Journal* **799**, 148 (2015)
- Biffi V., Dolag K., & Böhringer H.: *Investigating the velocity structure and X-ray observable properties of simulated galaxy clusters with PHOX*. *Monthly Notices of the Royal Astronomical Society* **428**, 1395 (2013)
- Binney J. & Tremaine S.: *Galactic Dynamics: Second Edition*. Princeton University Press (2008)
- Blakeslee J. P., Holden B. P., Franx M., Rosati P., Bouwens R. J., Demarco R., Ford H. C., Homeier N. L., Illingworth G. D., Jee M. J., et al.: *Clusters at Half Hubble Time: Galaxy Structure and Colors in RX J0152.7-1357 and MS 1054-03*. *The Astrophysical Journal* **644**, 30 (2006)
- Blom C., Forbes D. A., Brodie J. P., Foster C., Romanowsky A. J., Spitler L. R., & Strader J.: *The SLUGGS survey: globular cluster system kinematics and substructure in NGC 4365*. *Monthly Notices of the Royal Astronomical Society* **426**, 1959 (2012a)
- Blom C., Spitler L. R., & Forbes D. A.: *Wide-field imaging of NGC 4365's globular cluster system: the third subpopulation revisited*. *Monthly Notices of the Royal Astronomical Society* **420**, 37 (2012b)
- Blumenthal G. R., Faber S. M., Flores R., & Primack J. R.: *Contraction of dark matter galactic halos due to baryonic infall*. *The Astrophysical Journal* **301**, 27 (1986)
- Bocquet S., Saro A., Dolag K., & Mohr J. J.: *Baryon impact on the halo mass function: Fitting formulae and implications for cluster cosmology*. *ArXiv e-prints* **1502.07357** (2015)

- Bois M., Bournaud F., Emsellem E., Alatalo K., Blitz L., Bureau M., Cappellari M., Davies R. L., Davis T. A., de Zeeuw P. T., et al.: *Formation of slowly rotating early-type galaxies via major mergers: a resolution study*. Monthly Notices of the Royal Astronomical Society **406**, 2405 (2010)
- Bois M., Emsellem E., Bournaud F., Alatalo K., Blitz L., Bureau M., Cappellari M., Davies R. L., Davis T. A., de Zeeuw P. T., et al.: *The ATLAS<sup>3D</sup> project – VI. Simulations of binary galaxy mergers and the link with fast rotators, slow rotators and kinematically distinct cores*. Monthly Notices of the Royal Astronomical Society **416**, 1654 (2011)
- Boissier S., Boselli A., Duc P.-A., Cortese L., van Driel W., Heinis S., Voyer E., Cucciati O., Ferrarese L., Côté P., et al.: *The GALEX Ultraviolet Virgo Cluster Survey (GUViCS). II. Constraints on star formation in ram-pressure stripped gas*. Astronomy & Astrophysics **545**, A142 (2012)
- Bolton A. S., Burles S., Koopmans L. V. E., Treu T., Gavazzi R., Moustakas L. A., Wayth R., & Schlegel D. J.: *The Sloan Lens ACS Survey. V. The Full ACS Strong-Lens Sample*. The Astrophysical Journal **682**, 964 (2008)
- Bolton A. S., Brownstein J. R., Kochanek C. S., Shu Y., Schlegel D. J., Eisenstein D. J., Wake D. A., Connolly N., Maraston C., Arneson R. A., & Weaver B. A.: *The BOSS Emission-Line Lens Survey. II. Investigating Mass-density Profile Evolution in the SLACS+BELLS Strong Gravitational Lens Sample*. The Astrophysical Journal **757**, 82 (2012)
- Borgani S., Dolag K., Murante G., Cheng L.-M., Springel V., Diaferio A., Moscardini L., Tormen G., Tornatore L., & Tozzi P.: *Hot and cooled baryons in smoothed particle hydrodynamic simulations of galaxy clusters: physics and numerics*. Monthly Notices of the Royal Astronomical Society **367**, 1641 (2006)
- Borgani S. & Viel M.: *The evolution of a pre-heated intergalactic medium*. Monthly Notices of the Royal Astronomical Society **392**, L26 (2009)
- Bouché N., Dekel A., Genzel R., Genel S., Cresci G., Förster Schreiber N. M., Shapiro K. L., Davies R. I., & Tacconi L.: *The Impact of Cold Gas Accretion Above a Mass Floor on Galaxy Scaling Relations*. The Astrophysical Journal **718**, 1001 (2010)
- Bournaud F. & Combes F.: *Formation of polar ring galaxies*. Astronomy & Astrophysics **401**, 817 (2003)
- Bournaud F., Jog C. J., & Combes F.: *Multiple minor mergers: formation of elliptical galaxies and constraints for the growth of spiral disks*. Astronomy & Astrophysics **476**, 1179 (2007)
- Bouwens R. J., Illingworth G. D., Labbe I., Oesch P. A., Trenti M., Carollo C. M., van Dokkum P. G., Franx M., Stiavelli M., González V., et al.: *A candidate redshift  $z \sim 10$  galaxy and rapid changes in that population at an age of 500 Myr*. Nature **469**, 504 (2011)
- Bovy J. & Rix H.-W.: *A Direct Dynamical Measurement of the Milky Way's Disk Surface Density Profile, Disk Scale Length, and Dark Matter Profile at  $4 \text{ kpc} < R < 9 \text{ kpc}$* . The Astrophysical Journal **779**, 115 (2013)

- Boylan-Kolchin M., Springel V., White S. D. M., Jenkins A., & Lemson G.: *Resolving cosmic structure formation with the Millennium-II Simulation*. Monthly Notices of the Royal Astronomical Society **398**, 1150 (2009)
- Breitschwerdt D.: *Astrophysics: Blown away by cosmic rays*. Nature **452**, 826 (2008)
- Brinchmann J. & Ellis R. S.: *The Mass Assembly and Star Formation Characteristics of Field Galaxies of Known Morphology*. The Astrophysical Journal Letters **536**, L77 (2000)
- Brodie J. P. & Strader J.: *Extragalactic Globular Clusters and Galaxy Formation*. Annual review of astronomy and astrophysics **44**, 193 (2006)
- Brodie J. P., Romanowsky A. J., Strader J., Forbes D. A., Foster C., Jennings Z. G., Pastorello N., Pota V., Usher C., Blom C., et al.: *The SAGES Legacy Unifying Globulars and Galaxies Survey (SLUGGS): Sample Definition, Methods, and Initial Results*. The Astrophysical Journal **796**, 52 (2014)
- Bullock J. S., Kolatt T. S., Sigad Y., Somerville R. S., Kravtsov A. V., Klypin A. A., Primack J. R., & Dekel A.: *Profiles of dark haloes: evolution, scatter and environment*. Monthly Notices of the Royal Astronomical Society **321**, 559 (2001)
- Bullock J. S. & Johnston K. V.: *Tracing Galaxy Formation with Stellar Halos. I. Methods*. The Astrophysical Journal **635**, 931 (2005)
- Burkert A., Naab T., Johansson P. H., & Jesseit R.: *SAURON's Challenge for the Major Merger Scenario of Elliptical Galaxy Formation*. The Astrophysical Journal **685**, 897 (2008)
- Burkert A. & Tremaine S.: *A Correlation Between Central Supermassive Black Holes and the Globular Cluster Systems of Early-type Galaxies*. The Astrophysical Journal **720**, 516 (2010)
- Buta R. J., Corwin H. G., & Odewahn S. C.: *The de Vaucouleurs Atlas of Galaxies*. Cambridge University Press (2007)
- Butcher H. & Oemler A., Jr.: *The evolution of galaxies in clusters. V. A study of populations since  $Z$  approximately equal to 0.5*. The Astrophysical Journal **285**, 426 (1984)
- Caon N., Capaccioli M., & D'Onofrio M.: *On the Shape of the Light Profiles of Early Type Galaxies*. Monthly Notices of the Royal Astronomical Society **265**, 1013 (1993)
- Cappellari M., Emsellem E., Krajnović D., McDermid R. M., Scott N., Verdoes Kleijn G. A., Young L. M., Alatalo K., Bacon R., Blitz L., et al.: *The ATLAS<sup>3D</sup> project – I. A volume-limited sample of 260 nearby early-type galaxies: science goals and selection criteria*. Monthly Notices of the Royal Astronomical Society **413**, 813 (2011a)
- Cappellari M., Emsellem E., Krajnović D., McDermid R. M., Serra P., Alatalo K., Blitz L., Bois M., Bournaud F., Bureau M., et al.: *The ATLAS<sup>3D</sup> project – VII. A new look at the morphology of nearby galaxies: the kinematic morphology-density relation*. Monthly Notices of the Royal Astronomical Society **416**, 1680 (2011b)

- Cappellari M., McDermid R. M., Alatalo K., Blitz L., Bois M., Bournaud F., Bureau M., Crocker A. F., Davies R. L., Davis T. A., et al.: *Systematic variation of the stellar initial mass function in early-type galaxies*. *Nature* **484**, 485 (2012)
- Cappellari M., McDermid R. M., Alatalo K., Blitz L., Bois M., Bournaud F., Bureau M., Crocker A. F., Davies R. L., Davis T. A., et al.: *The ATLAS<sup>3D</sup> project – XX. Mass-size and mass- $\sigma$  distributions of early-type galaxies: bulge fraction drives kinematics, mass-to-light ratio, molecular gas fraction and stellar initial mass function*. *Monthly Notices of the Royal Astronomical Society* **432**, 1862 (2013)
- Carlberg R. G., Yee H. K. C., Morris S. L., Lin H., Hall P. B., Patton D., Sawicki M., & Shepherd C. W.: *Galaxy Clustering Evolution in the CNOC2 High-Luminosity Sample*. *The Astrophysical Journal* **542**, 57 (2000)
- Carollo D., Beers T. C., Lee Y. S., Chiba M., Norris J. E., Wilhelm R., Sivarani T., Marsteller B., Munn J. A., Bailer-Jones C. A. L., et al.: *Two stellar components in the halo of the Milky Way*. *Nature* **450**, 1020 (2007)
- Chabrier G.: *Galactic Stellar and Substellar Initial Mass Function*. *Publications of the Astronomical Society of the Pacific* **115**, 763 (2003)
- Chelouche D.: *The Case for Standard Irradiated Accretion Disks in Active Galactic Nuclei*. *The Astrophysical Journal* **772**, 9 (2013)
- Chevance M., Weijmans A.-M., Damjanov I., Abraham R. G., Simard L., van den Bergh S., Caris E., & Glazebrook K.: *On the Shapes and Structures of High-redshift Compact Galaxies*. *The Astrophysical Journal Letters* **754**, L24 (2012)
- Churazov E., Sazonov S., Sunyaev R., Forman W., Jones C., & Böhringer H.: *Supermassive black holes in elliptical galaxies: switching from very bright to very dim*. *Monthly Notices of the Royal Astronomical Society* **363**, L91 (2005)
- Clowe D., Bradač M., Gonzalez A. H., Markevitch M., Randall S. W., Jones C., & Zaritsky D.: *A Direct Empirical Proof of the Existence of Dark Matter*. *The Astrophysical Journal Letters* **648**, L109 (2006)
- Cocato L., Gerhard O., Arnaboldi M., Das P., Douglas N. G., Kuijken K., Merrifield M. R., Napolitano N. R., Noordermeer E., Romanowsky A. J., et al.: *Kinematic properties of early-type galaxy haloes using planetary nebulae*. *Monthly Notices of the Royal Astronomical Society* **394**, 1249 (2009)
- Cocato L., Arnaboldi M., & Gerhard O.: *Signatures of accretion events in the haloes of early-type galaxies from comparing PNe and GCs kinematics*. *Monthly Notices of the Royal Astronomical Society* **436**, 1322 (2013)
- Colless M., Dalton G., Maddox S., Sutherland W., Norberg P., Cole S., Bland-Hawthorn J., Bridges T., Cannon R., Collins C., et al.: *The 2dF Galaxy Redshift Survey: spectra and redshifts*. *Monthly Notices of the Royal Astronomical Society* **328**, 1039 (2001)

- Conroy C. & van Dokkum P. G.: *The Stellar Initial Mass Function in Early-type Galaxies From Absorption Line Spectroscopy. II. Results*. The Astrophysical Journal **760**, 71 (2012)
- Cooper A. P., Martínez-Delgado D., Helly J., Frenk C., Cole S., Crawford K., Zibetti S., Carballo-Bello J. A., & GaBany R. J.: *The Formation of Shell Galaxies Similar to NGC 7600 in the Cold Dark Matter Cosmogony*. The Astrophysical Journal Letters **743**, L21 (2011)
- Cortesi A., Arnaboldi M., Coccato L., Merrifield M. R., Gerhard O., Bamford S., Romanowsky A. J., Napolitano N. R., Douglas N. G., Kuijken K., et al.: *The Planetary Nebula Spectrograph survey of S0 galaxy kinematics. Data and overview*. Astronomy & Astrophysics **549**, A115 (2013)
- Côté P., Marzke R. O., & West M. J.: *The Formation of Giant Elliptical Galaxies and Their Globular Cluster Systems*. The Astrophysical Journal **501**, 554 (1998)
- Cox T. J., Dutta S. N., Di Matteo T., Hernquist L., Hopkins P. F., Robertson B., & Springel V.: *The Kinematic Structure of Merger Remnants*. The Astrophysical Journal **650**, 791 (2006)
- Danovich M., Dekel A., Hahn O., Ceverino D., & Primack J.: *Four phases of angular-momentum buildup in high-z galaxies: from cosmic-web streams through an extended ring to disc and bulge*. Monthly Notices of the Royal Astronomical Society **449**, 2087 (2015)
- D'Arrest H. L.: *Zweites Verzeichniss von neuen Nebelflecken, aufgefunden am Kopenhagener Refractor im Winter 1864/65*. Astronomische Nachrichten **65**, 1 (1865)
- Davis S. W. & Laor A.: *The Radiative Efficiency of Accretion Flows in Individual Active Galactic Nuclei*. The Astrophysical Journal **728**, 98 (2011)
- Davis T. A., Bureau M., Young L. M., Alatalo K., Blitz L., Cappellari M., Scott N., Bois M., Bournaud F., Davies R. L., et al.: *The ATLAS<sup>3D</sup> project – V. The CO Tully-Fisher relation of early-type galaxies*. Monthly Notices of the Royal Astronomical Society **414**, 968 (2011)
- de Sitter W.: *Einstein's theory of gravitation and its astronomical consequences*. Monthly Notices of the Royal Astronomical Society **76**, 699 (1916a)
- de Sitter W.: *On Einstein's theory of gravitation and its astronomical consequences. Second paper*. Monthly Notices of the Royal Astronomical Society **77**, 155 (1916b)
- de Sitter W.: *Einstein's theory of gravitation and its astronomical consequences. Third paper*. Monthly Notices of the Royal Astronomical Society **78**, 3 (1917)
- de Vaucouleurs G.: *Recherches sur les Nebuleuses Extragalactiques*. Annales d'Astrophysique **11**, 247 (1948)
- de Vaucouleurs G.: *Classifying Galaxies*. Leaflet of the Astronomical Society of the Pacific **7**, 329 (1957)
- de Vaucouleurs G.: *General Physical Properties of External Galaxies*. Handbuch der Physik **53**, 311 (1959)
- de Vaucouleurs G.: *Revised Classification of 1500 Bright Galaxies*. The Astrophysical Journal Supplement **8**, 31 (1963)

- Deason A. J., Belokurov V., Evans N. W., & McCarthy I. G.: *Elliptical Galaxy Masses Out to Five Effective Radii: The Realm of Dark Matter*. The Astrophysical Journal **748**, 2 (2012)
- Deason A. J., Belokurov V., Koposov S. E., & Rockosi C. M.: *Touching The Void: A Striking Drop in Stellar Halo Density Beyond 50 kpc*. The Astrophysical Journal **787**, 30 (2014)
- Dehnen W.: *A Family of Potential-Density Pairs for Spherical Galaxies and Bulges*. Monthly Notices of the Royal Astronomical Society **265**, 250 (1993)
- Dehnen W. & Aly H.: *Improving convergence in smoothed particle hydrodynamics simulations without pairing instability*. Monthly Notices of the Royal Astronomical Society **425**, 1068 (2012)
- Dekel A., Stoehr F., Mamon G. A., Cox T. J., Novak G. S., & Primack J. R.: *Lost and found dark matter in elliptical galaxies*. Nature **437**, 707 (2005)
- Dekel A. & Birnboim Y.: *Galaxy bimodality due to cold flows and shock heating*. Monthly Notices of the Royal Astronomical Society **368**, 2 (2006)
- Dekel A., Birnboim Y., Engel G., Freundlich J., Goerdt T., Mumcuoglu M., Neistein E., Pichon C., Teyssier R., & Zinger E.: *Cold streams in early massive hot haloes as the main mode of galaxy formation*. Nature **457**, 451 (2009)
- Di Matteo P., Jog C. J., Lehnert M. D., Combes F., & Semelin B.: *Generation of rotationally dominated galaxies by mergers of pressure-supported progenitors*. Astronomy & Astrophysics **501**, L9 (2009)
- Dicke R. H., Peebles P. J. E., Roll P. G., & Wilkinson D. T.: *Cosmic Black-Body Radiation*. The Astrophysical Journal **142**, 414 (1965)
- Diemer B. & Kravtsov A. V.: *Dependence of the Outer Density Profiles of Halos on Their Mass Accretion Rate*. The Astrophysical Journal **789**, 1 (2014)
- Dolag K., Bartelmann M., & Lesch H.: *SPH simulations of magnetic fields in galaxy clusters*. Astronomy & Astrophysics **348**, 351 (1999)
- Dolag K., Jubelgas M., Springel V., Borgani S., & Rasia E.: *Thermal Conduction in Simulated Galaxy Clusters*. The Astrophysical Journal Letters **606**, L97 (2004)
- Dolag K., Vazza F., Brunetti G., & Tormen G.: *Turbulent gas motions in galaxy cluster simulations: the role of smoothed particle hydrodynamics viscosity*. Monthly Notices of the Royal Astronomical Society **364**, 753 (2005)
- Dolag K., Borgani S., Murante G., & Springel V.: *Substructures in hydrodynamical cluster simulations*. Monthly Notices of the Royal Astronomical Society **399**, 497 (2009)
- Dressler A.: *Galaxy morphology in rich clusters – Implications for the formation and evolution of galaxies*. The Astrophysical Journal **236**, 351 (1980)
- Duc P.-A., Cuillandre J.-C., Karabal E., Cappellari M., Alatalo K., Blitz L., Bournaud F., Bureau M., Crocker A. F., Davies R. L., et al.: *The ATLAS<sup>3D</sup> project – XXIX. The new look of early-type galaxies and surrounding fields disclosed by extremely deep optical images*. Monthly Notices of the Royal Astronomical Society **446**, 120 (2015)

- Dutton A. A., van den Bosch F. C., Dekel A., & Courteau S.: *A Revised Model for the Formation of Disk Galaxies: Low Spin and Dark Halo Expansion*. The Astrophysical Journal **654**, 27 (2007)
- Ebrova I., Jungwiert B., Canalizo G., Bennert N., & Jilkova L.: *Shell Galaxies: Dynamical Friction, Gradual Satellite Decay and Merger Dating*. In: Smith B., Higdon J., Higdon S., & Bastian N. (eds.): *Galaxy Wars: Stellar Populations and Star Formation in Interacting Galaxies*. Astronomical Society of the Pacific Conference Series **423**, 236 (2010)
- Efstathiou G.: *A model of supernova feedback in galaxy formation*. Monthly Notices of the Royal Astronomical Society **317**, 697 (2000)
- Einasto J.: *On the Construction of a Composite Model for the Galaxy and on the Determination of the System of Galactic Parameters*. Trudy Astrofizicheskogo Instituta Alma-Ata **5**, 87 (1965)
- Einasto J.: *Galactic Models and Stellar Orbits (Invited Lecture)*. In: Mavridis L. N. (ed.): *Stars and the Milky Way System*. 291 (1974)
- Einasto J., Kaasik A., & Saar E.: *Dynamic evidence on massive coronas of galaxies*. Nature **250**, 309 (1974)
- Einstein A.: *Zur allgemeinen Relativitatstheorie*. Sitzungsberichte der Koniglich Preuischen Akademie der Wissenschaften (Berlin), 778 (1915)
- Einstein A.: *Kosmologische Betrachtungen zur allgemeinen Relativitatstheorie*. Sitzungsberichte der Koniglich Preuischen Akademie der Wissenschaften (Berlin), 142 (1917)
- Eisenstein D. J., Weinberg D. H., Agol E., Aihara H., Allende Prieto C., Anderson S. F., Arns J. A., Aubourg . E., Bailey S., Balbinot E., et al.: *SDSS-III: Massive Spectroscopic Surveys of the Distant Universe, the Milky Way, and Extra-Solar Planetary Systems*. Astronomical Journal **142**, 72 (2011)
- Eke V. R., Baugh C. M., Cole S., Frenk C. S., Norberg P., Peacock J. A., Baldry I. K., Bland-Hawthorn J., Bridges T., Cannon R., et al.: *Galaxy groups in the 2dFGRS: the group-finding algorithm and the 2PIGG catalogue*. Monthly Notices of the Royal Astronomical Society **348**, 866 (2004)
- Emsellem E., Cappellari M., Krajnovic D., van de Ven G., Bacon R., Bureau M., Davies R. L., de Zeeuw P. T., Falcon-Barroso J., Kuntschner H., et al.: *The SAURON project – IX. A kinematic classification for early-type galaxies*. Monthly Notices of the Royal Astronomical Society **379**, 401 (2007)
- Emsellem E., Cappellari M., Krajnovic D., Alatalo K., Blitz L., Bois M., Bournaud F., Bureau M., Davies R. L., Davis T. A., et al.: *The ATLAS<sup>3D</sup> project – III. A census of the stellar angular momentum within the effective radius of early-type galaxies: unveiling the distribution of fast and slow rotators*. Monthly Notices of the Royal Astronomical Society **414**, 888 (2011)
- Espada D., Munoz-Mateos J. C., Gil de Paz A., Sabater J., Boissier S., Verley S., Athanassoula E., Bosma A., Leon S., Verdes-Montenegro L., et al.: *Star Formation in the Extended Gaseous Disk of the Isolated Galaxy CIG 96*. The Astrophysical Journal **736**, 20 (2011)

- Faber S. M. & Jackson R. E.: *Velocity dispersions and mass-to-light ratios for elliptical galaxies*. The Astrophysical Journal **204**, 668 (1976)
- Faber S. M. & Gallagher J. S.: *Masses and mass-to-light ratios of galaxies*. Annual review of astronomy and astrophysics **17**, 135 (1979)
- Fabjan D., Borgani S., Tornatore L., Saro A., Murante G., & Dolag K.: *Simulating the effect of active galactic nuclei feedback on the metal enrichment of galaxy clusters*. Monthly Notices of the Royal Astronomical Society **401**, 1670 (2010)
- Fakhouri O. & Ma C.-P.: *The nearly universal merger rate of dark matter haloes in  $\Lambda$ CDM cosmology*. Monthly Notices of the Royal Astronomical Society **386**, 577 (2008)
- Fakhouri O. & Ma C.-P.: *Environmental dependence of dark matter halo growth – I. Halo merger rates*. Monthly Notices of the Royal Astronomical Society **394**, 1825 (2009)
- Falcón-Barroso J. & Knapen J. H.: *Secular Evolution of Galaxies*. Cambridge University Press (2013)
- Fall S. M. & Efstathiou G.: *Formation and rotation of disc galaxies with haloes*. Monthly Notices of the Royal Astronomical Society **193**, 189 (1980)
- Fall S. M.: *Galaxy formation – Some comparisons between theory and observation*. In: Athanasoula E. (ed.): *Internal Kinematics and Dynamics of Galaxies*. IAU Symposium **100**, 391 (1983)
- Fall S. M. & Rees M. J.: *A theory for the origin of globular clusters*. The Astrophysical Journal **298**, 18 (1985)
- Fall S. M. & Romanowsky A. J.: *Angular Momentum and Galaxy Formation Revisited: Effects of Variable Mass-to-light Ratios*. The Astrophysical Journal Letters **769**, L26 (2013)
- Feldmann R., Carollo C. M., Mayer L., Renzini A., Lake G., Quinn T., Stinson G. S., & Yepes G.: *The Evolution of Central Group Galaxies in Hydrodynamical Simulations*. The Astrophysical Journal **709**, 218 (2010)
- Feldmann R., Carollo C. M., & Mayer L.: *The Hubble Sequence in Groups: The Birth of the Early-type Galaxies*. The Astrophysical Journal **736**, 88 (2011)
- Fernández Lorenzo M., Cepa J., Bongiovanni A., Pérez García A. M., Ederoclite A., Lara-López M. A., Pović M., & Sánchez-Portal M.: *Evolution of the fundamental plane of  $0.2 < z < 1.2$  early-type galaxies in the EGS*. Astronomy & Astrophysics **526**, A72 (2011)
- Fernández Lorenzo M., Sulentic J., Verdes-Montenegro L., & Argudo-Fernández M.: *The stellar mass-size relation for the most isolated galaxies in the local Universe*. Monthly Notices of the Royal Astronomical Society **434**, 325 (2013)
- Féron C., Hjorth J., McKean J. P., & Samsing J.: *A Search for Disk-Galaxy Lenses in the Sloan Digital Sky Survey*. The Astrophysical Journal **696**, 1319 (2009)
- Ferrarese L., Côté P., Jordán A., Peng E. W., Blakeslee J. P., Piatek S., Mei S., Merritt D., Milosavljević M., Tonry J. L., & West M. J.: *The ACS Virgo Cluster Survey. VI. Isophotal Analysis and the Structure of Early-Type Galaxies*. The Astrophysical Journal Supplement **164**, 334 (2006)

- Ferreras I., La Barbera F., de la Rosa I. G., Vazdekis A., de Carvalho R. R., Falcón-Barroso J., & Ricciardelli E.: *Systematic variation of the stellar initial mass function with velocity dispersion in early-type galaxies*. Monthly Notices of the Royal Astronomical Society **429**, L15 (2013)
- Forbes D. A., Brodie J. P., & Grillmair C. J.: *On the Origin of Globular Clusters in Elliptical and cD Galaxies*. Astronomical Journal **113**, 1652 (1997)
- Forbes D. A. & Ponman T. J.: *On the relationship between age and dynamics in elliptical galaxies*. Monthly Notices of the Royal Astronomical Society **309**, 623 (1999)
- Forbes D. A., Ponman T., & O'Sullivan E.: *The baryonic haloes of elliptical galaxies: radial distribution of globular clusters and diffuse hot gas*. Monthly Notices of the Royal Astronomical Society **425**, 66 (2012)
- Förster Schreiber N. M., Genzel R., Bouché N., Cresci G., Davies R., Buschkamp P., Shapiro K., Tacconi L. J., Hicks E. K. S., Genel S., et al.: *The SINS Survey: SINFONI Integral Field Spectroscopy of  $z \sim 2$  Star-forming Galaxies*. The Astrophysical Journal **706**, 1364 (2009)
- Förster Schreiber N. M., Shapley A. E., Erb D. K., Genzel R., Steidel C. C., Bouché N., Cresci G., & Davies R.: *Constraints on the Assembly and Dynamics of Galaxies. I. Detailed Rest-frame Optical Morphologies on Kiloparsec Scale of  $z \sim 2$  Star-forming Galaxies*. The Astrophysical Journal **731**, 65 (2011)
- Forte J. C., Faifer F., & Geisler D.: *Globular clusters as tracers of stellar bimodality in elliptical galaxies: the case of NGC 1399*. Monthly Notices of the Royal Astronomical Society **357**, 56 (2005)
- Foster C., Arnold J. A., Forbes D. A., Pastorello N., Romanowsky A. J., Spitler L. R., Strader J., & Brodie J. P.: *The SLUGGS survey: outer triaxiality of the fast rotator elliptical NGC 4473*. Monthly Notices of the Royal Astronomical Society **435**, 3587 (2013)
- Foster C., Lux H., Romanowsky A. J., Martínez-Delgado D., Zibetti S., Arnold J. A., Brodie J. P., Ciardullo R., GaBany R. J., Merrifield M. R., et al.: *Kinematics and simulations of the stellar stream in the halo of the Umbrella Galaxy*. Monthly Notices of the Royal Astronomical Society **442**, 3544 (2014)
- Fouqué P., Solanes J. M., Sanchis T., & Balkowski C.: *Structure, mass and distance of the Virgo cluster from a Tolman-Bondi model*. Astronomy & Astrophysics **375**, 770 (2001)
- Freeman K. C.: *On the Disks of Spiral and so Galaxies*. The Astrophysical Journal **160**, 811 (1970)
- Friedmann A.: *Über die Krümmung des Raumes*. Zeitschrift für Physik **10**, 377 (1922)
- Gallagher J. S., III & Ostriker J. P.: *A Note on Mass Loss during Collisions between Galaxies and the Formation of Giant Systems*. Astronomical Journal **77**, 288 (1972)
- Gamow G.: *Expanding Universe and the Origin of Elements*. Physical Review **70**, 572 (1946)
- Gamow G.: *The Evolution of the Universe*. Nature **162**, 680 (1948)

- Gao L., Loeb A., Peebles P. J. E., White S. D. M., & Jenkins A.: *Early Formation and Late Merging of the Giant Galaxies*. The Astrophysical Journal **614**, 17 (2004)
- Gao L., Navarro J. F., Cole S., Frenk C. S., White S. D. M., Springel V., Jenkins A., & Neto A. F.: *The redshift dependence of the structure of massive  $\Lambda$  cold dark matter haloes*. Monthly Notices of the Royal Astronomical Society **387**, 536 (2008)
- Gaspari M., Ruszkowski M., & Oh S. P.: *Chaotic cold accretion on to black holes*. Monthly Notices of the Royal Astronomical Society **432**, 3401 (2013)
- Gavazzi R., Treu T., Rhodes J. D., Koopmans L. V. E., Bolton A. S., Burles S., Massey R. J., & Moustakas L. A.: *The Sloan Lens ACS Survey. IV. The Mass Density Profile of Early-Type Galaxies out to 100 Effective Radii*. The Astrophysical Journal **667**, 176 (2007)
- Genel S., Bouché N., Naab T., Sternberg A., & Genzel R.: *The Growth of Dark Matter Halos: Evidence for Significant Smooth Accretion*. The Astrophysical Journal **719**, 229 (2010)
- Genzel R., Burkert A., Bouché N., Cresci G., Förster Schreiber N. M., Shapley A., Shapiro K., Tacconi L. J., Buschkamp P., Cimatti A., et al.: *From Rings to Bulges: Evidence for Rapid Secular Galaxy Evolution at  $z \sim 2$  from Integral Field Spectroscopy in the SINS Survey*. The Astrophysical Journal **687**, 59 (2008)
- Gerhard O. E.: *N-body simulations of disc-halo galaxies – Isolated systems, tidal interactions and merging*. Monthly Notices of the Royal Astronomical Society **197**, 179 (1981)
- Gerhard O., Kronawitter A., Saglia R. P., & Bender R.: *Dynamical Family Properties and Dark Halo Scaling Relations of Giant Elliptical Galaxies*. Astronomical Journal **121**, 1936 (2001)
- Gnedin O. Y., Kravtsov A. V., Klypin A. A., & Nagai D.: *Response of Dark Matter Halos to Condensation of Baryons: Cosmological Simulations and Improved Adiabatic Contraction Model*. The Astrophysical Journal **616**, 16 (2004)
- Gnedin O. Y., Ceverino D., Gnedin N. Y., Klypin A. A., Kravtsov A. V., Levine R., Nagai D., & Yepes G.: *Halo Contraction Effect in Hydrodynamic Simulations of Galaxy Formation*. ArXiv e-prints **1108.5736** (2011)
- Goldstein H., Poole C., & Safko J.: *Classical mechanics*. Addison-Wesley (2002)
- González-García A. C., Balcells M., & Olshevsky V. S.: *Line-of-sight velocity distributions of elliptical galaxies from collisionless mergers*. Monthly Notices of the Royal Astronomical Society **372**, L78 (2006)
- González-García A. C., Oñorbe J., Domínguez-Tenreiro R., & Gómez-Flechoso M. Á.: *Shape and kinematics of elliptical galaxies: evolution due to merging at  $z < 1.5$* . Astronomy & Astrophysics **497**, 35 (2009)
- Goto T., Okamura S., Yagi M., Sheth R. K., Bahcall N. A., Zabel S. A., Crouch M. S., Sekiguchi M., Annis J., Bernardi M., et al.: *Morphological Butcher–Oemler Effect in the SDSS “Cut and Enhance” Galaxy Cluster Catalog*. Publications of the Astronomical Society of Japan **55**, 739 (2003a)

- Goto T., Yamauchi C., Fujita Y., Okamura S., Sekiguchi M., Smail I., Bernardi M., & Gomez P. L.: *The morphology-density relation in the Sloan Digital Sky Survey*. Monthly Notices of the Royal Astronomical Society **346**, 601 (2003b)
- Gratton R. G., Carretta E., & Bragaglia A.: *Multiple populations in globular clusters. Lessons learned from the Milky Way globular clusters*. The Astronomy and Astrophysics Review **20**, 50 (2012)
- Grogin N. A. & Geller M. J.: *An Imaging and Spectroscopic Survey of Galaxies within Prominent Nearby Voids. I. The Sample and Luminosity Distribution*. Astronomical Journal **118**, 2561 (1999)
- Guedes J., Callegari S., Madau P., & Mayer L.: *Forming Realistic Late-type Spirals in a  $\Lambda$ CDM Universe: The Eris Simulation*. The Astrophysical Journal **742**, 76 (2011)
- Gunn J. E. & Gott J. R., III: *On the Infall of Matter Into Clusters of Galaxies and Some Effects on Their Evolution*. The Astrophysical Journal **176**, 1 (1972)
- Haardt F. & Madau P.: *Radiative Transfer in a Clumpy Universe. II. The Ultraviolet Extragalactic Background*. The Astrophysical Journal **461**, 20 (1996)
- Hayes M., Schaerer D., & Östlin G.: *The H-alpha luminosity function at redshift 2.2. A new determination using VLT/HAWK-I*. Astronomy & Astrophysics **509**, L5 (2010)
- Hernquist L.: *Tidal triggering of starbursts and nuclear activity in galaxies*. Nature **340**, 687 (1989)
- Hernquist L. & Katz N.: *TREESPH – A unification of SPH with the hierarchical tree method*. The Astrophysical Journal Supplement **70**, 419 (1989)
- Hernquist L. & Quinn P. J.: *Formation of shell galaxies. II. Nonspherical potentials*. The Astrophysical Journal **342**, 1 (1989)
- Hernquist L.: *An analytical model for spherical galaxies and bulges*. The Astrophysical Journal **356**, 359 (1990)
- Herrmann K. A., Ciardullo R., Feldmeier J. J., & Vinciguerra M.: *Planetary Nebulae in Face-On Spiral Galaxies. I. Planetary Nebula Photometry and Distances*. The Astrophysical Journal **683**, 630 (2008)
- Herrmann K. A. & Ciardullo R.: *Planetary Nebulae in Face-On Spiral Galaxies. III. Planetary Nebula Kinematics and Disk Mass*. The Astrophysical Journal **705**, 1686 (2009)
- Hickson P.: *Systematic properties of compact groups of galaxies*. The Astrophysical Journal **255**, 382 (1982)
- Hilz M., Naab T., Ostriker J. P., Thomas J., Burkert A., & Jesseit R.: *Relaxation and stripping – The evolution of sizes, dispersions and dark matter fractions in major and minor mergers of elliptical galaxies*. Monthly Notices of the Royal Astronomical Society **425**, 3119 (2012)
- Hilz M., Naab T., & Ostriker J. P.: *How do minor mergers promote inside-out growth of ellipticals, transforming the size, density profile and dark matter fraction?* Monthly Notices of the Royal Astronomical Society **429**, 2924 (2013)

- Hirschmann M., Dolag K., Saro A., Bachmann L., Borgani S., & Burkert A.: *Cosmological simulations of black hole growth: AGN luminosities and downsizing*. Monthly Notices of the Royal Astronomical Society **442**, 2304 (2014)
- Hoffman L., Cox T. J., Dutta S., & Hernquist L.: *The Imprint of Dissipation on the Shapes of Merger Remnant LOSVDs*. The Astrophysical Journal **705**, 920 (2009)
- Hoffman L., Cox T. J., Dutta S., & Hernquist L.: *Orbital Structure of Merger Remnants. I. Effect of Gas Fraction in Pure Disk Mergers*. The Astrophysical Journal **723**, 818 (2010)
- Holden B. P., van der Wel A., Kelson D. D., Franx M., & Illingworth G. D.: *M/L<sub>B</sub> and Color Evolution for a Deep Sample of M\* Cluster Galaxies at z ~ 1: The Formation Epoch and the Tilt of the Fundamental Plane*. The Astrophysical Journal **724**, 714 (2010)
- Holmberg E.: *On the Clustering Tendencies among the Nebulae. II. A Study of Encounters Between Laboratory Models of Stellar Systems by a New Integration Procedure*. The Astrophysical Journal **94**, 385 (1941)
- Hopkins P. F., Hernquist L., Cox T. J., Dutta S. N., & Rothberg B.: *Dissipation and Extra Light in Galactic Nuclei. I. Gas-Rich Merger Remnants*. The Astrophysical Journal **679**, 156 (2008)
- Hubble E. P.: *NGC 6822, a remote stellar system*. The Astrophysical Journal **62**, 409 (1925)
- Hubble E. P.: *Extragalactic nebulae*. The Astrophysical Journal **64**, 321 (1926)
- Hubble E. P.: *The classification of spiral nebulae*. The Observatory **50**, 276 (1927)
- Hubble E. P.: *Distribution of luminosity in elliptical nebulae*. The Astrophysical Journal **71**, 231 (1930)
- Hubble E. P.: *Realm of the Nebulae*. Yale University Press (1936)
- Hubble E.: *A Relation between Distance and Radial Velocity among Extra-Galactic Nebulae*. Proceedings of the National Academy of Science **15**, 168 (1929)
- Humphrey P. J. & Buote D. A.: *The slope of the mass profile and the tilt of the Fundamental Plane in early-type galaxies*. Monthly Notices of the Royal Astronomical Society **403**, 2143 (2010)
- Hyde J. B. & Bernardi M.: *The luminosity and stellar mass Fundamental Plane of early-type galaxies*. Monthly Notices of the Royal Astronomical Society **396**, 1171 (2009)
- Ibata R. A., Lewis G. F., McConnachie A. W., Martin N. F., Irwin M. J., Ferguson A. M. N., Babul A., Bernard E. J., Chapman S. C., Collins M., et al.: *The Large-scale Structure of the Halo of the Andromeda Galaxy. I. Global Stellar Density, Morphology and Metallicity Properties*. The Astrophysical Journal **780**, 128 (2014)
- Jaffe W.: *A simple model for the distribution of light in spherical galaxies*. Monthly Notices of the Royal Astronomical Society **202**, 995 (1983)
- Jaffé Y. L., Smith R., Candlish G. N., Poggianti B. M., Sheen Y.-K., & Verheijen M. A. W.: *BUD-HIES II: a phase-space view of HI gas stripping and star formation quenching in cluster galaxies*. Monthly Notices of the Royal Astronomical Society **448**, 1715 (2015)

- Jesseit R., Naab T., & Burkert A.: *The Validity of the Adiabatic Contraction Approximation for Dark Matter Halos*. The Astrophysical Journal Letters **571**, L89 (2002)
- Jesseit R., Naab T., & Burkert A.: *Orbital structure of collisionless merger remnants: on the origin of photometric and kinematic properties of elliptical and S0 galaxies*. Monthly Notices of the Royal Astronomical Society **360**, 1185 (2005)
- Jesseit R., Naab T., Peletier R. F., & Burkert A.: *2D kinematics of simulated disc merger remnants*. Monthly Notices of the Royal Astronomical Society **376**, 997 (2007)
- Jesseit R., Cappellari M., Naab T., Emsellem E., & Burkert A.: *Specific angular momentum of disc merger remnants and the  $\lambda_R$ -parameter*. Monthly Notices of the Royal Astronomical Society **397**, 1202 (2009)
- Johansson P. H. & Efstathiou G.: *A model for the metallicity evolution of damped Lyman  $\alpha$  systems*. Monthly Notices of the Royal Astronomical Society **371**, 1519 (2006)
- Johansson P. H., Burkert A., & Naab T.: *The Evolution of Black Hole Scaling Relations in Galaxy Mergers*. The Astrophysical Journal Letters **707**, L184 (2009a)
- Johansson P. H., Naab T., & Burkert A.: *Equal- and Unequal-Mass Mergers of Disk and Elliptical Galaxies with Black Holes*. The Astrophysical Journal **690**, 802 (2009b)
- Johansson P. H., Naab T., & Ostriker J. P.: *Forming Early-type Galaxies in  $\Lambda$ CDM Simulations. I. Assembly Histories*. The Astrophysical Journal **754**, 115 (2012)
- Jones L. R., Ponman T. J., Horton A., Babul A., Ebeling H., & Burke D. J.: *The nature and space density of fossil groups of galaxies*. Monthly Notices of the Royal Astronomical Society **343**, 627 (2003)
- Jorgensen I., Franx M., & Kjaergaard P.: *The Fundamental Plane for cluster E and S0 galaxies*. Monthly Notices of the Royal Astronomical Society **280**, 167 (1996)
- Junk V., Walch S., Heitsch F., Burkert A., Wetzstein M., Schartmann M., & Price D.: *Modelling shear flows with smoothed particle hydrodynamics and grid-based methods*. Monthly Notices of the Royal Astronomical Society **407**, 1933 (2010)
- Kafle P. R., Sharma S., Lewis G. F., & Bland-Hawthorn J.: *On the Shoulders of Giants: Properties of the Stellar Halo and the Milky Way Mass Distribution*. The Astrophysical Journal **794**, 59 (2014)
- Kanipe J. & Webb D.: *The Arp Atlas of Peculiar Galaxies: A Chronicle and Observer's Guide*. Willmann-Bell, Inc. (2006)
- Kant I.: *Allgemeine Naturgeschichte und Theorie des Himmels*. Reprinted by tredition GmbH, Hamburg (1755, reprint)
- Karl S. J., Naab T., Johansson P. H., Kotarba H., Boily C. M., Renaud F., & Theis C.: *One Moment in Time – Modeling Star Formation in the Antennae*. The Astrophysical Journal Letters **715**, L88 (2010)

- Karl S. J., Lunttila T., Naab T., Johansson P. H., Klaas U., & Juvela M.: *Constrained simulations of the Antennae galaxies: comparison with Herschel-PACS observations*. Monthly Notices of the Royal Astronomical Society **434**, 696 (2013)
- Kartha S. S., Forbes D. A., Spitler L. R., Romanowsky A. J., Arnold J. A., & Brodie J. P.: *The SLUGGS survey: the globular cluster systems of three early-type galaxies using wide-field imaging*. Monthly Notices of the Royal Astronomical Society **437**, 273 (2014)
- Katz N. & White S. D. M.: *Hierarchical galaxy formation – Overmerging and the formation of an X-ray cluster*. The Astrophysical Journal **412**, 455 (1993)
- Katz N., Weinberg D. H., & Hernquist L.: *Cosmological Simulations with TreeSPH*. The Astrophysical Journal Supplement **105**, 19 (1996)
- Khochfar S. & Burkert A.: *Orbital parameters of merging dark matter halos*. Astronomy & Astrophysics **445**, 403 (2006)
- Khochfar S. & Silk J.: *A Simple Model for the Size Evolution of Elliptical Galaxies*. The Astrophysical Journal Letters **648**, L21 (2006)
- Kinman T. D., Suntzeff N. B., & Kraft R. P.: *The structure of the galactic halo outside the solar circle as traced by the blue horizontal branch stars*. Astronomical Journal **108**, 1722 (1994)
- Klypin A. A., Trujillo-Gomez S., & Primack J.: *Dark Matter Halos in the Standard Cosmological Model: Results from the Bolshoi Simulation*. The Astrophysical Journal **740**, 102 (2011)
- Klypin A., Yepes G., Gottlober S., Prada F., & Hess S.: *MultiDark simulations: the story of dark matter halo concentrations and density profiles*. ArXiv e-prints **1411.4001** (2014)
- Knapp G. R.: *Cold Gas and Star Formation in Elliptical Galaxies*. In: Carral P. & Cepa J. (eds.): *Star Formation in Early Type Galaxies*. Astronomical Society of the Pacific Conference Series **163**, 119 (1999)
- Kochanek C. S.: *Part 2: Strong gravitational lensing*. In: Meylan G., Jetzer P., North P., Schneider P., Kochanek C. S., & Wambsganss J. (eds.): *Saas-Fee Advanced Course 33: Gravitational Lensing: Strong, Weak and Micro*. 91 (2006)
- Komatsu E., Smith K. M., Dunkley J., Bennett C. L., Gold B., Hinshaw G., Jarosik N., Larson D., Nolta M. R., Page L., et al.: *Seven-year Wilkinson Microwave Anisotropy Probe (WMAP) Observations: Cosmological Interpretation*. The Astrophysical Journal Supplement **192**, 18 (2011)
- Koopmans L. V. E., Treu T., Bolton A. S., Burles S., & Moustakas L. A.: *The Sloan Lens ACS Survey. III. The Structure and Formation of Early-Type Galaxies and Their Evolution since  $z \sim 1$* . The Astrophysical Journal **649**, 599 (2006)
- Kormendy J.: *Brightness distributions in compact and normal galaxies. II. Structure parameters of the spheroidal component*. The Astrophysical Journal **218**, 333 (1977)
- Kormendy J. & Richstone D.: *Inward Bound—The Search For Supermassive Black Holes In Galactic Nuclei*. Annual review of astronomy and astrophysics **33**, 581 (1995)

- Kormendy J. & Bender R.: *A Proposed Revision of the Hubble Sequence for Elliptical Galaxies*. The Astrophysical Journal Letters **464**, L119 (1996)
- Kotarba H., Karl S. J., Naab T., Johansson P. H., Dolag K., Lesch H., & Stasyszyn F. A.: *Simulating Magnetic Fields in the Antennae Galaxies*. The Astrophysical Journal **716**, 1438 (2010)
- Krajnović D., Emsellem E., Cappellari M., Alatalo K., Blitz L., Bois M., Bournaud F., Bureau M., Davies R. L., Davis T. A., et al.: *The ATLAS<sup>3D</sup> project – II. Morphologies, kinematic features and alignment between photometric and kinematic axes of early-type galaxies*. Monthly Notices of the Royal Astronomical Society **414**, 2923 (2011)
- Kravtsov A. V.: *The Size–Virial Radius Relation of Galaxies*. The Astrophysical Journal Letters **764**, L31 (2013)
- Kreckel K., Platen E., Aragón-Calvo M. A., van Gorkom J. H., van de Weygaert R., van der Hulst J. M., & Beygu B.: *The Void Galaxy Survey: Optical Properties and HI Morphology and Kinematics*. Astronomical Journal **144**, 16 (2012)
- Kreckel K., van Gorkom J. H., Beygu B., van de Weygaert R., van der Hulst J. M., Aragón-Calvo M. A., & Peletier R. F.: *The Void Galaxy Survey: Galaxy Evolution and Gas Accretion in Voids*. ArXiv e-prints **1410.6597** (2014)
- Kronawitter A., Saglia R. P., Gerhard O., & Bender R.: *Orbital structure and mass distribution in elliptical galaxies*. Astronomy & Astrophysics Supplement **144**, 53 (2000)
- La Barbera F., de Carvalho R. R., de la Rosa I. G., Sorrentino G., Gal R. R., & Kohl-Moreira J. L.: *The Nature of Fossil Galaxy Groups: Are They Really Fossils?* Astronomical Journal **137**, 3942 (2009)
- La Barbera F., de Carvalho R. R., de La Rosa I. G., & Lopes P. A. A.: *SPIDER – II. The Fundamental Plane of early-type galaxies in grizYJHK*. Monthly Notices of the Royal Astronomical Society **408**, 1335 (2010a)
- La Barbera F., de Carvalho R. R., de La Rosa I. G., Lopes P. A. A., Kohl-Moreira J. L., & Capelato H. V.: *SPIDER – I. Sample and galaxy parameters in the grizYJHK wavebands*. Monthly Notices of the Royal Astronomical Society **408**, 1313 (2010b)
- La Barbera F., Lopes P. A. A., de Carvalho R. R., de La Rosa I. G., & Berlind A. A.: *SPIDER – III. Environmental dependence of the Fundamental Plane of early-type galaxies*. Monthly Notices of the Royal Astronomical Society **408**, 1361 (2010c)
- Lackner C. N., Cen R., Ostriker J. P., & Joung M. R.: *Building galaxies by accretion and in situ star formation*. Monthly Notices of the Royal Astronomical Society **425**, 641 (2012)
- Lagos C. d. P., Davis T. A., Lacey C. G., Zwaan M. A., Baugh C. M., Gonzalez-Perez V., & Padilla N. D.: *The origin of the atomic and molecular gas contents of early-type galaxies – I. A new test of galaxy formation physics*. Monthly Notices of the Royal Astronomical Society **443**, 1002 (2014)

- Lagos C. d. P., Padilla N. D., Davis T. A., Lacey C. G., Baugh C. M., Gonzalez-Perez V., Zwaan M. A., & Contreras S.: *The origin of the atomic and molecular gas contents of early-type galaxies – II. Misaligned gas accretion*. Monthly Notices of the Royal Astronomical Society **448**, 1271 (2015)
- Lane R. R., Salinas R., & Richtler T.: *Dark matter deprivation in the field elliptical galaxy NGC 7507*. Astronomy & Astrophysics **574**, A93 (2015)
- Lange R., Driver S. P., Robotham A. S. G., Kelvin L. S., Graham A. W., Alpaslan M., Andrews S. K., Baldry I. K., Bamford S., Bland-Hawthorn J., et al.: *Galaxy And Mass Assembly (GAMA): mass-size relations of  $z < 0.1$  galaxies subdivided by Sérsic index, colour and morphology*. Monthly Notices of the Royal Astronomical Society **447**, 2603 (2015)
- Lesch H. & Hanasz M.: *Strong magnetic fields and cosmic rays in very young galaxies*. Astronomy & Astrophysics **401**, 809 (2003)
- Lim J., Ao Y., & Dinh-V-Trung: *Radially Inflowing Molecular Gas in NGC 1275 Deposited by an X-Ray Cooling Flow in the Perseus Cluster*. The Astrophysical Journal **672**, 252 (2008)
- Lindner U., Einasto M., Einasto J., Freudling W., Fricke K., Lipovetsky V., Pustilnik S., Izotov Y., & Richter G.: *The distribution of galaxies in voids*. Astronomy & Astrophysics **314**, 1 (1996)
- Longair M. S.: *Galaxy Formation*. Springer (2008)
- Longair M. S.: *High Energy Astrophysics*. Cambridge University Press (2011)
- Lynden-Bell D.: *Statistical mechanics of violent relaxation in stellar systems*. Monthly Notices of the Royal Astronomical Society **136**, 101 (1967)
- Lynden-Bell D. & Lynden-Bell R. M.: *Ghostly streams from the formation of the Galaxy's halo*. Monthly Notices of the Royal Astronomical Society **275**, 429 (1995)
- Lyskova N., Churazov E., Zhuravleva I., Naab T., Oser L., Gerhard O., & Wu X.: *Testing a simple recipe for estimating galaxy masses from minimal observational data*. Monthly Notices of the Royal Astronomical Society **423**, 1813 (2012)
- Malin D. F. & Carter D.: *Giant shells around normal elliptical galaxies*. Nature **285**, 643 (1980)
- Maller A. H., Berlind A. A., Blanton M. R., & Hogg D. W.: *The Intrinsic Properties of SDSS Galaxies*. The Astrophysical Journal **691**, 394 (2009)
- Malumuth E. M. & Richstone D. O.: *The evolution of clusters of galaxies. II. Tidal stripping versus mergers as a function of richness*. The Astrophysical Journal **276**, 413 (1984)
- Mamon G. A.: *Are cluster ellipticals the products of mergers?* The Astrophysical Journal Letters **401**, L3 (1992)
- Marsan Z. C., Marchesini D., Brammer G. B., Stefanon M., Muzzin A., Fernández-Soto A., Geier S., Hainline K. N., Intema H., Karim A., et al.: *Spectroscopic Confirmation of an Ultra Massive and Compact Galaxy at  $z = 3.35$ : a Detailed Look at an Early Progenitor of Local Giant Ellipticals*. The Astrophysical Journal **801**, 133 (2015)

- Martínez-Delgado D., Gabany R. J., Crawford K., Zibetti S., Majewski S. R., Rix H.-W., Fliri J., Carballo-Bello J. A., Bardalez-Gagliuffi D. C., Peñarrubia J., et al.: *Stellar Tidal Streams in Spiral Galaxies of the Local Volume: A Pilot Survey with Modest Aperture Telescopes*. *Astronomical Journal* **140**, 962 (2010)
- Martinez-Delgado D., D’Onghia E., Chonis T. S., Beaton R. L., Teuwen K., GaBany R. J., Grebel E. K., & Morales G.: *Discovery of a stellar tidal stream around the Whale galaxy, NGC 4631*. ArXiv e-prints **1410.6368** (2014)
- Mathews W. G. & Brighenti F.: *Rapid Cooling of Dusty Gas in Elliptical Galaxies*. *The Astrophysical Journal Letters* **590**, L5 (2003)
- Matthews T. A., Morgan W. W., & Schmidt M.: *A Discussion of Galaxies Identified with Radio Sources*. *The Astrophysical Journal* **140**, 35 (1964)
- McDonald M., Bayliss M., Benson B. A., Foley R. J., Ruel J., Sullivan P., Veilleux S., Aird K. A., Ashby M. L. N., Bautz M., et al.: *A massive, cooling-flow-induced starburst in the core of a luminous cluster of galaxies*. *Nature* **488**, 349 (2012)
- McDonald M., Swinbank M., Edge A. C., Wilner D. J., Veilleux S., Benson B. A., Hogan M. T., Marrone D. P., McNamara B. R., Wei L. H., et al.: *The State of the Warm and Cold Gas in the Extreme Starburst at the Core of the Phoenix Galaxy Cluster (SPT-CLJ2344-4243)*. *The Astrophysical Journal* **784**, 18 (2014)
- McKee C. F. & Ostriker J. P.: *A theory of the interstellar medium – Three components regulated by supernova explosions in an inhomogeneous substrate*. *The Astrophysical Journal* **218**, 148 (1977)
- Menanteau F., Hughes J. P., Sifón C., Hilton M., González J., Infante L., Barrientos L. F., Baker A. J., Bond J. R., Das S., et al.: *The Atacama Cosmology Telescope: ACT-CL J0102-4915 “El Gordo,” a Massive Merging Cluster at Redshift 0.87*. *The Astrophysical Journal* **748**, 7 (2012)
- Méndez R. H., Riffeser A., Kudritzki R.-P., Matthias M., Freeman K. C., Arnaboldi M., Capaccioli M., & Gerhard O. E.: *Detection, Photometry, and Slitless Radial Velocities of 535 Planetary Nebulae in the Flattened Elliptical Galaxy NGC 4697*. *The Astrophysical Journal* **563**, 135 (2001)
- Méndez R. H., Teodorescu A. M., Kudritzki R.-P., & Burkert A.: *Kinematics of Planetary Nebulae in the Outskirts of the Elliptical Galaxy NGC 4697*. *The Astrophysical Journal* **691**, 228 (2009)
- Merritt D.: *Relaxation and tidal stripping in rich clusters of galaxies. I. Evolution of the mass distribution*. *The Astrophysical Journal* **264**, 24 (1983)
- Merritt D., Graham A. W., Moore B., Diemand J., & Terzić B.: *Empirical Models for Dark Matter Halos. I. Nonparametric Construction of Density Profiles and Comparison with Parametric Models*. *Astronomical Journal* **132**, 2685 (2006)
- Metevier A. J., Romer A. K., & Ulmer M. P.: *The Butcher-Oemler Effect at Moderate Redshift*. *Astronomical Journal* **119**, 1090 (2000)
- Meza A., Navarro J. F., Steinmetz M., & Eke V. R.: *Simulations of Galaxy Formation in a  $\Lambda$ CDM Universe. III. The Dissipative Formation of an Elliptical Galaxy*. *The Astrophysical Journal* **590**, 619 (2003)

- Miceli A., Rest A., Stubbs C. W., Hawley S. L., Cook K. H., Magnier E. A., Krisciunas K., Howell E., & Koehn B.: *Evidence for Distinct Components of the Galactic Stellar Halo from 838 RR Lyrae Stars Discovered in the LONEOS-I Survey*. The Astrophysical Journal **678**, 865 (2008)
- Mihos J. C. & Hernquist L.: *Gasdynamics and Starbursts in Major Mergers*. The Astrophysical Journal **464**, 641 (1996)
- Milgrom M.: *A modification of the Newtonian dynamics as a possible alternative to the hidden mass hypothesis*. The Astrophysical Journal **270**, 365 (1983a)
- Milgrom M.: *A modification of the Newtonian dynamics – Implications for galaxies*. The Astrophysical Journal **270**, 371 (1983b)
- Milgrom M.: *A Modification of the Newtonian Dynamics – Implications for Galaxy Systems*. The Astrophysical Journal **270**, 384 (1983c)
- Milne E. A.: *World-Structure and the Expansion of the Universe*. Zeitschrift für Astrophysik **6**, 1 (1933a)
- Milne E. A.: *Note on H. P. Robertson's paper on World-Structure*. Zeitschrift für Astrophysik **7**, 180 (1933b)
- Mo H. J., Mao S., & White S. D. M.: *The formation of galactic discs*. Monthly Notices of the Royal Astronomical Society **295**, 319 (1998)
- Mo H., van den Bosch F. C., & White S.: *Galaxy Formation and Evolution*. Cambridge University Press (2010)
- Moore B., Quinn T., Governato F., Stadel J., & Lake G.: *Cold collapse and the core catastrophe*. Monthly Notices of the Royal Astronomical Society **310**, 1147 (1999)
- Morgan W. W.: *A Preliminary Classification of the Forms of Galaxies According to Their Stellar Population*. Publications of the Astronomical Society of the Pacific **70**, 364 (1958)
- Mosleh M., Williams R. J., & Franx M.: *On the Robustness of  $z = 0-1$  Galaxy Size Measurements through Model and Non-parametric Fits*. The Astrophysical Journal **777**, 117 (2013)
- Moster B. P., Macciò A. V., Somerville R. S., Johansson P. H., & Naab T.: *Can gas prevent the destruction of thin stellar discs by minor mergers?* Monthly Notices of the Royal Astronomical Society **403**, 1009 (2010)
- Murante G., Arnaboldi M., Gerhard O., Borgani S., Cheng L. M., Diaferio A., Dolag K., Moscardini L., Tormen G., Tornatore L., & Tozzi P.: *The Diffuse Light in Simulations of Galaxy Clusters*. The Astrophysical Journal Letters **607**, L83 (2004)
- Muzzin A., Marchesini D., Stefanon M., Franx M., McCracken H. J., Milvang-Jensen B., Dunlop J. S., Fynbo J. P. U., Brammer G., Labbé I., & van Dokkum P. G.: *The Evolution of the Stellar Mass Functions of Star-forming and Quiescent Galaxies to  $z = 4$  from the COSMOS/UltraVISTA Survey*. The Astrophysical Journal **777**, 18 (2013)

- Naab T., Burkert A., & Hernquist L.: *On the Formation of Boxy and Disky Elliptical Galaxies*. The Astrophysical Journal Letters **523**, L133 (1999)
- Naab T. & Burkert A.: *Statistical Properties of Collisionless Equal- and Unequal-Mass Merger Remnants of Disk Galaxies*. The Astrophysical Journal **597**, 893 (2003)
- Naab T., Jesseit R., & Burkert A.: *The influence of gas on the structure of merger remnants*. Monthly Notices of the Royal Astronomical Society **372**, 839 (2006a)
- Naab T., Khochfar S., & Burkert A.: *Properties of Early-Type, Dry Galaxy Mergers and the Origin of Massive Elliptical Galaxies*. The Astrophysical Journal Letters **636**, L81 (2006b)
- Naab T., Johansson P. H., Ostriker J. P., & Efstathiou G.: *Formation of Early-Type Galaxies from Cosmological Initial Conditions*. The Astrophysical Journal **658**, 710 (2007)
- Naab T., Johansson P. H., & Ostriker J. P.: *Minor Mergers and the Size Evolution of Elliptical Galaxies*. The Astrophysical Journal Letters **699**, L178 (2009)
- Naab T. & Ostriker J. P.: *Are Disk Galaxies the Progenitors of Giant Ellipticals?* The Astrophysical Journal **690**, 1452 (2009)
- Naab T., Oser L., Emsellem E., Cappellari M., Krajnović D., McDermid R. M., Alatalo K., Bayet E., Blitz L., Bois M., et al.: *The ATLAS<sup>3D</sup> project – XXV. Two-dimensional kinematic analysis of simulated galaxies and the cosmological origin of fast and slow rotators*. Monthly Notices of the Royal Astronomical Society **444**, 3357 (2014)
- Napolitano N. R., Arnaboldi M., Freeman K. C., & Capaccioli M.: *Planetary nebulae as mass tracers of their parent galaxies: Biases in the estimate of the kinematical quantities*. Astronomy & Astrophysics **377**, 784 (2001)
- Napolitano N. R., Romanowsky A. J., Coccato L., Capaccioli M., Douglas N. G., Noordermeer E., Gerhard O., Arnaboldi M., de Lorenzi F., Kuijken K., et al.: *The Planetary Nebula Spectrograph elliptical galaxy survey: the dark matter in NGC 4494*. Monthly Notices of the Royal Astronomical Society **393**, 329 (2009)
- Napolitano N. R., Romanowsky A. J., Capaccioli M., Douglas N. G., Arnaboldi M., Coccato L., Gerhard O., Kuijken K., Merrifield M. R., Bamford S. P., et al.: *The P.N.S Elliptical Galaxy Survey: a standard  $\Lambda$ CDM halo around NGC 4374?* Monthly Notices of the Royal Astronomical Society **411**, 2035 (2011)
- Napolitano N. R., Pota V., Romanowsky A. J., Forbes D. A., Brodie J. P., & Foster C.: *The SLUGGS survey: breaking degeneracies between dark matter, anisotropy and the IMF using globular cluster subpopulations in the giant elliptical NGC 5846*. Monthly Notices of the Royal Astronomical Society **439**, 659 (2014)
- Navarro J. F. & White S. D. M.: *Simulations of dissipative galaxy formation in hierarchically clustering universes. 2. Dynamics of the baryonic component in galactic haloes*. Monthly Notices of the Royal Astronomical Society **267**, 401 (1994)

- Navarro J. F., Frenk C. S., & White S. D. M.: *The Structure of Cold Dark Matter Halos*. The Astrophysical Journal **462**, 563 (1996)
- Navarro J. F., Frenk C. S., & White S. D. M.: *A Universal Density Profile from Hierarchical Clustering*. The Astrophysical Journal **490**, 493 (1997)
- Navarro J. F., Hayashi E., Power C., Jenkins A. R., Frenk C. S., White S. D. M., Springel V., Stadel J., & Quinn T. R.: *The inner structure of  $\Lambda$ CDM haloes – III. Universality and asymptotic slopes*. Monthly Notices of the Royal Astronomical Society **349**, 1039 (2004)
- Navarro J. F., Ludlow A., Springel V., Wang J., Vogelsberger M., White S. D. M., Jenkins A., Frenk C. S., & Helmi A.: *The diversity and similarity of simulated cold dark matter haloes*. Monthly Notices of the Royal Astronomical Society **402**, 21 (2010)
- Negroponte J. & White S. D. M.: *Simulations of mergers between disc-halo galaxies*. Monthly Notices of the Royal Astronomical Society **205**, 1009 (1983)
- Neronov A. & Vovk I.: *Evidence for Strong Extragalactic Magnetic Fields from Fermi Observations of TeV Blazars*. Science **328**, 73 (2010)
- Newberg H. J., Yanny B., Rockosi C., Grebel E. K., Rix H.-W., Brinkmann J., Csabai I., Hennessy G., Hindsley R. B., Ibata R., et al.: *The Ghost of Sagittarius and Lumps in the Halo of the Milky Way*. The Astrophysical Journal **569**, 245 (2002)
- Newman A. B., Ellis R. S., Treu T., & Bundy K.: *Keck Spectroscopy of  $z > 1$  Field Spheroidals: Dynamical Constraints on the Growth Rate of Red “Nuggets”*. The Astrophysical Journal Letters **717**, L103 (2010)
- Newman A. B., Treu T., Ellis R. S., & Sand D. J.: *The Density Profiles of Massive, Relaxed Galaxy Clusters. II. Separating Luminous and Dark Matter in Cluster Cores*. The Astrophysical Journal **765**, 25 (2013)
- Newman A. B., Ellis R. S., & Treu T.: *Luminous and Dark Matter Profiles from Galaxies to Clusters: Bridging the Gap with Group-scale Lenses*. ArXiv e-prints **1503.05282** (2015)
- Novak G. S., Jonsson P., Primack J. R., Cox T. J., & Dekel A.: *On galaxies and homology*. Monthly Notices of the Royal Astronomical Society **424**, 635 (2012)
- Oñorbe J., Domínguez-Tenreiro R., Sáiz A., & Serna A.: *Bright and dark matter in elliptical galaxies: mass and velocity distributions from self-consistent hydrodynamical simulations*. Monthly Notices of the Royal Astronomical Society **376**, 39 (2007)
- Obreschkow D. & Glazebrook K.: *Fundamental Mass-Spin-Morphology Relation Of Spiral Galaxies*. The Astrophysical Journal **784**, 26 (2014)
- Onodera M., Renzini A., Carollo M., Cappellari M., Mancini C., Strazzullo V., Daddi E., Arimoto N., Gobat R., Yamada Y., et al.: *Deep Near-infrared Spectroscopy of Passively Evolving Galaxies at  $z \gtrsim 1.4$* . The Astrophysical Journal **755**, 26 (2012)
- Oort J. H.: *Some Problems Concerning the Structure and Dynamics of the Galactic System and the Elliptical Nebulae NGC 3115 and 4494*. The Astrophysical Journal **91**, 273 (1940)

- Oser L., Ostriker J. P., Naab T., Johansson P. H., & Burkert A.: *The Two Phases of Galaxy Formation*. The Astrophysical Journal **725**, 2312 (2010)
- Oser L., Naab T., Ostriker J. P., & Johansson P. H.: *The Cosmological Size and Velocity Dispersion Evolution of Massive Early-type Galaxies*. The Astrophysical Journal **744**, 63 (2012)
- Padoan P., Jimenez R., & Jones B.: *On star formation in primordial protoglobular clouds*. Monthly Notices of the Royal Astronomical Society **285**, 711 (1997a)
- Padoan P., Nordlund A., & Jones B. J. T.: *The universality of the stellar initial mass function*. Monthly Notices of the Royal Astronomical Society **288**, 145 (1997b)
- Pan D. C., Vogeley M. S., Hoyle F., Choi Y.-Y., & Park C.: *Cosmic voids in Sloan Digital Sky Survey Data Release 7*. Monthly Notices of the Royal Astronomical Society **421**, 926 (2012)
- Peebles P. J. E. & Dicke R. H.: *Origin of the Globular Star Clusters*. The Astrophysical Journal **154**, 891 (1968)
- Peebles P. J. E.: *Origin of the Angular Momentum of Galaxies*. The Astrophysical Journal **155**, 393 (1969)
- Peebles P. J. E.: *Rotation of Galaxies and the Gravitational Instability Picture*. Astronomy & Astrophysics **11**, 377 (1971)
- Peebles P. J. E.: *Dark matter and the origin of galaxies and globular star clusters*. The Astrophysical Journal **277**, 470 (1984)
- Peng E. W., Ford H. C., & Freeman K. C.: *The Planetary Nebula System and Dynamics in the Outer Halo of NGC 5128*. The Astrophysical Journal **602**, 685 (2004a)
- Peng E. W., Ford H. C., & Freeman K. C.: *The Globular Cluster System of NGC 5128. II. Ages, Metallicities, Kinematics, and Formation*. The Astrophysical Journal **602**, 705 (2004b)
- Peng E. W., Jordán A., Côté P., Blakeslee J. P., Ferrarese L., Mei S., West M. J., Merritt D., Milosavljević M., & Tonry J. L.: *The ACS Virgo Cluster Survey. IX. The Color Distributions of Globular Cluster Systems in Early-Type Galaxies*. The Astrophysical Journal **639**, 95 (2006)
- Peng E. W., Jordán A., Blakeslee J. P., Mieske S., Côté P., Ferrarese L., Harris W. E., Madrid J. P., & Meurer G. R.: *The Color-Magnitude Relation for Metal-Poor Globular Clusters in M87: Confirmation from Deep HST/ACS Imaging*. The Astrophysical Journal **703**, 42 (2009)
- Penzias A. A. & Wilson R. W.: *A Measurement of Excess Antenna Temperature at 4080 Mc/s*. The Astrophysical Journal **142**, 419 (1965)
- Perlmutter S., Aldering G., della Valle M., Deustua S., Ellis R. S., Fabbro S., Fruchter A., Goldhaber G., Groom D. E., Hook I. M., et al.: *Discovery of a supernova explosion at half the age of the universe*. Nature **391**, 51 (1998)
- Pillepich A., Vogelsberger M., Deason A., Rodriguez-Gomez V., Genel S., Nelson D., Torrey P., Sales L. V., Marinacci F., Springel V., et al.: *Halo mass and assembly history exposed in the faint outskirts: the stellar and dark matter haloes of Illustris galaxies*. Monthly Notices of the Royal Astronomical Society **444**, 237 (2014)

- Planck Collaboration, Ade P. A. R., Aghanim N., Arnaud M., Ashdown M., Atrio-Barandela F., Aumont J., Baccigalupi C., Balbi A., Banday A. J., et al.: *Planck intermediate results. V. Pressure profiles of galaxy clusters from the Sunyaev-Zeldovich effect*. *Astronomy & Astrophysics* **550**, A131 (2013)
- Planck Collaboration, Ade P. A. R., Aghanim N., Arnaud M., Ashdown M., Aumont J., Baccigalupi C., Banday A. J., Barreiro R. B., Bartlett J. G., et al.: *Planck 2015 results. XIII. Cosmological parameters*. ArXiv e-prints **1502.01589** (2015)
- Plummer H. C.: *On the problem of distribution in globular star clusters*. *Monthly Notices of the Royal Astronomical Society* **71**, 460 (1911)
- Pointecouteau E., Arnaud M., & Pratt G. W.: *The structural and scaling properties of nearby galaxy clusters. I. The universal mass profile*. *Astronomy & Astrophysics* **435**, 1 (2005)
- Pontzen A. & Governato F.: *How supernova feedback turns dark matter cusps into cores*. *Monthly Notices of the Royal Astronomical Society* **421**, 3464 (2012)
- Pota V., Forbes D. A., Romanowsky A. J., Brodie J. P., Spitler L. R., Strader J., Foster C., Arnold J. A., Benson A., Blom C., et al.: *The SLUGGS Survey: kinematics for over 2500 globular clusters in 12 early-type galaxies*. *Monthly Notices of the Royal Astronomical Society* **428**, 389 (2013)
- Prada F., Klypin A. A., Cuesta A. J., Betancort-Rijo J. E., & Primack J.: *Halo concentrations in the standard  $\Lambda$  cold dark matter cosmology*. *Monthly Notices of the Royal Astronomical Society* **423**, 3018 (2012)
- Pratt G. W. & Arnaud M.: *XMM-Newton observations of three poor clusters: Similarity in dark matter and entropy profiles down to low mass*. *Astronomy & Astrophysics* **429**, 791 (2005)
- Preston G. W., Shectman S. A., & Beers T. C.: *Detection of a galactic color gradient for blue horizontal-branch stars of the halo field and implications for the halo age and density distributions*. *The Astrophysical Journal* **375**, 121 (1991)
- Price D. J.: *Modelling discontinuities and Kelvin Helmholtz instabilities in SPH*. *Journal of Computational Physics* **227**, 10040 (2008)
- Prieur J.-L.: *The shell system around NGC 3923 and its implications for the potential of the galaxy*. *The Astrophysical Journal* **326**, 596 (1988)
- Purcell C. W., Kazantzidis S., & Bullock J. S.: *The Destruction of Thin Stellar Disks Via Cosmologically Common Satellite Accretion Events*. *The Astrophysical Journal Letters* **694**, L98 (2009)
- Qu Y., Di Matteo P., Lehnert M., van Driel W., & Jog C. J.: *The slowing down of galaxy disks in dissipationless minor mergers*. *Astronomy & Astrophysics* **515**, A11 (2010)
- Quinn P. J.: *On the formation and dynamics of shells around elliptical galaxies*. *The Astrophysical Journal* **279**, 596 (1984)
- Rashkov V., Pillepich A., Deason A. J., Madau P., Rockosi C. M., Guedes J., & Mayer L.: *A “Light,” Centrally Concentrated Milky Way Halo?* *The Astrophysical Journal Letters* **773**, L32 (2013)

- Rejkuba M., Harris W. E., Greggio L., Harris G. L. H., Jerjen H., & Gonzalez O. A.: *Tracing the Outer Halo in a Giant Elliptical to 25  $R_{\text{eff}}$* . *The Astrophysical Journal Letters* **791**, L2 (2014)
- Remus R.-S.: *The Evolution of Galaxies in Groups*. Diploma thesis, Ludwig-Maximilians-Universität München (2009)
- Remus R.-S., Burkert A., Dolag K., Johansson P. H., Naab T., Oser L., & Thomas J.: *The Dark Halo–Spheroid Conspiracy and the Origin of Elliptical Galaxies*. *The Astrophysical Journal* **766**, 71 (2013)
- Remus R.-S., Dolag K., Bachmann L. K., Beck A. M., Burkert A., Hirschmann M., & Teklu A.: *Disk Galaxies in the Magneticum Pathfinder Simulations*. In: Ziegler B. L., Combes F., Dannerbauer H., & Verdugo M. (eds.): *Galaxies in 3D across the Universe*. IAU Symposium **309**, 145 (2015a)
- Remus R.-S., Dolag K., & Burkert A.: *The Dark Halo–Spheroid Conspiracy Reloaded: Evolution with Redshift*. In: Cappellari M. & Courteau S. (eds.): *Galaxy Masses as Constraints of Formation Models*. IAU Symposium **311**, 116 (2015b)
- Retana-Montenegro E., van Hese E., Gentile G., Baes M., & Frutos-Alfaro F.: *Analytical properties of Einasto dark matter haloes*. *Astronomy & Astrophysics* **540**, A70 (2012)
- Ricciardelli E., Cava A., Varela J., & Quilis V.: *The star formation activity in cosmic voids*. *Monthly Notices of the Royal Astronomical Society* **445**, 4045 (2014)
- Richtler T., Salinas R., Lane R. R., Hilker M., & Schirmer M.: *Isolated elliptical galaxies and their globular cluster systems. II. NGC 7796 – globular clusters, dynamics, companion*. *Astronomy & Astrophysics* **574**, A21 (2015)
- Riess A. G., Filippenko A. V., Challis P., Clocchiatti A., Diercks A., Garnavich P. M., Gilliland R. L., Hogan C. J., Jha S., Kirshner R. P., et al.: *Observational Evidence from Supernovae for an Accelerating Universe and a Cosmological Constant*. *Astronomical Journal* **116**, 1009 (1998)
- Riffeser A., Seitz S., & Bender R.: *The M31 Microlensing Event WeCAPP-GL1/POINT-AGAPE-S3: Evidence for a MACHO Component in the Dark Halo of M31?* *The Astrophysical Journal* **684**, 1093 (2008)
- Romanowsky A. J., Douglas N. G., Arnaboldi M., Kuijken K., Merrifield M. R., Napolitano N. R., Capaccioli M., & Freeman K. C.: *A Dearth of Dark Matter in Ordinary Elliptical Galaxies*. *Science* **301**, 1696 (2003)
- Romanowsky A. J., Strader J., Spitler L. R., Johnson R., Brodie J. P., Forbes D. A., & Ponman T.: *Mapping The Dark Side with DEIMOS: Globular Clusters, X-Ray Gas, and Dark Matter in the NGC 1407 Group*. *Astronomical Journal* **137**, 4956 (2009)
- Romanowsky A. J. & Fall S. M.: *Angular Momentum and Galaxy Formation Revisited*. *The Astrophysical Journal Supplement* **203**, 17 (2012)
- Rosenblatt E. I., Faber S. M., & Blumenthal G. R.: *Pregalactic formation of globular clusters in cold dark matter*. *The Astrophysical Journal* **330**, 191 (1988)

- Rubin V. C., Burbidge E. M., Burbidge G. R., Crampin D. J., & Prendergast K. H.: *The Rotation and Mass of NGC 7331*. The Astrophysical Journal **141**, 759 (1965)
- Rubin V. C. & Ford W. K., Jr.: *Rotation of the Andromeda Nebula from a Spectroscopic Survey of Emission Regions*. The Astrophysical Journal **159**, 379 (1970)
- Rubin V. C., Thonnard N., & Ford W. K., Jr.: *Extended rotation curves of high-luminosity spiral galaxies. IV. Systematic dynamical properties, Sa→Sc*. The Astrophysical Journal Letters **225**, L107 (1978)
- Rubin V. C., Ford W. K. J., & Thonnard N.: *Rotational properties of 21 Sc galaxies with a large range of luminosities and radii, from NGC 4605 ( $R = 4$  kpc) to UGC 2885 ( $R = 122$  kpc)*. The Astrophysical Journal **238**, 471 (1980)
- Ruff A. J., Gavazzi R., Marshall P. J., Treu T., Auger M. W., & Braut F.: *The SL2S Galaxy-scale Lens Sample. II. Cosmic Evolution of Dark and Luminous Mass in Early-type Galaxies*. The Astrophysical Journal **727**, 96 (2011)
- Russell H. R., McNamara B. R., Edge A. C., Hogan M. T., Main R. A., & Vantyghem A. N.: *Radiative efficiency, variability and Bondi accretion on to massive black holes: the transition from radio AGN to quasars in brightest cluster galaxies*. Monthly Notices of the Royal Astronomical Society **432**, 530 (2013)
- Salpeter E. E.: *The Luminosity Function and Stellar Evolution*. The Astrophysical Journal **121**, 161 (1955)
- Sandage A.: *The Hubble atlas of galaxies*. Carnegie Institution (1961)
- Saro A., Liu J., Mohr J. J., Aird K. A., Ashby M. L. N., Bayliss M., Benson B. A., Bleem L. E., Bocquet S., Brodwin M., et al.: *Constraints on the CMB temperature evolution using multiband measurements of the Sunyaev-Zel'dovich effect with the South Pole Telescope*. Monthly Notices of the Royal Astronomical Society **440**, 2610 (2014)
- Saulder C., van den Bosch R. C. E., & Mieske S.: *Dozens of compact and high velocity-dispersion early-type galaxies in Sloan Digital Sky Survey*. ArXiv e-prints **1503.05117** (2015)
- Scannapieco C., Tissera P. B., White S. D. M., & Springel V.: *Effects of supernova feedback on the formation of galaxy discs*. Monthly Notices of the Royal Astronomical Society **389**, 1137 (2008)
- Schauer A. T. P.: *Tracing the Kinematics of Galaxies: Planetary Nebulae in NGC 4244*. Master's thesis, Ludwig-Maximilians-Universität München (2014a)
- Schauer A. T. P.: *The Mystery of the  $\sigma$ -Bump: A new Signature for Major Mergers?* Master's thesis, Ludwig-Maximilians-Universität München (2014b)
- Schauer A. T. P., Remus R.-S., Burkert A., & Johansson P. H.: *The Mystery of the  $\sigma$ -Bump – A New Signature for Major Mergers in Early-type Galaxies?* The Astrophysical Journal Letters **783**, L32 (2014)

- Schaye J., Dalla Vecchia C., Booth C. M., Wiersma R. P. C., Theuns T., Haas M. R., Bertone S., Duffy A. R., McCarthy I. G., & van de Voort F.: *The physics driving the cosmic star formation history*. Monthly Notices of the Royal Astronomical Society **402**, 1536 (2010)
- Schaye J., Crain R. A., Bower R. G., Furlong M., Schaller M., Theuns T., Dalla Vecchia C., Frenk C. S., McCarthy I. G., Helly J. C., et al.: *The EAGLE project: simulating the evolution and assembly of galaxies and their environments*. Monthly Notices of the Royal Astronomical Society **446**, 521 (2015)
- Schlachtberger D. P.: *The Origin of Cold Gas in the Center of Massive Elliptical Galaxies*. Master's thesis, Ludwig-Maximilians-Universität München (2014)
- Schuberth Y., Richtler T., Hilker M., Dirsch B., Bassino L. P., Romanowsky A. J., & Infante L.: *The globular cluster system of NGC 1399. V. dynamics of the cluster system out to 80 kpc*. Astronomy & Astrophysics **513**, A52 (2010)
- Scott N., Graham A. W., & Schombert J.: *The Supermassive Black Hole Mass-Spheroid Stellar Mass Relation for Sérsic and Core-Sérsic Galaxies*. The Astrophysical Journal **768**, 76 (2013)
- Semler D. R., Šuhada R., Aird K. A., Ashby M. L. N., Bautz M., Bayliss M., Bazin G., Bocquet S., Benson B. A., Bleem L. E., et al.: *High-redshift Cool-core Galaxy Clusters Detected via the Sunyaev-Zel'dovich Effect in the South Pole Telescope Survey*. The Astrophysical Journal **761**, 183 (2012)
- Sereno M., Fedeli C., & Moscardini L.: *Comparison of weak lensing by NFW and Einasto halos and systematic errors*. ArXiv e-prints **1504.05183** (2015)
- Sérsic J. L.: *Influence of the atmospheric and instrumental dispersion on the brightness distribution in a galaxy*. Boletín de la Asociación Argentina de Astronomía La Plata Argentina **6**, 41 (1963)
- Shen S., Mo H. J., White S. D. M., Blanton M. R., Kauffmann G., Voges W., Brinkmann J., & Csabai I.: *The size distribution of galaxies in the Sloan Digital Sky Survey*. Monthly Notices of the Royal Astronomical Society **343**, 978 (2003)
- Shih H.-Y. & Méndez R. H.: *Possible Stellar Streams in the Edge-on Spiral NGC 891 Discovered from Kinematics of Planetary Nebulae*. The Astrophysical Journal Letters **725**, L97 (2010)
- Smoot G. F., Bennett C. L., Kogut A., Wright E. L., Aymon J., Boggess N. W., Cheng E. S., de Amici G., Gulkis S., Hauser M. G., et al.: *Structure in the COBE differential microwave radiometer first-year maps*. The Astrophysical Journal Letters **396**, L1 (1992)
- Sonnenfeld A., Treu T., Gavazzi R., Marshall P. J., Auger M. W., Suyu S. H., Koopmans L. V. E., & Bolton A. S.: *Evidence for Dark Matter Contraction and a Salpeter Initial Mass Function in a Massive Early-type Galaxy*. The Astrophysical Journal **752**, 163 (2012)
- Sonnenfeld A., Gavazzi R., Suyu S. H., Treu T., & Marshall P. J.: *The SL2S Galaxy-scale Lens Sample. III. Lens Models, Surface Photometry, and Stellar Masses for the Final Sample*. The Astrophysical Journal **777**, 97 (2013a)

- Sonnenfeld A., Treu T., Gavazzi R., Suyu S. H., Marshall P. J., Auger M. W., & Nipoti C.: *The SL2S Galaxy-scale Lens Sample. IV. The Dependence of the Total Mass Density Profile of Early-type Galaxies on Redshift, Stellar Mass, and Size*. The Astrophysical Journal **777**, 98 (2013b)
- Sonnenfeld A., Nipoti C., & Treu T.: *Purely Dry Mergers do not Explain the Observed Evolution of Massive Early-type Galaxies since  $z \sim 1$* . The Astrophysical Journal **786**, 89 (2014)
- Spergel D. N., Bean R., Doré O., Nolta M. R., Bennett C. L., Dunkley J., Hinshaw G., Jarosik N., Komatsu E., Page L., et al.: *Three-Year Wilkinson Microwave Anisotropy Probe (WMAP) Observations: Implications for Cosmology*. The Astrophysical Journal Supplement **170**, 377 (2007)
- Spitzer L., Jr.: *The Dynamics of the Interstellar Medium. III. Galactic Distribution*. The Astrophysical Journal **95**, 329 (1942)
- Springel V.: *Modelling star formation and feedback in simulations of interacting galaxies*. Monthly Notices of the Royal Astronomical Society **312**, 859 (2000)
- Springel V., White S. D. M., Tormen G., & Kauffmann G.: *Populating a cluster of galaxies – I. Results at  $z = 0$* . Monthly Notices of the Royal Astronomical Society **328**, 726 (2001)
- Springel V. & Hernquist L.: *Cosmological smoothed particle hydrodynamics simulations: the entropy equation*. Monthly Notices of the Royal Astronomical Society **333**, 649 (2002)
- Springel V. & Hernquist L.: *Cosmological smoothed particle hydrodynamics simulations: a hybrid multiphase model for star formation*. Monthly Notices of the Royal Astronomical Society **339**, 289 (2003)
- Springel V.: *The cosmological simulation code GADGET-2*. Monthly Notices of the Royal Astronomical Society **364**, 1105 (2005)
- Springel V., Di Matteo T., & Hernquist L.: *Black Holes in Galaxy Mergers: The Formation of Red Elliptical Galaxies*. The Astrophysical Journal Letters **620**, L79 (2005a)
- Springel V., Di Matteo T., & Hernquist L.: *Modelling feedback from stars and black holes in galaxy mergers*. Monthly Notices of the Royal Astronomical Society **361**, 776 (2005b)
- Springel V. & Hernquist L.: *Formation of a Spiral Galaxy in a Major Merger*. The Astrophysical Journal Letters **622**, L9 (2005)
- Springel V., White S. D. M., Jenkins A., Frenk C. S., Yoshida N., Gao L., Navarro J., Thacker R., Croton D., Helly J., et al.: *Simulations of the formation, evolution and clustering of galaxies and quasars*. Nature **435**, 629 (2005c)
- Springel V., Wang J., Vogelsberger M., Ludlow A., Jenkins A., Helmi A., Navarro J. F., Frenk C. S., & White S. D. M.: *The Aquarius Project: the subhaloes of galactic haloes*. Monthly Notices of the Royal Astronomical Society **391**, 1685 (2008)
- Springel V.: *E pur si muove: Galilean-invariant cosmological hydrodynamical simulations on a moving mesh*. Monthly Notices of the Royal Astronomical Society **401**, 791 (2010)

- Stadel J., Potter D., Moore B., Diemand J., Madau P., Zemp M., Kuhlen M., & Quilis V.: *Quantifying the heart of darkness with GHALO – a multibillion particle simulation of a galactic halo*. Monthly Notices of the Royal Astronomical Society **398**, L21 (2009)
- Steinborn L. K., Dolag K., Hirschmann M., Prieto M. A., & Remus R.-S.: *A refined sub-grid model for black hole accretion and AGN feedback in large cosmological simulations*. Monthly Notices of the Royal Astronomical Society **448**, 1504 (2015)
- Steinmetz M. & Navarro J. F.: *The Cosmological Origin of the Tully-Fisher Relation*. The Astrophysical Journal **513**, 555 (1999)
- Sulentic J. W., Verdes-Montenegro L., Bergond G., Lisenfeld U., Durbala A., Espada D., Garcia E., Leon S., Sabater J., Verley S., et al.: *The AMIGA sample of isolated galaxies. II. Morphological refinement*. Astronomy & Astrophysics **449**, 937 (2006)
- Sunyaev R. A. & Zeldovich I. B.: *Microwave background radiation as a probe of the contemporary structure and history of the universe*. Annual review of astronomy and astrophysics **18**, 537 (1980)
- Szapudi I., Kovács A., Granett B. R., Frei Z., Silk J., Burgett W., Cole S., Draper P. W., Farrow D. J., Kaiser N., et al.: *Detection of a Supervoid Aligned with the Cold Spot of the Cosmic Microwave Background*. ArXiv e-prints **1405.1566** (2014a)
- Szapudi I., Kovács A., Granett B. R., Frei Z., Silk J., Garcia-Bellido J., Burgett W., Cole S., Draper P. W., Farrow D. J., et al.: *The Cold Spot in the Cosmic Microwave Background: the Shadow of a Supervoid*. ArXiv e-prints **1406.3622** (2014b)
- Szomoru A., van Gorkom J. H., Gregg M. D., & Strauss M. A.: *An HI Survey of the Bootes Void. II. The Analysis*. Astronomical Journal **111**, 2150 (1996)
- Szomoru D., Franx M., & van Dokkum P. G.: *Sizes and Surface Brightness Profiles of Quiescent Galaxies at  $z \sim 2$* . The Astrophysical Journal **749**, 121 (2012)
- Szomoru D., Franx M., van Dokkum P. G., Trenti M., Illingworth G. D., Labbé I., & Oesch P.: *The Stellar Mass Structure of Massive Galaxies from  $z = 0$  to  $z = 2.5$ : Surface Density Profiles and Half-mass Radii*. The Astrophysical Journal **763**, 73 (2013)
- Tanaka M., Chiba M., Komiyama Y., Guhathakurta P., Kalirai J. S., & Iye M.: *Structure and Population of the Andromeda Stellar Halo from a Subaru/Suprime-Cam Survey*. The Astrophysical Journal **708**, 1168 (2010)
- Teklu A. F.: *Angular Momentum Distribution in Galactic Halos*. Master's thesis, Ludwig-Maximilians-Universität München (2014)
- Teklu A. F., Remus R.-S., Dolag K., Beck A. M., Burkert A., Schmidt A. S., Schulze F., & Steinborn L. K.: *Connecting Angular Momentum and Galactic Dynamics: The complex Interplay between Spin, Mass, and Morphology*. ArXiv e-prints **1503.03501** (2015a)
- Teklu A., Remus R.-S., Dolag K., & Burkert A.: *The Angular Momentum Dichotomy*. In: Ziegler B. L., Combes F., Dannerbauer H., & Verdugo M. (eds.): *Galaxies in 3D across the Universe*. IAU Symposium **309**, 349 (2015b)

- Teyssier R., Pires S., Prunet S., Aubert D., Pichon C., Amara A., Benabed K., Colombi S., Refregier A., & Starck J.-L.: *Full-sky weak-lensing simulation with 70 billion particles*. *Astronomy & Astrophysics* **497**, 335 (2009)
- Thomas J., Saglia R. P., Bender R., Thomas D., Gebhardt K., Magorrian J., Corsini E. M., & Wegner G.: *Dynamical modelling of luminous and dark matter in 17 Coma early-type galaxies*. *Monthly Notices of the Royal Astronomical Society* **382**, 657 (2007)
- Thomas J., Saglia R. P., Bender R., Thomas D., Gebhardt K., Magorrian J., Corsini E. M., & Wegner G.: *Dark Matter Scaling Relations and the Assembly Epoch of Coma Early-Type Galaxies*. *The Astrophysical Journal* **691**, 770 (2009)
- Thomas J., Saglia R. P., Bender R., Thomas D., Gebhardt K., Magorrian J., Corsini E. M., Wegner G., & Seitz S.: *Dynamical masses of early-type galaxies: a comparison to lensing results and implications for the stellar initial mass function and the distribution of dark matter*. *Monthly Notices of the Royal Astronomical Society* **415**, 545 (2011)
- Toft S., Gallazzi A., Zirm A., Wold M., Zibetti S., Grillo C., & Man A.: *Deep Absorption Line Studies of Quiescent Galaxies at  $z \sim 2$ : The Dynamical-mass–Size Relation and First Constraints on the Fundamental Plane*. *The Astrophysical Journal* **754**, 3 (2012)
- Tojeiro R., Masters K. L., Richards J., Percival W. J., Bamford S. P., Maraston C., Nichol R. C., Skibba R., & Thomas D.: *The different star formation histories of blue and red spiral and elliptical galaxies*. *Monthly Notices of the Royal Astronomical Society* **432**, 359 (2013)
- Toomre A. & Toomre J.: *Galactic Bridges and Tails*. *The Astrophysical Journal* **178**, 623 (1972)
- Toomre A.: *Gravitational interactions between galaxies*. In: Shakeshaft J. R. (ed.): *The Formation and Dynamics of Galaxies*. IAU Symposium **58**, 347 (1974)
- Toomre A.: *Mergers and Some Consequences*. In: Tinsley B. M., Larson R. B. G., & Campbell D. (eds.): *Evolution of Galaxies and Stellar Populations*. 401 (1977)
- Tornatore L., Borgani S., Matteucci F., Recchi S., & Tozzi P.: *Simulating the metal enrichment of the intracluster medium*. *Monthly Notices of the Royal Astronomical Society* **349**, L19 (2004)
- Tornatore L., Borgani S., Dolag K., & Matteucci F.: *Chemical enrichment of galaxy clusters from hydrodynamical simulations*. *Monthly Notices of the Royal Astronomical Society* **382**, 1050 (2007)
- Torrey P., Snyder G. F., Vogelsberger M., Hayward C. C., Genel S., Sijacki D., Springel V., Hernquist L., Nelson D., Kriek M., et al.: *Synthetic galaxy images and spectra from the Illustris simulation*. *Monthly Notices of the Royal Astronomical Society* **447**, 2753 (2015)
- Torri E., Meneghetti M., Bartelmann M., Moscardini L., Rasia E., & Tormen G.: *The impact of cluster mergers on arc statistics*. *Monthly Notices of the Royal Astronomical Society* **349**, 476 (2004)
- Tortora C., Romanowsky A. J., & Napolitano N. R.: *An Inventory of the Stellar Initial Mass Function in Early-type Galaxies*. *The Astrophysical Journal* **765**, 8 (2013)

- Tortora C., La Barbera F., Napolitano N. R., Romanowsky A. J., Ferreras I., & de Carvalho R. R.: *Systematic variations of central mass density slopes in early-type galaxies*. Monthly Notices of the Royal Astronomical Society **445**, 115 (2014a)
- Tortora C., Napolitano N. R., Saglia R. P., Romanowsky A. J., Covone G., & Capaccioli M.: *Evolution of central dark matter of early-type galaxies up to  $z \sim 0.8$* . Monthly Notices of the Royal Astronomical Society **445**, 162 (2014b)
- Tremaine S. D.: *Summary – Structure and Dynamics of Elliptical Galaxies*. In: de Zeeuw P. T. (ed.): *Structure and Dynamics of Elliptical Galaxies*. IAU Symposium **127**, 367 (1987)
- Trenti M., Padoan P., & Jimenez R.: *The formation of globular clusters through minihalo-minihalo mergers*. ArXiv e-prints **1502.02670** (2015)
- Treu T. & Koopmans L. V. E.: *The Internal Structure and Formation of Early-Type Galaxies: The Gravitational Lens System MG 2016+112 at  $z = 1.004$* . The Astrophysical Journal **575**, 87 (2002)
- Treu T. & Koopmans L. V. E.: *Massive Dark Matter Halos and Evolution of Early-Type Galaxies to  $z \sim 1$* . The Astrophysical Journal **611**, 739 (2004)
- Treu T., Auger M. W., Koopmans L. V. E., Gavazzi R., Marshall P. J., & Bolton A. S.: *The Initial Mass Function of Early-Type Galaxies*. The Astrophysical Journal **709**, 1195 (2010)
- Treu T., Dutton A. A., Auger M. W., Marshall P. J., Bolton A. S., Brewer B. J., Koo D. C., & Koopmans L. V. E.: *The SWELLS survey – I. A large spectroscopically selected sample of edge-on late-type lens galaxies*. Monthly Notices of the Royal Astronomical Society **417**, 1601 (2011)
- Treu T. & Ellis R. S.: *Gravitational Lensing – Einstein’s Unfinished Symphony*. ArXiv e-prints **1412.6916** (2014)
- Trujillo I., Förster Schreiber N. M., Rudnick G., Barden M., Franx M., Rix H.-W., Caldwell J. A. R., McIntosh D. H., Toft S., Häussler B., et al.: *The Size Evolution of Galaxies since  $z \sim 3$ : Combining SDSS, GEMS, and FIRES*. The Astrophysical Journal **650**, 18 (2006)
- Tully R. B. & Fisher J. R.: *A new method of determining distances to galaxies*. Astronomy & Astrophysics **54**, 661 (1977)
- Usher C., Forbes D. A., Brodie J. P., Foster C., Spitler L. R., Arnold J. A., Romanowsky A. J., Strader J., & Pota V.: *The SLUGGS survey: calcium triplet-based spectroscopic metallicities for over 900 globular clusters*. Monthly Notices of the Royal Astronomical Society **426**, 1475 (2012)
- Utomo D., Blitz L., Davis T., Rosolowsky E., Bureau M., Cappellari M., & Sarzi M.: *Giant Molecular Clouds in the Early-Type Galaxy NGC4526*. ArXiv e-prints **1502.01017** (2015)
- van de Sande J., Kriek M., Franx M., van Dokkum P. G., Bezanson R., Whitaker K. E., Brammer G., Labbé I., Groot P. J., & Kaper L.: *The Stellar Velocity Dispersion of a Compact Massive Galaxy at  $z = 1.80$  Using X-Shooter: Confirmation of the Evolution in the Mass-Size and Mass-Dispersion Relations*. The Astrophysical Journal Letters **736**, L9 (2011)

- van de Sande J., Kriek M., Franx M., van Dokkum P. G., Bezanson R., Bouwens R. J., Quadri R. F., Rix H.-W., & Skelton R. E.: *Stellar Kinematics of  $z \sim 2$  Galaxies and the Inside-out Growth of Quiescent Galaxies*. The Astrophysical Journal **771**, 85 (2013)
- van de Sande J., Kriek M., Franx M., Bezanson R., & van Dokkum P. G.: *The Fundamental Plane of Massive Quiescent Galaxies Out to  $z \sim 2$* . The Astrophysical Journal Letters **793**, L31 (2014)
- van den Bosch F. C., Abel T., Croft R. A. C., Hernquist L., & White S. D. M.: *The Angular Momentum of Gas in Protogalaxies. I. Implications for the Formation of Disk Galaxies*. The Astrophysical Journal **576**, 21 (2002)
- van der Wel A., Holden B. P., Zirm A. W., Franx M., Rettura A., Illingworth G. D., & Ford H. C.: *Recent Structural Evolution of Early-Type Galaxies: Size Growth from  $z = 1$  to  $z = 0$* . The Astrophysical Journal **688**, 48 (2008)
- van der Wel A., Rix H.-W., Wuyts S., McGrath E. J., Koekemoer A. M., Bell E. F., Holden B. P., Robaina A. R., & McIntosh D. H.: *The Majority of Compact Massive Galaxies at  $z \sim 2$  are Disk Dominated*. The Astrophysical Journal **730**, 38 (2011)
- van der Wel A., Franx M., van Dokkum P. G., Skelton R. E., Momcheva I. G., Whitaker K. E., Brammer G. B., Bell E. F., Rix H.-W., Wuyts S., et al.: *3D-HST+CANDELS: The Evolution of the Galaxy Size-Mass Distribution since  $z = 3$* . The Astrophysical Journal **788**, 28 (2014)
- van Dokkum P. G., Kriek M., & Franx M.: *A high stellar velocity dispersion for a compact massive galaxy at redshift  $z = 2.186$* . Nature **460**, 717 (2009)
- van Dokkum P. G. & Conroy C.: *Confirmation of Enhanced Dwarf-sensitive Absorption Features in the Spectra of Massive Elliptical Galaxies: Further Evidence for a Non-universal Initial Mass Function*. The Astrophysical Journal Letters **735**, L13 (2011)
- van Dokkum P. G. & Conroy C.: *The Stellar Initial Mass Function in Early-type Galaxies from Absorption Line Spectroscopy. I. Data and Empirical Trends*. The Astrophysical Journal **760**, 70 (2012)
- Vogelsberger M., Genel S., Springel V., Torrey P., Sijacki D., Xu D., Snyder G., Nelson D., & Hernquist L.: *Introducing the Illustris Project: simulating the coevolution of dark and visible matter in the Universe*. Monthly Notices of the Royal Astronomical Society **444**, 1518 (2014)
- Vollmer B., Wong O. I., Braine J., Chung A., & Kenney J. D. P.: *The influence of the cluster environment on the star formation efficiency of 12 Virgo spiral galaxies*. Astronomy & Astrophysics **543**, A33 (2012)
- von Albrecht M.: *Ovid, Metamorphosen, Lateinisch–Deutsch*. Philipp Reclam jun., Stuttgart (1994)
- Walsh J. R., Rejkuba M., & Walton N. A.: *An imaging and spectroscopic study of the planetary nebulae in NGC 5128 (Centaurus A)*. Planetary nebulae catalogues. Astronomy & Astrophysics **574**, A109 (2015)
- Wegner G. A., Corsini E. M., Thomas J., Saglia R. P., Bender R., & Pu S. B.: *Further Evidence for Large Central Mass-to-light Ratios in Early-type Galaxies: The Case of Ellipticals and Lenticulars in the A262 Cluster*. Astronomical Journal **144**, 78 (2012)

- Wei L. H., Kannappan S. J., Vogel S. N., & Baker A. J.: *Gas Mass Fractions and Star Formation in Blue-Sequence E/S0 Galaxies*. The Astrophysical Journal **708**, 841 (2010)
- White S. D. M.: *The dynamics of rich clusters of galaxies*. Monthly Notices of the Royal Astronomical Society **177**, 717 (1976)
- White S. D. M.: *Simulations of merging galaxies*. Monthly Notices of the Royal Astronomical Society **184**, 185 (1978)
- White S. D. M.: *Can mergers make slowly rotating elliptical galaxies*. The Astrophysical Journal Letters **229**, L9 (1979a)
- White S. D. M.: *Further simulations of merging galaxies*. Monthly Notices of the Royal Astronomical Society **189**, 831 (1979b)
- Wiersma R. P. C., Schaye J., & Smith B. D.: *The effect of photoionization on the cooling rates of enriched, astrophysical plasmas*. Monthly Notices of the Royal Astronomical Society **393**, 99 (2009)
- Williams R. J., Quadri R. F., Franx M., van Dokkum P., Toft S., Kriek M., & Labbé I.: *The Evolving Relations Between Size, Mass, Surface Density, and Star Formation in  $3 \times 10^4$  Galaxies Since  $z = 2$* . The Astrophysical Journal **713**, 738 (2010)
- Wilman D. J., Balogh M. L., Bower R. G., Mulchaey J. S., Oemler A., Jr, & Carlberg R. G.: *The CNOC2 sample of intermediate redshift galaxy groups – the powerhouse of galaxy evolution*. ArXiv Astrophysics e-prints (2005)
- Wolf M.: *Notiz: Ein merkwürdiger Haufen von Nebelflecken*. Astronomische Nachrichten **155**, 127 (1901)
- Woodley K. A.: *The Centaurus Group and the Outer Halo of NGC 5128: Are They Dynamically Connected?* Astronomical Journal **132**, 2424 (2006)
- Wright E. L., Meyer S. S., Bennett C. L., Bogges N. W., Cheng E. S., Hauser M. G., Kogut A., Lineweaver C., Mather J. C., Smoot G. F., et al.: *Interpretation of the cosmic microwave background radiation anisotropy detected by the COBE Differential Microwave Radiometer*. The Astrophysical Journal Letters **396**, L13 (1992)
- Wright T.: *An Original Theory or new Hypothesis of the Universe, founded upon the Laws of Nature*. Reprinted by Cambridge University Press (1750, reprint from 2014)
- Yee H. K. C., Morris S. L., Lin H., Carlberg R. G., Hall P. B., Sawicki M., Patton D. R., Wirth G. D., Ellingson E., & Shepherd C. W.: *The CNOC2 Field Galaxy Redshift Survey. I. The Survey and the Catalog for the Patch CNOC 0223+00*. The Astrophysical Journal Supplement **129**, 475 (2000)
- York D. G., Adelman J., Anderson J. E., Jr, Anderson S. F., Annis J., Bahcall N. A., Bakken J. A., Barkhouser R., Bastian S., Berman E., et al.: *The Sloan Digital Sky Survey: Technical Summary*. Astronomical Journal **120**, 1579 (2000)

- Young L. M., Bureau M., Davis T. A., Combes F., McDermid R. M., Alatalo K., Blitz L., Bois M., Bournaud F., Cappellari M., et al.: *The ATLAS<sup>3D</sup> project – IV. The molecular gas content of early-type galaxies*. Monthly Notices of the Royal Astronomical Society **414**, 940 (2011)
- Young L. M., Scott N., Serra P., Alatalo K., Bayet E., Blitz L., Bois M., Bournaud F., Bureau M., Crocker A. F., et al.: *The Atlas<sup>3D</sup> project – XXVII. Cold Gas and the Colours and Ages of Early-type Galaxies*. ArXiv e-prints **1312.6318** (2013)
- Zeldovich Y. B. & Sunyaev R. A.: *The Interaction of Matter and Radiation in a Hot-Model Universe*. Astrophysics and Space Science **4**, 301 (1969)
- Zenteno A., Song J., Desai S., Armstrong R., Mohr J. J., Ngeow C.-C., Barkhouse W. A., Allam S. S., Andersson K., Bazin G., et al.: *A Multiband Study of the Galaxy Populations of the First Four Sunyaev-Zel'dovich Effect Selected Galaxy Clusters*. The Astrophysical Journal **734**, 3 (2011)
- Zhao D. H., Mo H. J., Jing Y. P., & Börner G.: *The growth and structure of dark matter haloes*. Monthly Notices of the Royal Astronomical Society **339**, 12 (2003)
- Zinn R.: *The globular cluster system of the galaxy. IV. The halo and disk subsystems*. The Astrophysical Journal **293**, 424 (1985)
- Zitrin A., Meneghetti M., Umetsu K., Broadhurst T., Bartelmann M., Bouwens R., Bradley L., Carrasco M., Coe D., Ford H., et al.: *CLASH: The Enhanced Lensing Efficiency of the Highly Elongated Merging Cluster MACS J0416.1-2403*. The Astrophysical Journal Letters **762**, L30 (2013)
- Zwicky F.: *On the Masses of Nebulae and of Clusters of Nebulae*. The Astrophysical Journal **86**, 217 (1937)

# List of Figures

1.1	Overview of the resolutions of the CMB maps provided by the COBE, WMAP, and Planck missions. . . . .	3
1.2	Temperature power spectrum from the Planck 2015 data release . . . . .	6
1.3	The star-formation rate in galaxies reaches its maximum at about $z = 2$ as detected from observations . . . . .	8
1.4	The cosmic web as seen from the SDSS survey . . . . .	9
1.5	Illustration of the Hubble Fork morphology classification of galaxies . . . . .	11
1.6	Peculiar galaxies: Adding complex systems to the classification . . . . .	13
1.7	Morphology density relation from SDSS (Goto et al., 2003b) and the Butcher-Oemler-Effect (Metevier et al., 2000) . . . . .	16
1.8	Classification as suggested by Cappellari et al. (2011b) from the results of the Atlas <sup>3D</sup> survey . . . . .	18
1.9	Kinematic “morphologies” as presented in Krajnović et al. (2011) . . . . .	19
1.10	Different density profiles in comparison . . . . .	31
1.11	Different Einasto profiles in comparison . . . . .	34
1.12	Mass-size relation at different redshifts and Fundamental Plane at $z = 0$ from van de Sande et al. (2013) and Bezanson et al. (2015) respectively . . . . .	37
2.1	“Merger” simulation from Holmberg (1941) and Toomre (1974) . . . . .	42
2.2	Visualization of a binary merger simulation . . . . .	47
2.3	Schematic view of the orbital encounter geometry . . . . .	48
2.4	2D illustration of the construction of the initial conditions for zoom-simulations . . . . .	51
2.5	Visualization of a cosmological Zoom-In simulation . . . . .	53
2.6	Overview of all boxes in the Magneticum Pathfinder simulation set . . . . .	56
2.7	Temperature map of Box2/hr of the Magneticum Pathfinder set. . . . .	58
2.8	Four example disk galaxies from Magneticum Box4 uhr . . . . .	59
2.9	Circularity for an elliptical and a disk galaxy from Magneticum Box4 uhr . . . . .	60
2.10	Stellar and total mass properties for galaxies in Magneticum Box4 uhr . . . . .	61
3.1	Density and velocity dispersion profiles for three example halos. . . . .	73
3.2	Combined total density profiles for all simulations . . . . .	74
3.3	Velocity dispersion slopes against density slopes . . . . .	75
3.4	Stellar velocity dispersion slopes versus density slopes . . . . .	75
3.5	Dark matter velocity dispersion slopes versus dark matter density slopes . . . . .	76
3.6	Stellar velocity dispersion slopes versus stellar density slopes . . . . .	76

3.7	Density and velocity dispersion profiles for a 20% and a 80% gas fraction merger . . .	79
3.8	Density slopes versus half-mass radius and stellar mass . . . . .	80
3.9	Density slopes versus dark matter fractions . . . . .	81
3.10	In-situ fraction versus density slopes . . . . .	82
3.11	Evolution of velocity dispersion slopes and density slopes with time for the binary mergers . . . . .	83
3.12	Evolution of the velocity dispersion and density slopes with redshift for the Zoom Simulations . . . . .	83
4.1	Mass-size relation for early type galaxies from simulations and observations at $z = 0$	92
4.2	Mass-size relation for early type galaxies from simulations and observations at $z = 0.5$ , $z = 1$ and $z = 2$ . . . . .	92
4.3	Central dark matter fractions versus mass at different redshifts . . . . .	95
4.4	In-situ fractions versus central dark matter fractions . . . . .	96
4.5	Evolution of the slope of the total radial density profile . . . . .	98
4.6	Velocity dispersion slopes against density slopes and velocity dispersion slope evolution for Magneticum spheroidals . . . . .	99
4.7	Correlations between central dark matter fractions, total density slopes and stellar mass density . . . . .	101
4.8	Total density slopes versus central dark matter fractions and stellar mass density at different redshifts . . . . .	103
4.9	Density slopes from mock observations of our simulated spheroidals . . . . .	105
4.10	Total density slope evolution for mock observations from our simulations . . . . .	106
5.1	Stellar distribution for two example galaxies from Magneticum Box4 uhr, showing substructure identification. . . . .	113
5.2	Stacked density profiles of all halos with $M_{\text{tot}} \approx 1 \times 10^{12} M_{\odot}$ from Box3 hr . . . . .	114
5.3	Density profiles of all halos with $M_{\text{tot}} \approx 1 \times 10^{12} M_{\odot}$ from Box4 uhr . . . . .	116
5.4	Histograms of the slopes of the individual stellar density profiles with $M_{\text{tot}} \approx 1 \times 10^{12} M_{\odot}$ from Box4 uhr at different redshifts. . . . .	117
5.5	Stacked density profiles of all halos with $M_{\text{tot}} \approx 1 \times 10^{12} M_{\odot}$ from Box4 uhr at different redshifts . . . . .	118
5.6	Galaxy properties versus slope of the outer stellar halo. . . . .	119
5.7	Stacked density profiles and outer stellar halo slopes $\gamma_{\text{out}}$ at 40 kpc to 100 kpc for different mass ranges . . . . .	121
5.8	Fits of different density profiles from the literature to the stacked halo profiles . . . . .	123
5.9	Histograms of the free parameters of the Einasto profiles for halos with $M_{\text{tot}} \approx 1 \times 10^{12} M_{\odot}$ from Box4 uhr . . . . .	124
5.10	Mean Slope of the Einasto profile fits versus total mass . . . . .	125
5.11	Slope versus scale radius of the Einasto profile fits to DM and stellar density profiles	126
5.12	Free parameters of the Einasto profile fits for dark matter versus stars in comparison .	127
5.13	Parameters of the Einasto profile fits versus different galaxy properties for galaxies with $M_{\text{tot}} \approx 1 \times 10^{12} M_{\odot}$ . . . . .	129
6.1	Random selection of 100 Tracer stars: Two examples for velocity profiles . . . . .	135
6.2	Scale height and LOSV-RMS-test for the random tracer populations . . . . .	136

6.3	Tracer populations for an example spheroidal (11 OBH2 13)	138
6.4	Histograms for the power-law-slopes and Sérsic indices for the 100 random draws of $N$ tracers	139
6.5	$1\sigma$ -deviations for different numbers of tracers for scale height, power-law index and Sérsic index	140
6.6	Power-Law and Sérsic density fits to the observed RGC and BGC density profiles of NGC 4365 and NGC 5846	143
6.7	Power-Law and Sérsic density fits to NGC 821, NGC 1407 and NGC 3377	144
6.8	Density slopes $\gamma$ versus the dark matter fraction within $5 R_{\text{eff}}$	145
6.9	The impact of the maximal radius $R_{\text{max}}$ on the observed density slopes	146
6.10	Visualisation of shells in a binary merger simulation	148
6.11	Shells in observations: NGC 474 and NGC 7252	148
6.12	Shells in density, velocity dispersion and phase-space	150
6.13	Evolution of the $\sigma$ -bump in density and velocity dispersion profiles	151
A.1	The $\sigma$ -bump in simulations and observations, from Schauer, Remus, et al. (2014)	165
A.2	Infall time of cold gas that is present in the gas disk of a simulated spheroidal galaxy	167
A.3	The $\lambda_{\text{R}}$ parameter for spheroids in Magneticum	171
A.4	Specific angular momentum versus stellar mass in observations and Magneticum	173
A.5	Mass-Size relation for the Magneticum Pathfinder Simulation Box4 uhr for disks and spheroidals	175
A.6	Fig. 9 taken from Steinborn et al. (2015): Stellar mass function at different redshifts	177
A.7	Illustration of cosmic rays and magnetic fields in voids, Fig. 2 from Beck et al. (2013)	179
A.8	Galaxy properties test for the new SPH scheme presented by Beck et al. (2015)	181
B.1	The most massive galaxy cluster in Magneticum Box4 uhr at $z = 0.38$	183
B.2	Galaxies in Magneticum at $z = 2.33$	184
B.3	Galaxies in Magneticum at $z = 0.38$	185



# List of Tables

1.1	Cosmological parameters from COBE, WMAP3, WMAP7, and Planck . . . . .	6
2.1	Binary merger simulation sample at a timestep of 3 Gyr . . . . .	49
2.2	CosmoZoom ellipticals sample at $z = 0$ . . . . .	54
2.3	CosmoZoom companion sample at $z = 0$ . . . . .	55
2.4	Magneticum Pathfinder simulations: An overview . . . . .	57
2.5	Magneticum BCGs at $z = 0$ from Box3 hr . . . . .	63
2.6	Magneticum spheroidals Box4 uhr at $z = 0$ . . . . .	64
2.8	Magneticum Box4 uhr Milky Way mass halos at $z = 0$ . . . . .	67
B.1	All galaxies with $M_{\text{tot}} > 1 \times 10^{11} M_{\odot}$ from Magneticum Box4 uhr at $z = 0$ . . . . .	187



# Acknowledgements

I want to thank a few people, without whom it would not have been possible to write this thesis.

First of all I would like to thank my “Doktorvater” Prof. Andreas Burkert for giving me the chance to write my PhD thesis with him and as part of his group. It was a turbulent, eventful, exciting and sometimes exhausting time. I enjoyed our scientific discussions very much, and I want to thank you for letting me travel all over the world to present my work in talks and posters.

Thanks are also due to Prof. Harald Lesch, for offering to be the second corrector of this thesis. Thanks also for all the discussions and interesting conversations throughout all the time I have been at the USM.

I also want to thank Klaus Dolag for inviting me to be a part of the *Magneticum Pathfinder* Team with all its new computational and scientific challenges and results, for his constant support on all scientific matters as well as his moral support whenever I was in need of some cheering up.

In most cases, things come differently than expected, and usually when deadlines are close. Thus, I especially want to thank Taziu Hoffmann for all the emergency stunts we had to perform, scientific discussions until late at night, his joy in learning about galaxies even though it is not his scientific field, and for the tremendous computational support and our public outreach design studio. You are one of the best friends one can wish for. And I also want to thank you for milk and chocolate, the best emergency food in the world.

Scientifically, every PhD thesis is a challenge for a new student, and writing the first paper is always a big step. Thus, I want to thank Peter H. Johansson, Thorsten Naab and Roland Jesseit for helping me with the first steps into the science of Galaxy formation and evolution, and for the continuing work we have been doing together. They also introduced me to the importance of a carefully designed figure to transport scientific language, although the problem of serifed letters in Python still remains to be solved.

Furthermore, I want to thank Alex Beck as well as Alfredo Zenteno, Rebekka Grellmann, Thorsten Ratzka and Steffi Pekruhl for the coffee-breaks, the fun, the discussions, the teaching and the shared good and bad times. I loved to work in the same institute with you, and I am glad that our friendship lasts even though most of you already left the USM. You made the time at USM a great one!

Additionally, I want to thank Anna Schauer, David Schlachtberger, Adelheid Teklu, Stefan Heigl and Lisa Steinborn. You were the first Master Students I had to supervise, and I enjoyed working with you. Thanks for your curiosity, all the annoying questions and your enthusiasm. You really proved to me the value of teaching!

A good scientific work always needs a counter-pole of private life! I am blessed with a few, however wonderful, friends: Christoph Bergemann, Matthias Goerner, Franziska Synatschke, Martin Trebbin and Regina Hoeschele. We have gone a long way together and I hope there will be much more. If I would ever have to build up a think tank: you would be the first ones to ask!

Finally, I want to thank the six most important people in my life, for simply being who you are. Moogie, Papa, Sabina, Eni, Charlie and my Sunshine, even if you sometimes freak me out, I love all of you, and I would not be who I am without you.